mathematics

Modeling and Simulation in Engineering

Edited by

Camelia Petrescu and Valeriu David

Printed Edition of the Special Issue Published in *Mathematics*

www.mdpi.com/journal/mathematics

MDPI

Modeling and Simulation in Engineering

Modeling and Simulation in Engineering

Editors

Camelia Petrescu
Valeriu David

MDPI • Basel • Beijing • Wuhan • Barcelona • Belgrade • Manchester • Tokyo • Cluj • Tianjin

Editors

Camelia Petrescu
Technical University of Iasi
Romania

Valeriu David
"Gheorghe Asachi" Technical University of Iasi
Romania

Editorial Office
MDPI
St. Alban-Anlage 66
4052 Basel, Switzerland

This is a reprint of articles from the Special Issue published online in the open access journal *Mathematics* (ISSN 2227-7390) (available at: https://www.mdpi.com/journal/mathematics/special_issues/Model_Simul_Eng).

For citation purposes, cite each article independently as indicated on the article page online and as indicated below:

LastName, A.A.; LastName, B.B.; LastName, C.C. Article Title. *Journal Name* **Year**, *Volume Number*, Page Range.

ISBN 978-3-0365-5939-1 (Hbk)
ISBN 978-3-0365-5940-7 (PDF)

© 2022 by the authors. Articles in this book are Open Access and distributed under the Creative Commons Attribution (CC BY) license, which allows users to download, copy and build upon published articles, as long as the author and publisher are properly credited, which ensures maximum dissemination and a wider impact of our publications.
The book as a whole is distributed by MDPI under the terms and conditions of the Creative Commons license CC BY-NC-ND.

Contents

About the Editors

Camelia Petrescu

Camelia Petrescu received an M.Sc. degree in Electrical Engineering (1982) from the Technical University of Iasi and a Ph.D. degree in Electrical Engineering from Politehnica University Bucharest, Romania (1994). She is a full professor at the Technical University of Iasi. Her areas of interest include analytical and numerical electromagnetic field analysis, optimization methods and electric power quality.

Valeriu David

Valeriu David received M.Sc. and Ph.D. degrees in electronic/electric engineering from the "Gheorghe Asachi" Technical University of Iasi, Romania, in 1983 and 1998, respectively. He is a full professor at the Technical University of Iasi and a Senior Member of IEEE. His teaching and research activities include electric and electronic measurements, estimation of biomedical and environmental parameters, survey of the electromagnetic environment, and electromagnetic absorbers/shields.

mathematics

MDPI

Editorial

Preface to the Special Issue on "Modelling and Simulation in Engineering"

Camelia Petrescu [1,*] and Valeriu David [2]

[1] Department of Electrotechnics, Faculty of Electrical Engineering, Gh. Asachi Technical University of Iași, 700050 Iași, Romania
[2] Department of Measurements and Materials, Faculty of Electrical Engineering, Gh. Asachi Technical University of Iași, 700050 Iași, Romania; valeriu.david@academic.tuiasi.ro
* Correspondence: cpetrescu@ac.tuiasi.ro

1. Introduction

The continuing achievements in Information Technology and Computer science in recent decades provide new tools for engineers in the design of devices and systems, with significant advances both in numerical and in analytical methods of analysis. Thus, modelling and simulation of processes have become mandatory stages prior to the experimental setup and are now part of the engineering culture.

The purpose of this Special Issue is to offer a platform for ongoing valuable research involving modelling and simulation methods in mathematical physics, to present new simulation software applications in engineering, and to also present recent advances in decision support systems or in the design of experiments.

The response of the scientific community was significant, with a total of 28 papers being submitted for consideration, of which 14 were accepted for publication after attentive peer-review by respected reviewers in the fields of the papers.

2. Description of Published Papers

In the following, a brief overview of the published papers is presented.

The paper by R.A. Hamid et al. [1] analyses a ferrofluid transport problem in a magnetic field, solved using the MATLAB bvp4c routine. The influence of the magnetic field and of the Stefan blowing parameters was investigated, leading to conclusions regarding the availability and stability of solutions.

The paper authored by Y. Li et al. [2] proposes a new estimation of the Hurst exponent used in long-term memory of time series and, in the context of this paper, in volatility modelling. In order to validate the new Hurst estimator tests are conducted for data taken from Chinese financial markets, with emphasis on truncated and non-truncated spot volatility.

The paper by F. Feng et al. [3] proposes an improved version of a RSE algorithm, previously developed by the same authors, used to recognize the complexity of non-fractals common in signals (roughness scaling extraction algorithm with first-order flattening (RSE-f1)). The speed of the newly proposed algorithm increases significantly (by 13 times), making it also faster than other typical algorithms. The new algorithm is then used to analyse the vibration signal from a mill in order to distinguish between the machine states (idle, stable, and chatter).

The paper by V. Saenko et al. [4] performs a study of the anomalous diffusion equation with a fractional derivative with respect to both time and coordinates, proposing a solution based on the Monte Carlo method. The numerical method for solving the anomalous diffusion equation, in which both the time derivative and the coordinate derivative can be of non-integer order, using a model of random realizations of particle trajectories, is proposed and applied in the analysis of the combustion process.

Citation: Petrescu, C.; David, V. Preface to the Special Issue on "Modelling and Simulation in Engineering". *Mathematics* **2022**, *10*, 2387. https://doi.org/10.3390/math10142387

Received: 28 June 2022
Accepted: 4 July 2022
Published: 7 July 2022

Publisher's Note: MDPI stays neutral with regard to jurisdictional claims in published maps and institutional affiliations.

Copyright: © 2022 by the authors. Licensee MDPI, Basel, Switzerland. This article is an open access article distributed under the terms and conditions of the Creative Commons Attribution (CC BY) license (https://creativecommons.org/licenses/by/4.0/).

The paper by A. Alahmer et al. [5] investigates the effect of using various biodiesel mixtures on the performance of a CI engine under full load and at different engine speeds. Specific parameters such as brake torque, brake power, fuel consumption and brake thermal efficiency are monitored, and an optimisation procedure based on fuzzy logic and particle swarm optimisation is carried out in order to determine the optimal engine speed and best fuel type. The results obtained show that the overall performance is fairly increased as compared to the experimental results.

The paper by K. Zhang et al. [6] studies calcium leaching in hydraulics applications, formulated as an inverse problem, which is studied using genetic algorithms and the finite element method. The objective function is constructed using the hydraulic head and leakage quantity time-series measurements. The proposed inverse analysis method is applied to predict the grout curtain hydraulic conductivity of a concrete dam in the leaching process, the simulation results being consistent with the monitored data.

The paper by N.F.H.M. Sohut et al. [7] analyses the unsteady 3D rotating hybrid nanofluid flow on a stretching sheet, by considering and representing the effects of some parameters. Thus, the specific system of partial differential equations was transformed to a system of ordinary differential equations, which were solved numerically using the MATLAB software.

The paper by G. Gordillo et al. [8] addresses the control of contaminant spill in water and, more generally, the problem of water quality control by using the gradient-descent method supplied with a first-order iterative process. The authors consider both the validation of the numerical technique and the possibilities and limitations of the applied method.

The paper by N.A. Yacob et al. [9] studies rotating flow in nanofluids over a permeable stretching/shrinking surface. The authors present the numerical results obtained with MATLAB software, starting from a mathematical model with carbon nanotubes (single and multi-walled), and analyse the heat and mass transfer characteristics, and also the stability of the considered solutions.

The paper by M.I. Dieste-Velasco [10] proposes an artificial neural network for fault diagnosis in analogue electronic circuits. This method is based on a small number of measurements and has been successfully tested to predict the hard faults in two electronic amplifiers.

The paper by V. Saenko et al. [11] analyses the possibility to obtain numerical solutions for fractional differential equations of anomalous diffusion. The kinetic equations that describe the process of walks are considered and their numerical solutions based on a local estimate of the Monte Carlo method are established, highlighting the advantages and limitations.

The paper authored by C. García-Hernández et al. [12] performs a study of the trochoidal milling path with variable feed. A process optimization is considered and a trochoidal milling test with the presentation and analysis of the obtained results is presented.

The paper by Y. Li et al. [13] proposes a surrogate for the original Kriging modelling method, which is tested in an air traffic control radar design simulation system. The proposed high-dimensional Kriging modelling method is characterised by a faster modelling efficiency and large possibilities for new applications.

D. Legatiuk proposes in [14] a new development of the category theory-based modelling methodology introduced in a previous paper that he co-authored. This methodology is based on representation of mathematical models by the help of categorical constructions. Two practical examples are used as illustrations for this method, namely the beam models and the aerodynamic models used in bridge engineering. The author points out that the category theory-based modelling methodology presented in the paper can be used in the model selection process after constructing a set of mathematical models and formulating criteria imposed on a model for a given practical problem.

3. Conclusions

As guest editors of the Special Issue Modelling and Simulation in Engineering, we would like to express our gratitude to all the authors who sent their articles for publication in this issue. We also express our gratitude and appreciation to the reviewers for their valuable observations, which helped improve the submitted papers.

We hope that the papers selected for this Issue will attract a significant audience in the scientific community and will further stimulate research involving modelling and simulation in mathematical physics and engineering.

Author Contributions: Conceptualization, C.P. and V.D.; writing—original draft preparation, C.P.; writing—review and editing, C.P. All authors have read and agreed to the published version of the manuscript.

Funding: This research received no external funding.

Conflicts of Interest: The authors declare no conflict of interest.

References

1. Hamid, R.A.; Nazar, R.; Naganthran, K.; Pop, I. Effects of Magnetic Fields, Coupled Stefan Blowing and Thermodiffusion on Ferrofluid Transport Phenomena. *Mathematics* **2022**, *10*, 1646. [CrossRef]
2. Li, Y.; Teng, Y. Estimation of the Hurst Parameter in Spot Volatility. *Mathematics* **2022**, *10*, 1619. [CrossRef]
3. Feng, F.; Yuan, M.; Xia, Y.; Xu, H.; Feng, P.; Li, X. Roughness Scaling Extraction Accelerated by Dichotomy-Binary Strategy and Its Application to Milling Vibration Signal. *Mathematics* **2022**, *10*, 1105. [CrossRef]
4. Saenko, V.V.; Kovalnogov, V.N.; Fedorov, R.V.; Generalov, D.A.; Tsvetova, E.V. Numerical Method for Solving of the Anomalous Diffusion Equation Based on a Local Estimate of the Monte Carlo Method. *Mathematics* **2022**, *10*, 511. [CrossRef]
5. Alahmer, A.; Rezk, H.; Aladayleh, W.; Mostafa, A.O.; Abu-Zaid, M.; Alahmer, H.; Mohamed, R.; Amel, G.; Alhussan, A.; Ghoniem, R.M. Modeling and Optimization of a Compression Ignition Engine Fueled with Biodiesel Blends for Performance Improvement. *Mathematics* **2022**, *10*, 420. [CrossRef]
6. Zhang, K.; Shen, Z.; Xu, L.; Shu, Y.; Yang, C. Inverse Modeling of Grout Curtain Hydraulic Conductivity Evolution Considering the Calcium Leaching Effect. *Mathematics* **2022**, *10*, 381. [CrossRef]
7. Sohut, N.F.H.M.; Soid, S.K.; Abu Bakar, S.; Ishak, A. Unsteady Three-Dimensional Flow in a Rotating Hybrid Nanofluid over a Stretching Sheet. *Mathematics* **2022**, *10*, 348. [CrossRef]
8. Gordillo, G.; Morales-Hernández, M.; García-Navarro, P. Solute Transport Control at Channel Junctions Using Adjoint Sensitivity. *Mathematics* **2022**, *10*, 93. [CrossRef]
9. Yacob, N.A.; Dzulkifli, N.F.; Salleh, S.N.A.; Ishak, A.; Pop, I. Rotating Flow in a Nanofluid with CNT Nanoparticles over a Stretching/Shrinking Surface. *Mathematics* **2022**, *10*, 7. [CrossRef]
10. Dieste-Velasco, M.I. Application of a Pattern-Recognition Neural Network for Detecting Analog Electronic Circuit Faults. *Mathematics* **2021**, *9*, 3247. [CrossRef]
11. Saenko, V.V.; Kovalnogov, V.N.; Fedorov, R.V.; Chamchiyan, Y.E. Numerical Solution to Anomalous Diffusion Equations for Levy Walks. *Mathematics* **2021**, *9*, 3219. [CrossRef]
12. García-Hernández, C.; Garde-Barace, J.J.; Valdivia-Sánchez, J.J.; Ubieto-Artur, P.; Bueno-Pérez, J.A.; Cano-Álvarez, B.; ÁngelAlcázar-Sánchez, M.; Valdivia-Calvo, F.; Ponz-Cuenca, R.; Huertas-Talón, J.-L.; et al. Trochoidal Milling Path with Variable Feed. Application to the Machining of a Ti-6Al-4V Part. *Mathematics* **2021**, *9*, 2701. [CrossRef]
13. Li, Y.; Shi, J.; Yin, Z.; Shen, J.; Wu, Y.; Wang, S. An Improved High-Dimensional Kriging Surrogate Modeling Method through Principal Component Dimension Reduction. *Mathematics* **2021**, *9*, 1985. [CrossRef]
14. Legatiuk, D. Mathematical Modelling by Help of Category Theory: Models and Relations between Them. *Mathematics* **2021**, *9*, 1946. [CrossRef]

mathematics

MDPI

Article

Mathematical Modelling by Help of Category Theory: Models and Relations between Them

Dmitrii Legatiuk

Chair of Applied Mathematics, Bauhaus-Universität Weimar, 99423 Weimar, Germany; dmitrii.legatiuk@uni-weimar.de

Abstract: The growing complexity of modern practical problems puts high demand on mathematical modelling. Given that various models can be used for modelling one physical phenomenon, the role of model comparison and model choice is becoming particularly important. Methods for model comparison and model choice typically used in practical applications nowadays are computation-based, and thus time consuming and computationally costly. Therefore, it is necessary to develop other approaches to working abstractly, i.e., without computations, with mathematical models. An abstract description of mathematical models can be achieved by the help of abstract mathematics, implying formalisation of models and relations between them. In this paper, a category theory-based approach to mathematical modelling is proposed. In this way, mathematical models are formalised in the language of categories, relations between the models are formally defined and several practically relevant properties are introduced on the level of categories. Finally, an illustrative example is presented, underlying how the category-theory based approach can be used in practice. Further, all constructions presented in this paper are also discussed from a modelling point of view by making explicit the link to concrete modelling scenarios.

Keywords: category theory; mathematical modelling; abstraction; formal approaches; functors

MSC: 00A71; 06A75; 18B99; 18C10

Citation: Legatiuk, D. Mathematical Modelling by Help of Category Theory: Models and Relations between Them. *Mathematics* **2021**, *9*, 1946. https://doi.org/10.3390/math9161946

Academic Editors: Camelia Petrescu and Valeriu David

Received: 24 July 2021
Accepted: 13 August 2021
Published: 15 August 2021

Publisher's Note: MDPI stays neutral with regard to jurisdictional claims in published maps and institutional affiliations.

Copyright: © 2021 by the author. Licensee MDPI, Basel, Switzerland. This article is an open access article distributed under the terms and conditions of the Creative Commons Attribution (CC BY) license (https://creativecommons.org/licenses/by/4.0/).

1. Introduction

The rapid development of modern technologies naturally leads to higher demands for the mathematical modelling process because practical problems nowadays require advanced coupled models. Moreover, typically several models can be used for modelling a given physical phenomenon, and thus a model selection process must be made. Evidently, the model selection influences the quality of a final coupled model. In this regard, one of the most important tasks of a modeller is understanding the role of individual models in a complete coupled model, as well as studying how different models are related along with the practical meaning of this relation.

In engineering applications, various factors leading to reduction of the quality of the final coupled model are typically referred to as uncertainties. According to [1], three types of uncertainties arising during the modelling process can be distinguished: (i) Model inputs, (ii) numerical approximation, and (iii) model form. While the first two types can be identified and treated by the help of computational and statistical methods, see for example [2,3] and references therein, the third type requires an extra treatment. The model form uncertainty implies that a conceptual modelling error has been made, i.e., basic physical assumptions of models have been violated. Considering that the impact of such conceptual modelling errors on the whole modelling process is much more profound, it is necessary to develop tools towards addressing conceptual modelling errors.

Consideration of mathematical models based only on their physical assumptions, i.e., without considering a specific engineering example or performing computations with a model, requires tools of abstract mathematics. Several approaches to using abstract

mathematics in applied mathematical modelling, such as graph theory [3], abstract Hilbert spaces [4,5], abstract algebraic approach [6,7], predicate logic [8,9], type theory [10,11], and category theory [12,13], have been proposed in recent years. In this paper, we aim at revisiting and further developing the category theory-based modelling methodology introduced in [13]. The motivation for using category theory for abstract description of mathematical models is based on several aspects: (i) The abstract nature of category theory allows description of very different objects and structures on common basis; (ii) a practical interpretation of abstract constructions provided by category theory-based modelling methodology is straightforward, and thus the methodology can really be used in engineering practice; (iii) category theory naturally provides scaling possibilities implying that description of more sophisticated objects and structures can be done by using the same principles as descriptions of their individual parts; (iv) finally, various applications of category theory scattering from modelling of dynamical systems [14] to ontological representation of knowledge [15] presented in recent years indicate that advantages of category theory are seen and accepted now not only by mathematicians, but also by people interested in applications.

As we have already mentioned, the category theory-based modelling methodology discussed in this paper has been originally proposed in [13]. After publishing this work, several new ideas on categorical modelling methodology providing a deeper understanding of mathematical models and modelling process have appeared in recent years. Therefore, it is necessary to revise ideas presented in [13] with new results and more refined categorical constructions. Moreover, it is worth to mention, that the use of category theory-based modelling methodology for analysis of models appearing in real-world engineering problems from the field of aeroelastic analysis of bridges has been presented in [16]. This work indicated practical advantages of using category theory for modelling purposes. To this end, the category theory-based modelling methodology presented in this paper aims at a consistent description of mathematical models and relations between them in the language of category theory. For the sake of clarity, we focus in this paper only on individual mathematical models, while coupled models will be treated in future research using results from the current paper as a basis.

Abstract categorical descriptions of mathematical models requires at first defining universal properties of models, which are properties shared by models in general, i.e., independent on a particular problem of an engineering field. If a universal model property is defined, then all categorical constructions used in one specific modelling application can be directly transferred to another field. Thus, we will start our construction with defining such a universal model property which is common for all models. Moreover, the main goal is to keep track of real physical and engineering interpretations of the constructions introduced in the category theory-based modelling methodology. The paper is organised as follows: Section 2 presents a general structure of categories of mathematical models together with a detailed discussion on practical interpretation of the introduced definition; after that, relations between mathematical models are discussed in Section 3; Section 4 formalises the problem of having different formulations of the same mathematical model by introducing the notion of convertible mathematical models; Section 5 provides an illustrative example how categorical constructions introduced in the previous sections can be used for comparison and analysis of models. Finally, in Section 6 we discuss a universal arrow in the framework of category theory-based modelling methodology, as well as establish a connection to an abstract algebraic approach, after we draw conclusions and discuss shortly the scope of future work. For making the paper self-contained, some basic definitions from category theory are presented in the Appendix A.

2. Categories of Mathematical Models

Before starting with categorical constructions, it is important to underline, that models used in practice can be generally classified in two types:

- physics-based models—models which are based on mathematical formalisations of physical laws and assumptions;
- data-driven models—models which are based on representations of data, e.g., results of experiments or measurements obtained from a monitoring system.

This paper deals with physics-based models, which are referred to simply as mathematical models, because this type of models is typically implied by the term mathematical modelling. Moreover, because mathematical models are based on physical assumptions formalised by the help of mathematical expressions, they provide a richer basis for abstract considerations, compared to data-driven models, which are very often black-box models not relying on any physical assumptions.

We start our construction with the introduction of concrete categories $\mathbf{Model}_i$, $i = 1, 2, \ldots$, which are associated with mathematical models used to describe a certain physical phenomenon, such as, for example, models of elasticity theory or heat conduction. The term "associated" has been used, because, strictly speaking, the objects of categories $\mathbf{Model}_i, i = 1, 2, \ldots$ are not mathematical models themself, but rather sets of basic physical assumptions on which the corresponding mathematical models are created. However, to keep notations short and transparent, we will refer to these categories simply as to categories of mathematical models. The following definition introduces basic structure of these categories:

Definition 1 (Category of mathematical models)**.** *Let* $\mathbf{Model}_1$ *be a category of mathematical models describing a given physical phenomenon. Then for all objects of* $\mathbf{Model}_1$ *the following assumptions hold:*

(i) *each object is a finite non-empty set – set of assumptions of a mathematical model, denoted by* $\mathbf{Set}_{\mathrm{A}}$*, where* A *is the corresponding mathematical model;*

(ii) *morphisms (arrows) are relations between these sets;*

(iii) *for each set of assumptions and its corresponding model exists a mapping*

$$\mathbf{Set}_{\mathrm{A}} \overset{S}{\mapsto} \mathrm{A};$$

(iv) *all objects are related to mathematical models acting in the same physical dimension.*

Let us now provide some motivation from the modelling perspective and comments for the assumptions used in this definition:

- Assumption (i). This assumption comes naturally from the modelling process: A mathematical model is created to describe a certain physical phenomenon or process, and evidently, it is possible only if physical background of the phenomenon or process is clearly stated, i.e., assumptions to be satisfied by the model are formulated. Moreover, for a stronger distinction between different mathematical models, the set of assumptions is understood in a broader sense: Not only basic physical assumptions are listed, but all further modifications and simplifications of the model, such as for example a linearisation of original equations, are also elements of the set of assumptions. The requirements for the set of assumptions to be finite comes from the fact that no model possess an infinite set of physical assumptions. Therefore, consideration of more general sets is not necessary.
  It is also important to remark that having finite sets as objects in the category is one possible way to approach mathematical models. Alternatively, one could think of working directly with mathematical expressions (equations) representing the models. However, in this case it will be more difficult to distinguish models, since the same set of assumptions can be formalised differently in terms of final equations, as we will see in Section 4.
- Assumption (ii). This assumption, in fact, introduces the structure of categories of mathematical models. The main point here is that instead of working with discrete categories, it is beneficial to study more elaborated structure. Since the objects in

categories of mathematical models are sets, it is natural to use relations between sets as morphism in the categories. We will make these relations more specific in Section 3.

- Assumption (iii). This assumption formally describes the process of obtaining the final form of a model, e.g., differential or integral equation, from basic physical assumptions. In this case, mapping S is, in fact, a formalisation process consisting in writing basic physical assumptions in terms of mathematical expressions, which constitute a mathematical model in the end of the formalisation process. Naturally, the formalisation process can be done by different means and approaches, for example first ideas on using type theory to describe the formalisation process towards detecting conceptual modelling errors have been presented in [10,11].
  We also would like to remark, that originally, mapping S has been called invertible in [13]. The invertibility in this case means, that set of assumptions can be uniquely reconstructed from the final form of a model. While that such a reconstruction is theoretically indeed possible, it is generally not unique. Even if we consider the following canonical parabolic equation

$$u_t = a^2 u_{xx},$$

  then without extra context it cannot be decided if this is a heat equation or a diffusion equation. Therefore, the invertibility of a mapping S has been dropped from Definition 1.
- Assumption (iv). This assumption ensures that we do not treat equally models from different dimensions.

It is also important to mention that according to Definition 1, models with different parameters, e.g., material constants, will be corresponded to the same set of assumptions. For example, if we consider the set of assumptions leading to the Lamé equation (partial differential equation with constant coefficients), then it is clear that infinite number of constant coefficients exists, but all these specific models are originated from the same set of assumptions. In general, models originating from the same set of assumptions, but having different material parameters are just particular instance of a general set of assumptions. This fact is particularly important for engineering applications, where stochasticity of material parameters in deterministic models is often considered as stochastic modelling. However, as we discussed above, the stochasticity only in material parameters does not change basic modelling assumptions, because the fact that a constant is chosen according to a certain probability law does not principally affect the assumption of having constant coefficients. In contrast, modelling of physical process by the help of stochastic partial differential equations is based on completely different modelling assumptions, see for example [17], and therefore, should not be put together with "classical" mathematical models.

3. Relations between Mathematical Models

This section is devoted to defining relations between sets of assumptions, which are objects in categories of mathematical models, as introduced in Definition 1. The main requirement for such relations is that their must define a universal model property, which is independent on a specific problem, meaning that boundary or initial conditions (but not coupling/transmission conditions!) should not have influence on the model property. For satisfying this requirement, the comparison of mathematical models by the help of universal model property called model complexity is proposed [13]:

Definition 2 (Complexity of mathematical models)**.** *Let* A *and* B *be mathematical models in a category* $\mathbf{Model}_1$*. We say that model* A *has higher complexity than model* B *if and only if* $\mathbf{Set}_A \subset \mathbf{Set}_B$*, but* $\mathbf{Set}_B \not\subset \mathbf{Set}_A$*. Consequently, two models are called equal, in the sense of complexity, iff* $\mathbf{Set}_B = \mathbf{Set}_A$*.*

The model complexity in this definition is defined relatively, since we do not describe it explicitly. From the point of view of physics, model complexity reflects the fact that a model which has less assumptions provides a more accurate description of a physical phenomenon under consideration. Thus, the model complexity is a relative quality measure of how good a mathematical model represents a given physical phenomenon. The relativity in the measure comes from the fact, that any comparison needs at least two objects, and one model cannot be assessed with respect to its ability represent the corresponding physical process, otherwise that would imply that the exact representation of the physical process is known a priori.

It is important to underline, that the notion of model complexity proposed in Definition 2 is neither related to the notion of complexity of an algorithm, nor to the notion of complexity used for statistical models, where the number of parameters is typically served as complexity measure. The advantage of the notion of model complexity introduced in Definition 2 is the fact that it does not depend on specific boundary or initial conditions, since typically basic model assumptions are not influenced by them. Nonetheless, if boundary conditions are essential for basic model assumptions, e.g., singular boundary conditions, then they will be automatically listed in the corresponding set of assumptions, since such boundary conditions are critical for describing the physical process. Thus, the model complexity introduced in Definition 2 is a universal model property.

Additionally, Definition 2 might sound a bit counterintuitive, since it states that a model satisfying less modelling assumption is more complex, and not of higher simplicity, as it could be expected as well. In fact, both points of view on the complexity are possible, and differ only in the general understanding of modelling assumptions. Definition 2 is based on the idea that modelling assumptions act as restrictions for a model, and thus implying that a model with less modelling assumptions is more general. Nonetheless, another perspective on the notion of model complexity still can be considered, which would reflect the opposite point of view that model assumptions are not restrictions, but rather generalisations of models. This discussion is also directly related to the following important remark:

Remark 1. *Sets of assumptions introduced in Definition 2 are assumed to be written by the help of a natural language. While intuitively it is clear how to formulate these sets, as well as how to compare them in the sense of model complexity, from the formal perspective it is not so straightforward. In fact, a formal comparison of sets of assumptions written in a natural language can be done only by the help of a detailed semantic analysis of these sentences, and only after that, sentences, and hence sets of assumptions, can be rigorously compared. As a possible way around this problem, stricter rules on formulating sets of assumptions might be imposed. In that case, a kind of basic "alphabet" containing allowed expressions and symbols could be introduced. Moreover, perhaps a combination of a natural language and mathematical expressions complemented by strict rules could be a suitable option. Different possibilities to address the problem of a rigorous comparison of sets of assumptions will be studied in future work.*

From the point of relational algebra, model complexity is a binary relation in a category of mathematical models. Hence, the objects in categories of mathematical models can be ordered by using model complexity. However, the ordering of objects defined by model complexity is only partial, and not total, since examples of mathematical models which should belong to the same category but cannot be ordered according to Definition 2 can be easily found, see for example aerodynamic models used in bridge engineering [16]. Naturally, in some cases mathematical models can constitute a category with totally ordered objects. To have a clear distinction between categories with partial and total ordering of objects, we introduce the following definition [16]:

Definition 3. *Let* $\mathbf{Model}_1$ *be a category of mathematical models in which n objects* $\mathbf{Set}_{A_j}$, $j = 1, \ldots, n$ *can be ordered according to Definition 2 as follows*

$$\mathbf{Set}_{A_i} \subset \mathbf{Set}_{A_j}, \text{ for } i < j \leq n.$$

Moreover, let X be the set of all modelling assumptions used in this category. Then category $\mathbf{Model}_1$ *contains totally ordered objects, and therefore is associated with totally ordered models, iff*

$$X = \mathbf{Set}_{\mathrm{A}_1} \cup \mathbf{Set}_{\mathrm{A}_2} \cup \ldots \cup \mathbf{Set}_{\mathrm{A}_n}, \text{ and } \mathbf{Set}_{\mathrm{A}_n} = X,$$

otherwise, the category $\mathbf{Model}_1$ *contains partially ordered objects corresponding to partially ordered models.*

As a direct consequence of this definition we have the following corollary:

Corollary 1. *In a totally ordered category* $\mathbf{Model}_1$ *with n objects always exist two unique objects:*

- *object* $\mathbf{Set}_{\mathrm{A}_1}$ *satisfying* $\mathbf{Set}_{\mathrm{A}_1} \subset \mathbf{Set}_{\mathrm{A}_i}$ $\forall i = 2, \ldots, n$, *which is called the most complex object, and the associated model* A_1 *is called the most complex model;*
- *object* $\mathbf{Set}_{\mathrm{A}_n}$ *satisfying* $\mathbf{Set}_{\mathrm{A}_n} = \mathbf{Set}_{\mathrm{A}_1} \cup \mathbf{Set}_{\mathrm{A}_2} \cup \ldots \cup \mathbf{Set}_{\mathrm{A}_n}$, *which is called the the simplest object element, and the associated model* A_n *is called the simplest model.*

It is worth to mention, that in the framework of introduced modelling formalism, the most complex object and the simplest object are, in fact, initial object and terminal object in categories of mathematical models, respectively. Note that, although categories of mathematical models have finite sets as objects, the initial and terminal objects are different to the ones in the classical category **Sets**, where these are given by the empty set and one-element set, correspondingly. The difference comes precisely from the modelling background of our categories, since while formally it is still possible to consider the empty and one-element sets as sets of assumptions of some (fictitious) models, it does not make sense from the modelling perspective.

The proof of Corollary 1 is straightforward, and we only would like to mention, that uniqueness of objects $\mathbf{Set}_{\mathrm{A}_1}$ and $\mathbf{Set}_{\mathrm{A}_n}$ follows immediately from Definition 2 and from the fact that a totally ordered category is considered. The situation is trickier in the case of partially ordered categories:

Proposition 1. *For a partially ordered category* $\mathbf{Model}_1$ *with n objects one of the following statements holds:*

(i) *the most complex object* $\mathbf{Set}_{\mathrm{A}_1}$ *and the simplest object* $\mathbf{Set}_{\mathrm{A}_n}$ *do not exist;*
(ii) *the most complex object* $\mathbf{Set}_{\mathrm{A}_1}$ *exists, while the simplest object* $\mathbf{Set}_{\mathrm{A}_n}$ *does not exist;*
(iii) *the most complex object* $\mathbf{Set}_{\mathrm{A}_1}$ *does not exist, while the simplest object* $\mathbf{Set}_{\mathrm{A}_n}$ *exists;*
(iv) *the most complex object* $\mathbf{Set}_{\mathrm{A}_1}$ *and the simplest object* $\mathbf{Set}_{\mathrm{A}_n}$ *exist simultaneously.*

Proof. We prove this proposition by straightforwardly constructing corresponding structures of partially ordered categories. We start the proof by proving cases (ii) and (iii) at first, since the proof of case (i) will be based on cases (ii) and (iii), and finally we will prove case (iv). We consider a category with one object $\mathbf{Set}_{\mathrm{A}_1}$, and the rest objects we construct explicitly from $\mathbf{Set}_{\mathrm{A}_1}$. Without loss of generality we assume that $\mathbf{Set}_{\mathrm{A}_1}$ contains at least one element, which will be denoted by $\mathrm{A}_1^{(1)}$. The objects $\mathbf{Set}_{\mathrm{A}_2}$ and $\mathbf{Set}_{\mathrm{A}_3}$ are then constructed from $\mathbf{Set}_{\mathrm{A}_1}$ by adding different elements $\mathrm{A}_1^{(2)}$ and $\mathrm{A}_1^{(3)}$ to $\mathbf{Set}_{\mathrm{A}_1}$, correspondingly, i.e., we obtain new sets of assumptions by adding two different assumptions. This construction is shown by the diagram

$$\begin{array}{ccc} & \mathbf{Set}_{\mathrm{A}_1} = \left\{\mathrm{A}_1^{(1)}\right\} & \\ \swarrow & & \searrow \\ \left\{\mathrm{A}_1^{(1)}, \mathrm{A}_1^{(2)}\right\} = \mathbf{Set}_{\mathrm{A}_2} & & \mathbf{Set}_{\mathrm{A}_3} = \left\{\mathrm{A}_1^{(1)}, \mathrm{A}_1^{(3)}\right\} \end{array}$$

implying that $\mathbf{Set}_{\mathrm{A}_1} \subset \mathbf{Set}_{\mathrm{A}_2}$ and $\mathbf{Set}_{\mathrm{A}_1} \subset \mathbf{Set}_{\mathrm{A}_3}$, but $\mathbf{Set}_{\mathrm{A}_2}$ and $\mathbf{Set}_{\mathrm{A}_2}$ are not related. Thus, $\mathbf{Set}_{\mathrm{A}_1}$ is the most complex object in this category, but no the simplest object exists. Thus, the case (ii) is proved.

The proof of case (iii) is analogues to case (ii), where only instead of adding extra assumptions, we remove different assumptions from the initial set. Thus, for simplicity, we assume that $\mathbf{Set}_{\mathrm{A}_1}$ has at least two different assumption. The rest of the proof follows immediately.

To prove case (i), we consider now two distinct objects $\mathbf{Set}_{\mathrm{A}_1}$ and $\mathbf{Set}_{\mathrm{A}_2}$ given by $\mathbf{Set}_{\mathrm{A}_1} = \left\{\mathrm{A}_1^{(1)}, \mathrm{A}_1^{(2)}, \mathrm{A}_1^{(3)}\right\}$ and $\mathbf{Set}_{\mathrm{A}_2} = \left\{\mathrm{A}_1^{(1)}, \mathrm{A}_1^{(2)}, \mathrm{A}_2^{(1)}\right\}$, respectively. Similar to cases (ii) and (iii), we construct now two other objects in two different ways as follows:

$$\begin{aligned} \mathbf{Set}_{\mathrm{A}_3} &= \left\{\mathrm{A}_1^{(1)}, \mathrm{A}_1^{(2)}, \mathrm{A}_1^{(3)}\right\} \setminus \left\{\mathrm{A}_1^{(2)}, \mathrm{A}_1^{(3)}\right\} = \left\{\mathrm{A}_1^{(1)}\right\}, \\ \mathbf{Set}_{\mathrm{A}_4} &= \left\{\mathrm{A}_1^{(1)}, \mathrm{A}_1^{(2)}, \mathrm{A}_1^{(3)}\right\} \setminus \left\{\mathrm{A}_1^{(1)}, \mathrm{A}_1^{(3)}\right\} = \left\{\mathrm{A}_1^{(2)}\right\}, \end{aligned}$$

and

$$\begin{aligned} \mathbf{Set}_{\mathrm{A}_3} &= \left\{\mathrm{A}_1^{(1)}, \mathrm{A}_1^{(2)}, \mathrm{A}_2^{(1)}\right\} \setminus \left\{\mathrm{A}_1^{(2)}, \mathrm{A}_2^{(1)}\right\} = \left\{\mathrm{A}_1^{(1)}\right\}, \\ \mathbf{Set}_{\mathrm{A}_4} &= \left\{\mathrm{A}_1^{(1)}, \mathrm{A}_1^{(2)}, \mathrm{A}_2^{(1)}\right\} \setminus \left\{\mathrm{A}_1^{(1)}, \mathrm{A}_2^{(1)}\right\} = \left\{\mathrm{A}_1^{(2)}\right\}. \end{aligned}$$

This construction is illustrated by the following diagram:

$$\begin{array}{ccccc} & & \mathbf{Set}_{\mathrm{A}_2} & & \\ & \swarrow & & \searrow & \\ \mathbf{Set}_{\mathrm{A}_3} & & & & \mathbf{Set}_{\mathrm{A}_4} \\ & \nwarrow & & \nearrow & \\ & & \mathbf{Set}_{\mathrm{A}_1} & & \end{array}$$

Thus, the constructed category is partially ordered, and since objects $\mathbf{Set}_{\mathrm{A}_1}$ and $\mathbf{Set}_{\mathrm{A}_2}$ are not related, this category does not contain neither the most complex nor the simplest objects, since no object satisfies assumptions of Corollary 1.

For proving case (iv), let us consider the object $\mathbf{Set}_{\mathrm{A}_1} = \left\{\mathrm{A}_1^{(1)}, \mathrm{A}_1^{(2)}, \mathrm{A}_1^{(3)}, \mathrm{A}_1^{(4)}\right\}$, and let us construct several other objects according to the following commutative diagram

$$\begin{array}{ccccc} & & \left\{\mathrm{A}_1^{(1)}\right\} & & \\ & \nearrow & \uparrow & \nwarrow & \\ \left\{\mathrm{A}_1^{(1)}, \mathrm{A}_1^{(4)}\right\} & & & & \left\{\mathrm{A}_1^{(1)}, \mathrm{A}_1^{(2)}\right\} \\ \uparrow & & & & \uparrow \\ \left\{\mathrm{A}_1^{(1)}, \mathrm{A}_1^{(2)}, \mathrm{A}_1^{(4)}\right\} & & & & \left\{\mathrm{A}_1^{(1)}, \mathrm{A}_1^{(2)}, \mathrm{A}_1^{(3)}\right\} \\ & \nwarrow & \uparrow & \nearrow & \\ & & \left\{\mathrm{A}_1^{(1)}, \mathrm{A}_1^{(2)}, \mathrm{A}_1^{(3)}, \mathrm{A}_1^{(4)}\right\} & & \end{array}$$

While the diagram is commutative, but the objects on the left side are not related to the objects of the right side in the sense of Definition 2. Thus, we have a partially ordered category, where both the most complex object $\left\{\mathrm{A}_1^{(1)}\right\}$ and the simplest object $\left\{\mathrm{A}_1^{(1)}, \mathrm{A}_1^{(2)}, \mathrm{A}_1^{(3)}, \mathrm{A}_1^{(4)}\right\}$ exist simultaneously. Hence, the proposition is proved. □

Next, we have the following theorem:

Theorem 1. *Consider a category* $\mathbf{Model}_1$ *with n objects. If the most complex object* $\mathbf{Set}_{\mathrm{A}_1}$ *and the simplest object* $\mathbf{Set}_{\mathrm{A}_n}$ *exist simultaneously in the category* $\mathbf{Model}_1$*, then* $\mathbf{Model}_1$ *is either a totally ordered category, or contains at least two totally ordered subcategories.*

Proof. The proof of the theorem follows immediately from Corollary 1, Proposition 1, and Definition 3. Looking at the proof of the case (iv) in Proposition 1, we see immediately that two totally ordered subcategories exist. The case of only one totally ordered subcategory is excluded by the assumption of simultaneous existence of the most complex and the simplest objects. Further, if the most complex and the simplest objects exist simultaneously and all objects in the category $\mathbf{Model}_1$ are related by the help of complexity, then it follows immediately that $\mathbf{Model}_1$ is a totally ordered category. □

Evidently, the last statement can be straightforwardly generalised as follows:

Theorem 2. *Every partially ordered category of mathematical models contains at least one totally ordered category of mathematical models as a subcategory.*

4. Convertible Mathematical Models

In this section, we will discuss the mappings S between sets of assumptions and the corresponding models appearing in Definition 1, and as we will see from the upcoming discussion, the role of mappings S provides clear reasoning why objects of categories of mathematical models are sets of assumptions and not the models themselves. The mappings S are generally not invertible, because they represent a formalisation process of basic modelling assumptions in terms of mathematical expressions. Moreover, these mappings are also not unique, since the same set of assumptions can be formalised differently. However, if objects in a category have been ordered (partially or totally) according their complexity, then the mappings will preserve this structure. Thus, these mappings are structure preserving mappings, i.e., they are functors.

Because the mappings between sets of assumptions and the corresponding mathematical models are functorial, then, in fact, the mathematical models constitute also a category. However, since final form of a model depends on the formalisation process, it is more difficult to work directly with categories of models, rather than to describe categories of sets of assumptions, as we have done already. Nonetheless, we will point out now some results related to the models directly. First, we summarise the above discussion in the following definition:

Definition 4. *Let* $\mathbf{Set}_{\mathrm{A}_1}$ *be an object in the category* $\mathbf{Model}_1$*, and let* B_1 *and* B_2 *be two possible model formulations associated with the object* $\mathbf{Set}_{\mathrm{A}_1}$ *via two functors F and G. Then the model formulations* B_1 *and* B_2 *are connected via a natural transformation of functors* ϑ*, and the model formulations* B_1 *and* B_2 *are called* ***convertible****. This construction corresponds to the commutative diagram*

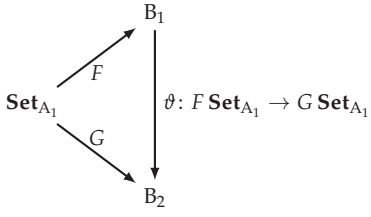

moreover, models which are instantiated by convertible model formulations will be called ***convertible models****.*

Obviously, because different model formulations are related to the same set of assumptions, the model complexity of these formulations remains the same. Thus, we have immediately the following corollary:

Corollary 2. *Convertible models have the same complexity.*

The discussion about convertible mathematical models underlines once more why sets of assumptions are considered as objects in categories of mathematical models, and not model formulations directly. Assume for a moment, that the latter would be the case and consider the following diagram with three objects for simplicity:

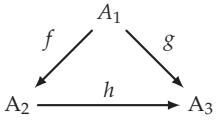

Moreover, assume additionally that the model formulations A_1 and A_2 are convertible in the sense of Definition 4, while the model formulation A_3 is not associated with the same set of assumptions. Thus, we would end up with two kinds of morphisms in the category: Morphism f plays the same role as the natural transformation ϑ in Definition 4, while morphisms g and h represent complexity-relation on the level of model formulations. Obviously, it is necessary to be able to distinguish between the two kinds of morphisms, which would imply much more complicated constructions for the structure of the category, as well as for relations between its objects.

As a simple immediate example indicating the necessity for considering convertible mathematical models, let us consider the classical model of linear elasticity describing deformations of an elastic body in a static case. The classical formulation of this model is given by the following system of equations

$$\begin{cases} \operatorname{div} \tilde{\sigma} + \rho\, \mathbf{K} = 0, \\ \tilde{\varepsilon} = \dfrac{1}{2}\Big[\nabla \mathbf{u} + (\nabla \mathbf{u})^{\mathrm{T}}\Big], \\ \tilde{\sigma} = 2\mu\left(\dfrac{\nu}{1-2\nu}\vartheta\, \tilde{\mathbf{E}} + \tilde{\varepsilon}\right), \end{cases} \qquad \vartheta = \operatorname{div} \mathbf{u} = \frac{\partial u_1}{\partial x_1} + \frac{\partial u_2}{\partial x_2} + \frac{\partial u_3}{\partial x_3}, \tag{1}$$

where $\tilde{\sigma}$ is a symmetric stress tensor, $\tilde{\varepsilon}$ is a symmetric strain tensor, $\mathbf{u}$ is a displacement vector, ρ is a material density, ν is the Poisson's ration, and $\mathbf{K}$ is the volume force. System of Equation (1) is the classical tensor version of elasticity equations, see for example [18]. However, the Lamé equation

$$\mu\, \Delta \mathbf{u} + (\lambda + \mu) \operatorname{grad} \operatorname{div} \mathbf{u} + \rho \mathbf{K} = 0, \tag{2}$$

is often used in practice as well. Furthermore, model of linear elasticity can be also written as follows

$$DMDu = 0, \text{ with } D = \sum_{k=1}^{3} \mathbf{e}_k \partial_k, \text{ and } u = u_0 + \mathbf{u}, \tag{3}$$

where the multiplication operator M is defined by

$$M\mathbf{u} := \frac{m-2}{2(m-1)} u_0 + \mathbf{u}, \quad m := \nu^{-1}.$$

Equation (3) is a quaternionic form of elasticity model with D denoting the Dirac operator, see [19] for all details on quaternionic analysis and its applications.

For the sake of clarity of further considerations, let us denote the models (1)–(3) as follows:

$$\begin{aligned}
\mathrm{B}_1 := &\begin{cases} \operatorname{div} \tilde{\sigma} + \rho\, \mathbf{K} = 0, \\ \tilde{\varepsilon} = \dfrac{1}{2}\left[\nabla \mathbf{u} + (\nabla \mathbf{u})^{\mathrm{T}}\right], \\ \tilde{\sigma} = 2\mu\left(\dfrac{\nu}{1-2\nu}\vartheta\, \tilde{\mathbf{E}} + \tilde{\varepsilon}\right), \end{cases} \qquad \vartheta = \operatorname{div} \mathbf{u} = \frac{\partial u_1}{\partial x_1} + \frac{\partial u_2}{\partial x_2} + \frac{\partial u_3}{\partial x_3}, \\
\mathrm{B}_2 := &\ \mu\, \Delta \mathbf{u} + (\lambda + \mu) \operatorname{grad} \operatorname{div} \mathbf{u} + \rho \mathbf{K} = 0, \\
\mathrm{B}_3 := &\ DMDu = 0, \text{ with } D = \sum_{k=1}^{3} \mathbf{e}_k \partial_k, \text{ and } u = u_0 + \mathbf{u}.
\end{aligned}$$

A possible representation of these models is provided by the diagram

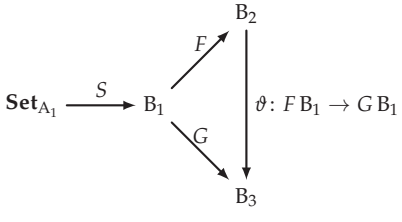

Here, functor S is a formalisation process of basic set of assumptions of linear elasticity $\mathbf{Set}_{\mathrm{A}_1}$ in the tensor form of model formulation B_1, after that, the tensor form can be further reformulated into the Lamé equation B_2, or into the quaternionic form B_3 via functorial mappings F and G. In some sense, the above diagram reflects traditional way of developing different model formulations: At first, the original form is introduced, and after that, several more specific forms better suitable for selected methods are introduced. Moreover, looking in particular at the quaternionic formulation B_3, it becomes clear that this form is not obtained directly through the formalisation process of $\mathbf{Set}_{\mathrm{A}_1}$ (at least no quaterninic-based modelling of linear elasticity has been reported till now), but through reformulation of either Lamé equation or the tensor form, see again [19].

5. Illustrative Examples

In this section, we illustrate the constructions of category theory-based modelling methodology presented in previous sections on two examples: First, we discuss classical models of beam theories, and after that, we discuss aerodynamic models used in bridge engineering. These examples have been already presented in works [13,16] at the time of first steps towards developing the category theory-based modelling methodology. Therefore, it is necessary to revisit these examples for underlying further development of the theory.

5.1. Categorical Modelling of Beam Theories

Transverse vibrations of one-dimensional beams are typically modelled by one of three common beam theories: Bernoulli–Euler theory, Rayleigh theory, and Timoshenko theory. Thus, let us consider a category of mathematical models, denoted by **Beam**, containing as objects sets of assumptions $\mathbf{Set}_{\mathrm{B-E}}$, $\mathbf{Set}_{\mathrm{R}}$, $\mathbf{Set}_{\mathrm{T}}$ corresponding to the Bernoulli–Euler, Rayleigh, and Timoshenko beam theories, respectively. We start our discussion on the construction of category **Beam** by explicitly listing the sets of assumptions, which are given in Table 1.

Table 1. Sets of assumptions of beam theories.

Assumptions	$\mathbf{Set}_{\mathrm{B-E}}$	$\mathbf{Set}_{\mathrm{R}}$	$\mathbf{Set}_{\mathrm{T}}$
1. Cross sections of a beam that are planes remain planes after the deformation process	+	+	+
2. Normal stresses on planes parallel to the axis of a beam are infinitesimal	+	+	+
3. A beam has a constant cross section	+	+	+
4. A beam is made of a homogeneous isotropic material	+	+	+
5. Cross sections of a beam perpendicular to its axis remain perpendicular to the deformed axis	+	+	
6. Rotation inertia of cross sections of a beam is omitted	+		

Remark 2. *The assumptions, as listed in Table 1, are formulated by the help of natural language, however in some cases it is more convenient to formulate sets of assumptions directly in terms of mathematical expressions, or as a mixture of both. While from the set-theoretic point of view such a freedom in writing sets of assumptions is not completely justified, it is acceptable in our setting because each set of assumption written in natural language can be rigorously formalised in terms of mathematical expressions. Thus, writing mathematical expressions in sets of assumptions can be considered as a kind of* ***syntactic sugar****, similar to programming languages terminology. Of course, this analogy not perfect but reflects a general point of view on writing sets of assumptions.*

Since derivation of beam models is well known, it will be omitted. Set of assumption $\mathbf{Set}_{\mathrm{B-E}}$ of the Bernoulli–Euler theory leads to the following beam equation:

$$\rho\, F \frac{\partial^2 u}{\partial t^2} + E\, I_y \frac{\partial^4 u}{\partial x^4} = 0,$$

where E is the Young's modulus of the material, I_y is the moment of inertia, *rho* is the density of material, and F is the area of cross section. Next, set of assumption $\mathbf{Set}_{\mathrm{R}}$ of the Rayleigh theory leads to the equation:

$$\rho\, F \frac{\partial^2 u}{\partial t^2} + E\, I_y \frac{\partial^4 u}{\partial x^4} - \rho\, I_y \frac{\partial^4 u}{\partial x^2 \partial t^2} = 0.$$

Finally, if the effect of bending of cross sections is taken into account, then set of assumption $\mathbf{Set}_{\mathrm{T}}$ of the Timoshenko theory is obtained, which leads to the system of differential equations:

$$\begin{cases} \rho F \dfrac{\partial^2 u}{\partial t^2} - \aleph \mu F \dfrac{\partial^2 u}{\partial x^2} + \aleph \mu F \dfrac{\partial \varphi}{\partial x} & = 0, \\ \rho I_y \dfrac{\partial^2 \varphi}{\partial t^2} - E I_y \dfrac{\partial^2 \varphi}{\partial x^2} + \aleph \mu F \left(\varphi - \dfrac{\partial u}{\partial x} \right) & = 0, \end{cases}$$

where φ is the angle of rotation of the normal to the mid-surface of the beam, $\aleph$ is the Timoshenko shear coefficient, which depends on the geometry of the beam, and μ is the

shear modulus. After some calculations this system can be reformulated in terms of only one partial differential equation for u as follows:

$$\rho F\frac{\partial^2 u}{\partial t^2}+E\,I_y\frac{\partial^4 u}{\partial x^4}-\rho\,I_y\left(1+\frac{E}{\aleph\,\mu}\right)\frac{\partial^4 u}{\partial x^2\partial t^2}+\frac{\rho^2 I_y}{\aleph\,\mu}\frac{\partial^4 u}{\partial t^4}=0.$$

Looking at the above beam models from the categorical perspective, we can summarise these models and their sets of assumptions as follows:

$$\begin{aligned}
\mathbf{Set}_{\mathrm{B-E}} &\overset{S}{\mapsto} \quad \rho F\frac{\partial^2 u}{\partial t^2}+E\,I_y\frac{\partial^4 u}{\partial x^4}=0 && =:\mathbf{A},\\
\mathbf{Set}_{\mathrm{R}} &\overset{S}{\mapsto} \quad \rho F\frac{\partial^2 u}{\partial t^2}+E\,I_y\frac{\partial^4 u}{\partial x^4}-\rho\,I_y\frac{\partial^4 u}{\partial x^2\partial t^2}=0 && =:\mathbf{B},\\
\mathbf{Set}_{\mathrm{T}} &\overset{S}{\mapsto} \quad \rho F\frac{\partial^2 u}{\partial t^2}+E\,I_y\frac{\partial^4 u}{\partial x^4}-\rho\,I_y\left(1+\frac{E}{\aleph\,\mu}\right)\frac{\partial^4 u}{\partial x^2\partial t^2}+\frac{\rho^2 I_y}{\aleph\,\mu}\frac{\partial^4 u}{\partial t^4}=0 && =:\mathbf{C}_1,\\
\mathbf{Set}_{\mathrm{T}} &\overset{S}{\mapsto} \quad \begin{cases} \rho F\dfrac{\partial^2 u}{\partial t^2}-\aleph\mu F\dfrac{\partial^2 u}{\partial x^2}+\aleph\mu F\dfrac{\partial\varphi}{\partial x} &= 0,\\ \rho I_y\dfrac{\partial^2\varphi}{\partial t^2}-EI_y\dfrac{\partial^2\varphi}{\partial x^2}+\aleph\mu F\left(\varphi-\dfrac{\partial u}{\partial x}\right) &= 0. \end{cases} && =:\mathbf{C}_2,
\end{aligned}$$

where S are formalisation mappings, as discussed before. It is worth making the remark:

Remark 3. *Note that, in general, mappings S can be different for each set of assumptions, or, can be the same if all equations are derived based on the same principle, e.g., the Hamilton's principle. If the fact that different formalisation processes have been used to obtain models from the sets of assumptions in one category is essential for the application, then it is necessary to indicate this fact by using sub-scripts, i.e., S_1, S_2, . . ., otherwise the general notation for the formalisation mappings might be kept.*

By using Definition 2, the category **Beam** can be straightforwardly equipped with the commutative diagram

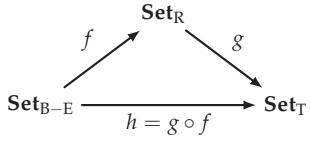

The morphisms f, g, and h indicate the simple fact, that one beam theory can be obtained from another by weakening basic assumptions. Moreover, the above diagram clearly indicate that the object $\mathbf{Set}_{\mathrm{T}}$ (Timoshenko theory) is the most complex, the object $\mathbf{Set}_{\mathrm{R}}$ (Rayleigh theory) has higher complexity than the object $\mathbf{Set}_{\mathrm{B-E}}$ (Bernoulli–Euler theory), which is the simplest object. The same ordering holds for the corresponding model instantiations. Next, let us list the following facts we know about the category **Beam**:

- it is a totally ordered category;
- the object $\mathbf{Set}_{\mathrm{B-E}}$ is the initial object of this category;
- the object $\mathbf{Set}_{\mathrm{T}}$ is the terminal object of this category;
- models $\mathbf{C}_1$ and $\mathbf{C}_2$ are convertible, since they represent different formulations of the assumptions of Timoshenko theory.

Note that, first three facts, as well as the commutative diagram presented above, do not require, in fact, models themself, because these facts are solely obtained simply from the sets of assumptions, i.e., by looking at the objects in the category **Beam**. Thus, the

categorical point of view introduced in the previous section reflects the following idea:

The principle difference between models lies not in their final form, but in the basic modelling assumptions these models are constructed from.

Finally, let us look at the level of models, where the following diagram is obtained

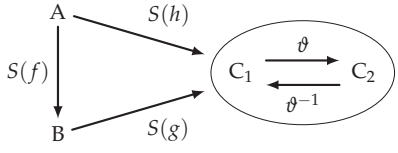

where ϑ denotes a natural transformation appearing in the definition of convertible models, recall Definition 4.

5.2. Category of Aerodynamic Models Revisited

Next, we briefly revisit the example of aerodynamic models used in bridge engineering presented in [16]. Since the idea is only briefly discuss categorical constructions introduced in previous sections, we will not present aerodynamic models in details, but we refer to works [20,21]. We consider the category **AeroModel** containing as objects the following sets of assumptions of mathematical models: (i) **ST** (steady model); (ii) **LST** (linear steady model); (iii) **QS** (quasi-steady model); (iv) **LQS** (linear quasi-steady model); (v) **LU** (linear unsteady model); (vi) **MQS** (modified quasi-steady model); (vii) **MBM** (mode-by-mode model); (viii) **CQS** (corrected quasi-steady model); (ix) **HNL** (hybrid nonlinear model); (x) **MNL** (modified nonlinear model); and, (xi) **NLU** (nonlinear unsteady model). The structure of category **AeroModel** is provided by the following diagram (adapted from [16]):

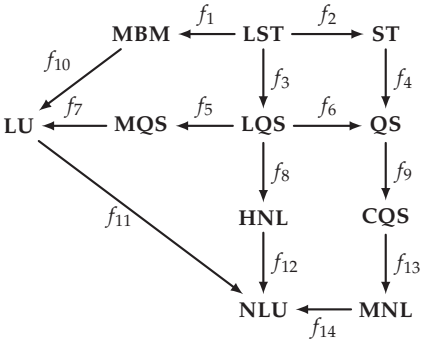

Let us now list some facts we know about the category **AeroModel**:

- it is a partially ordered category;
- the object **LST** is the initial object of this category;
- the object **NLU** is the terminal object of this category;
- according to Theorem 1 several totally ordered subcategories exists, which are

1. $\mathbf{LST} \xrightarrow{f_2} \mathbf{ST} \xrightarrow{f_4} \mathbf{QS} \xrightarrow{f_9} \mathbf{CQS} \xrightarrow{f_{13}} \mathbf{MNL} \xrightarrow{f_{14}} \mathbf{NLU}$
2. $\mathbf{LST} \xrightarrow{f_3} \mathbf{LQS} \xrightarrow{f_6} \mathbf{QS} \xrightarrow{f_9} \mathbf{CQS} \xrightarrow{f_{13}} \mathbf{MNL} \xrightarrow{f_{14}} \mathbf{NLU}$
3. $\mathbf{LST} \xrightarrow{f_3} \mathbf{LQS} \xrightarrow{f_8} \mathbf{HNL} \xrightarrow{f_{12}} \mathbf{NLU}$
4. $\mathbf{LST} \xrightarrow{f_3} \mathbf{LQS} \xrightarrow{f_5} \mathbf{MQS} \xrightarrow{f_7} \mathbf{LU} \xrightarrow{f_{11}} \mathbf{NLU}$
5. $\mathbf{LST} \xrightarrow{f_1} \mathbf{MBM} \xrightarrow{f_{10}} \mathbf{LU} \xrightarrow{f_{11}} \mathbf{NLU}$

Additionally, we can say that no models associated to the objects of **AeroModel** are convertible, but for that it is necessary to take a look at the derivation of models, see again [16] and references therein.

6. Further Characterisations of Mathematical Models and Conclusions

In this section, we present some further ideas on characterisations of mathematical models. One of the most important aspect of applications of category theory is a definition of a universal mapping property (UMP), or simply, a universal arrow, which provides, in fact, a categorical characterisation of objects, see [22,23] for details. Hence, it is important to discuss the universal arrow definition also in the context of category theory-based modelling methodology.

Let us consider a formalisation functor $S\colon$ **Model** $\to$ **M**, where **M** denotes formally a category of instantiations of mathematical models corresponding to the objects in **Model**. Let m be an object of **M**, then a universal arrow from m to S is a pair $\langle r, u\rangle$ consisting of an object r of **Model** and an arrow $r\colon m \to Sr$ of **M**, such that to every pair $\langle d, f\rangle$ with d an object of **Model** and $f\colon c \to Sd$ an arrow of **M**, there is a unique arrow $f'\colon r \to d$ of **Model** with $Sf' \circ u = f$. Practical meaning of a universal arrow in the context of category theory-based modelling methodology is that to the same set of assumption can correspond only convertible model formulations.

Finally, we would like to provide another possible definition of a mathematical model in general, which would summarise our discussion in this paper:

Definition 5. *A mathematical model* $\mathfrak{M}$ *is a triple* $\mathfrak{M} = \langle$**Set**$, \mathcal{M}, S\rangle$*, where*

- **Set** *is the set of assumptions of the model;*
- $\mathcal{M}$ *is an instantiation of the model in terms of mathematical expressions and equations;*
- S *is a formalisation mapping, which formalises the set of assumptions* **Set** *into the model instantiation* $\mathcal{M}$*.*

Relations between the models can be introduced again by the help of Definition 2. Definition 5 proposes an abstract description of a mathematical model similar to the abstract algebraic approach presented in [6]. Thus, a connection between the category theory-based modelling methodology and abstract algebraic approach is established. Hence, both approaches to the modelling process in engineering might complement each other, and therefore, the connection between both approaches will be studied in future research.

In this paper, we have revisited the category theory-based modelling methodology proposed in recent years. The main idea of this modelling methodology is representation of mathematical models by the help of categorical constructions. We have presented revised results from previous works, as well as new results and ideas supporting a deeper understanding of the modelling process in engineering. Moreover, two illustrative practical examples, namely categorical perspective of beam models and on aerodynamic models from bridge engineering, have been revisited. As it can be clearly seen from the examples, the category theory-based modelling methodology presented in this paper is indeed appli-

cable in practice and provides various characterisations of mathematical models, relations between them, and final formulations of models. Finally, we have describe a universal arrow in the framework of the proposed modelling methodology.

Additionally, we would like to remark how the category theory-based modelling methodology presented in this paper can be used in a model selection process. After constructing a category of mathematical models, we can formulate criteria which must be satisfied by a model for a given practical problem, and thus a subcategory of models satisfying these criteria can be constructed. Because we are on the abstract level of models, it is difficult to introduce a quantifiable criterion for the optimal model choice. Nonetheless, on the abstract level, the simplest model satisfying the criteria can be regarded as "the optimal choice" in this case, because generally there is no need for overcomplicating the model. Furthermore, the difference in model assumptions, and thus in model complexity, can be quantified by the help of numerical calculations, as it has been illustrated in [16] for the case of aerodynamic models.

The scope of future research is related to a revision and deeper understanding of coupled mathematical models. A categorical description of a coupled mathematical model will use constructions and ideas introduced in this paper. However, due to the more complex nature of coupled models, it is expected that more refined and advanced constructions will be necessary for a proper description of such models. Moreover, further ideas on a formal model comparison and model selection procedure, as well as a more strict approach to the formulation of sets of assumptions, will be considered in future work.

Funding: This research is supported by the German Research Foundation (DFG) through grant LE 3955/4-1.

Institutional Review Board Statement: Not applicable.

Informed Consent Statement: Not applicable.

Data Availability Statement: Not applicable.

Acknowledgments: I would like to thank the reviewers for very helpful comments, which help not only improving the paper, but also brought new ideas for future research.

Conflicts of Interest: The author declares no conflict of interest.

Appendix A. Some Basic Definitions from Category Theory

Following the classical works in category theory [22,23], we list here few important definitions.

Definition A1. *A category consists of the following data:*

- *Objects:* $A, B, C, \ldots$
- *Arrows (morphisms):* $f, g, h, \ldots$
- *For each arrow* f*, there are given objects* $\mathrm{dom}(f)$ *and* $\mathrm{cod}(f)$ *called the domain and codomain of* f*, respectively. We write*

$$f\colon A \longrightarrow B \quad or \quad A \xrightarrow{f} B$$

  to indicate that $A = \mathrm{dom}(f)$ *and* $B = \mathrm{cod}(f)$*.*
- *Given arrows* $f\colon A \longrightarrow B$ *and* $g\colon B \longrightarrow C$*, that is, with* $\mathrm{cod}(f) = \mathrm{dom}(g)$*, there is given an arrow*

$$g \circ f\colon A \longrightarrow C$$

  called the composite of f *and* g*.*
- *For each object* A*, there is given an arrow*

$$1_A\colon A \longrightarrow A$$

called the identity arrow of A.

These data are required to satisfy the following laws:

- *Associativity:* $h \circ (g \circ f) = (h \circ g) \circ f$ *for all* $f\colon A \longrightarrow B$, $g\colon B \longrightarrow C$, $h\colon C \longrightarrow D$.
- *Unit:* $f \circ 1_A = f = 1_B \circ f$ *for all* $f\colon A \longrightarrow B$.

Definition A2. *A functor*

$$F\colon \mathbf{C} \longrightarrow \mathbf{D}$$

between categories **C** *and* **D** *is a mapping of objects to objects and arrows to arrows, in such a way that*

(a) $F(f\colon A \longrightarrow B) = F(f)\colon F(A) \longrightarrow F(B)$,
(b) $F(1_A) = 1_{F(A)}$,
(c) $F(g \circ f) = F(g) \circ F(f)$.

That is, F respects domains and codomains, identity arrows, and composition.

Definition A3. *For categories* **C**, **D** *and functors* $F, G\colon \mathbf{C} \longrightarrow \mathbf{D}$ *a natural transformation* $\vartheta\colon F \longrightarrow G$ *is a family of arrows in* **D**

$$(\vartheta_C\colon FC \longrightarrow GC)_{C \in \mathbf{C}},$$

such that, for any $f\colon C \longrightarrow C'$ *in* **C**, *one has* $\vartheta_{C'} \circ F(f) = G(f) \circ \vartheta_C$, *that is, the following diagram commutes:*

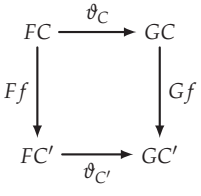

Definition A4. *In any category* **C**, *and object*

- 0 *is initial if for any object C there is a unique morphism* $0 \longrightarrow C$,
- 1 *is terminal if for any object C there is a unique morphism* $C \longrightarrow 1$.

Definition A5. *A subcategory* **S** *of a category* **C** *is a collection of some of the objects and some of the arrows of* **C**, *which includes with each arrow f both the object* $\mathrm{dom} f$ *and the object* $\mathrm{cod} f$, *with each object s its identity arrow* $1_{\mathbf{S}}$ *and with each pair of composable arrows* $s \longrightarrow s' \longrightarrow s''$ *their composite.*

References

1. Oberkampf, W.L.; Roy, C.J. *Verification and Validation in Scientific Computing*; Cambridge University Press: New York, NY, USA, 2010.
2. Babuska, I.; Oden, J. Verification and validation in computational engineering and science: Basis concepts. *Comput. Methods Appl. Mech. Eng.* **2004**, *193*, 4057–4066. [CrossRef]
3. Keitel, H.; Karaki, G.; Lahmer, T.; Nikulla, S.; Zabel, V. Evaluation of coupled partial models in structural engineering using graph theory and sensitivity analysis. *Eng. Struct.* **2011**, *33*, 3726–3736. [CrossRef]
4. Dutailly, J.C. *Hilbert Spaces in Modelling of Systems*; 2014; 47p. Available online: https://hal.archives-ouvertes.fr/hal-00974251 (accessed on 1 August 2021).
5. Dutailly, J.C. *Common Structures in Scientific Theories*; 2014; 34p. Available online: https://hal.archives-ouvertes.fr/hal-01003869 (accessed on 1 August 2021).
6. Legatiuk, D.; Smarsly, K. An abstract approach towards modeling intelligent structural systems. In Proceedings of the 9th European Workshop on Structural Health Monitoring, Manchester, UK, 10–13 July 2018.

7. Nefzi, B.; Schott, R.; Song, Y.Q.; Staples, G.S.; Tsiontsiou, E. An operator calculus approach for multi-constrained routing in wireless sensor networks. In Proceedings of the 16th ACM International Symposium on Mobile Ad Hoc Networking and Computing, New York, NY, USA, 22–25 June 2015
8. Vassilyev, S.N. Method of reduction and qualitative analysis of dynamic systems: I. *J. Comput. Syst. Int.* **2006**, *45*, 17–25. [CrossRef]
9. Vassilyev, S.N.; Davydov, A.V.; Zherlov, A.K. Intelligent control via new efficient logics. In Proceedings of the 17th World Congress The International Federation of Automatic Control, Seoul, Korea, 6–11 July 2008.
10. Gürlebeck, K.; Nilsson, H.; Legatiuk, D.; Smarsly, K. Conceptual modelling: Towards detecting modelling errors in engineering applications. *Math. Methods Appl. Sci.* **2020**, *43*, 1243–1252. [CrossRef]
11. Legatiuk, D.; Nilsson, H. Abstract modelling: Towards a typed declarative language for the conceptual modelling phase. In Proceedings of the 8th International Workshop on Equation-Based Object-Oriented Modeling Languages and Tools, Weßling, Germany, 1 December 2017.
12. Foley, J.D.; Breiner, S.; Subrahmanian, E.; Dusel, J.M. Operands for complex system design specification, analysis and synthesis. *Proc. R. Soc.* **2021**, *477*. [CrossRef]
13. Gürlebeck, K.; Hofmann, D.; Legatiuk, D. Categorical approach to modelling and to coupling of models. *Math. Methods Appl. Sci.* **2017**, *40*, 523–534. [CrossRef]
14. Behrisch, M.; Kerkhoff, S.; Pöschel, R.; Schneider, F.M.; Siegmund, S. Dynamical systems in categories. *Appl. Categ. Struct.* **2015**, *25*, 29–57. [CrossRef]
15. Spivak, D.; Kent, R. Ologs: A categorical framework for knowledge representation. *PLoS ONE* **2012**, *7*, e24274. [CrossRef] [PubMed]
16. Kavrakov, I.; Legatiuk, D.; Gürlebeck, K.; Morgenthal, G. A categorical perspective towards aerodynamic models for aeroelastic analyses of bridges. *R. Soc. Open Sci.* **2019**, *6*, 181848. [CrossRef] [PubMed]
17. Holden, H.; Øksendal, B.; Ubøe, J.; Zhang, T. *Stochastic Partial Differential Equations. A Modeling, White Noise Functional Approach*; Springer Science+Business Media: New York, NY, USA, 2010.
18. Lurie, A.I. *Theory of Elasticity*; Foundations of Engineering Mechanics; Springer: Berlin/Heidelberg, Germany, 2005.
19. Gürlebeck, K.; Habetha, K.; Sprößig, W. *Application of Holomorphic Functions in Two and Higher Dimensions*; Springer International Publishing: Berlin/Heidelberg, Germany, 2016.
20. Kavrakov, I.; Morgenthal, G. A comparative assessment of aerodynamic models for buffeting and flutter of long-span bridges. *Engineering* **2017**, *3*, 823–838. [CrossRef]
21. Kavrakov, I.K.; Morgenthal, G. A synergistic study of a CFD and semi-analytical models for aeroelastic analysis of bridges in turbulent wind conditions. *J. Fluids Struct.* **2018**, *82*, 59–85. [CrossRef]
22. Awodey, S. *Category Theory*; Oxford University Press Inc.: New York, NY, USA, 2010.
23. Mac Lane, S. *Categories for the Working Mathematician*; Springer: New York, NY, USA, 1978.

mathematics

MDPI

Article

An Improved High-Dimensional Kriging Surrogate Modeling Method through Principal Component Dimension Reduction

Yaohui Li [1,2], Junjun Shi [1,2], Zhifeng Yin [1,*], Jingfang Shen [2], Yizhong Wu [3] and Shuting Wang [3]

[1] College of Mechanical and Electrical Engineering, Xuchang University, Xuchang 461000, China; lyh@xcu.edu.cn (Y.L.); sjj_516@webmail.hzau.edu.cn (J.S.)
[2] College of Science, Huazhong Agricultural University, Wuhan 430070, China; sjf_712@mail.hzau.edu.cn
[3] National CAD Supported Software Engineering Centre, Huazhong University of Science and Technology, Wuhan 430074, China; cad.wyz@mail.hust.edu.cn (Y.W.); wangst@mail.hust.edu.cn (S.W.)
* Correspondence: 11996002@xcu.edu.cn

Abstract: The Kriging surrogate model in complex simulation problems uses as few expensive objectives as possible to establish a global or local approximate interpolation. However, due to the inversion of the covariance correlation matrix and the solving of Kriging-related parameters, the Kriging approximation process for high-dimensional problems is time consuming and even impossible to construct. For this reason, a high-dimensional Kriging modeling method through principal component dimension reduction (HDKM-PCDR) is proposed by considering the correlation parameters and the design variables of a Kriging model. It uses PCDR to transform a high-dimensional correlation parameter vector in Kriging into low-dimensional one, which is used to reconstruct a new correlation function. In this way, time consumption of correlation parameter optimization and correlation function matrix construction in the Kriging modeling process is greatly reduced. Compared with the original Kriging method and the high-dimensional Kriging modeling method based on partial least squares, the proposed method can achieve faster modeling efficiency under the premise of meeting certain accuracy requirements.

Keywords: surrogate model; Kriging; high-dimensional problems; principal component dimension reduction

Citation: Li, Y.; Shi, J.; Yin, Z.; Shen, J.; Wu, Y.; Wang, S. An Improved High-Dimensional Kriging Surrogate Modeling Method through Principal Component Dimension Reduction. *Mathematics* **2021**, *9*, 1985. https://doi.org/10.3390/math9161985

Academic Editors: Camelia Petrescu, Valeriu David, Alessandro Niccolai and Mario Versaci

Received: 23 June 2021
Accepted: 13 August 2021
Published: 19 August 2021

Publisher's Note: MDPI stays neutral with regard to jurisdictional claims in published maps and institutional affiliations.

Copyright: © 2021 by the authors. Licensee MDPI, Basel, Switzerland. This article is an open access article distributed under the terms and conditions of the Creative Commons Attribution (CC BY) license (https://creativecommons.org/licenses/by/4.0/).

1. Introduction

The surrogate model [1–5], also called a "response surface model", a "meta model", an "approximate model" or a "simulator", has been applied to different engineering design fields. Commonly used surrogate models include PRS (polynomial response surface) [6,7], Kriging [8–12], RBF (radial basis function) [13,14], SVR (support vector regression) [15,16] and MARS (multiple adaptive spline regression). According to [17] et al., Kriging (also known as Gaussian process model) is widely used. The main reason for this is that the Kriging model can attain better approximation accuracy compared to the other methods mentioned above, and it can handle simple or complex, linear or nonlinear, low-dimensional or high-dimensional problems. Secondly, Kriging can predict the uncertainty of unknown points, and its basis function usually has adjustable parameters. Moreover, the Kriging model can ensure the smoothness of the function, high execution efficiency and good accuracy.

Although Kriging was developed nearly 70 years ago and has been widely used in various fields, it always has some shortcomings in the process of dealing with high-dimensional problems. As shown in [18], using the DACE toolbox in MATLAB and 150 points to construct a Kriging model for a 50-dimensional problem requires 240 to 400 s, which is time consuming. For high-dimensional problems, constructing a Kriging model requires a great deal of computational cost, which limits the application of the Kriging model to high-dimensional problems.

To solve the key problem of the "curse of dimensionality", scholars have proposed various feasible strategies. A new method [19] combining Kriging modeling technology and a dimensionality reduction method has been proposed. This method uses slice inverse regression technology and constructs a new projection vector to reduce the original input vector without losing the basic information of the model's response. In the sub-region after dimensionality reduction, a new Kriging correlation function is constructed using the tensor product of multiple correlation function projection directions. By studying the correlation coefficient and distance correlation of the Kriging model, an effective Kriging modeling method [20] based on a new spatial correlation function is created to promote modeling efficiency. There are also gradient enhancement Kriging methods that use partial gradient sets to balance modeling efficiency and model accuracy. Chen et al. [21] mainly use feature selection techniques to predict the impact of each input variable on the output and rank them, and then select the gradient according to empirical evaluation rules. Mohamed A. et al. [22] also proposed a new gradient enhancement alternative model method based on partial least squares, which greatly reduced the number of correlation parameters to enhance modeling efficiency. In addition, a new method based on principal component analysis (PCA) [23] has been proposed to approximate high-dimensional proxy models. It seeks the best linear combination coefficient that can be provided with the smallest error without using any integral. S. Marelli et al. [24] combined Kriging, polynomial chaos expansion and kernel PCA to prove and verify that the proposed high-dimensional proxy modeling method can effectively solve high-dimensional problems.

The above mentioned dimensionality reduction method reduces modeling time while ensuring that certain model accuracy requirements are met. After all, things have two sides. The improvement in modeling efficiency leads to a loss in accuracy to a certain extent. Therefore, how to improve modeling efficiency as much as possible while reducing the loss in accuracy requires further study.

For this reason, a high-dimensional Kriging modeling method through principal component dimension reduction (HDKM-PCDR) is proposed. Through this method, the PCDR strategy can convert high-dimensional correlation parameters in the Kriging model into low-dimensional ones, which are used to reconstruct new correlation functions. The process of establishing correlation functions such as these can reduce the time consumption of correlation parameter optimization and correlation function matrix construction in the modeling process. Compared with the original Kriging method and the high-dimensional Kriging modeling method based on partial least squares, this method has better modeling efficiency under the premise of meeting certain accuracy requirements. In addition, the high-dimensional modeling method proposed in this article for the Kriging model will provide other researchers with new ideas and directions for the high-dimensional modeling research of surrogate models.

The remaining sections of this article are as follows. The second section introduces the characteristics of the Kriging model and its correlation parameter. The third section introduces the key issues of the proposed method and the specific implementation process in detail. In the fourth section, several high-dimensional benchmark functions and a simulation example are tested. Finally, conclusions are drawn and future research directions are envisioned.

2. Kriging Model

For experimental design sample $\mathbf{X} = [\boldsymbol{x}_1, \ldots, \boldsymbol{x}_\mathrm{m}]^\mathrm{T} (\mathbf{X} \in \Re^{m \times n})$ and corresponding objective $Y = [y_1, \ldots, y_m]^\mathrm{T} (Y \in \Re^{m \times 1})$, the Kriging surrogate model combining polynomial regression and stochastic process can be expressed as

$$Y(\boldsymbol{x}) = \mathbf{F}\boldsymbol{\beta} + Z(\boldsymbol{x}) \tag{1}$$

where parameter $Y(\boldsymbol{x})$ is a predicted function of interest. In this regression matrix $\mathbf{F}$ with $\mathbf{F} \in \Re^{m \times p}$, its elements are usually calculated by the first-order or second-order regression function of known observation points, and sometimes $\mathbf{F}$ can also be a constant regression

matrix. The weight $\boldsymbol{\beta}$ of the regression function is a p-dimensional column vector. The random process $Z(\boldsymbol{x})$ with zero mean and variance can be stated as

$$\mathrm{E}\left[Z(\boldsymbol{x})\right] = 0,\ \mathrm{E}\left[Z(\boldsymbol{x})Z\left(\boldsymbol{w}\right)\right] = \sigma^2 R(\boldsymbol{\theta}, \boldsymbol{\omega}, \boldsymbol{x}) \tag{2}$$

where $\boldsymbol{\theta}$ is the correlation parameter and σ^2 is the process variance. For any two different observations $\boldsymbol{\omega}$ and $\boldsymbol{x}$, the spatial correlation kernel function R ($\boldsymbol{\theta}$, $\boldsymbol{\omega}$, $\boldsymbol{x}$) is shown in Equation (3).

$$R(\boldsymbol{\theta}, \boldsymbol{\omega}, \boldsymbol{x}) = \prod_{i=1}^{n} R_i(\theta_i,\ \omega_i - x_i) \tag{3}$$

After determining the correlation among all sample points, the differentiability of the surface, the smoothness of the Kriging model and the influence of nearby points can be regulated by R ($\boldsymbol{\theta}$, $\boldsymbol{\omega}$, $\boldsymbol{x}$). There are generally seven choices for the spatial correlation function. However, the most widely used is the Gaussian correlation model [25,26]. It can be expressed by

$$R_i\left(\theta_i, w^k - x^k\right) = \exp\left(-\theta_i \left| w^k - x^k \right|^2\right) \tag{4}$$

According to the above analysis, the covariance correlation matrix $\mathbf{R}$ can be stated by Formula (5).

$$\mathbf{R}_{m\times m} = \begin{bmatrix} R(\boldsymbol{x}_1, \boldsymbol{x}_1) & R(\boldsymbol{x}_1, \boldsymbol{x}_2) & \cdots & R(\boldsymbol{x}_1, \boldsymbol{x}_m) \\ R(\boldsymbol{x}_2, \boldsymbol{x}_1) & R(\boldsymbol{x}_2, \boldsymbol{x}_2) & \cdots & R(\boldsymbol{x}_2, \boldsymbol{x}_m) \\ \vdots & \vdots & \ddots & \vdots \\ R(\boldsymbol{x}_m, \boldsymbol{x}_1), & R(\boldsymbol{x}_m, \boldsymbol{x}_2) & \cdots & R(\boldsymbol{x}_m, \boldsymbol{x}_m) \end{bmatrix} \tag{5}$$

Due to unbiased estimation, the regression problem $\mathbf{F}\boldsymbol{\beta} \approx Y$ has a generalized least squares solution $\hat{\boldsymbol{\beta}} = \left(\mathbf{F}^{\mathrm{T}}\mathbf{R}^{-1}\mathbf{F}\right)^{-1}\mathbf{F}^{\mathrm{T}}\mathbf{R}^{-1}\mathbf{Y}$ and a variance estimate $\hat{\sigma}^2 = (\mathbf{Y} - \mathbf{F}\hat{\boldsymbol{\beta}})^T\mathbf{R}^{-1}(\mathbf{Y} - \mathbf{F}\hat{\boldsymbol{\beta}})/m$.

As seen in Formula (2), process variance σ^2 and correlation parameter $\boldsymbol{\theta}$ are closely related among matrix $\mathbf{R}$. The unconstrained optimization problem of the maximum likelihood estimation in Equation (6) is maximized to determine optimal parameter $\boldsymbol{\theta}$.

$$-(m\ln\sigma^2 + \ln|\mathbf{R}|)/2 \tag{6}$$

3. HDKM-PCDR Method

3.1. Use PCDR to Generate New Low-Dimensional Kernel Function

The mathematical theory of the principal component (PC) dimensionality reduction method is PCA, which is used here to reduce the dimensionality of the Kriging design variables. It uses the idea of dimensionality reduction. Under the premise of losing little potential function information, all indicators are transformed into several comprehensive ones by the multivariate statistical method. These comprehensive indicators after conversion are called principal components (PCs). Different linear combinations of original design variables can constitute different PCs. Under the condition that the PCs are independent of each other and meet the accuracy, the PCs after dimensionality reduction have greater advantages in modeling efficiency than the original variables. These are especially suitable for research into high-dimensional complex problems.

Suppose that the study of a certain problem involves n indicators denoted by $x^1, x^2, \ldots, x^n$. Therefore, the n-dimensional random vector $\boldsymbol{x} = \left(x^1, x^2, \ldots, x^n\right)^{\mathrm{T}}$ for any sampling point is formed by these n indicators. A new compound variable v in Equation (7) can be obtained by linear transformation of $\boldsymbol{x}$; then, v is the PC we seek. If the first h ($h <= n$) PCs

are selected, this is equivalent to reducing the number of indicators from n to h (that is, from n dimension to h dimension).

$$\begin{cases} v_1 = u_{11}x^1 + u_{12}x^2 + \ldots + u_{1n}x^n \\ v_2 = u_{21}x^1 + u_{22}x^2 + \ldots + u_{2n}x^n \\ \cdots\cdots \\ v_n = u_{n1}x^1 + u_{n2}x^2 + \ldots + u_{nn}x^n \end{cases} \tag{7}$$

The greater the variance in the principal component v_i, the greater the amount of original data information carried. We always hope that the PCs ($z_i = \boldsymbol{u}_i^{\mathrm{T}} x$) are independent of each other and have the largest possible variance. However, in fact, if there is no restriction on $\boldsymbol{u}_i$, it may make the variance increase arbitrarily; the problem will therefore become meaningless. For this reason, linear transformation needs to follow the following principles:

Principle 1. *Ensure that* $\boldsymbol{u}_i^{\mathrm{T}}\boldsymbol{u}_i$ *is equal to 1, that is,* $u_{i1}^2 + u_{i2}^2 + \ldots + u_{in}^2 = 1 \quad (i = 1, 2, \ldots, n)$;

Principle 2. *Make* v_i *and* v_j *irrelevant, that is* $\mathrm{cov}(v_i, v_j) = 0$, $i \neq j$; $i, j = 1, 2, \ldots, n$;

Principle 3. *Ensure that* v_1 *is the one with the largest variance among all linear combinations of* $x^1, x^2, \ldots, x^n$ *that satisfy principle 1;* v_2 *is the one with the largest variance among all linear combinations of* $x^1, x^2, \ldots, x^n$ *when it is not correlated with* v_1 *; follow this rule, etc.,* v_n *is the one with the largest variance among all linear combinations of* $x^1, x^2, \ldots, x^n$ *when it is not correlated with* $v_1, v_2, \ldots, v_{n-1}$.

Based on the above three principles, the determined composite variable $v_1, v_2, \ldots, v_n$ is the first to the nth PC of the original variable. And the variances of the composite variable $v_1, v_2, \ldots, v_n$ are arranged in descending order.

According to the above analysis, the specific calculation process of the PCDR method is described as follows:

Step 1: Calculation of the covariance matrix. Suppose and offer the covariance matrix of the sample data is $\sum = \sigma^2\mathbf{R} = \left(s_{ij}\right)_{n\times n}$.

Step 2: Find the eigenvalue λ_i of $\sum$ and the corresponding unit eigenvector $\boldsymbol{u}_i$, and arrange the eigenvalues λ_i of the covariance matrix $\sum$ as $\lambda_1, \lambda_2, \ldots, \lambda_n$ $(\lambda_1 \geq \lambda_2 \ldots \lambda_n)$ in order of magnitude, and the corresponding unit eigenvectors $\boldsymbol{u}_1, \boldsymbol{u}_2, \ldots, \boldsymbol{u}_d$ are the coefficient vectors of the principal component $v_i(\ i = 1, 2, \ldots, n)$, respectively.

Step 3: Choice of PCs. The variance value of each PC v_i is equal to the corresponding λ_i [27]. Therefore, the contribution rate CR_i of the eigenvalue (or variance) is used to reflect the amount of information; that is, $CR_i = \lambda_i / \sum_{i=1}^{n} \lambda_i$.

Then, the value h can be determined by the cumulative contribution rate of variance in Equation (8).

$$CR(h) = \sum_{i=1}^{h} \lambda_i / \sum_{i=1}^{n} \lambda_i \tag{8}$$

When the cumulative contribution rate is greater than 80%, we believe that the PC can reflect the characteristic of the original variable to a certain extent, and the corresponding parameter h is the final selected principal component number:

Step 4: Determine a new conversion matrix according to the known sample data and using the formula $z_i = u_{i1}x^1 + u_{i2}x^2 + \ldots + u_{id}x^d (i = 1, \ldots, h)$ to calculate the value of the h PCs; meanwhile, the n*h transformation matrix is obtained. This matrix is used as a weight to replace Formula (3) and recalculate the new kernel function in a more efficient way.

Step 5: Generate new kernel function. First, the linear mapping expression is defined and shown in Equation (9).

$$\begin{array}{c} F_l : B \to B \\ \boldsymbol{x} \mapsto \left[u_l^1 x_1, \ldots, u_l^n x_n\right] \quad l = 1, \ldots, h \end{array} \tag{9}$$

where B is a hypercube belonging to $\Re^d$ and is represented by the product of the space interval in each direction. The corresponding kernel function is expressed as

$$R_l(\theta_l, F_l(x), F_l(\boldsymbol{w})) = \prod_{i=1}^{n} \exp\left(-\theta_l \left| u_l^i w^i - u_l^i x^i \right|^2\right) \tag{10}$$

Finally, through the tensor product of h kernel functions, a new kernel function based on Kriging and PCA (KPCA), as shown in Equation (11), can be generated. For new spatial correlation kernel function, we can use the reduced-dimensional Formula (11) to replace the high-dimensional Formula (3) so as to improve the modeling efficiency of the Kriging model.

$$\begin{aligned} R_{\mathrm{KPCA}}(\boldsymbol{x}, \boldsymbol{w}) &= \prod_{l=1}^{h} R_l(F_l(\boldsymbol{x}), F_l(\boldsymbol{w})) \\ &= \prod_{l=1}^{h} \prod_{i=1}^{n} \exp\left(-\theta_l \left| u_l^i w^i - u_l^i x^i \right|^2\right), \ \forall \boldsymbol{x}, \boldsymbol{w} \in B \end{aligned} \tag{11}$$

Next, take the two-dimensional GP function as an example to describe the dimensionality reduction process of the PCDR more clearly. First, use the LHD sampling method to randomly select 20 sample points, which are shown in Figure 1a. Next, calculate the covariance matrix of the sample points and use the eigenvector with the largest eigenvalue in the matrix as the first principal direction (the dotted line in Figure 1a). The first principal direction is essentially the coefficient in the linear transformation vector. In this way, the linear transformation of Equation (7) maps the original data points to the direction of the first principal component (as shown in Figure 1b). Thus far, the first four steps in the PCDR method are completed. The fifth step is to calculate a new spatial kernel function through the data points after dimensionality reduction, and then complete the low-dimensional Kriging modeling.

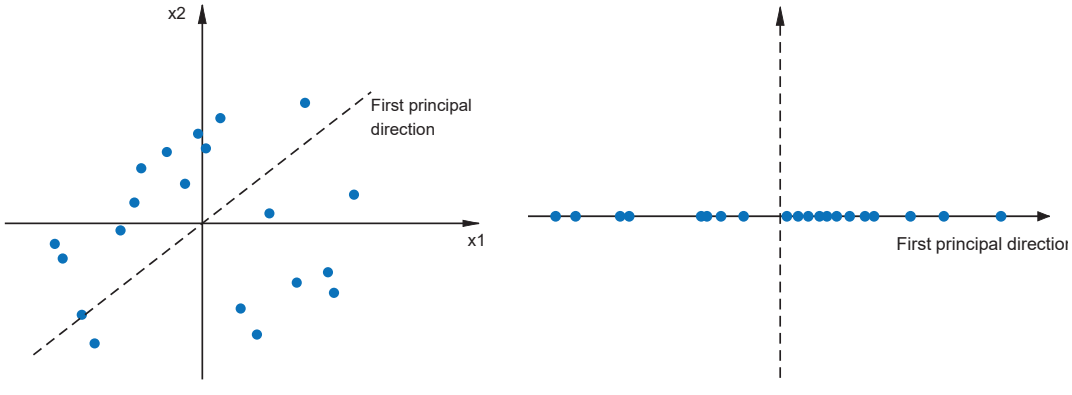

Figure 1. Take the GP function as an example, and the selection of the first principal component in the process of turning two-dimensional data into one-dimensional data. In (**a**), the 20 sample points are obtained through LHD sampling. After calculating the covariance matrix using these 20 sampling points, the first principal direction (the dotted line) is formed by the eigenvector with the largest eigenvalue in the matrix. In (**b**), the original 20 sampling points are mapped to the first principal direction through the linear transformation of Equation (7).

3.2. Specific Implementation of HDKM-PCDR Method

The process of the HDKM-PCDR is shown and stated in detail in Figure 2. Additionally, its specific implementation steps are presented as follows:

Step 1: Initial sampling. LHD (Latin Hypercube Design) method [28] is employed to generate the initial sample points. To facilitate comparison with other methods, different initial sampling points will be selected for different real function evaluation times.
Step 2: Build or update sample data. If the sampling data are obtained by the initial LHD method, we will establish the sample data set {**S**, **Y**} for the first time. If a new sampling point (s, y) is generated by LHD in the optimization process, we will update the sample data set, i.e., [**S**, s] $\rightarrow$ **S**, [**Y**, y] $\rightarrow$ **Y**.
Step 3: Generate new low-dimensional kernel function.
Step 4: Use new kernel function to rapidly construct the Kriging model.
Step 5: Generate a new candidate point by Latin Hypercube Design.
Step 6: Check the evaluation number of the expensive function.
Step 7: Expensive function evaluation at the new update point.

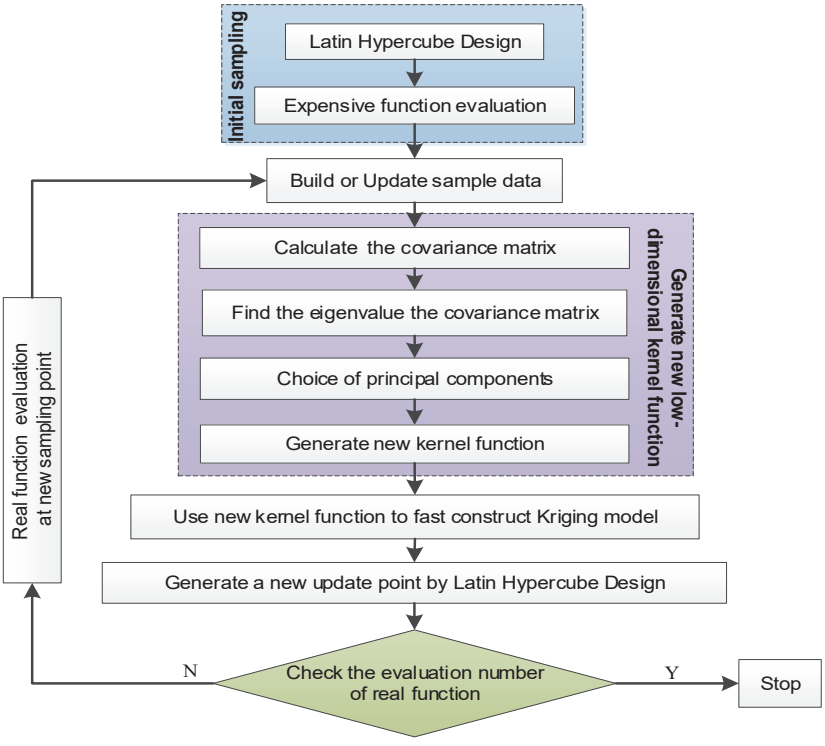

Figure 2. The implementation process of the HDKM-PCDR method.

4. Numerical Test

The KPLS method was proposed by Bouhlel et al. in 2016, and [29,30] demonstrated that the KPLS method is highly effective at solving high-dimensional problems. The KPLS combining PLS (partial least squares) technique and Kriging model uses the least squares dimensionality reduction method in the process of establishing the Kriging model, which reduces the number of hyper-parameter calculations of the model to be consistent with the number of PCs retained by the PLS, thereby accelerating the construction of the Kriging

model. For this reason, we can prove the effectiveness of HDKM-PCDR by comparing HDKM-PCDR with the KPLS method. If the test result of HDKM-PCDR is better, it can prove the effectiveness of the HDKM-PCDR method. In addition, Kriging is also used as a comparison method to verify the applicability of the HDKM-PCDR method for solving high-dimensional problems.

To compare HDKM-PCDR and KPLS methods in a better and more detailed way, this work keeps the number of PCs retained in the two methods consistent. The modeling time and modeling error of the two methods are tested when one principal component, two PCs and three PCs are retained, respectively.

According to the characteristics of the function's multimodality, the complexity degree (the number of valleys or ridges) and the level of dimensionality, the 20-dimensional Griewank function, the 40-dimensional SUR function, the 60-dimensional DixonPrice function and the 80-dimensional Michalewicz function shown below are chosen as the Benchmark functions.

Griewank function:

$$y(\boldsymbol{x}) = \sum_{i=1}^{20} \frac{x_i^2}{4000} - \prod_{i=1}^{20} \cos(\frac{x_i}{\sqrt{i}}) + 1 \quad -600 \le x_i \le 600 \tag{12}$$

SUR function:

$$y(\boldsymbol{x}) = (x_1 - 1)^2 + (x_{40} - 1)^2 + 40\sum_{i=1}^{39} (40 - i)(x_i^2 - x_{i+1})^2 \quad -3 \le x_i \le 2 \tag{13}$$

DixonPrice function:

$$y(\boldsymbol{x}) = (x_1 - 1)^2 + \sum_{i=2}^{60} i(2x_i^2 - x_{i-1})^2 \quad -10 \le x_i \le 10 \tag{14}$$

Michalewicz function:

$$y(\boldsymbol{x}) = -\sum_{i=1}^{80} \sin(x_i) \sin^{160}(\frac{ix_i^2}{\pi}) \quad 0 \le x_i \le \pi \tag{15}$$

For each test function, it is tested in two cases. The first case is to obtain 10 initial sampling points through LHD, and then new sampling points will be added until the total number of samples reaches 100. The second case is to obtain 20 initial sampling points; when the total number of samples reaches 200, stop the HDKM-PCDR method. The total number of sampling points here is reflected in Tables 1–4. For the test in each case, in order to reflect the robustness and effectiveness of the HDKM-PCDR, the average value of ten repeated runs is taken as the final test result.

Table 1. Test results on time and RMSE for the Griewank function.

Test Method	100 Sample Points		200 Sample Points	
	Time (s)	RMSE	Time (s)	RMSE
Kriging	7.5573	11.9916	74.1562	8.6062
HDKM-PCDR-1	0.7652	10.3085	6.5901	6.6526
KPLS-1	0.8119	10.1789	6.6855	6.8414
HDKM-PCDR-2	1.3173	9.6095	13.7230	5.4336
KPLS-2	1.3510	9.9492	13.7983	6.8227
HDKM-PCDR-3	2.5512	9.3348	30.8119	5.4700
KPLS-3	2.7733	9.8196	30.9308	6.7632

Table 2. Test results on time and RMSE for the SUR function.

Test Method	100 Sample Points		200 Sample Points	
	Time (s)	RMSE	Time (s)	RMSE
Kriging	18.2212	1.3791×10^4	216.5188	1.1123×10^4
HDKM-PCDR-1	1.2272	1.2820×10^4	12.8934	8.8252×10^3
KPLS-1	1.9691	1.2301×10^4	14.1654	7.0127×10^3
HDKM-PCDR-2	2.2761	1.1949×10^4	23.5094	7.6304×10^3
KPLS-2	2.3510	1.2795×10^4	24.1808	8.4033×10^3
HDKM-PCDR-3	4.1168	1.2322×10^4	55.3962	8.3669×10^3
KPLS-3	4.7523	1.2576×10^4	55.7409	8.7498×10^3

Table 3. Test results on time and RMSE of the DixonPrice function.

Test Method	100 Sample Points		200 Sample Points	
	Time (s)	RMSE	Time (s)	RMSE
Kriging	61.4766	2.8969×10^5	664.3026	2.1001×10^5
HDKM-PCDR-1	2.9292	2.8021×10^5	24.3048	1.9415×10^5
KPLS-1	2.8138	2.8041×10^5	25.0655	1.9264×10^5
HDKM-PCDR-2	4.8741	2.7954×10^5	54.7819	1.8945×10^5
KPLS-2	5.9279	2.7961×10^5	56.8854	1.8879×10^5
HDKM-PCDR-3	15.2038	2.6808×10^5	126.8160	1.8643×10^5
KPLS-3	13.6838	2.6488×10^5	137.2857	1.8654×10^5

Table 4. Time and RMSE of the Michalewicz function.

Test Method	100 Sample Points		200 Sample Points	
	Time (s)	RMSE	Time (s)	RMSE
Kriging	126.6239	0.1296	1289.3620	0.0925
HDKM-PCDR-1	3.4028	0.1276	25.9314	0.0916
KPLS-1	3.6180	0.1276	26.9781	0.0918
HDKM-PCDR-2	4.7722	0.1248	53.1837	0.0920
KPLS-2	5.0228	0.1264	53.8481	0.0923
HDKM-PCDR-3	19.3122	0.1241	184.6957	0.0915
KPLS-3	32.3037	0.1238	285.4663	0.0908

The results of the time consumption and modeling error (RMSE-Root Mean Square Error) of the four test functions are shown in Tables 1–4. The time is the total modeling time spent during the whole sampling process for all sample points. The RMSE in these tables can be obtained by using "leave one out cross" validation [31]. The concrete expression of RMSE is shown in Equation (12). Here, parameter k represents the number of samples in the current data. If the Kriging model is used to estimate the variance of point $\boldsymbol{x}_i$, we first need to reconstruct the Kriging model with the remaining k-1 sampling points, except for point $\boldsymbol{x}_i$. Then, calculate the estimated variance $\hat{s}_i^2$ of point $\boldsymbol{x}_i$ by using the newly built Kriging model and Formula (8). After repeating k times to complete the variance estimation of these k sampling points, the average value can be calculated to obtain the RMSE with Equation (12).

$$\mathrm{RMSE} = \frac{1}{k}\sqrt{\sum_{i=1}^{k} \hat{s}_i^2} \tag{16}$$

Under the condition of different sample points, box plots of 10 test results of each test function are, respectively, shown in Figures 3–6 to further demonstrate the stability and effectiveness of the HDKM-PCDR method, as well as to express it intuitively.

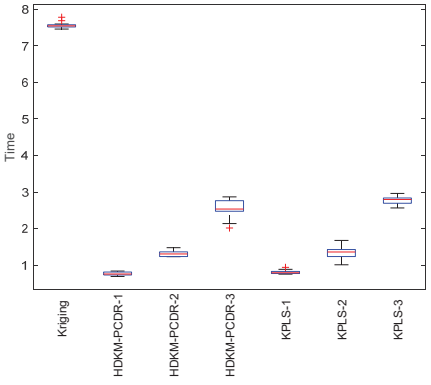

(**a**) Time for 100 sampling points.

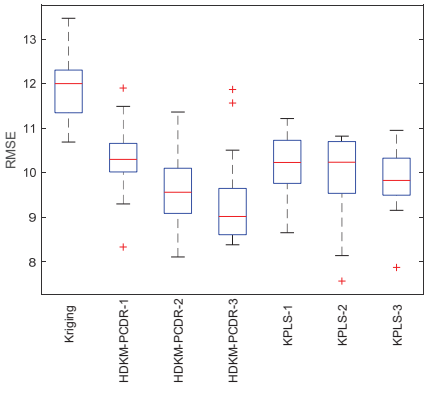

(**b**) RMSE for 100 sampling points.

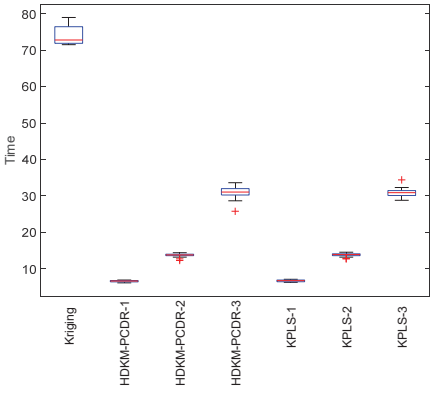

(**c**) Time for 200 sampling points.

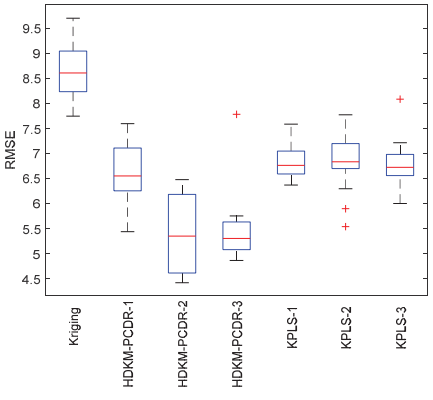

(**d**) RMSE for 200 sampling points.

Figure 3. Time and RMSE of the Griewank function.

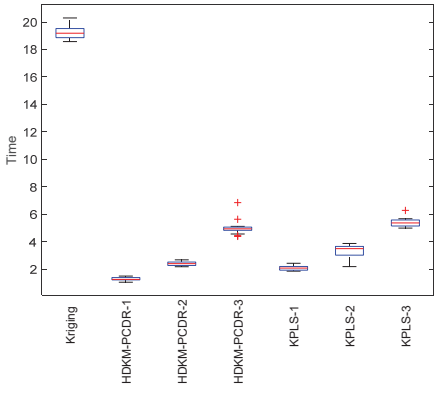

(**a**) Time for 100 sampling points.

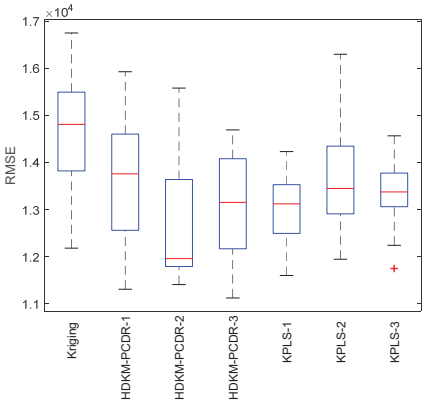

(**b**) RMSE for 100 sampling points.

Figure 4. *Cont.*

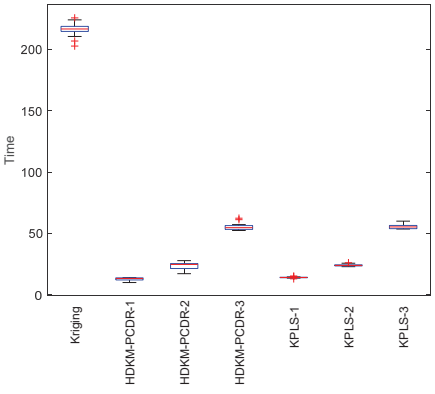

(**c**) Time for 200 sampling points.

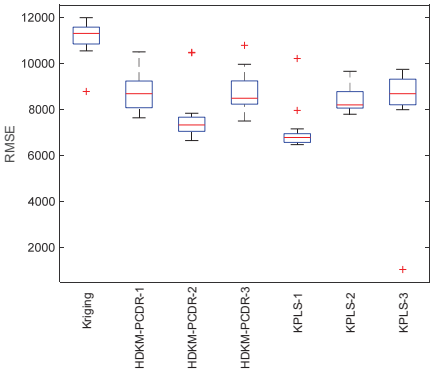

(**d**) RMSE for 200 sampling points.

Figure 4. Time and RMSE of the SUR function.

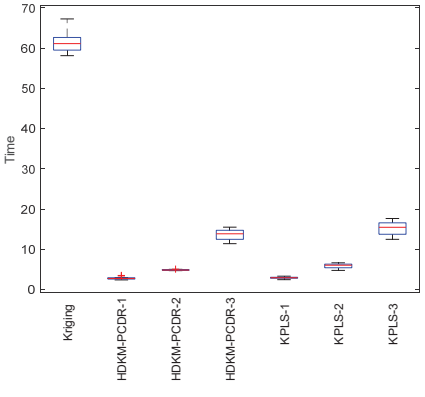

(**a**) Time for 100 sampling points.

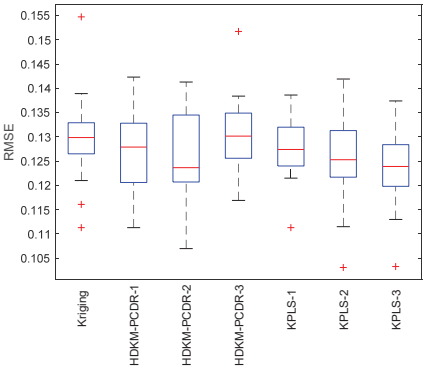

(**b**) RMSE for 100 sampling points.

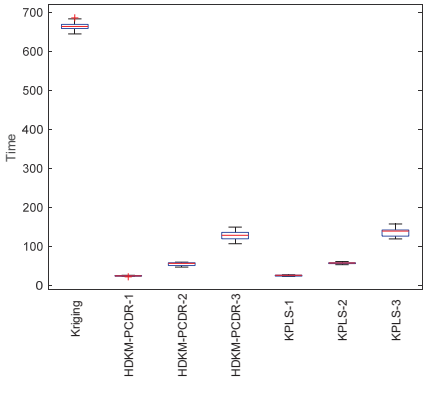

(**c**) Time for 200 sampling points.

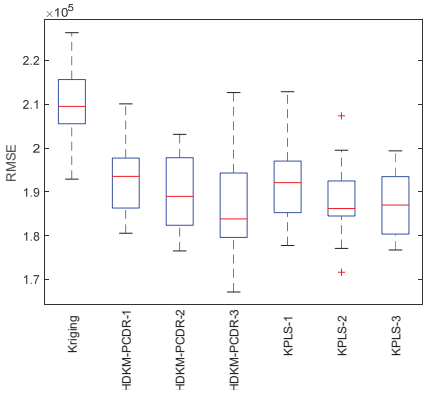

(**d**) RMSE for 200 sampling points.

Figure 5. Time and RMSE of the DixonPrice function.

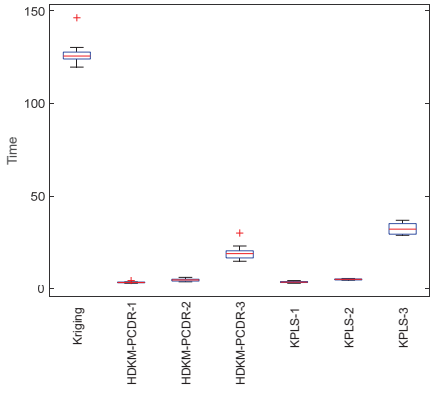

(**a**) Time for 100 sampling points.

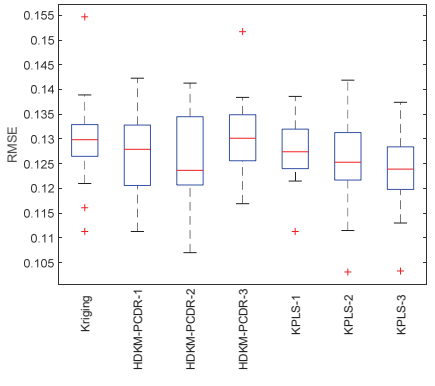

(**b**) RMSE for 100 sampling points.

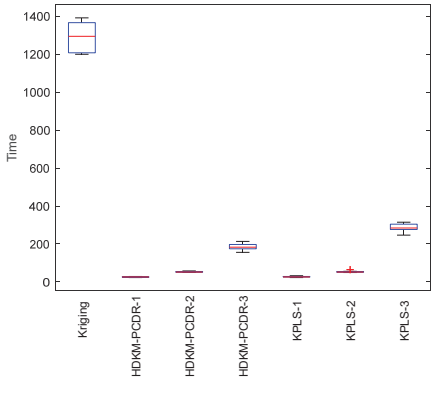

(**c**) Time for 200 sampling points.

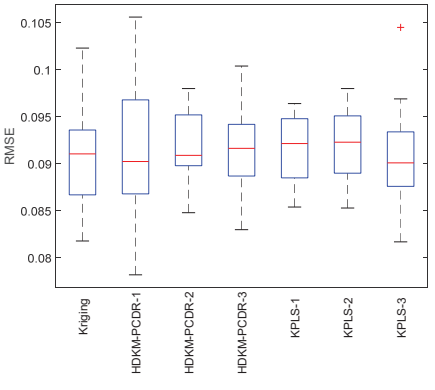

(**d**) RMSE for 200 sampling points.

Figure 6. Time and RMSE of the Michalewicz function.

First, let us take a look at the modeling time test results of the algorithms from subgraphs (a) and (c) in Figures 3–6. Compared with ordinary Kriging and KPLS methods, from the median (red solid line) of the time box plots and the size (the area formed by the upper quartile and the lower quartile) of the box, the median line value shown by the proposed method is the lowest, and the frame area is also the smallest. In addition, it has fewer outliers. For example, in the Griewank function test of 200 sampling points, the HDKM-PCDR-3 method and the KPLS-3 method have abnormal points. However, the abnormal points generated by the HDKM-PCDR-3 method are located below the box plot, while the abnormal point of KPLS-3 is located above the box plot. This shows that the time consumed by HDKM-PCDR-3 in the ten test cycles has a smaller value in a certain test, while KPLS-3 has a larger value. Therefore, the proposed method has the shortest modeling time in the process of each test, and the fluctuation of the time spent in these ten modeling times is not large. These test results show that the HDKM-PCDR modeling method has better stability and efficiency.

The modeling time and model accuracy in each of the four tables are the average of the results obtained after ten runs of each benchmark function. All tests were performed in Matlab2018a by a Lenovo machine equipped with an i5–4590 3.3 GHz CPU and 4 GB RAM. As expected, for these four benchmark functions, the HDKM-PCDR method and the KPLS method under the dimensionality reduction condition use 100 and 200 sampling points to

establish the Kriging model. The corresponding time spent and the approximate accuracy of the model are better than the Kriging method without direct dimensionality reduction. For the HDKM-PCDR method and the KPLS using the idea of dimensionality reduction, the modeling time shown by the HDKM-PCDR-n (n = 1, 2, 3) method stays ahead of the KPLS-n (n = 1, 2, 3) method under the condition of reducing the same dimensions. For Griewank, SUR and DixonPrice functions, although the modeling time of the proposed method is slightly lower than that of KPLS, the total modeling time of the two methods is not much different. For the more complex Michalewicz function, the HDKM-PCDR-3 method takes only a little more than half of the time of the KPLS-3 method, which also shows that the HDKM-PCDR method has higher efficiency in dealing with multi-dimensional and multi-peak complex problems. In terms of model accuracy, except for the KPLS-1 method at 100 points, the test results of Griewank function using the proposed method perform best. Other than the KPLS-1 method in the case of 100 points and 200 points, the RMSE obtained by the HDKM-PCDR method to test the SUR function meets the high accuracy requirements. For the DixonPrice and Michalewicz functions, the two methods are evenly matched, and both have advantages. However, considering modeling time and model accuracy, the proposed method is slightly better.

Next, let us look at the test results of the modeling accuracy of the algorithm from sub-graphs (b) and (d) in Figures 3–6. Theoretically speaking, the RMSE (model accuracy) of the ordinary Kriging method without dimensionality reduction should be the best. However, as can be seen from subgraphs (b) and (d), the fact is just the opposite. Judging from the median RMSE in the Griewank function test results, the HDKM-PCDR performs better than the KPLS. For SUR function, in addition to KPLS-1, the accuracy results in other cases are still slightly better than the proposed method. For the DixonPrice function and the Michalewicz function, these two dimensionality reduction methods are evenly matched, and each has its own merits. However, KPLS-2 and KPLS-3 both showed better performance of abnormal points in some test functions, which is better than the proposed method. However, in general, the proposed method is still stronger than KPLS, and can ensure that the accuracy of the problem after dimensionality reduction meets certain requirements.

In summary, the following conclusions can be drawn for all the above test results: (1) Compared to the non-dimensionality reduction Kriging method, regardless of the modeling time and the accuracy of the model, the HDKM-PCDR method and the KPLS method using dimensionality reduction have been improved. (2) The modeling time of the HDKM-PCDR method is almost always shorter than that of the KPLS method while retaining the same number of PCs. Additionally, with the increase in the dimension and the number of sample points, the efficiency advantage of the HDKM-PCDR method becomes more and more obvious. The main reason for this is that the proposed method reduces the size of the hyperparameter correlation matrix in the Kriging model, which is equivalent to simplifying the internal structure of the Kriging model, thereby improving the efficiency of Kriging modeling. (3) However, in terms of modeling accuracy, for different functions, the proposed method and the KPLS method have their own advantages in accuracy. For example, HDKM-PCDR's test results of Griewank function show that its modeling accuracy is higher. The results of the proposed method and the KPLS method for the other three benchmark functions are basically evenly divided. The main reason is explained as follows: the reduction in the proposed method is mainly for the reduction in the dimensions of the related hyperparameters, which directly leads to the reduction in the correlation matrix, while the KPLS method also considers the PLS method and the Kriging estimation of the sampling points. These two different reduction methods consider different angles for the reduction problem, resulting in approximate accuracy sometimes being better than KPLS; sometimes, KPLS is better than the proposed method, but the overall accuracy values are not much different and are even close. (4) In some special circumstances, when the dimensionality of the problem is higher after dimensionality reduction, the model's accuracy will decrease instead. For example, when the Michalewicz function is tested

at 200 sampling points, it appears that the accuracy of HDKM-PCDR-1 and KPLS-1 are better than HDKM-PCDR-2 and KPLS-2. The reason for this result may be that the sample point contains a large amount of information when it is reduced to one-dimensional data. In other words, the weight of the function on a certain dimensional variable is too large. However, this situation is rare seen in practice.

5. Air Traffic Control Radar Design

With the continuous and rapid development of China's air traffic field, air traffic control technology has higher and higher requirements for the perception of future air traffic situations. In order to ensure the flight safety of aircraft and the normal operation of air traffic in real time, a radar detection system has been set up. This radar detection system can monitor the flight range of an aircraft in real time. In this case, unfortunate events such as missing aircraft can be avoided.

In order to better design the above air traffic control radar, we simulated an air traffic control (ATC) radar design through Simulink simulation software in MATLAB. The simulation model can be divided into three main subsystems: radar, aircraft and weather. The specific air traffic control model diagram is shown in Figure 7. The air traffic control radar simulation system designed in this paper introduces real-time data such as flight information, radar signals, weather forecast, aircraft resistance and flight mileage as simulation parameters in the simulation process. In order to make the parameters of the radar system design easier to change and easier to determine their values, this model provides a GUI (see Figure 8). The parameters of radar and weather can be changed through the GUI. The effect of different parameters can be seen on the oscilloscope screen during simulation. The oscilloscope screen shows the actual range of the aircraft and the change over time in the aircraft's range estimated by radar under certain parameter settings.

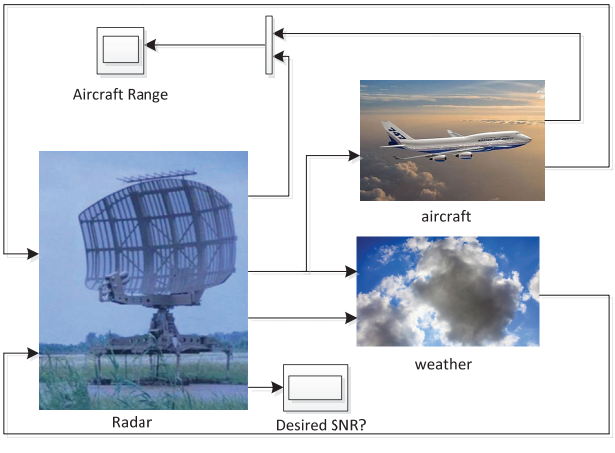

Figure 7. Air traffic control system.

This paper takes the design variables as the parameter settings of the air traffic control radar design simulation system, so that the simulation results can be obtained by Simulink. Since the simulation result changes with time, the maximum range of radar detection is taken as the simulation result and output to the MATLAB workspace. Based on the simulation results and the HDKM-PCDR method, one, two and three principal components are retained to construct the Kriging model, and the modeling time and modeling error in the three cases are recorded. In addition, the Kriging model was directly established with the data obtained from the simulation, and modeling time and modeling error were also recorded.

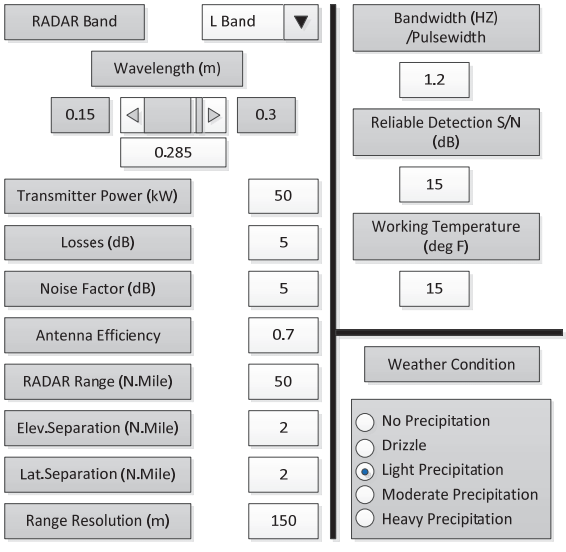

Figure 8. Air traffic radar design parameters.

Figure 9 shows the results of modeling time and modeling error in a modeling process. In order to better compare the time for the HDKM-PCDR method to establish Kriging and to directly establish the Kriging model, the time in Figure 7 has removed the time used for simulation. In this modeling process, there are 10 initial sample points, and the corresponding expensive estimates of the sample points are obtained through simulation. The Kriging model is established by the HDKM-PCDR method, and the modeling time at this time (excluding time for simulation estimation) is recorded as a first-time value. In each iteration, a sample point is added, and the corresponding expensive estimate is simulated; modeling time at this time (excluding the time for the simulation estimate) is recorded as a time value. Repeat the iterative process until final sample number is 100, and then stop the iterative process.

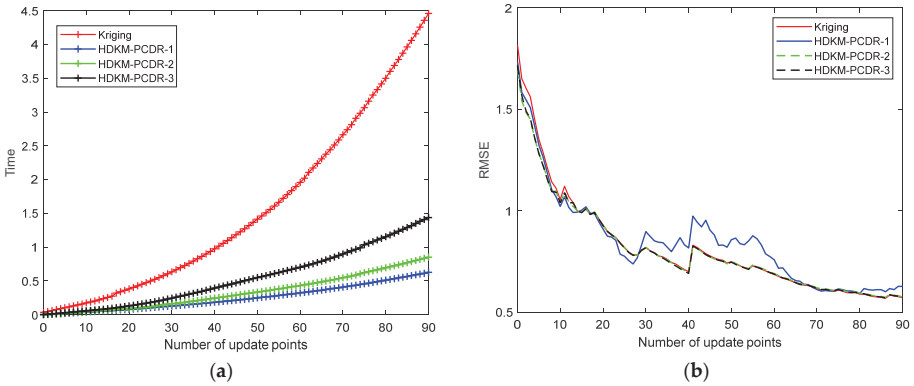

(**a**) (**b**)

Figure 9. (**a**) Test results on modeling time of air traffic control systems throughout the Kriging, HDKM-PCDR-1, HDKM-PCDR-2 and HDKM-PCDR-3 methods. (**b**) Test results on RMSE of air traffic control systems throughout the Kriging, HDKM-PCDR-1, HDKM-PCDR-2 and HDKM-PCDR-3 methods.

The following two conclusions can be drawn from the figure: (a) It can be seen from the figure that, as the number of sample points increases, the time required for HDKM-PCDR and Kriging to build a model gradually increases. However, with the increase in the number of sample points, the time required to directly establish the Kriging model is greater than the time required to establish the model of HDKM-PCDR. In the end, the time difference is 8 times, 6 times and 3.2 times, respectively. (b) It can be seen from the figure that the modeling error is gradually reduced as the number of sample points increases. The modeling error of the HDKM-PCDR-1 method is unstable and large, but it is not much different from the modeling error of the Kriging method. The modeling errors of the HDKM-PCDR-2 and HDKM-PCDR-3 methods are very close to those of the Kriging method. In summary, the HDKM-PCDR method can improve the modeling efficiency of the Kriging model when the modeling accuracy loss is small.

6. Conclusions

The complexity of engineering problems causes calculating time to be expensive. Therefore, the Kriging surrogate model is used to reduce this burden. However, when using the Kriging model to approximate high-dimensional problems, the modeling process is also time consuming. The most time is spent during the inversion of the covariance correlation matrix and the solving of the Kriging correlation parameter. To this end, a high-dimensional Kriging modeling method through principal component dimension reduction (HDKM-PCDR) is proposed. In this method, the PCDR way of considering design variables and correlation parameters can convert the high-dimensional correlation parameter in Kriging into a low-dimensional one, which is used to reconstruct a new correlation function. In this way, it will reduce the time spent optimizing correlation parameters and constructing the correlation function matrix in the Kriging modeling process. Compared with the original Kriging method and the high-dimensional Kriging modeling based on partial least squares, the proposed method has better modeling efficiency while meeting certain accuracy requirements.

When dealing with high-dimensional problems, the proposed method has certain deficiencies in relation to model accuracy. In principal component dimensionality reduction, it is necessary to ensure that the cumulative contribution rate of the first few principal components extracted reaches a higher level (that is, the variable after dimensionality reduction has a higher amount of information). In this case, when the correlation between the original design variables is weak, too many principal components may be selected, which is not conducive to improvements in Kriging modeling efficiency. In future research, we will further explore new sampling strategies by combining factors such as prediction target, variance, and distance. In this way, more promising sampling points can be obtained to improve the model accuracy.

Author Contributions: Conceptualization, Y.L.; methodology, Y.L. and J.S. (Junjun Shi); software, J.S. (Junjun Shi); writing—original draft, Y.L.; writing—review and editing, Y.L., J.S. (Junjun Shi), Z.Y., J.S. (Jingfang Shen), Y.W. and S.W. All authors have read and agreed to the published version of the manuscript.

Funding: This research was funded by National Natural Science Foundation of China (No. 51775472), Science and Technology Innovation Talents in Universities of Henan Province (No. 21HASTIT027) and Henan Excellent Youth Fund Project (No. 202300410346), Training plan of Young Backbone Teachers in Universities of Henan Province (No. 2020GGJS209).

Institutional Review Board Statement: Not applicable.

Informed Consent Statement: Not applicable.

Conflicts of Interest: The authors declare no conflict of interest.

References

1. Jensen, W.A. Response surface methodology: Process and product optimization using designed experiments. *J. Qual. Technol.* **2017**, *49*, 186. [CrossRef]
2. Fan, Y.; Lu, W.; Miao, T.; Li, J.; Lin, J. Multiobjective optimization of the groundwater exploitation layout in coastal areas based on multiple surrogate models. *Environ. Sci. Pollut. Res. Int.* **2020**, *27*, 19561–19576. [CrossRef]
3. Dubourg, V.; Sudret, B.; Bourinet, J.M. Reliability-based design optimization using kriging surrogates and subset simulation. *Struct. Multidiscip. Optim.* **2011**, *44*, 673–690. [CrossRef]
4. Kaymaz, I. Application of kriging method to structural reliability problems. *Struct. Saf.* **2005**, *27*, 133–151. [CrossRef]
5. Azizsoltani, H.; Gaxiola-Camacho, J.R.; Haldar, A. Site-specific seismic design of damage tolerant structural systems using a novel concept. *Bull. Earthq. Eng.* **2018**, *16*, 3819–3843. [CrossRef]
6. Fan, C.; Huang, Y.; Wang, Q. Sparsity-promoting polynomial response surface: A new surrogate model for response prediction. *Adv. Eng. Softw.* **2014**, *77*, 48–65. [CrossRef]
7. Rashki, M.; Azarkish, H.; Rostamian, M.; Bahrpeyma, A. Classification correction of polynomial response surface methods for accurate reliability estimation. *Struct. Saf.* **2019**, *81*, 101869. [CrossRef]
8. Li, T.; Yang, X. An efficient uniform design for Kriging-based response surface method and its application. *Comput. Geotech.* **2019**, *109*, 12–22. [CrossRef]
9. Van Stein, B.; Wang, H.; Kowalczyk, W.; Emmerich, M.; Bäck, T. Cluster-based Kriging approximation algorithms for complexity reduction. *Appl. Intell.* **2019**, *50*, 778–791. [CrossRef]
10. Namura, N.; Shimoyama, K.; Obayashi, S. Kriging surrogate model with coordinate transformation based on likelihood and gradient. *J. Glob. Optim.* **2017**, *68*, 827–849. [CrossRef]
11. Li, Y.; Shi, J.; Cen, H.; Shen, J.; Chao, Y. A kriging-based adaptive global optimization method with generalized expected improvement and its application in numerical simulation and crop evapotranspiration. *Agric. Water Manag.* **2021**, *245*, 106623. [CrossRef]
12. Li, Y.; Shi, J.; Shen, J.; Cen, H.; Chao, Y. An adaptive Kriging method with double sampling criteria applied to hydrogen preparation case. *Int. J. Hydrog. Energy* **2020**, *45*, 31689–31705. [CrossRef]
13. Dou, S.-Q.; Li, J.-J.; Kang, F. Health diagnosis of concrete dams using hybrid FWA with RBF-based surrogate model. *Water Sci. Eng.* **2019**, *12*, 188–195. [CrossRef]
14. Durantin, C.; Rouxel, J.; Désidéri, J.-A.; Glière, A. Multifidelity surrogate modeling based on radial basis functions. *Struct. Multidiscip. Optim.* **2017**, *56*, 1061–1075. [CrossRef]
15. Yan, C.; Shen, X.; Guo, F. An improved support vector regression using least squares method. *Struct. Multidiscip. Optim.* **2017**, *57*, 2431–2445. [CrossRef]
16. Hamed, Y.; Alzahrani, A.I.; Shafie, A.; Mustaffa, Z.; Ismail, M.C.; Eng, K.K. Two steps hybrid calibration algorithm of support vector regression and K-nearest neighbors. *Alex. Eng. J.* **2020**, *59*, 1181–1190. [CrossRef]
17. Keshtegar, B.; Mert, C.; Kisi, O. Comparison of four heuristic regression techniques in solar radiation modeling: Kriging method vs RSM, MARS and M5 model tree. *Renew. Sustain. Energy Rev.* **2018**, *81*, 330–341. [CrossRef]
18. Liu, B.; Zhang, Q.; Gielen, G. A Gaussian Process Surrogate Model Assisted Evolutionary Algorithm for Medium Scale Expensive Optimization Problems. *IEEE Trans. Evol. Comput.* **2014**, *18*, 180–192. [CrossRef]
19. Zhou, Y.; Lu, Z. An enhanced Kriging surrogate modeling technique for high-dimensional problems. *Mech. Syst. Signal. Process.* **2020**, *140*, 106687. [CrossRef]
20. Fu, C.; Wang, P.; Zhao, L.; Wang, X. A distance correlation-based Kriging modeling method for high-dimensional problems. *Knowl. Based Syst.* **2020**, *206*, 106356. [CrossRef]
21. Chen, L.; Qiu, H.; Gao, L.; Jiang, C.; Yang, Z. A screening-based gradient-enhanced Kriging modeling method for high-dimensional problems. *Appl. Math. Model.* **2019**, *69*, 15–31. [CrossRef]
22. Bouhlel, M.A.; Martins, J. Gradient-enhanced kriging for high-dimensional problems. *Eng. Comput.* **2019**, *35*, 157–173. [CrossRef]
23. Hajikolaei, K.H.; Wang, G.G. High Dimensional Model Representation With Principal Component Analysis. *J. Mech. Des.* **2013**, *136*, 011003. [CrossRef]
24. Lataniotis, C.; Marelli, S.; Sudret, B. EXTENDING CLASSICAL SURROGATE MODELING TO HIGH DIMENSIONS THROUGH SUPERVISED DIMENSIONALITY REDUCTION: A DATA-DRIVEN APPROACH. *Int. J. Uncertain. Quantif.* **2020**, *10*, 55–82. [CrossRef]
25. Martin, J.D. Computational Improvements to Estimating Kriging Metamodel Parameters. *J. Mech. Des.* **2009**, *131*, 084501. [CrossRef]
26. Martin, J.D.; Simpson, T.W. Use of kriging models to approximate deterministic computer models. *AIAA J.* **2005**, *43*, 853–863. [CrossRef]
27. Chauhan, D.; Mathews, R. *Review on Dimensionality Reduction Techniques*; Springer International Publishing: Cham, Switzerland, 2020; Volume 49, pp. 356–362.
28. Tang, B. Latin Hypercube Designs. In *Encyclopedia of Statistics in Quality and Reliability*; Wiley: Hoboken, NJ, USA, 2008.
29. Bouhlel, M.A.; Bartoli, N.; Otsmane, A.; Morlier, J. An Improved Approach for Estimating the Hyperparameters of the Kriging Model for High-Dimensional Problems through the Partial Least Squares Method. *Math. Probl. Eng.* **2016**, *2016*, 1–11. [CrossRef]

30. Bouhlel, M.A.; Bartoli, N.; Otsmane, A.; Morlier, J. Improving kriging surrogates of high-dimensional design models by Partial Least Squares dimension reduction. *Struct. Multidiscip. Optim.* **2016**, *53*, 935–952. [CrossRef]
31. Vehtari, A.; Gelman, A.; Gabry, J. Practical Bayesian model evaluation using leave-one-out cross-validation and WAIC. *Stat. Comput.* **2017**, *27*, 1413–1432. [CrossRef]

mathematics

MDPI

Article

Trochoidal Milling Path with Variable Feed. Application to the Machining of a Ti-6Al-4V Part

César García-Hernández [1,*], Juan-José Garde-Barace [2], Juan-Jesús Valdivia-Sánchez [2], Pedro Ubieto-Artur [1], José-Antonio Bueno-Pérez [3], Basilio Cano-Álvarez [4], Miguel-Ángel Alcázar-Sánchez [4], Francisco Valdivia-Calvo [2], Rubén Ponz-Cuenca [5], José-Luis Huertas-Talón [1,2] and Panagiotis Kyratsis [6]

[1] Department of Design and Manufacturing Engineering, University of Zaragoza, 50018 Zaragoza, Spain; pubieto@unizar.es (P.U.-A.); jhuertas@unizar.es (J.-L.H.-T.)
[2] CPIFP "Corona de Aragón", 50009 Zaragoza, Spain; garde.juanjose@cpicorona.es (J.-J.G.-B.); valdivia.juanjesus@cpicorona.es (J.-J.V.-S.); fvaldivia@educa.aragon.es (F.V.-C.)
[3] IES "Jaume Huguet", 43800 Tarragona, Spain; jbueno@xtec.cat
[4] CIFP "Virgen de Gracia", 13500 Ciudad Real, Spain; basilio@cifpvirgendegracia.com (B.C.-Á.); miguelangel.alcazar@cifpvirgendegracia.com (M.-Á.A.-S.)
[5] Marena, S.L., 50171 Zaragoza, Spain; ruben.ponz@marenasl.com
[6] Department of Industrial Design Engineering, University of Western Macedonia, GR 50100 Kozani, Greece; pkyratsis@uowm.gr
* Correspondence: garcia-hernandez.cesar@unizar.es

Abstract: Trochoidal milling is a well-stablished machining strategy which still allows for the introduction of new approaches. This strategy can be applied to any kind of material, although it is usually associated to advanced materials, such as titanium and nickel alloys. This study is based on the adaptation of the feed speed of a milling tool with Ti-6Al-4V, so the chip width can be maintained constant without modifying the path geometry. A singularity in the experimental stage was to mill an Archimedes spiral groove instead of the conventional straight grooves. This made it possible to obtain a concave wall as well as a convex one and to optimize the amount of material used. The time efficiency compared to a constant feed, was slightly superior to 20%, reducing tool wear also. These techniques require milling machines with high mechanical and kinematic performance, as well as the absence of clearance between joints and a high acceleration capacity.

Keywords: trochoidal milling; variable feed; spiral groove; CAM

Citation: García-Hernández, C.; Garde-Barace, J.-J.; Valdivia-Sánchez, J.-J.; Ubieto-Artur, P.; Bueno-Pérez, J.-A.; Cano-Álvarez, B.; Alcázar-Sánchez, M.-Á.; Valdivia-Calvo, F.; Ponz-Cuenca, R.; Huertas-Talón, J.-L.; et al. Trochoidal Milling Path with Variable Feed. Application to the Machining of a Ti-6Al-4V Part. *Mathematics* **2021**, *9*, 2701. https://doi.org/10.3390/math9212701

Academic Editor: Camelia Petrescu

Received: 27 September 2021
Accepted: 22 October 2021
Published: 25 October 2021

Publisher's Note: MDPI stays neutral with regard to jurisdictional claims in published maps and institutional affiliations.

Copyright: © 2021 by the authors. Licensee MDPI, Basel, Switzerland. This article is an open access article distributed under the terms and conditions of the Creative Commons Attribution (CC BY) license (https://creativecommons.org/licenses/by/4.0/).

1. Introduction

The main objective of trochoidal milling is to use all the effective tool length in order to make the cut [1]. The cutting force on the tool depends on the chip section and produces the tool flection; furthermore, the cutting power is proportional to the cutting force. A similar cutting force can appear due to the elimination of a large chip width a_e and a small axial depth of cut a_p, or the removal of a small chip width and a large axial cut, Figure 1.

The force application point on the right of Figure 1 is more distant from the handle clamp, so the flection torque is bigger and the breaking probability increases.

This justifies the increase of a_p as much as possible, due to its limited influence [2] in tool wear and surface quality [3]. The reduction of a_e produces a decrease of the chip width, reducing heat generation and improving tool wear.

In this study, the values of the a_p are equal to triple the tool diameter, while a_e is almost 0.06D, which can be considered as finishing conditions, allowing cutting speeds over 90 m/min. The decrease of tool wear facilitates the possibility of using sharper cutting edges (less cutting force). Those cutting edges are micro-rounded in order to raise their robustness, Figure 2.

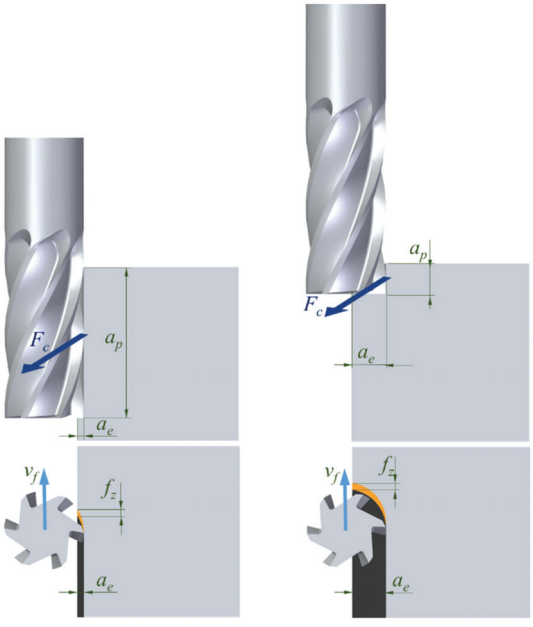

Figure 1. Relation between a_p and a_e for the same section.

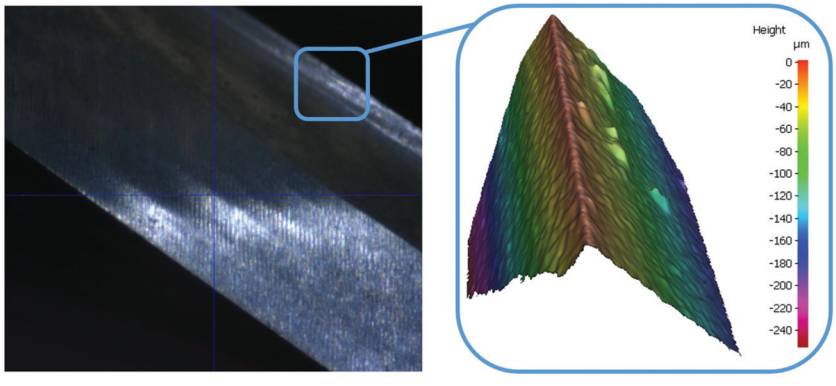

Figure 2. Micro-rounded mill cutting edge.

In theory, for the same values of the chip section ($a_p \times a_e$), the number of passes required to complete the machining would be the same. Nevertheless, if the chip width decreases there are new advantages:

- The tooth gap can be smaller for the same feed (the chip width is reduced), so more teeth can be implemented and, for the same feed per tooth, the final feed rises and, as a result, the machining time decreases.
- As a consequence, the mill core has a wider section, being able to support bigger flection and torque forces, Figure 3. This bigger rigidity makes possible to decrease deformation and vibrations, being more suitable for materials with superior cutting requirements [4], such as titanium and nickel alloys.

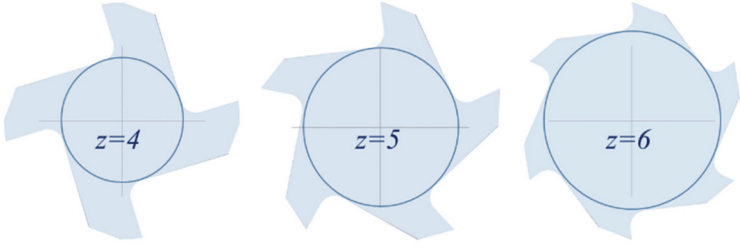

Figure 3. For the same tool diameter, with more teeth, there is a tool core increase.

Figure 1 shows a straight peripheral milling, which could also follow a curved path, as in trochoidal milling, being internally generated. The chip widths are different, as shown in Figures 4 and 5. There are three different kinds of feed per tooth, which are coincident in straight milling.

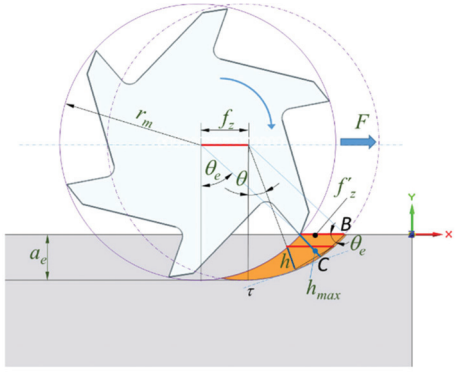

Figure 4. Engagement angle and chip thickness in lineal path.

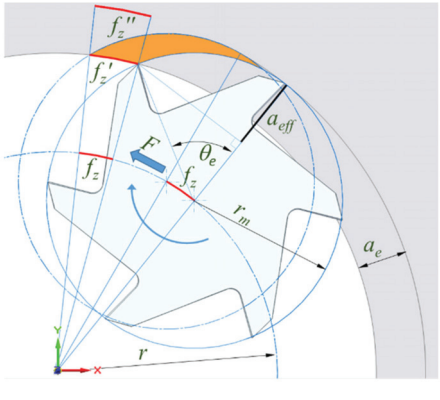

Figure 5. Engagement angle and chip depth in the interior arch.

The engagement angle, θ_e, is an important parameter in peripheral millings. Different studies [5–7] have been based on determining this parameter and maintaining it constant.

2. Materials and Methods

2.1. Selection of the Radial Cut Depth

The radial cut depth was selected as a parameter for the trochoidal milling. The chip thickness, h, is a parameter that tool manufacturers use [8–10]. The process to obtain this parameter has been previously published in different classical books [11–14]; nevertheless, it has been mentioned below in order to clearly establish the approximations adopted in this study.

Parameters θ_e and h are clearly related, as shown in Figure 4, considering the maximum chip thickness and approximating the CB chord to the tangent in B. This approximation is valid because the feed per tooth, f_z, is small in comparison to the mill dimensions. In this case, the feed per tooth, f'_z, on the milling surface, is equal to the feed per tooth, f_z, in the centre of the mill:

$$\sin\theta_e = \frac{h_{max}}{f_z{}'} \tag{1}$$

$$\cos\theta_e = \frac{r_m - a_e}{r_m} \tag{2}$$

Converting the cosine in sine and replacing (2) in (1):

$$\sqrt{1 - \left(1 + \left(\frac{a_e}{r_m}\right)^2 - 2\frac{a_e}{r_m}\right)} = \frac{h_{max}}{f_z{}'} \tag{3}$$

Other aspects to take into account include:

- Considering that a_e is small in comparison to the milling tool radius r_m.
- Avoiding the use of the squared parenthesis. According to the previous aspect, it is not significant compared to the other equation terms.
- Using the milling tool diameter instead of the radius.

Finally, the previous expression (3), can be written as follows:

$$h_{max} = 2f_z{}'\sqrt{\frac{a_e}{D}} \tag{4}$$

Applying the mean value theorem to Equation (1), the mean thickness can be obtained:

$$h_m = 2\frac{f_z{}'a_e}{D\theta_e} \tag{5}$$

Which can also be written as:

$$h_m = f_z{}'\sqrt{\frac{a_e}{D}} \tag{6}$$

Milling tool manufacturers give the cutting values referring to the feed per tooth f_z, which is required to determine the feed:

$$F = f_z{\cdot}z{\cdot}N \tag{7}$$

For the straight milling path, $f_z = f_z{}'$.

In trochoidal milling, the path of the milling tool is not straight, but curved. The most frequent path describes a real trochoid, although other curves can be applied to maintain the engagement angle θ_e as constant as possible.

It is necessary to pay attention to the curved paths, noting that the most interesting path for this purpose is the interior (concave) path, as in Figure 5, where the curvature and depth are constant. The engagement angle is:

$$\cos\theta_e = \frac{r_m - a_{eff}}{r_m} \tag{8}$$

Equation (8) is similar to Equation (2), but includes the effective radial depth a_{eff}, which has a much higher value, compared to a_e. Furthermore, the feed per tooth and, therefore, the feed in (7) are different in the centre of the milling tool, which is the point to be programmed in the numeric control (NC) machine, and in the most external point (highest cut radius), as shown in Figure 5.

$$f_z = f_z{}'' \frac{r}{r + r_m} = f_z{}' \frac{r}{r + r_m - a_e} \tag{9}$$

Analysing Figures 4 and 5, it can be observed that:

- For the same feed in the milled part, the programmed feed must be lower in the interior tool path.
- According to Figure 5 and Equations (2) and (8), for the interior tool path, the engagement angle is higher for the same radial depth, a_e, as a_{eff} is larger than a_e.
- As the value of the feed per tooth is low in comparison to the milling tool dimensions, the arch of fz' is close to a straight line. Thus, the mean thickness can be approximated to the previous case, considering a_{eff} instead of a_e:

$$h_m = f_z{}' \sqrt{\frac{a_{eff}}{D}} \tag{10}$$

- As a_e is constant, the values of the engagement angle and the effective axial depth are constant. However, they are not constant in trochoidal milling.

Moreover, the following considerations must be taken into account:

- Avoiding an excessive decrease of the chip width, as the friction of the part with the tool edge increases, heat is generated [15]. On the contrary, the increase of the chip effective width causes a decrease of friction and cut pressure [16].
- The mean chip depth should not be decreased. For this reason, in this study, to let h_m be constant when a_{eff} varies, the feed per tooth fz' will be continuously modified.

In the experimental stage, f_z was selected according to the tool manufacturer's technical advice in relation to the straight-line peripheral milling for surface finishing. With that value in Equation (6), h_m can be obtained. This value makes it possible to obtain $f_z{}'$ in Equation (10). The instantaneous feed per tooth in the centre of the milling tool can be obtained with (9) for each instantaneous a_e.

The trochoidal path is similar to the case in Figure 5, although the axial depth a_e is not constant and, consequently, neither is a_{eff}. For this reason, the engagement angle θ_e is variable.

Figure 6 shows a simplified approximation of the trochoidal milling path as a series of semi-circular arches with a step equal to axial depth, with values from zero to a_{emax}.

The effective axial feed is considered the variable to be studied in the experimental stage. Its maximum value can be observed in Figure 7, when the first contact point of the milling tool is in line with the two centres (of trochoid arch and of milling tool).

The position angle γ of a point of the trochoidal path, referred to the axis of the rotation centre, will be obtained. It must be noticed that this is an approximation in which the maximum axial depth is much lower than the slot width, being as that the value of b equal to half of this slot width.

The goal is to determine the angle ωt (which is the position of the milling tool in the trochoidal path) and the maximum value of a_{eff}.

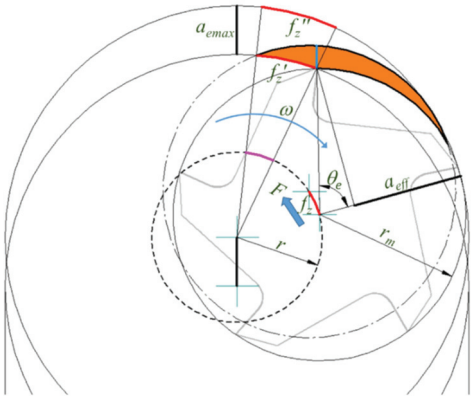

Figure 6. Trochoidal path approximation.

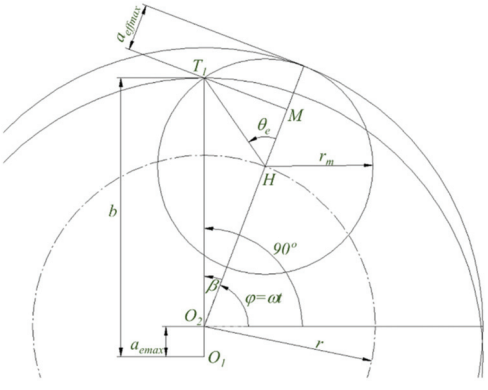

Figure 7. Instant in which a_{effmax} is reached.

In the triangle O_2HT_1, with $r = b - r_m$:

$$r_m{}^2 = (b - a_{emax})^2 + r^2 - 2(b - a_{emax})r\cos\beta$$

$$\cos\beta = \frac{(b - a_{emax})^2 + r^2 - r_m{}^2}{2(b - a_{emax})r} \tag{11}$$

$$\varphi_{aeffmax} = \frac{\pi}{2} - \cos^{-1}\left(\frac{(b - a_{emax})^2 + r^2 - r_m{}^2}{2(b - a_{emax})r}\right) \tag{12}$$

$$O_2M = (b - e_{emax})\cos\beta$$
$$a_{effmax} = b - O_2M$$

$$a_{effmax} = b - \frac{(b - a_{emax})^2 + r^2 - r_m{}^2}{2r} \tag{13}$$

Figure 8 shows the calculation of the effective radial depth a_{eff}. To do so, there are two possibilities: using analytic geometry or trigonometry. In both cases, the coordinate origin is placed in O_2.

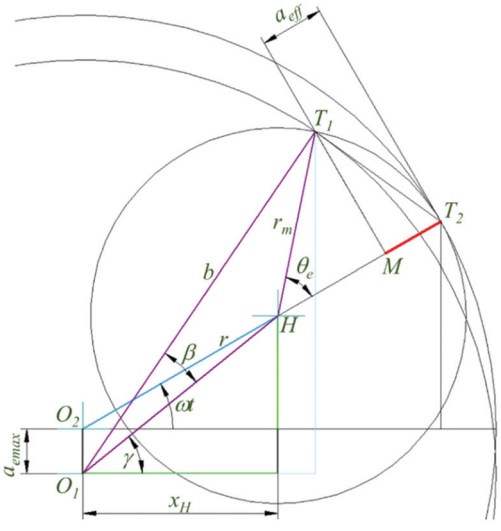

Figure 8. Obtaining the effective radial depth.

For the first method, solving equations with the centre in O_1 and in H, T_1 is obtained.

$$\left.\begin{array}{c} x^2 + (y - a_{emax})^2 = b^2 \\ (x - r\cos\omega t)^2 + (y - r\sin\omega t) = {r_m}^2 \end{array}\right\} \Rightarrow \left\{\begin{array}{l} x_{T1} = x \\ y_{T1} = y \end{array}\right. \tag{14}$$

Solving equations of the circles with centres in O_2 and H, T_2 can be obtained:

$$\left.\begin{array}{c} x^2 + y^2 = b^2 \\ (x - r\cos\omega t)^2 + (y - r\sin\omega t)^2 = {r_m}^2 \end{array}\right\} \Rightarrow \left\{\begin{array}{l} x_{T2} = x \\ y_{T2} = y \end{array}\right. \tag{15}$$

The coordinates of M can be obtained with the equation of the straight line which contains O_2 and T_2, intersected with the line which contains T_1 and is perpendicular to the previous one:

$$\left.\begin{array}{c} y = \frac{y_{T2}}{x_{T2}} x \\ y = y_{T1} + \frac{-x_{T2}}{y_{T2}}(x - x_{T1}) \end{array}\right\} \Rightarrow \left\{\begin{array}{l} x_M = x \\ y_M = y \end{array}\right. \tag{16}$$

Now, the effective width MT_2 can be obtained:

$$a_{eff} = \sqrt{(x_{T2} - x_M)^2 + (y_{T2} - y_M)^2} \tag{17}$$

It is important to consider the double solutions of (14) and (15) in the change of quadrant, as well as the divisions by zero in (16).

The second method is based on the application of trigonometry:

$$O_1T_1 = O_2T_2 = b$$

$$x_2 = b\cos\omega t \quad y_2 = b\sin\omega t \tag{18}$$

$$O_2H = O_2T_2 - HT_2 = r = b - r_m$$

$$x_H = (b - r_m)\cos\omega t \quad y_H = (b - r_m)\sin\omega t \tag{19}$$

$$O_1H = \sqrt{{x_H}^2 + (y_H + a_{emax})^2} \tag{20}$$

In the triangle O_1HT_1, the cosine theorem is applied:

$$r_m{}^2 = b^2 + O_1H^2 - 2b{\cdot}O_1H{\cdot}\cos\beta$$

$$\cos\beta = \frac{b^2 + O_1H^2 - r_m{}^2}{2b{\cdot}O_1H} \tag{21}$$

$$\cos\gamma = \frac{x_H}{O_1H} \tag{22}$$

The coordinates of point T_1 are determined as follows:

$$\begin{aligned} x_1 &= b{\cdot}\cos(\gamma+\beta) \\ y_1 &= b{\cdot}\sin(\gamma+\beta) - a_{emax} \end{aligned} \tag{23}$$

The side T_1T_2 of the triangle T_1HT_2:

$$T_1T_2 = \sqrt{(x_2-x_1)^2 + (y_2-y_1)^2} \tag{24}$$

The engagement angle is obtained with the cosine theorem in the isosceles triangle T_1HT_2:

$$T_1T_2{}^2 = r_m{}^2 + r_m{}^2 - 2r_m{\cdot}r_m{\cdot}\cos\theta_e \tag{25}$$

$$\cos\theta_e = 1 - \frac{T_1T_2{}^2}{2r_m{}^2} \tag{26}$$

With this, the segment HM is:

$$HM = r_m\cos\theta_e$$

And the effective radial depth can be obtained:

$$a_{eff} = HT2 - HgM = r_m(1-\cos\theta_e) \tag{27}$$

A different method, based in parametric CAD, was applied with Solid Edge™, as shown in Figure 9, with the values of the angle ωt from a table of variables and a spreadsheet. This method was important to verify the results of the two previous calculations.

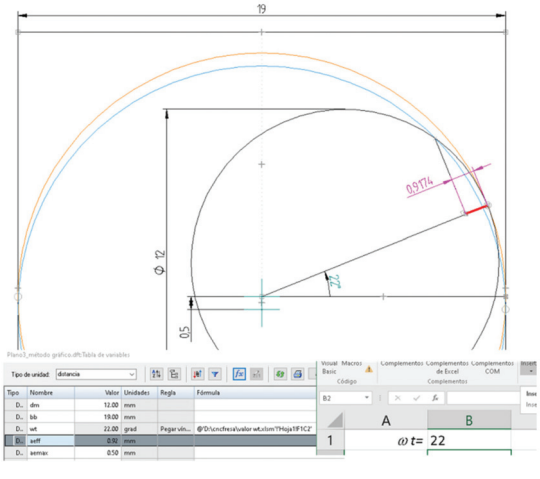

Figure 9. Graphical method to verify a_{eff}.

In the NC program, the feed was variable in order to maintain constant the value of the chip width, improving the process efficiency [17]. This variation in the feed F is possible thanks to the kinematics of the milling machines and the NC, which can process large numbers of program lines [18], such as the was used in this case.

Finally, the trigonometry-based method was chosen to simplify implementation in the NC programming. This option made it possible to avoid divisions by zero or considering double solutions, as previously detailed.

2.2. NC Program of a Trochoid with Adaptive Feed

The trochoidal path [19] described by the centre of the milling tool is the combination of two simultaneous movements. Figure 10 shows a circular path with radius r and a straight movement with a speed v.

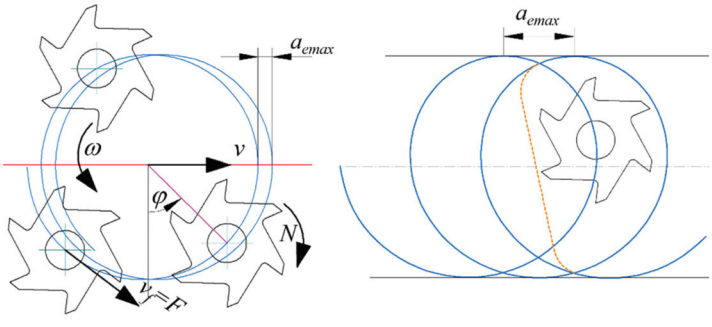

Figure 10. Generation of the straight-line path.

The movement of the milling tool centre is a straight line, but this carrier route can be any 2D or 3D curve. Finally, the straight-line path will be transformed into an Archimedes spiral.

To decrease the processing time, the in and out paths are usually modified to shorten the milled area with a straight line (with initial and final tangential arches) at a higher feed [20].

The described angle depends on the angular speed ω at which the centre of the milling tool plots the circular path which, if the value of ω is constant, is $\varphi=\omega t$. This value of ω can be variable, as analysed below:

The feed of the tool should be adapted to the chip thickness for each instant. When the chip thickness is the maximum, the feed is the minimum (this is similar to a progressive entry, but without constant slope), as shown in Figure 11. In the following segment of the turn, the feed of the milling tool is at the minimum at the beginning and progressively increases until reaching its maximum value as a function of the effective depth.

The previous variation is not lineal. The maximum value of the effective radial depth is in Equation (12). Its variation depends on Equation (27), following the steps between Equations (18) and (26). The graph displayed in Figure 12 was obtained with the following values: b = 0.5 mm, D_m = 12 mm, a_{emax} = 0.5 mm. The maximum value of the effective radial depth is 1.32 mm, and the corresponding ωt angle is 65.3°.

Equations for the straight trochoidal path, with constant feed, are developed below. These equations will be the base for adapting the feed and transform the straight path into a spiral trajectory.

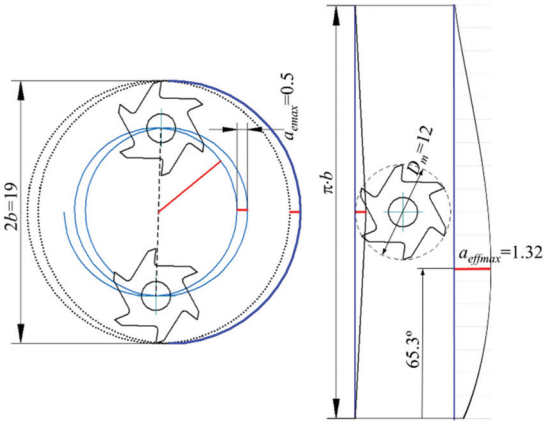

Figure 11. Equivalence between trochoidal and peripheral ramp milling with variable slope.

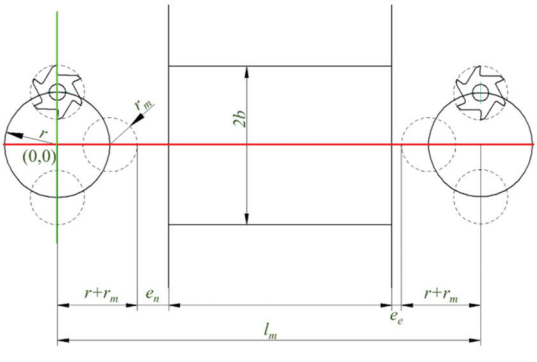

Figure 12. Milling time calculation.

The angular speed ω, is obtained from the feed per tooth f_z, the number of teeth z, the cutting speed V_c and the milling tool diameter D_m. The rotation frequency of the milling tool is:

$$N = \frac{1000V_c}{\pi D} \tag{28}$$

The feed of the cutter on the path:

$$v_f = f_z \cdot z \cdot N \tag{29}$$

This feed is also the tangential speed of the tool centre path, so:

$$v_f = \omega \cdot r \rightarrow \omega = \frac{v_f}{r} = \frac{f_z \cdot z \cdot N}{r} \tag{30}$$

Units can be found in the initial variable table.
The rotated angle is:

$$\varphi = \omega \cdot t \tag{31}$$

For the time, T, required for the tool centre to describe a complete rotation ($\varphi = 2\pi$), the simultaneous lineal movement of the path must trace the maximum radial depth ae_{max}.

$$T = \frac{ae_{max}}{v} = \frac{2\pi}{\omega} \rightarrow v = \frac{\omega}{2\pi} ae_{max} \tag{32}$$

Replacing the ω of Equation (30) in (32):

$$v = \frac{f_z \cdot z \cdot N \cdot ae_{max}}{2\pi \cdot r} \tag{33}$$

With all this, it is possible to obtain the trochoidal path equation, depending on the milling parameters, by combining the lineal and rotational movements:

$$\begin{array}{c} x = vt + r\cos(\omega t + \varphi_0) \\ y = r\sin(\omega t + \varphi_0) \end{array} \tag{34}$$

Time goes from 0 to a final value t_f (Figure 12):

$$t_f = \frac{l_m}{v} \tag{35}$$

The time increase to obtain the points (x, y) that define the tool centre path can be calculated from the maximum chordal error [21]. The objective is to replace arches by segments by means of the G1 command for lineal interpolation, as well as by the activation of the high-speed functions in the NC.

When the arch of the trochoid, traced by the tool edge, is approximated to a circumference arch (Figure 13):

$$\Delta\varphi = 2\cos^{-1}\left(1 - \frac{e}{r + r_m}\right) \tag{36}$$

Obtaining:

$$\Delta t = \frac{\Delta\varphi}{\omega} \qquad 0 < t < t_f \tag{37}$$

The obtained points will be used to establish the feed in every segment. Thus, Equations (29)–(35) depend on mean feed, although for each time increment (37) there is a specific feed value, v_f, which provides a different v for each φ.

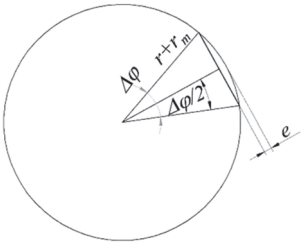

Figure 13. Polygonal approximation of the circumference.

Previous equations were programmed using MS Excel™ and Visual Studio™, obtaining higher processing speeds with the latter. The cutting parameters were established according to the technical advice in two manufacturer's websites: Sandvik™ [22] and Seco™ [23]. The depth value was increased up to 35 mm for a 12 mm milling tool, with an effective cutting length of 36 mm, according to the indications of the local manufacturer (Marena, S.L., Zaragoza, Spain). This made it possible to test the performance of the milling tool in a 19 mm wide groove (so the radius of the trochoidal arch is 3.5 mm).

Instead of the total straight path, a single period is traced in order to use, for each interval between points, a different feed (10) with an effective thickness (27).

Equation (37) was not considered due to the variable values of feed, because the angular movement was not constant. The process was:

- The points that define a step of the trochoidal path were obtained using (36).
- ω was obtained from (30), using the feed f_z for peripheral milling.

- Introducing the previous values of $\Delta\varphi$ and ω in (37), Δt is obtained.
- With (33), v is obtained.
- Using (34), the coordinates of the trochoidal arc (0 to π) were obtained, with $\Delta\varphi$.
- For each of the previous coordinates (x, y), the effective chip width was obtained (27).
- The mean value of chip width was obtained from (6), for the peripheral milling, with $a_e = a_{emax}$.
- With (10), the value of f'_z can be found.
- As the cut is interior, Equation (11) makes it possible to find the corrected f_z for each point. When a_{effmax} is reached, f_z is at the minimum, being maximum in the trochoid limits (Figure 11).
- Finally, rotation (38) and translation are applied to the points obtained in the previous step. This step is described below.

The two reasons to mill a spiral groove (Figure 14) are:

- The cost of a cylinder (∅ = 183 mm) of Ti-6Al-4V was significantly lower than a rectangular plate. In fact, the local provider had a leftover, which made it more affordable.
- The milled part has concave and convex walls. While the values of the radius of these walls are not constant, this situation is closer to reality and can be consider a novelty compared to previous tests with trochoidal milling [24–27].

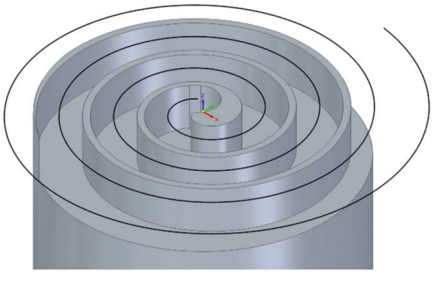

Figure 14. Spiral groove.

The point with coordinates (x_i, y_i) belongs to the arch of one of the trochoidal steps (Figure 15). A rotation is applied to this point:

$$\begin{aligned} xp_i &= x_i \cos\tau - y_i \sin\tau \\ yp_i &= x_i \sin\tau + y_i \cos\tau \end{aligned} \tag{38}$$

The rotation is given by the direction τ, which is tangent to the spiral path, Figure 16. After this rotation, a translation is applied to the spiral point (x_s, y_s), where the tangent was obtained.

The coordinates of the point S (x_s, y_s) are:

$$\begin{aligned} x_s &= k\phi_s \cos\phi_s \\ y_s &= k\phi_s \sin\phi_s \end{aligned} \tag{39}$$

The direction of the spiral tangent is obtained from:

$$\begin{aligned} dx_s &= \cos\phi_s - \phi_s \sin\phi_s \\ dy_s &= \sin\phi_s + \phi_s \cos\phi_s \end{aligned} \tag{40}$$

To obtain the direction of rotation, τ, the arc tangent of dy/dx must be calculated. It must be considered that a division by zero can be solved as follows:

```
Select Case dx
    Case 0
If dy > 0 Then τ = Pi/2 + Pi Else τ = -Pi/2 + Pi
    Case Else
τ = Math.Atan2(dy, dx) + Pi
End Select
```
(41)

It can be noticed that π has been added in the previous code, so when the spiral path is from the outside to the inside, the tangent direction is contrary to the one in Figure 16.

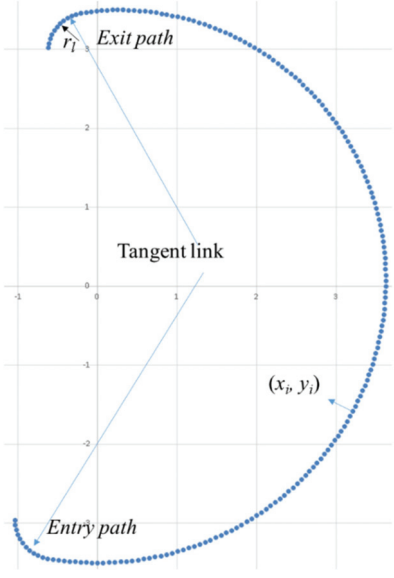

Figure 15. Trochoidal path step.

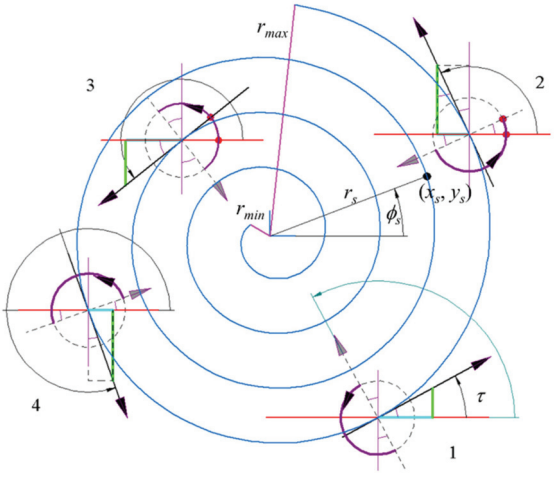

Figure 16. Rotation and translation for adapting the point (x_i, y_i) to the spiral path.

The Visual Net function ATAN2 made it possible to obtain the arc tangent and to distinguish the sign properly.

The entry and exit paths shown in Figure 15 are circular arches, where a value of the minimum radius depends on the acceleration performance of the machine [28], given by:

$$a_n = \frac{v_f}{{r_l}^2} = \frac{f_z \cdot z \cdot N}{{r_l}^2} \tag{42}$$

In order to avoid additional calculations, the entry and exit paths can be extended, as shown in Figure 17, following the same trochoidal path. From the exit, the maximum feed can be used (G0 can be too fast for some milling machines). In the entry point, the required feed is recovered.

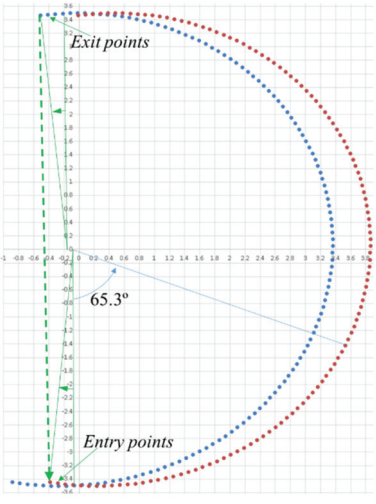

Figure 17. Extension of the entry and exit paths.

The essential points of the trochoidal path in Figure 15, in addition to those additional ones for the entry and exit, are previously calculated, storing their coordinates and feed (x, y, F) in numeric arrays. The entry and exit points are also stored with the assigned feed.

The next step would be distributing the points of the trochoid step along the spiral. Dividing the spiral length [29] by the step (a_{emax}) gives the number of the generated trochoidal arches. Several expressions can be used to define the length of the spiral arch. Applying differential calculus:

$$\Delta l_m = \frac{1}{2} k \left[\phi \sqrt{1+\phi^2} + \ln\left(\phi + \sqrt{1+\phi^2} \right) \right]_{\phi_i}^{\phi_e} \tag{43}$$

When the spiral step decreases, an approximated expression of this length can be deduced:

$$r_s = k\phi \tag{44}$$

Using the mean value of the radius:

$$r_m = \frac{r_i + r_e}{2} = k \frac{\phi_i + \phi_e}{2} \tag{45}$$

Multiplying the mean radius by the covered arch, the arch length can be obtained, approximating with:

$$\Delta l_m = \frac{k}{2} \left({\phi_e}^2 - {\phi_i}^2 \right) \tag{46}$$

The number of trochoidal arches is:

$$n_{sp} = \frac{\Delta l_m}{a_{emax}} \tag{47}$$

This solution was applied to the integer value plus one, because a verification of the accumulated length would make possible to stop calculations, not exceeding the value of Δl_m, obtained with (43).

From Equation (36), for a given value of the chordal error, the angle increment can be obtained. As the angle traced by the trochoid is π radians, the number of points (without entry and exit points) included in Figure 15 are:

$$n_t = \text{truncate}\left(\frac{\pi}{\Delta\varphi}\right) + 1 \tag{48}$$

In an open path, the number of the defined points is equal to the gaps plus one.

The entry and exit points are added to the previous ones (48), as shown in Figure 17.

$$\begin{aligned} n_i &= \text{truncate}\left(\tfrac{\varphi_i}{\Delta\varphi}\right) + 1 \\ n_o &= \text{truncate}\left(\tfrac{\varphi_o}{\Delta\varphi}\right) + 1 \end{aligned} \tag{49}$$

2.3. Practical Development

The trochoidal milling test was developed with a cylinder of titanium grade 5 with the previously mentioned dimensions. The initial cylinder was cut in three parts, with an appropriate saw, to develop the experimental stage using milling machines with the same features in three different vocational training centres, from Zaragoza, Valls and Puertollano (Spain), Figure 18.

Figure 18. One of the three NC milling machines.

The dimensions of the spiral groove and the working conditions for the peripheral milling were placed in a Visual Net form, Figure 19.

Intermediate calculations were obtained from Equation (46), making it possible to solve the final angle without any numerical approximation from the arch length and the initial angle. With this equation, a small error is generated.

For each point of the trochoidal path arch (Figures 16 and 18), the rotation of Equation (38) was obtained with:

- The substitution of angle φ_e (46).
- The substitution of the length increment Δl_m by the value of a_{emax} divided by the value obtained from (48).

The angle previously obtained is introduced again in (46), repeating the process until the spiral final angle.

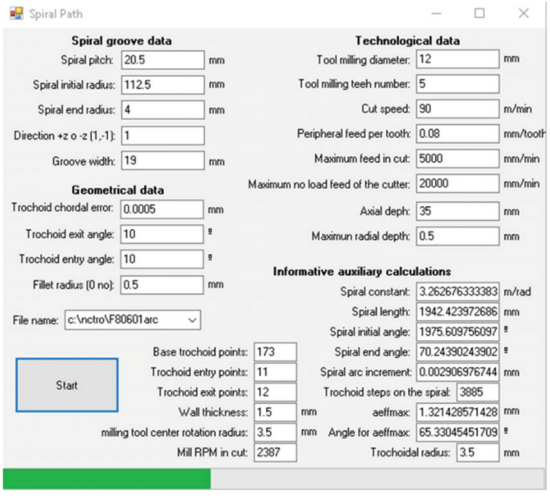

Figure 19. Visual Net data form.

3. Results

Before the milling stage, two different CAM dealers were asked for the roughing of a straight groove with the dimensions shown in Figure 19 and a length of 100 mm, applying trochoidal paths (Figure 20a,b). It was also developed by us, using two additional CAM (Figure 21). From these results, a complete trochoidal arch was isolated. The only restriction was to apply the *Y* axis as the milling direction.

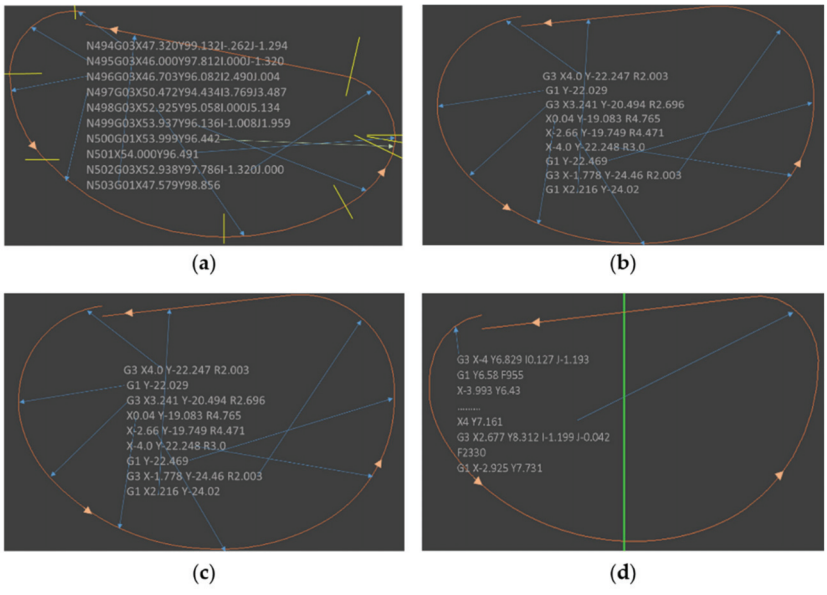

Figure 20. Four CAM trajectories applied.

These CAM codes make possible to identify when the milling tool is not cutting (highest feed) and it is cutting (recommended feed, which remains constant).

The geometry is similar with all the CAM codes, although they describe an elliptical trochoidal path, being the semi-axes of (b) and (d) oriented in the opposite direction to (a) and (c). The intention is to replace the position and the value of a_{effmax} and to decrease the value or $\varphi_{aeffmax}$.

(a) and (b) are based on circular arches, while (c) and (d) are described by a series of points, following the path.

(b) and (c) add two straight segments, in parallel to the milling direction, in order to improve the finishing.

The entry and exit paths are circular arches (G3) in all of the cases.

The slope and transformation of an elliptical trochoidal path was previously studied [30]. In this research, the elliptical trochoid was graphically analysed, as seen in Figures 9 and 21.

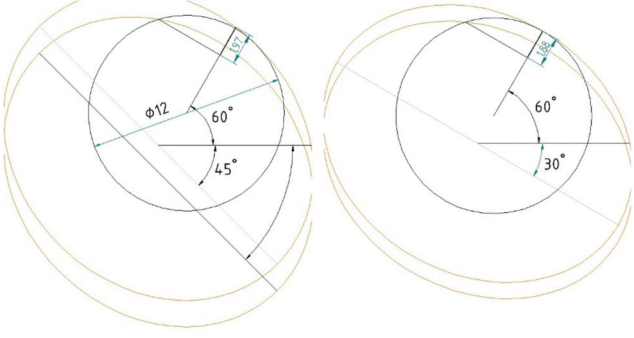

Figure 21. Graphical analysis obtaining of a_{eff} in an elliptical trochoidal path.

Figure 22 shows the variation of a_{eff} and the milling displacement angle with increments of 5°.

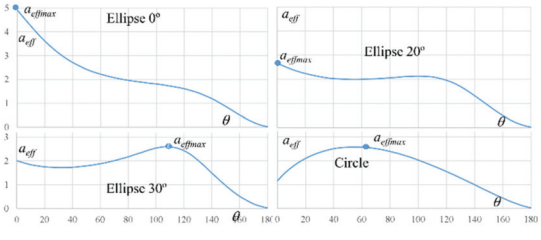

Figure 22. a_{eff} for the circular and elliptical trochoidal paths.

The 20° elliptical path keeps the value of a_{eff} more stable, being necessary to optimize its parameters [30,31]. However, the circular trochoidal path was tested, with the objective of studying the feed per tooth variation to maintain the chip thickness constant.

Figure 23 shows the path of the milling tool centre, combining Figures 15 and 16, thus extending the trochoidal arch and rounding entry and exit paths.

During the tests, the milling tool "marena 965" (Figure 24) was used [32], with z = 5 teeth, ∅ = 12 mm, maximum cutting length = 36 mm. The cutting speed was 90 m/min and the feed was 0.08 mm/tooth for peripheral milling, with a_e = 0.5 mm and p = 35 mm. With these conditions, the spiral path was milled several times with three similar machines (Figure 17).

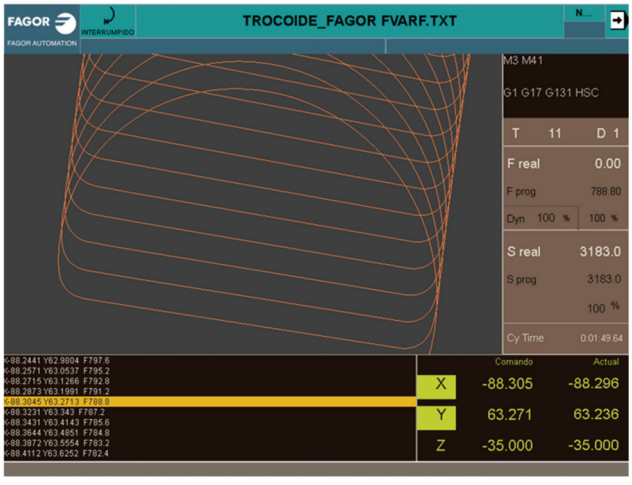

Figure 23. Trochoidal roughing adapted to a spiral groove.

Figure 24. Milling tool used in the experiments.

Figure 25 shows the path in the NC display (FAGOR 8060^{TM}).

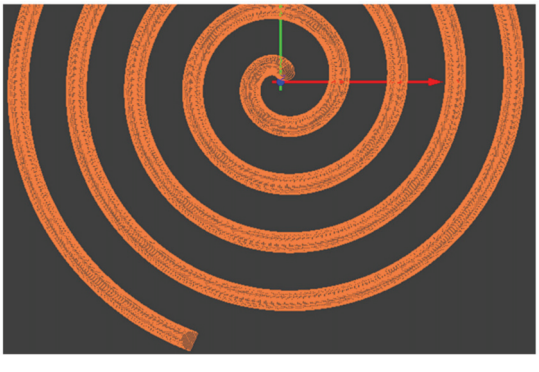

Figure 25. Trochoidal-spiral path.

Figure 26 shows the real spiral after milling it (left), and the initial (a), intermediate (b) and final (c) Titanium chips.

Figure 26. One of the milling processes and types of chips (**a**–**c**).

Finally, Figures 27 and 28 show the tool wear obtained with constant F and with variable F, respectively.

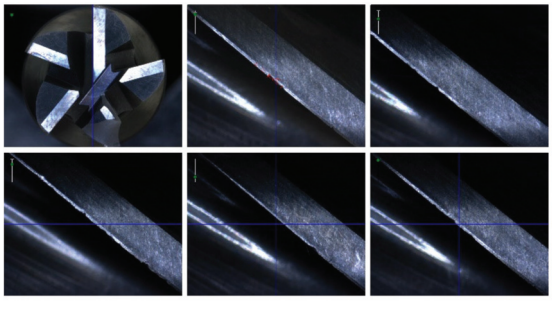

Figure 27. Tool wear for constant F.

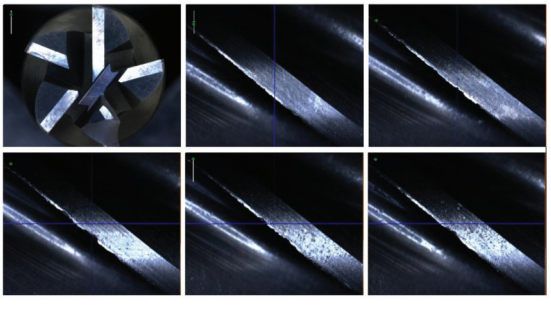

Figure 28. Tool wear for variable F.

4. Discussion

As shown in Figure 22, the 20° elliptical path can be interesting because a_{eff} stays more stable, although its value is higher, decreasing the feed per tooth. In contrast, the 0° elliptical path starts with a high value of a_{eff}, making it necessary to decrease the feed per tooth, although it could be increased at the exit.

The circular trochoidal path was chosen because its initial a_{eff} is not high, obtaining its maximum value before tracing the centre of the semitrochoid. The feed per tooth has a high value at the entry and decreases until a_{effmax} and, after it, its value increases to the exit. From the exit to the following entry, the feed value can be significantly increased.

After analysing references [30] and [31], it would be interesting to test these new paths by varying the *F* in further research.

The tool holders must be hydraulic, particularly when the loads are high or the feeds vary a lot during the milling process, because other kinds of tool holders (e.g.,: Weldon or clamps) were not able to maintain the position of the tool.

In both milling processes, a frontal tool tooth was broken (Figures 27 and 28). The tool wear was slightly lighter with variable *F* and the tool coating was not peeled in any case. The diameter deviation between teeth, before and after the milling, was below 5 micrometres.

The milling process with variable *F*, even adapting S [28,32], suggests improvements which should be tested in further research.

An additional possibility would be elevating the milling tool in the exit points (helicoidally), descending in the entry points (Figures 15 and 17). This possibility was not implemented, according to the tool manufacturer indications (to avoid stress in the *Z* spindle and the entrapment of chip residues).

5. Conclusions

The machining time with the conditions shown in Figure 19, was 1 h 17 min with constant *F*, and 51 min with variable *F*. When the cutting speed was raised to 100 m/min and the feed per tooth was 0.07 mm, the machining times were 1 h 36 min and 59 min, respectively.

The wear of the tool edge decreases with the variable *F* strategy.

Finally, it was concluded that the variable *F* strategy was advantageous, but it can only be applied with milling machines that allow high acceleration of their axes (*X*, *Y*).

It is possible to reduce the energy consumption as well as the time required, increasing tool life and improving the sustainability of machining processes, thanks to several aspects. These aspects include the improved features of current machine tools, new machining strategies and advances in tool cooling, e.g., using cryogenic products [33] with phase change. It is also possible to use cryogenic cooling to improve the effectiveness of lubrication [34,35], significantly reducing the quantity required. Another interesting option is based on adding nanoparticles [36] to reduce tool wear or by locally applying a process of laser preheating [37].

Author Contributions: Conceptualization, C.G.-H., P.U.-A., J.-L.H.-T. and P.K.; methodology, C.G.-H., J.-J.G.-B., J.-J.V.-S., P.U.-A., J.-L.H.-T. and P.K.; software, J.-L.H.-T.; validation, C.G.-H., J.-J.G.-B., J.-A.B.-P., B.C.-Á., M.-Á.A.-S., F.V.-C., R.P.-C. and J.-L.H.-T.; formal analysis, C.G.-H. and J.-L.H.-T.; investigation, C.G.-H., P.U.-A., J.-A.B.-P., B.C.-Á., M.-Á.A.-S., F.V.-C., J.-L.H.-T. and P.K.; resources, J.-J.G.-B.; data curation, C.G.-H. and J.-L.H.-T.; writing—original draft preparation, C.G.-H., J.-J.G.-B., J.-J.V.-S. and J.-L.H.-T.; writing—review and editing, C.G.-H., P.U.-A., R.P.-C., J.-L.H.-T. and P.K.; supervision, C.G.-H., J.-J.G.-B., J.-J.V.-S., P.U.-A., J.-A.B.-P., B.C.-Á., M.-Á.A.-S., F.V.-C., R.P.-C. and J.-L.H.-T.; project administration, J.-J.G.-B. and F.V.-C.; funding acquisition, J.-J.G.-B. and F.V.-C. All authors have read and agreed to the published version of the manuscript.

Funding: This research was funded by the Spanish "Secretaría de Estado de Educación y Formación Profesional" grant for applied innovation and knowledge transfer in vocational training: AFP 19/00017, 16 September 2019.

Data Availability Statement: All data generated or analysed during this study are included in this published article.

Acknowledgments: The authors want to thank the following: Pixel Sistemas, for the CAM code in Solid Edge CAM Pro; Hexagon, for the CAM code in EDGECAM; Students of the NC and CAM modules, for simulating the NC and CAM code during the remote (due to COVID-19) practical sessions; Kiomac S.L., for the technical advice; Ysamco S.L., for preparing the Ti6V4Al parts; Marena S.L., for facilitating the access to all the required milling tools and for the technical advice.

Conflicts of Interest: The authors declare no conflict of interest.

References

1. Harvey Tools. *Hem Guidebook a Machinist's Guide to Increasing Shop Productivity with High Efficiency Milling*; Harvey Performance Company, LLC: Rowley, MA, USA, 2017; Volume 9, pp. 38–40.
2. Pérez, J.; Llorente, J.I.; Sanchez, J.A. Advanced cutting conditions for the milling of aeronautical alloys. *J. Mater. Process. Technol.* **2000**, *100*, 1–11.
3. Okokpujie, I.P.; Okonkwo, U.C. Effects of cutting parameters on surface roughness during end milling of aluminium under minimum quantity lubrication (MQL). *Int. J. Sci. Res.* **2015**, *4*, 2937–2942.
4. Available online: https://www.harveyperformance.com/in-the-loupe/flute-count-matters/ (accessed on 7 May 2021).
5. Jacso, A.; Matyasi, G.; Szalay, T. The fast constant engagement offsetting method for generating milling tool paths. *Int. J. Adv. Manuf. Technol.* **2019**, *103*, 4293–4305. [CrossRef]
6. Choy, H.S.; Chan, K.W. A corner-looping based tool path for pocket milling. *Comput. Aided Des.* **2003**, *35*, 155–166. [CrossRef]
7. Wu, S.; Zhao, Z.; Wang, C.Y.; Xie, Y.; Ma, W. Optimization of toolpath with circular cycle transition for sharp corners in pocket milling. *Int. J. Adv. Manuf. Technol.* **2016**, *86*, 2861–2871. [CrossRef]
8. Masters in Solid Carbide Tooling. SCT Special Carbide Tooling. 2020; pp. 144–145. Available online: https://sct-tools.com/wp-content/uploads/2020/06/Catalog_2020_Downloads_SCT_Tools_.pdf (accessed on 7 May 2021).
9. 2017 Master Cataloge. WIDIA. pp. 1266–1272. Available online: https://s7d2.scene7.com/skins/Kennametal/A-15-04580_Master17_Catalog_Metric_LRpdf (accessed on 7 May 2021).
10. Trochoidal Shank End Mill with Variable Helix. S. v. Bassewitz GmbH & Co. KG (pp. 4 y 7). Available online: https://www.bassewitz.com/en/ (accessed on 7 May 2021).
11. Solar, Z.C. *Problemas de Tecnología de la Fresadora. Biblioteca Tecnológica de la Fabricación Mecánica*; Biblioteca Tecnológica de la Fabricación Mecánica: Gijón, Spain, 1970; p. 49.
12. Boothroyd, G. Fundamentos del corte de los metales y de las máquinas herramientas/. *Geoffrey Boothroyd. Mcgraw Hill. Lat. SA.* **1975**, *Book*, 29–37.
13. Micheletti, G.F.; Doménech, T.L. Mecanizado por arranque de viruta: Tecnología mecánica. *Blume* **1980**, *Book*, 150–153.
14. Peláez Vara, J. *La Fresadora. Colección La Máquina Herramienta (TOMO II)*; Ediciones CEDEL: Barcelona, Spain, 1992; pp. 43–44.
15. Richardson, D.J.; Keavey, M.A.; Dailami, F. Modelling of cutting induced workpiece temperatures for dry milling. *Int. J. Mach. Tools Manuf.* **2006**, *46*, 1139–1145. [CrossRef]
16. Rao, B.; Shin, Y.C. Analysis on high-speed face-milling of 7075-T6 aluminum using carbide and diamond cutters. *Int. J. Mach. Tools Manuf.* **2001**, *41*, 1763–1781. [CrossRef]
17. Perez, H.; Rios, J.; Diez, E.; Vizan, A. Increase of material removal rate in peripheral milling by varying feed rate. *J. Mater. Process. Technol.* **2008**, *201*, 486–490. [CrossRef]
18. Fagor Automation. Manual de Programación CNC 8060 8065. Available online: https://www.fagorautomation.com (accessed on 14 May 2021).
19. Otkur, M.; Lazoglu, I. Trochoidal milling. *Int. J. Mach. Tools Manuf.* **2007**, *47*, 1324–1332. [CrossRef]
20. Pleta, A.; Mears, L. Cutting force investigation of trochoidal milling in nickel-based superalloy. *Procedia Manuf.* **2016**, *5*, 1348–1356. [CrossRef]
21. Talón, J.L.H.; Boria, D.R.; Muro, L.B.; Gómez, C.L.; Zurdo, J.J.M.; Calvo, F.V.; Barace, J.J.G. Functional check test for high-speed milling centres of up to five axes. *Int. J. Adv. Manuf. Technol.* **2011**, *55*, 39–51. [CrossRef]
22. Sanvik Coromant. Fresado (PDF Format). pp. 121–122. Available online: https://www.sandvik.coromant.com/es-es/knowledge/milling/milling-holes-cavities-pockets/pages/slicing-trochoidal-milling.aspx (accessed on 21 May 2021).
23. Seco, Fresas Enterizas JABRO. (PDF Format), p. 420. Available online: https://usercontent.azureedge.net/Content/UserContent/Documents/027782.pdf (accessed on 21 May 2021).
24. Gross, D.; Friedl, F.; Meier, T.; Hanenkamp, N. Comparison of linear and trochoidal milling for wear and vibration reduced machining. *Procedia CIRP* **2020**, *90*, 563–567. [CrossRef]
25. Karkalos, N.E.; Karmiris-Obratański, P.; Kurpiel, S.; Zagórski, K.; Markopoulos, A.P. Investigation on the Surface Quality Obtained during Trochoidal Milling of 6082 Aluminum Alloy. *Machines* **2021**, *9*, 75. [CrossRef]
26. Waszczuk, K.; Skowronek, H.; Karolczak, P.; Kowalski, M.; Kołodziej, M. Influence of the Trochoidal Tool Path on Quality Surface of Groove Walls. *Adv. Sci. Technology. Res. J.* **2019**, *13*, 38–42. [CrossRef]
27. Santhakumar, J.; Iqbal, U.M. Role of trochoidal machining process parameter and chip morphology studies during end milling of AISI D3 steel. *J. Intell. Manuf.* **2021**, *32*, 649–665. [CrossRef]
28. Garde-Barace, J.J.; Huertas-Talón, J.L.; Valdivia-Calvo FBueno-Pérez, J.A.; Cano-Álvarez, B.; Álcazar-Sánchez, M.A.; Ponz-Cuenca, R.; Tzotzis, A. Velocidad de corte constante en fresado. *IMHE Ed. Técnicas IZARO* **2021**, *476*, 80–98.
29. Aguirre, N. La espiral de Arquímedes en un proyecto de modelación matemática. *Rev. Educ. Matemática* **2008**, *23*, 1–10.
30. Huang, X.; Wu, S.; Liang, L.; Li, X.; Huang, N. Efficient trochoidal milling based on medial axis transformation and inscribed ellipse. *Int. J. Adv. Manuf. Technol.* **2020**, *111*, 1069–1076. [CrossRef]
31. Klocke, F.; Bergs, T.; Busch, M.; Rohde, L.; Witty, M.; Cabral, G.F. Integrated approach for a knowledge-based process layout for simultaneous 5-axis milling of advanced materials. *Adv. Tribol.* **2011**, *2011*, 1–7. [CrossRef]
32. Käsemodel, R.B.; de Souza, A.F.; Voigt, R.; Basso, I.; Rodrigues, A.R. CAD/CAM interfaced algorithm reduces cutting force, roughness, and machining time in free-form milling. *Int. J. Adv. Manuf. Technol.* **2020**, *107*, 1883–1900. [CrossRef]

33. Huertas, J.L.; Faci, E.; Ros, E. CO_2, la mejor opción. *IMHE* **2006**, *330*, 59–78.
34. Jamil, M.; Zhao, W.; He, N.; Gupta, M.K.; Sarikaya, M.; Khan, A.M.; Sanjay, M.R.; Siengchin, S.; Pimenov, D.Y. Sustainable milling of Ti–6Al–4V: A trade-off between energy efficiency, carbon emissions and machining characteristics under MQL and cryogenic environment. *J. Clean. Prod.* **2021**, *281*, 1–14. [CrossRef]
35. Albertelli, P.; Mussi, V.; Strano, M.; Monno, M. Experimental investigation of the effects of cryogenic cooling on tool life in Ti6Al4V milling. *Int. Adv. Manuf. Technol.* **2021**. Available online: https://link.springer.com/article/10.1007%2Fs00170-021-07161-9#citeas (accessed on 21 May 2021).
36. Eltaggaz, A.; Nouzil, I.; Deiab, I. Machining Ti-6Al-4V Alloy Using Nano-Cutting Fluids: Investigation and Analysis. *J. Manuf. Mater. Process* **2021**, *5*, 42.
37. Kim, D.-H.; Lee, C.-M. Experimental Investigation on Machinability of Titanium Alloy by Laser-Assisted End Milling. *Metals* **2021**, *11*, 1552. [CrossRef]

mathematics

MDPI

Article

Numerical Solution to Anomalous Diffusion Equations for Levy Walks

Viacheslav V. Saenko [1,2,*], Vladislav N. Kovalnogov [1], Ruslan V. Fedorov [1,*] and Yuri E. Chamchiyan [1]

[1] Laboratory for Interdisciplinary Problems of Energy Reproduction, Ulyanovsk State Technical University, 32, Severny Venets St., 432027 Ulyanovsk, Russia; kvn@ulstu.ru (V.N.K.); y.chamchiyan@ulstu.ru (Y.E.C.)
[2] S.P. Kapitsa Scientific Research Institute of Technology, Ulyanovsk State University, 42, L. Tolstoy St., 432017 Ulyanovsk, Russia
* Correspondence: vvsaenko@inbox.ru (V.V.S.); r.fedorov@ulstu.ru (R.V.F.)

Abstract: The process of Levy random walks is considered in view of the constant velocity of a particle. A kinetic equation is obtained that describes the process of walks, and fractional differential equations are obtained that describe the asymptotic behavior of the process. It is shown that, in the case of finite and infinite mathematical expectation of paths, these equations have a completely different form. To solve the obtained equations, the method of local estimation of the Monte Carlo method is described. The solution algorithm is described and the advantages and disadvantages of the considered method are indicated.

Keywords: Levy walks; anomalous diffusion; fractional material derivative; combustion process; local estimate; Monte Carlo method

MSC: 58J65; 60J60; 60J70; 65C05

Citation: Saenko, V.V.; Kovalnogov, V.N.; Fedorov, R.V.; Chamchiyan, Y.E. Numerical Solution to Anomalous Diffusion Equations for Levy Walks. *Mathematics* **2021**, *9*, 3219. https://doi.org/10.3390/math9243219

Academic Editors: Camelia Petrescu and Valeriu David

Received: 20 November 2021
Accepted: 7 December 2021
Published: 13 December 2021

Publisher's Note: MDPI stays neutral with regard to jurisdictional claims in published maps and institutional affiliations.

Copyright: © 2021 by the authors. Licensee MDPI, Basel, Switzerland. This article is an open access article distributed under the terms and conditions of the Creative Commons Attribution (CC BY) license (https://creativecommons.org/licenses/by/4.0/).

1. Introduction

At present, the theory of anomalous diffusion is rarely used to describe the combustion processes of a substance, although there are all the prerequisites for this. For example, when a substance is burning, various kinds of turbulence are developing. As a result, the diffusion packet width $\Delta(t)$ stops obeying the law $\Delta(t) \propto t^{\gamma}$ with an exponent $\gamma = 1/2$ and starts growing with time by the law with an exponent $\gamma \neq 1/2$, which testifies to the appearance of anomalous diffusion. Signs of the appearance of anomalous diffusion at thermal transport in a low-dimensional system are indicated in the papers [1,2]. This assumption is also supported by experimental data. For example, in the work [3], the thermal radiation in the combustion chamber during the combustion of natural gas and acetylene was studied, depending on the level of fuel enrichment with oxygen. Time series analysis showed that the combustion process at any oxygen concentration is subdiffusive in nature.

The assumption about the formation of anomalous diffusion during the combustion of a substance allows us to introduce into consideration the fractional differential equations of anomalous diffusion. An effective coefficient of heat conductivity for the Levy–Fokker–Plank equation was obtained in the papers [4,5]. In the papers [6–8], to describe the combustion process, it is proposed to use the fractional differential equation of anomalous diffusion:

$$ {}_0D_t^{\beta} u = \partial_{xx} u + f(u), \quad t > 0, \quad 0 < x < L, \tag{1} $$

where ${}_0D_t^{\beta}$ is the fractional Riemann–Liouville derivative [9] of the order $0 < \beta < 1$ by time and ∂_{xx} is the classical particular derivative of the second order by coordinate. In the paper [10], a two-dimensional combustion model with a fractional time derivative was studied. To solve the obtained equation of diffusion, the authors develop an adaptive

finite-difference discontinuous Galerkin method. A modification of the Equation (1) in the case of the dependence of the diffusivity on temperature and relaxation time has been considered in the article [11]. In the papers [8,12], a fractional-differential combustion model with the first derivative with respect to time and a fractional derivative with respect to the spatial variable is considered:

$$\partial_t u = \frac{\partial^\alpha}{\partial |x|^\alpha} u + f(u), \quad u(x,0) = u_0(x), \quad u(a,t) = u(b,t) = 0. \tag{2}$$

Here, ∂_t is the partial time derivative, and $\frac{\partial^\alpha}{\partial |x|^\alpha}$ is the fractional-differential Riesz operator [9]. To solve this equation, a finite-difference scheme using an adaptive strategy is described in the papers [8,12]. In the paper [13], a fractional-differential generalization of the kinetic equation was obtained that describes the relationship between the radius of the ball and time in the model of the combustion of a fireball, theoretically predicted by the Soviet physicist Ya.B. Zeldovich [14].

However, when using the Equations (1) and (2), it should be kept in mind that they are based on the process of Continuous Time Random Walk (CTRW) [15–22]. This process assumes that a particle instantly moves from one point in space to another at a random distance $R_i, i = 1, 2, 3, \ldots$, and then rests at this point for a random time $T_i, i = 1, 2, 3, \ldots$ All these random values R_i and T_i are independent of each other and between one another and they are distributed by the laws $p_R(x) \propto x^{-\alpha-1}, x \to \infty$ and $q_T(t) \propto t^{-\beta-1}, t \to \infty$, respectively.

Depending on the value α, the path distribution has different properties. If $\alpha = 2$, then the distribution has finite mathematical expectation and variance, at $1 < \alpha < 2$, mathematical expectation is finite and variance is infinite, at $0 < \alpha \leqslant 1$ both mathematical expectation and variance are infinite. The instantaneousness of jumps means that, for an arbitrarily small time interval from the initial one, the particle can be at an arbitrarily large distance from the source. In some cases, this non-physical behavior of a particle does not lead to any contradiction with the experiment. For example, in the case of the normal diffusion ($\alpha = 2, \beta = 1$), when the distribution of paths and rest times have a finite variance, the process is described by the classical diffusion equation, the solution to which is expressed in terms of the normal distribution. It is well known that the normal distribution is nonzero on the entire number axis, which indicates the infinite velocity of the particle in the inherent walk model. However, in view of the finite variance of the distribution of paths, the infinite velocity of motion is compensated for by a small value of the paths. The situation is completely different in the case of anomalous diffusion. As the exponent α decreases, the probability of greater paths increases and at values $\alpha < 1$ this probability turns out to be significant. Therefore, it is necessary to use the anomalous diffusion model with a certain degree of caution, especially when considering problems with limited spatial geometry or processes limited in time, for example, to describe combustion processes in furnaces.

One of the ways to eliminate the difficulty described above is to introduce a constant final velocity of the particle. One of the first works in which a constant velocity of particle motion was introduced into the model of anomalous diffusion is the work [23]. In this paper, the authors called this model Levy walks. Further study of this model was carried out in the works [24–26]. The work [27] is devoted to the study of Levy walks in bounded and semi-bounded spaces. In the work [28], kinetic equations of anomalous diffusion with a finite velocity are obtained, the root-mean-square deviation is investigated, and an exact solution to the kinetic equation in the one-dimensional case is obtained. The work [29] is devoted to the study of statistical moments for the case of Levy random walks with a random finite velocity without traps, and the case of multidimensional walks with traps of arbitrary type with constant velocity is considered in the works and the case of multidimensional walks with traps of arbitrary type with constant velocity is considered in the works [30–33]. The work [34] examines the influence of the final velocity on the spatial distribution of particles in Levy walks with exponential traps. In this work, it

was found that, in the case $1 < \alpha \leqslant 2$, taking account of the constant velocity of particle motion is reduced to a decrease in the diffusion coefficient in the equation of anomalous diffusion (2). In the case $\alpha < 1$ distributions take *W*-like or *U*-like form and cannot be described by the Equation (2). The papers [35–37] study the process of Levy random walks without traps and it was shown that in the case of infinite mathematical expectation of the distribution of paths, the asymptotic distributions have *U*-like and *W*-like form. In the paper [38] an expression for current within framework of the Levy walks model was obtained. The obtained expression generalize the Fourier's law to the case of anomalous thermal transport for the Levy diffusion model.

The work [39] succeeded in addressing the problem of describing Levy random walks in the case $\alpha < 1$. In this work, it was shown that, in the case of an infinite mathematical expectation of the distribution of paths, to take account of the finite velocity, it is necessary to replace the fractional Laplacian in the equation of anomalous diffusion by a material derivative of a fractional order. Later, the authors of the works [40–44] come to the same conclusion. The solution to the equation of anomalous diffusion with a material derivative of the fractional order was obtained in the works [44–46]. In these works, it was shown that the solution to this equation is expressed in terms of the Lamperti distribution.

In this paper, we consider a method for the numerical solution to the equations of anomalous diffusion taking account of the constant finite velocity of the particle motion between collisions. The work is organized as follows. In Section 2, a kinetic equation describing the considered process of walks is derived. In Section 3, fractional differential equations and the solutions of these equations are obtained, describing the asymptotic (at $t \to \infty$ and $x \to \infty$) distribution of particles. It was shown that, in the case of an infinite mathematical expectation of the distribution of paths ($0 < \alpha < 1$) and finite mathematical expectation $1 < \alpha < 2$, the behavior of the process is described by completely different equations. In Section 4, a numerical method for solving the kinetic equation based on the method of local density estimation is considered.

2. Kinetic Equation of the Random Walk Process

To obtain the kinetic equation, we will use the approach proposed in the paper [28], which was developed in the paper [47]. We will consider the density of collisions $f(\mathbf{r}, \mathbf{p}, t)$, where $\mathbf{r}$ is the radius-vector of the particle, $\mathbf{p}$—is the particle momentum, t—is time. The value $f(\mathbf{r}, \mathbf{p}, t)d\mathbf{r}\,d\mathbf{p}\,dt$ is the number of collisions in the volume element $d\mathbf{r}$ of the vicinity of the point $\mathbf{r}$ for the interval of time dt, at which the momentum of the particle takes on a value from $\mathbf{p}$ to $\mathbf{p} + d\mathbf{p}$. We will consider the nonrelativistic case $\mathbf{p} = m\mathbf{v}$. Without loss of generality, we assume that $m = 1$. The paper [47] shows that, with the presence n of discrete states, the value $f(\mathbf{r}, \mathbf{v}, t)$ can be represented in the form:

$$f(\mathbf{r}, \mathbf{v}, t) = \sum_{j=1}^{n} f_j(\mathbf{r}, \mathbf{v}, t), \tag{3}$$

where

$$f_j(\mathbf{r}, \mathbf{v}, t) = s_j(\mathbf{r}, \mathbf{v}, t) + \sum_{i=1}^{n} c_{ij} \int_0^t k_i(\tau)d\tau \int W_{ij}(\mathbf{\Omega}', \mathbf{\Omega})d\mathbf{\Omega}' \times \int f_i(\mathbf{r} - v'\mathbf{\Omega}'\tau, v'\mathbf{\Omega}', t - \tau)h_{ij}(v', v)dv'. \tag{4}$$

Here, $k_i(\tau)$ is the probability density distribution of the residence time in the state i, c_{ij}—the probabilities of transition from the state i into the state j, $W_{ij}(\mathbf{\Omega}', \mathbf{\Omega})$ is the probability density that before collision the velocity had the direction $\mathbf{\Omega}'$, after collision the direction took the value $\mathbf{\Omega}$, $h_{ij}(v', v)$ is the density of the probability of the change in velocity from the value v' to v, $s_j(\mathbf{r}, \mathbf{v}, t)$ is the density of new particle sources in the state

j, $\mathbf{v} = v\mathbf{\Omega}$, $v = |\mathbf{v}|$, $d\mathbf{v} = dv\, d\mathbf{\Omega}$, the summation is carried out over all possible previous states. The values c_{ij}, $W_{ij}(\mathbf{\Omega}', \mathbf{\Omega})$ and $h_{ij}(v', v)$ are normalized:

$$\sum_{j=1}^{n} c_{ij} = 1, \quad \int W_{ij}(\mathbf{\Omega}', \mathbf{\Omega}) d\mathbf{\Omega} = 1, \quad \int h_{ij}(v', v) dv = 1. \tag{5}$$

The transition from the density of collisions $f(\mathbf{r}, \mathbf{v}, t)$ to the phase density $\psi(\mathbf{r}, \mathbf{v}, t)$ is carried out with the help of the integral,

$$\psi(\mathbf{r}, \mathbf{v}, t) = \int_0^t K(\tau) f(\mathbf{r} - v\mathbf{\Omega}\tau, v\mathbf{\Omega}, t - \tau) d\tau, \tag{6}$$

where $K(t) = \int_t^\infty k(\tau) d\tau$. Substituting (3) in (6) we get that the phase density has the form of the sum,

$$\psi(\mathbf{r}, \mathbf{v}, t) = \sum_{j=1}^{n} \psi_j(\mathbf{r}, \mathbf{v}, t), \tag{7}$$

where

$$\psi_j(\mathbf{r}, \mathbf{v}, t) = \int_0^t K_j(\tau) f_j(\mathbf{r} - v\mathbf{\Omega}\tau, v\mathbf{\Omega}, t - \tau) d\tau, \tag{8}$$

where $K_j(t) = \int_t^\infty k_j(\tau) d\tau$. The physical interpretation of the last expression is simple. To detect the particle in the state j of the vicinity $d\mathbf{r}$ of the point $\mathbf{r}$ with the velocity in the interval from $\mathbf{v}$ to $\mathbf{v} + d\mathbf{v}$ at the moment of time from t to $t + dt$ the particle must pass to this state at the point $\mathbf{r} - v\mathbf{\Omega}\tau$ at the moment of time $t - \tau$ and stay in this state during the time greater than τ. Transition to the density of particles $\rho(\mathbf{r}, t)$ is carried out with the help of the integral,

$$\rho(\mathbf{r}, t) = \int \psi(\mathbf{r}, \mathbf{v}, t) d\mathbf{v}. \tag{9}$$

The system of Equations (4), (7) and (8), together with conditions (5) describes practically any process of random walks with n discrete states under fairly general assumptions about the scattering indicatrix $W_{ij}(\mathbf{\Omega}', \mathbf{\Omega})$ and the law of redistribution of speed $h_{ij}(v', v)$. In this work, using these equations, we obtain kinetic equations describing Levy walks with a constant velocity of motion between two successive scatterings of a particle.

We define the process of walks as follows. There is only this state—the state of motion ($n = 1$). A particle moves at a constant velocity v between two successive collisions. After the collision, the particle changes its direction, which is determined by the scattering indicatrix $W(\mathbf{\Omega})$. After which, the particle continues to move in a new direction with the same constant velocity v. Random times between two successive collisions of a particle $T_i, i = 1, 2, 3, \ldots$ are independent random values. Since the motion occurs with a finite speed, then for times T_i the particle covers the path $R_i = vT_i, i = 1, 2, 3, \ldots$. The values R_i are the paths of particles.

Since there is only one state, then in Equations (4), (7) and (8), we need to put $n = 1$, $c_{11} = 1$. We will also assume that the source can be represented in the form $s(\mathbf{r}, \mathbf{v}, t) = s(\mathbf{r}, t) h_s(v) W_s(\mathbf{\Omega})$ and, for brevity, we omit the subscript indicating the status number. As a result, we obtain:

$$\psi(\mathbf{r}, \mathbf{v}, t) = \int_0^t K(\tau) f(\mathbf{r} - v\mathbf{\Omega}\tau, v\mathbf{\Omega}, t - \tau) d\tau, \tag{10}$$

$$f(\mathbf{r}, \mathbf{v}, t) = s(\mathbf{r}, t) h_s(v) W_s(\mathbf{\Omega}) + \int_0^t k(\tau) d\tau \int W(\mathbf{\Omega}', \mathbf{\Omega}) d\mathbf{\Omega}' \int f(\mathbf{r} - v'\mathbf{\Omega}'\tau, v'\mathbf{\Omega}', t - \tau) h(v', v) dv'. \tag{11}$$

The motion velocity between two successive collisions will be denoted by v_0. Let us also assume that the direction of motion after each collision does not depend on the previous direction of motion. In view of the foregoing, we get:

$$h(v', v) = h_s(v) = \delta(v - v_0), \quad W(\mathbf{\Omega}', \mathbf{\Omega}) = W_s(\mathbf{\Omega}) = W(\mathbf{\Omega}).$$

Now, substituting these expressions in Equation (11), we obtain:

$$f(\mathbf{r}, \mathbf{v}, t) = W(\mathbf{\Omega})\delta(v - v_0)\left(s(\mathbf{r}, t) + \int_0^t k(\tau)d\tau \int d\mathbf{\Omega}' \int f(\mathbf{r} - v'\mathbf{\Omega}'\tau, v'\mathbf{\Omega}', t - \tau)dv'\right). \tag{12}$$

From this relation, it is clear that, in cases when the densities of transition probabilities $h(v', v)$ and $W_{ij}(\mathbf{\Omega}', \mathbf{\Omega})$ do not depend on the previous value v' and $\mathbf{\Omega}'$, then the density of the collision can be represented in the form of the product $f(\mathbf{r}, v\mathbf{\Omega}, t) = W(\mathbf{\Omega})h(v)F(\mathbf{r}, \mathbf{t})$. Thus, we obtain:

$$f(\mathbf{r}, v\mathbf{\Omega}, t) = W(\mathbf{\Omega})\delta(v - v_0)F(\mathbf{r}, \mathbf{t}). \tag{13}$$

Now substituting this relation in (12) and by integrating over $dv\, d\mathbf{\Omega}$ we get the equation for $F(\mathbf{r}, t)$:

$$\begin{aligned} F(\mathbf{r}, t) &= s(\mathbf{r}, t) + \int_0^t k(\tau)d\tau \int W(\mathbf{\Omega}')d\mathbf{\Omega}' \int F(\mathbf{r} - v'\mathbf{\Omega}'\tau, t - \tau)\delta(v' - v_0)dv' \\ &= s(\mathbf{r}, t) + \int_0^t k(\tau)d\tau \int F(\mathbf{r} - v_0\mathbf{\Omega}'\tau, t - \tau)W(\mathbf{\Omega}')d\mathbf{\Omega}'. \end{aligned} \tag{14}$$

Here, we used the normalization condition $\int W(\mathbf{\Omega}')d\mathbf{\Omega}' = 1$. The physical meaning of the quantity $F(\mathbf{r}, t)$ is quite simple. This is the density of collisions in the volume element $d\mathbf{r}$ of the vicinity of the point $\mathbf{r}$.

Let us now pass from the collision density to the phase density $\psi(\mathbf{r}, \mathbf{v}, t)$, and then to the density of particles $\rho(\mathbf{r}, t)$. To this end, we put the expression (13) in (10). As result, we obtain:

$$\psi(\mathbf{r}, \mathbf{v}, t) = \int_0^t K(\tau)W(\mathbf{\Omega})\delta(v - v_0)F(\mathbf{r} - v\mathbf{\Omega}\tau, t - \tau)d\tau.$$

Now integrating this expression over $dv\, d\mathbf{\Omega}$ and taking account of the ratio (9), we get the equation for the density of particles:

$$\rho(\mathbf{r}, t) = \int_0^t K(\tau)d\tau \int W(\mathbf{\Omega})F(\mathbf{r} - v_0\mathbf{\Omega}\tau, t - \tau)d\mathbf{\Omega}. \tag{15}$$

For the further solution to the obtained equations, it turns out to be convenient to pass from the time τ to the particle path ξ. By substituting the integration variable $\tau = \xi/v_0$, in Equations (14) and (15), we get:

$$\rho(\mathbf{r}, t) = \frac{1}{v_0}\int_0^{v_0 t} P(\xi)d\xi \int F(\mathbf{r} - \xi\mathbf{\Omega}, t - \xi/v_0)W(\mathbf{\Omega})d\mathbf{\Omega}, \tag{16}$$

$$F(\mathbf{r}, t) = s(\mathbf{r}, t) + \int_0^{v_0 t} p(\xi)d\xi \int F(\mathbf{r} - \xi\mathbf{\Omega}', t - \xi/v_0)W(\mathbf{\Omega}')d\mathbf{\Omega}'.. \tag{17}$$

Here, the following notation was introduced: $p(\xi) = \frac{1}{v_0}k(\xi/v_0)$ is the density of probability of the path distribution and $K(\frac{\xi}{v_0}) \equiv P(\xi) = \int_\xi^\infty p(y)dy$.

From this system of equations, it is possible to exclude the equation for $F(\mathbf{r},t)$. To do this, we will substitute Equation (17) in (16) and change the order of integration in the second summand. As a result, we obtain the equation for density,

$$\rho(\mathbf{r},t)=\frac{1}{v_0}\int_0^{v_0t}P(\xi)d\xi\int s(\mathbf{r}-\xi\mathbf{\Omega},t-\xi/v_0)W(\mathbf{\Omega})d\mathbf{\Omega} + \int_0^{v_0t}p(\xi)d\xi\int\rho(\mathbf{r}-\xi\mathbf{\Omega}',t-\xi/v_0)W(\mathbf{\Omega}')d\mathbf{\Omega}'. \quad (18)$$

The first summand in this equation describes unscattered radiation. The second summand describes multiply scattered radiation. This equation describes the random walk of a particle with constant velocity in three-dimensional space with an arbitrary distribution of paths.

Let us simplify the problem and consider one-dimensional particle walks. Let the random walk process occur along the axis x. In this case, the function $W(\mathbf{\Omega})$ takes the form:

$$W(\mathbf{\Omega})=W(\theta,\varphi)=\frac{1}{\sin\theta}(\omega_1\delta(\varphi)+\omega_2\delta(\varphi-\pi))\delta(\theta-\pi/2), \quad (19)$$

where ω_1 and ω_2 are the probabilities of motion in the positive and negative directions of the axis Ox respectively and $\omega_1+\omega_2=1$. Now substituting (19) in Equation (18) and considering that $\mathbf{\Omega}=(\sin\theta\cos\varphi,\sin\theta\sin\varphi,\cos\theta)$, $\rho(\mathbf{r},t)=\rho(x,y,z,t)$, $s(\mathbf{r},t)=s(x,y,z,t)$, $d\mathbf{\Omega}=\sin\theta d\theta d\varphi$ and integrating the resulting equation over the angular variables, we obtain:

$$\rho(x,y,z,t)=\frac{1}{v_0}\int_0^{v_0t}P(\xi)(\omega_1 s(x-\xi,y,z,t-\xi/v_0)+\omega_2 s(x+\xi,y,z,t-\xi/v_0))d\xi + \int_0^{v_0t}p(\xi)(\omega_1\rho(x-\xi,y,z,t-\xi/v_0)+\omega_2\rho(x+\xi,y,z,t-\xi/v_0))d\xi.$$

Since random walks along the axis Ox are considered, then,

$$\rho(x,y,z,t)=\rho(x,t)\delta(y)\delta(z),\quad s(x,y,z,t)=s(x,t)\delta(y)\delta(z).$$

Now substituting these expressions into the previous equation and integrating over the variables y and z, we finally obtain:

$$\rho(x,t)=\frac{1}{v_0}\int_0^{v_0t}P(\xi)(\omega_1 s(x-\xi,t-\xi/v_0)+\omega_2 s(x+\xi,t-\xi/v_0))d\xi + \int_0^{v_0t}p(\xi)(\omega_1\rho(x-\xi,t-\xi/v_0)+\omega_2\rho(x+\xi,t-\xi/v_0))d\xi. \quad (20)$$

The first component in this equation describes unscattered particles that, after escaping from the source, did not have a single collision and move in positive and negative directions, respectively. The second component describes multiply scattered particles, which at the moment of time $t-\xi/v_0$ had a collision and after that they began their motion in positive and negative directions, respectively.

3. Asymptotic Solution to a Kinetic Equation

An asymptotic solution to this equation can be found. To do this, we perform the Fourier–Laplace transform:

$$\hat{\rho}(k,\lambda)=\int_0^\infty dt\int_{-\infty}^{\infty}e^{ikx-\lambda t}\rho(x,t)dx \quad (21)$$

of the Equation (20). As a result, we obtain:

$$\hat{\rho}(k,\lambda) = \frac{1}{v_0}\hat{s}_2(k,\lambda)\left(\omega_1\hat{P}(\lambda/v_0 - ik) + \omega_2\hat{P}(\lambda/v_0 + ik)\right) + \hat{\rho}(k,\lambda)(\omega_1\hat{p}(\lambda/v_0 - ik) + \omega_2\hat{p}(\lambda/v_0 + ik)).$$

As a result, we obtained a simple algebraic equation, the solution to this equation has the form:

$$\hat{\rho}(k,\lambda) = \frac{\frac{1}{v_0}\hat{s}(k,\lambda)\left(\omega_1\hat{P}(\lambda/v_0 - ik) + \omega_2\hat{P}(\lambda/v_0 + ik)\right)}{1 - \omega_1\hat{p}(\lambda/v_0 - ik) - \omega_2\hat{p}(\lambda/v_0 + ik)}.$$

Let there be a point instantaneous source $s(x,t) = \delta(x)\delta(t)$. This means that $\hat{s}(k,\lambda) = 1$. Considering that

$$\hat{P}(\lambda) = \int_0^\infty e^{-\lambda\xi}P(\xi)d\xi = \frac{1-\hat{p}(\lambda)}{\lambda},$$

we obtain

$$\hat{\rho}(k,\lambda) = \frac{1/v_0}{1 - W(k,v_0,\lambda)}\left(\omega_1\frac{1-\hat{p}\left(\frac{\lambda}{v_0} - ik\right)}{\frac{\lambda}{v_0} - ik} + \omega_2\frac{1-\hat{p}\left(\frac{\lambda}{v_0} + ik\right)}{\frac{\lambda}{v_0} + ik}\right), \tag{22}$$

where $W(k,v,\lambda) = \omega_1\hat{p}(\lambda/v - ik) - \omega_2\hat{p}(\lambda/v + ik)$. This solution describes the spatial distribution of particles with random walks of a particle at a constant velocity, with an arbitrary distribution of paths. This solution is not new and was obtained earlier (see, for example, [40,42,48–52]). In this paper, we will consider the asymptotic solution to this equation in the case when the distribution of paths has asymptotics of the form:

$$p(x) \propto \alpha x_0^\alpha x^{-\alpha-1}, \quad 0 < \alpha < 2, \quad x \to \infty, \tag{23}$$

where $x_0 = (\Gamma(1-\alpha)\sin(\frac{\pi}{2}(1-\alpha)))^{-1/\alpha}$. The cases of other distributions of paths are considered in the work [52].

Let us consider the case $0 < \alpha < 1$. In this case, the Laplace transform of the density (23) has the form (see [33]):

$$\hat{p}(\lambda) \approx 1 - (\lambda x_0)^\alpha\Gamma(1-\alpha), \quad \lambda \to 0.$$

Now substituting this expression into the solution (22), we obtain:

$$\hat{\rho}(k,\lambda) = \frac{\omega_1(\lambda - ikv_0)^{\alpha-1} + \omega_2(\lambda + ikv_0)^{\alpha-1}}{\omega_1(\lambda - ikv_0)^\alpha + \omega_2(\lambda + ikv_0)^\alpha}. \tag{24}$$

This expression completely coincides with the result obtained in [37,49,53]. Taking account of the fact that the multiplier $(\lambda \pm ikv)^\alpha$ is the Fourier–Laplace transform of the fractional material derivative [40,54],

$$(\lambda \pm \imath kv)^\alpha\hat{f}(k,\lambda) = \int_0^\infty dt\int_{-\infty}^\infty e^{\imath kx - \lambda t}f(x,t)\left(\frac{\partial}{\partial t} \pm v\frac{\partial}{\partial x}\right)^\alpha dx,$$

we obtain that the process is described by the fractional differential equation [44,53–55]:

$$\left[\omega_1\left(\frac{\partial}{\partial t} - v_0\frac{\partial}{\partial x}\right)^\alpha + \omega_2\left(\frac{\partial}{\partial t} + v_0\frac{\partial}{\partial x}\right)^\alpha\right]\rho(x,t) = = \left[\omega_1\left(\frac{\partial}{\partial t} - v_0\frac{\partial}{\partial x}\right)^{\alpha-1} + \omega_2\left(\frac{\partial}{\partial t} + v_0\frac{\partial}{\partial x}\right)^{\alpha-1}\right]\delta(x)\delta(t). \tag{25}$$

By changing the variable $s = ik$ in (24), one can perform the inverse transformation using the method described in the work [56] (see also [37]). As result, we have:

$$\rho(x,t) = \frac{2\sin(\pi\alpha)}{\pi v_0 t} \frac{\omega_1\omega_2\left(1-(x/v_0t)^2\right)^{\alpha-1}}{\omega_1^2(1-x/v_0t)^{2\alpha}+\omega_2^2(1+x/v_0t)^{2\alpha}+2\omega_1\omega_2(1-(x/v_0t)^2)\cos(\pi\alpha)}. \tag{26}$$

In the case $1 < \alpha < 2$, the distribution (23) has a mathematical expectation. In view of the fact that the Laplace transform of density (23) takes the form (see [33]):

$$\hat{p}(\lambda) \approx 1 - m_1\lambda + m_2\lambda^\alpha, \quad \lambda \to 0,$$

where $m_1 = \frac{\alpha x_0}{\alpha-1}$, $m_2 = \frac{x_0^\alpha\Gamma(2-\alpha)}{\alpha-1}$. Now substituting this expression in (22) and considering asymptotics $\lambda \to 0$, $k \to 0$, $|\lambda/kv| \to 0$, we get:

$$\rho(k,\lambda) \approx \frac{1}{\lambda + ikv_0(\omega_2-\omega_1) - \frac{m_2}{m_1}(\omega_1(-ikv_0)^\alpha + \omega_2(ikv_0)^\alpha)}. \tag{27}$$

To obtain an equation describing the process of random walks, we rewrite this expression in the form:

$$\lambda\hat{\rho}(k,\lambda) - 1 = \hat{\rho}(k,\lambda)\left(ikv_0(\omega_1-\omega_2) + \frac{m_2}{m_1}(\omega_1(-ikv_0)^\alpha + \omega_2(ikv_0)^\alpha)\right).$$

Let us simplify the problem and consider symmetric random walks $\omega_1 = \omega_2 = 1/2$, we obtain:

$$\lambda\hat{\rho}(k,\lambda) - 1 = \hat{\rho}(k,\lambda)\frac{m_2}{2m_1}v_0^\alpha|k|^\alpha((-i)^\alpha + i^\alpha).$$

In view of the fact that $\frac{1}{2}((-i)^\alpha + i^\alpha) = \cos(\frac{\pi}{2}\alpha)$ we get:

$$\lambda\hat{\rho}(k,\lambda) - 1 = -D_\alpha\hat{\rho}(k,\lambda)|k|^\alpha. \tag{28}$$

Here, $D_\alpha = \frac{m_2}{m_1}v_0^\alpha\sin\left(\frac{\pi}{2}(\alpha-1)\right)$. To perform the inverse Fourier–Laplace transform of this equation, we need the Riesz fractional differentiation operator:

$$\frac{\partial^\nu}{\partial|x|^\nu} = \frac{-1}{2\cos(\pi\nu/2)}({}_{-\infty}D_x^\nu + {}^{\infty}D_x^\nu).$$

The Fourier transform of this operator has the form (see, for example, [9]):

$$\int_{-\infty}^{\infty} e^{ikx}\frac{\partial^\nu f(x)}{\partial|x|^\nu}dx = -|k|^\nu\hat{f}(k).$$

Taking this relation into account, it is possible to perform the inverse Fourier–Laplace transform of Equation (28). As a result, we obtain the equation of anomalous diffusion:

$$\frac{\partial\rho(x,t)}{\partial t} = D_\alpha\frac{\partial^\alpha\rho(x,t)}{\partial|x|^\alpha}, \tag{29}$$

with the initial condition $\rho(x,0) = \delta(x)\delta(t)$.

The solution to this equation can be obtained by performing the inverse Fourier–Laplace transform of the solution (27). It has already been done in the works [52,53]. As a result, the inverse Fourier–Laplace transform has the form:

$$\rho(x,t) = \frac{1}{(D_\alpha t)^{1/\alpha}}g\Big((x-\omega vt)(D_\alpha t)^{-1/\alpha};\alpha,\omega,0,1\Big),$$

where $g(x;\alpha,\omega,0,1)$ is the density of the standard stable law and $\omega = \omega_1 - \omega_2$. In the case of symmetric walks $\omega_1 = \omega_2 = 1/2$, this expression takes the form:

$$\rho(x,t) = \frac{1}{(D_\alpha t)^{1/\alpha}} g\Big(x(D_\alpha t)^{-1/\alpha};\alpha,0,0,1\Big). \tag{30}$$

As we can see, the equation solution (29) is expressed in terms of a symmetrical stable law [20,57,58].

Thus, taking account of the constant velocity of the particle in the Levy walk model leads to the need to consider two cases $0 < \alpha < 1$ and $1 < \alpha < 2$. The principal difference between these two cases is that, at $0 < \alpha < 1$, the mathematical expectation of the distribution (23) is equal to infinity and in the case $1 < \alpha < 2$, the mathematical expectation is finite. It is this fact that leads to different asymptotic distributions of particles. In the case of an infinite mathematical $0 < \alpha < 1$ the probability of the appearance of large paths turns out to be significant, and leads to the fact that the overwhelming majority of particles move along the front of the distribution $x = \pm vt$. This is especially clear at values $\alpha < 0.6$. In this case, the *U*—like form of the asymptotic distribution of particles is formed. As the parameter α increases, the share of large paths decreases. This leads to the appearance of multiply scattered particles, which form a hump in the central part of the distributions. As a result, the *W*—like asymptotic distribution of particles is formed. These solutions are not new and were obtained earlier when considering random walks with constant velocity [49,52,53], and when considering similar models of random walks [37,42,48,59,60] (see also the overview work [50]). In the case of the finite mathematical expectation ($1 < \alpha < 2$), the process of random walks of a particle with a constant velocity falls under the action of the generalized central limit theorem. As a result, the asymptotic distribution of the particle coordinate is described by a stable law. In this case, the influence of the final velocity is reduced to a decrease in the diffusion coefficient $D \to D_\alpha$ [34].

As we can see, in the case of the finite mathematical expectation and infinite mathematical expectation, not only are the asymptotic distributions different, but so are the equations describing the process of random walks. In the case of the finite mathematical expectation, the random walk process is described by the anomalous diffusion equation with the first time derivative (29), and the influence of the finite velocity is reduced to replacing the diffusion coefficient in this equation. In the case of the infinite mathematical expectation for taking account of the finite velocity of motion, as noted in the work [34], it is no longer sufficient to simply replace the diffusion coefficient. For this, it is necessary to replace the operator of the fractional Laplacian with the material derivative of the fractional order, which was first noted in the work [39]. Later, the authors of the works [40–44] come to the conclusion like this. Thus, in the case $0 < \alpha < 1$ in asymptotics $t \to \infty$ the random walk process is described by Equation (25).

4. Numerical Solution to a Kinetic Equation

It should be noted that the numerical methods for solving Equation (29) are well investigated (see, for example, [8,12]). For a more detailed familiarization with the methods of numerical solutions of equations with fractional derivatives we refer the reader to the reviews [61,62]. However, there are no numerical methods for solving Equation (25) or similar equations with the material derivative of the fractional order. At least, the authors are not familiar with works devoted to methods of the numerical solution of such equations.

We consider a method for a numerical solution to Equations (25) and (29), which is based on the Monte Carlo method. From Section 2, it is clear that the random walk process of a particle with a constant velocity is described by an integral transport equation, which in the one-dimensional case takes the form (20). This allows the use of the Monte Carlo method to find a solution to this equation. The advantage of Monte Carlo methods is that they allow one to find a solution in multidimensional problems, as well as for various boundary and initial conditions.

From Section 2, the simplest method of numerical solution immediately follows based on modeling trajectories and histogram estimates of the particle distribution density. Each trajectory starts at a moment in time $t = 0$ from the origin of coordinates $x = 0$. We will consider one-dimensional symmetric walks $\omega_1 = \omega_2 = 1/2$. Therefore, from the origin of coordinates, a particle with equal probability moves to the right or to the left at a random distance R_1, spending time $T_1 = R_1/v_0$ on it. After that, the direction of motion is again modeled and with equal probability the particle continues to move to the right or to the left, moving a random distance R_2, spending time $T_2 = R_2/v_0$ on it. After that, the process continues in the same way. The construction of the trajectory continues as long as the condition is met:

$$\sum_{k=1}^{N(T^*)} T_k \leqslant T^*, \tag{31}$$

where T^* is a given moment in time at which it is necessary to find a solution. As soon as this condition is no longer met, the trajectory is terminated and a new trajectory begins. Random paths R_k, $k = 1, 2, \ldots$ are distributed with a density,

$$p(x) = \begin{cases} \alpha x_0^{\alpha} x^{-\alpha-1} & x \geqslant x_0, \\ 0 & x < x_0. \end{cases}$$

Thus, random quantities R_k, $k = 1, 2, \ldots$ are modeled according to the formula $R = x_0 \zeta^{-1/\alpha}$, where ζ is a uniformly distributed random variable on a segment $(0, 1]$.

To construct the simplest histogram estimate for the solution to the kinetic equation, the entire area of interest $\Delta = [a, b]$ is broken down into non-overlapping intervals $\Delta_i = (x_i, x_{i+1}]$, $i = 1, 2, \ldots M-1$, $x_1 = a, x_M = b$. To construct a histogram, the trajectory is modeled until the condition is met (31). As soon as this condition ceases to be met, the trajectory is terminated and the contribution from this trajectory is calculated:

$$h_j(\Delta_i) = \frac{I(\Delta_i)}{\Delta_i},$$

where $I(\Delta_i)$ is the interval indicator Δ_i,

$$I(\Delta_i) = \begin{cases} 1, & x^* \in \Delta_i, \\ 0, & x^* \notin \Delta_i, \end{cases}$$

where x^* is the coordinate of a particle at the moment of time T^*. As a result, the estimate of the density for the interval Δ_i is given by the expression:

$$\tilde{\rho}(\Delta_i, t) = \frac{1}{N} \sum_{j=1}^{N} h_j(\Delta_i), \tag{32}$$

where summation is performed over the ensemble N of independent trajectories.

Despite the simplicity of this estimate, it has several disadvantages. Firstly, the estimate of the solution $\tilde{\rho}(\Delta_i, t)$ is sought for the interval Δ_i. This is the source of the systematic (horizontal) component of the error δ_x. Secondly, this estimate also contains the statistical component of the error $\hat{\delta}$, which decreases like $N^{-1/2}$ at $N \to \infty$. It is impossible to eliminate these errors completely; one can only reduce their value. However, a decrease in one of these values leads to an increase in the other value or to an increase in the calculation time.

It is possible to get rid of the systematic component of the error completely δ_x, if to consider one of the varieties of a local estimate. As in the case of the histogram estimate, the problem is to estimate the probability density of detecting a particle at the point x^* at the moment of time T^*. The main element of solving the problem of transport theory by the Monte Carlo method—trajectory modeling remains unchanged. The difference lies in

the estimation method. In the case of a local estimate, the probability of a particle reaching a point is calculated (x^*, T^*), provided that the next collision is the final one.

To find this probability, let us consider the process of a random walk. Suppose that the density needs to be estimated at the point x^* at the moment of time T^* (see Figure 1). We will consider symmetrical random walks $\omega_1 = \omega_2 = 1/2$. The particle trajectory begins at the point $x = 0$ at the moment of time $t = 0$. Let the particle, as a result of a random walk at the moment of time t', reach the point x'. To estimate the density at the point x^*, it is necessary to calculate the probability of transition from the point (x', t') to the point (x^*, T^*). It is obvious that, to get from the point (x', t') to the point (x^*, T^*), there are two possible alternatives of the trajectory continuation (see, Figure 1). The first option is to cover the distance ξ_1 in the positive direction of the axis Ox. Then, to scatter at the point (x'_1, t'_1) and to cover the distance greater than ξ_2 in the negative direction of the axis Ox. The second option is to cover the distance ξ_2 first in the negative direction of the axis Ox. Then, to scatter at the point (x'_2, t'_2) and to cover the distance greater than ξ_1 in the positive direction of the axis Ox. Since the particle is moving with a constant velocity v_0 all the time, then the paths ξ_1 and ξ_2 will take time $\tau_1 = \xi_1/v_0$ and $\tau_2 = \xi_2/v_0$. The values of the paths ξ_1 and ξ_2 are determined by the formulas:

$$\xi_1 = \tfrac{1}{2}(v_0(T^* - t') + (x^* - x')), \quad \xi_2 = \tfrac{1}{2}(v_0(T^* - t') - (x^* - x')).$$

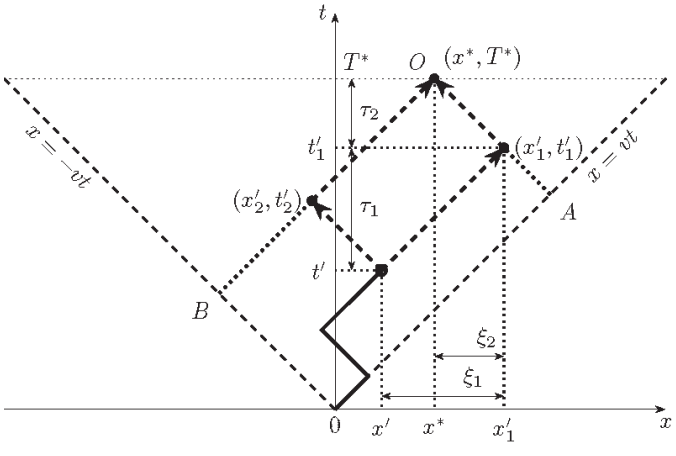

Figure 1. Possible continuation of the particle trajectory for constructing a local estimate.

Thus, the probability of transition from the point (x', t') to the point (x^*, T^*) is determined by the formula:

$$\psi(x^*, x', T^*, t') = \tfrac{1}{4}(p(\xi_1)P(\xi_2) + p(\xi_2)P(\xi_1)), \tag{33}$$

where $P(\xi) = \int_\xi^\infty p(\xi')d\xi'$, and the multiplier $1/4$ appears as a result of the fact that, on the considered section of the trajectory, the particle changes its direction of motion twice. This transition probability is calculated after each particle scattering.

Theoretically, the contribution to the sought density can be made at the point x^* by those particles that can get to the point x^* from the current point without having a single scatter in the remaining time. Suppose that, as a result of random walks, the particle is scattered at the point x'_1 at the moment of time t'_1 (see Figure 1). Thus, staying at the point x'_1 at the moment of time t'_1, the particle can be found at the point x^* at the moment of time T^* if its path ξ satisfies the inequality $\xi \geqslant |x^* - x'_1|$. In this case, the contribution to the density estimate has the form,

$$\psi_{unsc}(x^*, x', T^*, t') = \tfrac{1}{2}P(|x^* - x'|),$$

where we need to substitute $x' = x'_1$, $t' = t'_1$. However, it should be noted that, for such a situation to be realized, during the random walk, the particle must undergo scattering at some point exactly lying on the segments OA or OB. Considering that the probability that the coordinate of a particle will take exactly a given value is equal to zero, then the contribution to the sought density from such particles will be zero. Nevertheless, unscattered particles make a significant contribution to the points lying on the half lines $x = \pm vt$. These half lines determine the front of the distribution. Beyond this front, the probability of detecting a particle is zero. In view of the fact that the source is at the point $x = 0$, then it is obvious that the probability to detect a particle at the point $x = 0$ at the moment of time $t = 0$ is equal to one. Therefore, if after its appearance, the particle did not have any scattering and its path $\xi \geqslant v_0 T^*$, then such particles reach the points $x = \pm v_0 T^*$ and form the front of the distribution. The contribution of such particles at the points $x = \pm v_0 T^*$ is calculated by the formula:

$$\psi_{unsc}(\pm v_0 T^*, 0, T^*, 0) = \tfrac{1}{2} P(v_0 T^*).$$

The particles will also form the front of the distribution which, after their appearance during scattering, did not change their original direction of motion. Density contribution at points $x = \pm v_0 T^*$ from such particles after each collision is calculated by a similar formula:

$$\psi(\pm v_0 T^*, x', T^*, t') = \tfrac{1}{2} P(|\pm v_0 T^* - x'|). \tag{34}$$

Here, x', t' is the coordinate and moment of time at which the particle scattered. It should be noted that if, after its appearance, the particle began its motion in the positive direction, then unscattered or multiply scattered in one direction particles contribute only at the point $v_0 T^*$. Particles that began their motion in the negative direction—to the point $-v_0 T^*$. As a result, the contribution to the density estimate from each individual trajectory has the form:

$$h_j(x^*, T^*) = \sum_{i=1}^{K(T^*)} \psi(x^*, x_i, T^*, t_i),$$

where $K(T^*)$ is the number of scatterings that occurred during the time interval $(0, T^*)$. To estimate the density at the points $x \neq \pm v_0 T^*$, the function $\psi(x^*, x_i, T^*, t_i)$ has the form (33), to estimate the density at the points $x = \pm v_0 T^*$ the function $\psi(x^*, x_i, T^*, t_i)$ takes the form (34). We finally obtain that the density at the point x^* at the moment of time T^*, is estimated by the formula:

$$\tilde{\rho}(x^*, T^*) = \frac{1}{N} \sum_{j=1}^{N} h_j(x^*, T^*), \tag{35}$$

where the summation is performed over an ensemble of N independent trajectories.

In Figure 2, the results of the numerical solution to the Equation (25) are given for the values $\varkappa = 0.5$, $v = 1$, $T^* = 1000$. Circles show the results of the histogram's estimation of the Monte Carlo method (32), asterisks are the results of the local estimate (35) and the solid line is the solution (26). The calculation results are transformed for the variable $-1 \leqslant \zeta \leqslant 1$ with the help of transformation $\rho(\zeta, t) = vt\rho(x/vt, t)$, where $-vt \leqslant x \leqslant vt$. As we can see from the figure, at the value $\varkappa = 0.5$, the results of all three solutions coincide. The figure also shows the advantages of the considered solution method. The results of the local estimate (35) do not contain the horizontal component of the error, which is present in the histogram estimate of the Monte Carlo method (32) and is connected with a finite quantity of the interval Δ_i. In view of the fact that the contribution from one trajectory to the point x^* is calculated $K(T^*)$ times, then this leads to a decrease in the statistical (vertical) error. In the figure, the magnitude of the statistical error does not exceed the size of the symbol. It should be noted that the solution (26) is an asymptotic solution and describes the distribution of particles at $t \to \infty$. As we can see from the figure, in the case $\varkappa = 0.5$ and time $T^* = 1000$, the results of all three methods of solution coincide. This means that

the process of the random walk of a particle has already entered the asymptotic regime. However, the moment when the random walk process enters the asymptotic regime for different values α is different.

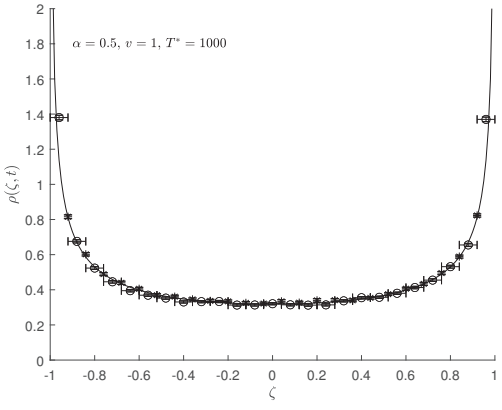

Figure 2. Particle distribution density at $\alpha = 0.5$, $v = 1.0$, $t = 1000$. Number of trajectories $N = 10^5$.

Figure 3 contains the solution results of a kinetic Equation (20) using the method of the histogram estimation (circles), the method of the local estimation (asterisks). Solution results are given for three times $T^* = 10^2, 10^3, 10^4$. The figure also shows the solution to the Equation (25) (solid curve), which describes the asymptotic distribution of particles. As we can see in the figure, for the value $\alpha = 0.8$ at the indicated times, the random walk process does not yet reach the asymptotic regime. However, when time T^* increases, the solutions to the kinetic equation gradually approach the asymptotic distribution. It can also be seen from the figure that, at times $T^* = 10^3$ and $T^* = 10^4$, the solutions to the histogram estimate of the Monte Carlo method and the local estimate coincide, which confirms the validity of the results of the local estimation method. It can be seen from this figure that, at large times $T^* = 10^3$ and $T^* = 10^4$, there is an increase in the magnitude of the statistical error in the results of the local estimation. This increase in the calculation error is due to the fact that, at greater times, the value of the contribution (33) turns out to be a small magnitude. As a result, the calculation error can already affect it.

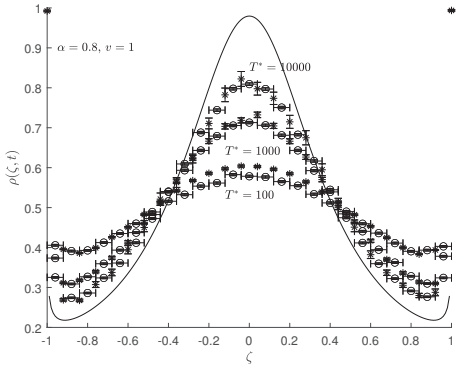

Figure 3. The density of particle distribution for the value $\alpha = 0.8$ and specified values T^*. Number of trajectories $N = 10^6$.

The solution to the kinetic equation for the case $\alpha > 1$ and specified values T^* is given in Figure 4. In this figure, the points are the results of solving the kinetic Equation (20)

with the use of the local estimation method, the solid curve is the solution (30). As in the previous cases, the calculation results are given for the variable $\zeta = x/vt$, where $-vt \leqslant x \leqslant vt$. The figure shows that, at times $T^* = 100$ and $T^* = 1000$, the random walk process has not yet reached the asymptotic regime. The asymptotic regime of random walks is reached at $T^* = 10^4$. As one can see, for a given time, the asymptotic solution (30) and the local estimation results are in good agreement with each other.

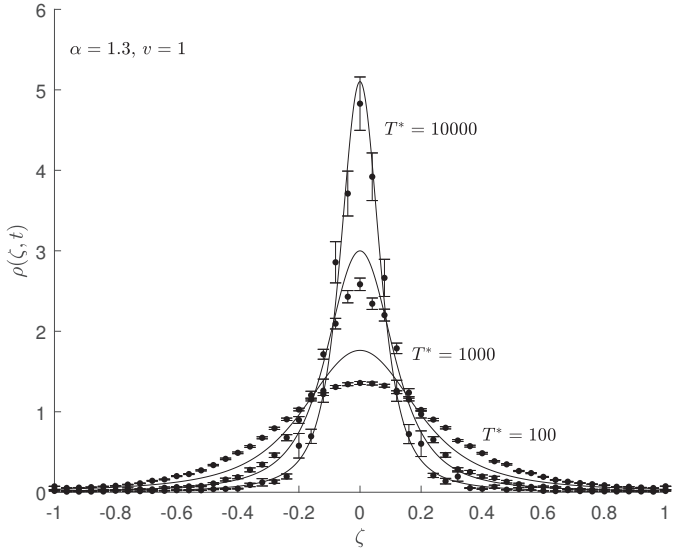

Figure 4. Density of the particle distribution for the value $\alpha = 1.3$ and specified values T^*. Number of trajectories $N = 10^5$.

One obvious shortcoming of the local estimation method should also be pointed out. In the considered method, it is necessary to calculate the contribution (33) after each scattering of a particle. This leads to an increase in the computational operations of the processor, which in turn leads to an increase in the calculation time in comparison with the histogram method for estimating the density. However, this increase in calculation time is a necessary price to pay for the clear advantages of the local estimation method. As noted earlier, the main benefit of the local estimation (35) is the possibility to find a solution at a given point x^*. This means that the results of the local estimation do not contain a systematic (horizontal) component of the error. If we give a set of points $x_i^*, i = 1, \ldots, n$, then one trajectory will contribute at once to all points of the set x_i^*. This allows the solution to be constructed as a smooth function of the coordinate x. If we also take into account that the contribution (33) is calculated after each particle scattering, then the contribution from one trajectory is calculated $K(T^*)$ times, where $K(T^*)$ is the number of scatterings of a particle in the interval $[0, T^*]$. This leads to a decrease in the statistical component of the error.

5. Conclusions

The use of the theory of anomalous diffusion to describe combustion processes is only at the initial stage of development. At present, there are a few works devoted to the studies undertaken in this area of research [3,6–8,10,12]. In all the works, to describe combustion processes, the use of the equations of anomalous diffusion (1) or (2) is proposed. As is known, these equations describe the asymptotic ($t \to \infty, x \to \infty$) distribution of particles in the CTRW process, which is based on the assumption of the instant travel of particles from one point of space to another. This non-physical behavior of the particle leads to the fact that, at a time instant that is arbitrarily close to the initial one, the particle can be at an

arbitrarily large distance from the source. Therefore, it is necessary to use these equations to describe the processes occurring in a limited area of space and develop them in time with a certain degree of caution.

An obvious way to eliminate the instantaneous movement of a particle is to introduce into consideration a constant final velocity of the movement of a particle, which was done in this work. Taking account of the constant velocity of motion shows that, depending on whether the mathematical expectation of the travel is finite or infinite, the asymptotic distribution of particles is described by completely different equations. In the case of the finite mathematical expectation of the path value ($1 < \alpha < 2$), the asymptotic process is described by the anomalous diffusion Equation (29), and the consideration of the finite velocity is reduced to the substitution of the anomalous diffusion coefficient $D \to D_\alpha$. In the case of the infinite mathematical expectation ($0 < \alpha < 1$), the consideration of the finite velocity leads to a completely different Equation (25) containing the fractional-order material derivative operator.

The main difficulty in using equations in fractional derivatives is to find solutions to these equations. Analytical methods for solving these equations are only at the stage of development. Therefore, the main method of solution is to apply numerical methods. In this paper, a numerical solution method is considered which is based on a local estimate of the Monte Carlo method. This method is based on the idea of modeling the trajectory of a particle's random walk. The idea of the proposed method consists of the following. Now, after each scattering of a particle, one should calculate the probability of transition from the scattering point to a given point at which it is necessary to estimate the particle density. By giving a set of points, the transition probability should be calculated for each point from the given set. The advantages of this method over the standard histogram estimation of the Monte Carlo method are obvious. Firstly, since the solution is estimated at a specified point, then the estimation results do not contain a systematic (horizontal) component of the error. Secondly, each trajectory will contribute to all points of the given set at once. Taking account of the fact that, before the termination of the simulation of the trajectory, the particle undergoes $K(T^*)$ of scatterings, then one trajectory will contribute $K(T^*)$ times to each point of the given set. This leads to a decrease in the statistical error. However, since now the transition probability is calculated after each particle scattering, this leads to an increase in the arithmetic operations of the processor. As a result, in comparison with the histogram estimate of the Monte Carlo method, more time is spent on modeling the same number of trajectories. However, an increase in the calculation time should be considered a necessary payment for the complete absence of horizontal error.

The calculations made show that the results of the local estimation of the Monte Carlo method are in good agreement with both the results of the histogram estimation of the Monte Carlo method and the results of solving Equations (25) and (29), describing the asymptotic behavior of the process. From the calculations presented it also follows that, at different values of the parameter α, the process of random walks reaches the asymptotic regime at different times. This indicates another advantage of using the Monte Carlo method. In fact, Equations (25) and (29) describe the asymptotic behavior of the process at $t \to \infty$, while the Monte Carlo method allows us to find a solution to the kinetic equation at any arbitrary moment in time and, thus, trace the evolution of the distribution of particles in time.

Author Contributions: Conceptualization, V.V.S.; methodology, V.V.S.; software, V.V.S.; validation, V.V.S. and Y.E.C.; investigation, V.V.S.; writing—original draft preparation, V.V.S.; writing—review and editing, V.V.S., V.N.K. and R.V.F.; visualization, V.V.S. and Y.E.C.; supervision, V.N.K.; project administration, R.V.F.; funding acquisition, V.N.K. and R.V.F. All authors have read and agreed to the published version of the manuscript.

Funding: This work was supported by the Megagrant of the Government of the Russian Federation in the framework of the federal project No. 075-15-2021-584.

Institutional Review Board Statement: Not applicable.

Informed Consent Statement: Not applicable.

Data Availability Statement: Not applicable.

Conflicts of Interest: The authors declare no conflict of interest.

References

1. Dhar, A. Heat transport in low-dimensional systems. *Adv. Phys.* **2008**, *57*, 457–537. [CrossRef]
2. Lepri, S.; Livi, R.; Politi, A. Thermal conduction in classical low-dimensional lattices. *Phys. Rep.* **2003**, *377*, 1–80. [CrossRef]
3. Souza, J.W.; Santos, A.A.; Guarieiro, L.L.; Moret, M.A. Fractal aspects in O 2 enriched combustion. *Phys. A Stat. Mech. Appl.* **2015**, *434*, 268–272. [CrossRef]
4. Li, S.N.; Cao, B.Y. Anomalous heat diffusion from fractional Fokker–Planck equation. *Appl. Math. Lett.* **2020**, *99*, 105992. [CrossRef]
5. Li, S.N.; Cao, B.Y. Anomalies of lévy-based thermal transport from the lévy-fokker-planck equation. *AIMS Math.* **2021**, *6*, 6868–6881. [CrossRef]
6. Xu, Y.; Zheng, Z. Quenching phenomenon of a time-fractional diffusion equation with singular source term. *Math. Methods Appl. Sci.* **2017**, *40*, 5750–5759. [CrossRef]
7. Xu, Q.; Xu, Y. Extremely low order time-fractional differential equation and application in combustion process. *Commun. Nonlinear Sci. Numer. Simul.* **2018**, *64*, 135–148. [CrossRef]
8. Xu, Y. Quenching phenomenon in a fractional diffusion equation and its numerical simulation. *Int. J. Comput. Math.* **2018**, *95*, 98–113. [CrossRef]
9. Samko, S.G.; Kilbas, A.A.; Marichev, O.I. *Fractional Integrals and Derivatives—Theory and Application*; Gordon and Breach: New York, NY, USA, 1973.
10. Xu, Q.; Xu, Y. Quenching study of two-dimensional fractional reaction–diffusion equation from combustion process. *Comput. Math. Appl.* **2019**, *78*, 1490–1506. [CrossRef]
11. Garra, R.; Giusti, A.; Mainardi, F. The fractional Dodson diffusion equation: A new approach. *Ric. Mat.* **2018**, *67*, 899–909. [CrossRef]
12. Wang, Z.; Xu, Y. Quenching of combustion explosion model with balanced space-fractional derivative. *Math. Methods Appl. Sci.* **2020**, *43*, 4472–4485. [CrossRef]
13. Pagnini, G. Nonlinear time-fractional differential equations in combustion science. *Fract. Calc. Appl. Anal.* **2011**, *14*, 80–93. [CrossRef]
14. Zeldovich, Y.B. *Theory of Combustion and Detonation of Gases*; Academy of Sciences (USSR): Moscow, Russia, 1944.
15. Montroll, E.W.; Weiss, G.H. Random Walks on Lattices. II. *J. Math. Phys.* **1965**, *6*, 167. [CrossRef]
16. Scher, H.; Lax, M. Stochastic transport in a disordered solid. I. Theory. *Phys. Rev. B* **1973**, *7*, 4491–4502. [CrossRef]
17. Scher, H.; Lax, M. Stochastic transport in a disordered solid. II. Impurity conduction. *Phys. Rev. B* **1973**, *7*, 4502–4519. [CrossRef]
18. Scher, H.; Montroll, E. Anomalous transit-time dispersion in amorphous solids. *Phys. Rev. B* **1975**, *12*, 2455–2477. [CrossRef]
19. Klafter, J.; Blumen, A.; Shlesinger, M.F. Stochastic pathway to anomalous diffusion. *Phys. Rev. A* **1987**, *35*, 3081–3085. [CrossRef]
20. Uchaikin, V.V. Montroll-Weiss problem, fractional equations, and stable distributions. *Int. J. Theor. Phys.* **2000**, *39*, 2087–2105. [CrossRef]
21. Uchaikin, V.V. Self-similar anomalous diffusion and Levy-stable laws. *Phys. Uspekhi* **2003**, *46*, 821–849. [CrossRef]
22. Zaslavsky, G.M. Chaos, fractional kinetics, and anomalous transport. *Phys. Rep.* **2002**, *371*, 461–580. [CrossRef]
23. Shlesinger, M.F.; West, B.J.; Klafter, J. Lévy dynamics of enhanced diffusion: Application to turbulence. *Phys. Rev. Lett.* **1987**, *58*, 1100–1103. [CrossRef]
24. Zumofen, G.; Klafter, J. Scale-invariant motion in intermittent chaotic systems. *Phys. Rev. E* **1993**, *47*, 851–863. [CrossRef] [PubMed]
25. Klafter, J.; Zumofen, G.; Shlesinger, M.F. Lévy walks in dynamical systems. *Phys. A Stat. Mech. Appl.* **1993**, *200*, 222–230. [CrossRef]
26. Klafter, J.; Zumofen, G. Levy statistics in a Hamiltonian system. *Phys. Rev. E* **1994**, *49*, 4873–4877. [CrossRef] [PubMed]
27. Drysdale, P.; Robinson, P. Lévy random walks in finite systems. *Phys. Rev. E* **1998**, *58*, 5382–5394. [CrossRef]
28. Uchaikin, V.V. Anomalous transport equations and their application to fractal walking. *Phys. A Stat. Mech. Appl.* **1998**, *255*, 65–92. [CrossRef]
29. Andersen, K.H.; Castiglione, P.; Mazzino, A.; Vulpiani, A. Simple stochastic models showing strong anomalous diffusion. *Eur. Phys. J. B* **2000**, *18*, 447–452. [CrossRef]
30. Uchaikin, V.V. Anomalous diffusion of particles with a finite free-motion velocity. *Theor. Math. Phys.* **1998**, *115*, 496–501. [CrossRef]
31. Jarovikova, I.V. Numerical Analysis of the Kinetic Models of Multivariate Diffusion. Ph.D. Thesis, Ulyanovsk State University, Ulyanovsk, Russia, 2001.
32. Uchaikin, V.V.; Yarovikova, I.V. Numerical solution to the non-stationary problem of anomalous kinetics by the method of momenta. *Comput. Math. Math. Phys.* **2003**, *43*, 1478–1490.

33. Saenko, V.V. The influence of the finite velocity on spatial distribution of particles in the frame of Levy walk model. *Phys. A Stat. Mech. Appl.* **2016**, *444*, 765–782. [CrossRef]
34. Zolotarev, V.M.; Uchaikin, V.V.; Saenko, V.V. Superdiffusion and stable laws. *J. Exp. Theor. Phys.* **1999**, *88*, 780–787. [CrossRef]
35. Ferrari, R.; Manfroi, a.J.; Young, W.R. Strongly and weakly self-similar diffusion. *Phys. D Nonlinear Phenom.* **2001**, *154*, 111–137. [CrossRef]
36. Zaburdaev, V.Y.; Schmiedeberg, M.; Stark, H. Random walks with random velocities. *Phys. Rev. Stat. Nonlinear Soft Matter Phys.* **2008**, *78*, 1–5. [CrossRef] [PubMed]
37. Froemberg, D.; Schmiedeberg, M.; Barkai, E.; Zaburdaev, V.Y. Asymptotic densities of ballistic Lévy walks. *Phys. Rev. E* **2015**, *91*, 022131. [CrossRef] [PubMed]
38. Dhar, A.; Saito, K.; Derrida, B. Exact solution of a Lévy walk model for anomalous heat transport. *Phys. Rev. E* **2013**, *87*, 010103. [CrossRef] [PubMed]
39. Zaburdaev, V.Y.; Chukbar, K.V. Enhanced superdiffusion and finite velocity of Levy flights. *J. Exp. Theor. Phys.* **2002**, *94*, 252–259. [CrossRef]
40. Sokolov, I.M.; Metzler, R. Towards deterministic equations for Lévy walks: The fractional material derivative. *Phys. Rev. E* **2003**, *67*, 010101. [CrossRef]
41. Chukbar, K.V.; Zaburdaev, V.Y. Comment on "Towards deterministic equations for Lévy walks: The fractional material derivative". *Phys. Rev. E Stat. Nonlinear Soft Matter Phys.* **2003**, *68*, 033101. [CrossRef]
42. Zaburdaev, V.Y. Random walk model with waiting times depending on the preceding jump length. *J. Stat. Phys.* **2006**, *123*, 871–881. [CrossRef]
43. Uchaikin, V.V. On the fractional derivative model of the transport of cosmic rays in the Galaxy. *JETP Lett.* **2010**, *91*, 105–109. [CrossRef]
44. Uchaikin, V.V.; Sibatov, R.T. On fractional differential models for cosmic ray diffusion. *Gravit. Cosmol.* **2012**, *18*, 122–126. [CrossRef]
45. Uchaikin, V.V.; Sibatov, R.T. Statistical model of fluorescence blinking. *J. Exp. Theor. Phys.* **2009**, *109*, 537–546. [CrossRef]
46. Froemberg, D.; Barkai, E. Random time averaged diffusivities for Lévy walks. *Eur. Phys. J. B* **2013**, *86*, 331. [CrossRef]
47. Saenko, V.V. Anomalous Diffusion Equations with Multiplicative Acceleration. *J. Exp. Theor. Phys.* **2018**, *126*, 462–478. [CrossRef]
48. Meerschaert, M.M.; Benson, D.A.; Scheffler, H.P.; Becker-Kern, P. Governing equations and solutions of anomalous random walk limits. *Phys. Rev. E Stat. Nonlinear Soft Matter Phys.* **2002**, *66*, 4–7. [CrossRef] [PubMed]
49. Uchaikin, V.V.; Sibatov, R.T. One-Dimensional Fractal Walk at a Finite Free Motion Velocity. *Tech. Phys. Lett.* **2004**, *30*, 316–318. [CrossRef]
50. Zaburdaev, V.Y.; Denisov, S.I.; Klafter, J. Lévy walks. *Rev. Mod. Phys.* **2015**, *87*, 483–530. [CrossRef]
51. Uchaikin, V.V.; Sibatov, R.T.; Byzykchi, A.N. Interpreting data on solar cosmic ray fluxes via the fractional derivative method. *Bull. Russ. Acad. Sci. Phys.* **2015**, *79*, 592–595. [CrossRef]
52. Uchaikin, V.V.; Sibatov, R.T.; Bezbatko, D.N. On a Generalization of One-Dimensional Kinetics. *Mathematics* **2021**, *9*, 1264. [CrossRef]
53. Uchaikin, V.V.; Sibatov, R.T.; Byzykchi, A.N. Cosmic rays propagation along solar magnetic field lines: A fractional approach. *Commun. Appl. Ind. Math.* **2014**, *6*, 479. [CrossRef]
54. Uchaikin, V.V.; Sibatov, R.T. Fractional Boltzmann equation for multiple scattering of resonance radiation in low-temperature plasma. *J. Phys. A Math. Theor.* **2011**, *44*, 145501. [CrossRef]
55. Uchaikin, V.V. Fractional phenomenology of cosmic ray anomalous diffusion. *Phys. Uspekhi* **2013**, *56*, 1074–1119. [CrossRef]
56. Godrèche, C.; Luck, J.M. Statistics of the occupation time of renewal processes. *J. Stat. Phys.* **2001**, *104*, 489–524. [CrossRef]
57. Mainardi, F.; Luchko, Y.; Pagnini, G. The fundamental solution of the space-time fractional diffusion equation. *Fract. Calc. Appl. Anal.* **2001**, *4*, 153–192.
58. Metzler, R.; Klafter, J. The random walk's guide to anomalous diffusion: A fractional dynamics approach. *Phys. Rep.* **2000**, *339*, 1–77. [CrossRef]
59. Magdziarz, M.; Szczotka, W.; Zebrowski, P. Langevin Picture of Lévy Walks and Their Extensions. *J. Stat. Phys.* **2012**, *147*, 74–96. [CrossRef]
60. Schmiedeberg, M.; Zaburdaev, V.Y.; Stark, H. On moments and scaling regimes in anomalous random walks. *J. Stat. Mech. Theory Exp.* **2009**, *2009*, P12020. [CrossRef]
61. Karniadakis, G.E. *Handbook of Fractional Calculus with Applications. Volume 3. Numerical Methods*; De Gruyter: Berlin, Germany, 2019; Volume 3. [CrossRef]
62. Garrappa, R. Numerical Solution of Fractional Differential Equations: A Survey and a Software Tutorial. *Mathematics* **2018**, *6*, 16. [CrossRef]

mathematics

MDPI

Article

Application of a Pattern-Recognition Neural Network for Detecting Analog Electronic Circuit Faults

M. Isabel Dieste-Velasco

Electromechanical Engineering Department, Higher Polytechnic School, University of Burgos, 09006 Burgos, Spain; midieste@ubu.es

Abstract: In this study, machine learning techniques based on the development of a pattern–recognition neural network were used for fault diagnosis in an analog electronic circuit to detect the individual hard faults (open circuits and short circuits) that may arise in a circuit. The ability to determine faults in the circuit was analyzed through the availability of a small number of measurements in the circuit, as test points are generally not accessible for verifying the behavior of all the components of an electronic circuit. It was shown that, despite the existence of a small number of measurements in the circuit that characterize the existing faults, the network based on pattern-recognition functioned adequately for the detection and classification of the hard faults. In addition, once the neural network has been trained, it can be used to analyze the behavior of the circuit versus variations in its components, with a wider range than that used to develop the neural network, in order to analyze the ability of the ANN to predict situations different from those used to train the ANN and to extract valuable information that may explain the behavior of the circuit.

Keywords: modeling; analog circuits; fault diagnosis; neural networks

Citation: Dieste-Velasco, M.I. Application of a Pattern-Recognition Neural Network for Detecting Analog Electronic Circuit Faults. *Mathematics* **2021**, *9*, 3247. https://doi.org/10.3390/math9243247

Academic Editors: Camelia Petrescu and Valeriu David

Received: 3 November 2021
Accepted: 12 December 2021
Published: 15 December 2021

Publisher's Note: MDPI stays neutral with regard to jurisdictional claims in published maps and institutional affiliations.

Copyright: © 2021 by the author. Licensee MDPI, Basel, Switzerland. This article is an open access article distributed under the terms and conditions of the Creative Commons Attribution (CC BY) license (https://creativecommons.org/licenses/by/4.0/).

1. Introduction

In analog electronic circuits, the limited access to measurement points makes determining faulty components a very complex task. On the other hand, when defining a set of measurement variables to characterize faults, many of the states that are generated by faults in the circuit are equivalent from the point of view of the values of the measured inputs, because the test points are generally not accessible to verify the behavior of all the components of the electronic circuit. In addition, performing measurements in each component of the circuit is not feasible from a practical point of view.

The present study deals with an application of supervised learning, based on the use of a pattern-recognition artificial neural network (ANN), for the detection of the individual hard faults (open circuits and short circuits) that may arise in an analog electronic circuit. The fact that the test points cannot be placed at all locations may cause several equivalent states to exist, depending on the points chosen to monitor the behavior of the circuit. This makes the detection of existing faults in an analog circuit a very complex task and much less developed than the same task in digital electronic circuits. In order to detect the hard faults that may arise in an electronic circuit, measurements are to be taken at accessible points in the circuit. Specifically, for the analysis to be carried out in this study, measurements of DC voltage and voltage gain were considered as input values so that it was possible to monitor the circuit and to determine, from these easily obtainable measures, whether the circuit was in a hard fault situation (open circuit or short circuit).

The first circuit under test (CUT) used in the present study was a single-stage small-signal BJT amplifier, in which it is difficult to detect the hard faults that may arise because some faults lead to an equivalent state, from the point of view of the inputs used to monitor the behavior of the circuit, and later a more complex CUT was also studied. First, in the present study, the outputs of the CUTs versus variations that may arise from the tolerances of the passive elements of the circuit were obtained through a Monte Carlo analysis by

using Cadence® OrCAD® (CA, USA) design electronic simulation software. The values thus obtained were then used to train the ANN applied to predict the faulty components of the circuit. Moreover, a dataset obtained from the simulation software was used to validate and test the obtained results. In addition, once the pattern-classification neural network had been obtained, it was used to predict the behavior of the circuit subject to variations in the faulty components at wider ranges than those used to develop the neural network. This was carried out to determine the ranges of the parameters from which it is possible to detect hard faults in the CUTs.

Nowadays, determining faults in analog electronic circuits is being deeply studied by several research studies. For example, as shown in a review of Binu and Kariyappa [1], fault diagnosis in electronic circuits has been extensively researched in the last few years, for which machine learning approaches have been widely applied for fault detection. As shown by Binu and Kariyappa [1], open circuits and short circuits are some of the main failure sources in analog electronic circuits, and these hard faults can be modeled by including a 1 Ω parallel resistance with the component in a short-circuit situation and a 1 MΩ series resistance with the component in an open-circuit situation.

As previously mentioned, fault diagnosis in analog electronic circuits is a very complex task and is much less developed than the equivalent task in digital electronic circuits. The methods for analyzing faults in analog electronic circuits may be classified, roughly speaking, into two main categories: simulation before test (SBT) and simulation after test (SAT), as shown in the research study of Aizenberg et al. [2].

In the SBT approach, the development of a fault dictionary is very useful for detecting the faults in a circuit. In that way, the main faults that may arise in the circuit are simulated along with the nominal behavior of the circuit. In addition, in order to detect the faults that can occur in the analog circuit, it is important to consider both ambiguity groups, that is, the set of components of the electronic circuit that do not provide a unique solution if considered as a potential fault, and the canonical ambiguity groups, where a canonical ambiguity group is a group that does not contain other ambiguity groups [2–4], because it is very difficult to determine which component is faulty within one of these ambiguity groups.

Over the last few years, soft computing techniques for modeling and analyzing the behavior of electronic devices, as well as other kind of devices, have been widely used. As a consequence, several research studies dealing with this subject have been developed, as can be observed, for example, in [5–9], among many others research studies. With regard to the application of ANNs for detecting faults in analog electronic circuits, the study of Gao et al. [10] could be mentioned, where a dual-input fault diagnosis model based on convolutional neural networks, gated recurrent unit networks, and a softmax classifier was proposed. Likewise, Zhang et al. [11] used a convolutional neuronal network and backward difference for soft fault diagnosis in analog circuits, where the circuits being tested were the Sallen–Key band-pass filter and a four-opamp biquad high-pass filter.

Another studyworth mentioning is that of Wang et al. [12], which used a long short-term memory neural network for fault detection and classification in modular multilevel converters in high-voltage direct current systems.

On the other hand, Xiao and Feng [13] used Monte Carlo analysis and SPICE simulation along with particle swarm optimization to tune the neural networks for analog fault diagnosis. Likewise, Aizenberg et al. [2] presented a method for detecting single parametric faults in analog circuits. They used a multi-valued neuron-based multilayer neural network (MLMVN) as a classifier, and a comparison with support vector machines (SVMs) was also presented in their study. These authors found that the MLMVN was highly accurate for classifying the fault class (FC) in the circuits under analysis in their study. Likewise, in the research of Kalpana et al. [14], Monte Carlo analysis was combined with machine learning techniques for fault diagnosis in analog circuits based on SBT.

Neural networks and genetic algorithms were also used in Tan et al. [15] for analog fault diagnosis, in which PSPICE simulations were used, and three different circuits were

analyzed. These authors applied back propagation neural networks with 28–36 hidden layers, depending on the CUT, and with a binary coding scheme for the outputs, where the open-circuit faults were modeled with 1×10^6 times the nominal parameters and the short circuit as 1×10^{-6} the nominal values of each element. On the other hand, Viveros-Wacher et al. [16] used a CMOS RF negative feedback amplifier as the CUT for diagnosing faults using ANNs.

Some other studies on diagnosing analog circuit faults used neural networks and fuzzy logic, as shown by Bo et al. [17], who used a negative feedback amplifier as the CUT. Simulation and deep learning were also used by Pawlowski et al. [18] for identifying circuit faults in post-market circuit boards. In other studies, Li et al. [19] used a radial basis function (RFB) neural network and a back propagation algorithm for fault detection in a differential amplifier circuit. An RBF and back propagation were also used by Wuming and Peiliang [20], who employed a particle swarm optimization algorithm to adjust the neural network. SPICE and a quantum Hopfield neural network were employed by Li et al. [21] for fault analysis in a Sallen–Key band pass filter. Likewise, Monte Carlo analysis combined with deep learning and convolutional neuronal networks were used in Moezi and Kargar [22] for fault detection in analog circuits. In another study, Mosin [23] applied a three-layer feedforward neural network for fault diagnosis, where a tan-sigmoid function was used as the transfer function for the input and intermediate layers, and a log-sigmoid function was employed for the output layer, with a Sallen–Key bandpass filter being the CUT.

Further studies are that of Grasso et al. [24], which applied a procedure based on multifrequency fault diagnosis, where the CUT was a two-stage CE audio amplifier, and that of Li and Xie [25], which used a method based on the cross-entropy between a circuit under nominal behavior and one with faults, where the CUT was analyzed by Monte Carlo simulation. Some other studies are that of Sheikhan and Sha'bani [26], which used a modular neural model for soft fault diagnosis in analog circuits; that of Liang et al. [27], which applied a support vector machine classifier and fuzzy feature selection for analog circuit fault diagnosis; and that of Wang et al. [28], which used a semi-supervised algorithm for parametric fault diagnosis in analog circuits, among many others.

The remainder of this article is structured as follows: In Section 2, the methodology used to develop the ANN used to detect circuit faults is shown. In Section 3, the results are presented. A discussion of these results is provided in Section 4. Finally, the main conclusions of this study are outlined in Section 5.

2. Fault Diagnosis Method

As previously mentioned, this study analyzed the application of a pattern-classification ANN to detect hard faults in two analog circuits in which the faults that could arise were difficult to diagnose because several faults could provide similar results, from the point of view of the selected test points used to monitor the behavior of the circuit, because the test points should be selected in accessible points of the circuit and cannot simply be located anywhere due to practical considerations. Therefore, to detect the faults that may arise in the circuit, three measurements of DC voltage and the gain voltage were considered as input variables in the first CUT and six measurements of DC voltage and the gain voltage were considered as input variables in the second one. In order to develop the ANN used in this study, the software Cadence® OrCAD® Design Systems was first used in order to carry out a Monte Carlo analysis of the tolerances of the passive components of the circuit. The first CUT is shown in Figure 1, for which it is assumed that only the DC voltage in the transistor and the gain voltage are available. In addition, a simulation was first used to determine the failure situations that presented ambiguity because it was not possible to determine precisely which was the faulty component.

Figure 1 shows the first CUT used in the present study, which is a single-stage small-signal BJT amplifier, similar to that shown in [29]. Likewise, Figure 1 shows the test points in this study. As can be observed, these test points are easily accessible. The nominal

values of the circuit's components are shown in Tables 1 and 2. First, the application of the pattern-recognition ANN to the CUT shown in Figure 1 is analyzed, and later, a more complex circuit that incorporates two amplification stages is analyzed in order to show that the ANN developed is capable of adequately predicting fault situations, as well as nominal behavior, in the second CUT.

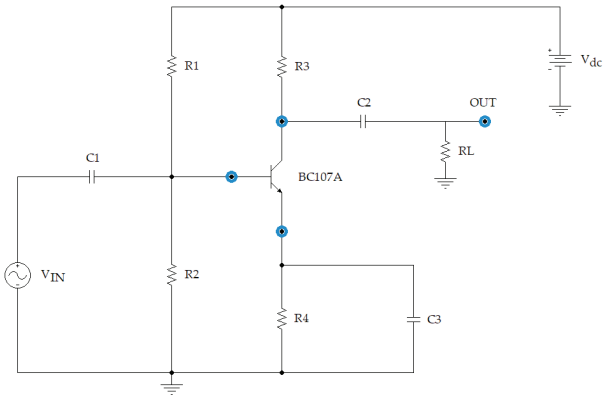

Figure 1. Electrical diagram of the first CUT (a single-stage small-signal BJT amplifier).

Table 1. Nominal values and tolerances of the passive components of the circuit.

	R_1 (kΩ)	R_2 (kΩ)	R_3 (kΩ)	R_4 (kΩ)	C_1 (μF)	C_2 (μF)	C_3 (μF)
Nominal value	15	2.7	5.6	1.8	82	10	56
Tolerance	10%	10%	10%	10%	20%	20%	20%

Table 2. Values of the load resistance and voltage sources of the circuit.

V_{IN} (Sinusoidal Voltage Source)	V_{dc} (Power Supply)	R_L (Load Resistance)
V_{INmax} = 10 mV; frequency = 1 kHz	20 V	8.2 kΩ

Table 3 shows the possible individual faults that may arise in the first CUT obtained when the hard faults (a short circuit (sc) or an open circuit (oc)) arise in the passive components. From Table 3, it is possible to see that, in this CUT, there are 14 individual hard faults, as well as the nominal behavior of the circuit {Nominal, R_{1oc}, R_{1sc}, R_{2oc}, R_{2sc}, R_{3oc}, R_{3sc}, R_{4oc},R_{4sc}, C_{1oc}, C_{1sc}, C_{2oc}, C_{2sc}, C_{3oc}, C_{3sc}}, which were coded as {F_{01}, F_{02}, F_{03}, F_{04}, F_{05}, F_{06}, F_{07}, F_{08}, F_{09}, F_{10}, F_{11}, F_{12}, F_{13}, F_{14}, F_{15} }. Therefore, these were the working modes that were analyzed. As previously mentioned, in order to characterize the behavior of the CUT, an electronic simulation was carried out by using Cadence® OrCAD® design electronic simulation software for each of the failure modes shown in Table 3. As can be observed, the faults were grouped into ambiguity groups, from the point of view of the inputs considered to diagnose the circuit's behavior, where a hard fault in a component of the circuit due to an open circuit (oc) was simulated by placing a resistance (R_{Fault} = 10 MΩ) in series with the component, and a hard fault due to a short circuit (sc) was simulated by placing a resistance (R_{Fault} = 1 Ω) in parallel with the component. The ambiguity groups were determined from the values of the inputs, which were obtained from an electronic simulation. These ambiguity groups (M_j classes) were coded as {M_{01}, M_{02}, M_{03}, M_{04}, M_{05}, M_{06}, M_{07}, M_{08}, M_{09}, M_{10}, M_{11}}. It should be mentioned that there are some fault events, such as those obtained, for example, in the M_{04} class, which include hard faults {F_{10}, F_{12}}, in the event of which it would not be possible to determine the faulty component. Moreover,

in case of a situation due to a catastrophic fault leading to an actual open circuit or a short circuit, the DC voltages and the gain voltage (Av) could be different from those obtained by the model employed in this study. These situations were obtained from the simulation when a 10 MΩ resistance was placed in series with the faulty component to simulate the open circuit (oc), and when a value of 1 Ω resistance was placed in parallel with the faulty component. Therefore, to consider the actual catastrophic fault, the values obtained in the test points were also obtained from the simulation and considered as additional inputs to those provided by the Monte Carlo analysis in order to train the ANN.

Table 3. Nominal behavior and hard faults grouped by ambiguity groups (M_j classes).

$\mathbf{M_{01}}$	$\mathbf{M_{02}}$	$\mathbf{M_{03}}$	$\mathbf{M_{04}}$	$\mathbf{M_{05}}$	$\mathbf{M_{06}}$	$\mathbf{M_{07}}$	$\mathbf{M_{08}}$	$\mathbf{M_{09}}$	$\mathbf{M_{10}}$	$\mathbf{M_{11}}$
F_{01}	F_{13}	$\{F_{02}, F_{05}, F_{11}\}$	$\{F_{10}, F_{12}\}$	F_{14}	$\{F_{09}, F_{15}\}$	F_{07}	F_{08}	F_{03}	F_{04}	F_{06}
Nominal	C_{2sc}	$\{R_{1oc}, R_{2sc}, C_{1sc}\}$	$\{C_{1oc}, C_{2oc}\}$	C_{3oc}	$\{R_{4sc}, C_{3sc}\}$	R_{3sc}	R_{4oc}	R_{1sc}	R_{2oc}	R_{3oc}

A Monte Carlo analysis considering the tolerances of the passive elements of the circuit shown in Table 1 was first carried out for each of the hard faults (open circuits and short circuits) in order to train the ANN, and 64 results were generated for each fault (63 results from the Monte Carlo analysis and 1 additional result from the actual catastrophic fault). Likewise, 64 results were obtained for the nominal behavior. These results were then used to train the pattern-recognition ANN considered in this study. Figure 2 shows the ANN applied, which was trained to detect the nominal behavior and the individual faults shown in Table 3. The hard faults that may arise in the circuit shown in Figure 1, as well as the nominal behavior, were characterized from the outputs of the ANN as shown in Equation (1):

$$S_j = column_{j-th}\{I\} \quad (1)$$

where S_j corresponds to the ANN outputs, so that the *j-th* output class corresponds to the *j-th* column of the identity matrix (I). The nominal behavior corresponds to $M_{01}(F_1)$ and the remaining classes shown in Table 3 correspond to the short-circuit and open-circuit faults, where the hard faults were grouped by the ambiguity groups obtained from the inputs used to characterize the behavior of the circuit. Therefore, the coding used to characterize a fault should provide a "1" in the position of the fault and "0" in the rest of the outputs, and hence, all outputs will have a "0" value except the *j-th* class (the fault class to be identified), which will have a "1" value. The same is applicable for the nominal value.

As can be observed, in Figure 2, the first ANN used in the present study was made up of an input layer that has four inputs (V_B, V_C, V_E, A_V), which correspond to the DC voltages in the base, collector, and emitter of the BJT transistor and to the gain voltage (A_V), respectively, as well as a single hidden layer (with two neurons and a hyperbolic tangent as the transfer function) and one output layer with a softmax transfer function, which is commonly used in pattern-recognition neural networks. As can be noted, the output layer has 11 outputs, which correspond to the 10 fault classes identified in the electronic circuit and to the nominal working mode.

As shown later in this study, with the configuration given in Figure 2, it is possible to have high accuracy in the ANN for detecting both the hard faults of the circuit and the nominal behavior. It should be mentioned that different ANN topologies were analyzed with one and two hidden layers and by using different training algorithms to adjust the ANN parameters. Finally, a Levenberg–Marquardt back propagation algorithm was selected to update the weights and biases of the ANN by using the Deep Learning Toolbox™ of MATLAB™ 2020a [30]. The ANN shown in Figure 2 was used, since it was able to provide accurate results without having to increase the number of neurons or the number of hidden layers. The metric used to test the models was the mean squared error (MSE). Different transfer functions were also analyzed in the hidden layer but, finally, a hyperbolic tangent was used in this study. On the other hand, the Levenberg–Marquardt algorithm was able to provide, in this case, more accurate results than the others analyzed, such as

the Scaled Conjugate Gradient. Therefore, the topology was that shown in Figure 2, where W_1 and b_1 are the weights and bias of the hidden layer, and W_2 and b_2 are those of the output layer. As previously mentioned, a hyperbolic tangent (f_1) was used as the transfer function in the hidden layer and a softmax transfer function (f_2) was used in the output layer.

$$Outputs = f_2(W_2 * f_1(W_1 * Inputs + b_1) + b_2) \quad (2)$$

As Figure 2 shows, the number of outputs was 11, where each output corresponds to the class identified (Mj); one of them represents the nominal behavior and the remaining classes representing the ambiguity groups, where the outputs of the ANN can be obtained from Equation (2). In order to obtain the results shown in this study, the Deep Learning Toolbox™ of MATLAB™ R2020a [30] was used.

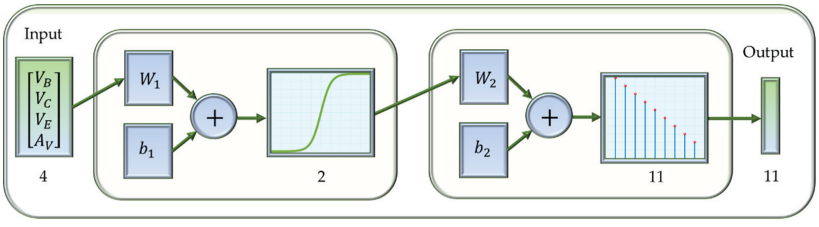

Figure 2. Pattern-recognition ANN applied in this study.

3. Results

After training the ANN shown in Figure 2 with the data obtained from the Monte Carlo simulations and following the procedure shown in the previous section, it was possible to obtain the confusion matrices shown in Figures 3–6, for training, validation, testing, and all data, respectively, where 70% of data were used for training, 15% for testing and 15% for the validation. As can be observed, in Figures 3–6, a perfect classification of the results was obtained with this ANN comprising a single hidden layer that contains two neurons.

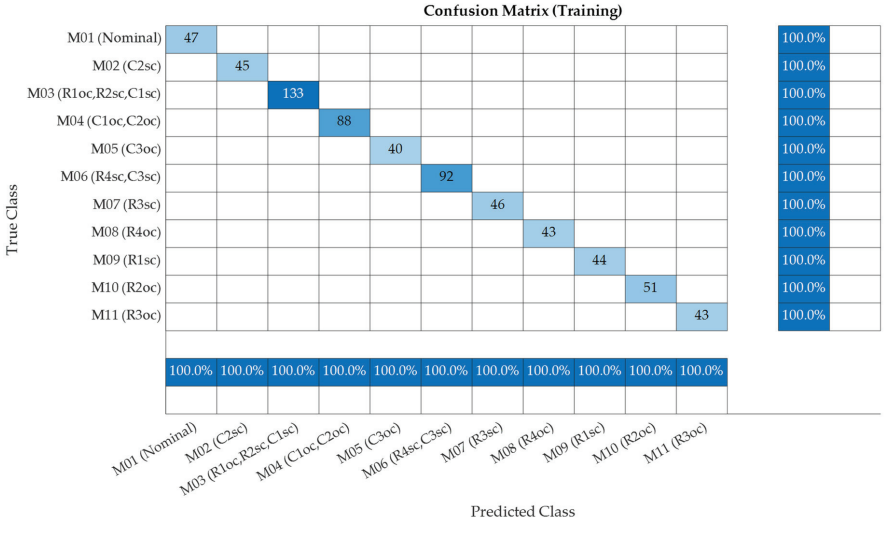

Figure 3. Confusion matrix obtained with the ANN (training data).

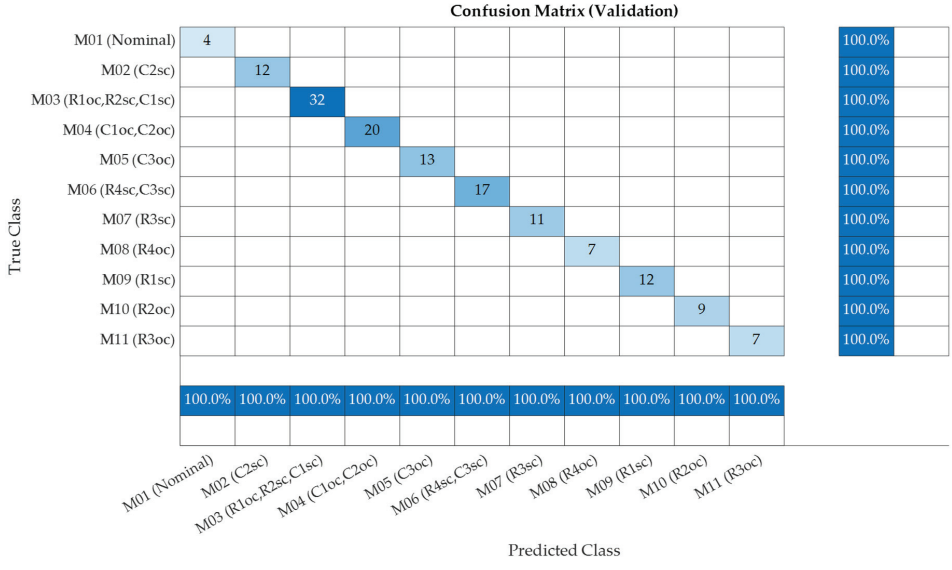

Figure 4. Confusion matrix obtained with the ANN (validation data).

Figure 3 shows the results obtained in the confusion matrix when 70% of the data from the Monte Carlo analysis were employed to train the ANN. It can be seen that there are fault classes that present a larger amount of data due to the fact that they agglutinate fault configurations that belong to the same ambiguity group. As can be seen, 100% of the data are classified correctly.

Figure 4 shows the results obtained in the confusion matrix when 15% of the Monte Carlo data were used for validation of the ANN, and Figure 5 shows the results for the test case. Similar to the results obtained during training, the ANN was able to diagnose 100% of the working modes correctly (hard faults and nominal behavior).

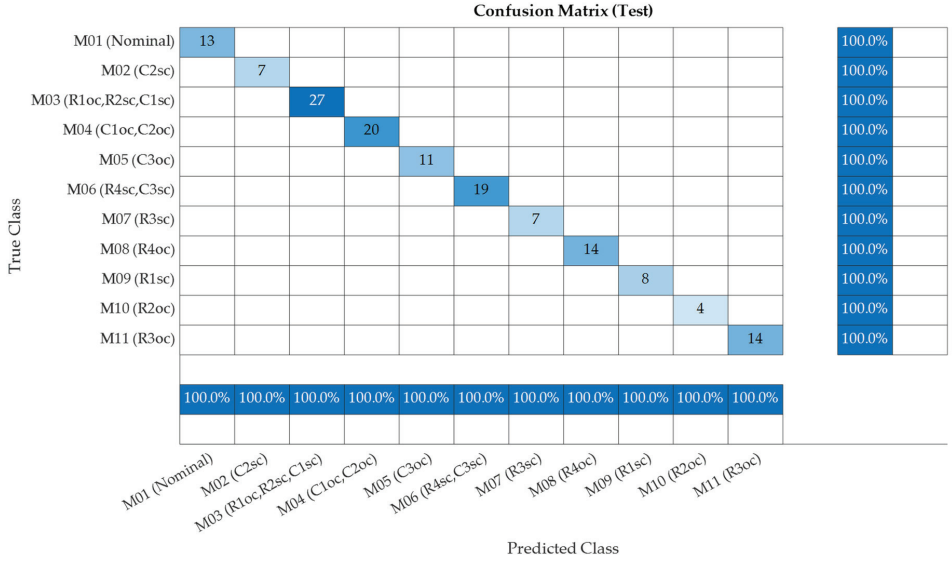

Figure 5. Confusion matrix obtained with the ANN (test data).

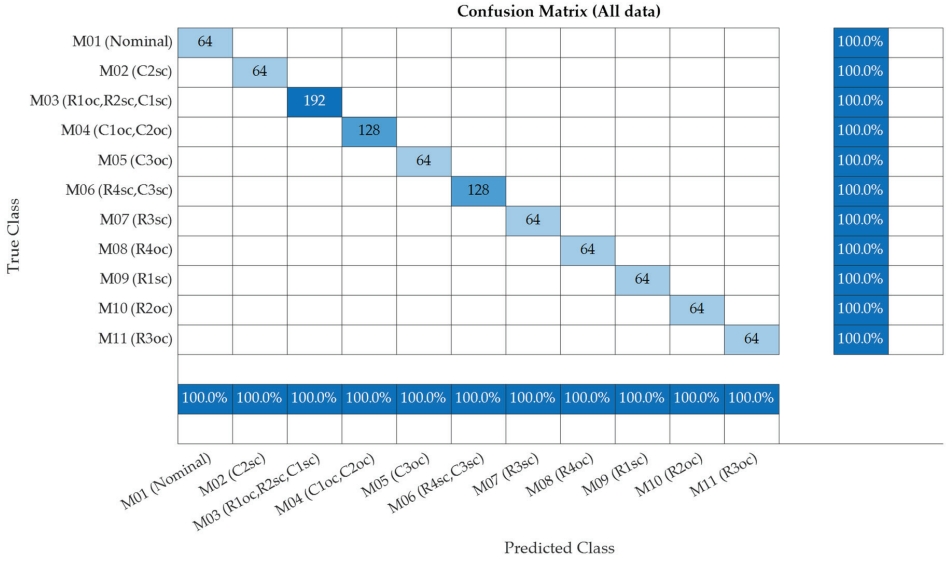

Figure 6. Confusion matrix obtained with the ANN (all data).

Figure 6 shows the results of the confusion matrix for each of the hard faults and for the nominal behavior considering all the Monte Carlo data. As previously mentioned, 64 values were used for each fault and for the nominal behavior in the Monte Carlo analysis by considering the tolerances of the components.

It can be noted in Figure 6 that, in the confusion matrix generated from all data, there are classes with a greater number of elements because the ambiguous failure modes were grouped into failure classes. Thus, for example, class M_{03} has 192 elements, since it encompasses three failure modes (R_{1oc}, R_{2sc}, C_{1sc}). In addition, it can be seen that 100% of the data were classified correctly.

Figure 7a shows the mean squared error (MSE) obtained with the ANN and Figure 7b shows the error histograms for training, validation, and testing.

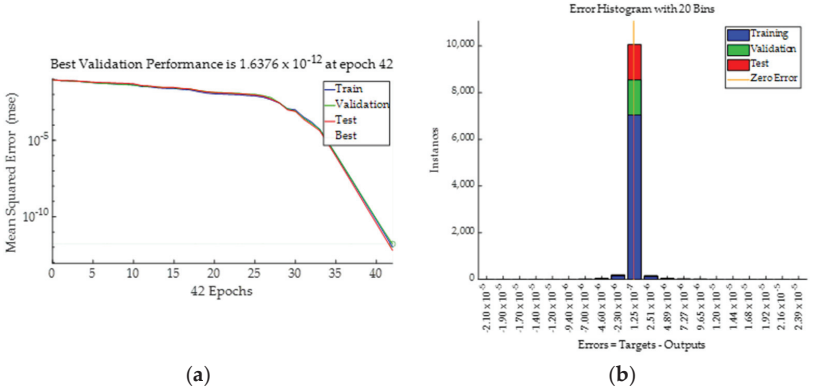

(**a**) (**b**)

Figure 7. (**a**) Validation performance (MSE) and (**b**) error histogram.

As Figure 8 shows, the ROC (receiver operating characteristic) curves have an area under the curve (AUC) of 1, which demonstrates that the pattern-recognition ANN developed was able to diagnose the working modes of the BJT amplifier once they were classified into the 11 classes shown in Table 3. In order to show that the pattern-recognition ANN is capable of predicting the behavior of other circuits, a two-stage small-signal BJT amplifier, such as that shown in Figure 9, was also analyzed in the present study.

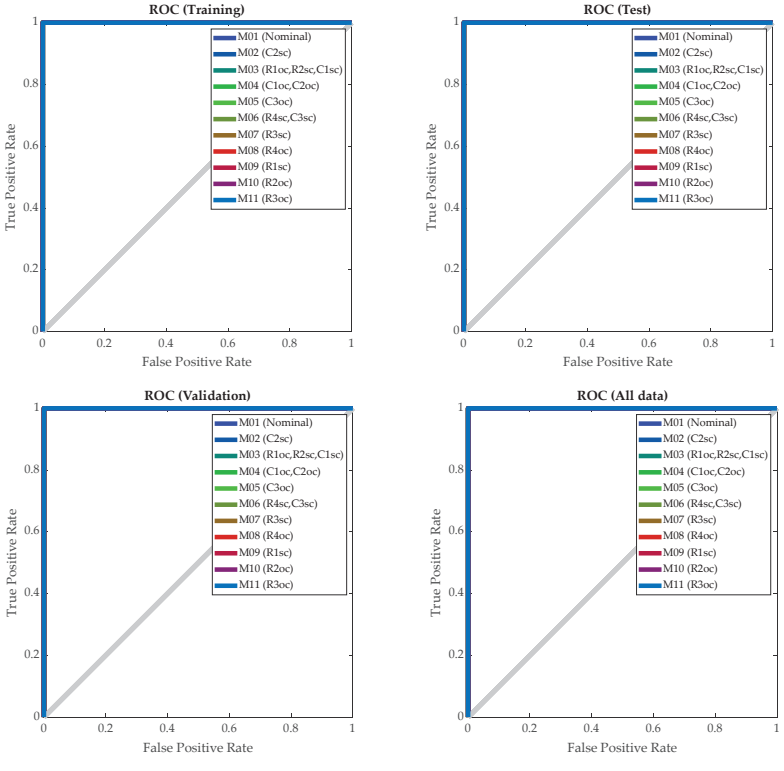

Figure 8. ROC curves.

The nominal values of the circuit's components are shown in Tables 4–6.

Table 4. Nominal values and tolerances of the passive components of the circuit (R).

	R_1 (kΩ)	R_2 (kΩ)	R_3 (kΩ)	R_4 (kΩ)	R_5 (kΩ)	R_6 (kΩ)	R_7 (kΩ)	R_8 (kΩ)
Nominal value	15	2.7	5.6	2.2	15	2.7	7.5	1.8
Tolerance	10%	10%	10%	10%	10%	10%	10%	10%

Table 5. Nominal values and tolerances of the passive components of the circuit (C).

	C_1 (μF)	C_2 (μF)	C_3 (μF)	C_4 (μF)	C_5 (μF)
Nominal value	100	1	0.56	10	47
Tolerance	20%	20%	20%	20%	20%

Table 6. Values of the load resistance and the voltage sources of the circuit.

V_{IN} (Sinusoidal Voltage Source)	V_{dc} (Power Supply)	R_L (Load Resistance)
V_{INmax} = 1 mV; frequency = 1 kHz	20 V	8.2 kΩ

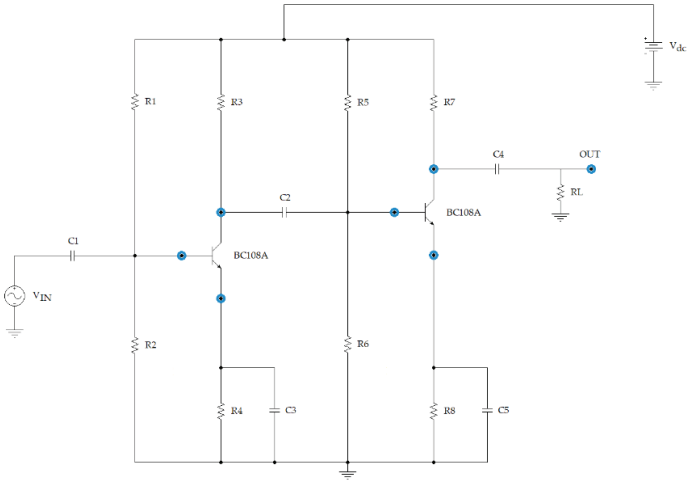

Figure 9. Electrical diagram of the second CUT (a two-stage small-signal BJT amplifier).

Table 7 shows the possible individual faults that may arise in the second CUT obtained when the hard faults (short circuit (sc) or open circuit (oc)) arise in the passive components. From Table 7, it is possible to see that, in this second CUT, there are 27 individual hard faults, as well as the nominal behavior of the circuit {nominal, C_{1oc}, C_{1sc}, C_{2oc}, C_{2sc}, C_{3oc}, C_{3sc}, C_{4oc}, C_{4sc}, C_{5oc}, C_{5sc}, R_{1oc}, R_{1sc}, R_{2oc}, R_{2sc}, R_{3oc}, R_{3sc}, R_{4oc}, R_{4sc}, R_{5oc}, R_{5sc}, R_{6oc}, R_{6sc}, R_{7oc}, R_{7sc}, R_{8oc}, R_{8sc} }, which were coded as {F_{01}, F_{02}, . . . , F_{26}, F_{27}}, where F_{01} corresponds to the nominal behavior. Therefore, these are the working modes that are analyzed in the second case. As can be observed, the faults were grouped into ambiguity groups, from the point of view of the inputs considered to diagnose the circuit's behavior, following the previously mentioned procedure, where a hard fault in a component of the circuit due to an open circuit (oc) was simulated by placing a resistance (R_{Fault} = 10 MΩ) in series with the component, and a hard fault due to a short circuit (sc) was simulated by placing a resistance (R_{Fault} = 1 Ω) in parallel with the component.

Table 7. Nominal behavior and hard faults in the second CUT grouped by ambiguity groups (M_j classes).

M_{01}	M_{02}	M_{03}	M_{04}	M_{05}	M_{06}	M_{07}	M_{08}	M_{09}
Nominal	C_{2sc}	{R_{1oc}, R_{2sc}, C_{1sc}}	{C_{1oc}, C_{2oc}, C_{4oc}}	C_{3oc}	{R_{4sc}, C_{3sc}}	R_{3sc}	R_{4oc}	R_{1sc}
M_{10}	**M_{11}**	**M_{12}**	**M_{13}**	**M_{14}**	**M_{15}**	**M_{16}**	**M_{17}**	**M_{18}**	**M_{19}**	**M_{20}**
R_{2oc}	R_{3oc}	{R_{8sc}, C_{5sc}}	{R_{5oc}, R_{6sc}}	C_{4sc}	C_{5oc}	R_{5sc}	R_{6oc}	R_{7oc}	R_{7sc}	R_{8oc}

As in the previous case, the ambiguity groups were determined from the values of the inputs, which were obtained from an electronic simulation. These ambiguity groups (M_j classes) were coded as {M_{01}, M_{02}, . . . , M_{19}, M_{20}} because, in this second case, 20 classes were detected. It should be mentioned that there are some fault events, such as those obtained, for example, in the M_{03} class, that include hard faults {R_{1oc}, R_{2sc}, C_{1sc}} for which it would not be possible to determine the faulty component. Moreover, in case of a situation due to a catastrophic fault leading to an actual open circuit or a short circuit, the DC voltages

and the gain voltage (Av) could be different to those obtained by the model employed in this study. Therefore, to consider an actual catastrophic fault, as in the previous case, the values obtained in the test points were also obtained from the simulation and considered as additional inputs to those provided by the Monte Carlo analysis in order to train the ANN.

Figure 10 shows the ANN for the second CUT, which is shown in Figure 9. As can be seen in this case, the number of inputs is seven, which correspond to the voltages at the base, emitter and collector of both transistors as well as the gain voltage (V_{B1}, V_{C1}, V_{E1}, V_{B2}, V_{C2}, V_{E2}, A_V), and the outputs are 20, corresponding to the detected fault classes and the nominal behavior. Similar to the previous case, the same network topology is used, although, in this case, there are four neurons in the hidden layer. As was done with the ANN developed for the first CUT, a Levenberg–Marquardt back propagation algorithm was selected to update the weights and biases of the ANN by using the Deep Learning Toolbox™ in MATLAB™ 2020a [30].

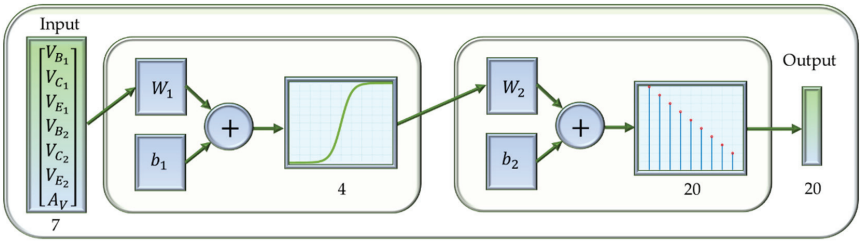

Figure 10. Pattern-recognition ANN applied to the second CUT.

Figure 11a shows the MSE values obtained versus the number of epochs, and Figure 11b shows the training state values for the ANN employed to analyze the faults in the second CUT.

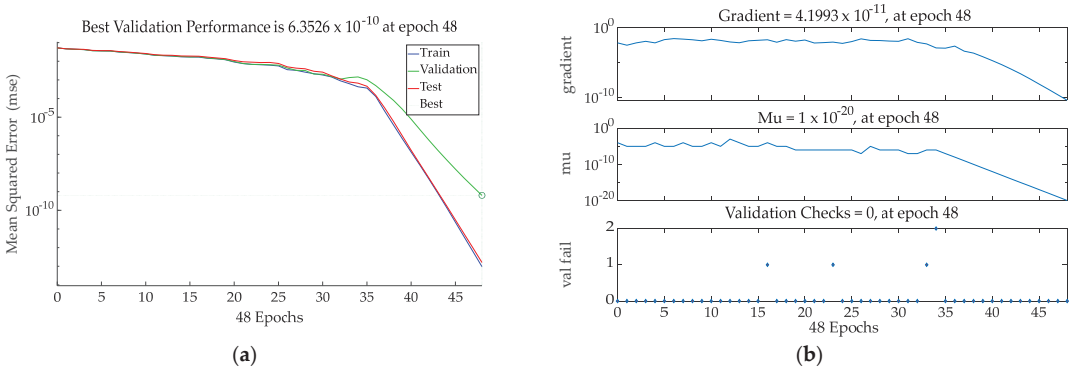

(**a**) (**b**)

Figure 11. (**a**) Validation performance (MSE) and (**b**) training state of the ANN for the second CUT.

Figure 12 shows the results obtained in the confusion matrix when 70% of the data from the Monte Carlo analysis were employed to train the ANN shown in Figure 10, which was employed to model the behavior of the second CUT. It can be seen that there are fault classes that present a larger amount of data due to the fact that they agglutinate fault configurations that belong to the same ambiguity group. As can be seen, 100% of the data are classified correctly in the second case, similar to the previous one. As can be observed, the fault classes do not have the same number of elements because the data used to train, validate, and test the ANN were randomly selected.

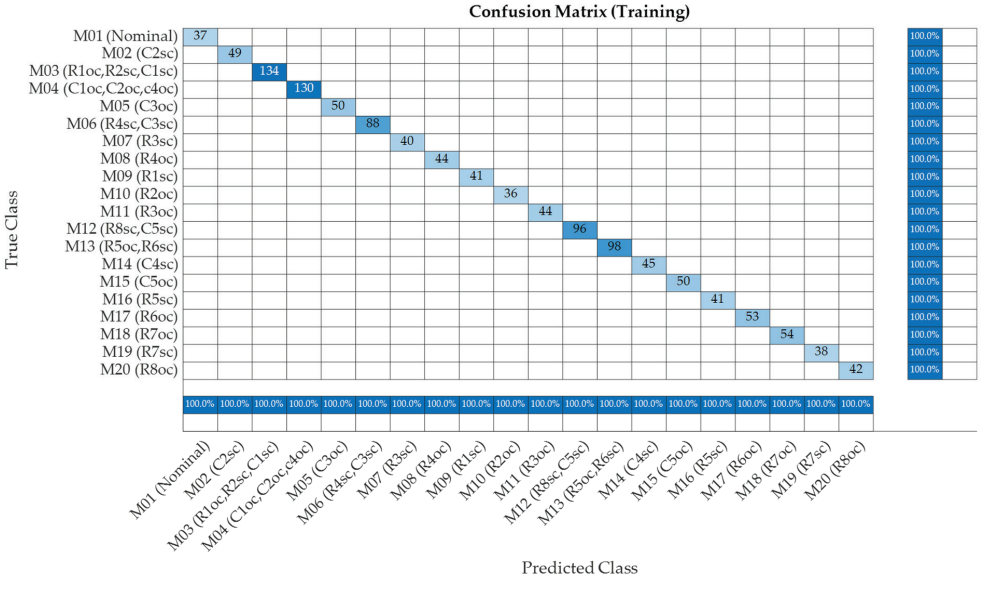

Figure 12. Confusion matrix obtained with the ANN (training data) for the second CUT.

Figure 13 shows the results obtained in the confusion matrix when 15% of the Monte Carlo data were used for validation of the ANN, and Figure 14 shows the results for the test case. Similar to the results obtained during training, the ANN was able to diagnose 100% of the working modes correctly (hard faults and nominal behavior). As can be observed, the same results as those obtained with the first CUT were obtained with the second CUT.

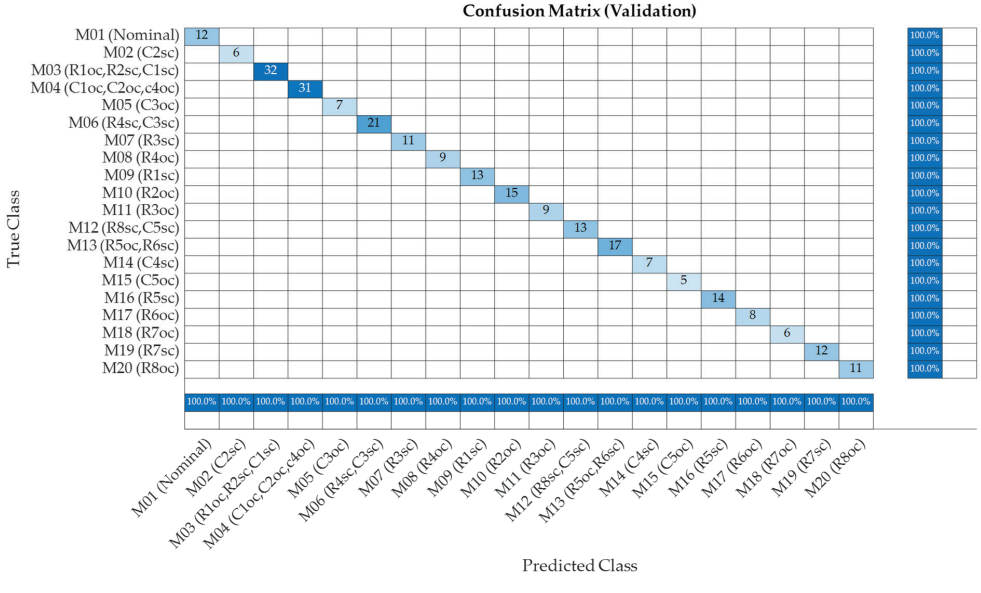

Figure 13. Confusion matrix obtained with the ANN (validation data) for the second CUT.

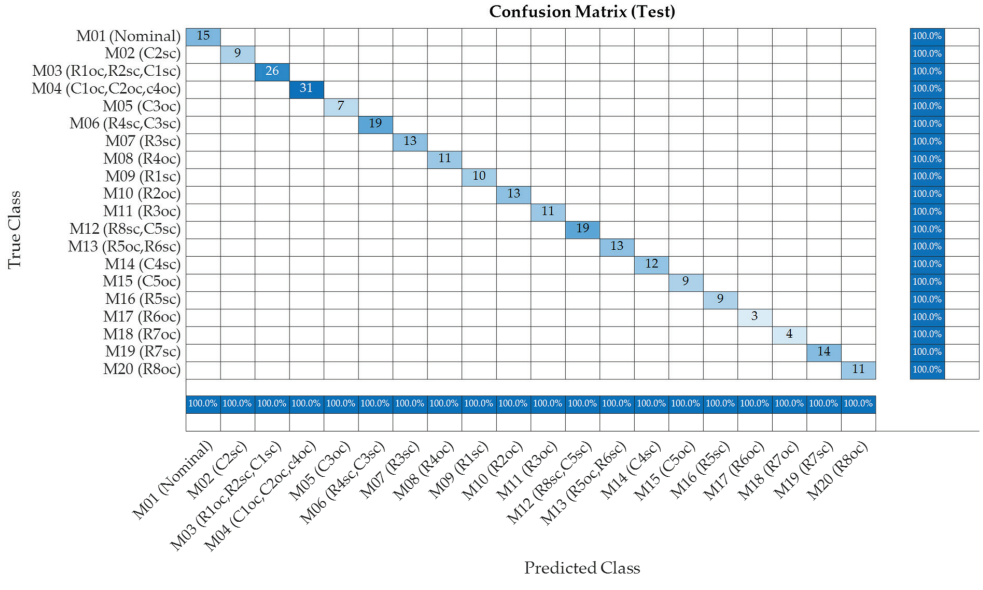

Figure 14. Confusion matrix obtained with the ANN (test data) for the second CUT.

Finally, Figure 15 shows the confusion chart for all data, and Figure 16 shows the ROC curve (all data) for the second CUT. In this curve, the true positive rate (TPR) versus the false positive rate (FPR) was plotted at different threshold settings. The ANN developed in this study is a perfect classifier for the electronic faults in the second CUT because it is perfectly able to distinguish each fault class for any FPR. Similar to the results obtained with the first CUT, it can be seen that 100% of the data were classified correctly.

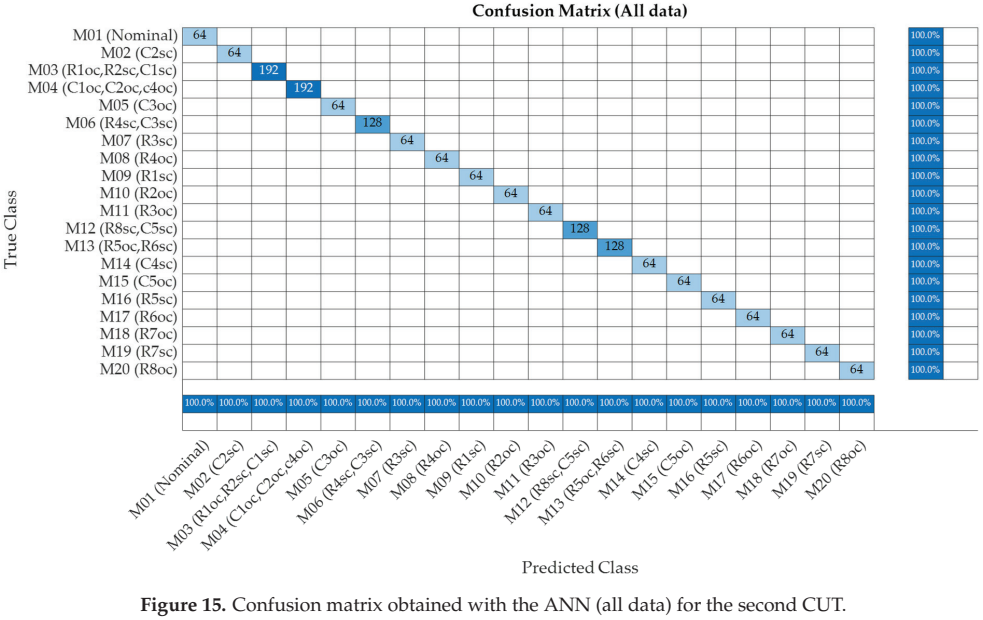

Figure 15. Confusion matrix obtained with the ANN (all data) for the second CUT.

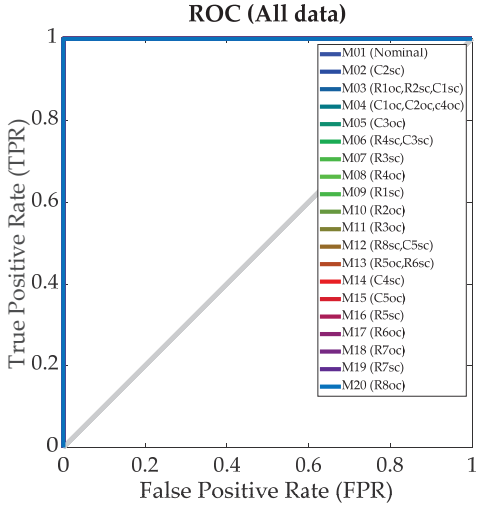

Figure 16. ROC curve (all data) for the second CUT.

4. Discussion

As Figures 8 and 16 show, the pattern-recognition ANN can correctly diagnose both the nominal behavior and the fault classes of the CUTs considered in the present study, with 100% of the data correctly classified when considering 64 Monte Carlo points for each fault and for the nominal behavior. However, in order to analyze the ability of the ANN to explain situations different from those used to train the ANN and to extract valuable information that may explain the behavior of the circuit, wider ranges of the fault resistances placed in series and in parallel with the components to simulate the hard faults in the CUT were used. These values were chosen in order to generate different fault scenarios to determine the ability of the developed ANN to diagnose possible fault situations before a hard fault occurs. To test the ANN with these fault resistances, a new Monte Carlo analysis was performed. In this later case, the number of runs generated for the fault resistance was 1024, for each fault, instead of the 64 runs used to train the ANN, following a uniform distribution, as shown in Figure 17a, for the case of a fault resistance in series with the faulty component to simulate an open circuit, and in Figure 17b for the case of a fault resistance in parallel with the faulty component to simulate a short circuit. On the other hand, the rest of the components of the CUT were allowed to vary within the specified tolerances.

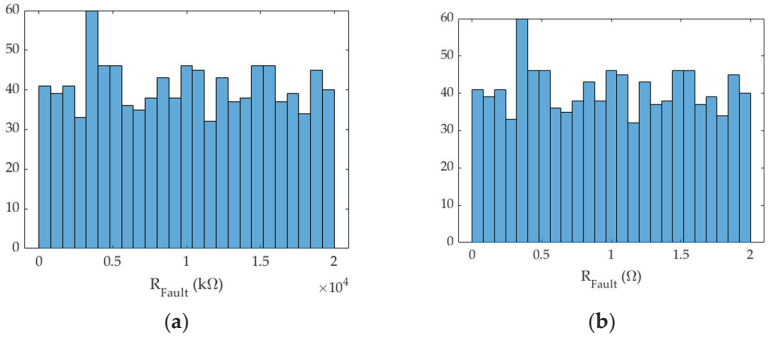

Figure 17. Histograms showing the 1024 values of the (**a**) series and (**b**) parallel fault resistances used in the Monte Carlo analysis (grouped into 25 bins).

That is, to train the neural network, an initial Monte Carlo analysis was performed for the CUT in which 64 runs were used for each fault event as well as for the nominal value. This results in a total of 960 input vectors (V_B, V_C, V_E, A_V) in the case of the first CUT and a total of 1728 input vectors (V_{B1}, V_{C1}, V_{E1}, V_{B2}, V_{C2}, V_{E2}, A_V) in the case of the second CUT. Therefore, this study employed a supervised learning technique in order to develop a pattern-recognition neural network. It should be noted that, in the case of the first CUT, 70% of these 960 data, obtained by Monte Carlo analysis, was used to train the neural network (i.e., 672 data). The remaining 15% of the data was used for validation and the other 15% for testing. The same procedure was followed for the second CUT (70% train, 15% test, 15% validation). Once the neural network was developed, the values predicted by the network for the different modes of operation were analyzed. This first Monte Carlo analysis was generated from the tolerances of the circuit components, which were considered commercial and standardized values with tolerances of 10% for resistors and 20% for capacitors. As shown in the present study, the proposed ANN is a perfect classifier since it is able to discriminate 100% of the data, not only with those used for training, but also with those used for validation and testing, in both CUTs. This can be observed in the ROC curves shown in Figure 8 (for the first CUT) and Figure 16 (for the second CUT). Once the network was developed, another Monte Carlo analysis was carried out to analyze how the ANN is able to predict other fault events, where the resistances used were different from those used to develop the ANN. This was done by varying the fault resistances (which are placed in series and in parallel with the potentially faulty components) with values of 10 MΩ ± 99.9% to simulate the open circuit and values of 1 Ω ± 99.9% for the short circuit. These values of the resistors are shown in Figure 17 and were chosen in order to generate different fault scenarios to determine the ability of the ANN to diagnose possible fault situations before a hard fault occurs. In the latter case, the Monte Carlo analysis was carried out using 1024 values for each fault event. From this, it was possible to obtain the outputs of the ANN for these fault events and to determine the thresholds from which the fault will be detected in each component. In the case of the nominal behavior, it was also considered that the tolerance of the components was increased by 50% relative to the nominal values, as shown in Figure 18, so that, in this case, the resistance tolerances were increased to 15% and up to a value of 30% in the case of the capacitors.

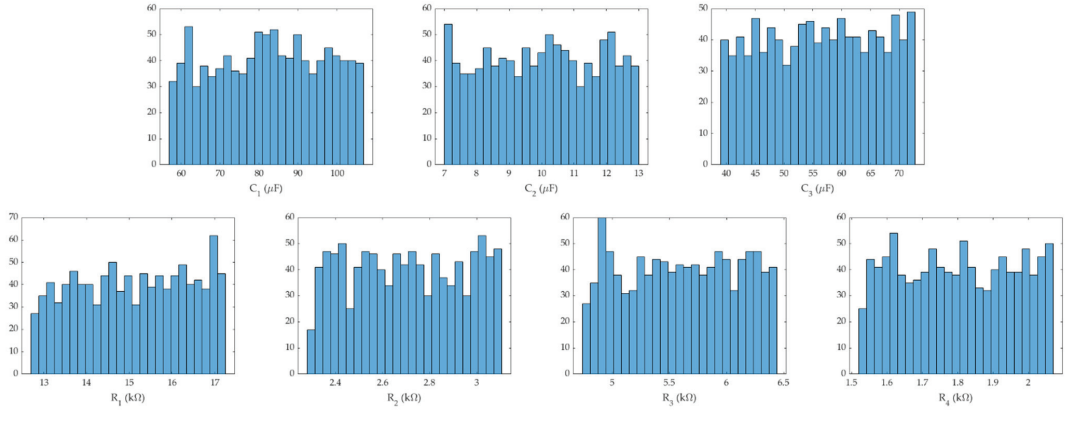

Figure 18. Histograms showing the 1024 values used in the Monte Carlo analysis (grouped into 25 bins) for each component in the case of the nominal behavior.

Figure 19 shows the results of the confusion matrix obtained in the case of a wider range of variation in the fault resistance, for the first CUT. As can be noted, the ANN was

able to correctly diagnose most of the fault classes that may arise in the first CUT, as well as the nominal behavior. A similar analysis could be carried out with the second CUT.

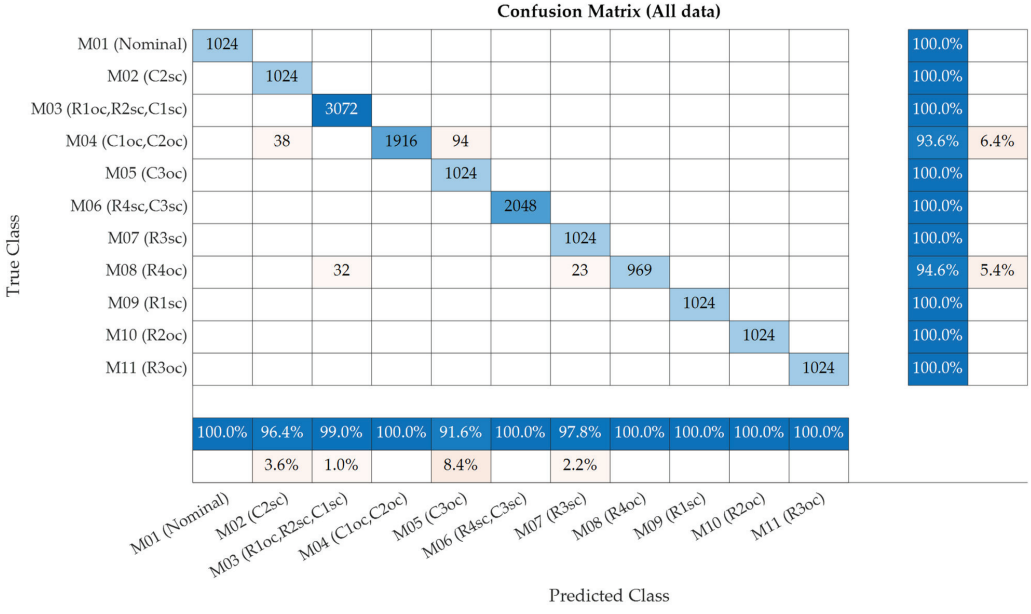

Figure 19. Predicted faults in the first CUT when the fault resistances had 99.9% variation.

Specifically, it can be observed in Figure 19 that, when the first CUT works with the nominal values of the passive components, with their tolerances increased by 50%, the ANN predicted nominal behavior in all cases (100%), which is logical, since the BJT amplifier considered as the first CUT in this study was robust to variations in the tolerances of the passive components, so it was not greatly affected by the fact that these tolerances were increased by 50% with respect to the design values, as can be observed in Figure 20.

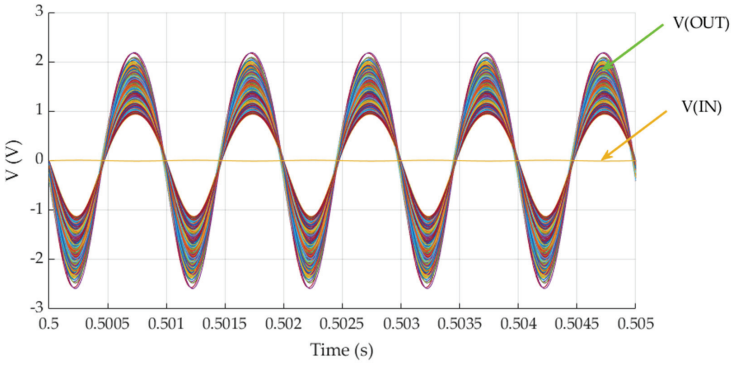

Figure 20. Response of the amplifier (Monte Carlo analysis of the nominal behavior) vs. variations in the components (increased by 50% with respect to the design values).

On the other hand, regarding the M_{02} and M_{03} classes, these were correctly diagnosed. In the case of M_{04}, there were some faults that were classified as M_{02} and M_{05} classes, which, at first, may seem like a detection failure by the ANN, but may have actually been

caused by the fact that varying the resistance in series with C_1 and C_2 within the range of values analyzed (by setting 99.9% variation in the series fault resistance) can lead to a similar configuration from the point of view of the DC voltages of the transistor. In any case, 93.6% of the cases analyzed were correctly detected. Additionally, in the case of M_{05}, M_{06}, and M_{07}, 100% of the cases were detected correctly. Moreover, regarding the M_{08} class the network predicted 94.6% of the faults. For the rest of the classes (M_{09}, M_{10}, and M_{11}), the ANN detected 100% of the faults.

Therefore, the ANN developed in this study could accurately predict the behavior of the first CUT when faced with variations in the fault resistance. Figures 21–26 show the values predicted by the ANN versus the values of the fault resistance.

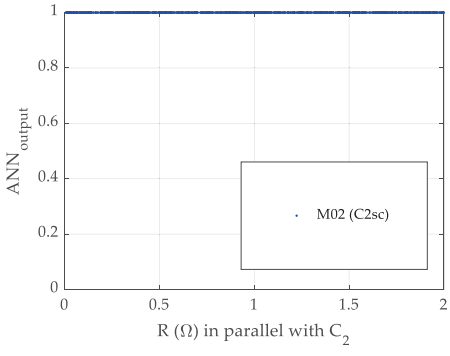

Figure 21. Predicted values (ANN) vs. fault resistance (R) in parallel with C_2.

Figure 21 shows the values predicted by the ANN for the fault class M_{02}. It can be noted that the ANN detected all the faults in the circuit for the values of parallel resistance considered.

Figure 22 shows the values predicted by the ANN for fault class M_{03}. It can be noted that the ANN detected all the faults in the circuit for the values of serial and parallel resistances (R) considered. Likewise, Figure 23a shows that, in the case of C_1 for low values of resistance in series (R) with the faulty component, some of these situations could be detected as $M_{02}\{C_{2sc}\}$ and $M_{05}\{C_{3oc}\}$ since the values of the fault resistance in series with C_1 presented a minimum value of 64 kΩ, which was obtained in this study through Monte Carlo analysis with 1024 runs. The same behavior was obtained in the case of C_2, although for different thresholds of resistance (R), as can be observed in Figure 23b.

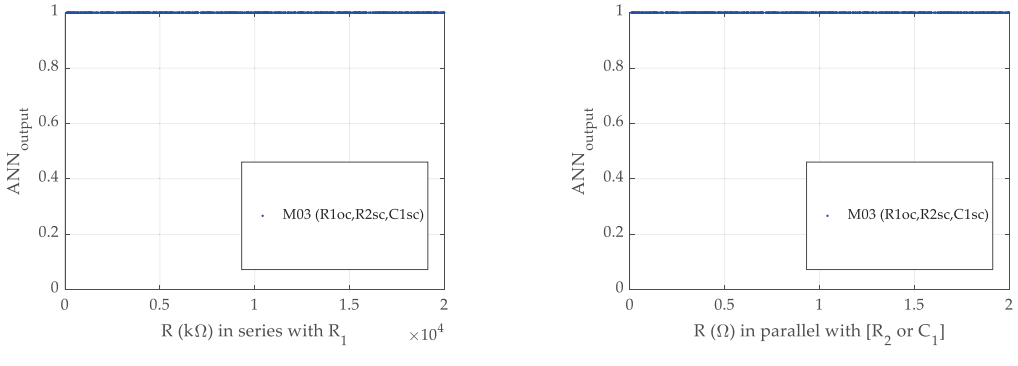

(**a**) (**b**)

Figure 22. Predicted values (ANN) vs. fault resistance (R) (**a**) in series with R_1 and (**b**) in parallel with R_2 or C_1.

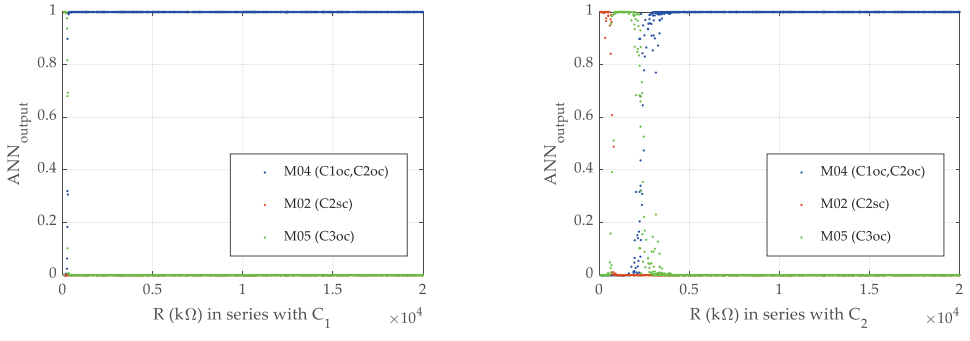

Figure 23. Predicted values (ANN) vs. fault resistance (R) (**a**) in series with C_1 and (**b**) in series with C_2.

Figure 24a shows the values predicted by the ANN for the hard faults of class M_{05} {C_{3oc}}, and Figure 24b shows those for the M_{06} {R_{4sc}, C_{3sc}} and M_{07} {R_{3sc}} fault classes. As can be observed, the ANN detected all the faults in the circuit.

Figure 25 shows the results predicted by the ANN for the M_{08} fault class (94.6% faults were detected). Finally, Figure 26 shows the results predicted for the remaining fault classes. As can be observed, 100% of fault data were correctly diagnosed in the case of R_{1sc} (M_{09}), R_{2oc} (M_{10}), and R_{3oc} (M_{11}).

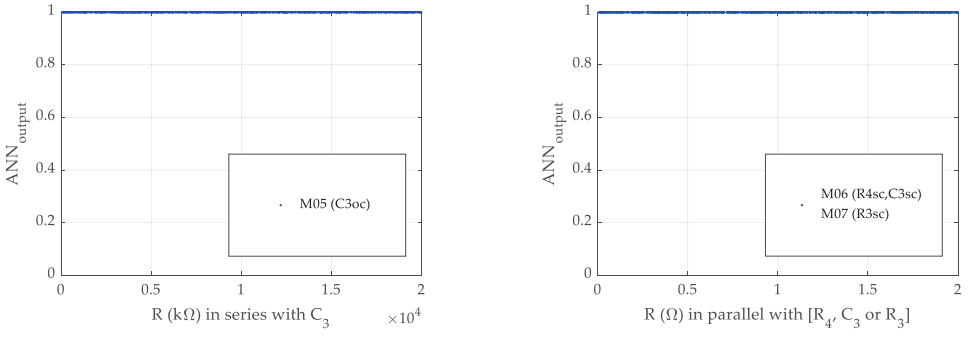

Figure 24. Predicted values (ANN) vs. fault resistance (R) (**a**) in series with C_3 and (**b**) in parallel with R_4, C_3, or R_3.

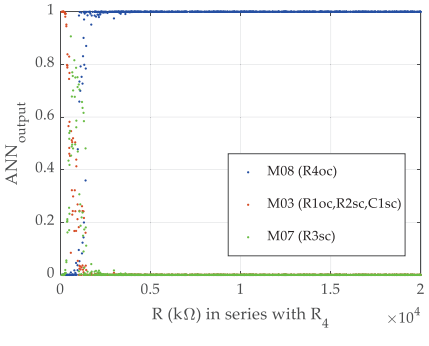

Figure 25. Predicted values (ANN) vs. fault resistance (R) in series with R_4.

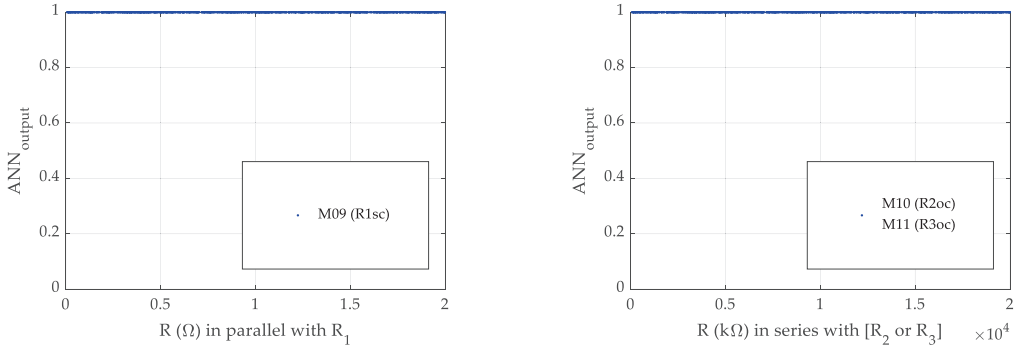

Figure 26. Predicted values (ANN) vs. fault resistance (R) (**a**) in parallel with R_1 and (**b**) in series with R_2 or R_3.

5. Conclusions

In the present study, a pattern-recognition neural network with a hyperbolic tangent as the transfer function in the hidden layer, along with a softmax transfer function in the output layer, was used to diagnose individual hard faults in two CUTs. First, a single-stage small-signal BJT amplifier was studied, followed by a two-stage small-signal BJT amplifier. It was shown that the ANN was able to predict the hard faults accurately in both CUTs considered in this work.

It was shown that a pattern-recognition ANN such as the one considered in this study can be used to model hard faults in the CUTs by training the ANN with a reduced number of measurements that have been taken at accessible points of the circuit and by using only one hidden layer with a reduced number of neurons.

Moreover, in case of applying the neural network to situations different from those used to train the neural network, where these situations have been modeled by expanding the ranges of failure resistance, it was shown that the ANN developed had high precision in diagnosing the failures in the first CUT, and it was able to explain situations different from those used to train the ANN and to extract valuable information that may explain the behavior of the circuit.

Funding: This research received no external funding.

Conflicts of Interest: The author declares no conflict of interest.

References

1. Binu, D.; Kariyappa, B.S. A survey on fault diagnosis of analog circuits: Taxonomy and state of the art. *AEU—Int. J. Electron. Commun.* **2017**, *73*, 68–83. [CrossRef]
2. Aizenberg, I.; Belardi, R.; Bindi, M.; Grasso, F.; Manetti, S.; Luchetta, A.; Piccirilli, M.C. A Neural Network Classifier with Multi-Valued Neurons for Analog Circuit Fault Diagnosis. *Electronics* **2021**, *10*, 349. [CrossRef]
3. Fedi, G.; Manetti, S.; Piccirilli, M.C.; Starzyk, J. Determination of an optimum set of testable components in the fault diagnosis of analog linear circuits. *IEEE Trans. Circuits Syst. I Fundam. Theory Appl.* **1999**, *46*, 779–787. [CrossRef]
4. Starzyk, J.A.; Pang, J.; Manetti, S.; Piccirilli, M.C.; Fedi, G. Finding ambiguity groups in low testability analog circuits. *IEEE Trans. Circuits Syst. I Fundam. Theory Appl.* **2000**, *47*, 1125–1137. [CrossRef]
5. Li, J.; Yu, H.; Cheng, W.T.; Schuermyer, C.; Dong, X. A supervised ANN method for memory failure signature classification. In Proceedings of the ICSICT 2012 IEEE 11th International Conference Solid State Integrated Circuit Technology, Xi'an, China, 29 October–1 November 2012; pp. 1–3. [CrossRef]
6. Guedidi, A.; Guettaf, A.; Cardoso, A.J.M.; Laala, W.; Arif, A. Bearing Faults Classification Based on Variational Mode Decomposition and Artificial Neural Network. In Proceedings of the 2019 IEEE 12th International Symposium on Diagnostics for Electrical Machines, Power Electronics and Drives SDEMPED 2019, Toulouse, France, 27–30 August 2019; pp. 391–397. [CrossRef]
7. Calcagno, S.; Morabito, F.C.; Versaci, M. A novel approach for detecting and classifying defects in metallic plates. *IEEE Trans. Magn.* **2003**, *39*, 1531–1534. [CrossRef]

8. Shao, Y.E.; Lin, S.-C. Using a Time Delay Neural Network Approach to Diagnose the Out-of-Control Signals for a Multivariate Normal Process with Variance Shifts. *Mathematics* **2019**, *7*, 959. [CrossRef]
9. Kerboua, A.; Metatla, A.; Kelailia, R.; Batouche, M. Fault Diagnosis in Induction Motor using Pattern Recognition and Neural Networks. In Proceedings of the 2018 International Conference on Signal, Image, Vision and their Applications SIVA 2018, Guelma, Algeria, 26–27 November 2018; pp. 1–7. [CrossRef]
10. Gao, T.; Yang, J.; Jiang, S.; Yang, C. A Dual-input Fault Diagnosis Model Based on Convolutional Neural Networks and Gated Recurrent Unit Networks for Analog Circuits. In Proceedings of the 2021 IEEE International Instrumentation and Measurement Technology Conference (I2MTC), Glasgow, Scotland, 17–20 May 2021; pp. 1–6. [CrossRef]
11. Zhang, C.; Zha, D.; Wang, L.; Mu, N. A Novel Analog Circuit Soft Fault Diagnosis Method Based on Convolutional Neural Network and Backward Difference. *Symmetry* **2021**, *13*, 1096. [CrossRef]
12. Wang, Q.; Yu, Y.; Ahmed, H.O.A.; Darwish, M.; Nandi, A.K. Open-Circuit Fault Detection and Classification of Modular Multilevel Converters in High Voltage Direct Current Systems (MMC-HVDC) with Long Short-Term Memory (LSTM) Method. *Sensors* **2021**, *21*, 4159. [CrossRef] [PubMed]
13. Xiao, Y.; Feng, L. A novel neural-network approach of analog fault diagnosis based on kernel discriminant analysis and particle swarm optimization. *Appl. Soft Comput. J.* **2012**, *12*, 904–920. [CrossRef]
14. Kalpana, V.; Maheswar, R.; Nandakumar, E. Multiple parametric fault diagnosis using computational intelligence techniques in linear filter circuit. *J. Ambient Intell. Humaniz. Comput.* **2020**, *11*, 5533–5545. [CrossRef]
15. Tan, Y.; He, Y.; Cui, C.; Qiu, G. A novel method for analog fault diagnosis based on neural networks and genetic algorithms. *IEEE Trans. Instrum. Meas.* **2008**, *57*, 2631–2639. [CrossRef]
16. Viveros-Wacher, A.; Rayas-Sánchez, J.E.; Brito-Brito, Z. Analog Gross Fault Identification in RF Circuits Using Neural Models and Constrained Parameter Extraction. *IEEE Trans. Microw. Theory Tech.* **2019**, *67*, 2143–2150. [CrossRef]
17. Bo, F.; Peng, X.; Junjie, L.; Ming, D. Analog circuit fault diagnosis based on neural network and fuzzy logic. In Proceedings of the 2009 Chinese Control and Decision Conference, Guilin, China, 17–19 June 2009; Volumes 380–384, pp. 199–202. [CrossRef]
18. Pawlowski, K.; Chkravarty, S.; Joginipelly, A.K. Simulation and Fault Diagnosis in Post-Manufacturing Mixed Signal Circuits. In Proceedings of the 2020 Pan Pacific Microelectronics Symposium (Pan Pacific), Hapuna Beach Prince Hotel, Waimea, HI, USA, 10–13 February 2020; pp. 1–6. [CrossRef]
19. Li, X.; Zhang, Y.; Wang, S.; Zhai, G. A method for analog circuits fault diagnosis by neural network and virtual instruments. In Proceedings of the 2011 3rd International Workshop on Intelligent Systems and Applications, Wuhan, China, 28–29 May 2011. [CrossRef]
20. Wuming, H.; Peiliang, W. Analog Circuit Fault Diagnosis Based on RBF Neural Network Optimized by PSO Algorithm. In Proceedings of the 2010 International Conference on Intelligent Computation Technology and Automation, Changsha, China, 11–12 May 2020; Volume 1, pp. 628–631. [CrossRef]
21. Li, P.; Chai, Y.; Cen, M.; Qiu, Y.; Zhang, K. Multiple fault diagnosis of analog circuit using quantum hopfield neural network. In Proceedings of the 2013 25th Chinese Control and Decision Conference (CCDC), Guiyang, China, 25–27 May 2013; pp. 4238–4243. [CrossRef]
22. Moezi, A.; Kargar, S.M. Simultaneous fault localization and detection of analog circuits using deep learning approach. *Comput. Electr. Eng.* **2021**, *92*, 107162. [CrossRef]
23. Mosin, S. Quality improvement of analog circuits fault diagnosis based on ANN using clusterization as preprocessing. In Proceedings of the 2015 IEEE East-West Design & Test Symposium (EWDTS), Batumi, Georgia, 26–29 September 2015; pp. 1–4. [CrossRef]
24. Grasso, F.; Manetti, S.; Piccirilli, M.C. An approach to analog fault diagnosis using genetic algorithms. In Proceedings of the 12th IEEE Mediterranean Electrotechnical Conference (IEEE Cat. No. 04CH37521), Dubrovnik, Croatia, 12–15 May 2004; Volume 1, pp. 111–114. [CrossRef]
25. Li, X.; Xie, Y. Analog circuits fault detection using cross-entropy approach. *J. Electron. Test. Theory Appl.* **2013**, *29*, 115–120. [CrossRef]
26. Sheikhan, M.; Sha'bani, A.A. PSO-optimized modular neural network trained by OWO-HWO algorithm for fault location in analog circuits. *Neural Comput. Appl.* **2013**, *23*, 519–530. [CrossRef]
27. Liang, H.; Zhu, Y.; Zhang, D.; Chang, L.; Lu, Y.; Zhao, X.; Guo, Y. Analog Circuit Fault Diagnosis Based on Support Vector Machine Classifier and Fuzzy Feature Selection. *Electronics* **2021**, *10*, 1496. [CrossRef]
28. Wang, L.; Zhou, D.; Tian, H.; Zhang, H.; Zhang, W. Parametric Fault Diagnosis of Analog Circuits Based on a Semi-Supervised Algorithm. *Symmetry* **2019**, *11*, 228. [CrossRef]
29. Dieste-Velasco, M.I. Application of a Fuzzy Inference System for Optimization of an Amplifier Design. *Mathematics* **2021**, *9*, 2168. [CrossRef]
30. Beale, M.H.; Hagan, M.T.; Demuth, H.B. *Deep Learning Toolbox™ User's Guide, R2020a, The MathWorks: Copyright 1992–2020*; The MathWorks Inc.: Natick, MA, USA, 2020.

mathematics

MDPI

Article

Rotating Flow in a Nanofluid with CNT Nanoparticles over a Stretching/Shrinking Surface

Nor Azizah Yacob [1], Nor Fadhilah Dzulkifli [1], Siti Nur Alwani Salleh [2], Anuar Ishak [3,*] and Ioan Pop [4]

[1] Faculty of Computer and Mathematical Sciences, Universiti Teknologi MARA Pahang, Jengka 26460, Pahang, Malaysia; norazizah872@uitm.edu.my (N.A.Y.); nfd@uitm.edu.my (N.F.D.)
[2] Faculty of Computer and Mathematical Sciences, Universiti Teknologi MARA Kedah, Merbok 08400, Kedah, Malaysia; sitinuralwani@uitm.edu.my
[3] Department of Mathematical Sciences, Faculty of Science and Technology, Universiti Kebangsaan Malaysia, Bangi 43600, Selangor, Malaysia
[4] Department of Mathematics, Babeş-Bolyai University, 400578 Cluj-Napoca, Romania; popm.ioan@yahoo.co.uk
* Correspondence: anuar_mi@ukm.edu.my; Tel.: +60-389215785

Abstract: The steady three-dimensional rotating flow past a stretching/shrinking surface in water and kerosene-based nanofluids containing single and multi-walled carbon nanotubes (CNTs) is investigated. The governing equations are converted to similarity equations, and then numerically solved using MATLAB software. The impacts of rotational, suction, and nanoparticle volume fraction on the flow and the thermal fields, as well as velocity and temperature gradients at the surface, are represented graphically and are analyzed. Further, the friction factor and the heat transfer rate for different parameters are presented in tables. It is found that the heat transfer rate increases with increasing nanoparticle volume fraction as well as suction parameter in water and kerosene-based nanofluids of single and multi-walled CNTs. However, the increment in the rotating flow parameter decreases the rate of heat transfer. Multi-walled carbon nanotubes and kerosene-based nanofluid contribute to heat transfer rates better than single-walled carbon nanotubes and water-based nanofluid, respectively. A unique solution exists for the stretching surface, while two solutions are obtained for the shrinking surface. Further analysis of their stabilities shows that only one of them is stable over time.

Keywords: carbon nanotubes; heat transfer; nanofluid; rotating; stretching/shrinking

Citation: Yacob, N.A.; Dzulkifli, N.F.; Salleh, S.N.A.; Ishak, A.; Pop, I. Rotating Flow in a Nanofluid with CNT Nanoparticles over a Stretching/Shrinking Surface. *Mathematics* **2022**, *10*, 7. https://doi.org/10.3390/math10010007

Academic Editors: Camelia Petrescu and Valeriu David

Received: 17 November 2021
Accepted: 15 December 2021
Published: 21 December 2021

Publisher's Note: MDPI stays neutral with regard to jurisdictional claims in published maps and institutional affiliations.

Copyright: © 2021 by the authors. Licensee MDPI, Basel, Switzerland. This article is an open access article distributed under the terms and conditions of the Creative Commons Attribution (CC BY) license (https://creativecommons.org/licenses/by/4.0/).

1. Introduction

Researchers have begun looking for fluids with high thermal conductivity in the last few decades since traditional fluids have low thermal conductivity. In 1873, Maxwell studied the dispersion of solid particles with a size of millimeters and micrometers in traditional fluids. However, the existence of these particles caused a drastic drop in pressure, clogged flow channels, caused sedimentation of the particles to occur faster and erosion on the channel, and certain particles are too large for the microsystem [1]. Choi and Eastman [1] proposed a new fluid called nanofluid, in which solid particles with sizes ranging from 1–100 nm are dispersed in traditional fluids such as water, oil, and ethylene glycol. This fluid is significant because of its unique chemical and physical properties, as well as its high thermal conductivity, which can improve the heat transfer rate [2]. Waqas et al. [3] investigated the impact of nanoparticle shape's factor in porous media and discovered that platelet and cylindrical shapes had the highest thermal conductivity compared to brick and spherical shapes. A comprehensive collection of nanofluids studies can be found in [4–9].

Recently, many studies have considered carbon nanotubes as nanoparticles since their thermal conductivity is better and higher than those of traditional fluids. Carbon nanotubes (CNTs) are a sheet of graphene rolled into a cylinder introduced by Iigima in 1991. Carbon nanotubes are classified as single-walled (SWCNT) and multi-walled (MWCNT). They have

a nanometer diameter size which is much smaller than other advanced semiconductor devices, and the length of nanotubes can exceed 1 micrometer. In addition, carbon nanotubes also offer unique electrical characteristics that other semiconductors lack. Further studies on unique features and review of carbon nanotubes can be found through investigation by Popov [10], Patel et al. [11], and Taherian et al. [12].

Due to their performance in optimizing thermal conductivity, researchers carried out many works to study the influence of carbon nanotubes availability and other effects in the fluids on the flow behavior. Khan et al. [13] investigated the fluid flow and heat transmission of CNTs nanofluid over a flat plate using three types of base fluids: water, engine oil, and kerosene. In comparison to water and kerosene-CNTs, they discovered that engine oil-CNTs have the highest heat transfer rate. Using a homogeneous model, Akbar et al. [14] investigated the stagnation-point flow of carbon nanotubes towards a stretching sheet with a magnetic field, velocity slip effect, and convective boundary condition. It was discovered that a higher magnetic field reduces the heat transfer rate at the surface and that single-walled carbon nanotubes have a higher heat transfer rate than multi-walled carbon nanotubes. Later, using similar CNTs nanofluid, Hayat et al. [15] explored the stagnation-point flow over a nonlinear stretching surface with homogeneous–heterogeneous reactions. Hussain et al. [16] studied a three-dimensional flow of carbon nanotubes nanofluids over a nonlinearly stretching sheet with heat generation/absorption effect in a porous medium. Sreedevi et al. [17] investigated the heat and mass transfer characteristics of nanofluids containing CNTs towards a vertical cone in a porous medium by considering the magnetic field, chemical reaction, and suction/injection parameters. The findings revealed that increasing the nanoparticle volume fraction improves the heat transfer rate, while employing multi-walled CNT. as nanoparticles enhance the heat transfer over single-walled CNT. The latter conclusion was similar to Anuar et al. [18], who analyzed the mixed convection flow towards a moving plate. However, Anuar et al. [18] obtained a different result when the nanoparticle volume fraction increased. Reddy and Sreedevi [19] studied the effects of thermal radiation and single-walled carbon nanotubes inside a square chamber. From their observation, increasing these two factors enhances the heat transfer rate. Ramzan et al. [20] applied the Cattaneo–Christov heat flux model to analyze the impact of nonlinear thermal radiation and thermal stratification on the unsteady magnetohydrodynamics (MHD) flow between two stretching rotatory discs in nanofluid with carbon nanotubes. They discovered that nonlinear thermal radiation gives rise to the temperature of both SWCNT and MWCNT. Relevant studies on CNT nanofluids can be found in [21–23].

Investigation of the rotating flow towards a stretching surface is vital due to its application in a variety of scientific, technical, and product applications, designing and modeling jet engines, pumps, and vacuum cleaners, as well as geophysical flows [24]. Numerical studies on rotating flow have been explored by many researchers such as Singh and Sathi [25], who obtained an exact solution using Laplace transform for an unsteady rotating flow over an infinite plate. Wang [26] was the first to study the rotating flow over a stretching sheet using a perturbation method to identify the velocity profiles of small parameter values. Later, Nazar et al. [27] extended the work of Wang [26] by considering an unsteady flow. This study was expanded by Ali et al. [28] to the shrinking surface, and they obtained dual solutions. Further, Sreelakshmi et al. [29] included the magnetic field and thermal radiation effects in their study. They reported that the magnetic field, thermal radiation parameter, and rotation parameter increase the heat transfer rate. Rosali et al. [30] investigated the rotating flow over an exponentially permeable shrinking surface and found dual solutions. Rana et al. [31] implemented the Boungiorno model to investigate the MHD flow across a stretching surface in a nanofluid and numerically solved using a finite element method. It was revealed that the local Nusselt number and the local Sherwood number drop with the growth of the rotational parameter. By combining the Boungiorno and Tiwari-Das models, Bakar et al. [32] solved a rotating flow towards a shrinking surface with three nanoparticles types: copper, alumina, and titania with water as the base fluid using a shooting method. Different from Rana et al. [31], they found dual solutions, and the

local Nusselt number and the local Sherwood number increase with rotational parameter. Further, Krishna [33] explored the MHD effect in a Jeffrey fluid on a porous surface with hall and ion slip.

Nadeem et al. [34] explored a rotating flow towards a stretching surface utilizing copper and titania as the nanoparticles with water as the base fluid by applying the Tiwari-Das model. They discovered that increasing the volume fraction of nanoparticles boosted the heat transfer rate while decreasing it with the rotation parameter. Hayat et al. [15] reported the analytical results of rotating flow with carbon nanotubes over a stretching porosity surface. Dzulkifli et al. [35] continued the study of Ali et al. [28] by considering the unsteady rotation flow on a stretched surface in a nanofluid with copper as nanoparticles. According to the findings, as the rotating parameter and nanoparticle volume percentage grew, the heat transfer rate dropped. Later, Salleh et al. [36] expanded the study by Nadeem et al. [34] to a permeable shrinking surface and obtained dual solutions. A stability analysis was carried out to inspect the stability of the solutions in the long run. As stated by Merkin [37] and Harris et al. [38], the upper branch is always stable, and this discovery is similar to the works made by Salleh et al. [36], Mustafa et al. [39], and Tshivhi and Makinde [40]. Hafeez et al. [41] explored the MHD rotating flow in a hybrid nanofluid using a finite element method. Mehdipour et al. [42] designed a rotating liquid sheet (RLS) contactor to explore carbon dioxide absorption from a gas stream using water-based SiO_2 and ZnO nanofluids. CO_2 absorption is more significant in the presence of ZnO than in the presence of SiO_2, and tube rotation can improve absorption performance.

Acharya et al. [43] conducted a comparative investigation of SWCNTs and MWCNTs in a rotating regime over a stretching sheet in the presence of a magnetic field using the RK-4 method. They noticed that increasing the volume fraction of SWCNTs and MWCNTs improved the nanofluid temperature. Later, Shah et al. [44] analyzed a similar investigation over a stretching sheet using an analytical method. Noranuar et al. [45] studied a non-coaxial rotation flow towards a permeable moving disk in an MHD Casson nanofluid. Hussain et al. [46] extended the work of Nadeem et al. [34] by considering engine oil as the base fluid with copper and aluminum dioxide as nanoparticles over a stretching surface with slip condition. They found that copper nanoparticles react as heat carriers better than aluminum oxide. Manjunatha et al. [47] recently performed a numerical analysis to study the effect of a magnetic field on the fluid flow over a rotating disc in a nanofluid using single and multi-walled carbon nanotubes as nanoparticles and water as the base fluid. They reported that a unique solution exists, and the increase in the magnetic field caused an increase in the radial velocity and temperature.

Based on the previous studies mentioned above, many researchers focused on a rotational flow/disk over a stretching surface rather than a permeable stretching/shrinking surface and only obtained a unique solution. A permeable stretching/shrinking surface is vital in industrial applications since the surface may not be static such as polymer extrusion process, liquid crystal, and ceramic production [48]. Therefore, the present study aims to extend the work of Nadeem et al. [34] and Salleh et al. [36] by exploring the impact of rotation flow parameter, suction and nanoparticle volume fraction on the heat and mass transfer characteristics of carbon nanotubes (SWCNTs and MWCNTs) over a permeable stretching/shrinking surface in a nanofluid. Since no studies have considered this mathematical model with carbon nanotubes nanoparticles, the results obtained are genuine and can contribute to the development of this field. The numerical results are obtained using the bvp4c solver in MATLAB software, and a stability analysis is performed to investigate the stability of the solutions as time evolves.

2. Mathematical Model Description

A steady 3D rotating boundary layer flow of a carbon nanotube past a stretching or shrinking surface is examined, and its physical model is illustrated in Figure 1. In Figure 1, x, y, and z are the Cartesian coordinates with x- and y-axes measured in the plane $z = 0$ where nanofluid is in the region $z \geq 0$. The boundary $z = 0$ is elastic and linearly stretched

or shrunk by two equal and opposite forces in the direction of the x-axis with the velocity $U_w = ax$. The fluid is rotating at an angular velocity Ω in the z-direction. It is assumed that the nanofluid has a uniform wall and ambient temperatures, T_w and T_∞, respectively. Based on the above assumptions, the governing equations of mass, momentum, and energy are (see Nadeem et al. [34] and Salleh et al. [36]):

$$\frac{\partial u}{\partial x} + \frac{\partial v}{\partial y} + \frac{\partial w}{\partial z} = 0 \tag{1}$$

$$u\frac{\partial u}{\partial x} + v\frac{\partial u}{\partial y} + w\frac{\partial u}{\partial z} - 2\Omega v = \frac{\mu_{nf}}{\rho_{nf}}\frac{\partial^2 u}{\partial z^2} \tag{2}$$

$$u\frac{\partial v}{\partial x} + v\frac{\partial v}{\partial y} + w\frac{\partial v}{\partial z} + 2\Omega u = \frac{\mu_{nf}}{\rho_{nf}}\frac{\partial^2 v}{\partial z^2} \tag{3}$$

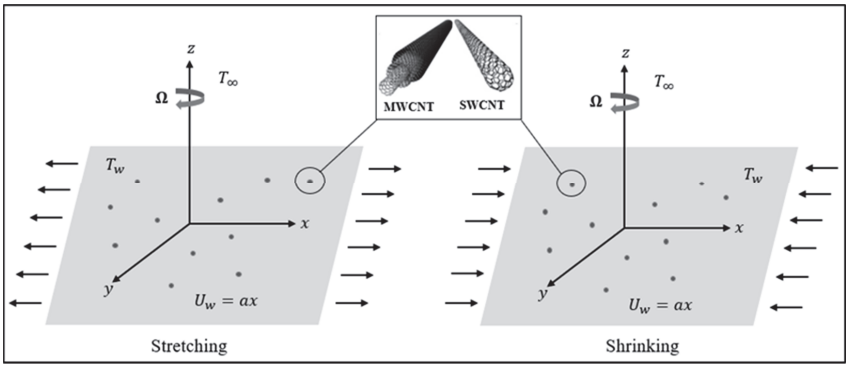

Figure 1. Physical model of the problem.

$$u\frac{\partial T}{\partial x} + v\frac{\partial T}{\partial y} + w\frac{\partial T}{\partial z} = \alpha_{nf}\frac{\partial^2 T}{\partial z^2} \tag{4}$$

The boundary conditions are

$$\begin{gathered} u = \varepsilon U_w,\ v = 0,\ w = -w_0,\ T = T_w \text{ at } z = 0, \\ u \to 0,\ v \to 0,\ T \to T_\infty \text{ as } z \to \infty \end{gathered} \tag{5}$$

where u, v, and w represent the velocity components in the x-, y-, and z-directions, respectively, T represents the fluid temperature, w_0 is the constant mass flux with $w_0 > 0$ indicates injection, while $w_0 < 0$ is for suction. Further, ε is the stretching or shrinking parameter with $\varepsilon > 0$ for stretching, $\varepsilon < 0$ for shrinking and $\varepsilon = 0$ for the static surface. In this study, we adopt the theoretical model proposed by Xue [49] as follows:

$$\begin{gathered} \mu_{nf} = \frac{\mu_f}{(1-\varphi)^{2.5}},\ \alpha_{nf} = \frac{k_{nf}}{(\rho C_p)_{nf}},\ \frac{k_{nf}}{k_f} = \frac{1-\varphi+2\varphi\frac{k_{cnt}}{k_{cnt}-k_f}\ln\frac{k_{cnt}+k_f}{2k_f}}{1-\varphi+2\varphi\frac{k_f}{k_{cnt}-k_f}\ln\frac{k_{cnt}+k_f}{2k_f}}, \\ \rho_{nf} = (1-\varphi)\rho_f + \varphi\rho_{cnt},\ (\rho C_p)_{nf} = (1-\varphi)(\rho C_p)_f + \varphi(\rho C_p)_{cnt}. \end{gathered} \tag{6}$$

In Equation (6), μ is dynamic viscosity, ρ is density, α is thermal diffusivity, k is thermal conductivity, C_p is the specific heat capacity at constant pressure, φ is nanoparticle volume fraction parameter in which the subscripts nf, f, and cnt, respectively, refer to nanofluid, fluid, and carbon nanotube.

The thermophysical properties of SWCNT and MWCNT for different base fluids namely, water (Pr = 6.2) and kerosene (Pr = 21) at the temperature 20–25 °C are given in Table 1 (Khan et al. [13]). Water and kerosene are chosen as the base fluids for comparison with the previous studies. Furthermore, water has the highest specific heat that can stabilize the temperature and is used as a cooling agent, while oil-based nanofluids are often utilized in industrial operations for lubrication or high-temperature applications [50]. The following similarity transformations (7) are introduced for solving Equations (2)–(4) together with the boundary conditions (5) that satisfy the continuity Equation (1).

$$u = axf'(\eta),\ v = axh(\eta),\ w = -\sqrt{av_f}f(\eta),\ \eta = \sqrt{\frac{a}{\nu_f}}z,\ \theta(\eta) = \frac{T - T_\infty}{T_w - T_\infty} \tag{7}$$

Table 1. Thermophysical properties of base fluids and carbon nanotubes.

Physical Properties	Base Fluids		Nanoparticles	
	Water (Pr = 6.2)	Kerosene (Pr = 21)	SWCNT	MWCNT
ρ (kg/m^3)	997	783	2600	1600
C_p (J/kgK)	4179	2090	425	796
k (W/mK)	0.613	0.145	6600	3000

From Equation (7), the velocity mass flux can be defined as

$$w_0 = -\sqrt{av_f}S \tag{8}$$

where $S = f(0)$, S is the suction parameter in which $S < 0$ for injection and $S > 0$ for suction. Substituting Equations (6) and (7) into Equations (2)–(5) yields

$$\frac{1}{(1-\varphi)^{2.5}\left[1-\varphi+\varphi\left(\rho_{cnt}/\rho_f\right)\right]}f''' + ff'' - f'^2 + 2\omega h = 0 \tag{9}$$

$$\frac{1}{(1-\varphi)^{2.5}\left[1-\varphi+\varphi\left(\rho_{cnt}/\rho_f\right)\right]}h'' + fh' - f'h - 2\omega f' = 0 \tag{10}$$

$$\frac{k_{nf}/k_f}{\Pr\left[1-\varphi+\varphi(\rho C_p)_{cnt}/(\rho C_p)_f\right]}\theta'' + f\theta' = 0 \tag{11}$$

The BCs (5) become

$$\begin{gathered}(0) = S,\ h(0) = 0,\ f'(0) = \varepsilon,\ \theta(0) = 1,\\ h(\eta) \to 0,\ f'(\eta) \to 0,\ \theta(\eta) \to 0 \text{ as } \eta \to \infty.\end{gathered} \tag{12}$$

In Equations (9)–(12), prime denotes the differentiation w.r.t. similarity variable η, $\omega = \Omega/a$ is the rotation parameter, and Pr is the Prandtl number.

The quantities of physical interest are the skin friction coefficients and the local Nusselt number (heat transfer rate at the surface). The skin friction coefficients in the x- and y-directions, respectively, are given by:

$$C_{fx} = \frac{\tau_{xz}}{\rho_f U_w^2},\ C_{fy} = \frac{\tau_{yz}}{\rho_f U_w^2} \tag{13}$$

The local Nusselt number Nu_x is defined as:

$$Nu_x = \frac{xq_w}{k_f(T_w - T_\infty)} \tag{14}$$

The shear stresses τ_{xz}, τ_{yz} and the heat flux q_w at the surface are given by:

$$\tau_{xz} = \mu_{nf}\left(\frac{\partial u}{\partial z}\right)_{z=0},\ \tau_{yz} = \mu_{nf}\left(\frac{\partial v}{\partial z}\right)_{z=0},\ q_w = -k_{nf}\left(\frac{\partial T}{\partial z}\right)_{z=0} \tag{15}$$

Using Equation (15), Equations (13) and (14) become

$$\begin{gathered} Re_x^{\frac{1}{2}} C_{fx} = \frac{1}{(1-\varphi)^{2.5}} f''(0),\ Re_x^{\frac{1}{2}} C_{fy} = \frac{1}{(1-\varphi)^{2.5}} h'(0), \\ Re_x^{-1/2}\, Nu_x = -\frac{k_{nf}}{k_f}\theta'(0). \end{gathered} \tag{16}$$

where $Re_x = Ux/\nu_f$ is the local Reynold number.

3. Stability Analysis

To investigate the stability of the solutions of Equations (9)–(12) over time, the unsteady case of Equations (2)–(4) are considered as [37,51]

$$\frac{\partial u}{\partial t} + u\frac{\partial u}{\partial x} + v\frac{\partial u}{\partial y} + w\frac{\partial u}{\partial z} - 2\Omega v = \frac{\mu_{nf}}{\rho_{nf}}\frac{\partial^2 u}{\partial z^2} \tag{17}$$

$$\frac{\partial v}{\partial t} + u\frac{\partial v}{\partial x} + v\frac{\partial v}{\partial y} + w\frac{\partial v}{\partial z} + 2\Omega u = \frac{\mu_{nf}}{\rho_{nf}}\frac{\partial^2 v}{\partial z^2} \tag{18}$$

$$\frac{\partial T}{\partial t} + u\frac{\partial T}{\partial x} + v\frac{\partial T}{\partial y} + w\frac{\partial T}{\partial z} = \alpha_{nf}\frac{\partial^2 T}{\partial z^2} \tag{19}$$

where t refers to time. Next, new dimensionless variables are introduced as follows:

$$\begin{gathered} \tau = \frac{Ut}{x},\ u = ax\frac{\partial f}{\partial \eta}(\eta,\tau),\ v = axh(\eta,\tau),\ w = -\sqrt{a\nu_f}f(\eta,\tau),\ \eta = \sqrt{\frac{a}{\nu_f}}z, \\ \theta(\eta,\tau) = \frac{T-T_\infty}{T_w-T_\infty} \end{gathered} \tag{20}$$

By utilizing Equation (20), Equations (17)–(19) become:

$$\frac{1}{(1-\varphi)^{2.5}\left[1-\varphi+\varphi\left(\rho_{cnt}/\rho_f\right)\right]}\frac{\partial^3 f}{\partial \eta^3} + f\frac{\partial^2 f}{\partial \eta^2} - \left(\frac{\partial f}{\partial \eta}\right)^2 + 2\omega h - \frac{\partial^2 f}{\partial \eta \partial \tau} = 0. \tag{21}$$

$$\frac{1}{(1-\varphi)^{2.5}\left[1-\varphi+\varphi\left(\rho_{cnt}/\rho_f\right)\right]}\frac{\partial^2 h}{\partial \eta^2} + f\frac{\partial h}{\partial \eta} - h\frac{\partial f}{\partial \eta} - 2\omega\frac{\partial f}{\partial \eta} - \frac{\partial h}{\partial \tau} = 0. \tag{22}$$

$$\frac{k_{nf}/k_f}{\Pr\left[1-\varphi+\varphi(\rho C_p)_{cnt}/(\rho C_p)_f\right]}\frac{\partial^2 \theta}{\partial \eta^2} + f\frac{\partial \theta}{\partial \eta} - \frac{\partial \theta}{\partial \tau} = 0 \tag{23}$$

where their respective boundary conditions are

$$\begin{gathered} f(0,\tau) = S,\ h(0,\tau) = 0,\ \frac{\partial f}{\partial \eta}(0,\tau) = \varepsilon,\ \theta(0,\tau) = 1, \\ h(\eta,\tau) \to 0,\ \frac{\partial f}{\partial \eta}(\eta,\tau) \to 0,\ \theta(\eta,\tau) \to 0 \text{ as } \eta \to \infty. \end{gathered} \tag{24}$$

The stability of the steady flow solutions $f(\eta) = f_0(\eta), h(\eta) = h_0(\eta)$, and $\theta(\eta) = \theta_0(\eta)$ can be determined by writing $f(\eta,\tau), h(\eta,\tau)$ and $\theta(\eta,\tau)$ as follows [51]:

$$\begin{gathered} f(\eta,\tau) = f_0(\eta) + e^{-\gamma\tau}F(\eta,\tau),\ h(\eta,\tau) = h_0(\eta) + e^{-\gamma\tau}H(\eta,\tau), \\ \theta(\eta,\tau) = \theta_0(\eta) + e^{-\gamma\tau}G(\eta,\tau). \end{gathered} \tag{25}$$

In Equation (25), $F(\eta,\tau)$, $H(\eta,\tau)$, and $G(\eta,\tau)$ are smaller relative to $f = f_0(\eta)$, $h = h_0(\eta)$ and $\theta = \theta_0(\eta)$, respectively, and γ is the eigenvalue. Substituting Equation (25) into Equations (21)–(24), the following system of linear eigenvalue problem is obtained:

$$\begin{aligned}\frac{1}{(1-\varphi)^{2.5}\left[1-\varphi+\varphi\left(\rho_{cnt}/\rho_f\right)\right]}\frac{\partial^3 F}{\partial\eta^3}+f_0\frac{\partial^2 F}{\partial\eta^2}+F\frac{\partial^2 f_0}{\partial\eta^2}-2\frac{\partial f_0}{\partial\eta}\frac{\partial F}{\partial\eta}+2\omega H\\ +\gamma\frac{\partial F}{\partial\eta}-\frac{\partial^2 F}{\partial\eta\partial\tau}=0\end{aligned} \tag{26}$$

$$\begin{aligned}\frac{1}{(1-\varphi)^{2.5}\left[1-\varphi+\varphi\left(\frac{\rho_{cnt}}{\rho_f}\right)\right]}\frac{\partial^2 H}{\partial\eta^2}+f_0\frac{\partial H}{\partial\eta}+F\frac{\partial h_0}{\partial\eta}-H\frac{\partial f_0}{\partial\eta}-h_0\frac{\partial F}{\partial\eta}+\gamma H\\ -\frac{\partial H}{\partial\tau}-2\omega\frac{\partial F}{\partial\eta}=0\end{aligned} \tag{27}$$

$$\frac{k_{nf}/k_f}{\Pr\left[1-\varphi+\varphi(\rho C_p)_{cnt}/(\rho C_p)_f\right]}\frac{\partial^2 G}{\partial\eta^2}+f_0\frac{\partial G}{\partial\eta}+F\frac{\partial\theta_0}{\partial\eta}+\gamma G-\frac{\partial G}{\partial\tau}=0 \tag{28}$$

subject to the boundary conditions

$$\begin{aligned}F(0,\tau)=0,\ H(0,\tau)=0,\ \tfrac{\partial F}{\partial\eta}(0,\tau)=0,\ G(0,\tau)=0\\ H(\eta,\tau)\to 0,\ \tfrac{\partial F}{\partial\eta}(\eta,\tau)\to 0,\ G(\eta,\tau)\to 0 \text{ as } \eta\to\infty.\end{aligned} \tag{29}$$

Following Weidman et al. [51], we take $\tau = 0$ to determine the initial decay or growth of the solutions in Equation (25) and functions F, H, and G can be written as $F_0(\eta)$, $H_0(\eta)$, and $G_0(\eta)$, respectively. Thus, Equations (26)–(29) can be simplified as

$$\frac{1}{(1-\varphi)^{2.5}\left[1-\varphi+\varphi\left(\rho_{cnt}/\rho_f\right)\right]}F_0'''+f_0F_0''+F_0f_0''-2f_0'F_0'+2\omega H_0+\gamma F_0'=0 \tag{30}$$

$$\frac{1}{(1-\varphi)^{2.5}\left[1-\varphi+\varphi\left(\frac{\rho_{cnt}}{\rho_f}\right)\right]}H_0''+f_0H_0'+F_0h_0'-H_0f_0'-h_0F_0'+\gamma H_0-2\omega F_0'=0 \tag{31}$$

$$\frac{1}{(1-\varphi)^{2.5}\left[1-\varphi+\varphi\left(\frac{\rho_{cnt}}{\rho_f}\right)\right]}H_0''+f_0H_0'+F_0h_0'-H_0f_0'-h_0F_0'+\gamma H_0-2\omega F_0'=0 \tag{32}$$

subjected to the conditions

$$\begin{aligned}F_0(0)=0,\ H_0(0)=0,\ F_0'^{(0)}=0,\ G_0(0)=0,\\ H_0(\eta)\to 0,\ F_0'(\eta)\to 0,\ G_0(\eta)\to 0 \text{ as } \eta\to\infty.\end{aligned} \tag{33}$$

According to Harris et al. [38], the value of the smallest eigenvalue γ can be computed by relaxing the boundary conditions on $F_0(\eta)$, $H_0(\eta)$ or $G_0(\eta)$. In this study, the condition $F_0'(\eta)\to 0$ as $\eta\to\infty$ is selected to be relaxed, thus, Equations (30)–(33) are solved along with a new boundary condition $F_0''(0)=1$ using bvp4c solver in MATLAB software.

4. Results and Discussion

The system of nonlinear ordinary differential Equations (8)–(10) associated with the boundary conditions (11) was numerically computed for the diverse values of physical emerging parameters, namely, rotation parameter ω, stretching or shrinking parameter ε, nanoparticle volume fraction parameter φ, and suction parameter S. Two types of base fluids, which are water ($\Pr = 6.2$) and kerosene ($\Pr = 21$), were considered using both SWCNT and MWCNT. Numerical outcomes are obtained through the function bvp4c in MATLAB software are displayed in graphs and tables [52]. The numerical values of the velocity gradients at the surface of x- component $f''(0)$ and y-component $h'(0)$ were compared with the previous work of Wang [26] and Mustafa et al. [53] in the absence of

stretching/shrinking parameter ($\varepsilon = 0$), nanoparticle volume fraction ($\varphi = 0$), and suction parameter ($S = 0$) for SWCNTs using water as the base fluid. Those values are listed in Table 2, and the acquired results were deemed adequate compared to previously obtained data by Wang [26] and Mustafa et al. [53]. Dual solutions are obtained as depicted in Figures 2–14, and it was worth performing a stability analysis as described in Section 2 to identify the stability of the solutions. The finding of stability analysis is discussed at the end of Section 3.

Table 2. Comparison values of $f''(0)$ and $h'(0)$ for multiple values of rotation parameter ω when $\varepsilon = \varphi = S = 0$ and Pr = 6.2 (water) for SWCNT.

ω	**Wang [26]**		**Mustafa et al. [53]**		**Present Study**	
	$f''(0)$	$h'(0)$	$f''(0)$	$h'(0)$	$f''(0)$	$h'(0)$
0	−1	0	−1	0	−1	0
0.5	−1.1384	−0.5128	−1.13838	−0.51276	−1.138381	−0.512760
1.0	−1.3250	−0.8371	−1.32503	−0.83709	−1.325029	−0.837098
2.0	−1.6523	−1.2873	−1.65235	−1.28726	−1.652352	−1.287259

In this paper, the results in Figures 2–14 and Tables 3–6 are presented to discuss the impact of various physical parameters on the physical quantities of interest, such as the local skin friction coefficients $Re_x^{1/2}C_{fx}$ and $Re_x^{1/2}C_{fy}$, and the local Nusselt number $Re_x^{-1/2}Nu_x$, which are proportional to $f''(0)$, $h'(0)$ and $-\theta'(0)$, respectively, as well as the velocity and temperature profiles. Figures 2 and 3 present the variation of $f''(0)$ and $h'(0)$ for several values of rotation parameter ω versus stretching or shrinking parameter ε for SWCNT using water as the base fluid. These figures reveal that rising ω causes the gradients $f''(0)$ and $h'(0)$ to grow. However, it is noted that $h'(0)$ becomes zero when there is no rotation in the flow or when $\omega = 0$. Further, a higher rotation rate causes fluid to move faster, which accelerates the velocity. The drag force between the fluid and the surface expedites and consequently increases the velocity gradient for both components. In addition, an increase in the values of $f''(0)$ and $h'(0)$ is due to the decrement in the momentum boundary layer thickness as ω increases (see Figure 7; Figure 8). Besides, as the stretching or shrinking parameter changes from the negative value to the positive one, both values of $f''(0)$ and $h'(0)$ seems to decrease. It happens because when the surface shrinks, less friction occurs on the surface than on the stretching surface. The rotating fluid forces the friction to appear in the flow significantly when the surface is being compressed. As a result, the velocity gradients rise for the shrinking surface compared to the stretching surface. Furthermore, the emergence of dual solutions is noticed when ε is in the region of $\varepsilon_c < \varepsilon \leq -0.8$. Meanwhile, unique solutions are obtained when $\varepsilon > -0.8$ and no solutions when $\varepsilon < \varepsilon_c$.

The variation of $f''(0)$ and $h'(0)$ and $-\theta'(0)$ for some values of nanoparticle volume fraction parameter φ versus suction parameter S are plotted in Figures 4–6 for MWCNT using kerosene as the base fluid. It is found from these plots that increasing the values of φ tends to diminish the $f''(0)$ and $-\theta'(0)$. However, the reverse effect is noted for $h'(0)$ since adding more nanoparticles in the flow will slow down the collision between the molecules of the base fluid and nanoparticles, which in turn reduces $f''(0)$.

Since the surface is compressed or stretched in the x-direction, thus, the effect of φ on $f''(0)$ is more pronounced than $h'(0)$. As noticed in Figure 5, there is a slight increase in the value of $h'(0)$ when φ increases. Besides, the reduction in $-\theta'(0)$, as displayed in Figure 6, is due to the thickening of the thermal boundary layer thickness as φ increases. This phenomenon prevents heat from the surface from being transferred to the surrounding fluid, and consequently, reduces $-\theta'(0)$. It is also revealed that as S intensifies, $f''(0)$ and $-\theta'(0)$ seem to increase, while the contrary phenomenon is noticed for $h'(0)$. The increment of $-\theta'(0)$ is influenced by the surface texture where suction causes heat to be transferred from the wall to the fluid. It is observed that non-unique solutions occur for the particular

values of the suction parameter and no solutions when $S < S_c$. Figure 4 reveals that in the case of regular fluid ($\varphi = 0$), dual solutions exist in the range of $S_c = 1.9965 < S \leq 2.31$. Meanwhile, as the value of φ increases from 0 to 0.02 and 0.04, dual solutions are obtained in the range of $S_c = 2.0265 < S \leq 2.34$ and $S_c = 2.0584 < S \leq 2.38$, respectively. As can be seen in Figures 2–5, the range of solutions that exist are different based on the pertinent parameters involved. Figures 2 and 3 show that when different values of ω are plotted versus ε, the range of solutions increases with an increasing rotation parameter ω. However, Figures 4 and 5 depict that it decreases when the nanoparticle volume fraction φ increases.

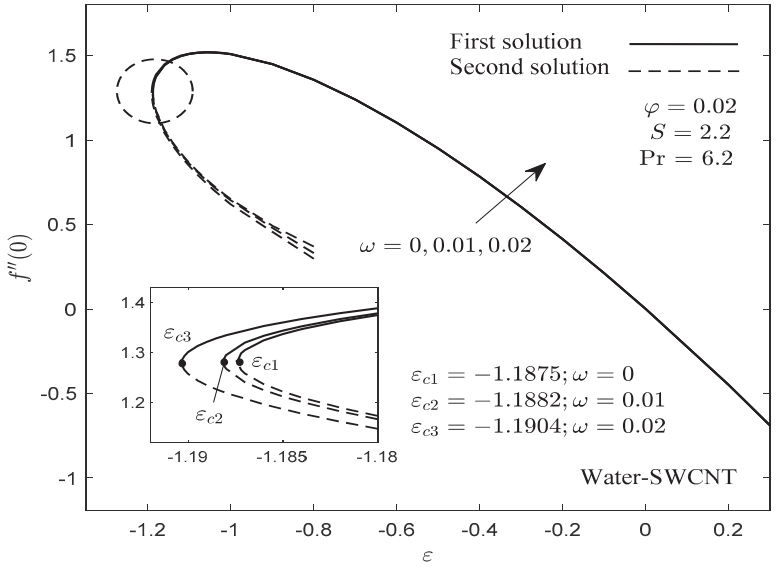

Figure 2. Values of $f''(0)$ for some values of ω versus ε.

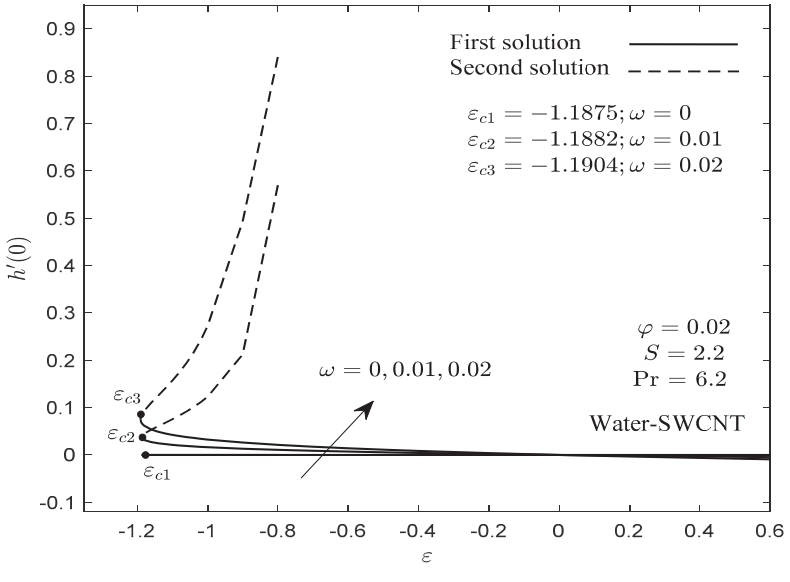

Figure 3. Values of $h'(0)$ for some values of ω versus ε.

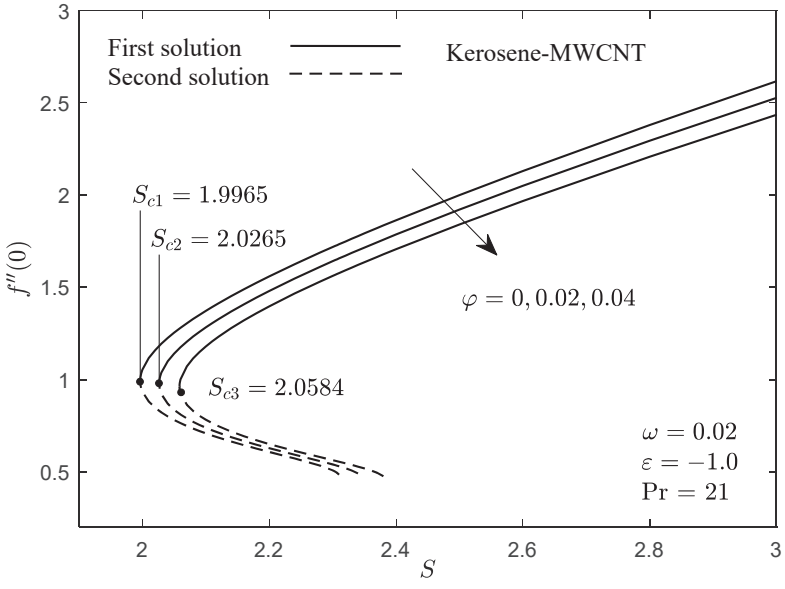

Figure 4. Values of $f''(0)$ for some values of φ versus S.

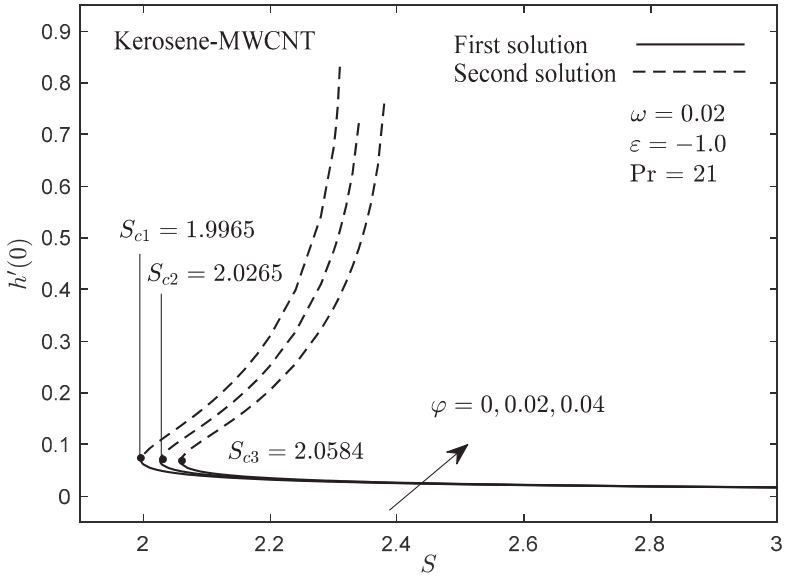

Figure 5. Values of $h'(0)$ for some values of φ versus S.

Figures 7–14 illustrate the velocities of x- and y-components, $f'(\eta)$ and $h(\eta)$ as well as the temperature profiles $\theta(\eta)$ for multiple values of ω, φ and S for different base fluids. As can be seen in Figures 7 and 8, both velocities of x- and y-components enhance with a higher rotation parameter for the first solution. An increase in the rotation rate will force the fluid to move rapidly and, in the meantime, accelerate both velocity components. This behavior will complicate the formation of the boundary layer thickness; thus, the boundary layer thickness becomes thinner. In contrast, the opposite phenomenon is reported for

the second solution. Furthermore, it is found that the velocity of x-component decreases; meanwhile, the velocity of y-component and the temperature fields for the first solution show an increment with the increasing φ as displayed in Figures 9–11, respectively.

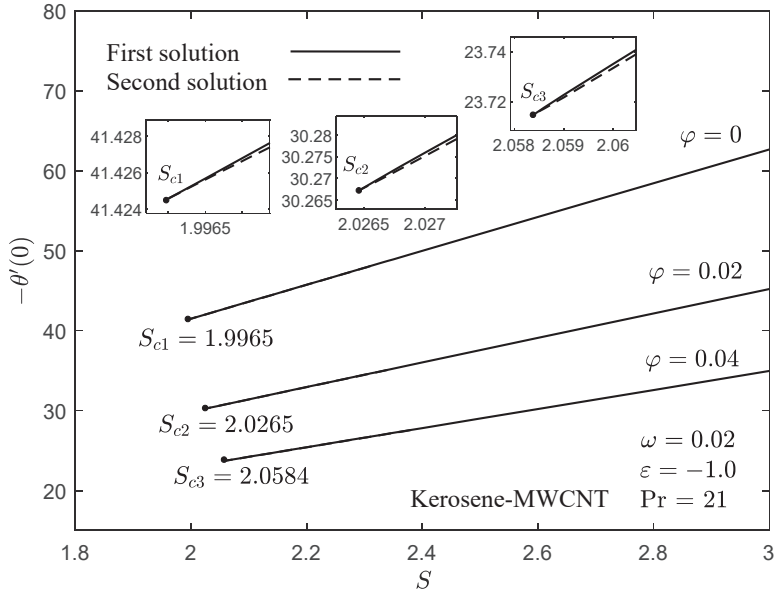

Figure 6. Values of $-\theta'(0)$ for some values of φ versus S.

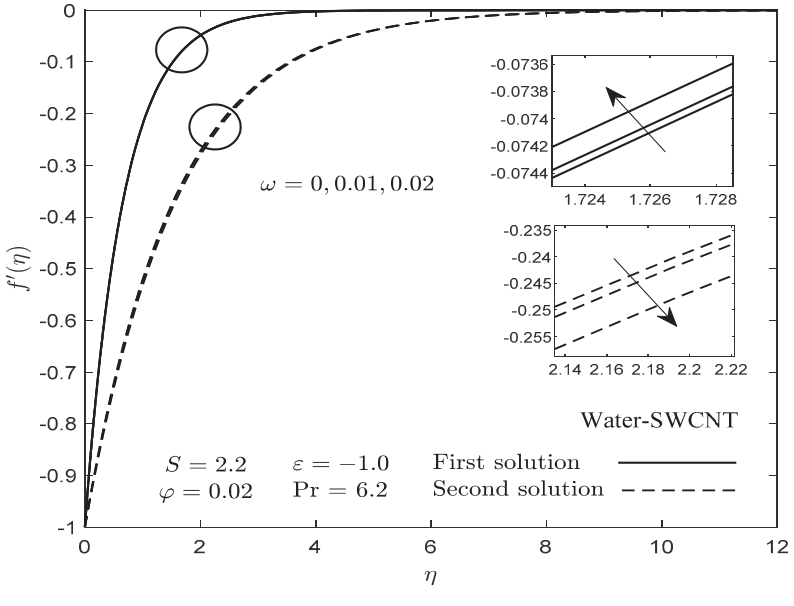

Figure 7. Velocity profiles of x-component $f'(\eta)$ for some values of ω.

The presence of more suspended particles in the flow decelerates the velocity of x-component because the surface is only compressed in the x-direction. Since the surface

is not compressed in the y-direction, the velocity of y-component increases due to less collision between the suspended molecules. The higher nanoparticle rate that thickens the thermal boundary layer thickness, as in Figure 11, will prevent heat diffusion from the surface to the fluid. As a result, the temperature of the flow rises. As the suction parameter enhances, the velocity of x-component for the first solution rises, while the opposite phenomenon is observed for both the velocity of y-component and temperature profiles as presented in Figures 12–14, respectively. Moreover, all the profiles obtained in this work satisfy the endpoint boundary conditions (11) asymptotically, thus supporting the numerical results gained for the current study. Further, the boundary layer thickness near the surface for the first solution is thinner than the second solution.

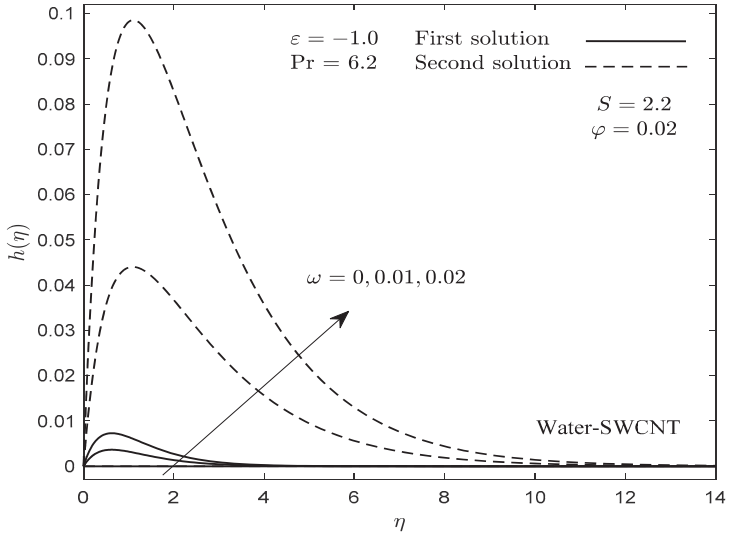

Figure 8. Velocity profiles of y-component $h(\eta)$ for some values of ω.

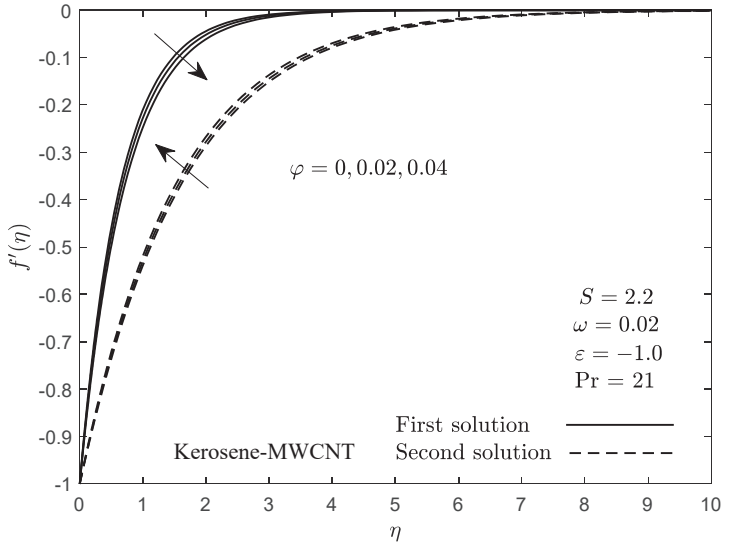

Figure 9. Velocity profiles of x-component $f'(\eta)$ for some values of φ.

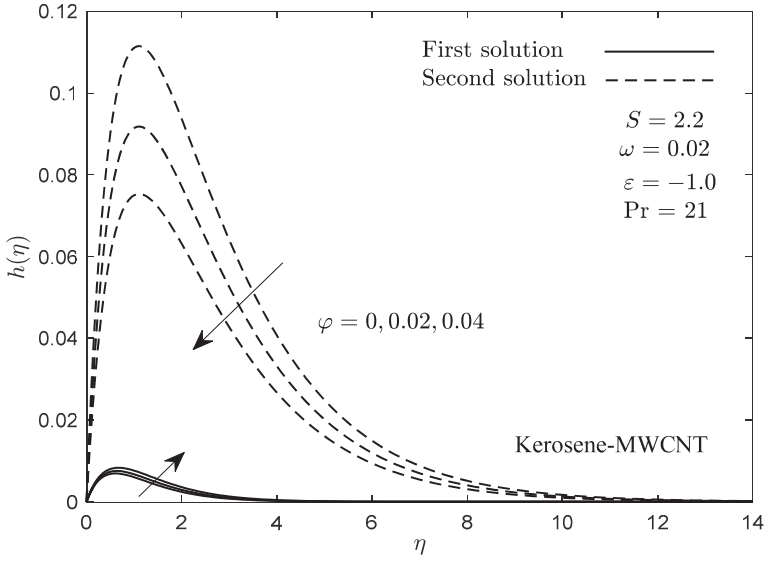

Figure 10. Velocity profiles of y-component $h(\eta)$ for some values of φ.

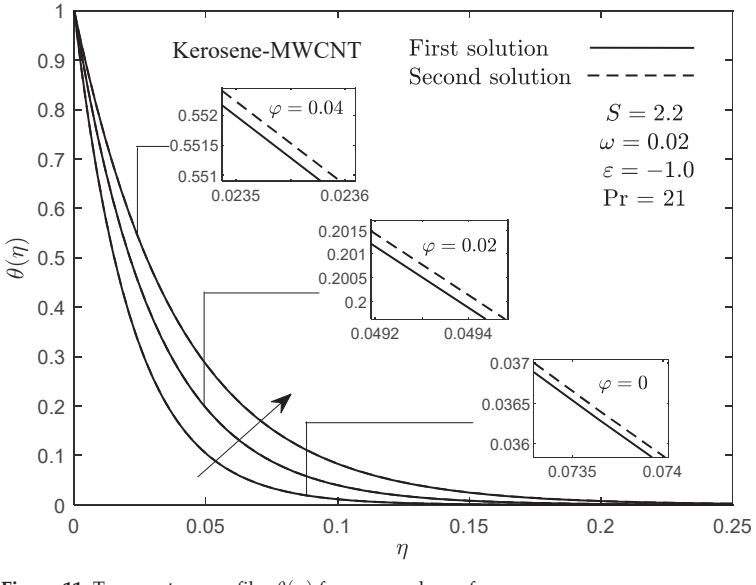

Figure 11. Temperature profiles $\theta(\eta)$ for some values of φ.

Tables 3 and 4 provide the numerical values of the skin friction coefficients of x-component $Re_x^{1/2}C_{fx}$ and y-component $Re_x^{1/2}C_{fy}$, for several values of φ, suction S, and ω for water and kerosene as the base fluids when $\varepsilon = 1.0$ (stretching case), respectively. It is observed from Tables 3 and 4, that an increase in φ tends to decrease $\left|Re_x^{1/2}C_{fx}\right|$ and $\left|Re_x^{1/2}C_{fy}\right|$ for both water-SWCNT and kerosene-MWCNT as reported by Anuar et al. [18]. This result differs from prior findings for copper, titanium, and alumina nanoparticles (see Nadeem et al. [34]; Mabood et al. [54]; Dinarvand et al. [55]). Furthermore, as the parameter S becomes more intense, the values of $Re_x^{1/2}C_{fx}$ increase, while $Re_x^{1/2}C_{fy}$ decreases for both

water-SWCNT and kerosene-MWCNT. This discovery demonstrates that the suction effect stimulates particle collisions which causes more friction in the x-direction. Moreover, the suction impact on the skin friction in x-component is more significant than y-component since the surface is stretched in the x-direction.

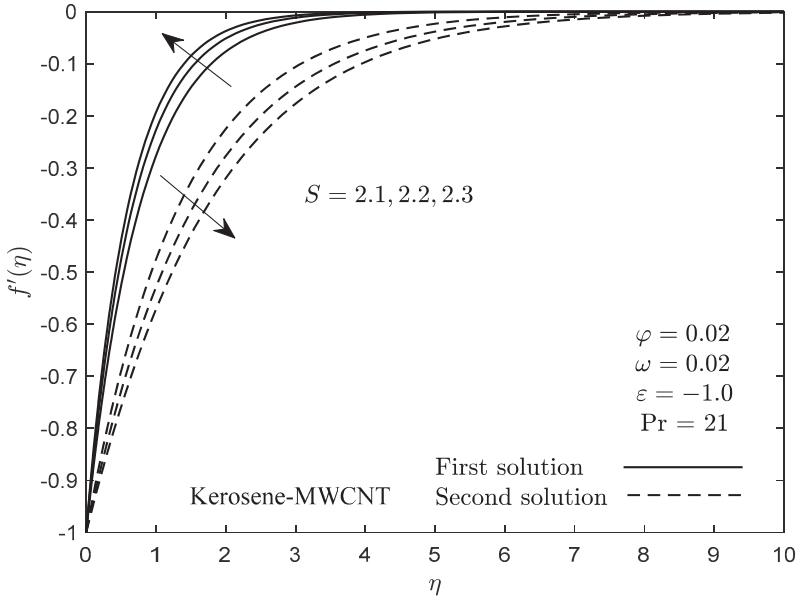

Figure 12. Velocity profiles of x-component $f'(\eta)$ for some values of S.

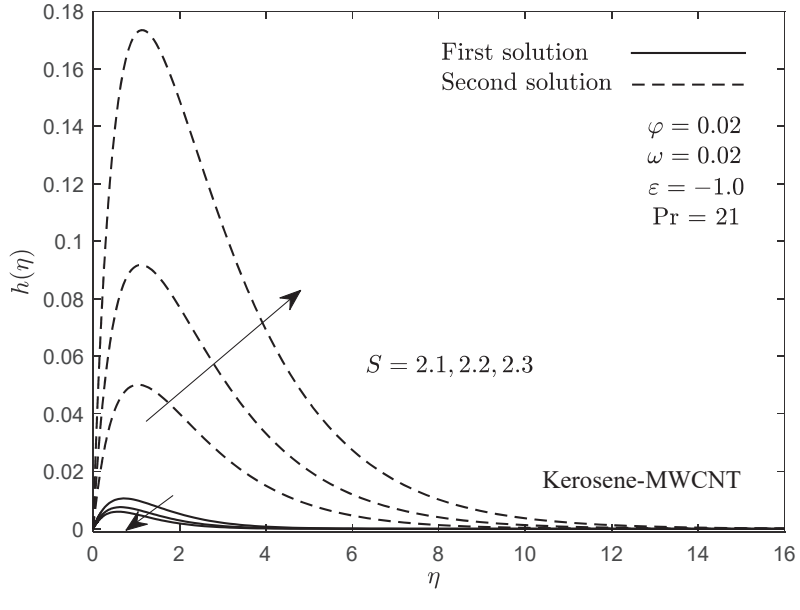

Figure 13. Velocity profiles of y-component $h(\eta)$ for some values of S.

In addition, both values of $\left|Re_x^{1/2}C_{fx}\right|$ and $\left|Re_x^{1/2}C_{fy}\right|$ increased with a higher rotation rate. Physically, a high rotation rate causes the fluid to rotate continuously and generates more friction on the surface. The skin friction coefficients of the x- and y-components for SWCNTs are clearly higher than for MWCNTs. It is also worth noting that kerosene-based fluid has a greater x- and y-components skin friction coefficient than those of water-based fluid. Moreover, a positive value of the skin friction coefficient indicates that the fluid exerts a drag force on the plate, whereas a negative sign suggests the opposite.

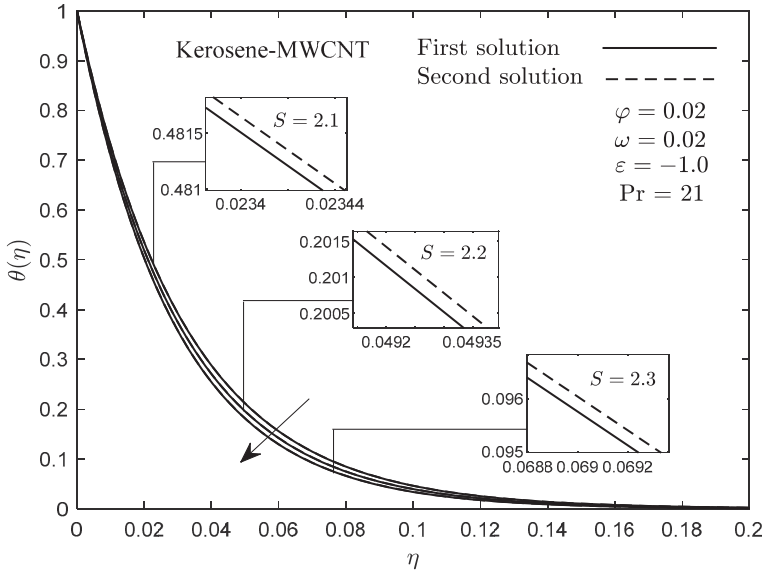

Figure 14. Temperature profiles $\theta(\eta)$ for some values of S.

Table 3. Values of $Re_x^{1/2}C_{fx}$ for different values of φ, S, and ω when $\varepsilon = 1.0$ (stretching case) for both water and kerosene base fluids.

			Water		**Kerosene**	
φ	S	ω	**SWCNT**	**MWCNT**	**SWCNT**	**MWCNT**
0.01	0	0	−1.02075	−1.01570	−1.02432	−1.01791
	2.1	0.1	−2.54543	−2.52381	−2.56079	−2.53326
		0.2	−2.55136	−2.52976	−2.56670	−2.53921
		0.3	−2.56096	−2.53939	−2.57628	−2.54882
	2.2	0.1	−2.63319	−2.61061	−2.64922	−2.62049
		0.2	−2.63865	−2.61610	−2.65467	−2.62596
		0.3	−2.64751	−2.62499	−2.66351	−2.63484
0.02	2.1	0.1	−2.58922	−2.54595	−2.61994	−2.56488
		0.2	−2.59532	−2.55210	−2.62602	−2.57101
		0.3	−2.60520	−2.56204	−2.63585	−2.58092
	2.2	0.1	−2.67828	−2.63311	−2.71036	−2.65286
		0.2	−2.68390	−2.63877	−2.71595	−2.65851
		0.3	−2.69302	−2.64796	−2.72502	−2.66767
0.03	2.1	0.1	−2.63333	−2.56839	−2.67943	−2.59680
		0.2	−2.63962	−2.57475	−2.68567	−2.60312
		0.3	−2.64979	−2.58501	−2.69577	−2.61335
	2.2	0.1	−2.72368	−2.65589	−2.77181	−2.68555
		0.2	−2.72948	−2.66175	−2.77756	−2.69138
		0.3	−2.73887	−2.67125	−2.78688	−2.70083

Table 4. Values of $Re_x^{1/2}C_{fy}$ for different values of φ, S, and ω when $\varepsilon = 1.0$ (stretching case) for both water and kerosene base fluids.

			Water		Kerosene	
φ	S	ω	SWCNT	MWCNT	SWCNT	MWCNT
0.01	0	0	−1.02075	0	0	0
	2.1	0.1	−0.07556	−0.07541	−0.07566	−0.07547
		0.2	−0.15042	−0.15011	−0.15063	−0.15025
		0.3	−0.22397	−0.22349	−0.22430	−0.22370
	2.2	0.1	−0.07342	−0.07328	−0.07352	−0.07334
		0.2	−0.14624	−0.14596	−0.14644	−0.14609
		0.3	−0.21792	−0.21749	−0.21822	−0.21768
0.02	2.1	0.1	−0.07735	−0.07705	−0.07756	−0.07718
		0.2	−0.15398	−0.15336	−0.15441	−0.15363
		0.3	−0.22925	−0.22829	−0.22992	−0.22871
	2.2	0.1	−0.07517	−0.07489	−0.07537	−0.07502
		0.2	−0.14972	−0.14915	−0.15012	−0.14940
		0.3	−0.22309	−0.22220	−0.22370	−0.22259
0.03	2.1	0.1	−0.07920	−0.07874	−0.07952	−0.07894
		0.2	−0.15765	−0.15670	−0.15830	−0.15712
		0.3	−0.23470	−0.23322	−0.23571	−0.23387
	2.2	0.1	−0.07698	−0.07655	−0.07727	−0.07674
		0.2	−0.15331	−0.15244	−0.15391	−0.15282
		0.3	−0.22841	−0.22706	−0.22934	−0.22766

Table 5. Values of $Re_x^{1/2}Nu_x$ for different values of φ, S and ω when $\varepsilon = 1.0$ (stretching case) for both water and kerosene base fluids.

			Water		Kerosene	
φ	S	ω	SWCNT	MWCNT	SWCNT	MWCNT
0.01	0	0	1.891986	1.882514	3.745629	3.726123
	2.1	0.1	13.36019	13.36137	44.48189	44.52129
		0.2	13.35999	13.36118	44.48181	44.52122
		0.3	13.35967	13.36086	44.48168	44.52109
	2.2	0.1	13.95826	13.95984	46.55247	46.59429
		0.2	13.95809	13.95968	46.55240	46.59422
		0.3	13.95781	13.95941	46.55230	46.59412
0.02	2.1	0.1	13.31519	13.31824	44.42055	44.49977
		0.2	13.31494	13.31799	44.42045	44.49967
		0.3	13.31453	13.31759	44.42027	44.49950
	2.2	0.1	13.90693	13.91074	46.48099	46.56501
		0.2	13.90671	13.91053	46.48090	46.56492
		0.3	13.90636	13.91019	46.48076	46.56478
0.03	2.1	0.1	13.26841	13.27395	44.35873	44.47819
		0.2	13.26810	13.27364	44.35859	44.47806
		0.3	13.26758	13.27315	44.35837	44.47784
	2.2	0.1	13.85391	13.86056	46.40909	46.53571
		0.2	13.85364	13.86030	46.40898	46.53560
		0.3	13.85320	13.85988	46.40879	46.53542

The numerical values of the local Nusselt number $Re_x^{-1/2}Nu_x$ for some values of nanoparticle volume fraction φ, suction S and rotation parameter ω are given in Table 5 when $\varepsilon = 1.0$ (stretching case). It is seen in Table 5 that the values of $Re_x^{-1/2}Nu_x$ increase with increasing φ for both water/kerosene-SWCNTs and water/kerosene-MWCNTs. However, the opposite observation was found for $-\theta'(0)$, as displayed in Figure 6. It demonstrates that the thermal conductivity formula affects the heat transfer rate at the surface since it involves nanoparticle volume fraction (see Equations (6) and (15)). As a result of this circumstance, numerous studies are attempting to acquire the most effective

thermal conductivity, as noted by Li et al. [56] and Fabre and Murshed [57]. However, a similar pattern was obtained for the values of $Re_x^{-1/2}Nu_x$ and $-\theta'(0)$, where a higher suction rate leading to an increase in $Re_x^{-1/2}Nu_x$ and $-\theta'(0)$. In contrast, the values of $Re_x^{-1/2}Nu_x$ and $-\theta'(0)$ decreased with the presence of the rotating fluid in the flow. This is due to the fluid rotation delaying heat transmission from the surface to the surrounding fluid, and the opposite trend occurs as suction increases.

Table 6. Minimum eigenvalues γ for multiple values of ω and ε when $\varphi = 0.02$, $S = 2.2$, and $\mathrm{Pr} = 6.2$ (water) for SWCNT.

ω	ε	First Solutions	Second Solutions
0.0	−1.1826	0.0891	−0.0861
	−1.1820	0.0946	−0.0912
	−1.1800	0.1110	−0.1063
0.01	−1.1849	0.0732	−0.0712
	−1.1840	0.0829	−0.0803
	−1.1800	0.1168	−0.1117
0.02	−1.1899	0.0268	−0.0265
	−1.1890	0.0473	−0.0464
	−1.1800	0.1333	−0.1267

In the absence of suction and rotation parameters when $\varphi = 0.01$, SWCNT produces higher heat transfer rate than MWCNT for both water and kerosene base fluids. Without any disturbances like rotation in the fluid and suction at the surface, heat is quickly diffused through the thin wall (SWCNT) compared to the thick wall (MWCNT). In contrast, when there are suction and rotation parameters, a higher heat transfer rate is obtained for MWCNT. It is also found that kerosene has a higher heat transfer rate than water since it has a greater Prandtl number ($\mathrm{Pr} = 21$) than water ($\mathrm{Pr} = 6.2$).

Basically, the solution is stable if the trajectories do not deviate significantly in response to a slight perturbation and have the same values of $f''(0)$, $h'(0)$, and $-\theta'(0)$ for η_∞. In this study, the second solution is not stable since the solution is only valid for certain values of boundary layer thicknesses compared to the first solution. However, the existence of second solutions cannot be ignored since they may have physical sense in some circumstances. In this study, the stability analysis proposed by Merkin [37] was performed to determine which solution was stable as time evolved, by solving Equations (30)–(33) using bvp4c solver in MATLAB software. The values of the smallest eigenvalue γ for some values of rotation and stretching or shrinking parameters are generated and tabulated in Table 6 for single-wall carbon nanotubes. It was found that the values of the smallest eigenvalues γ for the first solutions were positive, whereas the second solutions had negative values. Referring to Equation (25), the flow was unstable since the initial growth of disturbance occurred for the negative value of γ. In contrast, the flow was stable when γ took the positive value, which implies an initial decay of disturbance in the system. It was noticed that as ε approached its critical value ε_c, the smallest eigenvalue tended to zero for both first and second solutions, as shown in Figure 15. This criterion indicates that the transition occurs at the turning point. Figure 15 also shows the region for the stable and unstable solutions.

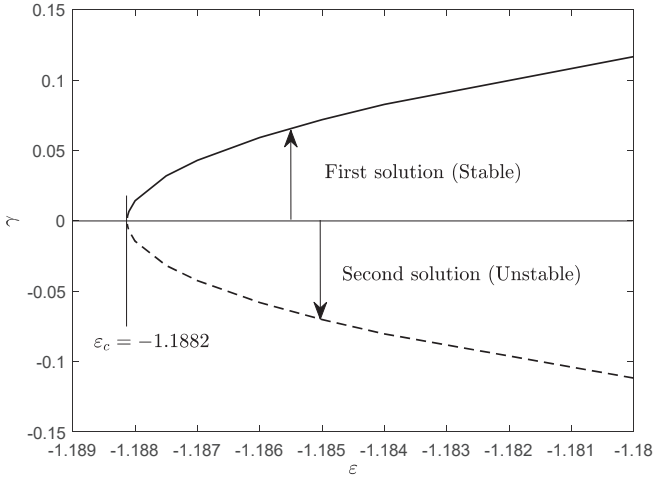

Figure 15. Minimum eigenvalues γ versus ε when $\omega = 0.01$, $\varphi = 0.02$, $S = 2.2$, and $\mathrm{Pr} = 6.2$ (water) for SWCNT.

5. Conclusions

In the present paper, the numerical results of a steady rotational flow past a stretching/shrinking surface in a nanofluid with carbon nanotube as the nanoparticles (SWCNTs and MWCNTs) were obtained using bvp4c solver in MATLAB and reported in Tables and graphs. One of the most important discoveries in this paper is that dual solutions exist for the shrinking surface, and we found that only the first solution is stable in the long run. Moreover, the heat transfer enhancement is higher in water-MWCNTs than in water-SWCNTs. Kerosene-based carbon nanotubes have a higher heat transfer rate than water-based carbon nanotubes. Other findings of this study can be summarized as follows:

- Increasing nanoparticle volume fraction tends to increase the heat transfer at the surface, while decreasing the temperature gradient in both nanofluids;
- The heat transfer rate at the surface is increased by suction parameter, whereas it decreases by rotating flow parameter in both nanofluids;
- In both nanofluids, increasing the nanoparticle volume fraction reduces the friction on the surface in the x and y directions, whereas rotational flow increases it;
- The friction in x direction is higher than in y direction in both nanofluids.

Author Contributions: Writing—original draft, N.A.Y.; formulation and methodology, N.F.D., N.A.Y. and S.N.A.S.; generating numerical results: S.N.A.S. and N.A.Y.; validation, N.A.Y.; writing—review and editing, A.I. and I.P.; supervising, A.I.; funding acquisition, A.I. All authors have read and agreed to the published version of the manuscript.

Funding: This research was funded by the Universiti Kebangsaan Malaysia (DIP-2020-001).

Institutional Review Board Statement: Not applicable.

Informed Consent Statement: Not applicable.

Data Availability Statement: Not applicable.

Acknowledgments: The first author would like to thank Universiti Teknologi MARA for supporting her sabbatical leave.

Conflicts of Interest: The authors declare no conflict of interest.

References

1. Choi, S.U.S.; Eastman, J.A. Enhancing Thermal Conductivity of Fluids with Nanoparticles. In Proceeding of the ASME International Mechanical Engineering Congress and Exposition, San Francisco, CA, USA, 12–17 November 1995; Volume 66, pp. 99–105.
2. Das, S.K.S.; Choi, U.S.; Yu, W.; Pradeep, T. *Nanofluids: Science and Technology*; John Wiley & Sons: Hoboken, NJ, USA, 2008; pp. 1–10.
3. Waqas, H.; Farooq, U.; Alghamdi, M.; Muhammad, T. Significance of surface-catalyzed reactions in SiO_2-H_2O nanofluid flow through porous media. *Case Stud. Therm. Eng.* **2021**, *27*, 101228. [CrossRef]
4. Subhashini, S.V.; Sumathi, R. Dual solutions of a mixed convection flow of nanofluids over a moving vertical plate. *Int. J. Heat Mass Transf.* **2014**, *71*, 117–124. [CrossRef]
5. Bachok, N.; Ishak, A.; Pop, I. Flow and heat transfer characteristics on a moving plate in a nanofluid. *Int. J. Heat Mass Transf.* **2012**, *55*, 642–648. [CrossRef]
6. Ahmadi, M.H.; Mirlohi, A.; Nazari, M.A.; Ghasempour, R. A review of thermal conductivity of various nanofluids. *J. Mol. Liq.* **2018**, *265*, 181–188. [CrossRef]
7. Othman, N.A.; Yacob, N.A.; Bachok, N.; Ishak, A.; Pop, I. Mixed convection boundary-layer stagnation point flow past a vertical stretching/shrinking surface in a nanofluid. *Appl. Therm. Eng.* **2017**, *115*, 1412–1417. [CrossRef]
8. Jamaludin, A.; Nazar, R.; Pop, I. Mixed convection stagnation point flow of a nanofluid past a permeable stretching/shrinking sheet in the presence of thermal radiation and heat source/sink. *Energies* **2019**, *12*, 788. [CrossRef]
9. Komeilibirjandi, A.; Raffiee, A.H.; Maleki, A.; Nazari, M.A.; Shadloo, M.S. Thermal conductivity prediction of nanofluids containing CuO nanoparticles by using correlation and artificial neural network. *J. Therm. Anal. Calorim.* **2019**, *139*, 2679–2689. [CrossRef]
10. Popov, V.N. Carbon nanotubes: Properties and application. *Mater. Sci. Eng. R Rep.* **2004**, *43*, 61–102. [CrossRef]
11. Patel, P.R.; Sharma, S.; Tiwari, S.K. Governing parameters for pull-out of carbon nanotubes from aluminium composites: A review. *Mater. Today Proc.* **2021**, *44*, 4827–4832. [CrossRef]
12. Taherian, H.; Alvarado, J.L.; Languri, E.M. Enhanced thermophysical properties of multi-walled carbon nanotubes based nanofluids. Part 1: Critical review. *Renew. Sustain. Energy Rev.* **2018**, *82*, 4326–4336. [CrossRef]
13. Khan, W.A.; Khan, Z.H.; Rahi, M. Fluid flow and heat transfer of carbon nanotubes along a flat plate with Navier slip boundary. *Appl. Nanosci.* **2014**, *4*, 633–641.
14. Akbar, N.S.; Khan, Z.H.; Nadeem, S. The combined effects of slip and convective boundary conditions on stagnation-point flow of CNT suspended nanofluid over a stretching sheet. *J. Mol. Liq.* **2014**, *196*, 21–25. [CrossRef]
15. Hayat, T.; Hussain, Z.; Alsaedi, A.; Asghar, S. Carbon nanotubes effects in the stagnation point flow towards a nonlinear stretching sheet with variable thickness. *Adv. Powder Technol.* **2016**, *27*, 1677–1688. [CrossRef]
16. Hussain, Z.; Hayat, T.; Alsaedi, A.; Ahmad, B. Three-dimensional convective flow of CNTs nanofluids with heat generation/absorption effect: A numerical study. *Comput. Methods Appl. Mech. Eng.* **2018**, *329*, 40–54. [CrossRef]
17. Sreedevi, P.; Reddy, P.S.; Chamkha, A.J. Magneto-hydrodynamics heat and mass transfer analysis of single and multi-wall carbon nanotubes over vertical cone with convective boundary condition. *Int. J. Mech. Sci.* **2018**, *135*, 646–655. [CrossRef]
18. Anuar, N.S.; Bachok, N.; Arifin, N.M.; Rosali, H. Role of multiple solutions in flow of nanofluids with carbon nanotubes over a vertical permeable moving plate. *Alex. Eng. J.* **2020**, *59*, 763–773. [CrossRef]
19. Reddy, P.S.; Sreedevi, P. Effect of thermal radiation and volume fraction on carbon nanotubes based nanofluid flow inside a square chamber. *Alex. Eng. J.* **2020**, *60*, 1807–1817. [CrossRef]
20. Ramzan, M.; Shah, S.R.Z.; Kumam, P.; Thounthong, P. Unsteady MHD carbon nanotubes suspended nanofluid flow with thermal stratification and nonlinear thermal radiation. *Alex. Eng. J.* **2020**, *59*, 1557–1566. [CrossRef]
21. Ul Haq, R.; Soomro, F.A.; Öztop, H.F.; Mekkaoui, T. Thermal management of water-based carbon nanotubes enclosed in a partially heated triangular cavity with heated cylindrical obstacle. *Int. J. Heat Mass Transf.* **2019**, *131*, 724–736. [CrossRef]
22. Reddy, P.S.; Jyothi, K.; Reddy, M.S. Flow and heat transfer analysis of carbon nanotubes based Maxwell nanofluid flow driven by rotating stretchable disks with thermal radiation. *J. Braz. Soc. Mech. Sci. Eng.* **2018**, *40*, 576. [CrossRef]
23. Li, X.; Chen, W.; Zou, C. The stability, viscosity and thermal conductivity of carbon nanotubes nanofluids with high particle concentration: A surface modification approach. *Powder Technol.* **2020**, *361*, 957–967. [CrossRef]
24. Peter, R.N.C. *Rotating Flow*; Elsevier: Woburn, UK, 2011; pp. 1–2.
25. Singh, M.P.; Sathi, H.L. An Exact Solution in Rotating Flow. *J. Math. Mech.* **1968**, *18*, 193–200. [CrossRef]
26. Wang, C.Y. Stretching a surface in a rotating fluid. *Z. Angew. Math. Phys. ZAMP* **1988**, *39*, 177–185. [CrossRef]
27. Nazar, R.; Amin, N.; Pop, I. Unsteady boundary layer flow due to a stretching surface in a rotating fluid. *Mech. Res. Comm.* **2004**, *31*, 121–128. [CrossRef]
28. Ali, F.M.; Nazar, R.; Arifin, N.M.; Pop, I. Unsteady shrinking sheet with mass transfer in a rotating fluid. *Int. J. Numer. Meth. Fluids* **2011**, *66*, 1465–1474. [CrossRef]
29. Sreelakshmi, K.; Nagendramma, V.; Sarojamma. Unsteady boundary layer flow induced by a stretching sheet in a rotating fluid with thermal radiation. *Procedia Eng.* **2015**, *127*, 678–685.
30. Rosali, H.; Ishak, A.; Nazar, R.; Pop, I. Rotating flow over an exponentially shrinking sheet with suction. *J. Mol. Liq.* **2015**, *211*, 965–969. [CrossRef]

31. Rana, P.; Bhargava, R.; Bég, O.A. Finite element simulation of unsteady magneto-hydrodynamic transport phenomena on a stretching sheet in a rotating nanofluid. *Proc. Inst. Mech. Eng. Part N J. Nanoeng. Nanosyst.* **2013**, *227*, 77–99. [CrossRef]
32. Bakar, N.A.A.; Bachok, N.; Arifin, N.M. Rotating flow over a shrinking sheet in nanofluid using Buongiorno model and thermophysical properties of nanoliquids. *J. Nanofluids* **2017**, *6*, 1215–1226. [CrossRef]
33. Krishna, M.V. Hall and ion slip effects on radiative MHD rotating flow of Jeffreys fluid past an infinite vertical flat porous surface with ramped wall velocity and temperature. *Int. Commun. Heat Mass Transf.* **2021**, *126*, 105399. [CrossRef]
34. Nadeem, S.; Rehman, A.U.; Mehmood, R. Boundary Layer Flow of Rotating Two Phase Nanofluid Over a Stretching Surface. *Heat Transf. Asian Res.* **2016**, *45*, 285–298. [CrossRef]
35. Dzulkifli, N.F.; Bachok, N.; Yacob, N.A.; Arifin, N.M.; Rosali, H. Unsteady boundary layer rotating flow and heat transfer in a copper-water nanofluid over a stretching sheet. *Malays. J. Math. Sci.* **2017**, *11*, 21–33.
36. Salleh, S.N.A.; Bachok, N.; Arifin, N.M. Stability analysis of a rotating flow toward a shrinking permeable surface in nanofluid. *Malays. J. Math. Sci.* **2019**, *38*, 19–32. [CrossRef]
37. Merkin, J.H. On dual solutions occurring in mixed convection in a porous medium. *J. Eng. Math.* **1986**, *20*, 171–179. [CrossRef]
38. Harris, S.D.; Ingham, D.B.; Pop, I. Mixed convection boundary-layer flow near the stagnation point on a vertical surface in a porous medium: Brinkman model with slip. *Transp. Porous Med.* **2009**, *77*, 267–285. [CrossRef]
39. Mustafa, I.; Abbas, Z.; Arif, A.; Javed, T.; Ghaffari, A. Stability analysis for multiple solutions of boundary layer flow towards a shrinking sheet: Analytical solution by using least square method. *Phys. A Stat. Mech. Appl.* **2020**, *540*, 123028. [CrossRef]
40. Tshivhi, K.S.; Makinde, O.D. Magneto-nanofluid coolants past heated shrinking/stretching surfaces: Dual solutions and stability analysis. *Results Eng.* **2021**, *10*, 100229. [CrossRef]
41. Hafeez, M.U.; Hayat, T.; Alsaedi, A.; Khan, M.I. Numerical simulation for electrical conducting rotating flow of Au (Gold)-Zn (Zinc)/EG (Ethylene glycol) hybrid nanofluid. *Int. Commun. Heat Mass Transf.* **2021**, *124*, 105234. [CrossRef]
42. Mehdipour, M.; Keshavarz, P.; Rahimpour, M.R. Rotating liquid sheet contactor: A new gas-liquid contactor system in CO_2 absorption by nanofluids. *Chem. Eng. Process. Process Intensif.* **2021**, *165*, 108447. [CrossRef]
43. Acharya, N.; Das, K.; Kundu, P.K. Rotating flow of carbon nanotube over a stretching surface in the presence of magnetic field: A comparative study. *Appl. Nanosci.* **2018**, *8*, 369–378. [CrossRef]
44. Shah, Z.; Bonyah, E.; Islam, S.; Gul, T. Impact of thermal radiation on electrical MHD rotating flow of carbon nanotubes over a stretching sheet. *AIP Adv.* **2019**, *9*, 015115. [CrossRef]
45. Noranuar, W.N.N.; Mohamad, A.Q.; Shafie, S.; Khan, I.; Jiann, L.Y.; Ilias, M.R. Non-coaxial rotation flow of MHD Casson nanofluid carbon nanotubes past a moving disk with porosity effect. *Ain Shams Eng. J.* **2021**, *12*, 4099–4110. [CrossRef]
46. Hussain, A.; Arshad, M.; Hassan, A.; Rehman, A.; Ahmad, H.; Baili, J.; Gia, T.N. Heat transport investigation of engine oil based rotating nanomaterial liquid flow in the existence of partial slip effect. *Case Stud. Therm. Eng.* **2021**, *28*, 101500. [CrossRef]
47. Manjunatha, P.T.; Punith Gowda, R.J.; Kumar, R.N.; Suresha, S.; Sarwe, D.U. Numerical simulation of carbon nanotubes nanofluid flow over vertically moving disk with rotation. *Partial Differ. Equ. Appl. Math.* **2021**, *4*, 100124. [CrossRef]
48. Anusha, T.; Mahabaleshwar, U.S.; Sheikhnejad, Y. An MHD of Nanofluid Flow Over a Porous Stretching/Shrinking Plate with Mass Transpiration and Brinkman Ratio. *Transp. Porous Med.* 2021, in press. [CrossRef]
49. Xue, Q.Z. Model for thermal conductivity of carbon nanotube-based composites. *Phys. Rev. B Condens. Matter.* **2005**, *368*, 302–307. [CrossRef]
50. Babar, H.; Ali, H.M. Towards hybrid nanofluids: Preparation, thermophysical properties, applications, and challenges. *J. Mol. Liq.* **2019**, *281*, 598–633. [CrossRef]
51. Weidman, P.D.; Kubitschek, D.G.; Davis, A.M.J. The effect of transpiration on self-similar boundary layer flow over moving surfaces. *Int. J. Eng. Sci.* **2006**, *44*, 730–737. [CrossRef]
52. Shampine, L.F.; Gladwell, I.; Thompson, S. *Solving ODEs with Matlab*; Cambridge University Press: New York, NY, USA, 2006; pp. 133–168.
53. Mustafa, M.; Mushtaq, A.; Hayat, T.; Alsaedi, A. Rotating flow of magnetite-water nanofluid over a stretching surface inspired by nonlinear thermal radiation. *PLoS ONE* **2016**, *11*, e0149304. [CrossRef]
54. Mabood, F.; Ibrahim, S.M.; Kumar, P.V.; Khan, W.A. Viscous dissipation effects on unsteady mixed convective stagnation point flow using Tiwari-Das nanofluid model. *Results Phys.* **2017**, *7*, 280–287. [CrossRef]
55. Dinarvand, S.; Hosseini, R.; Pop, I. Axisymmetric mixed convective stagnation-point flow of a nanofluid over a vertical permeable cylinder by Tiwari-Das nanofluid model. *Powder Technol.* **2017**, *311*, 147–156. [CrossRef]
56. Li, J.; Zhang, X.; Xu, B.; Yuan, M. Nanofluid research and applications: A review. *Int. Commun. Heat Mass Transf.* **2021**, *127*, 105543. [CrossRef]
57. Fabre, E.; Murshed, S.M.S. A comprehensive review of thermophysical properties and prospects of ionanocolloids in thermal energy applications. *Renew. Sustain. Energy Rev.* **2021**, *151*, 111593. [CrossRef]

mathematics

MDPI

Article

Solute Transport Control at Channel Junctions Using Adjoint Sensitivity

Geovanny Gordillo [1,2], Mario Morales-Hernández [1,*] and Pilar García-Navarro [1]

[1] Fluid Mechanics, EINA-I3A, Universidad de Zaragoza, C/María de Luna 3, 50018 Zaragoza, Spain; ggordillo@unizar.es (G.G.); pigar@unizar.es (P.G.-N.)
[2] Departamento de Ciencias de La Vida, Universidad de Las Fuerzas Armadas ESPE, Av. Gral. Rumiñahui s/n, Sangolqui 171103, Ecuador
* Correspondence: mmorales@unizar.es

Abstract: Water quality control and the control of contaminant spill in water in particular are becoming a primary need today. Gradient descent sensitivity methods based on the adjoint formulation have proved to be encouraging techniques in this context for river and channel flows. Taking into account that most channels and rivers include junctions with other branches, the objective of this study is to explore the adjoint technique on a channel network to reconstruct the upstream boundary condition of the convection-reaction equation. For this purpose, the one-dimensional shallow water equations and the transport equation for a reactive solute are considered. The control is formulated through the gradient-descent technique supplied with a first-order iterative process. Both the physical and the adjoint equations are supplied with suitable internal boundary conditions at the junction and are numerically solved using a finite volume upwind scheme. The results reveal that the adjoint technique is capable of reconstructing the inlet solute concentration boundary condition in an acceptable number of iterations for both steady state and transient configurations using a downstream measurement location. It was also observed that the reconstruction of the boundary condition tends to be less effective the further away the measurement station is from the target.

Keywords: adjoint; gradient-descent; junctions; transport equation

Citation: Gordillo, G.; Morales-Hernández, M.; García-Navarro, P. Solute Transport Control at Channel Junctions Using Adjoint Sensitivity. *Mathematics* **2022**, *10*, 93. https://doi.org/10.3390/math10010093

Academic Editors: Camelia Petrescu and Valeriu David

Received: 3 November 2021
Accepted: 24 December 2021
Published: 28 December 2021

Publisher's Note: MDPI stays neutral with regard to jurisdictional claims in published maps and institutional affiliations.

Copyright: © 2021 by the authors. Licensee MDPI, Basel, Switzerland. This article is an open access article distributed under the terms and conditions of the Creative Commons Attribution (CC BY) license (https://creativecommons.org/licenses/by/4.0/).

1. Introduction

Simulation tools based on hydrodynamic models combined with solute transport have become an essential tool to help decision makers [1], with efficiency and accuracy being both the fundamental keys of any mathematical model. Particularly, the geometry of the cross sections as well as the presence of junctions must be included into the model, having this last feature a greater impact on the physical and chemical properties of water. The numerical simulation of water flow at channel junctions has been addressed by several authors. In [2], it was concluded that it is possible to model the flow in a junction when the Froude numbers are low assuming the same water stage at the junction for every channel. Hsu et al. [3] derived an analytical approach through the junction over subcritical flows and uniform beds. The validation of their model was supported by three experimental tests with different junction angles, showing a good correlation between the numerical data and experimental values. The hydrodynamic details of flows at junctions have also been studied in [4–8] with experimental data and with field measurements. Likewise, the flow propagation in open-channel junctions was analyzed in [9], showing acceptable numerical results for supercritical transitions with small junction angles.

The influence of geometry in large-scale junctions was evaluated by [10]. It was concluded that there is a domain of the Kelvin–Helmholtz (KH) mode and the wake mode within the mixing interface, as the angle of the junction is altered. Based on the flow structure in the confluences, Constantinescu et al. [11] determined that the mixing interface can be either in the KH mode or in the wake mode. Both cases are dominated by quasi

two-dimensional (2-D) eddies whose growth in the first case is boosted by the KH instability whereas, in the latter case, the mixing interface is populated by eddies with opposing senses of rotation. The influence of the mixing interface eddies and vortical characteristics on the mean velocity and turbulent kinetic energy patterns was also analyzed in [12]. Using the detached eddy simulation model, they were able to capture in detail the flow and turbulent structure in the confluence zone. This behavior was verified by a real data event at the confluence of the Kaskaskia River and Copper Slough. The morphological characteristics of the channel were also considered in [13,14]. In these studies, it was observed that sediment deposition is within and beyond the flow separation region, forming a large bank-attached bar.

On the other hand, the chemical change generated by the junction of two streams has been much more limited due to the requirements on the experimental data. Burguete et al. [15] demonstrated the innovative aspects for fertigation in furrows and level furrow systems with solute transport. This work was validated against experimental data and incorporated a computationally efficient approach of the internal boundary conditions to ensure the conservation of global mass. The behavior of the concentrations at junctions was also analyzed in [16]. Detailed analysis at the junction showed that the concentration distributions were controlled mainly by the shear layer and the two helical cells. The detailed study for dynamic phosphorus contamination was also considered in [17,18], showing and application for the Huiji and Ying rivers in eastern China. Additionally, it was demonstrated that there is an alteration of the flow and the mixing interface in junctions of two tributaries in natural rivers with large bed discordance due to the temperature differences in the two inflows [19]. Particularly, the mixing interface is proved to be very sensitive to inflow changes due to seasonal variations, which may cause significant differences in density [20].

The quality of the predictions supplied by numerical models is strongly related with the quality of the data used (initial conditions, boundary conditions or model parameters). This information is not always available for different reasons, and thus, retrieval techniques such as trial and error methods are necessary, sometimes resulting in tedious and not very intuitive processes especially when there is not enough modeling experience. To overcome this drawback, the gradient-descent method emerges as an alternative due to the use of the functional gradient where the minimum of the objective function is efficiently found. In this context, based on existing works [21–26], the adjoint method is considered to reconstruct a part or all of the necessary information in predictive simulation models. In particular, it is possible to efficiently reconstruct the boundary condition of a water quality model [27].

With this technique, the sensitivity of an objective function to the parameters of the system—initial, boundaries or decay coefficients—can be found by solving the adjoint equation backwards in time. This sensitivity is used in an iterative process, producing a sequence of improved solutions that ends up providing the desired values.

In this work, a one-dimensional (1D) hydrodynamic model combined with the advection-reaction equation on a channel junction are used for the predictive simulation of the flow evolution and solute transport, respectively. The adjoint methodology is adopted to find a procedure to reconstruct the boundary condition of the transport equation using a measure of the error at a location downstream the junction. To meet this objective, the flow, the transport and the adjoint equations are solved using an explicit finite volume method. Particular attention is paid to the following aspects: (a) reconstruction of the inlet boundary condition of one or more solutes from downstream measurements after a junction; (b) validation of the numerical technique against steady state and unsteady scenarios of both flow and concentration; (c) characterization of the main strengths and limitations of the adjoint method; (d) test the reconstruction of the information, with different decay rates when more than one solute acts.

The rest of the paper is structured as follows: Section 2 presents the governing equations of the physical system together with the numerical method chosen to solve them. The adjoint formulation is provided in Section 3 and is also presented together with the

numerical discretization used. In Section 4, the proposed model control is validated with some synthetic cases. The results of the model are presented in Section 5. Finally, the conclusions are presented for some test cases are discussed in Section 6.

2. Flow Equations and Numerical Model

The 1D Saint Venant equations are here considered to model the water flow [28] while the advection-reaction equation is used to model the solute transport with a first order decay process [29,30]. Diffusion–dispersion effects (particularly longitudinal dispersion) are important when modeling the behavior of solutes in rivers, mainly in accidental pollution problems [31,32]. However, for the sake of clarity, they have not been included in this work. The main reason for this is to simplify the development of this methodology without introducing another degree of freedom and extra uncertainty in the derivation of the equations and their resolution. Additionally, boundary conditions are needed for the whole set of the equations both at the inlet and outlet points and at the junctions. All these items are explained in the following paragraphs.

2.1. 1D Shallow Water Equations

The cross-sectional averaged 1D system of mass and momentum equations can be expressed as follows [33]:

$$\begin{aligned} &\frac{\partial A}{\partial t} + \frac{\partial Q}{\partial x} = q_L \\ &\frac{\partial Q}{\partial t} + \frac{\partial}{\partial x}\left(\frac{Q^2}{A} + gI_1\right) = g[I_2 + A(S_o - S_f)] \end{aligned} \tag{1}$$

where $A[\mathrm{L}^2]$ is the wetted cross section area, $Q[\mathrm{L}^3\mathrm{T}^{-1}]$ is the discharge, $q_L[\mathrm{L}^2\mathrm{T}^{-1}]$ is the lateral inflow per unit width, $g[\mathrm{LT}^{-2}]$ is the acceleration due to gravity, $I_1[\mathrm{L}^3]$ represents the hydrostatic pressure force term, and $I_2[\mathrm{L}^2]$ accounts for the pressure forces due to channel width change. The remaining two terms S_o $[\mathrm{LL}^{-1}]$ and S_f $[\mathrm{LL}^{-1}]$ represent the bed slope and friction slope, the latter formulated with the semi-empirical Manning's law:

$$S_o = -\frac{\partial z}{\partial x}, \qquad S_f = \frac{n^2|Q|Q}{A^2 R_h^{4/3}}, \tag{2}$$

being $z[\mathrm{L}]$ the bed level, $R_h[\mathrm{L}]$ the hydraulic radius and $n[\mathrm{TL}^{-1/3}]$ the Manning's roughness coefficient.

2.2. 1D Advection–Reaction Equation

The continuous change of concentration within the hydrodynamic system is generally affected by the advection and reaction processes. The formulation of this transport equation along every river or channel reach averaged in the cross section can be expressed as [34]:

$$\frac{\partial(A\phi)}{\partial t} + \frac{\partial(Q\phi)}{\partial x} = -AR, \tag{3}$$

where $\phi[\mathrm{ML}^{-3}]$ is the cross sectional average concentration of the solute, and R $[\mathrm{ML}^{-3}\mathrm{T}^{-1}]$ is the first order rate or decay process:

$$R = \kappa\phi, \tag{4}$$

where κ $[\mathrm{T}^{-1}]$ is the reaction constant. As many transport equations as solutes must be considered together with the corresponding reaction terms in the case of more than one reactive solute in the system. This is accomplished simply by generalizing the concentration ϕ_j and R_j in (3) where the subscript j indicates the number of reactive solutes [35].

2.3. Numerical Model

The numerical solution of Equations (1) and (3) is achieved by applying an explicit upwind finite volume method based on Roe's linearization. This scheme has been proved to be robust, well-balanced and efficient and has been verified in multiple scenarios: for the 1D and 2D the frameworks [36–38].

Following [15,38], the system (1) can be solved for each computational cell i of size Δx:

$$\mathbf{U}_i^{n+1} = \mathbf{U}_i^n - \frac{\Delta t}{\Delta x}\left[\left(\sum_m \tilde{\lambda}^+ \tilde{\gamma}\tilde{\mathbf{e}}\right)_{i-1/2}^m + \left(\sum_m \tilde{\lambda}^- \tilde{\gamma}\tilde{\mathbf{e}}\right)_{i+1/2}^m\right]^n, \tag{5}$$

where $\mathbf{U} = (A, Q)$, n is the discrete time level, and $\tilde{\lambda}$ and $\tilde{\mathbf{e}}$ are the eigenvalues and eigenvectors, respectively; $\tilde{\gamma}$ is the linearized term that contains the fluxes and source strengths; m is the eigenvalues counter, and Δt is the time step size. This expression (5) is solved for the interior points in each of the channels considered in the system.

The complete discretization of the transport equation follows [39]:

$$(A\phi)_i^{n+1} = (A\phi)_i^n - \frac{\Delta t}{\Delta x}\left[(q\phi)_{i+1/2}^{\downarrow} - (q\phi)_{i-1/2}^{\downarrow}\right]^n + \Delta t (AR)_i^n, \tag{6}$$

where the variables $q^{\downarrow}$ and $\phi^{\downarrow}$ are defined in order to decouple conservatively this equation from the hydrodynamic system. This formulation ensures solute positivity and a non-oscillatory solution in both space and time [35]. The scheme in (6) is used to solve for each solute at all the interior points of each channel.

2.4. Junction Boundary Conditions

Appropriate boundary conditions are needed to solve the system of flow and solute equations formed by (1) and (3). The number of boundary conditions at the inlet, outlet and junction points depends on the flow regime [2]. For the sake of simplification, this work only considers sub-critical cases. Regarding the flow equations, it is enough to impose one boundary condition upstream and downstream. Generally, a discharge hydrograph $Q(t)$ is imposed upstream while a gauging curve or a water surface level is set downstream. As for the solute, only an upstream boundary condition is required.

When considering junctions such as the one represented in Figure 1, internal boundary conditions are needed. In the present work, uniform water surface level together with discharge continuity at the junction is assumed [40]:

$$\begin{aligned} &(h+z)_{imax,1} = (h+z)_{0,2} = (h+z)_{imax,3}, \\ &Q_{0,2} = Q_{imax,1} \pm Q_{imax,3}, \end{aligned} \tag{7}$$

where the number of cells goes from 0 to *imax* in each channel. As for the internal condition of the solute, a mass balance at the junction is formulated as in [15]:

$$(Q\phi)_{0,2} = (Q\phi)_{imax,1} \pm (Q\phi)_{imax,3}. \tag{8}$$

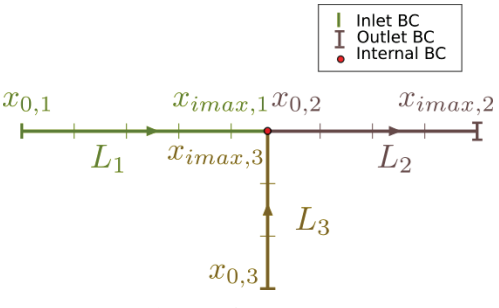

Figure 1. Spatial domain of junctions.

3. Adjoint Equations and Gradient Descent Method

3.1. Solute Transport Adjoint Equation

This study focuses on identifying the sensitivity of the objective function to the inlet boundary condition of one or more solutes on a network of channels with junctions. For this purpose, an objective function is defined in order to measure the error between the values of the concentration predicted by the numerical simulation and those measured at a certain location (x_M):

$$J(p) = \frac{1}{2}\int_0^T \int_0^L \left[\delta_D(x - x_M)(\phi(p) - \widehat{\phi})^2\right] dxdt, \tag{9}$$

where $\delta_D()$ is the Dirac-delta function, $\phi(p)$ is the computed concentration based on a parameter p which the functional depends on, $\widehat{\phi}$ is the target at location x_M, $T[\mathrm{T}]$ is the total simulation time, and $L[\mathrm{L}]$ refers to the length of the computational domain.

The method to derive the adjoint equation from the configuration shown in Figure 1, where the measurement point is assumed in channel 2, is summarized in the following steps: (1) The transport Equation (3) is multiplied by an adjoint variable ($\sigma\,[\mathrm{MTL}^{-5}]$) and integrated in space and time for each channel k:

$$\begin{aligned} I = &\int_0^T \int_{x_{0,1}}^{x_{imax,1}} \sigma_1 \left[\frac{\partial(A\phi)}{\partial t} + \frac{\partial(Q\phi)}{\partial x} + AR\right]_1 dxdt \\ &+ \int_0^T \int_{x_{0,2}}^{x_{imax,2}} \sigma_2 \left[\frac{\partial(A\phi)}{\partial t} + \frac{\partial(Q\phi)}{\partial x} + AR\right]_2 dxdt \\ &+ \int_0^T \int_{x_{0,3}}^{x_{imax,3}} \sigma_3 \left[\frac{\partial(A\phi)}{\partial t} + \frac{\partial(Q\phi)}{\partial x} + AR\right]_3 dxdt = 0. \end{aligned} \tag{10}$$

(2) Integrating (10) by parts, the partial derivatives are passed over to the adjoint variable:

$$\begin{aligned} I = &\int_0^T \int_{x_{0,1}}^{x_{imax,1}} \left[-(A\phi)\frac{\partial\sigma}{\partial t} - (Q\phi)\frac{\partial\sigma}{\partial x} + A\sigma R\right]_1 dxdt \\ &+ \int_0^T \sigma Q\phi\Big|_{x_{0,1}}^{x_{imax,1}} dt + \int_{x_{0,1}}^{x_{imax,1}} \sigma A\phi\Big|_0^T dx \\ &+ \int_0^T \int_{x_{0,2}}^{x_{imax,2}} \left[-(A\phi)\frac{\partial\sigma}{\partial t} - (Q\phi)\frac{\partial\sigma}{\partial x} + A\sigma R\right]_2 dxdt \\ &+ \int_0^T \sigma Q\phi\Big|_{x_{0,2}}^{x_{imax,2}} dt + \int_{x_{0,2}}^{x_{imax,2}} \sigma A\phi\Big|_0^T dx \\ &+ \int_0^T \int_{x_{0,3}}^{x_{imax,3}} \left[-(A\phi)\frac{\partial\sigma}{\partial t} - (Q\phi)\frac{\partial\sigma}{\partial x} + A\sigma R\right]_3 dxdt \\ &+ \int_0^T \sigma Q\phi\Big|_{x_{0,3}}^{x_{imax,3}} dt + \int_{x_{0,3}}^{x_{imax,3}} \sigma A\phi\Big|_0^T dx = 0. \end{aligned} \tag{11}$$

(3) As $I = 0$, we can redefine (9) as $J = J + I$ and taking the first variation of the functional with respect to ϕ leads to

$$
\begin{aligned}
\delta J = & \int_0^T \int_{x_{0,1}}^{x_{imax,1}} \left[-(A\delta\phi)\frac{\partial \sigma}{\partial t} - (Q\delta\phi)\frac{\partial \sigma}{\partial x} + A\frac{\partial R}{\partial \phi}\delta\phi \right]_1 dxdt \\
& + \int_0^T \sigma Q \delta\phi \Big|_{x_{0,1}}^{x_{imax,1}} dt \int_{x_{0,1}}^{x_{imax,1}} \sigma A \delta\phi \Big|_0^T dx \\
& + \int_0^T \int_{x_{0,2}}^{x_{imax,2}} \delta_D(x - x_M)\frac{\partial \xi}{\partial \phi}\delta\phi dxdt + \\
& + \int_0^T \int_{x_{0,2}}^{x_{imax,2}} \left[-(A\delta\phi)\frac{\partial \sigma}{\partial t} - (Q\delta\phi)\frac{\partial \sigma}{\partial x} + A\frac{\partial R}{\partial \phi}\delta\phi \right]_2 dxdt \\
& + \int_0^T \sigma Q \delta\phi \Big|_{x_{0,2}}^{x_{imax,2}} dt + \int_{x_{0,2}}^{x_{imax,2}} \sigma A \delta\phi \Big|_0^T dx \\
& + \int_0^T \int_{x_{0,3}}^{x_{imax,3}} \left[-(A\delta\phi)\frac{\partial \sigma}{\partial t} - (Q\delta\phi)\frac{\partial \sigma}{\partial x} + A\frac{\partial R}{\partial \phi}\delta\phi \right]_3 dxdt \\
& + \int_0^T \sigma Q \delta\phi \Big|_{x_{0,3}}^{x_{imax,3}} dt + \int_{x_{0,3}}^{x_{imax,3}} \sigma A \delta\phi \Big|_0^T dx,
\end{aligned} \tag{12}
$$

with

$$
\xi = \frac{1}{2}(\phi(p) - \widehat{\phi})^2. \tag{13}
$$

(4) With the aim of finding the sensitivities of the objective function with respect to the upstream boundary condition of the first channel, certain restrictions are applied:

$$
\begin{aligned}
& \sigma(x_k, T) = 0, k = 1, ..., 3, \\
& \delta\phi(x_k, 0) = 0, k = 1, ..., 3, \\
& \delta\phi(x_{imax,2}, t) = \delta\phi(x_{0,3}, t) = 0.
\end{aligned} \tag{14}
$$

(5) The adjoint equations are formulated at every channel reach k:

$$
\left[-A\frac{\partial \sigma}{\partial t} - Q\frac{\partial \sigma}{\partial x} + \frac{\partial \xi}{\partial \phi} - A\sigma\frac{\partial R}{\partial \phi} \right]_k = 0. \qquad k = 1, .., 3 \tag{15}
$$

The adjoint advection–reaction equations are in charge of transporting the error registered at the measurement station (x_M) to the reconstruction point, which is in this case the inlet boundary of channel 1.

(6) Now, applying the constraints of Equations (14) and (15) on expression (12) leads to

$$
\delta J = \int_0^T \left[\left(\sigma Q \delta\phi \right)_{x_{imax,1}} - \left(\sigma Q \delta\phi \right)_{x_{0,1}} - \left(\sigma Q \delta\phi \right)_{x_{0,2}} + \left(\sigma Q \delta\phi \right)_{x_{imax3}} \right] dt. \tag{16}
$$

(7) Like the flow and transport equations, the adjoint equations also require an internal boundary condition at the junction.

$$
\left(\sigma Q \delta\phi \right)_{x_{imax1}} - \left(\sigma Q \delta\phi \right)_{x_{0,2}} + \left(\sigma Q \delta\phi \right)_{x_{imax,3}} = 0. \tag{17}
$$

(8) Accordingly, the sensitivity of the objective function to the boundary condition of channel 1 is

$$
\nabla J = \frac{\delta J}{\delta \phi}\Big|_{(0,t)_1} = -(\sigma Q)(0,t)_1. \tag{18}
$$

Therefore, the regulation can be applied by means of the perturbation in the value of the boundary condition $\phi(0,t)$ using the discrete version of (18) at every time t^n. This development is part of an iterative process that is detailed later.

Note that the technique described above is analogous to reconstruct the boundary condition at channel 3.

3.2. Numerical Model and Gradient Descent Method

The adjoint equations (15) can be discretized (see Figure 2) following the same procedure used in (6). Therefore, the expression that updates the adjoint variables at cell i for time t^n is [27]:

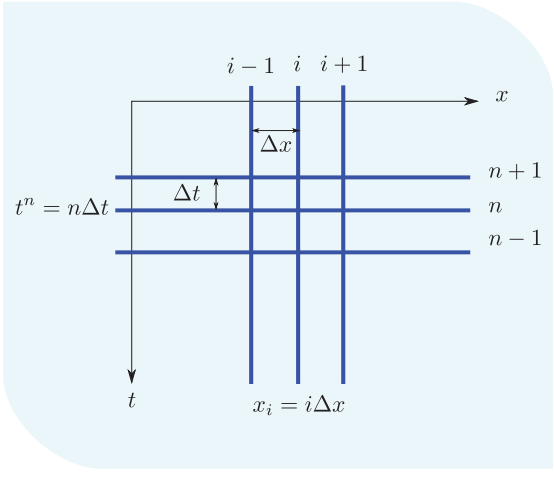

Figure 2. Discretization of time and space in the adjoint equation.

$$\sigma_i^n = \sigma_i^{n+1} + \frac{\Delta t}{\Delta x}\left[\left(u^-\delta\sigma\right)_{i-1/2}^{n+1} + \left(u^+\delta\sigma\right)_{i+1/2}^{n+1}\right] + \Delta t(\sigma R)_i + \Delta t\left(\frac{\partial\xi}{\partial\phi}\frac{1}{A}\right)_i \tag{19}$$

where $u = Q/A$ is the cross sectional average flow velocity. It is worth highlighting that finding the solution of the adjoint variable σ for each channel requires to solve the system backwards in time, that is, updating the time as $t^n = t^{n+1} - \Delta t$. Note that the upwind contributions (positive or negative superindex in the flow velocity) are opposite to those on the transport equation. As seen, the solution of Equation (19) also requires some information such as the time step Δt, the flow velocity u_i^n and the wetted area A_i^n at every time level t^n. For this purpose, all the information regarding the hydrodynamic part is saved at each time step and at each computational cell in a previous first forward simulation. Due to the explicit character of the scheme, the time step size is restricted by stability reasons in order to fulfill the CFL condition [35,41].

To obtain the best reconstructed values for the boundary condition, the gradient-descent method is used. The form of the iterative algorithm is described as follows:

$$\phi(0,t)^{\overline{n}+1} = \phi(0,t)^{\overline{n}} - \epsilon^{\overline{n}}(\nabla J)^{\overline{n}}, \tag{20}$$

where $\overline{n}$ indicates the level of the iteration, ϵ is the step length, and ∇J is the gradient of J. Accordingly, as long as all the hydrodynamic information is available, only of the adjoint equation (backwards) and the transport equation (forward) are necessary to converge to the minimum of the function with a certain tolerance.

The step length ϵ is considered a constant value and is obtained through trial and error. Regarding the target, the location of the measuring station x_M does not follow a defined rule; however, according to a previous work [42], it is known that this location could be crucial when reconstructing the information at a given point.

Figure 3 illustrates the flowchart followed to reconstruct the information of the solute boundary condition. This process is summarized in two fundamental stages: the so-called

flow simulation and the control simulation. In the flow simulation, the flow equations are solved using (5) with the known initial and boundary conditions, while the transport equation is computed with an estimated boundary condition (initial guess, generally 0) using (6). All the hydrodynamic information necessary for the next stage is stored during this process.

For the control simulation, two main parts are considered: the forward simulation and the backward simulation. This process is repeated until the functional is below a tolerance. The backward simulation calculates the value of the adjoint variable using (19) and the available velocity field and time step size at each time level and at each computational cell. The upstream boundary condition, i.e., the new value of the concentration at every time level, is obtained through the gradient method using (20).

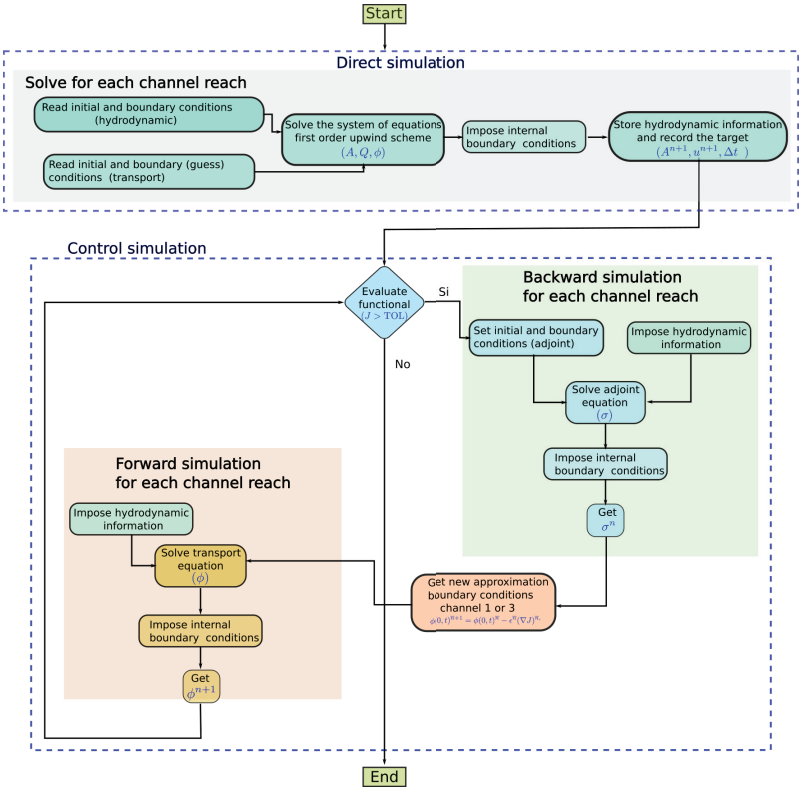

Figure 3. Scheme to reconstruct the information of the boundary condition through the adjoint and gradient-descent method.

4. Test Cases

The robustness and accuracy of the proposed technique is verified with some synthetic cases. In all of them, a first simulation is performed using a known upstream boundary condition in order to store time series of concentration values at the measurement point to be used as the target. These values are then used as the "experimental data" for the adjoint technique in order to evaluate the ability of the proposed method to reconstruct the upstream solute boundary condition.

The optimization process starts by solving the transport equation with an initial guess inlet solute boundary condition $\phi(0,t)_1 = 0\,\mathrm{g/m^3}$. The adjoint equation is then solved backwards to obtain the sensitivity for the optimization algorithm. The process is repeated

until the functional value is below a tolerance level. This procedure is applied in all cases presented.

4.1. Cases 1 and 2: Steady State of Both Flow and Concentration

In this scenario, we consider a 90° junction of three 10 m wide rectangular flat and frictionless channels of lengths L_1, L_2 and L_3 and widths B_1, B_2 and B_3 as shown in Figure 4. The initial conditions are

$$\begin{aligned} Q(x,0)_1 &= 1\,\mathrm{m}^3/\mathrm{s} & \text{Œ(x,0)}_1 &= 1\,\mathrm{g}/\mathrm{m}^3 & \mathrm{x} &\in [0, \mathrm{L}_1] \\ Q(x,0)_2 &= 2\,\mathrm{m}^3/\mathrm{s} & \text{Œ(x,0)}_2 &= 0.5\,\mathrm{g}/\mathrm{m}^3 & \mathrm{x} &\in [0, \mathrm{L}_2] \\ Q(x,0)_3 &= 1\,\mathrm{m}^3/\mathrm{s} & \text{Œ(x,0)}_3 &= 0\,\mathrm{g}/\mathrm{m}^3 & \mathrm{x} &\in [0, \mathrm{L}_3] \end{aligned}$$

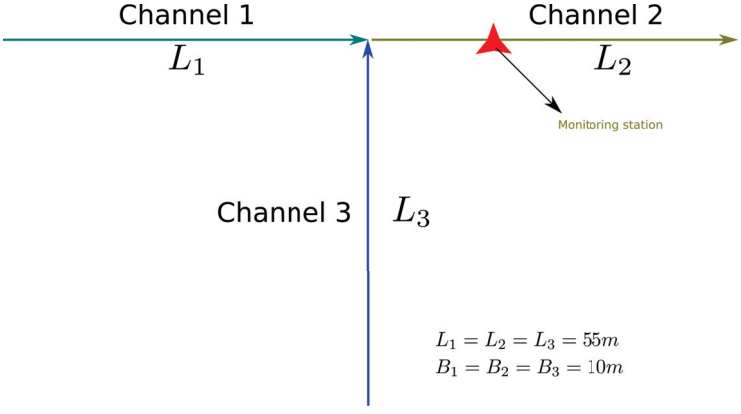

Figure 4. Case 1. Schematic of the three channels at a 90° confluence.

The inlet flow boundary condition is defined by the following values: $Q(0,t)_1 = Q(0,t)_3 = 1\ \mathrm{m}^3/\mathrm{s}$ for both channel 1 and channel 3 for $t \in [0, T]$. The solute inlet boundary condition for channel 3 is $\phi(x,0)_3 = 0\,\mathrm{g}/\mathrm{m}^3$ for $x \in [0, L_3]$. The inlet boundary condition for the solute of the first channel to be reconstructed by means of the control is $\phi(0,t)_1 = 1\ \mathrm{g}/\mathrm{m}^3$ for $t \in [0, T]$. For this case, the reaction constant $\kappa = 0$.

The measurement station is located in channel 2 at $x_M = 25.5\,\mathrm{m}$ (see Figure 4). As previously mentioned, these values are obtained through a first simulation with all the known parameters.

The time evolution of the solute concentration both at the inlet of channel 1 and at the target location in channel 2 obtained with CFL = 1, $\Delta x = 1$ m and $\epsilon = 7$ are shown in Figure 5. The numerical solution with the proposed scheme is plotted for iterations 1, 2, 5, 10, 15 and 20 (colored lines) for both the boundary conditions (a) and the target (b). The numerical solution of the last iteration converges to the theoretical solution (black line) with an acceptable accuracy. Small differences show up at the beginning of the simulation ($t \in [0, 150\,\mathrm{s}]$) for the boundary reconstruction. This behavior has already been reported and analyzed in the literature [27] and is attributed to the numerical diffusion. The target is however successfully achieved at iteration 20.

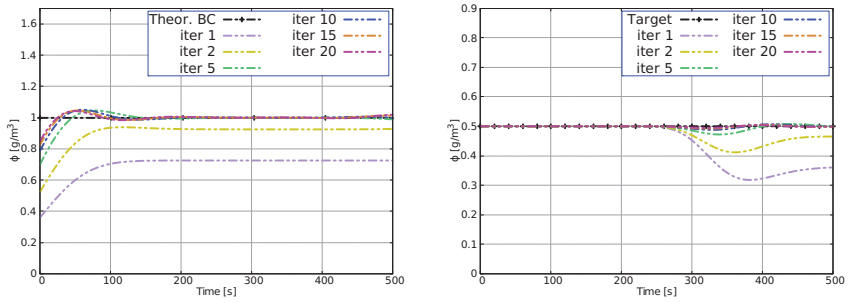

(**a**) (**b**)

Figure 5. Case 1. Evolution of the reconstruction of the boundary condition (**a**) and evolution of the target (**b**) at some iterations.

This test case has been repeated to evaluate the influence of the mesh size using the following number of cells (MNC): 100, 200 and 400. The results of both the reconstruction of the boundary condition in the last iteration and the evolution of the objective functional are plotted in Figure 6. Particularly, Figure 6a shows the variations that occur at the beginning of the simulation. They can be attributed to the numerical diffusion as well that tends to decrease as the mesh number of cells (MNC) increases.

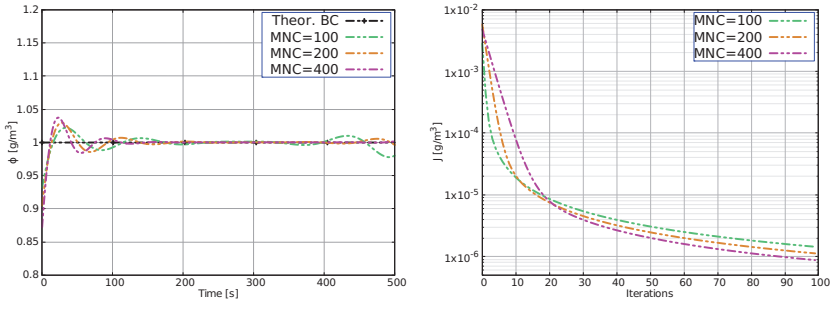

(**a**) (**b**)

Figure 6. Case 1. Reconstruction of the boundary condition at iteration 100 (**a**) and evolution of the objective function at each iteration (**b**) for different number of cells.

The results of the objective function also show the same trend, i.e., its value decreases as the number of cells increases. Furthermore, it is evident that the functional does not decrease in the same way for the range of iterations, especially in the first 20 iterations. For example, for a fixed $J = 1.0 \times 10^{-4}$, the number of iterations is different: ten iteration for MNC = 400, three iterations for MNC = 100. This trend changes after 20 iterations.

In the context of Case 1, new cases are considered (Case 2), to test the influence of the inlet discharge of channel. For this purpose, three scenarios were carried out. The initial conditions (I.C.) and boundary conditions (B.C.) of the flow of the three scenarios are displayed in Table 1.

Table 1. Initial and inlet boundary conditions to evaluate the reconstruction of the inlet boundary condition of the solute at channel 3.

Case	I.C. $Q(x,0)$ m^3/s			B.C. $Q(0,t)$ m^3/s	
	Channel 1	**Channel 2**	**Channel 3**	**Channel 1**	**Channel 3**
Case 2.1	1	1.5	0.5	1	0.5
Case 2.2	1	2	1	1	1
Case 2.3	1	3	2	1	2

The initial condition of the solute for the three channels and for the three proposed cases is $\phi(x,0) = 1\,\mathrm{g/m^3}$, and the boundary condition is determined by the following expression:

$$\phi(0,t)_1 = \begin{cases} 1 & 0 \leq t \leq 100\,\mathrm{s} \\ 0 & t \geq 100\,\mathrm{s} \end{cases} \qquad \phi(0,t)_3 = \begin{cases} 1 & 0 \leq t \leq 2000\,\mathrm{s} \\ 0 & t \geq 2000\,\mathrm{s} \end{cases}$$

The results show that the value of the functional tends to decrease the higher the inlet flow is. The discussion and the Root Mean Square Error (RMSE) of this set of test cases is presented later.

4.2. Case 3: Unsteady Flow with Gaussian Pulse for Both Flow and Concentration

This test case considers the same configuration displayed in Figure 4. The following initial conditions for both flow and solute are imposed:

$$\begin{aligned} Q(x,0)_1 &= 1.14\,\mathrm{m^3/s} & \phi(x,0)_1 &= 0\,\mathrm{g/m^3} & \mathrm{x} &\in [0, \mathrm{L}_1] \\ Q(x,0)_2 &= 2.14\,\mathrm{m^3/s} & \phi(x,0)_2 &= 0.46\,\mathrm{g/m^3} & \mathrm{x} &\in [0, \mathrm{L}_2] \\ Q(x,0)_3 &= 1\,\mathrm{m^3/s} & \phi(x,0)_3 &= 1\,\mathrm{g/m^3} & \mathrm{x} &\in [0, \mathrm{L}_3] \end{aligned}$$

The hydrodynamic inlet boundary condition for channel 1 is defined with a Gaussian function expressed as

$$Q(0,t)_1 = ae^{-\frac{(t-b)^2}{2c^2}} \qquad a = 3,\ b = 250,\ c = 180 \quad t \in [0,T] \tag{21}$$

The solute boundary condition $\phi(0,t)_1$ used to generate the target to be reconstructed by the adjoint method follows:

$$\phi(0,t)_1 = ae^{-\frac{(t-b)^2}{2c^2}}. \qquad a = 2,\ b = 250,\ c = 30 \quad t \in [0,T] \tag{22}$$

On the other hand, the inlet boundary conditions at channel 3 are defined as

$$Q(0,t)_3 = \begin{cases} 1\,\mathrm{m^3/s} & t \in [0, 100\,\mathrm{s}] \\ 3\,\mathrm{m^3/s} & t \in [100\,\mathrm{s}, 200\,\mathrm{s}] \\ 1\,\mathrm{m^3/s} & t \in [200\,\mathrm{s}, 500\,\mathrm{s}] \end{cases} \qquad \phi(0,t)_3 = 1\,\mathrm{g/m^3} \quad t \in [0,T] \tag{23}$$

No reaction or decay processes are considered ($\kappa = 0$). The downstream measurement station is located in channel 2 at $x_M = 5.5$ m. As for the optimization method, $\epsilon = 8$. The numerical results are plotted in Figure 7. The method efficiently reconstructs the signals regardless of their distributions. Particularly, the shape of the target (see Figure 7b) containing a plateau and the Gaussian pulse coming from the input signals from channels 1 and 3 are satisfactory achieved. With only 15 iterations, it is possible to reconstruct the boundary condition at channel 1 and achieve a great level of accuracy at the target (channel 2) without any non-physical concentrations or oscillations.

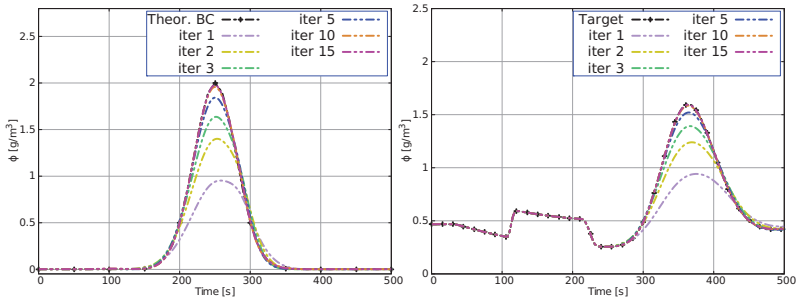

(**a**) (**b**)

Figure 7. Case 3. Evolution of the reconstruction of the boundary condition (**a**) and evolution of the target (**b**) in some iterations.

4.3. Case 4: Analysis of the Influence of the Measurement Station, Geometry and the Type of Reconstruction

The purpose of the next set of cases is to observe the influence of the location of the measurement station and the geometry of the case (length, slope) in the performance of the adjoint technique for the reconstruction of the upstream solute boundary condition of either channel 1 or channel 3. The configuration of the channel system is similar to that shown in Figure 4. Initial conditions for these scenarios are

$$\begin{aligned} Q(x,0)_1 &= 1\,\mathrm{m}^3/\mathrm{s} & \phi(x,0)_1 &= 0\,\mathrm{g}/\mathrm{m}^3 & \mathrm{x} &\in [0, \mathrm{L}_1] \\ Q(x,0)_2 &= 2\,\mathrm{m}^3/\mathrm{s} & \phi(x,0)_2 &= 0\,\mathrm{g}/\mathrm{m}^3 & \mathrm{x} &\in [0, \mathrm{L}_2] \\ Q(x,0)_3 &= 1\,\mathrm{m}^3/\mathrm{s} & \phi(x,0)_3 &= 0\,\mathrm{g}/\mathrm{m}^3 & \mathrm{x} &\in [0, \mathrm{L}_3] \end{aligned}$$

The boundary conditions for all the cases presented are

$$Q(0,t)_1 = \begin{cases} 1 & t \in [0, 100\,\mathrm{s}] \\ 2 & t \in [100, 1100\,\mathrm{s}] \\ 1 & t \geq 1100\,\mathrm{s} \end{cases} \quad \phi(0,t)_1 = \begin{cases} 0 & t \in [0, 100\,\mathrm{s}] \\ 2 & t \in [100, 1100\,\mathrm{s}] \\ 0 & t \geq 1100\,\mathrm{s} \end{cases}$$

$$Q(0,t)_3 = \begin{cases} 0.5 & t \in [0, 100\,\mathrm{s}] \\ 1 & t \in [100, 1100\,\mathrm{s}] \\ 0.5 & t \geq 1100\,\mathrm{s} \end{cases} \quad \phi(0,t)_3 = \begin{cases} 0 & t \in [0, 100\,\mathrm{s}] \\ 1 & t \in [100, 1100\,\mathrm{s}] \\ 0 & t \geq 1100\,\mathrm{s} \end{cases}$$

The roughness coefficient is 0.035 $\mathrm{sm}^{-1/3}$, and $\Delta x = 5$ m. This analysis is carried out by changing the length, slope and target location as shown in Table 2. The results with $\epsilon = 1$, CFL = 1 and number of total iterations equal to 100 are plotted in Figure 8. According to the location of the measurement station (Figure 2a), the study shows that the further it is from the reconstruction point, the bigger that value of the functional is. Regarding the length, the functional adopts different forms according to the reconstruction, and when the reconstruction is on channel 1 (see Figure 2b), there are small differences between the functional. However, when the information of channel 3 is reconstructed (Figure 2d), there are large variations, especially when the length of channel 3 is 1500 m. On the other hand, when the slope is 2%, the value of the functional decreases considerably with respect to the 1% slope (see Figure 2c).

Table 2. Case 4. Location of the target measuring station (channel 2) and geometric properties.

Channel Recons.	Case	L_1 (m)	L_2 (m)	L_3 (m)	$(S_o)_{1-3}$	x_M (m)
channel 1	Case 3.1	1000	1000	1000	1%	100
	Case 3.2	1000	1000	1000	1%	500
	Case 3.3	1000	1000	1000	1%	900
	Case 3.4	500	1000	1000	1%	100
	Case 3.5	1000	1000	1000	1%	100
	Case 3.6	1500	1000	1000	1%	100
	Case 3.7	1000	1000	1000	0.5%	100
	Case 3.8	1000	1000	1000	1%	100
	Case 3.9	1000	1000	1000	1.5%	100
channel 3	Case 3.10	1000	1000	500	1%	100
	Case 3.11	1000	1000	1000	1%	100
	Case 3.12	1000	1000	1500	1%	100

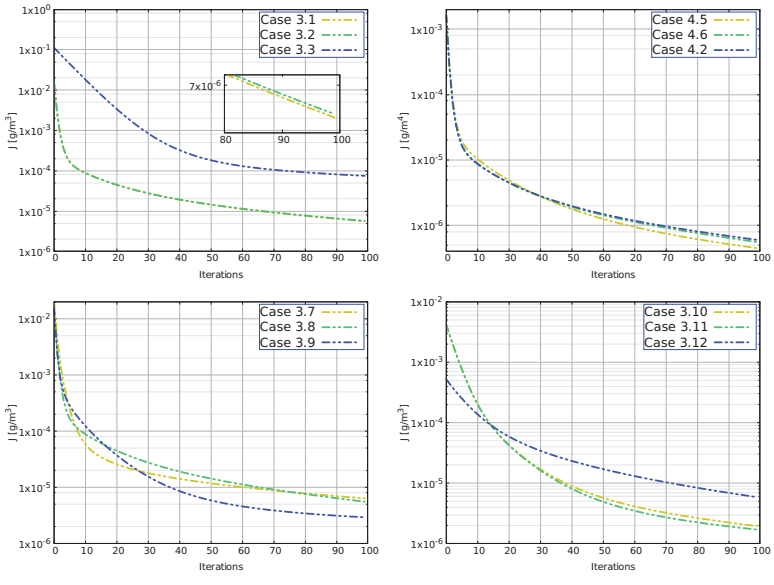

Figure 8. Case 4. Evolution of the functional in the different proposed scenarios.

4.4. Case 5: Unsteady Flow with Step Pulse for Both Flow and Concentration with Reaction

The purpose of this case is to observe the behavior of the reconstruction of the channel 1 upstream boundary condition given by a solute step pulse on the same configuration of Case 1 in presence of reaction. The initial conditions are set according to

$$\begin{aligned} Q(x,0)_1 &= 1\,\mathrm{m}^3/\mathrm{s} && \mathrm{x} \in [0, \mathrm{L}_1] \\ Q(x,0)_2 &= 2\,\mathrm{m}^3/\mathrm{s} && \mathrm{x} \in [0, \mathrm{L}_2] \\ Q(x,0)_3 &= 1\,\mathrm{m}^3/\mathrm{s} && \mathrm{x} \in [0, \mathrm{L}_3] \\ \phi(x,0)_1 = \phi(x,0)_2 &= \phi(x,0)_3 = 1\,\mathrm{g}/\mathrm{m}^3 && \mathrm{x} \in [0, \mathrm{L}_\mathrm{k}] \end{aligned} \tag{24}$$

and the boundary conditions are

$$Q(0,t)_1 = \begin{cases} 1\,\mathrm{m}^3/\mathrm{s} & t \in [0, 100\,\mathrm{s}] \\ 3\,\mathrm{m}^3/\mathrm{s} & t \in [100\,\mathrm{s}, 400\,\mathrm{s}] \\ 1\,\mathrm{m}^3/\mathrm{s} & t \in [400\,\mathrm{s}, 1000\,\mathrm{s}] \end{cases} \quad \phi(0,t)_1 = \begin{cases} 1\,\mathrm{g}/\mathrm{m}^3 & t \in [0, 100\,\mathrm{s}] \\ 3\,\mathrm{g}/\mathrm{m}^3 & t \in [100\,\mathrm{s}, 400\,\mathrm{s}] \\ 1\,\mathrm{g}/\mathrm{m}^3 & t \in [400\,\mathrm{s}, 1000\,\mathrm{s}] \end{cases}$$

$$Q(0,t)_3 = \begin{cases} 1\mathrm{m}^3/\mathrm{s} & t \in [0, 200\,\mathrm{s}] \\ 3\,\mathrm{m}^3/\mathrm{s} & t \in [200\,\mathrm{s}, 600\,\mathrm{s}] \\ 1\,\mathrm{m}^3/\mathrm{s} & t \in [600\,\mathrm{s}, 1000\,\mathrm{s}] \end{cases} \quad \phi(0,t)_3 = \begin{cases} 1\,\mathrm{g}/\mathrm{m}^3 & t \in [0, 200\,\mathrm{s}] \\ 3\,\mathrm{g}/\mathrm{m}^3 & t \in [200\,\mathrm{s}, 600\,\mathrm{s}] \\ 1\,\mathrm{g}/\mathrm{m}^3 & t \in [600\,\mathrm{s}, 1000\,\mathrm{s}] \end{cases}$$

The reaction solute constant decay is set to $\kappa = 1 \times 10^{-3}\ \mathrm{s}^{-1}$ for all channels. With these conditions, $\Delta x = 1$ m and $x_M = 5.5$ m at channel 2, the flow, the transport and the adjoint equation are solved following the iterative procedure. Figure 9 plots the time evolution of the flow at x_M and follows the imposed conditions, achieving a bounded and oscillation-free solution.

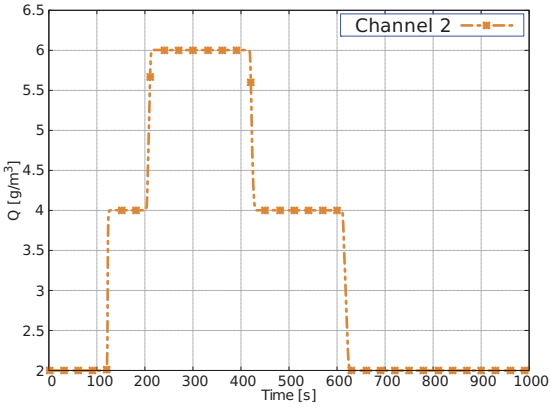

Figure 9. Case 5. Temporal evolution of flow-rate at $x_{M,2}$ = 5.5 m.

Figure 10 shows the numerical solutions at some iterations for both the reconstruction of the boundary condition and the target. Figure 10a shows small variations in the last iteration that can be attributed to the considered solute pulse shape, differences that are totally reduced when the signal to be reconstructed is smoother (Case 4) also observed in [27]. Figure 10b shows the target reached in only 60 iterations with satisfactory results.

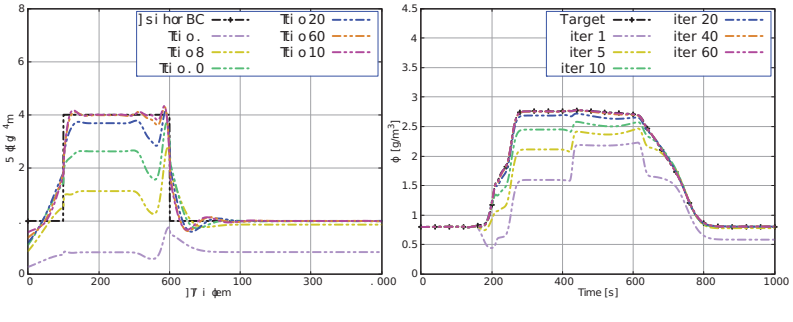

(**a**) (**b**)

Figure 10. Case 5. Evolution of the reconstruction of the boundary condition (**a**) and evolution of the target (**b**) in some iterations.

4.5. Case 6: Unsteady Flow with Two Solutes and Friction

In this case, two solutes ϕ_1 and ϕ_2 with different decay rates k_{ϕ_1} and k_{ϕ_2}, respectively, are considered. The hydraulic characteristics (see Figure 4) include now slope and friction for all channels: $S_0 = 0.001$ and $n = 0.035\ \mathrm{sm}^{-1/3}$. The initial conditions for the flow are

$$\begin{array}{llll} Q(x,0)_1 = 1.14\,\mathrm{m}^3/\mathrm{s} & \phi_1(x,0)_1 = 0\,\mathrm{g/m}^3 & \text{Œ}_2(\mathrm{x},0)_1 = 0\,\mathrm{g/m}^3 & \mathrm{x} \in [0, \mathrm{L}_1] \\ Q(x,0)_2 = 1.35\,\mathrm{m}^3/\mathrm{s} & \phi_1(x,0)_2 = 0\,\mathrm{g/m}^3 & \text{Œ}_2(\mathrm{x},0)_2 = 0\,\mathrm{g/m}^3 & \mathrm{x} \in [0, \mathrm{L}_2] \\ Q(x,0)_3 = 0.21\,\mathrm{m}^3/\mathrm{s} & \phi_1(x,0)_3 = 0\,\mathrm{g/m}^3 & \text{Œ}_2(\mathrm{x},0)_3 = 0\,\mathrm{g/m}^3 & \mathrm{x} \in [0, \mathrm{L}_3] \end{array}$$

On the other hand, the flow boundary conditions for channels 1 and 3 are a transient configuration defined by (21) using $a_1 = 3, b_1 = 250, c_1 = 180$ for channel 1 and $a_3 = 2.5$, $b_3 = 400, c_3 = 180$ for channel 3. The theoretical solute upstream boundary conditions to be reconstructed are highlighted in grey in Table 3 and are also defined by Equation (22). The remaining parameters and the decay rates are defined in Table 3.

Table 3. Case 6. Gaussian function parameters and decay rates of the three channels.

Channel	Variables							
	$\phi_1(0,t)$			$\phi_2(0,t)$			Decay Rate (s^{-1})	
	a	b	c	a	b	c	k_{ϕ_1}	k_{ϕ_2}
channel 1	2	250	30	4	250	30	1×10^{-5}	2×10^{-2}
channel 2		-			-		4×10^{-3}	2×10^{-3}
channel 3	1	400	30	2	400	30	8×10^{-6}	1.5×10^{-6}

The measurement station is located downstream of the junctions at $x_M = 35.5$ m in channel 2. The mesh size used in this test case is $\Delta x = 1$ m, with a CFL = 1 and a step length $\epsilon = 10$. The numerical results are plotted in the Figure 11. Figure 11a shows the numerical solution of the flow measured at x_M free of disturbances. Figure 11b,d displays the reconstructions of the inlet boundary condition for solutes ϕ_1 and ϕ_2, respectively, showing an acceptable convergence to a stable solution after 100 iterations.

Figure 11c,e shows the target for ϕ_1 and ϕ_2 after some iterations (dashed lines in colors), requiring 100 iterations to successfully converge to the registered downstream shape.

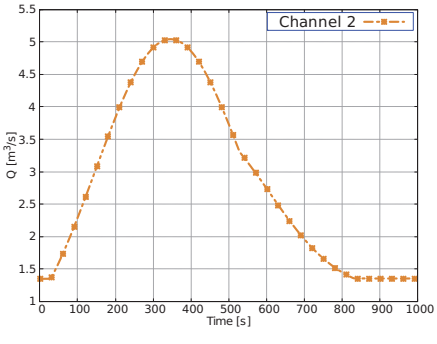

(**a**)

Figure 11. *Cont.*

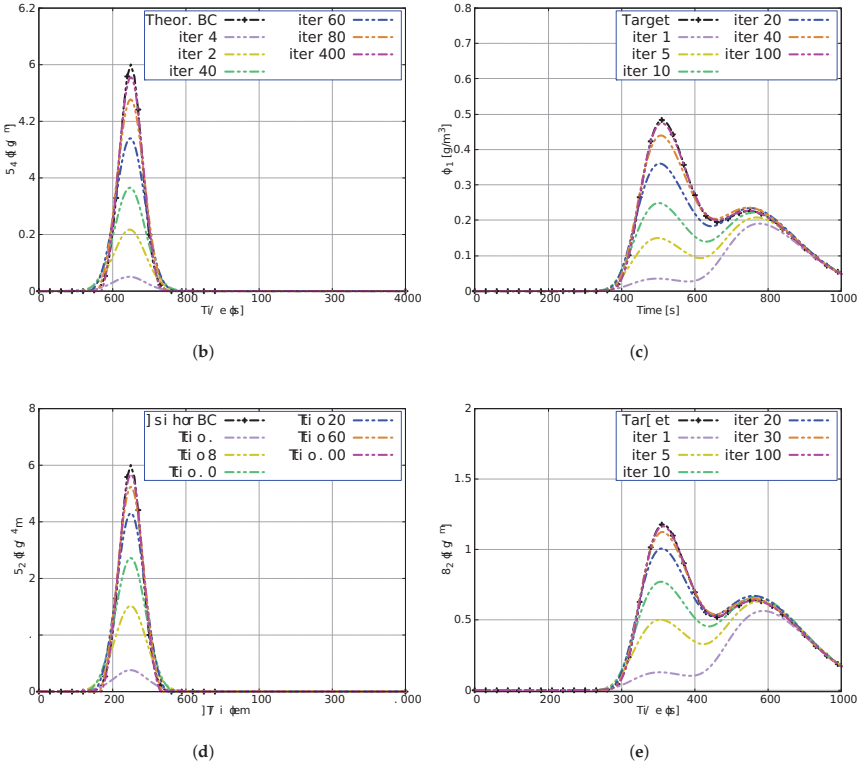

Figure 11. Case 4. Temporal evolution of flow-rate at $x_{M,2} = 35.5$ m (**a**) and reconstruction of the boundary condition ϕ_1 and ϕ_2 (**b**,**d**) and target at $x_{M,2} = 35.5$ m (**c**,**e**).

5. Discussion

This study presents a predictive explicit model for surface flow and transport of a non-conservative solute in a channel junction together with the adjoint formulation of the conservative and non-conservative transport equations. All the test cases used are synthetic and followed the channel network shown in Figure 4. In this section, the numerical results, the keys of the scheme, the combination of the hydrodynamic, transport, adjoint and first-order gradient models, and the limitations of the proposed strategy are analyzed.

The technique is completely stable under the CFL condition when considering the hydrodynamic source terms (slope and friction) and the source term of the adjoint and physical transport equation (decay rate). Together with appropriate junction boundary conditions, this technique is demonstrated to solve satisfactorily both steady state and unsteady scenarios in a channel junction.

Optimization models considered in the literature frequently require hundreds of calls of both the hydrodynamic and transport models to find the best accordance between computed and observed state variables (model components) by variation of a number of parameters [43,44], so a model with these features will require considerable computational burden. Among the different alternatives for the inverse modeling offered by predictive models, the adjoint formulation has demonstrated to be an efficient and flexible tool. This works explores the extension of the adjoint technique to reconstruct the solute boundary condition in hydrodynamic models with solute transport at junction of channels.

The adjoint equations are solved using the same numerical scheme, computational grid and time step size as the physical equations. Moreover, they are supplied with the

hydrodynamic information previously stored in the first simulation. This allows the error to be transported from the measurement point to the control point. Consequently, the gradient is used in the optimization method, allowing the boundary condition to be reconstructed efficiently and with relevant accuracy in all the scenarios proposed in this work. This is justified by the value of the functional in the last iteration, generally reduced by a 99.9% factor.

The versatility of the method to reconstruct the information at different channels has also been demonstrated. This was evidenced in Case 4 where the convergence of the functional achieves satisfactory results in both cases (Figure 8b,d). These results are evidenced with the evaluation of the root mean square error (RMSE) of the reconstructed upstream boundary condition at the last iteration (see Table 4). The evaluation criterion used reveals that the predictive precision and the fit of the model by means of the adjoint method have a better performance when the solute transported in unsteady flow is Gaussian. For this case, an RMSE = 0.0088 g/m^3 is reached compared to an RMSE = 0.361 g/m^3 in Case 3.3 when the solute pulse is a stepwise function.

Table 4. Root mean square error of the reconstructed boundary conditions.

Case	RMSE (g/m^3)
Case 1	0.02013
Case 2 MNC 100	0.0101
Case 2 MNC 200	0.0105
Case 2 MNC 400	0.0123
Case 2.1	0.208
Case 2.2	0.085
Case 2.3	0.034
Case 3.1	0.299
Case 3.2	0.3
Case 3.3	0.361
Case 3.4	0.298
Case 3.5	0.299
Case 3.6	0.301
Case 3.7	0.359
Case 3.8	0.299
Case 3.9	0.284
Case 3.10	0.196
Case 3.11	0.198
Case 3.12	0.314
Case 4	0.008
Case 5	0.154
Case 6	0.025

This work is an encouraging step forward to extend the method presented in [27] for water quality optimization analysis in branched channel or river networks. However, the main limitation of the model is the oscillatory trend for the reconstruction of a stepwise signal, leading to notable differences, especially in sudden changes in concentration. An example of this is Case 5, where the concentration varies sharply from 1 to 3 g/m^3 in a period of time of 1s (see Figure 10a). Another potential downside of the method is the necessity of storing of all the flow information in each computational cell and each time step. This downside could be overcome with techniques such as check pointing [45] which can be analyzed in future works of this nature.

6. Conclusions

This study reveals that the transport equation model can serve as a first step to understand the relationships between the channel network and the control of the concentration

of a solute downstream junction. The results showed that the accuracy of the boundary condition reconstruction depends largely on the shape of the signal to be reconstructed. However, these variations can be reduced by refining the computational mesh and increasing the number of iterations. The numerical solutions also indicate that, as the measurement station moves away from the reconstruction point, the final functional value in the last iteration becomes larger. Furthermore, it is demonstrated that few iterations in both steady state and unsteady scenarios are required to reconstruct the inlet boundary conditions of one or more solutes at a time.

Finally, the efficiency of the technique requires that the same computational mesh, the hydrodynamic characteristics and time step size be used when solving the transport equation and the adjoint equation in the optimization process. Besides this restriction, the optimization model presented in this work has been proved to be robust, accurate and efficient for different hydrodynamic and solute configurations.

Author Contributions: Conceptualization, G.G., M.M.-H. and P.G.-N.; methodology, M.M.-H. and P.G.-N.; software, G.G. and M.M.-H.; validation, G.G., M.M.-H. and P.G.-N.; formal analysis, G.G., M.M.-H. and P.G.-N.; investigation, G.G., M.M.-H. and P.G.-N.; resources, G.G., M.M.-H. and P.G.-N.; data curation, G.G.; writing—original draft preparation, G.G.; writing—review and editing, M.M.-H. and P.G.-N.; visualization, G.G.; supervision, M.M.-H. and P.G.-N.; project administration, P.G.-N.; funding acquisition, P.G.-N. All authors have read and agreed to the published version of the manuscript.

Funding: This work is funded by the Spanish Ministry of Science and Innovation under the research project PGC2018-094341-B-I00.

Data Availability Statement: Not applicable.

Conflicts of Interest: The authors declare no conflict of interest.

References

1. Chapra, S.C. Engineering water quality models and TMDLs. *J. Water Resour. Plan. Manag.* **2003**, *129*, 247–256. [CrossRef]
2. Garcia-Navarro, M.; Savirón, J. Numerical simulation of unsteady flow at open channel junctions. *J. Hydraul. Res.* **1992**, *30*, 595–609. [CrossRef]
3. Hsu, C.C.; Lee, W.J.; Chang, C.H. Subcritical open-channel junction flow. *J. Hydraul. Eng.* **1998**, *124*, 847–855. [CrossRef]
4. Best, J.; Roy, A. Mixing layer distortion at the confluence of unequal depth channels. *Nature* **1991**, *350*, 411–413. [CrossRef]
5. Best, J.L. Flow dynamics at river channel confluences: Implications for sediment transport and bed morphology. In *Recent Developments in Fluvial Sedimentology, 39*; Ethridge, F., Flores, M., Harvey, M., Eds.; Society of Economic Paleontologists and Mineralogists, Special Publication: Tulsa, OK, USA, 1987; pp. 27–35.
6. Best, J.L. Sediment transport and bed morphology at river channel confluences. *Sedimentology* **1988**, *35*, 481–498. [CrossRef]
7. Kenworthy, S.T.; Rhoads, B.L. Hydrologic control of spatial patterns of suspended sediment concentration at a stream confluence. *J. Hydrol.* **1995**, *168*, 251–263. [CrossRef]
8. Tong-Huan, L.; Yi-Kui, W.; Xie-Kang, W.; Huan-Feng, D.; Xu-Feng, Y. Morphological environment survey and hydrodynamic modeling of a large bifurcation-confluence complex in Yangtze River, China. *Sci. Total Environ.* **2020**, *737*, 139705.
9. Ghostine, R.; Vazquez, J.; Terfous, A.; Mose, R.; Ghenaim, A. Comparative study of 1D and 2D flow simulations at open-channel junctions. *J. Hydraul. Res.* **2012**, *50*, 164–170. [CrossRef]
10. Constantinescu, G.; Miyawaki, S.; Rhoads, B.; Sukhodolov, A. Numerical evaluation of the effects of planform geometry and inflow conditions on flow, turbulence structure, and bed shear velocity at a stream confluence with a concordant bed. *J. Geophys. Res. Earth Surf.* **2014**, *119*, 2079–2097. [CrossRef]
11. Constantinescu, G.; Miyawaki, S.; Rhoads, B.; Sukhodolov, A. Numerical analysis of the effect of momentum ratio on the dynamics and sediment-entrainment capacity of coherent flow structures at a stream confluence. *J. Geophys. Res.* **2012**, *117*, F04028. [CrossRef]
12. Constantinescu, G.; Miyawaki, S.; Rhoads, B.; Sukhodolov, A.; Kirkil, G. Structure of turbulent flow at a river confluence with momentum and velocity ratios close to 1: Insight provided by an eddy-resolving numerical simulation. *Water Resour. Res.* **2011**, *47*, W05507. [CrossRef]
13. Gualtieri, C.; Filizola, N.; de Oliveira, M.; Santos, A.M.; Ianniruberto, M. A field study of the confluence between Negro and Solimões Rivers. Part 1: Hydrodynamics and sediment transport. *Comptes Rendus Geosci.* **2018**, *350*, 31–42. [CrossRef]
14. Ianniruberto, M.; Trevethan, M.; Pinheiro, A.; Andrade, J.F.; Dantas, E.; Filizola, N.; Santos, A.; Gualtieri, C. A field study of the confluence between Negro and Solimões Rivers. Part 2: Bed morphology and stratigraphy. *Comptes Rendus Geosci.* **2018**, *350*, 43–54. [CrossRef]

15. Burguete, J.; Zapata, N.; García-Navarro, P.; Maïkaka, M.; Playán, E.; Murillo, J. Fertigation in furrows and level furrow systems. I: Model description and numerical tests. *J. Irrig. Drain. Eng.* **2009**, *135*, 401–412. [CrossRef]
16. Tang, H.; Zhang, H.; Yuan, S. Hydrodynamics and contaminant transport on a degraded bed at a 90-degree channel confluence. *Environ. Fluid Mech.* **2018**, *18*, 443–463. [CrossRef]
17. Xiao, Y.; Xia, Y.; Yuan, S.y.; Tang, H.w. Flow structure and phosphorus adsorption in bed sediment at a 90° channel confluence. *J. Hydrodyn. Ser. B* **2017**, *29*, 902–905. [CrossRef]
18. Yuan, S.; Tang, H.; Xiao, Y.; Xia, Y.; Melching, C.; Li, Z. Phosphorus contamination of the surface sediment at a river confluence. *J. Hydrol.* **2019**, *573*, 568–580. [CrossRef]
19. Cheng, Z.; Constantinescu, G. Stratification effects on flow hydrodynamics and mixing at a confluence with a highly discordant bed and a relatively low velocity ratio. *Water Resour. Res.* **2018**, *54*, 4537–4562. [CrossRef]
20. Gualtieri, C.; Ianniruberto, M.; Filizola, N. On the mixing of rivers with a difference in density: The case of the Negro/Solimões confluence, Brazil. *J. Hydrol.* **2019**, *578*, 124029. [CrossRef]
21. Lacasta, A.; Morales-Hernández, M.; Brufau, P.; García-Navarro, P. Application of an adjoint-based optimization procedure for the optimal control of internal boundary conditions in the shallow water equations. *J. Hydraul. Res.* **2018**, *56*, 111–123. [CrossRef]
22. Neupauer, R.M. Adjoint sensitivity analysis of contaminant concentrations in water distribution systems. *J. Eng. Mech.* **2011**, *137*, 31–39. [CrossRef]
23. Piasecki, M. Optimal wasteload allocation procedure for achieving dissolved oxygen water quality objectives. I: Sensitivity analysis. *J. Environ. Eng.* **2004**, *130*, 1322–1334. [CrossRef]
24. Sanders, B.F.; Katopodes, N.D. Adjoint sensitivity analysis for shallow-water wave control. *J. Eng. Mech.* **2000**, *126*, 909–919. [CrossRef]
25. Katopodes, N.D. *Free-Surface Flow: Environmental Fluid Mechanics*; Butterworth-Heinemann: Oxford, UK, 2018.
26. Marchuk, G.I. *Mathematical Models in Environmental Problems*; Elsevier: Amsterdam, The Netherlands, 2011; Volume 16.
27. Gordillo, G.; Morales-Hernández, M.; García-Navarro, P. A gradient-descent adjoint method for the reconstruction of boundary conditions in a river flow nitrification model. *Environ. Sci. Process. Impacts* **2020**, *22*, 381–397. [CrossRef]
28. Kundu, P.; Cohen, I.; Dowling, D. *Fluid Mechanics*; Waltham: Singapore, 2012.
29. Chapra, S.C. *Surface Water-Quality Modeling*; Waveland Press: Long Grove, IL, USA, 2008; pp. 175–183.
30. Thomann, R.V.; Mueller, J.A. *Principles of Surface Water Quality Modeling and Control*; Harper & Row, Publishers: New York, NY, USA, 1987.
31. Ramezani, M.; Noori, R.; Hooshyaripor, F.; Deng, Z.; Sarang, A. Numerical modelling-based comparison of longitudinal dispersion coefficient formulas for solute transport in rivers. *Hydrol. Sci. J.* **2019**, *64*, 808–819. [CrossRef]
32. Cheme, E.K.; Mazaheri, M. The effect of neglecting spatial variations of the parameters in pollutant transport modeling in rivers. *Environ. Fluid Mech.* **2021**, *21*, 587–603. [CrossRef]
33. Abbott, M.; Minns, A. *Computational Hydraulics: Elements of the Theory of Free Surface Flows*; MB Abbott. Pitman Publishing: London, UK, 1979.
34. Ji, Z.G. *Hydrodynamics and Water Quality: Modeling Rivers, Lakes, and Estuaries*; John Wiley & Sons: Hoboken, NJ, USA, 2017.
35. Gordillo, G.; Morales-Hernández, M.; García-Navarro, P. Finite volume model for the simulation of 1D unsteady river flow and water quality based on the WASP. *J. Hydroinform.* **2020**, *22*, 327–345. [CrossRef]
36. Murillo, J.; Navas-Montilla, A. A comprehensive explanation and exercise of the source terms in hyperbolic systems using Roe type solutions. Application to the 1D-2D shallow water equations. *Adv. Water Resour.* **2016**, *98*, 70–96. [CrossRef]
37. Fernández-Pato, J.; Morales-Hernández, M.; García-Navarro, P. Implicit finite volume simulation of 2D shallow water flows in flexible meshes. *Comput. Methods Appl. Mech. Eng.* **2018**, *328*, 1–25. [CrossRef]
38. Morales-Hernández, M.; García-Navarro, P.; Burguete, J.; Brufau, P. A conservative strategy to couple 1D and 2D models for shallow water flow simulation. *Comput. Fluids* **2013**, *81*, 26–44. [CrossRef]
39. Morales-Hernández, M.; Murillo, J.; García-Navarro, P. Diffusion–dispersion numerical discretization for solute transport in 2D transient shallow flows. *Environ. Fluid Mech.* **2019**, *19*, 1217–1234. [CrossRef]
40. Fernández-Pato, J.; García-Navarro, P. Finite volume simulation of unsteady water pipe flow. *Drink. Water Eng. Sci.* **2014**, *7*, 83–92. [CrossRef]
41. Murillo, J.; García-Navarro, P. Weak solutions for partial differential equations with source terms: Application to the shallow water equations. *J. Comput. Phys.* **2010**, *229*, 4327–4368. [CrossRef]
42. Piasecki, M. Optimal wasteload allocation procedure for achieving dissolved oxygen water quality objectives. II: Optimal load control. *J. Environ. Eng.* **2004**, *130*, 1335–1344. [CrossRef]
43. Lacasta, A.; Morales-Hernández, M.; Burguete, J.; Brufau, P.; García-Navarro, P. Calibration of the 1D shallow water equations: A comparison of Monte Carlo and gradient-based optimization methods. *J. Hydroinform.* **2017**, *19*, 282–298. [CrossRef]
44. MIKE21, D.; MIKE3 Flow Model, F. *Hydrodynamic and Transport Module Scientific Documentation*; DHI Water & Environment: Hørsholm, Denmark, 2009.
45. Lacasta, A.; García-Navarro, P. A GPU accelerated adjoint-based optimizer for inverse modeling of the two-dimensional shallow water equations. *Comput. Fluids* **2016**, *136*, 371–383. [CrossRef]

mathematics

MDPI

Article

Unsteady Three-Dimensional Flow in a Rotating Hybrid Nanofluid over a Stretching Sheet

Noor Farizza Haniem Mohd Sohut [1], Siti Khuzaimah Soid [2], Sakhinah Abu Bakar [1] and Anuar Ishak [1,*]

[1] Department of Mathematical Sciences, Universiti Kebangsaan Malaysia, Bangi 43600, Malaysia; p106827@siswa.ukm.edu.my (N.F.H.M.S.); sakhinah@ukm.edu.my (S.A.B.)
[2] Faculty of Computer and Mathematical Sciences, Universiti Teknologi MARA, Shah Alam 40450, Malaysia; khuzaimah@tmsk.uitm.edu.my
* Correspondence: anuar_mi@ukm.edu.my

Abstract: The problem of an unsteady 3D boundary layer flow induced by a stretching sheet in a rotating hybrid nanofluid is studied. A dimensionless set of variables is employed to transform the system of partial differential equations (PDEs) to a set of nonlinear ordinary differential equations (ODEs). Then, the system of ODEs is solved numerically using the MATLAB software. The impacts of different parameters, such as copper nanoparticles volume fraction, radiation, rotation, unsteadiness, and stretching parameters are graphically displayed. It is found that two solutions exist for the flow induced by the stretching sheet. Furthermore, the increasing nanoparticle volume fraction enhances the skin friction coefficient. It is noticed that the skin friction coefficient, as well as the heat transfer rate at the surface, decrease as the rotating parameter increases. Additionally, the thermal radiation as well as the unsteadiness parameter stimulate the temperature.

Keywords: unsteady flow; rotation; heat transfer; hybrid nanofluid; stretching sheet; radiation

Citation: Mohd Sohut, N.F.H.; Soid, S.K.; Abu Bakar, S.; Ishak, A. Unsteady Three-Dimensional Flow in a Rotating Hybrid Nanofluid over a Stretching Sheet. *Mathematics* **2022**, *10*, 348. https://doi.org/10.3390/math10030348

Academic Editors: Camelia Petrescu and Valeriu David

Received: 23 December 2021
Accepted: 22 January 2022
Published: 24 January 2022

Publisher's Note: MDPI stays neutral with regard to jurisdictional claims in published maps and institutional affiliations.

Copyright: © 2022 by the authors. Licensee MDPI, Basel, Switzerland. This article is an open access article distributed under the terms and conditions of the Creative Commons Attribution (CC BY) license (https://creativecommons.org/licenses/by/4.0/).

1. Introduction

The investigation into heat transfer is useful in various engineering applications, such as transpiration cooling, drag reduction, thrust bearing, and radial diffuser design [1]. Usually, fluids are used as heat transporters, such as in heating and cooling processes in transportation systems and industrial processes. It is also noticed that the stretching sheet has gained researchers' attention for years. Researchers have conducted various studies on the physical phenomena and heat transmissions past a stretching plate. It has numerous important applications in industrial production, including the extrusion of plastic sheets, the process of condensation of metallic plates, and glass filer fabrication [2]. The study of flow and heat transfer is of significant importance since the quality of the final product depends on the large extent of the skin friction coefficient and the heat transfer rate at the surface [2]. Recently, the investigation of flow over a stretching sheet has been broadened to many different cases that make the study more interesting. For instance, Shahid et al. [3] studied the effects of swimming gyrotactic microorganisms using Darcy law and Vafai et al. [4] explored the effects of Dufour, Soret, and radiation on the Powell–Eyring fluid flow.

Even though the study of steady-state flows has the greatest practical significance, many scholars are now paying close attention to the study of unsteady-state flows. Steady flow can be defined as a flow in which the fluid characteristics at a given location in the system stay constant throughout time. In contrast, the unsteady flow is defined otherwise, which is time-dependent flow. Sears and Telionis [5] reported the numerical studies of steady and unsteady distinguishing boundary layer flow with Goldstein's type singularities, and a possible comparison between the position of the singularity in relation to the time curves and the point of vanishing wall shear can be made. They discovered a significant difference between vanishing wall shear and separation. The unsteady (transient) boundary

layer that is time-varying consists of mostly start-up processes, such as the movements from rest or transitions from one steady-state to another or occasional movements [6]. According to Liao [7], the unsteady flow problem may be resolved in the same manner as the steady-state similarities governed by the nonlinear ODEs. The study found that solving the problem for unsteady flow is as easy as steady flow using the homotopy analysis method (HAM). Suali et al. [8] considered both shrinking and stretching sheets with injection or suction to explore the unsteady flow towards a stagnation point on the sheet. According to this study, the spectrum of dual outcomes rises with mass suction, whereas it reduces with mass injection. The problems related to the unsteady flow can also be found in numerous literature [9–16].

The applications involved the problem of rotating flow, such as flywheels, cutting discs, rotating machinery, computer storage devices, electrical items, and many others [17]. Anuar et al. [18] stated that the fluid flow with a rotating plane was initially introduced by Kármán [19] using the momentum integral method. In the year 1988, Wang [20] explored the rotating fluid flow of the stretching plate. The solutions were determined by the rotation rate parameter, and it was found that the perturbation solutions for small and large rotation rates were comparable to other works of literature. A few years later, Rajeswari and Nath [21] broadened Wang's problem to include the unsteady flow problem by combining the finite-difference scheme with the quasilinearization technique. Takhar et al. [22] have also extended Wang's analysis to include the magnetic field. The application that is related to the present magnetic-rotational model was the chilling process in amalgamation reactors of liquid metal blankets. Yacob et al. [23] investigated a steady rotating flow in a nanofluid containing carbon nanotubes past a stretching/shrinking surface. Carbon nanotubes can be classified into single-walled (SWCNT) and multi-walled (MWCNT). They discovered that the heat transfer enhancement is greater in water-MWCNTs than in water-SWCNTs. Moreover, recent studies in this area may be found in references [24–27].

Nanofluid is a new amalgamation formed, as stated by Choi [28]. A nanofluid is formed by adding tiny particles in nano-dimensions to the base fluid. Nanofluids have higher thermal conductivity and are more effective in heat transport activities compared to their base fluid. Hence, it is also well acknowledged and accepted empirically and conceptually that dispersing nanoparticles in a liquid may improve the liquid's thermo-physical properties [29]. Nanotechnology has advanced rapidly in recent years, and by combining many nanoparticle elements, stability issues and low heat conductivity can be addressed. Nanofluids will save energy, improve thermal efficiency, speed up processes, and increase the life of the equipment. Using a finite element simulation, Rana et al. [24] observed the unsteady magnetohydrodynamic (MHD) boundary layer rotating nanofluid flow on a stretching plate. Apart from that, nanofluid provides a number of advantages, including less component degradation and blockage in tiny channels than fluid containing micro-to millimeter-sized particles in suspension [30]. Similar problems in nanofluid but with different approaches were published by Ghadimi et al. [31], Noor et al. [32], Ahmad et al. [33], and Khan et al. [34].

Due to its importance in providing greater properties than nanofluid, hybrid nanofluid has recently been a topic of discussion. It's employed in heat transfer applications using particles that are less than 100 nanometers in size. Higher energy efficiency, lower operating costs, and greater performance are among the contributions of the high thermal conductivity of a hybrid nanofluid [35]. Hybrid nanofluids have recently piqued the curiosity of many academics as a novel technological idea. Using a two-step technique, Suresh et al. [36] studied the combination of Al_2O_3-Cu/H_2O hybrid nanofluid. They found that the distinct nanoparticles improved the parameters of the hybrid nanofluid. Later, Suresh et al. [37] discussed the heat transport and the impacts of the alumina-copper/H_2O hybrid nanofluid. Numerical research of the 3D hybrid nanofluid flux with Newtonian heating and Lorentz force effects on a stretching plate was conducted by Devi and Devi [38]. Later, they continued the investigation across a stretching plate on increasing heat transmission in a copper-alumina/H_2O hybrid nanofluid [35].

Moreover, Waini et al. [39] investigated the unsteady hybrid nanofluid flow and heat transmission through a stretching, as well as a shrinking surface. For a particular unsteadiness parameter range, dual solutions exist; the results demonstrate that increasing the nanoparticle volume percentage of Cu for the first solution will improve the skin friction coefficient, while the second solutions show the opposite. Furthermore, the unsteady hybrid nanofluid flow on a porous biaxial stretching or shrinking plate, the effects of buoyancy and stagnation flow on an exponentially stretching or shrinking vertical plate, heat transfer, and MHD flow over a porous stretching/shrinking wedge, as well as the flow past a permeable non-isothermal shrinking surface were reviewed by Waini et al. [40–43]. The stability analysis was conducted by Zainal et al. [44] for the unsteady 3D magnetohydrodynamic hybrid nanofluid for Homann flow. Hayat and Nadeem [45] described how heat dissipation might be improved using Ag-CuO/H_2O hybrid nanofluid. Later, Hayat et al. [26] extended the study of rotational flow with partial slip and radiation effects. Subsequently, Anuar et al. [18] explored copper-alumina/water hybrid nanofluid with radiation on a rotating surface. They reported the stability of the solutions over time. The study of hybrid nanofluid flows has been diversified by Khan et al. [46] to various nanoparticle shape factors and for different base fluids.

Motivated by the earlier studies on rotating hybrid nanofluids, the present work intends to explore the rotation and radiation impacts on the unsteady 3D rotating flow of a hybrid nanofluid over a stretching sheet. The boundary value problem is solved numerically using the MATLAB software. The model is adopted from Rana et al. [24] and Devi and Devi [35], where the hybrid nanofluid Al_2O_3-Cu/H_2O is considered in this study. Rana et al. [24] studied the unsteady magnetohydrodynamic flow on a stretching sheet in a rotating nanofluid. The influences of the related parameters are visually depicted, and the numerical findings obtained are compared with the existing literature. The novelty of this study can also be seen in the discovery of dual solutions when the surface of the sheet is stretched. This discovery also has applications in a variety of sectors of science and technology, and it is useful for engineers as well as scientists to understand the behavior of the boundary layer flow.

2. Problem Formulation

The unsteady rotating flow of a hybrid nanofluid on a stretching sheet is considered as demonstrated in Figure 1, where (x, y, z) are cartesian coordinates with the sheet at $z = 0$. The stretching velocities in the x and y directions are denoted by $u_w(x, t)$ and $v_w(x, t)$, respectively, while ω is the uniform angular velocity of the rotation, see Figure 1. Moreover, the ambient temperature of the fluid is T_∞ and the sheet temperature is T_w. The hybrid nanofluid Al_2O_3-Cu/H_2O is considered in this study. The desired hybrid nanofluid is formed by scatting copper nanoparticles in water to create Cu-H_2O nanofluid, and then aluminum oxide nanoparticles are added into that Cu-H_2O nanofluid.

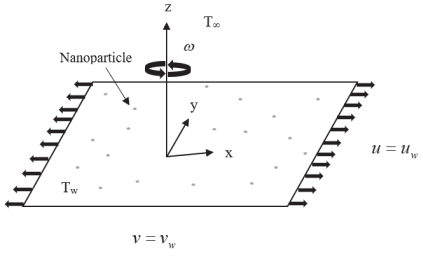

Figure 1. Physical configuration.

The governing equations are adopted from Refs. [2,20,21,25], and may be written as

$$\frac{\partial u}{\partial x} + \frac{\partial v}{\partial y} + \frac{\partial w}{\partial z} = 0 \tag{1}$$

$$\frac{\partial u}{\partial t}+u\frac{\partial u}{\partial x}+v\frac{\partial u}{\partial y}+w\frac{\partial u}{\partial z}=2\omega v+\frac{\mu_{hnf}}{\rho_{hnf}}\frac{\partial^2 u}{\partial z^2} \tag{2}$$

$$\frac{\partial v}{\partial t}+u\frac{\partial v}{\partial x}+v\frac{\partial v}{\partial y}+w\frac{\partial v}{\partial z}=-2\omega u+\frac{\mu_{hnf}}{\rho_{hnf}}\frac{\partial^2 v}{\partial z^2} \tag{3}$$

$$\frac{\partial w}{\partial t}+u\frac{\partial w}{\partial x}+v\frac{\partial w}{\partial y}+w\frac{\partial w}{\partial z}=\frac{\mu_{hnf}}{\rho_{hnf}}\frac{\partial^2 w}{\partial z^2} \tag{4}$$

$$\frac{\partial T}{\partial t}+u\frac{\partial T}{\partial x}+v\frac{\partial T}{\partial y}+w\frac{\partial T}{\partial z}=\frac{k_{hnf}}{(\rho C_p)_{hnf}}\frac{\partial^2 T}{\partial z^2}-\frac{1}{(\rho C_p)_{hnf}}\frac{\partial q_r}{\partial z} \tag{5}$$

The boundary conditions are

$$\begin{array}{lll} u=u_w(x,t)=\frac{cx}{1-\alpha t}, & v=0, \quad w=0, & T=T_w \quad \text{at } z=0 \\ u\to 0, & v\to 0, & T\to T_\infty \quad \text{as } z\to\infty \end{array} \tag{6}$$

where (u, v, w) are the velocity components along the (x, y, z) directions, t refers to time, T is the fluid temperature, $c>0$ for the stretching sheet and q_r is the radiative heat flux, k_{hnf} is the thermal conductivity, μ_{hnf} is the dynamic viscosity, ρ_{hnf} is the density, $(\rho C_p)_{hnf}$ is the heat capacity, and σ_{hnf} is the electrical conductivities. The thermophysical properties are given in [47] as presented in Table 1.

Table 1. Thermophysical properties.

Properties	Hybrid Nanofluid
Density	$\rho_{hnf}=\phi_{Al_2O_3}\rho_{Al_2O_3}+\phi_{Cu}\rho_{Cu}+\left(1-\phi_{hnf}\right)\rho_f$
Dynamic viscosity	$\mu_{hnf}=\mu_f\left(1-\phi_{Al_2O_3}-\phi_{Cu}\right)^{-2.5}$
Thermal conductivity	$\frac{k_{hnf}}{k_f}=\left\{\frac{\phi_{Al_2O_3}k_{Al_2O_3}+\phi_{Cu}k_{Cu}}{\phi_{Al_2O_3}+\phi_{Cu}}+2k_f+2\left(\phi_{Al_2O_3}k_{Al_2O_3}+\phi_{Cu}k_{Cu}\right)-2\left(\phi_{Al_2O_3}+\phi_{Cu}\right)k_f\right\}\times$ $\left\{\frac{\phi_{Al_2O_3}k_{Al_2O_3}+\phi_{Cu}k_{Cu}}{\phi_{Al_2O_3}+\phi_{Cu}}+2k_f-\left(\phi_{Al_2O_3}k_{Al_2O_3}+\phi_{Cu}k_{Cu}\right)+\left(\phi_{Al_2O_3}+\phi_{Cu}\right)k_f\right\}^{-1}$
Heat capacity	$(\rho C_p)_{hnf}=\phi_{Al_2O_3}(\rho C_p)_{Al_2O_3}+\phi_{Cu}(\rho C_p)_{Cu}+\left(1-\phi_{hnf}\right)(\rho C_p)_f$

Where $\phi_{hnf}=\phi_{Al_2O_3}+\phi_{Cu}$.

In Table 1, ϕ denotes the nanoparticle volume fraction where $\phi=0$ indicates the regular fluid, $\phi_{Al_3O_2}$ correlates to Al_2O_3, and ϕ_{Cu} correlates to Cu. The physical properties of the nanoparticles and the base fluid are given in Table 2, as reported in [48].

Table 2. Thermophysical properties of nanoparticles and water (base liquid).

Physical Properties	Al_2O_3	Cu	Water
C_p(J/KgK)	765	385	4179
$\rho\left(\mathrm{kg/m^3}\right)$	3970	8933	997.1
k(W/mK)	40	400	0.613
$\beta\times 10^{-5}$(1/K)	0.85	1.67	21

Following Bataller [49], Ishak [50], Magyari and Pantokratoras [51], and Roşca, Roşca and Pop [52], the Rosseland approximation is applied to exhibit q_r as

$$q_r=-\frac{4}{3}\frac{\sigma^*}{k^*}\frac{\partial T^4}{\partial y} \tag{7}$$

where q_r, k^* and σ^* respectively indicate the radiative heat flux, mean absorption coefficient, and the Stefan–Boltzmann constant. By neglecting higher-order terms and employing the

Taylor series, T^4 may be approximated as $T^4 \approx 4T_\infty^3 T - 3T_\infty^4$. Equation (5) is now may be written as

$$\frac{\partial T}{\partial t} + u\frac{\partial T}{\partial x} + v\frac{\partial T}{\partial y} + w\frac{\partial T}{\partial z} = \frac{1}{(\rho C_p)_{hnf}}\left(k_{hnf} + \frac{16\sigma^* {T_\infty}^3}{3k^*}\right)\frac{\partial^2 T}{\partial z^2} \tag{8}$$

The given transformation variables are according to Maqsood et al. [25],

$$\begin{gathered} u = \tfrac{ax}{1-\alpha t} f'(\eta), \qquad v = \tfrac{ax}{1-\alpha t} h(\eta), \qquad w = -\sqrt{\tfrac{a\nu_f}{1-\alpha t}} f(\eta) \\ \theta(\eta) = \tfrac{T-T_\infty}{T_w - T_\infty}, \qquad \eta = z\sqrt{\tfrac{a/\nu_f}{1-\alpha t}} \end{gathered} \tag{9}$$

where $(')$ denotes differentiation w.r.t. η, $a > 0$ is the stretching constant along the x direction, α is a parameter indicating the flow unsteadiness, ν_f is the kinematic viscosity of the base fluid, and the nonlinear rotating angular velocity is $\omega = \omega^*/(1-\alpha t)$.

Substituting the similarity variables (9) into Equations (1)–(4) and (8) yields

$$\frac{\mu_{hnf}/\mu_f}{\rho_{hnf}/\rho_f} f''' + ff'' - f'^2 + 2\Omega h - \beta\left(f' + \frac{\eta}{2}f''\right) = 0 \tag{10}$$

$$\frac{\mu_{hnf}/\mu_f}{\rho_{hnf}/\rho_f} h'' + fh' - f'\,h - 2\Omega f' - \beta\left(h + \frac{\eta}{2}h'\right) = 0 \tag{11}$$

$$\frac{1}{\Pr}\frac{1}{(\rho C_p)_{hnf}/(\rho C_p)_f}\left(\frac{k_{hnf}}{k_f} + \frac{4}{3}Rd\right)\theta'' + f\theta' - \beta\frac{\eta}{2}\theta' = 0 \tag{12}$$

The boundary conditions are as follows:

$$\begin{gathered} f(0) = 0, \quad f'(0) = \lambda, \quad h(0) = 0, \quad \theta(0) = 1 \\ f'(\eta) \to 0, \quad h(\eta) \to 0, \quad \theta(\eta) \to 0 \quad \text{as } \eta \to \infty \end{gathered} \tag{13}$$

where Ω is the rotation parameter, β the unsteadiness parameter, Pr indicates the Prandtl number, Rd the radiation parameter, and $\lambda > 0$ is the stretching parameter respectively defined as

$$\Omega = \frac{\omega^*}{a}, \qquad \beta = \frac{\alpha}{a}, \qquad \Pr = \frac{\nu_f}{\alpha_f}, \qquad Rd = \frac{4\sigma^* {T_\infty}^3}{k^* k_f}, \qquad \lambda = \frac{c}{a} \tag{14}$$

It is noted that $\lambda > 0$ is for stretching sheet, $\lambda < 0$ for shrinking sheet, and $\lambda = 0$ corresponds to static sheet.

We notice that the regular fluid $(\phi_{Al_2O_3} = \phi_{Cu} = 0)$ and the absence of rotating parameter $(\Omega = 0)$, Equation (10) becomes Equation (15) which is consistent with Equation (6) as in Fang et al. [53].

$$f''' + ff'' - f'^2 - \beta\left(f' + \frac{\eta}{2}f''\right) = 0 \tag{15}$$

The quantities of physical interest are the skin friction coefficients and the local Nusselt number which are given as follows:

$$\begin{gathered} C_{fx} = \frac{\mu_{hnf}}{\rho_f {u_e}^2(x)}\left(\frac{\partial u}{\partial z}\right)_{z=0}, \qquad C_{fy} = \frac{\mu_{hnf}}{\rho_f {u_e}^2(x)}\left(\frac{\partial v}{\partial z}\right)_{z=0}, \\ Nu_x = -\frac{x k_{hnf}}{k_f(T_f - T_\infty)}\left(\frac{\partial T}{\partial z}\right)_{z=0} + x(q_r)_{z=0} \end{gathered} \tag{16}$$

Using Equations (10) and (17) yields

$$\begin{gathered} {\mathrm{Re}_x}^{1/2} C_{fx} = \frac{\mu_{hnf}}{\mu_f} f''(0), \qquad {\mathrm{Re}_x}^{1/2} C_{fy} = \frac{\mu_{hnf}}{\mu_f} h'(0), \\ {\mathrm{Re}_x}^{-1/2} Nu_x = -\left(\frac{k_{hnf}}{k_f} + \frac{4}{3}Rd\right)\theta'(0) \end{gathered} \tag{17}$$

where Re_x is the local Reynolds number defined as $\mathrm{Re}_x = u_e(x)x/\nu_f$.

3. Results and Discussion

The governing non-linear ordinary differential equations (ODEs) (10)–(12) subjected to the boundary conditions (13) are solved numerically using the built-in function "bvp4c" available in the MATLAB software. The detailed settings are described in [54]. The validation for the skin friction coefficient in x and y directions $f''(0)$ and $h'(0)$, respectively, is obtained, which agrees with Wang [20], Nazar et al. [2], and Rana et al. [24]. The comparisons are for the stretching surface, $\lambda = 1$ in the absence of solid volume fraction ($\phi_1 = \phi_2 = 0$) at a steady state for different values of Ω as presented in Table 3. For convenient purposes, the subscripts '1′ and '2′ indicate the alumina (Al_2O_3) and the copper (Cu), respectively.

Table 3. Comparison of $f''(0)$ and $h'(0)$ for $\beta = 0$, $\lambda = 1$ and variation of Ω.

Ω	Wang [20]		Nazar et al. [2]		Rana et al. [24]		Present Study	
	$f''(0)$	$h'(0)$	$f''(0)$	$h'(0)$	$f''(0)$	$h'(0)$	$f''(0)$	$h'(0)$
0	−1	0	−1	0	−1	0	−1	0
0.5	−1.1384	−0.5128	−1.1384	−0.5128	−1.1384	−0.5128	−1.1384	−0.5128
1.0	−1.3250	−0.8371	−1.3250	−0.8371	−1.3250	−0.8371	−1.3250	−0.8371
2.0	−1.6523	−1.2873	−1.6523	−1.2873	−1.6523	−1.2873	−1.6523	−1.2873
5.0	-	-	-	-	−2.3903	−2.1502	−2.3903	−2.1502

The effects of non-dimensional parameters like Cu nanoparticle volume fraction ϕ_2, rotating parameter Ω, radiation parameter Rd, and unsteadiness parameter β, are discussed and illustrated in Figures 2–9. We can see from these diagrams that there are two solutions within the first and second solutions when $\lambda > 0$. The solutions are found up to a specific critical value $\lambda = \lambda_c$.

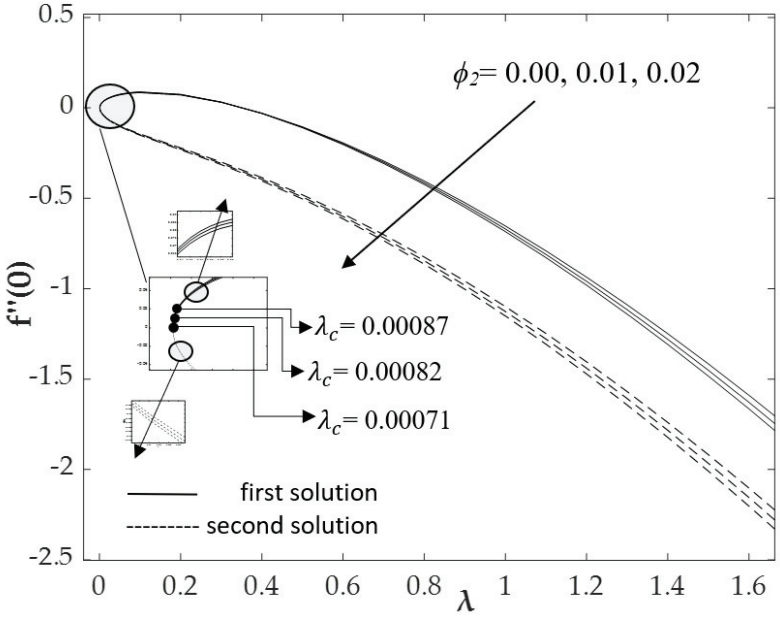

Figure 2. Variations of the skin friction coefficient in the x direction, $f''(0)$, with stretching parameter λ for various values of ϕ_2.

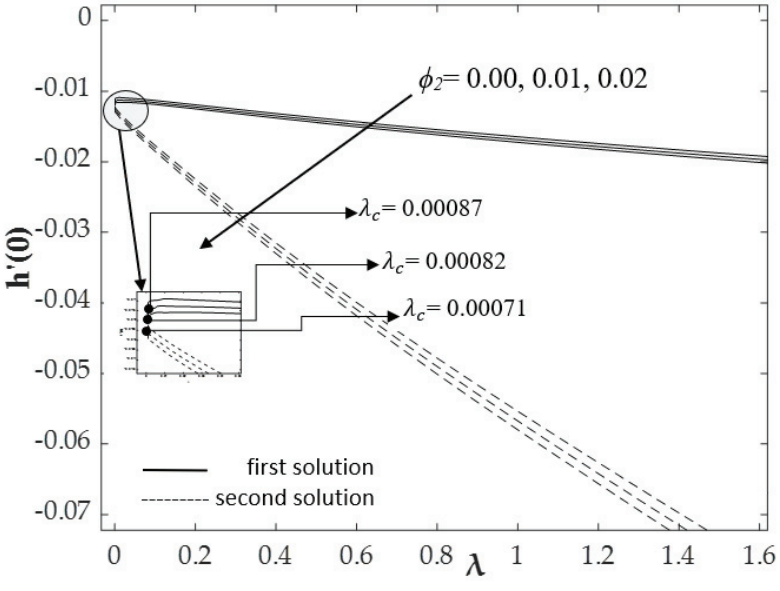

Figure 3. Variations of the skin friction coefficient in the y direction, $h'(0)$, with stretching parameter λ for various values of ϕ_2.

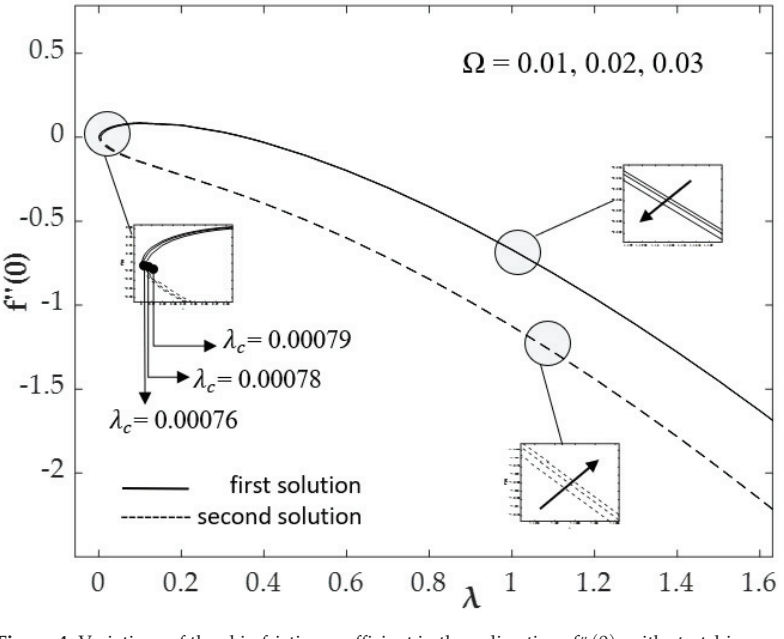

Figure 4. Variations of the skin friction coefficient in the x direction, $f''(0)$, with stretching parameter λ for various values of Ω.

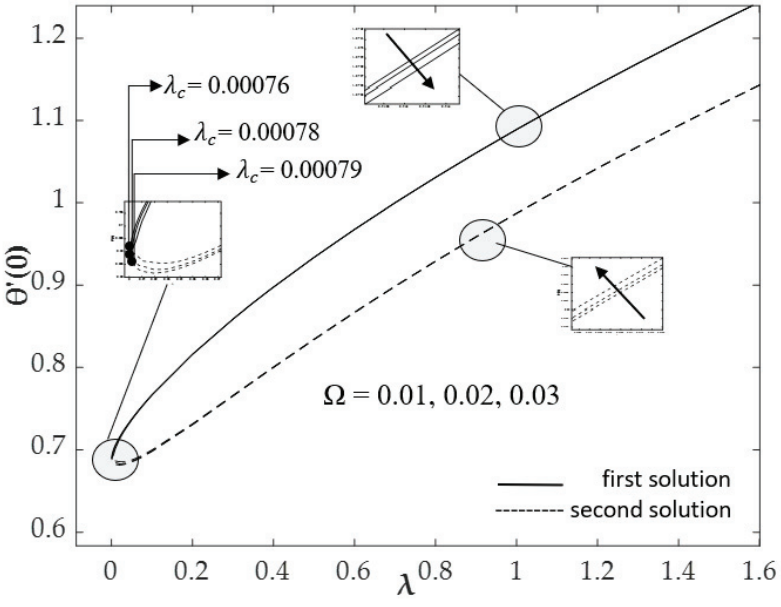

Figure 5. Variations of the local Nusselt number $-\theta'(0)$ with stretching parameter λ for different values of Ω.

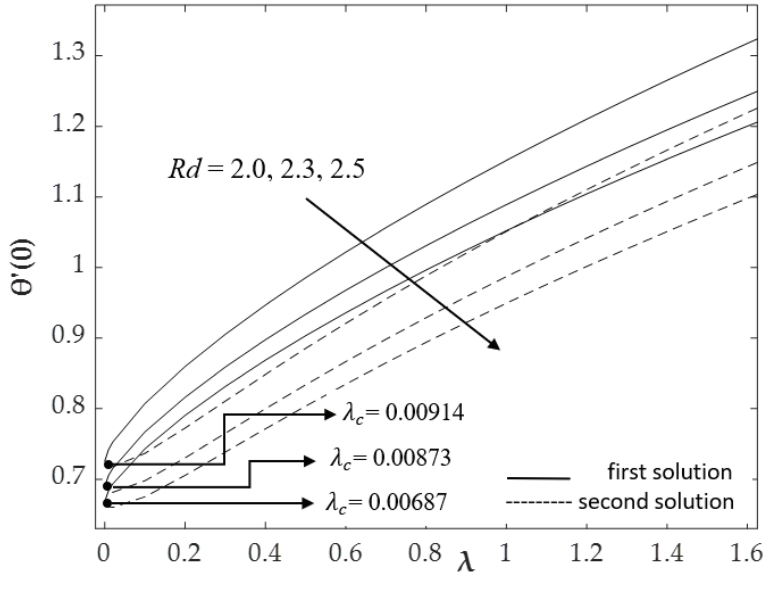

Figure 6. Variations of the local Nusselt number $-\theta'(0)$ with stretching parameter λ for different values of *Rd*.

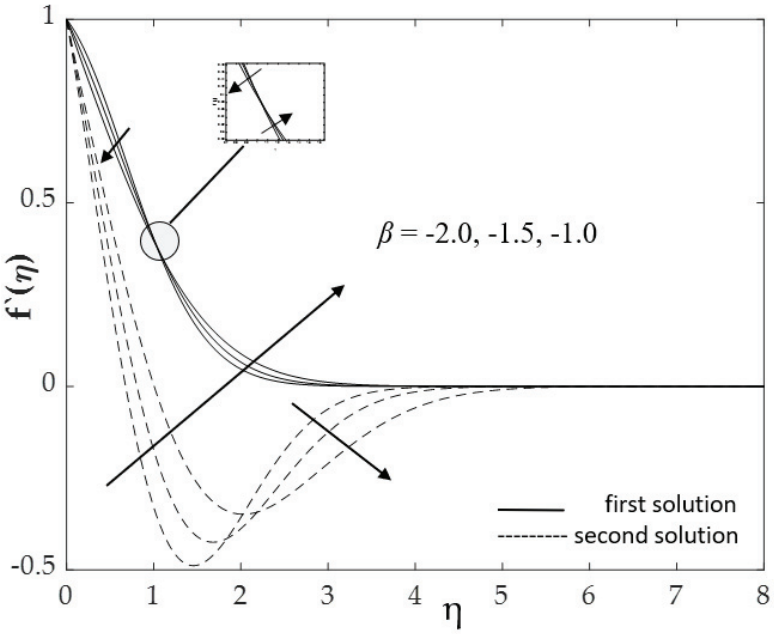

Figure 7. Velocity profiles in the x direction $f'(\eta)$, for different values of β when $Rd = 2.3$, $\lambda = 1$, $\phi_1 = \phi_2 = 0.01$, Pr $= 6.2$ and $\Omega = 0.01$.

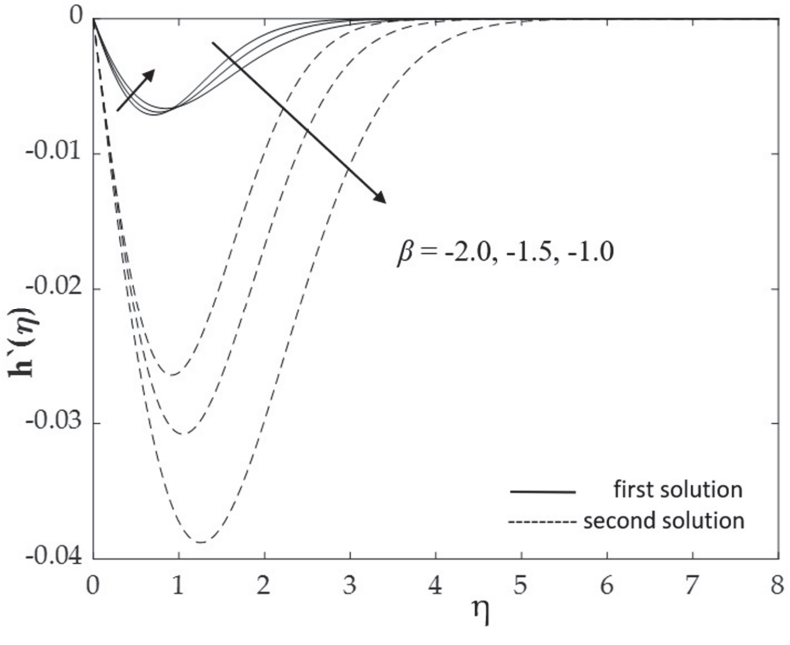

Figure 8. Velocity profiles in the y direction $h(\eta)$, for different values of β when $Rd = 2.3$, $\lambda = 1$, $\phi_1 = \phi_2 = 0.01$, Pr $= 6.2$ and $\Omega = 0.01$.

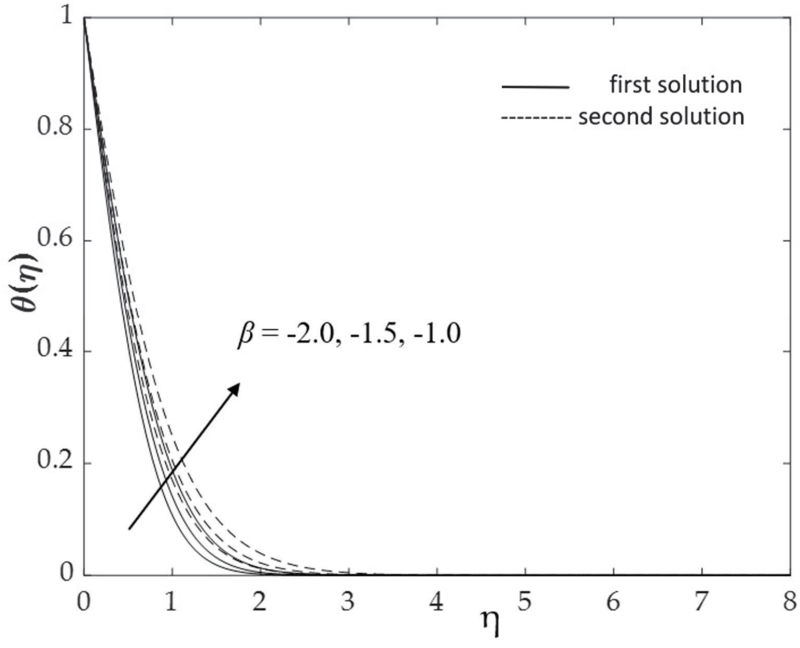

Figure 9. Temperature distribution $\theta(\eta)$ for different values of β when Pr $= 6.2$, $Rd = 2.3$, $\lambda = 1$, $\phi_1 = \phi_2 = 0.01$ and $\Omega = 0.01$.

Figures 2 and 3 depict the changes in the skin friction $f''(0)$ in the x direction and $h'(0)$ in the y direction, respectively, for the various values of ϕ_2 when Pr $= 6.2$, $Rd = 2.3$, $\beta = -1$, $\phi_1 = 0.01$ and $\Omega = 0.01$. It is discovered that as the Cu nanoparticle volume fraction ϕ_2 increases, the values of $f''(0)$ and $h'(0)$ decrease (increase in absolute sense) for both solutions. There are two solutions for a particular range of stretching strength $\lambda > 0$. It is noted that the critical value λ_c for Cu/H_2O nanofluid ($\phi_1 = 0.01$, $\phi_2 = 0.00$) is 0.00087 and for the hybrid nanofluid Al_2O_3-Cu/H_2O ($\phi_1 = 0.01$, $\phi_2 = 0.01,\ 0.02$) are 0.00082 and 0.00071, respectively. It is found that the critical values λ_c decrease when the values of ϕ_2 increase. When compared to the nanofluid, the hybrid nanofluid has a higher concentration of nanoparticles. In particular, a higher concentration of nanoparticles will lead to the boundary layer separation being delayed. In Figure 2, the magnitude of $f''(0)$ rises in perfect sync with the Cu nanoparticle volume fraction ϕ_2. It is noted that the solid surface exerts a drag force on the fluid for negative values of $f''(0)$. Meanwhile, if the stretching strength is less $(0.05 < \lambda < 0.4)$, it has the opposite behavior, in which the fluid exerts a drag force on the sheet, represented by positive values of $f''(0)$. The solution exists up to the critical values of λ as shown in Figure 2, where λ_c = 0.00087, 0.00082, and 0.00071 for Cu nanoparticle volume fraction parameter ϕ_2 =0.00, 0.01, and 0.02, respectively. It is noted that there are positive and negative values of $f''(0)$. The positive values indicate a drag force imposed by the fluid on the solid surface, while the negative sign implies a drag force imposed by the solid surface on the fluid. On the other hand, the case $f''(0) = 0$ indicates that the fluid-solid contact is free of friction moving at the same velocity. Overall, the higher the ratio of stretching, the higher the drag force on the surface. There are significant effects on the second solution in Figure 3, where the y-direction skin friction coefficient, $h'(0)$ is always negative for $\lambda > 0$ as the drag force is dominant on the solid surface. The effects of drag force in the y direction are less than the effects in the x direction.

In addition, Figures 4 and 5 elucidate the variation in the skin friction $f''(0)$ in the x direction and heat transfer $-\theta'(0)$ for various values of the rotating parameter Ω when

Pr = 6.2, Rd = 2.3, $\beta = -1$, and $\phi_1 = \phi_2 = 0.01$. It is observed that the critical values λ_c are getting bigger with the increasing values of the rotating parameter Ω. The critical values of λ for the rotating parameter $\Omega = 0.01$, 0.02, and 0.03 are λ_c =0.00076, 0.00078, and 0.00079, respectively. The increment values of the rotating parameter depend on the rotation rate, as well as the stretching rate [25]. Figure 4 shows that $f''(0)$ decreases as Ω increases for the first solution, but it increases for the second solution, which is consistent with the results presented in Figure 2. Even though the gap is small, due to the small variation of the rotating parameter Ω, but the existence of the dual solutions can still be seen. However, Figure 5 shows the opposite results, where for the first solution, increasing Ω leads to a decrease in the heat transfer rate $-\theta'(0)$, while for the second solution, it rises.

The variations of heat transfer rate $-\theta'(0)$ with λ for various values of radiation parameter Rd when Pr = 6.2, $\Omega = 0.01$, $\beta = -1$, and $\phi_1 = \phi_2 = 0.01$ are presented in Figure 6. We note that as Rd increases, the absolute value of $-\theta'(0)$ decreases. The critical values, $\lambda_c = 0.00914$, 0.00873, and 0.00687 for Rd =2.0, 2.3, and 2.5, respectively, are also presented in this figure. It is noted that Rd gives no effect on the skin friction coefficients for both the x and y directions, which is expected since the velocity field is not affected by the thermal field, see Equations (10)–(13).

Figures 7–9 elucidate the effects of the unsteadiness parameter β on the fluid velocity in the x and y directions, as well as the fluid temperature. Initially, by increasing β, the velocity of the first solution decreases, while the velocity of the second solution increases. However, the opposite behavior is seen in the velocity in the y direction. When the fluid moves towards inviscid flow, the directional movement of the velocity changes in the x direction for first and second solutions, while the movement of velocity in the y direction is consistent with decreasing towards the quiescent fluid. These scenarios imply thickening of the velocity boundary layer. In addition, the temperature increases for both solutions. It shows a consistent analysis that the thermal boundary layer thickness is also rising.

4. Conclusions

The problem of the unsteady 3D rotating hybrid nanofluid flow on a stretching sheet was explored. The governing PDEs were transformed to ODEs using a suitable similarity transformation. The effects of the involved parameters on the physical quantities of interest were visually shown and analyzed. The existence of double solutions was discovered for the stretching situation. In addition, the higher concentration of the nanoparticle volume fraction slowed down the boundary layer flow separation. The function $h(\eta)$ was found to be negative, which explains that the counterclockwise fluid rotation influences the fluid flow in the negative y direction. The positive skin friction coefficient shows that the fluid imposes a drag force on the solid surface, while the negative value implies the contrary. The results showed that the radiation parameter, Rd, emits the heat energy into the boundary layer, thus leading to a temperature rise of the hybrid nanofluid and subsequently enhancing the heat transfer rate of the fluid.

Author Contributions: Writing—original draft, N.F.H.M.S.; methodology, N.F.H.M.S., S.K.S.; generating numerical results, N.F.H.M.S., S.K.S.; validation, S.A.B., A.I.; writing—review and editing, S.A.B., A.I.; supervising, S.K.S., S.A.B., A.I.; funding acquisition, A.I. All authors have read and agreed to the published version of the manuscript.

Funding: This research was funded by Universiti Kebangsaan Malaysia (DIP-2020-001).

Institutional Review Board Statement: Not applicable.

Informed Consent Statement: Not applicable.

Conflicts of Interest: The authors declare no conflict of interest.

Nomenclature

a, c	constants
C_∞	ambient concentration
C_f	skin friction coefficient
C_p	specific heat at constant pressure ($Jkg^{-1}K^{-1}$)
(ρC_p)	heat capacitance of the fluid ($JK^{-1}m^{-3}$)
f'	velocity in the x-direction
h	velocity in the y-direction
k	thermal conductivity of the fluid ($Wm^{-1}K^{-1}$)
k^*	Rosseland mean absorption coefficient (m^{-1})
Nu_x	local Nusselt number
Pr	Prandtl number
q_r	radiative heat flux (Wm^{-2})
Rd	radiation parameter
Re_x	local Reynolds number
t	time (s)
T	fluid temperature (K)
T_∞	ambient temperature (K)
T_w	surface temperature (K)
u, v, w	velocity component in the x-, y- and z- directions (ms^{-1})
u_w	velocity in the x direction (ms^{-1})
v_w	velocity in the y direction (ms^{-1})
x, y, z	Cartesian coordinates (m)
Greek Symbols	
α	a parameter indicates the flow unsteadiness
β	unsteadiness parameter
η	similarity variable
θ	dimensionless temperature
λ	stretching parameter
μ	dynamic viscosity ($kgm^{-1}s^{-1}$)
ν	kinematic viscosity of the fluid (m^2s^{-1})
ρ	density of the fluid (kgm^{-3})
σ	electric conductivity (Sm^{-1})
σ^*	Stefan-Boltzmann constant ($Wm^{-2}K^{-4}$)
ϕ	nanoparticle volume fraction
Ω	rotating parameter
ω	angular velocity (rad s^{-1})
Subscripts	
f	base fluid
hnf	hybrid nanofluid
Superscript	
$'$	differentiation with respect to η

References

1. Attia, H.A. Steady three-dimensional hydromagnetic stagnation point flow towards a stretching sheet with heat generation. *Ital. J. Pure Appl. Math.* **2010**, *2010*, 9–18.
2. Nazar, R.; Amin, N.; Pop, I. Unsteady boundary layer flow due to a stretching surface in a rotating fluid. *Mech. Res. Commun.* **2004**, *31*, 121–128. [CrossRef]
3. Shahid, A.; Huang, H.; Bhatti, M.M.; Zhang, L.; Ellahi, R. Numerical investigation on the swimming of gyrotactic microorganisms in nanofluids through porous medium over a stretched surface. *Mathematics* **2020**, *8*, 380. [CrossRef]
4. Vafai, K.; Khan, A.A.; Fatima, G.; Sait, S.M.; Ellahi, R. Dufour, Soret and radiation effects with magnetic dipole on Powell-Eyring fluid flow over a stretching sheet. *Int. J. Numer. Methods Heat Fluid Flow* **2021**, *31*, 1085–1103. [CrossRef]
5. Sears, W.R.; Telionis, D.P. Boundary-layer separation in unsteady flow. *SIAM J. Appl. Math.* **1975**, *28*, 215–235. [CrossRef]
6. Schlichting, H.; Gersten, K. *Boundary-Layer Theory*; Springer: Berlin/Heidelberg, Germany, 2016; ISBN 9783662529195.
7. Liao, S. Unsteady boundary-layer flows. In *Homotopy Analysis Method in Nonlinear Differential Equations*; Springer: Berlin/Heidelberg, Germany, 2012; pp. 403–421.

8. Suali, M.; Nik Long, N.M.A.; Ariffin, N.M. Unsteady stagnation point flow and heat transfer over a stretching/shrinking sheet with suction or injection. *J. Appl. Math.* **2012**, *2012*, 781845. [CrossRef]
9. Mukhopadhyay, S.; Andersson, H.I. Effects of slip and heat transfer analysis of flow over an unsteady stretching surface. *Heat Mass Transf. Stoffuebertragung* **2009**, *45*, 1447–1452. [CrossRef]
10. Nadeem, S.; Hussain, M.; Naz, M. MHD stagnation flow of a micropolar fluid through a porous medium. *Meccanica* **2010**, *45*, 869–880. [CrossRef]
11. Mukhopadhyay, S.; De, P.R.; Bhattacharyya, K.; Layek, G.C. Casson fluid flow over an unsteady stretching surface. *Ain Shams Eng. J.* **2013**, *4*, 933–938. [CrossRef]
12. Naganthran, K.; Nazar, R.; Pop, I. Unsteady stagnation-point flow and heat transfer of a special third grade fluid past a permeable stretching/shrinking sheet. *Sci. Rep.* **2016**, *6*, 24632. [CrossRef]
13. Bachok, N.; Ishak, A.; Pop, I. Unsteady boundary-layer flow and heat transfer of a nanofluid over a permeable stretching/shrinking sheet. *Int. J. Heat Mass Transf.* **2012**, *55*, 2102–2109. [CrossRef]
14. Soid, S.K.; Ishak, A.; Pop, I. Unsteady MHD flow and heat transfer over a shrinking sheet with ohmic heating. *Chin. J. Phys.* **2017**, *55*, 1626–1636. [CrossRef]
15. Dzulkifli, N.F.; Bachok, N.; Yacob, N.A.; Arifin, N.M.; Rosali, H. Unsteady stagnation-point flow and heat transfer over a permeable exponential stretching/shrinking sheet in nanofluid with slip velocity effect: A stability analysis. *Appl. Sci.* **2018**, *8*, 2172. [CrossRef]
16. Khan, U.; Waini, I.; Ishak, A.; Pop, I. Unsteady hybrid nanofluid flow over a radially permeable shrinking/stretching surface. *J. Mol. Liq.* **2021**, *331*, 115752. [CrossRef]
17. Childs, P.R.N. Rotating Flow. In *Rotating Cylinders, Annuli, and Spheres*; Elsevier Inc.: Amsterdam, The Netherlands, 2011; pp. 177–247. ISBN 9780123820983.
18. Anuar, N.S.; Bachok, N.; Pop, I. Radiative hybrid nanofluid flow past a rotating permeable stretching/shrinking sheet. *Int. J. Numer. Methods Heat Fluid Flow* **2020**, *31*, 914–932. [CrossRef]
19. Kármán, T.V. Über laminare und turbulente Reibung. *ZAMM J. Appl. Math. Mech. Zeitschrift Angew. Math. Mech.* **1921**, *1*, 233–252. [CrossRef]
20. Wang, C.Y. Stretching a surface in a rotating fluid. *ZAMP Zeitschrift Angew. Math. Phys.* **1988**, *39*, 177–185. [CrossRef]
21. Rajeswari, V.; Nath, G. Unsteady flow over a stretching surface in a rotating fluid. *Int. J. Eng. Sci.* **1992**, *30*, 747–756. [CrossRef]
22. Takhar, H.S.; Chamkha, A.J.; Nath, G. Flow and heat transfer on a stretching surface in a rotating fluid with a magnetic field. *Int. J. Therm. Sci.* **2003**, *42*, 23–31. [CrossRef]
23. Yacob, N.A.; Dzulkifli, N.F.; Nur, S.; Salleh, A.; Ishak, A. Rotating flow in a nanofluid with CNT nanoparticles over a stretching/shrinking surface. *Mathematics* **2022**, *10*, 7. [CrossRef]
24. Rana, P.; Bhargava, R.; Bég, O.A. Finite element simulation of unsteady magneto-hydrodynamic transport phenomena on a stretching sheet in a rotating nanofluid. *Proc. Inst. Mech. Eng. Part N J. Nanoeng. Nanosyst.* **2013**, *227*, 77–99. [CrossRef]
25. Maqsood, N.; Mustafa, M.; Khan, J.A. Numerical tackling for viscoelastic fluid flow in rotating frame considering homogeneous-heterogeneous reactions. *Results Phys.* **2017**, *7*, 3475–3481. [CrossRef]
26. Hayat, T.; Nadeem, S.; Khan, A.U. Rotating flow of Ag-CuO/H2O hybrid nanofluid with radiation and partial slip boundary effects. *Eur. Phys. J. E* **2018**, *41*, 75. [CrossRef] [PubMed]
27. Tassaddiq, A.; Khan, S.; Bilal, M.; Gul, T.; Mukhtar, S.; Shah, Z.; Bonyah, E. Heat and mass transfer together with hybrid nanofluid flow over a rotating disk. *AIP Adv.* **2020**, *10*, 055317. [CrossRef]
28. Choi, S.U.S.; Eastmen, J.A. Enhancing thermal conductivity of fluids with nanoparticles. In Proceedings of the Conference: 1995 International Mechanical Engineering Congress and Exhibition, San Francisco, CA, USA, 12–17 November 1995.
29. Uddin, M.J.; Sohail, A.; Bég, O.A.; Ismail, A.I.M. Numerical solution of MHD slip flow of a nanofluid past a radiating plate with Newtonian heating: A Lie group approach. *Alex. Eng. J.* **2018**, *57*, 2455–2464. [CrossRef]
30. Zulkifli, S.N.; Sarif, N.M.; Salleh, M.Z.; Azmi, E.F. MHD stagnation point flow of micropolar nanofluid with Soret and Dufour effects. *J. Phys. Conf. Ser.* **2019**, *1366*, 012015. [CrossRef]
31. Ghadimi, A.; Saidur, R.; Metselaar, H.S.C. A review of nanofluid stability properties and characterization in stationary conditions. *Int. J. Heat Mass Transf.* **2011**, *54*, 4051–4068. [CrossRef]
32. Noor, N.F.M.; Haq, R.U.; Nadeem, S.; Hashim, I. Mixed convection stagnation flow of a micropolar nanofluid along a vertically stretching surface with slip effects. *Meccanica* **2015**, *50*, 2007–2022. [CrossRef]
33. Ahmad, A.; Asghar, S.; Afzal, S. Flow of nanofluid past a Riga plate. *J. Magn. Magn. Mater.* **2016**, *402*, 44–48. [CrossRef]
34. Khan, U.; Zaib, A.; Ishak, A. Magnetic field effect on Sisko fluid flow containing gold nanoparticles through a porous curved surface in the presence of radiation and partial slip. *Mathematics* **2021**, *9*, 921. [CrossRef]
35. Devi, S.S.U.; Devi, S.P.A. Heat transfer enhancement of Cu−Al2O3/water hybrid nanofluid flow over a stretching sheet. *J. Niger. Math. Soc.* **2017**, *36*, 419–433.
36. Suresh, S.; Venkitaraj, K.P.; Selvakumar, P.; Chandrasekar, M. Synthesis of Al2O3-Cu/water hybrid nanofluids using two step method and its thermo physical properties. *Colloids Surf. A Physicochem. Eng. Asp.* **2011**, *388*, 41–48. [CrossRef]
37. Suresh, S.; Venkitaraj, K.P.; Selvakumar, P.; Chandrasekar, M. Effect of Al 2O 3-Cu/water hybrid nanofluid in heat transfer. *Exp. Therm. Fluid Sci.* **2012**, *38*, 54–60. [CrossRef]

38. Devi, S.S.U.; Devi, S.P.A. Numerical investigation of three-dimensional hybrid Cu-Al2O3/water nanofluid flow over a stretching sheet with effecting Lorentz force subject to Newtonian heating. *Can. J. Phys.* **2016**, *94*, 490–496. [CrossRef]
39. Waini, I.; Ishak, A.; Pop, I. Unsteady flow and heat transfer past a stretching/shrinking sheet in a hybrid nanofluid. *Int. J. Heat Mass Transf.* **2019**, *136*, 288–297. [CrossRef]
40. Waini, I.; Ishak, A.; Pop, I. Hybrid nanofluid flow and heat transfer over a permeable biaxial stretching/shrinking sheet. *Int. J. Numer. Methods Heat Fluid Flow* **2019**, *30*, 3497–3513. [CrossRef]
41. Waini, I.; Ishak, A.; Pop, I. Hybrid nanofluid flow towards a stagnation point on an exponentially stretching/shrinking vertical sheet with buoyancy effects. *Int. J. Numer. Methods Heat Fluid Flow* **2020**, *31*, 216–235. [CrossRef]
42. Waini, I.; Ishak, A.; Pop, I. MHD flow and heat transfer of a hybrid nanofluid past a permeable stretching/shrinking wedge. *Appl. Math. Mech.* **2020**, *41*, 507–520. [CrossRef]
43. Waini, I.; Ishak, A.; Pop, I. Hybrid nanofluid flow over a permeable non-isothermal shrinking surface. *Mathematics* **2021**, *9*, 538. [CrossRef]
44. Zainal, N.A.; Nazar, R.; Naganthran, K.; Pop, I. Unsteady three-dimensional MHD non-axisymmetric homann stagnation point flow of a hybrid nanofluid with stability analysis. *Mathematics* **2020**, *8*, 784. [CrossRef]
45. Hayat, T.; Nadeem, S. Heat transfer enhancement with Ag–CuO/water hybrid nanofluid. *Results Phys.* **2017**, *7*, 2317–2324. [CrossRef]
46. Khan, U.; Zaib, A.; Pop, I.; Abu Bakar, S.; Ishak, A. Stagnation point flow of a micropolar fluid filled with hybrid nanoparticles by considering various base fluids and nanoparticle shape factors. *Int. J. Numer. Methods Heat Fluid Flow* **2022**. [CrossRef]
47. Takabi, B.; Salehi, S. Augmentation of the heat transfer performance of a sinusoidal corrugated enclosure by employing hybrid nanofluid. *Adv. Mech. Eng.* **2014**, *2014*, 147059. [CrossRef]
48. Oztop, H.F.; Abu-Nada, E. Numerical study of natural convection in partially heated rectangular enclosures filled with nanofluids. *Int. J. Heat Fluid Flow* **2008**, *29*, 1326–1336. [CrossRef]
49. Bataller, R.C. Radiation effects for the Blasius and Sakiadis flows with a convective surface boundary condition. *Appl. Math. Comput.* **2008**, *206*, 832–840. [CrossRef]
50. Ishak, A. Thermal boundary layer flow over a stretching sheet in a micropolar fluid with radiation effect. *Meccanica* **2010**, *45*, 367–373. [CrossRef]
51. Magyari, E.; Pantokratoras, A. Note on the effect of thermal radiation in the linearized Rosseland approximation on the heat transfer characteristics of various boundary layer flows. *Int. Commun. Heat Mass Transf.* **2011**, *38*, 554–556. [CrossRef]
52. Roşca, N.C.; Roşca, A.V.; Pop, I. Axisymmetric flow of hybrid nanofluid due to a permeable non-linearly stretching/shrinking sheet with radiation effect. *Int. J. Numer. Methods Heat Fluid Flow* **2020**, *31*, 2330–2346. [CrossRef]
53. Fang, T.G.; Zhang, J.; Yao, S.S. Viscous flow over an unsteady shrinking sheet with mass transfer. *Chin. Phys. Lett.* **2009**, *26*, 014703. [CrossRef]
54. Shampine, L.F.; Gladwell, I.; Thompson, S. *Solving ODEs with MATHLAB*; Cambridge University Press: Cambridge, UK, 2003; ISBN 9780521824040.

mathematics

MDPI

Article

Inverse Modeling of Grout Curtain Hydraulic Conductivity Evolution Considering the Calcium Leaching Effect

Kailai Zhang [1], Zhenzhong Shen [1,2], Liqun Xu [1,*], Yongkang Shu [1] and Chao Yang [1]

[1] College of Water Conservancy and Hydropower Engineering, Hohai University, Nanjing 210098, China; 160202020006@hhu.edu.cn (K.Z.); zhzhshen@hhu.edu.cn (Z.S.); shuyongkang@hhu.edu.cn (Y.S.); yangchao96@hhu.edu.cn (C.Y.)

[2] State Key Laboratory of Hydrology-Water Resources and Hydraulic Engineering, Hohai University, Nanjing 210098, China

* Correspondence: xlq@hhu.edu.cn

Abstract: The calcium leaching effect inevitably increases the grout curtain hydraulic conductivity. It is diffucult to sample and obtain the leaching-related calculation parameters for deep-buried grout curtains. This study introduced the inversion method into the calcium leaching analysis to get proper leaching-related calculation parameters and accurate results. An inverse analysis model was proposed using the genetic algorithm (GA) and finite element analysis technology to solve the calcium leaching problems. The objective function is constructed using the hydraulic head and leakage quantity time-series measurements, which improves the uniqueness and reliability of the inverse results. The proposed method was applied to the inverse analysis of the hydraulic conductivity evolution of the grout curtain in a concrete dam foundation. The predicted water heads and leakage quantity are consistent with the monitored data, indicating the rationality of this simulation. The grout curtain hydraulic conductivity prediction in 100 years is also presented. The results illustrate the feasibility of the proposed method for determining leaching-related parameters and the hydraulic conductivity prediction in the leaching process.

Keywords: inverse modeling; calcium leaching; grout curtain; hydraulic conductivity

Citation: Zhang, K.; Shen, Z.; Xu, L.; Shu, Y.; Yang, C. Inverse Modeling of Grout Curtain Hydraulic Conductivity Evolution Considering the Calcium Leaching Effect. *Mathematics* **2022**, *10*, 381. https://doi.org/10.3390/math10030381

Academic Editors: Camelia Petrescu and Valeriu David

Received: 14 December 2021
Accepted: 24 January 2022
Published: 26 January 2022

Publisher's Note: MDPI stays neutral with regard to jurisdictional claims in published maps and institutional affiliations.

Copyright: © 2022 by the authors. Licensee MDPI, Basel, Switzerland. This article is an open access article distributed under the terms and conditions of the Creative Commons Attribution (CC BY) license (https://creativecommons.org/licenses/by/4.0/).

1. Introduction

In grouting projects, cement slurry is injected into rock fractures to improve the foundation engineering properties such as permeability, strength, and deformation resistance [1–3]. Hydraulic conductivity is a crucial hydrologic parameter of the grout curtains and foundation rock. For foundation rocks, the hydraulic conductivity is generally not changed with time, while for the grout curtains and concrete face slabs, the hydraulic conductivity is constantly changed under the effect of calcium leaching [4]. Calcium leaching occurs when the calcium compounds in the cement matrix dissolve in a low pH or alkaline solution. In the calcium leaching process, the decomposition of calcium hydroxide (CH) and calcium silicate hydrate (C-S-H) significantly degrade the cement-based material engineering performance. For example, the Fengman concrete gravity dam has been demolished and reconstructed for severe calcium leaching and leakage issues. The annual average leached quantity of the dam body is about 9.6 t, and the dam foundation is about 8.0 t [5]. After nearly 40 years of operation, the overall concrete slabs strength of the Gutianxi flat-slab buttress dam decreased from 49.6 MPa to 37.9 MPa, by 23.6% [6].

The simulation of the leaching process could guide the safe operation of the project. Many scholars have studied the modeling of the leaching process. Gerard et al. [7], Wan et al. [8,9], and Phung et al. [10] proposed different solid−liquid equations for diffusion-driven leaching. For advection-diffusion-driven leaching, Ulm et al. [11] proposed a calcium compound decomposition rate equation based on the chemo-poro-plasticity theory. Gawin [12,13] adopted this equation and proposed a pure water hydro-chemo-mechanical

leaching model of concrete. Calcium leaching significantly increased the hydraulic conductivity of cement-based materials. The reported data show that the hydraulic conductivity of the leached cement paste specimen increased by three orders of magnitude [14].

The hydraulic conductivity is often defined as a function of porosity in leaching simulations. Saito [15] proposed an exponential formula between porosity and permeability. This equation works well in accelerated electrochemical tests on mortars and was adopted by Gawin [12,13]. To better understand the leaching effect on the increase in hydraulic conductivity, the evolution of pore structures should be considered. The Kozeny−Carman (KC) relation introduced microstructure parameters into permeability, including the channel shapes, specific surface areas, and tortuosity [16]. This relation could provide a more accurate characterization of hydraulic conductivity, and has been widely used in cement-based materials [17–20]. Phung [10] adopted the Kozeny−Carman (KC) relation for modeling the cement pastes hydraulic conductivity evolution in the leaching process. However, it is difficult to obtain the correct calculation parameters in the KC relation. On the one hand, no calcium leaching test is carried out to determine the parameters. On the other hand, it is not easy to obtain samples for testing as the anti-seepage structures such as concrete core walls and grout curtains are deeply buried.

Inverse modeling is an alternative way to obtain the numerical calculation parameters. Extensive studies have shown the efficiency of inverse modeling for determining the hydraulic conductivity of foundation rocks and seepage-proof systems [21–28]. Most previous studies pursue steady or transient flow conditions in the inverse calculation of aquifer parameters. These studies are generally aimed at seepage problems or fluid−structure interaction problems [29,30], and the calcium leaching effect is not considered. Under the calcium leaching effect, deterioration of the grout curtain will lead to an increase of up-lift pressure and leakage, and endangered dam safety and benefits. At present, there is no research on applying the inverse modeling method to predicting grout curtain hydraulic conductivity. Furthermore, the parameters that are to be inversed in the calcium leaching process are still unknown.

The present study aimed to determine the calcium leaching parameters and predict the hydraulic conductivity evolution of grout curtains in the leaching process. Thus, a new inverse modeling approach is proposed considering the interaction between transient flow and calcium leaching. The genetic algorithm (GA) is adopted to reduce the computational cost. The proposed procedure is applied to the inverse modeling of a grout curtain degradation induced by calcium leaching in the foundation of a concrete gravity dam. Combined with site characterization data, the calcium leaching parameters are obtained. The hydraulic conductivity evolution of the grout curtain in 100 years is also presented.

2. Calcium Leaching Effect on the Grout Curtain

2.1. Calcium Leaching in the Grout Curtain

The main chemical reactions equations of the calcium leaching process are given in Equation (1) [31,32]:

$$\begin{aligned} \mathrm{Ca(OH)_2} &\rightleftharpoons \mathrm{Ca^{2+}} + 2\mathrm{OH^-} \\ n\mathrm{CaO \cdot SiO_2 \cdot nH_2O} &\rightleftharpoons n\mathrm{Ca^{2+}} + \mathrm{H_3SiO_4^-} + [2n - 1]\mathrm{H_2O} \end{aligned} \tag{1}$$

The calcium ions in the pore solution of the grout curtain are assumed to be in thermodynamic equilibrium with the calcium compound in the cement materix [7]. When the Ca^{2+} ion concentration decreases below 22 mol/m^3, CH starts to decompose; when the calcium ion concentration is lower than 19 mol/m^3, C-S-H starts to decay [10]. Decomposition of calcium compounds increases the grout curtain porosity and hydraulic conductivity, degrading the anti-seepage performance.

2.2. Characterization of Hydraulic Conductivity Evolution

To characteristic the mortars hydraulic conductivity evolution in the leaching process, Saito [15] proposed an exponential relation between porosity and hydraulic conductivity.

This formula works well in accelerated electrochemical tests on mortars and has been adopted by Kuhl [31,32] and Gawin [12,13]. However, the pore structures of the cement-based materials are not considered in this relation. The Kozeny−Carman model introduces the hydraulic radius and tortuosity, which characterizes the pore space geometry into the hydraulic conductivity of the cement-based materials, as shown in Equation (2) [10].

$$\begin{cases} K = \chi \frac{\varphi^3}{(1-\varphi)^2} \\ \chi = \frac{1}{\tau^2 S_a^2 F_s} \end{cases} \tag{2}$$

where K is the permeability coefficient (m^2), χ is the microstructure parameter (m^2), φ is the capillary porosity, τ is the tortuosity, S_a is the specific pore surface (m^2/m^3), and F_s is the shape factor.

Phung [10] introduced the lumped term Ω to calculate the shape factor F_s and tortuosity τ. The lumped term Ω is defined in Equation (3).

$$\begin{cases} \Omega = \frac{1}{\tau^2 F_s} \\ \Omega_0 = \frac{1}{n}\Omega_l \\ \Omega = \Omega_0 - (\Omega_0 - \Omega_l)\, d_l^2 \end{cases} \tag{3}$$

where Ω_0 and Ω_l are the lumped term for intact and leached materials, respectively, and d_l is the degradation degree. The degradation degree is defined as the ratio between the current CH content and the initial values, as shown in Equation (4) [10].

$$d_l = \begin{cases} 1, & C_{CH} = 0 \\ \frac{C_{CH}}{C_{CH}^0}, & C_{CH} > 0 \end{cases} \tag{4}$$

where d_l is the leaching degree, and C_{CH}^0 and C_{CH} are the initial and current concentrations of CH, (mol/m^3), respectively.

Due to the solid skeleton dissolution, the porosity of the grout curtain increases according to Equation (5) [12,13].

$$\begin{cases} \varphi = \varphi_0 + \Delta\varphi \\ \Delta\varphi = \frac{M_{diss}}{\rho^{diss}} \int \frac{1}{\eta} A_s dt \end{cases} \tag{5}$$

where φ and φ_0 are current and initial porosity of the grout curtain, respectively; $\Delta\varphi$ is the increase of the grout curtain porosity due to the leaching process; $\frac{M_{diss}}{\rho^{diss}}$ is the average molar volume of dissolved components of the solid skeleton (in this study, $\frac{M_{diss}}{\rho^{diss}}$ is taken as 0.056 mol/m^3); η is determined by the micro-diffusion of the Ca^{2+}; and A_s is the chemical affinity.

In this study, the inverse parameters are presented in Table 1. Among them, lumped term and initial specific pore surface are related to the initial hydraulic conductivity—lumped term increased times n is the parameter that controls the increase of hydraulic conductivity due to the decomposition of CH. The leached specific pore surface controls the increase of hydraulic conductivity due to decomposition of CH and C-S-H. The lumped term increase times, and initial and leached specific pore surface ranges are taken from Phung's test results. More details are presented in reference [10]. The rock hydarulic conductivity range is determined by the water pressure test.

Table 1. Parameters in the Kozeny−Carman (KC) relation [10].

Parameter	Notation	Unit	Parameter Range
Lumped term	Ω_0	1	1000~20,000
Lumped term increased times	n	1	500~2000
Initial specific pore surface	S_{a0}	10^6/m	10~50
Leached specific pore surface	S_{al}	10^6/m	100~500
Rock hydraulic conductivity	k_r	m/s	1.0×10^{-6}~1.0×10^{-8}

3. The Objective Function

To improve the accuracy of the inverse modeling, this study utilizes the time-series measurements of both the piezometric head and leakage quantity. Suppose that the number of hydraulic conductivities of different rock layers yet to be determined is m, and vector K is defined to denote the hydraulic conductivities of the medium with $K = [k_0, k_1, k_2, \ldots, k_m]^T$, in which $k_{1\sim m}$ is the hydraulic conductivity of the ith rock layer. M denotes the number of piezometers in the domain, and $H_i^m = [H_{i1}^m, H_{i1}^m, H_{i1}^m, \ldots]^T (i = 1, 2, \ldots, M)$ denotes the time series measurements at piezometer i, where H_i^m is the measured water head at piezometer i and at time t. Similarly, the leakage measured is denoted by L, and the time-series measurements from the measuring weir are $L_j^m = [L_1^m, L_2^m, L_3^m, \ldots], (j = 1, 2, 3, \ldots, N)$, where L_j^m is the leakage measurement at time N. The objective function for the inverse problem is defined in Equation (6)

$$\begin{gathered} \min \mathrm{f} = w_H \left(\sum_{i=1}^{M} \frac{||H_i(K) - H_i^m||_2^2}{||H_i^m||_2^2} \right)^{\frac{1}{2}} + w_L \left(\sum_{j=1}^{N} \frac{||L_j(K) - L_j^m||_2^2}{||L_j^m||_2^2} \right)^{\frac{1}{2}} \\ w_H + w_L = 1.0 \\ K_{low} < K < K_{up} \end{gathered} \tag{6}$$

where $||\cdot||_2$ is the Euclidean norm of a vector, and $H_i(K)$ and $L_j(K)$ are the time series results of the water head at piezometer i and leakage quantity numerically obtained with a given parameters vector K, respectively. w_H and w_L are the weight coefficient to ensure a balance of the relative errors of the measured water head and leakage quantity, respectively. In this study, the weights of the measured water head and leakage quantity are assumed to be the same. The sum of w_H and w_L equals 1.0. K_{low} and K_{up} represent the lower and upper bounds of the possible hydraulic conductivity values of the rock layers and grout curtains. respectively.

The objective function defined in Equation (6) requires the best fit of the time series measurements of both the water head and the leakage quantity. This study assumes the hydraulic conductivity of the rock layer is an isotropic constant, while for the grout curtain, the hydraulic conductivity increases over the leaching time. This study adopts the Kozeny−Carman (KC) relation to model the grout curtain hydraulic conductivity evolution in the leaching process. The porosity is chosen as the coupling parameter to connect the calcium leaching effect and hydraulic conductivity. The KC relation contains the lumped term for sound materials Ω_0, lumped term increased times n, initial and leached specific pore surface S_{a0} and S_{al}. These parameters have significant impacts on the grout curtain hydraulic conductivity evolution. This study aims to obtain the representative values of these parameters. In addition, the hydraulic conductivity of the rock layer should also be inversed.

4. Calcium Leaching Model

4.1. Basic Assumptions

Calcium leaching in concrete dams is a complex process that involves the decomposition of multiple components such as CH, C-S-H, ettringite, and un-hydrated cement particles. The leached Ca^{2+} ions may react with carbon dioxide in the air to form $CaCO_3$. To simplify the problem, the following assumptions are applied:

(1) The cement has been completely hydrated, the influence of the rehydration and the leaching of un-hydrated cement particles are ignored;
(2) Only the decomposition of CH and C-S-H are considered;
(3) Ca^{2+} ions in the solution are not reacting to form any new compounds;
(4) As the grout curtain is deep-buried in the foundation, the materials are and remain saturated over time, and the isothermal conditions are also preserved;
(5) The flow in the grout curtain is laminar, and Darcy's law could describe the flow rate.

4.2. Governing Equation

The governing equations of the advection-diffusion driven leaching in the concrete dams are presented in Equation (7) [33].

$$\begin{cases} u = -\frac{k}{\rho g}\nabla P \\ \frac{\partial(\varepsilon_p \rho)}{\partial t} + \nabla(\rho u) = Q_m \\ \frac{\partial c}{\partial t} + \nabla(-D\nabla c) + u\nabla c = R \end{cases} \tag{7}$$

In this Equation, u is the flow rate (m/s), k is the permeability (m^2), ρ is the water density (kg/m^3), g is the gravitational acceleration (m/s^2), P is the pore water pressure (Pa), ε_p is the porosity, t is the time (s), Q_m is a mass source term ($kg/(m^3 \cdot s)$), c is the Ca^{2+} ions concentration of the species (mol/m^3), D is the diffusion coefficient (m^2/s), and R is the chemical reaction rate ($mol/(m^3 \cdot s)$).

The chemical reactions in the leaching process are the decomposition of the calcium compounds in the solid skeleton. The decomposition rate is presented in Equation (8) [11–13]:

$$\begin{cases} \frac{\partial s_{Ca}}{\partial t} = \frac{1}{\eta} A_s \\ \eta = RT\tau_{leach} \\ A_s = RT \ln\left(\frac{c_{Ca}}{c_{Ca}^{eq}}\right) - \int_{S_{Ca}^{eq}}^{S_{Ca}} \kappa(\bar{s}) d\bar{s} \\ \kappa(s_{Ca}) = \frac{RT}{c_{Ca}} \left(\frac{ds_{Ca}}{dc_{Ca}}\right)^{-1} \end{cases} \tag{8}$$

In this equation, s_{Ca} is the calcium content in the cement materix (mol/m^3), η is the micro-diffusion of Ca^{2+} ions ($mol/(J \cdot s)$), A_s is the chemical affinity (J/m^3), R is the gas constant ($J/(mol \cdot K)$), T is the temperature (K), τ_{leach} is the characteristic time of leaching s, c_{Ca} is the Ca^{2+} ion concentration in the pore solution (mol/m^3), (c_{Ca}^{eq}, s_{Ca}^{eq}) is the equilibrium concentration, and $\kappa(s_{Ca})$ is the equilibrium constant.

4.3. Diffusivity

Bentz [34–36] proposed the effective diffusion model for cement-based materials. We can calculate the effective diffusivity from cement hydration and the water−cement ratio. Bentz's model holds for a standard non-leached cement matrix. For leached cement-based materials, Van Eijk and Brouwers [37] proposed a revised formula, as seen in Equation (9).

$$\begin{aligned} \frac{D_e}{D_0} &= 0.0025 - 0.07\varphi_c(x,0)^2 - 1.8H(\varphi_c(x,0) - 0.18)(\varphi_c(x,0) - 0.18)^2 \\ &+ 0.14\varphi_c(x,t)^2 + 3.6H(\varphi_c(x,t) - 0.16)(\varphi_c(x,t) - 0.16)^2 = D(\varphi) \end{aligned} \tag{9}$$

where $\varphi_c(x,0)$ is the initial capillary porosity, $H()$ is the Heaviside function, and $\varphi_c(x,t)$ is the capillary porosity. D_0 is the diffusivity of Ca^{2+} ion in water, $D_0 = 4.5 \times 10^{-10}$ m^2/s.

Equation (9) has been widely used in calcium leaching simulations, such as by Wan [8,9]. In this study, we also adopted this equation.

5. Hydraulic Conductivity Prediction Model Optimized by GA

5.1. Genetic Algorithm

The genetic algorithm (GA) is a free-derivative method based on natural selection and evaluation [38]. The genetic algorithm has been widely used as an optimizing tool in many engineering problems, including in dam seepage inverse analysis [39–43]. This study adopted GA to obtain the globally optimal hydraulic conductivity of rock layers and grout curtains. The population size was 50, the function tolerance was 1.0×10^{-6}, and the constraint tolerance was 0.001. In this way, the objective function of Equation (6) is minimized, and reasonable results can be obtained.

5.2. Mathematical Framework of the Model

The procedure for the inversion of the parameters is shown in Figure 1. The calcium leaching inverse model of the coupled seepage and chemical reactions are numerically solved with COMSOL, compiled with Matlab software. The calculations steps are presented as follows:

Step 1: Input all the initial parameters, including the materials property, initial and boundary conditions, and the variation range of the parameters to be inversed;
Step 2: Solve the calcium leaching model and obtain the seepage characteristics;
Step 3: Calculate the objective functions value F and evaluate the precision requirement;
Step 4: Generate the new solvable groups according to the operational approach of the GA;
Step 5: Steps (2) to (4) are repeated until the objective functions meet the precision requirements;
Step 6: Output the optional objective function values and predict the grout curtain hydraulic conductivity evolution.

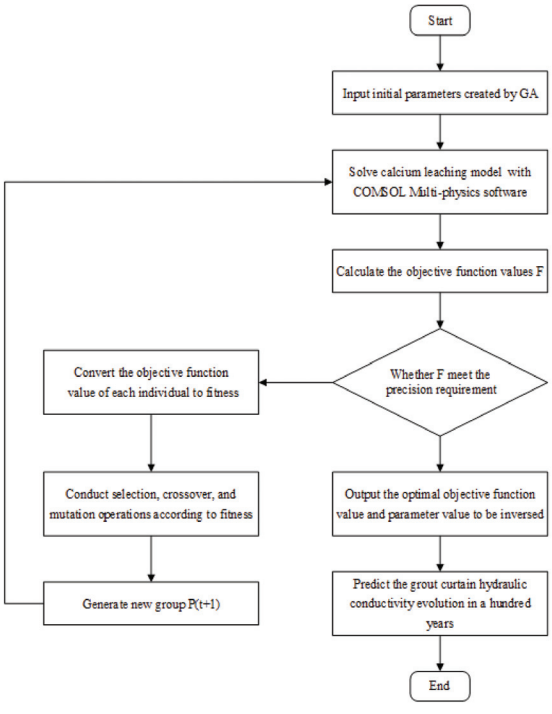

Figure 1. Flowchart of the inverse modeling.

6. Application: A Case Study of the Shimantan Concrete Gravity Dam

6.1. General Description

The Shimantan reservoir is located in Wugang City, Henan Province. The Shimantan dam is a complete roller compacted concrete (RCC) gravity dam with a height of 40.5 m. The maximum width of the dam body is 31.74 m. There are 22 dam sections, with a total length of 645 m. The Shimantan dam started to store water in 1997. The dam foundation is composed of quartz sandstone. The longitudinal wave velocity of the foundation rock is varied from 4000 m/s to 5000 m/s, and is regarded as a relatively uniform elastomer. After 16 years of operation, a severe calcium leaching phenomenon was observed. The location and the calcium leaching phenomena in the corridors of the Shimantan dam are presented in Figure 2.

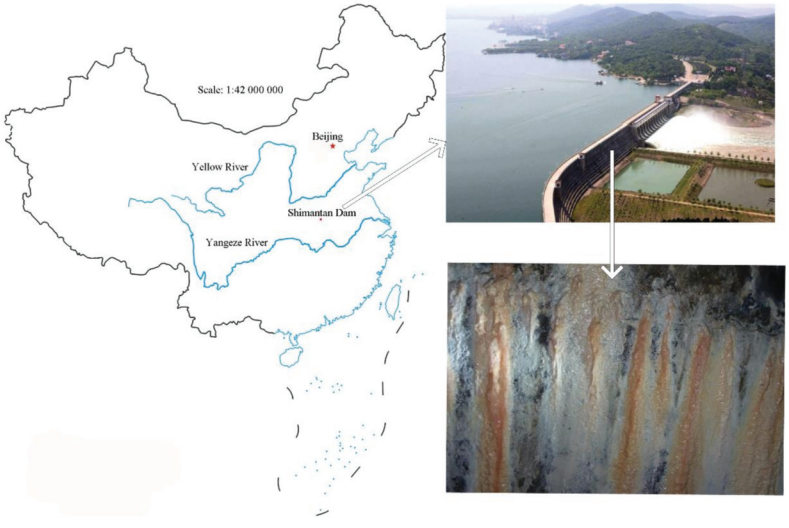

Figure 2. Shimantan concrete gravity dam location and the calcium leaching in the corridors.

6.2. Computational Model

In this study, the foundation of the Shimantan dam is taken as an example to verify the proposed model. The finite element model of the Shimantan dam foundation is built based on actual size. We extended the foundation two times the dam's height at both the upstream and downstream sides of the dam. The foundation's height is considered two times the dam's height. The thickness of curtain grouting is 2 m and reaches into slightly weathered rock by 3 m. The key wall is located at the top of the curtain, with a 32 m and a thickness of 1m. This study simplifies the key-wall and rock foundation's bonded surface into straight. In total, 4157 finite elements are used in this model. The maximum element width is 2.5 m, and the minimum element width is 0.1 m. The finite element meshes of the model are presented in Figure 3. The finite elements families used in this study are four-node convection/diffusion quadrilateral elements.

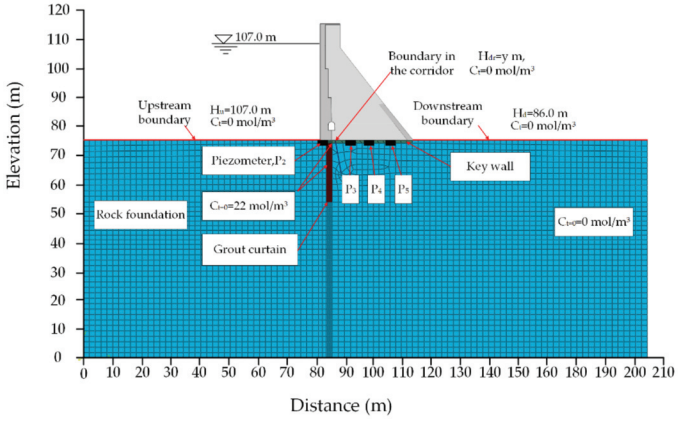

Figure 3. 2D finite element meshes and boundary conditions of the inverse model.

6.3. Calculation Parameters

As the grout curtain has been in operation for more than 20 years, it is not easy to obtain the initial components of the grout materials. In this study, the inverse parameters of the grout curtain adopt Phung's test parameters of Sample 3. The CH and C-S-H contents are 3027 and 6054 mol/m^3, respectively [14]. The parameters of the rock and grout curtain are presented in Table 2. The parameters of non-equilibrium solid−liquid dissolution follow Gawin's model [12]. The calculation parameters are presented in Table 3.

Table 2. Numerical parameters used for simulation.

Material	Parameter	Notation	Value
Rock	Initial porosity	φ_f	0.10
Rock	Initial diffusivity	D_{r0}	1.47×10^{-11} m^2/s
Concrete	Initial porosity	φ_{k0}	0.10
Concrete	Initial diffusivity	D_{k0}	7.11×10^{-12}
Concrete	CH content	C_{CH_K}	3027 mol/m^3
Concrete	C-S-H content	C_{C-S-H_K}	6054 mol/m^3
Grout curtain	CH content	C_{CH}	3027 mol/m^3
Grout curtain	C-S-H content	C_{C-S-H}	6054 mol/m^3
Grout curtain	Initial porosity	φ_{g0}	0.15
Grout curtain	Initial diffusivity	D_{g0}	9.87×10^{-12} m^2/s
Grout curtain	Intact/leached bulk density	ρ_0/ρ_L	30.6/145.8

Table 3. Values of the non-equilibrium decomposition model of calcium compounds [12].

Skeleton Compound	Ca^{2+} (mol/m^3)	ds_{Ca}/dc_{Ca}	Diffusivity (m^2/s)	τ_{leach} (s)	$\frac{1}{\eta}$ (mol/(J · s))
CH	19–22	2142	1.44×10^{-9}	1.17×10^{4}	3.45×10^{-8}
C-S-H	2–19	203	1.62×10^{-9}	5.88×10^{2}	0.7×10^{-8}
C-S-H	0–2	1910	1.83×10^{-9}	6.52×10^{3}	6.2×10^{-8}

6.4. Initial and Boundary Conditions

The initial and boundary conditions for the calcium leaching model are present in Figure 3. The applied boundary conditions are the same as the working conditions. The pore solution is assumed to be saturated for the grout curtain zones, according to previous studies such as [9,10]. The upstream water head is 107.0 m, and the downstream head is 86.0 m. The upstream water head boundary is applied on the bottom of the reservoir basin at an elevation of 76.0 m. The distance is from 0 m to 80.0 m. The downstream water head

boundary is applied on the downstream side foundation surface at an elevation of 76.0 m. The distance is from 116 m to 204 m. The water head boundary in the corridor is 85.0 m. The distance is from 85.6 m to 85.7 m. The calcium ion concentration boundary at the upstream side, downstream side, and corridor is 0 mol/m^3. The distribution of the calcium ion concentration boundary is the same as for the water head boundary. The initial calcium ion concentrations in the grout curtain and key-wall are 22 mol/m^3. The initial calcium ion concentration in the rock foundation is 0 mol/m^3. The long-term observations of upstream and downstream water levels are presented in Figure 4. Data observations shown in Figures 4–6 are obtained from the Shimantan reservoir project management report. The time-series measurements adopt the annual average values presented in Figures 5 and 6.

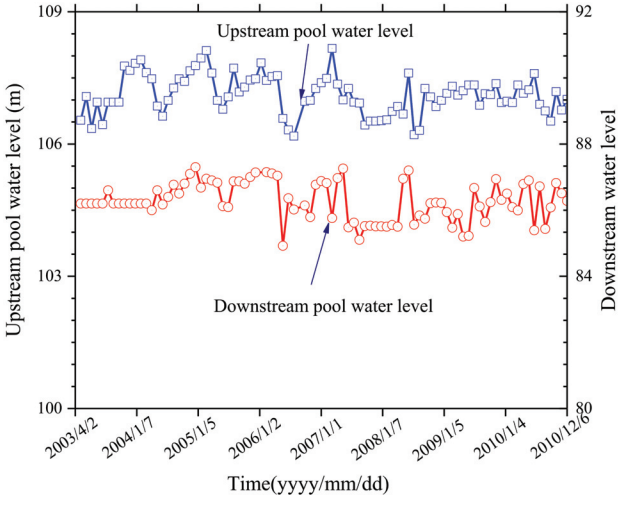

Figure 4. Long-term observations of upstream and downstream water level.

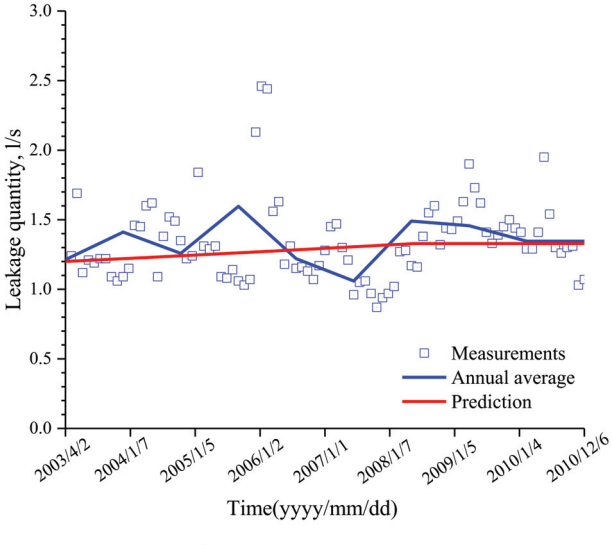

Figure 5. Comparison of the simulated leakage quantity and monitored data.

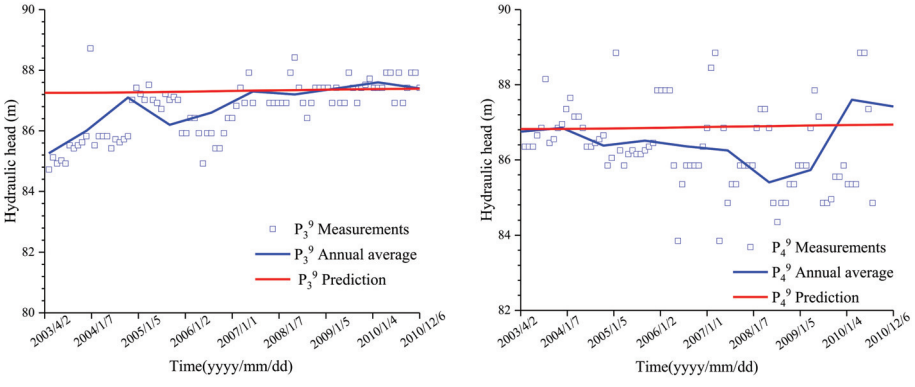

Figure 6. Comparison of measured and simulated hydraulic heads at piezometer: (**a**) hydraulic head at piezometer P_3^9 and (**b**) hydraulic head at piezometer P_4^9.

6.5. Results

6.5.1. Verification of the Results

The predicted results are listed in Table 4.

Table 4. Inverse analysis results of the grout curtain and rock layers.

Parameter	Ω_0	n	S_{a0}	S_{al}	k_r
Values	12,251.43	1125.31	3.21×10^7	3.13×10^8	1.0×10^{-7}

Figure 5 compares the simulated dam foundation leakage quantity and the monitored data. The monitored data recorded the leakage quantity of the dam foundation from 2003 to 2010. As we can see from Figure 5, with the increase in time, the leakage quantity increases from 1.20 L/s to 1.33 L/s. The predicted leakage quantity fluctuates between the average annual monitored values. The predictions are basically consistent with the monitored data, indicating the rationality of this simulation.

Figure 6 presents a comparison of measured and simulated water heads at piezometers P_3^9 and P_4^9. The upstream hydraulic head fluctuates around 107.0 m, and the downstream hydraulic head fluctuates around 86.0 m. The positions of piezometers P_3^9 and P_4^9 are presented in Figure 1. The square dots are the measured data from 2003 and 2010. As we can infer from the figure, the predicted water head at P_3^9 increases from 87.25m to 87.40m. The predicted water head at P_4^9 increases from 86.82 m to 86.93 m. The predicted water heads are basically consistent with the monitored data, indicating the rationality of this simulation.

The bar graphs of the water head and leakage relative error are presented in Figures 7 and 8. The relative error is computed from the D-value between the annual average measurements and predicted values divided by the yearly average measures. As we infer from the figures, the presented maximum water head relative error is 2.4% and the maximum leakage quantity relative error is 24.1%. The scatter field data showed a comparative considerable leakage relative error. Overall, the predicted leakage and water head are consistent with the monitored data.

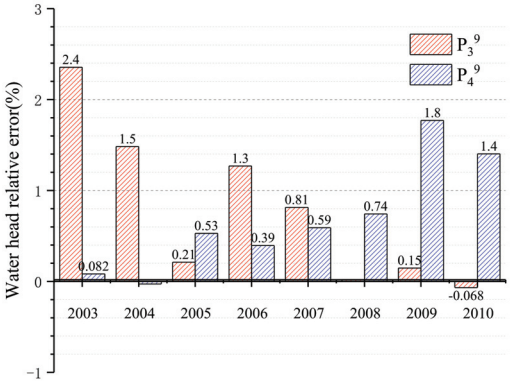

Figure 7. Bar graph of the water head relative error.

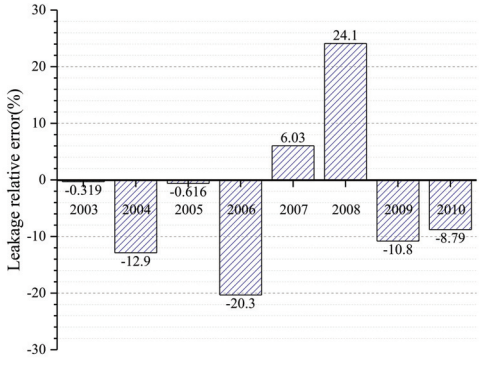

Figure 8. Bar graph of the dam foundation leakage relative error.

6.5.2. Hydraulic Conductivity of the Grout Curtain

Figure 9a presents the grout curtain porosity evolution in the leaching process. As we can infer from the porosity contour distribution, the porosity of the upper part is larger than the middle and bottom parts. The porosity of the upstream side is larger than the downstream side. Figure 9b presents porosity evolution in 100 years at H = 63.0 m. After 100 years of leaching duration, the maximum porosity on the upstream side is 0.21 and the minimum porosity at the downstream side is 0.17. Figure 9c shows the grout curtain porosity evolution at the different positions after 50 years of leaching duration. The elevation of these three positions is 72.0, 63.0, and 54.0 m. The maximum porosity at the elevation of 72.0 m is 0.02 larger than the other two positions.

Figure 10a presents the grout curtain hydraulic conductivity evolution in the leaching process. The hydraulic conductivity evolution is similar to the porosity. The hydraulic conductivity at the upper and upstream sides is more significant than in the other regions. Figure 10b presents the hydraulic conductivity evolution in 100 years at H = 63.0 m. The maximum hydraulic conductivity on the upstream is 1.8×10^{-6} m/s and the minimum porosity at the downstream side is 1.9×10^{-7} m/s. The hydraulic conductivity of the upstream side is one order of magnitude larger than the downstream side. Figure 10c shows the evolution of the hydraulic conductivity at different positions after 50 years of leaching. The hydraulic conductivity at an elevation of 72.0 m is half an order of magnitude larger than for the other two elevations. According to the above analysis, the most vulnerable parts of the grout curtain are the upper and upstream sides.

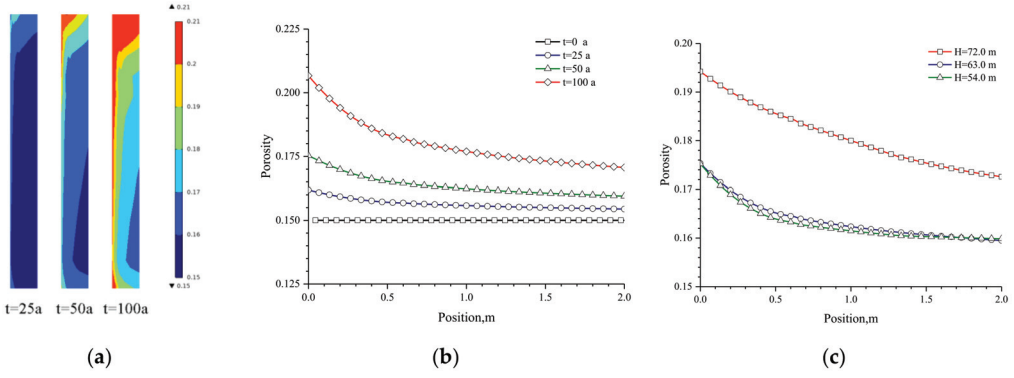

Figure 9. Grout curtain porosity evolution in the leaching process: (**a**) porosity contour distribution, (**b**) porosity evolution at H = 63.0 m in 100 years, and (**c**) porosity evolution at different positions.

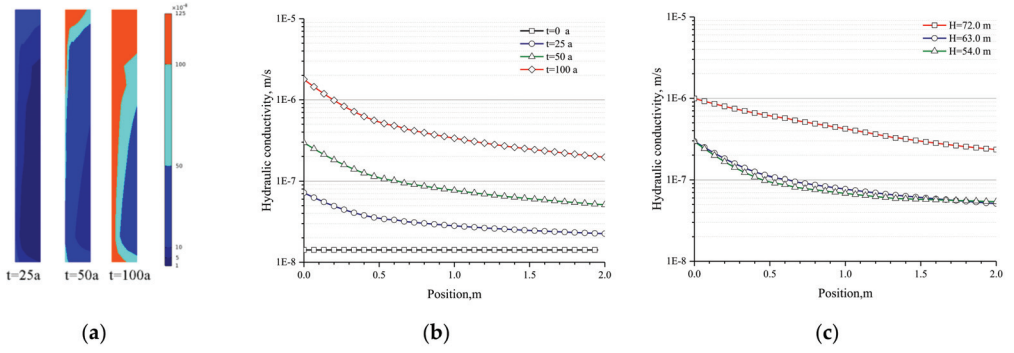

Figure 10. Grout curtain hydraulic conductivity evolution in the leaching process: (**a**) hydraulic conductivity contour distribution, (**b**) hydraulic conductivity evolution at H = 63.0 m in a hundred years, and (**c**) hydraulic conductivity evolution at different positions.

7. Conclusions

Accurate determination of the hydraulic conductivity of the anti-seepage structures, such as grout curtains, concrete face slabs, and core walls, is challenging. Under the calcium leaching effect, the hydraulic conductivity of the grout curtain is not constant. The evolution of grout curtain hydraulic conductivity in the leaching process is closely related to the project safety and benefits. It is not easy to sample and obtain the calculation parameters for deep-buried grout curtains. This study introduced the inversion analysis into the calcium leaching analysis in order to obtain proper calculation parameters and accurate results. This method can analyze the new curtain and the curtain built for many years.

The proposed inverse analysis model provides a new way to obtain calcium leaching parameters. The genetic algorithm (GA) is adopted to reduce the computational cost. The time-series measurements, including the hydraulic head and leakage quantity, were adopted to construct the objective function, which improves the uniqueness and reliability of the inverse results. The proposed inverse analysis method is applied to predict the grout curtain hydraulic conductivity of a concrete dam in the leaching process. The predictions are basically consistent with the monitored data, indicating the rationality of this model. The simulation results of this study show that the increase in the permeability coefficient at the connection between the curtain and tooth wall is more significant than that at other

parts. It is necessary to strengthen the grout curtain and key-wall joint monitoring to prevent leakage, abnormal uplift pressure, and for other problems induced by calcium leaching.

The calcium leaching problem is common in hydraulic engineering anti-seepage structures such as concrete face slabs and grout curtains. Compared with the grout curtains, the hydraulic conductivity evolutions of the concrete face slabs in the leaching process is more complex, involving the interaction of stress state, seepage flow, and chemical reactions. The inverse modeling of concrete face slabs hydraulic conductivities needs further study.

Author Contributions: Conceptualization, K.Z. and L.X.; methodology, Z.S.; software, K.Z.; validation, Y.S. and C.Y.; formal analysis, L.X.; investigation, K.Z.; resources, Z.S.; data curation, C.Y.; writing—original draft preparation, K.Z.; writing—review and editing, K.Z.; visualization, Y.S.; supervision, Z.S.; project administration, Z.S.; funding acquisition, L.X. All authors have read and agreed to the published version of the manuscript.

Funding: This research was funded by the National Natural Science Foundation of China, grant number 52179130; the Postgraduate Research and Practice Innovation Program of Jiangsu Province, grant number KYCX18/0598; and the Fundamental Research Funds for the Central Universities, grant number 2018B630/X14.

Institutional Review Board Statement: Not applicable.

Informed Consent Statement: Not applicable.

Data Availability Statement: Not applicable.

Conflicts of Interest: The authors declare no conflict of interest.

References

1. Ribeiro, D.; Cardoso, R. A review on models for the prediction of the diameter of jet grouting columns. *Eur. J. Environ. Civ. Eng.* **2016**, *21*, 641–669. [CrossRef]
2. Liangchao, Z.; Hakansson, U.; Cvetkovic, V. Two-phase cement grout propagation in homogeneous water-saturated rock fractures. *Int. J. Rock Mech. Min. Sci.* **2018**, *106*, 243–249.
3. Zhong, D.; Liu, Z.; Su, Z.; Li, K.; Li, X. Predicting and controlling the cement intake during curtain grouting of dam foundations. *Eur. J. Environ. Civ. Eng.* **2020**, *2020*, 1–27. [CrossRef]
4. Kailai, Z.; Zhenzhong, S.; Lei, G. Advances in cement-based materials leaching test. *Adv. Sci. Technol. Water Resour.* **2018**, *38*, 86–94. (In Chinese)
5. Longze, P.; Shuming, Z.; Weiping, G. Analysis on the Corrosion of Percolating Water to the Concrete of Fengman Dam. *Water. Resour. Hydrop Eng.* **2000**, *31*, 34–36. (In Chinese)
6. Xing, L.; Xu, S. Deterioration and its treatment of Gutianxi Cascade-III Dam. *Water Power* **2005**, *31*, 69–71. (In Chinese)
7. Gerard, B.; Le Bellego, C.; Bernard, O. Simplified modelling of calcium leaching of concrete in various environments. *Mater. Struct.* **2002**, *38*, 632–640. [CrossRef]
8. Keshu, W.; Lin, L.; Wei, S. Solid–liquid equilibrium curve of calcium in 6mol/L ammonium nitrate solution. *Cem. Concr. Res.* **2013**, *53*, 44–50.
9. Keshu, W.; Lin, L.; Wei, S. Experimental and modelling research of the accelerated calcium leaching of cement paste in ammonium nitrate solution. Constr. *Build. Mater.* **2013**, *40*, 832–846.
10. Phung, Q.T.; Maes, N.; Jacques, D.; Perko, J.; De Schutter, G.; Ye, G. Modelling the evolution of microstructure and transport properties of cement pastes under conditions of accelerated leaching. Constr. *Build. Mater.* **2016**, *115*, 179–192. [CrossRef]
11. Ulm, F.; Torrenti, J.; Adenot, F. Chemoporoplasticity of calcium leaching in concrete. *J. Eng. Mech.* **1999**, *125*, 1200–1211. [CrossRef]
12. Gawin, D.; Pesavento, F.; Schrefler, B.A. Modeling of cementitious materials exposed to isothermal calcium leaching, considering process kinetics and advective water flow. Part 1: Theoretical model. *Int. J. Solids Struct.* **2008**, *45*, 6221–6240. [CrossRef]
13. Gawin, D.; Pesavento, F.; Schrefler, B.A. Modeling of cementitious materials exposed to isothermal calcium leaching, considering process kinetics and advective water flow. Part 2: Numerical solution. *Int. J. Solids Struct.* **2008**, *45*, 6241–6268. [CrossRef]
14. Phung, Q.T.; Maes, N.; Jacques, D.; De Schutter, G.; Ye, G. Investigation of the changes in microstructure and transport properties of leached cement pastes accounting for mix composition. *Cem. Concr. Res.* **2016**, *79*, 217–234. [CrossRef]
15. Hiroshi, S.; Akira, D. Leaching tests on different mortars using accelerated electrochemical method. *Cem. Concr. Res.* **2000**, *30*, 1815–1825.
16. Nelio, H.; Juan, C.B.; Wagner, F.S. A three-parameter Kozeny–Carman generalized equation for fractal porous media. *Chem. Eng. Sci.* **2010**, *65*, 4432–4442.

17. Henderson, N.; Brettas, J.C.; Sacco, W.F. Applicability of the three-parameter Kozeny–Carman generalized equation to the description of viscous fingering in simulations of water flood in heterogeneous porous media. *Adv. Eng. Softw.* **2015**, *85*, 73–80. [CrossRef]
18. Katagiri, J.; Konno, Y.; Yoneda, J.; Temma, N. Pore-scale modeling of flow in particle packs containing grain-coating and pore-filling hydrates: Verification of a Kozeny-Carman-based permeability reduction model. *J. Nat. Gas Sci. Eng.* **2017**, *45*, 537–551. [CrossRef]
19. Lala, A.M.S. Modifications to the Kozeny-Carman model to enhance petrophysical relationships. *Explor. Geophys.* **2017**, *49*, 1–19. [CrossRef]
20. Zhang, K.-L.; Sheng, Z.-Z.; Xu, L.-Q.; Tan, J.-C.; Yang, C. Durability control index of anti-seepage curtain considering the effect of advection-diffusion-driven leaching. *J. Hydraul. Eng.* **2020**, *51*, 169–179. (In Chinese)
21. Zhou, C.-B.; Liu, W.; Chen, Y.-F.; Hu, R.; Wei, K. Inverse modeling of leakage through a rockfill dam foundation during its construction stage using transient flow model, neural network and genetic algorithm. *Eng. Geol.* **2015**, *187*, 183–195. [CrossRef]
22. Chegbeleh, L.P.; Akabzaa, T.M.; Akudago, J.A.; Yidana, S.M. Investigation of critical hydraulic gradient and its application to the design and construction of bentonite-grout curtain. *Environ. Earth Sci.* **2019**, *78*, 1–10. [CrossRef]
23. Chi, S.; Ni, S.; Liu, Z. Back Analysis of the Permeability Coefficient of a High Core Rockfill Dam Based on a RBF Neural Network Optimized Using the PSO Algorithm. *Math. Probl. Eng.* **2015**, *118*, 1–15.
24. Tan, J.; Xu, L.; Zhang, K.; Yang, C. A Biological Immune Mechanism-Based Quantum PSO Algorithm and Its Application in Back Analysis for Seepage Parameters. *Math. Probl. Eng.* **2020**, *2020*, 1–13. [CrossRef]
25. Ren, J.; Shen, Z.-Z.; Yang, J.; Yu, C.-Z. Back analysis of the 3D seepage problem and its engineering applications. *Environ. Earth Sci.* **2016**, *75*, 1–8. [CrossRef]
26. Virbulis, J.; Bethers, U.; Saks, T.; Sennikovs, J.; Timuhins, A. Hydrogeological model of the Baltic Artesian Basin. *Hydrogeol. J.* **2013**, *21*, 845–862. [CrossRef]
27. Borazjani, S.; Hemmati, N.; Behr, A.; Genolet, L.; Mahani, H.; Zeinijahromi, A.; Bedrikovetsky, P. Determining water-oil relative permeability and capillary pressure from steady-state coreflood tests. *J. Pet. Sci. Eng.* **2021**, *205*, 108810. [CrossRef]
28. Bahrami, A.; Aghamir, F.; Bahrami, M.; Khodaverdiloo, H. Inverse modeling towards parameter estimation of the nonlinear soil hydraulic functions using developed multistep outflow procedure. *J. Hydrol.* **2020**, *590*, 125446. [CrossRef]
29. Chen, Y.F.; Zhou, C.B.; Sheng, Y.Q. Formulation of strain-dependent hydraulic conductivity for a fractured rock mass. *Int. J. Rock Mech. Min. Sci.* **2007**, *44*, 981–996. [CrossRef]
30. Chen, Y.; Hu, S.; Zhou, C.; Jing, L. Micromechanical modeling of anisotropic damage-induced permeability variation in crystalline rocks. *Rock Mech. Rock. Eng.* **2014**, *47*, 1775–1791. [CrossRef]
31. Kuhl, D.; Falko, B.; Meschke, G. Coupled chemo-mechanical deterioration of cementitious materials. Part I: Modeling. *Int. J. Solids Struct.* **2004**, *41*, 15–40. [CrossRef]
32. Kuhl, D.; Falko, B.; Meschke, G. Coupled chemo-mechanical deterioration of cementitious materials Part II: Numerical methods and simulations. *Int. J. Solids Struct.* **2004**, *41*, 41–67. [CrossRef]
33. Morteza, D. Hydrodynamic dispersion due to a variety of flow velocity profiles in a porous-walled microfluidic channel. *Int. J. Heat Mass Tran.* **2019**, *41*, 41–67.
34. Garboczi, E.J.; Bentz, D.P. Computer simulation of the diffusivity of cement-based materials. *J. Mater. Sci.* **1992**, *27*, 2083–2092. [CrossRef]
35. Bentz, D.; Jensen, O.; Coats, A.; Glasser, F. Influence of silica fume on diffusivity in cement-based materials: I. Experimental and computer modeling studies on cement pastes. *Cem. Concr. Res.* **2000**, *30*, 953–962. [CrossRef]
36. Bentz, D.P. Influence of silica fume on diffusivity in cement-based materials: II. Multi-scale modeling of concrete diffusivity. *Cem. Concr. Res.* **2000**, *30*, 1121–1129. [CrossRef]
37. Van Eijk, R.J.; Brouwers, H.J.H. Study of the realation between hydrated portland cement composition and leaching resistance. *Cem. Concr. Res.* **1998**, *28*, 815–828. [CrossRef]
38. Javadi, A.A.; Farmani, R.; Tan, T.P. A hybrid intelligent genetic algorithm. *Adv. Eng. Inform.* **2005**, *19*, 255–262. [CrossRef]
39. Zhang, X.; Chen, X.; Li, J. Improving Dam Seepage Prediction Using Back-Propagation Neural Network and Genetic Algorithm. *Math. Probl. Eng.* **2020**, *2020*, 1–8.
40. Shahrokhabadi, S.; Toufigh, M.M. The solution of unconfined seepage problem using Natural Element Method (NEM) coupled with Genetic Algorithm (GA). *Appl. Math. Model.* **2013**, *37*, 2775–2786. [CrossRef]
41. Al-Juboori, M.; Datta, B. Performance evaluation of a genetic algorithm-based linked simulation-optimization model for optimal hydraulic seepage-related design of concrete gravity dams. *J. Appl. Water Eng. Res.* **2019**, *7*, 173–197. [CrossRef]
42. Deng, X.; Yuan, D.; Yang, D.; Zhang, C. Back Analysis of Geomechanical Parameters of Rock Masses Based on Seepage-Stress Coupled Analysis. *Math. Probl. Eng.* **2017**, *2017*, 1–13. [CrossRef]
43. Hong, J.-M.; Chen, Y.-F.; Liu, M.-M.; Zhou, C.-B. Inverse modelling of groundwater flow around a large-scale underground cavern system considering the excavation-induced hydraulic conductivity variation. *Comput. Geotech.* **2017**, *81*, 346–359. [CrossRef]

mathematics

MDPI

Article

Modeling and Optimization of a Compression Ignition Engine Fueled with Biodiesel Blends for Performance Improvement

Ali Alahmer [1,*], Hegazy Rezk [2], Wail Aladayleh [1], Ahmad O. Mostafa [1], Mahmoud Abu-Zaid [3], Hussein Alahmer [4], Mohamed R. Gomaa [5,6], Amel A. Alhussan [7] and Rania M. Ghoniem [8,*]

1 Department of Mechanical Engineering, Faculty of Engineering, Tafila Technical University, P.O. Box 179, Tafila 66110, Jordan; wadaileh@ttu.edu.jo (W.A.); a.omar@ttu.edu.jo (A.O.M.)
2 Department of Electrical Engineering, College of Engineering at Wadi Addawaser, Prince Sattam Bin Abdulaziz University, AI-Kharj 16278, Saudi Arabia; hr.hussien@psau.edu.sa
3 Mechanical Engineering Department, Mutah University, Alkarak 61710, Jordan; abuzaid@mutah.edu.jo
4 Department of Automated Systems, Faculty of Artificial Intelligence, Al-Balqa Applied University, Al-Salt 19117, Jordan; dr.halahmer@bau.edu.jo
5 Mechanical Engineering Department, Faculty of Engineering, Al-Hussein Bin Talal University, Ma'an 71111, Jordan; Behiri@bhit.bu.edu.eg
6 Mechanical Engineering Department, Benha Faculty of Engineering, Benha University, Benha 13512, Egypt
7 Department of Computer Sciences, College of Computer and Information Sciences, Princess Nourah bint Abdulrahman University, P.O. Box 84428, Riyadh 11671, Saudi Arabia; Aaalhussan@pnu.edu.sa
8 Department of Information Technology, College of Computer and Information Sciences, Princess Nourah bint Abdulrahman University, P.O. Box 84428, Riyadh 11671, Saudi Arabia
* Correspondence: a.alahmer@ttu.edu.jo (A.A.); RMGhoniem@pnu.edu.sa (R.M.G.); Tel.: +962-798277537 (A.A.)

Citation: Alahmer, A.; Rezk, H.; Aladayleh, W.; Mostafa, A.O.; Abu-Zaid, M.; Alahmer, H.; Gomaa, M.R.; Alhussan, A.A.; Ghoniem, R.M. Modeling and Optimization of a Compression Ignition Engine Fueled with Biodiesel Blends for Performance Improvement. *Mathematics* **2022**, *10*, 420. https://doi.org/10.3390/math10030420

Academic Editors: Camelia Petrescu and Valeriu David

Received: 25 December 2021
Accepted: 25 January 2022
Published: 28 January 2022

Publisher's Note: MDPI stays neutral with regard to jurisdictional claims in published maps and institutional affiliations.

Copyright: © 2022 by the authors. Licensee MDPI, Basel, Switzerland. This article is an open access article distributed under the terms and conditions of the Creative Commons Attribution (CC BY) license (https://creativecommons.org/licenses/by/4.0/).

Abstract: Biodiesel is considered to be a promising alternative option to diesel fuel. The main contribution of the current work is to improve compression ignition engine performance, fueled by several biodiesel blends. Three metrics were used to evaluate the output performance of the compression ignition engine, as follows: brake torque (BT), brake specific fuel consumption (BSFC), and brake thermal efficiency (BTE), by varying two input parameters (engine speed and fuel type). The engine speeds were in the 1200–2400 rpm range. Three biodiesel blends, containing 20 vol.% of vegetable oil and 80 vol.% of pure diesel fuel, were prepared and tested. In all the experiments, pure diesel fuel was employed as a reference for all biodiesel blends. The experimental results revealed the following findings: although all types of biodiesel blends have low calorific value and slightly high viscosity, as compared to pure diesel fuel, there was an improvement in both BT and brake power (BP) outputs. An increase in BSFC by 7.4%, 4.9%, and 2.5% was obtained for palm, sunflower, and corn biodiesel blends, respectively, as compared to that of pure diesel. The BTE of the palm oil biodiesel blend was the lowest among other biodiesel blends. The suggested work strategy includes two stages (modeling and parameter optimization). In the first stage, a robust fuzzy model is created, depending on the experimental results, to simulate the output performance of the compression ignition engine. The particle swarm optimization (PSO) algorithm is used in the second stage to determine the optimal operating parameters. To confirm the distinction of the proposed strategy, the obtained outcomes were compared to those attained by response surface methodology (RSM). The coefficient of determination (R^2) and the root-mean-square-error (RMSE) were used as comparison metrics. The average R^2 was increased by 27.7% and 29.3% for training and testing, respectively, based on the fuzzy model. Using the proposed strategy in this work (integration between fuzzy logic and PSO) may increase the overall performance of the compression ignition engine by 2.065% and 8.256%, as concluded from the experimental tests and RSM.

Keywords: optimization; fuzzy model; response surface methodology; diesel engine performance; biodiesel

1. Introduction

Recently, the energy crisis, environmental contamination, and climate change are considered the most critical difficulties facing the country [1–6]. Therefore, the increased awareness of potential environmental risks on human health has been focused on keeping engine emissions under control. Diesel fuel has a crucial problem related to exhaust, vibration, and acoustic emissions [7–11]. Biodiesel is considered an eco-friendly, bio-degradable, energy efficient, renewable, scientifically feasible, and non-toxic fuel alternative [12–14]. Besides, it is considered one of the safest fuels, because it has a high flash point amongst all conventional fuels [15], and can operate diesel engines with little or no adjustments [16]. Biodiesel can be produced from a variety of animal fats, as well as vegetable oils, processed with a catalyst and alcohol. For example, the utilization of palm oil as biodiesel is recognized as palm oil methyl ester, which is growing rapidly in popularity, due to its huge productivity and low prices. Biodiesel produced from palm oil is categorized by a high amount of saturated fatty acids and displays tremendous combustion characteristics, such as the calorific value and cetane number, despite its high kinematic viscosity at low temperatures [17]. The continuous improvement of the cetane number will actually impact the injection time, the coefficients of combustion variables, and heat release aspects, according to Labeckas and Slavinskas [18]. Various mixtures and fuel attributes have a significant impact in the ignition delay and evaporation processes, within similar experimental settings. Generally, most of the biodiesel blends have a high cetane number, no sulfur, no aromatics, and they contain up to 11 wt% oxygen. The National Renewable Energy Laboratory (NREL) [19] reported that the oxygen concentration in biodiesel fuel, including vegetable oil blends, ranges from 2.5% to 11%, for biodiesel blends of 20% and 100% by volume. In contrast, pure diesel does not contain any oxygen molecules. The significant oxygen concentration in the biodiesel enhances the combustion efficiency and decreases some of the exhaust emissions. Conversely, the main crucial drawback of biodiesel, in terms of high viscosity, leads to many difficulties in the atomization and pumping processes. Therefore, there was a need for a transesterification process. Furthermore, biodiesel fuels have greater surface tension and viscosity than regular diesel fuels, and these differences become crucial in cold circumstances, because the rate of fuel injection is greatly influenced, and the combustion mechanism might be influenced as a result. Additives have been used in biodiesel fuels to improve the biodiesel cold filter plugging point (CFPP) property and, consequently, improve the properties of the flow at low temperatures, to make them more appropriate for low-temperature operations [20]. Other drawbacks are the lower calorific value, which is about 80% of the heating value compared to that of pure diesel, low oxidation stability, high pour point, and low volatility [21,22]. To address the difficulties related to biodiesel fuel having a high viscosity, the following techniques could be adopted [23–26]: (i) Use small blend ratios with pure diesel [23]. It is commonly recognized that up to 20% of biodiesel blends can be used without engine modifications; (ii) Make a micro-emulsification by the use of ethanol or methanol [24]; (iii) Use nanoparticles as fuel additives to lower the density and viscosity of the fuel mixture [25,26]. In terms of feasibility issues, Rajak et al. [27] examined the economics of diesel fuel compared to biodiesel fuels made from Jatropha curcas and Moringa oleifera. According to the authors, the cost of diesel is nearly equal to the cost of alternative biofuels. The prior viewpoint was examined in detail and scientifically interpreted by Tasca et al. [28–30]. Yee et al. [30] introduced the concept of life cycle assessment (LCA), to investigate and assess whether biodiesel fuel is a sustainable fuel. The three phases of the LCA analysis were as follows: biodiesel transesterification process, agricultural processes, and oil milling. For each process, the energy and greenhouse gas balances were computed. According to the findings, the use of palm biodiesel was found to be more ecologically friendly than regular diesel fuel, with a significant 38% reduction in CO_2 emissions per liter combusted.

1.1. A Literature Review of Biodiesel Engine Performance

Numerous previous works have been conducted to assess the impacts of different types of biodiesel blends on engine durability, injection manner, exhaust emission, performance, heat losses and availability, spray formation, engine vibration analysis, catalyst synthesis for biodiesel production, and acoustic emissions [31–36]. Nalgundwar et al. [37] stated that a higher cetane of palm biodiesel blends is the reason for improved brake power and results in reduced ignition delay, which makes combustion start in advance. Moreover, a higher cetane number is required for the higher engine rotational speed. Sanjid et al. [38] compared the performances of two types of biodiesels; namely, mustard and palm biodiesel fuels, with volume blends of 10% and 20%. The results showed that the BSFC for mustard biodiesel is 1% and 3.5% higher than palm biodiesel blends of 10% and 20%, respectively. Ndayishimiye and Tazerout [39] examined the engine performance of a diesel engine fueled with palm oil blends. The authors found a small increase in BSFC and BTE, compared to pure diesel fuel.

Patel et al. [40] suggested the employment of biodiesel fuel instead of pure diesel to make some modifications in diesel engines, especially for the fuel filter, fuel pumps, and injector needle, to overcome the higher viscosity of biodiesel fuel and, therefore, to improve its performance.

1.2. Literature Review on Engine Performance Optimization Approaches

To avoid financial constraints and time-consuming experiments, scholars have employed different modeling techniques, including artificial intelligence (AI), in terms of an artificial neural network (ANN) tool, and fuzzy modeling in modeling engine performances and exhaust emissions [41–44]. Accordingly, the correlation coefficient between the experimental data and ANN predictions can accurately forecast the engine efficiency and exhaust emissions powered with biodiesel mixes [45].

The fuzzy model is a more advantageous method to estimate the parameters of the diesel engine that maximized the engine performance, as compared to other techniques, such as the computational fluid dynamics reaction kinetic model, because it necessitates less time and effort [46,47]. On the other hand, computational techniques for studying internal combustion engines have several drawbacks. To avoid this, Salam and Verma [48] innovated an alternate, non-traditional way to explore the challenge of empirical redundancy in engine operation and behavioral characterization. This study provided a unique empirical approach to assess the relative empirical importance of chosen variables of interest, addressing the comprehensibility of engine operation. Furthermore, Salam and Verma [49,50] employed redundancy to create a sequence of variables of interest, depending on their importance in the ICE operation. Dey et al. [51] examined the performance of a single-cylinder compression ignition (CI) engine, fueled by palm/diesel and ethanol biofuel blends, using two models of ANN and RSM. The results revealed that the optimized engine performance, in terms of BTE and BSFC, was obtained from a blend of 20% palm biodiesel, mixed with 5% ethanol and 75% pure diesel at full load. Krishnamoorthi et al. [52] maximized the diesel engine performance responses with two approaches (ANN tool and RSM). The engine was powered with diesel/vegetable oil/diethyl ether blends at different engine loads, along with various compression ratios. The error percentage of the two approaches was rated less than 5%. Therefore, the authors stated that the application of previous approaches plays a crucial role in improving engine performance. Dey et al. [53] and Reang et al. [54] employed the fuzzy-based Taguchi technique, to boost CI performance and reduce emission characteristics for a CI engine, with varying engine loads and varied biodiesel blends. Shirneshan et al. [55] used response surface techniques to investigate the effects of biodiesel–ethanol fuel mixes on the performance of a CI engine. Parameter optimizations were also performed, using the genetic method. According to the findings, increasing the quantity of ethanol in the gasoline combination reduced BP and BT by around 30%. Because ethanol has a lower calorific value than biodiesel, the BSFC of fuel blends increased by roughly 16% with a larger proportion of ethanol. To

minimize and identify the proper number of experimental trials, the Taguchi experimental approach could be utilized [56]. Rith et al. [57] employed RSM and the desired function to optimize a dual gas-diesel fuel engine, with several objectives. The goal was to use the desired function to optimize the desirability of SFC and specific exhaust emissions, at a high engine speed of 3000 rpm. The optimal desirability of 0.829 was reached with input parameters of 11° BTDC. Ghanbari et al. [58] examined how the percentage of alumina nanoparticles in biodiesel blends affected the exhaust emissions and performance of a CI engine. Furthermore, the authors designed empirical correlations, using RSM, to simulate diesel engine performance and exhaust emissions powered by nano biodiesel fuel mixes. The findings of the experiments demonstrated that alumina nanoparticles are a useful addition to diesel–biodiesel blends, to boost engine performance and reduce exhaust emissions. Devarajan et al. [59] examined CI engine performance by adding nanoparticles of silver oxide as additives, in various weight fractions, to a palm oil biodiesel. According to the results, the addition of nanoparticles to biodiesel improves the igniting behavior.

1.3. Research Gap, Objectives, and Originality

Although there are many articles in the literature about engine performance using different biodiesel fuel blends, there is still a gap in its modeling-based AI and modern optimization of the diesel engine. The current research aims to investigate a diesel engine, operated at full load conditions and at various engine speeds. In this work, engine performance has been studied extensively for an unmodified diesel engine, fueled with corn, sunflower, and palm biodiesel blends. Then, based on the experimental results, a robust fuzzy model, to simulate the output performance of the compression ignition engine, was created. Finally, a PSO algorithm was used to establish the best operating parameters. To confirm the distinction of the proposed strategy, the obtained outcomes were compared to those attained by RSM. Therefore, the novelty of this study relates to the integration between fuzzy logic and particle swarm optimization, to determine the optimal engine speed and the best fuel type that maximizes the output BT and BTE and significantly minimizes the BSFC.

1.4. Manuscript Organization

The rest of the manuscript is structured as follows: The experimental setup is discussed, in terms of biodiesel preparation, biodiesel characteristics, experimental equipment and procedure, engine performance measurements, proposed modeling and optimization, including fuzzy modeling, ANOVA test, and PSO in section two. The influence of biodiesel blends on diesel engine performance in terms of BT, BSFC, and BTE under full load and at various engine speeds was examined in section three, using the observed experimental results, combined with the uncertainty analysis. In addition, in section three, the outcomes of modeling and optimization, using fuzzy-based modeling logic, PSO algorithm to determine the optimal engine speed and best fuel type that maximize output BT and BTE, while momentarily minimizing the BSFC, RSM based on ANOVA test, and the best input parameters and related output performance from the RSM-based optimization method, were discussed and analyzed. In section four, we compared the performance of the experimental, RSM, and suggested strategies. Finally, the findings of the investigation were summarized in section five, which leads to the conclusion.

2. Experimental Setup, Equipment, Procedure, Modeling, and Optimization

A set of tests were carried out using a single-cylinder, water-cooled, four-stroke, and a direct injection PETTER PHIW Lister LV1 CI engine, with a compression ratio of 17:1, which is primarily powered by pure diesel fuel. The details of diesel engine specifications are demonstrated in Table 1. All tested fuels, which were pure diesel, corn biodiesel, sunflower biodiesel, and palm biodiesel, were implemented without making any adjustments to the diesel engine. The schematic diagram of an experimental diesel test engine is depicted in Figure 1.

Table 1. Technical data of PETTER PHIW diesel engine.

Technical Data	Specification
Type	Lister LV1
Maximum Power	9 HP (6.7 kW) @ 3000 rpm
Maximum torque	25 Nm @ 2000 rpm
Number of cylinders	Single
Engine Operation	Four Stroke
Nominal speed range	1000–3000 rpm
Bore ∗ Stroke	85.73 × 82.55 mm
Compression ratio	0.70902778
Connecting rod length	188.5 mm
Combustion chamber	Direct injection
Piston shape	Bowl-in-piston
Orifice diameter of the nozzle	0.250 mm
Fuel injector holes	3
Valve number/cylinder	2
Pressure @ injector opens	180 bars
Intake valve opening/closing	15^0 CA BTDC/41^0 CA ABDC
Exhaust valve opening/closing	41^0 CA BBDC/15^0 CA ATDC
Dynamometer	Swinging field DC machine with torque measurement by load

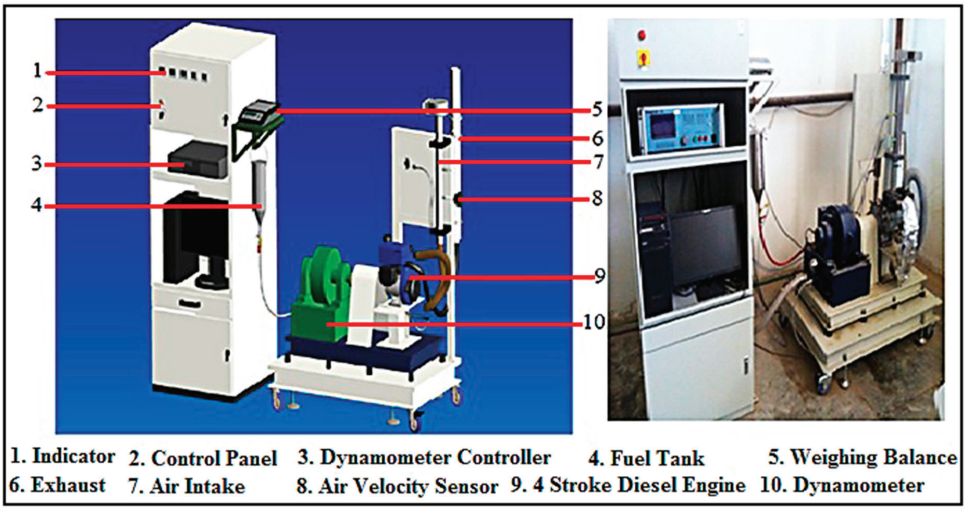

Figure 1. Schematic diagram of an experimental diesel test engine.

2.1. Biodiesel Preparation

As displayed in Table 2, numerous techniques have been used, including blending with transesterification, petrodiesel, pyrolysis, and microemulsification [60–64]. In our experimental test, three different biodiesel blends, consisting of 20 vol.% of vegetable oil and 80 vol.% of pure diesel fuel (namely, corn, sunflower, and palm biodiesels) were prepared according to the following procedure and depicted in Figure 2: 4 g of sodium hydroxide was added to 200 cm^3 of methanol in an electrical blender at low speed for around 2 min. The reaction heats up the mixture. It was vigorously stirred until all of the sodium hydroxide was fully dissolved in the methanol to form sodium methoxide. 1000 cm^3 of vegetable oil was preheated to 65 °C and added gradually to the previous mixture, while the electrical blender continued operating for around 30 min. After blending, the solution was left for 4 h of reaction time to settle down. Finally, the solution is separated

by gravity into two layers; one at the top is the biodiesel and one at the bottom is glycerin. Darker colored glycerin was gathered in a distinct layer at the bottom of the container, with an obvious line of separation from the pale liquid above, which was biodiesel. To eliminate all traces of glycerin and contaminants, the biodiesel product must be rinsed. The washing technique involves adding hot water to the biodiesel and allowing it to settle for 12 h in a separating funnel. The bottom layer was gradually removed until the sample was transparent. To eliminate the water content, the purified biodiesel was poured into a beaker and heated to 55 °C. Table 3 displays the percentage of fatty acids in oil materials used [60,64,65]. The measured fuel properties are recorded in Table 4, accompanied by equipment specifications.

Table 2. A summary of alternative biodiesel preparation approaches [60–64].

Technique	Preparation Process	Features	Drawbacks
Transesterification	Alcohol (methanol or ethanol) and catalyst were used to react the vegetable/animal oils. Following that, the combination of glycerol and methyl/ethyl esters (biodiesel) will be separated and purified before being used.	Relatively low cost with a high conversion, moderate processing settings, product qualities comparable to diesel and large-scale manufacturing	Low levels of water and free fatty acids in the raw resources were required, as well as lengthy separation and purification stages, the possibility of side reactions, and the formation of a substantial volume of effluent.
Blending	Pre-heated vegetable/animal oils were mixed with diesel in a 10–40% (*w*/*w*) ratio. The diesel engine was then coupled with the oil-diesel mixture.	There is no need for a chemical process (it is non-polluting), no technical adjustments, and it is simple to apply.	Inadequate spraying behaviour, weak atomization, improper fuel combustion, and difficulties in fueling by conventional engines caused by the high viscosity, unreliable, low volatility, and rise in vegetable/animal oil component.
Microemulsification	The vegetable/animal oils were dissolved in an alcohol-based solvent and a surfactant until they reached the desired viscosity.	Simple method that does not pollute the environment.	High viscosity, limited stability, and the possibility of sticking, incomplete combustion, and carbon deposition.
Pyrolysis	The vegetable/animal oils were preheated to a high temperature, usually exceeding 350 degrees Celsius, and then decomposed. It did not matter if the catalyst was there or not. Several products were examined depends on the individual product's boiling temperature range.	Practical technique, easy (no washing, drying, or filtration is necessary), waste, and pollution-free.	High temperatures and costly equipment are required, and the biodiesel produced is of low purity

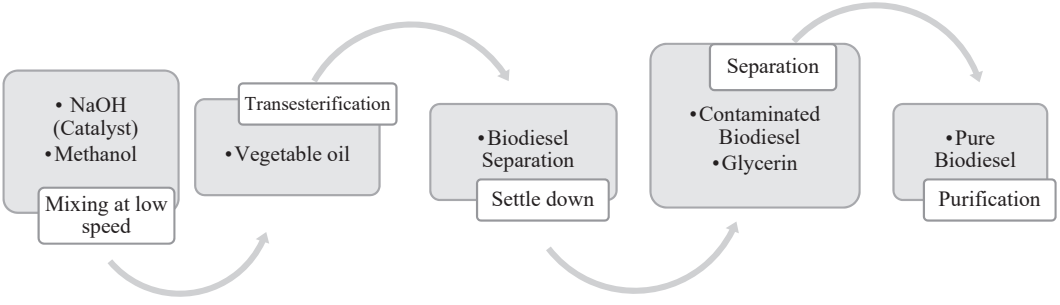

Figure 2. Production steps of vegetable oil biodiesel.

Table 3. Percentage of fatty acids in oil materials used [60,64,65].

Sources	% (wt) Palmitic (C16:0)	% (wt) Stearic (C18:0)	% (wt) Oleic (C18:1)	% (wt) Linoleic (C18:2)	% (wt) Linolenic (C18:3)
Palm oil	45	4	39	11	- *
Sunflower	3–10	1–10	14–35	55–75	<0.3
Corn	8–10	1–4	30–50	3456	0.5–1.5

* Not specified.

According to the following equation [66,67], the % error related to the experimental quantities was determined as depicted in Table 4.

$$\text{Error } \% = \frac{\text{Apparatus Accuracy}}{\text{Minimum value of apparatus measured}} \times 100\% \quad (1)$$

Table 4. Measured fuel blend properties of all tested fuel [60,68–73].

Properties	Diesel	Corn Biodiesel	Palm Biodiesel	Sunflower Biodiesel	Test method	Equipment	Accuracy	Error
Cetane Number	47	53	61	52	ASTM D613	-	-	
Flash Point, °C	52	74.74	72	86	ASTM D-93	Point-automatic NPM 440 (Norma Lab, France)	-	-
Iodine Value (cg I/g oil)	-	103–140	35–61	110–143	ASTM D5554-15	FTIR spectroscopy	-	-
Saponification Number	-	202	186–209	200	ASTM D5558-95	FTIR spectroscopy	-	-
Pour point, °C	−32	−18	−10	−5.0	ASTM D97	Cloud And Pour Point Apparatus	-	-
Cloud point, °C	−18	−15	−5	4.0	ASTM D2500	Cloud And Pour Point Apparatus	-	-
Specific gravity@ 15 °C	0.83	0.855	0.85	0.853	IP 190/93	Capillary stoppered Pycnometer	$\pm 10^{-3}$ g/cm^3	±0.12%

Table 4. *Cont.*

Properties	Diesel	Corn Biodiesel	Palm Biodiesel	Sunflower Biodiesel	Test method	Equipment	Accuracy	Error
Viscosity at 40 °C (cSt)	3.85	4.772	5.281	4.963	ASTM D445	EMILA rotary viscometer apparatus	±0.1 cP	±2.6%
Heating Value (MJ/kg)	43.5	39.5	40.1	39.8	ASTM D240	automated adiabatic bomb calorimeter	±0.04 MJ/kg	±0.1%

2.2. Engine Performance Measurements

A trunnion-mounted, swinging field of a direct current (DC) electrical machine capable of absorbing a maximum load of 10 kW at a speed of 4000 rpm was utilized as the dynamometer. The rated BT was 50 Nm. Torque was measured with a precision of ±0.2–0.3% of full scale (FS), whereas rotational speed measurement accuracy was ±1 r/min. The engine was driven by a speed-increasing tooth belt. A strain gauge load cell system with mechanical overload protection was included, as well as appropriate calibration equipment. For speed measurement and feedback to the control system, a toothed wheel and magnetic pick-up were employed. A dynamometer attached with a DC motor to produce a load was used to evaluate the engine brake power. A varying field current regulated the load and operation. Therefore, this dynamometer can work at different loads and speeds according to any required amount of torque. Because the test used a regular engine speed, the dynamometer power absorption unit absorbed the power generated by the engine to drive a DC motor that works as a generator to produce a load. This absorption unit delivered a variable quantity of braking torque to operate the engine at the desired rotation. Moreover, the braking power absorption unit on the engine was executed using an electronic control unit. The dynamometer control system is a microprocessor-controlled, completely regenerative thyristor drive that enables the dynamometer to run a motor or generator at a constant speed. A strain gauge load cell sensor was used to assess engine load. The magnetic pick-up sensor was used to monitor engine speed using a dented wheel on the dynamometer shaft. The performance test measurements are regulated according to the following procedure: The engine warms up until the cooling water and lubricating oil reach the set operating temperatures. After that, the choke is opened gradually by turning the lever to its widest setting. The speed control lever is set to the low-speed position and warms it up without applying the load for a few minutes. The speed control lever is gradually moved towards the high-speed position and set to the required engine speed. The tested fuel is applied. The following parameters were recorded: a digital tachometer was utilized to quantify the engine speed, the dynamometer was employed to measure a BT, temperatures of the exhaust gases, lubricating oil, and cooling water were monitored with a thermocouple type K of resistance temperature detectors (RTD) integrated with a high-temperature surface probe with accuracy of ±1.6 °C. Finally, install the air velocity sensor in the air intake duct, ensuring that the sensor element is aligned with the airflow and in the middle of the duct with an accuracy of ±0.3% full-scale deflection (FSD). The twin bulb glass burette and timer were used to calculate the fuel consumption rate with an accuracy of (±0.05 cm^3).

The previous steps were repeated for different biodiesel fuel blends. Before conducting any test, the engine and dynamometer were calibrated and regulated to their default values. After the engine was stabilized, all of the measurement data were logged. For each tested fuel, the experiments were repeated three times and the average of the measurements was taken.

2.3. Modeling and Optimization

There are two stages to the suggested modeling and optimization technique. The first phase involves fuzzy modeling based on an experimental dataset to predict the compression ignition engine's output performance. To confirm the distinction of the fuzzy model proposed in this work, the obtained results are compared to those attained by ANOVA. The second phase is determining the engine speed and the best types of fuel using PSO. Unlike mathematical methods, the definition of the model structure that makes up the system rule base is the first step in the fuzzy modeling technique. Thus, the relation between inputs and outputs are represented by fuzzy IF-THEN rules. In the case under study, the Takagi–Sugeno fuzzy was adopted to build the fuzzy rules because it can track the nonlinear input data. The inputs' membership functions were selected as the Gaussian shape. The rules are typically established depending on dataset inputs [74]. The following expressions are simply adopting the form of a fuzzy rule statement for a two-input single-output system:

$$\text{IF } x \text{ is } \text{MF}_x \text{ and } y \text{ is } \text{MF}_y \text{ THEN } z \text{ is } \text{MF}_z \tag{2}$$

where, MF_x, and MF_y are the fuzzy membership functions for two inputs, x and y, respectively; MF_z is the fuzzy membership function for a single output z.

One of the most well-known optimizers is PSO. Kennedy and Eberhart proposed the initial form of PSO. The main concept of PSO is derived from the natural flocking behavior of birds [75]. The original PSO is fairly simple and straightforward. Every particle has the potential to be a prospective solution. It consists of the two following vectors: velocity and position. The values for each of the variables in the problem are included in the location vector. The velocity is taken into account while changing the position of particles. For each dimension and particle separately, the velocity determines the magnitude and direction of step size. Further information on the mathematical representation and physical dispersion can be found in [76]. The following is a description of the updating process for particle velocity and location.

$$v^{t+1} = v^t + c_1 r_1 (P^t_{best} - x^t) + c_2 r_2 (g^t_{best} - x^t) \tag{3}$$

$$x^{t+1} = x^t + v^{t+1} \tag{4}$$

where, V indicates velocity, P_{best} is the best solution, g_{best} is the best solution globally. c_1 and c_2 denote cognitive and social aspects, r_1 and r_2 are random values, and t represents the number of iterations.

Figure 3 displays a schematic diagram of the experimental approach integrated with an optimization process.

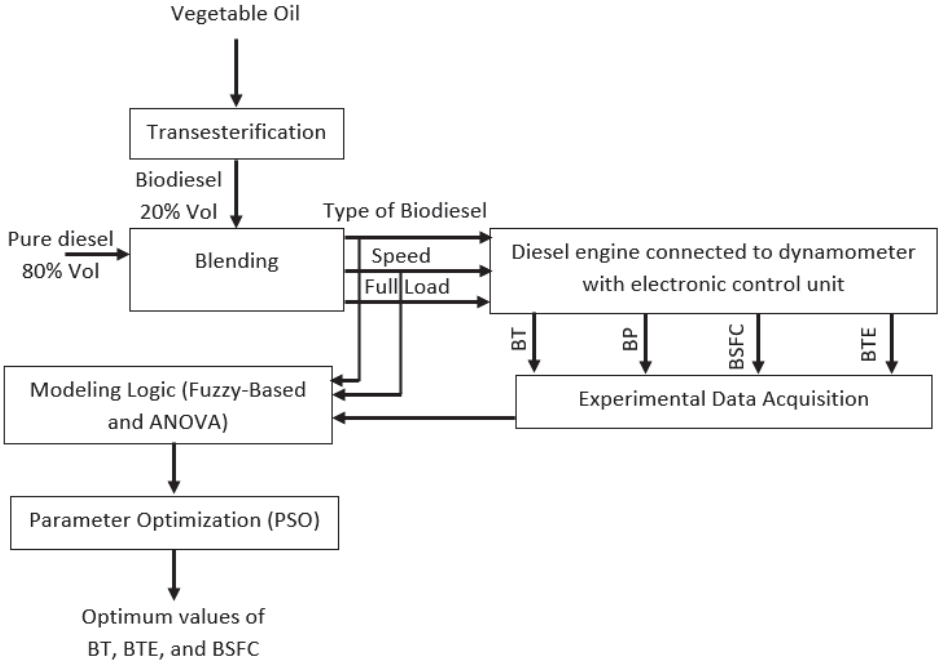

Figure 3. A schematic diagram of the experimental approach integrated with an optimization process.

3. Results and Discussion

The generated experimental findings provide a thorough examination of the impact of biodiesel blends on diesel engine performance, under full load and at different engine speeds.

3.1. Engine Performance Analysis

The effects of biodiesel blends on the CI engine BT, BP, BSFC, and BTE, at different engine speeds, have been investigated and discussed in the following sections.

3.1.1. Engine Brake Torque (BT) and Brake Power (BP)

The variations of BT and BP output of the diesel engine, at various engine speeds, powered by different biodiesel blends, are displayed in Figures 4 and 5, respectively. As depicted in Figures 4 and 5, the BT of a diesel engine increases with the engine speed, peaking at 1800 rpm, and then decreasing as the engine speed increases. The decrease might be attributed to the higher friction loss and a lack of air consumption at high speeds [77,78]. Although all types of biodiesels have a lower calorific value and a slightly higher viscosity than pure diesel, engine BT and BP are improved. On average, palm, sunflower, and corn biodiesels improved brake power by 8.7%, 5.4%, and 2.5%, respectively, as compared to pure diesel. The higher content of oxygen in all blends of biodiesel, which improves the combustion behavior to become more complete [43], might be responsible for the increased brake power. Typically, the diesel fuel is pumped into the engine according to volumetric measures. The density of all forms of biodiesel mixes is greater than pure diesel. As a consequence, for the same fuel volume, a higher fuel flow rate must be injected into the engine cylinder. Because of the high viscosity of biodiesel blends, there was less internal leakage in the diesel fuel pump [79]. Lapuerta et al. [80] attributed the change in brake power not only to the change in fuel mass supplied, but also due to the fact that the volume pumped was greater (1.2–3.2%) when biodiesel was used, especially in full-load

settings. Biodiesel has a greater viscosity, which lowers backflow over the piston clearance for the injection pump. Furthermore, as the injection temperature was increased, the disparity in fuel delivery reduced, indicating that the viscosity of the fuel had decreased. However, when the injection temperatures for diesel and biodiesel were altered to achieve comparable viscosities, the volume of diesel fuel injection was somewhat higher, due to its lower density, which boosts flow rate across orifices. The increased lubricity of biodiesel may contribute to reducing friction loss, resulting in more effective braking [16]. Mekonen and Sahoo [81] proposed a method of preheating intake air, to increase the braking power of palm biodiesel engines. Preheating the intake air decreases the ignition delay, allowing the obtainable oxygen in the combustion chamber to be utilized for combustion, resulting in completing combustion and improved energy conversion. Furthermore, preheating the intake air has a significant impact on fuel atomization, resulting in full combustion and, hence, increased brake power. Many studies [82,83] have shown that increasing the biodiesel content ratio reduces the heating value and increases the viscosity of biodiesel, resulting in erratic combustion, which reduces engine BT and BP. On the other hand, the reduced fuel leakages in the injection pumping system, the advanced combustion process, and better biodiesel lubricity have all been identified in response to the aforementioned power regeneration.

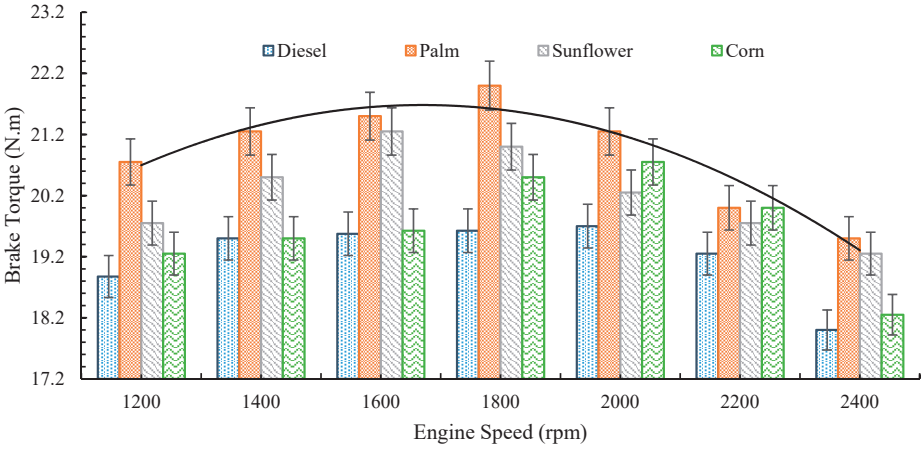

Figure 4. Variation of BT output vs. engine speed for different biodiesel blends.

3.1.2. Brake Specific Fuel Consumption (BSFC)

Figure 6 depicts the nature of BSFC against engine speed, for pure diesel and various kinds of biodiesel fuel. The BSFC gradually declines with engine speed, until it hits a minimum, then increases with engine speed. This was the case for all of the tested fuels. Greater heat loss towards the combustion chamber walls, which decreases combustion efficiency and increases fuel consumption, is a major cause of this reduction. The rise in BSFC is due to an increase in engine friction at high engine speeds. Another finding was that all biodiesel mixes had greater BSFC than pure diesel, especially at low engine speeds. The indirect reasons for the increased specific fuel consumption are as follows: (i) lesser formation of a finer dispersion, due to relatively low biodiesel vaporization (micro-explosion), (ii) less air entrained in the spray due to decreased momentum and penetrating force, and (iii) decrease in the local excess air ratio due to the biodiesel being replaced. In comparison to pure diesel, palm, sunflower, and corn biodiesels showed, on average, an increase in BSFC of 7.4%, 4.9%, and 2.5%, respectively. Because all biodiesel mixes have a lower calorific value than pure diesel, they require greater fuel consumption to generate the same braking power output. Since palm biodiesel has the highest kinematic viscosity, which leads to poor fuel atomization and mixture formation, it has a higher rise in BSFC

than the other tested fuels [84]. Another observation was that at high engine speeds, above 2000 rpm, there was a small difference in BSFC for all biodiesel mixes, compared to pure diesel. It indicates that all biodiesel fuels tested may get an increase in combustion efficiency. This enhancement is attributed to increased diffusion rates for biodiesel fuel vapor inside the combustion chamber, which stimulates the formation of an air–fuel mixture prior to beginning the ignition, in the form of fine spray, related to fast evaporation. Due to an increase in the cetane number, the studied biodiesel fuel blends featured a shorter ignition delay, resulting in more power combustion efficiency and less fuel burning in pre-mixed combustion [85]. According to Fayad et al. [86], increasing the proportion of biodiesel in fuel mixes increases the BSFC, for various engine loads and speeds. Further investigations have shown similar outcomes [83,87,88].

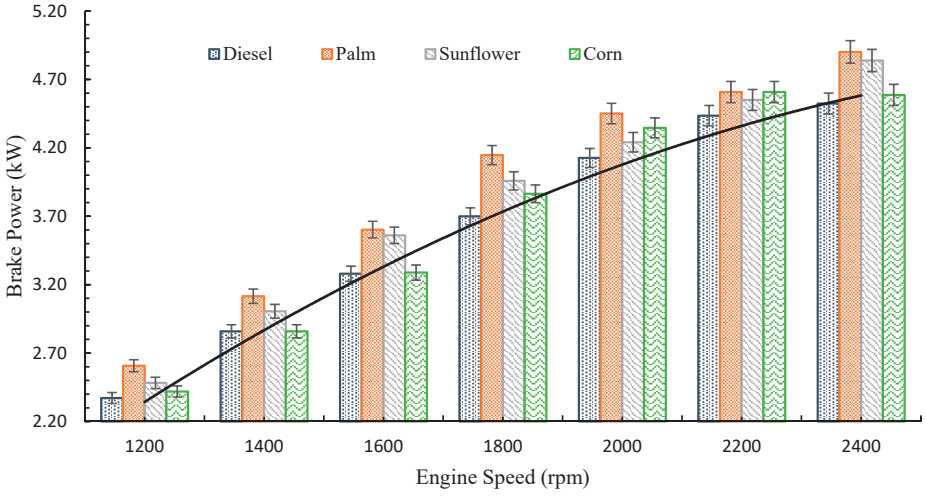

Figure 5. Variation of brake power vs. engine speed for different biodiesel blends.

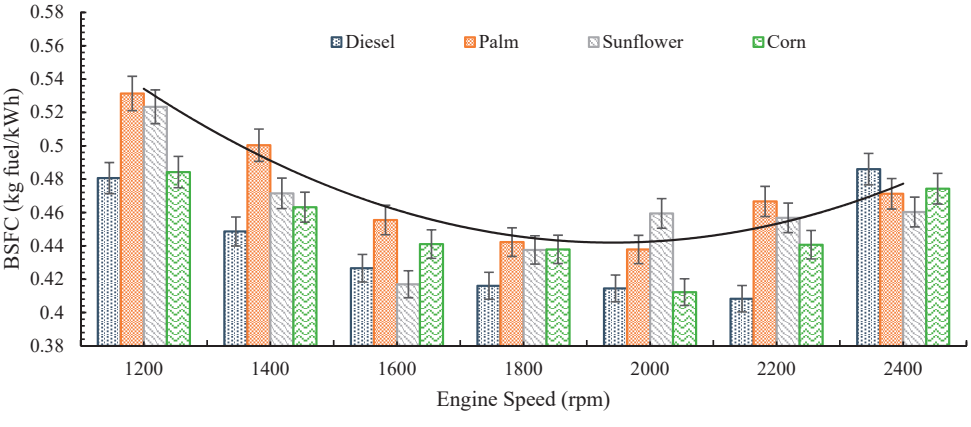

Figure 6. Variation of BSFC vs. engine speed for different biodiesel blends.

3.1.3. Brake Thermal Efficiency (BTE)

The fluctuation of BTE for pure diesel and various biodiesel blends, over a range of engine speeds, is displayed in Figure 7. The BTE steadily improves with engine speed, until it reaches a maximum value, as depicted in this figure. This then lowers, as the engine

speed rises. This trend might be explained by the fact that cylinder walls take a long time to transmit heat, especially at low speeds, resulting in a considerable amount of fuel being required to compensate for the increased heat loss. The braking power increases as the engine speed rises, resulting in better BTE. Due to the high inertia of the moving parts, friction power increases fast at higher speeds, which might be a result of the decrease in BTE. Another observation is that, as compared to pure diesel, all biodiesel blends have a poorer BTE. In comparison to pure diesel, palm, sunflower, and corn biodiesel had, on average, BTE drops of 6.7%, 4.4%, and 2.4%, respectively. The use of biodiesel fuel causes higher thermal friction losses, which transfer to the cylinder walls and engine coolant. The brake BTE is known to be inversely related to the BSFC and heating value [89]. For all biodiesel blends, for example, BSFC increased, while the heating value dropped. In this scenario, however, the brake-specific fuel consumption increase is more prominent. This explains why, despite their low heating value, biodiesel blends have a lower BTE. Furthermore, as compared to pure diesel, biodiesel blends have a shorter ignition delay, which implies that combustion begins sooner. As a result of the shorter ignition delay, more heat is lost to the environment, requiring more power for the piston to complete the compression stroke. According to Khiraiya et al. [90], the kinematic viscosity of palm biodiesel is 150% that of pure diesel fuel. Palm biodiesel requires a greater injection pressure than diesel, due to its higher kinematic viscosity, resulting in smaller diameter droplets and poorer BTE. In terms of fuel injection system design, sound speed and bulk modulus data are critical. In the fuel injection system, the speed of sound and the bulk modulus of the fuel have a significant impact on the fuel injection time. The propagation of pressure waves, from the fuel injection pump to the injectors, requires a few degrees of crank angle, especially in pump-line-nozzle injection systems [91]. According to Szybist et al. [92], biodiesel has a higher bulk modulus and sound velocity, as well as its higher viscosity, resulting in earlier injection starts. This, combined with any increment in the cetane number, has the potential to dramatically speed up and advance the combustion process. Traditional diesel engines require delayed combustion to reduce pressure and temperature peaks in the combustion chamber. A delay will result in a reduction in BTE and braking power. When the injection starts, and therefore the combustion process is advanced, the combustion process is re-centered, and the BP improves [93]. Many researchers reached the same conclusions [37,87,90,94–96]. However, a few scholars [21,23,97] observed the opposite pattern. They attributed the enhanced BTE to the oxygenated biodiesel fuel's better combustion characteristics, or to the lower friction loss as a result of increased lubricity. Because of the tight tolerances in the injectors and injection system, high lubricity is essential for diesel fuels. More friction and wear between moving elements inside the injection system may occur if a diesel fuel with low lubricity is utilized.

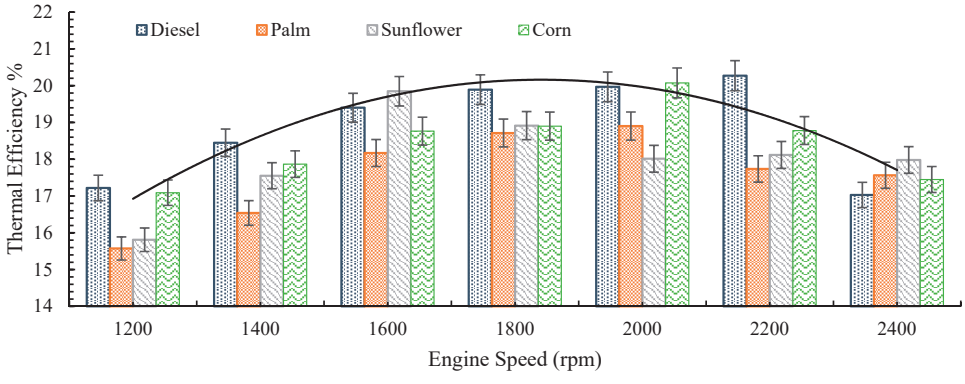

Figure 7. Variation of thermal efficiency vs. engine speed for different biodiesel blends.

Table 5 presents a brief quantitative comparison of the current work to previous studies published in the literature.

Table 5. Comparison of the current work to previous studies published in the literature [39,86,98–103].

Reference	Engine Type	Fuel	Test Conditions	BP	BSFC	BTE
Ozsezen et al. [98]	Six cylinders	Palm	Constant speed @ 1500 rpm, variable load	Reduced 2.5%	Increased 7.5%	Reduced 0.48%
Dulger and Kaplan [99]	Four cylinders	Sunflower	Variable speed @ Full load	Reduced 10%	Increased 2–5%	-
Fayad et al. [86]	Four cylinders	Sunflower	Variable speed @ Full load	-	Increased 23–35.7	Reduced 27%–30.4%
Lin et al. [100]	Single cylinder	Corn oil methyl ester	Variable speed and variable load	Increased 0.4%	Increased 10%	-
		Palm oil methyl ester		Increased 1.5	Increased 14.4%	-
Ndayishimiye and Tazerout [39]	Single cylinder	Palm	Constant speed @ 1500 rpm, variable load	-	10% Increased	Reduced 1–2%
Canakci et al. [101]	Four cylinder	Palm	Variable speed @Full load	Reduced 0–7%	11% Increased	Reduced 8%
Suryanarayanan et al. [102]	Single cylinder	Sunflower	Constant speed @ 1500 rpm, variable load	-	Increased 6–12%	Increased 2–5%
Reddy et al. [103]	Single cylinder	Corn seed	Constant speed @ 1500 rpm, variable load	-	8% Increased	Reduced 3.2%
Current Study	Single cylinder	Palm	Variable speed @Full load	Increased 8.7%	Increased 7.4%	Reduced 6.7%
		Sunflower		Increased 5.4%	Increased 4.9%	Reduced 4.4%
		Corn		Increased 2.5%	Increased 2.5%	Reduced 2.4%

3.2. Uncertainty Analysis

The outcomes evaluated from the experimental tests were commonly estimated from measured physical parameters. These values have some errors, due to their uncertainty measurements. Therefore, to compute the difference between the experimentally measured value and the typical true value of a quantity, an uncertainty analysis was used to certify the reliability of the calculated physical quantities. The technique, suggested by Holman [104], was anticipated to measure the experimental uncertainties. According to this technique, if the outcome, R, is a set function of the variables $x_1, x_2, x_3 \ldots x_n$, and $\omega_1, \omega_2, \omega_3 \ldots \omega_n$ are the uncertainties in the independent variables. Therefore, uncertainty in the results ω_R is evaluated by Equation (5) [105], as follows:

$$\omega_R = \pm\sqrt{\left(\frac{\partial R}{\partial X_1}\omega_{X_1}\right)^2 + \left(\frac{\partial R}{\partial X_2}\omega_{X_2}\right)^2 + \left(\frac{\partial R}{\partial X_3}\omega_{X_3}\right)^2 + \ldots + \left(\frac{\partial R}{\partial X_n}\omega_{X_n}\right)^2} \quad (5)$$

The quantity of uncertainty percentage is calculated by Equation (6), as follows:

$$\text{Percentage Analysis} = \frac{\omega_R}{|R|} \times 100\%. \quad (6)$$

For instance, the uncertainty error in braking power (BP) is evaluated as a function of rotating engine speed (N) and torque (T).

$$\mathrm{BP} = f(N,T)\Delta\mathrm{BP} = \sqrt{\left(\frac{\partial \mathrm{BP}}{\partial N}\Delta N\right)^2 + \left(\frac{\partial \mathrm{BP}}{\partial T}\Delta T\right)^2} \quad (7)$$

In regard to Equation (5), the uncertainties for measured physical quantities, such as BT, BP, BSFC, and BTE were evaluated as ±1.82%, ±1.68, ±1.94%, and ± 2.02% respectively, which indicates the evaluated results are reliable.

3.3. Modeling and Optimization

3.3.1. Fuzzy-Based Modeling Logic

The following three outputs were utilized to replicate the CI engine's output performance: BT, BTE, and BSFC. The output performance of the CI engine was investigated by varying the following two input parameters: engine speed and fuel type. The tests were conducted at various engine speeds, ranging from 1200 to 2400 rpm. Pure diesel, palm oil, sunflower oil, and corn oil were the four types of fuel examined. The experimental dataset was split into two parts, with a ratio of 70:30 training:testing stages. The fuzzy model structure is a Sugeno-type, adaptive network-based fuzzy inference system (ANFIS). In addition, the fuzzy rules were developed using the subtractive clustering approach, which yielded 10 fuzzy rules. For the fuzzification procedure, the MFs inputs were chosen as the Gaussian shape, and just 10 epochs were determined to be adequate for training. During training and testing, the following three metrics were used to assess the accuracy of a fuzzy model: mean square error (MSE), root-mean-square error (RMSE), and R^2. The values of the statistical metrics of the fuzzy model response are shown in Table 6.

Table 6. Statistical evaluation for the fuzzy-based models.

MSE			**Coefficient of Determination (R^2)**		
Train	**Test**	**All**	**Train**	**Test**	**All**
First fuzzy model of brake Torque					
6.71×10^{-6}	0.0805	0.0259	1	0.9145	0.9713
Second fuzzy model of thermal efficiency					
5.99×10^{-8}	0.1736	0.0558	1	0.845	0.9626
Third fuzzy model of BSFC					
1.53×10^{-7}	0.0002	0.0001	0.9998	0.7845	0.9408
Average					
2.31×10^{-6}	8.48×10^{-2}	2.73×10^{-2}	1	0.84801	0.9581

Considering Table 6 for the modeling of the BT, the MSE values are 6.71×10^{-6} and 0.0805, and the coefficients of determination values represent 1.00 and 0.9145, for the training and testing, respectively. This indicates the advantageous nature of fuzzy modeling. For modeling the BTE, the MSE values are 5.99×10^{-8} and 0.1736, and the R^2 values are 1.00 and 0.845, for training and testing, respectively. For modeling the BSFC, the MSE values are 1.53×10^{-7} and 0.0002, and the R^2 values are 0.9998 and 0.7845, for training and testing, respectively.

The graphical description is essential to evaluate the fuzzy-based model. As a result, the training and testing phase prediction accuracies were emphasized by graphing the model's predictions against their associated targets, as shown in Figure 8. The forecasts are clearly distributed tightly over the % line, indicating that the model's performance accuracy is confirmed.

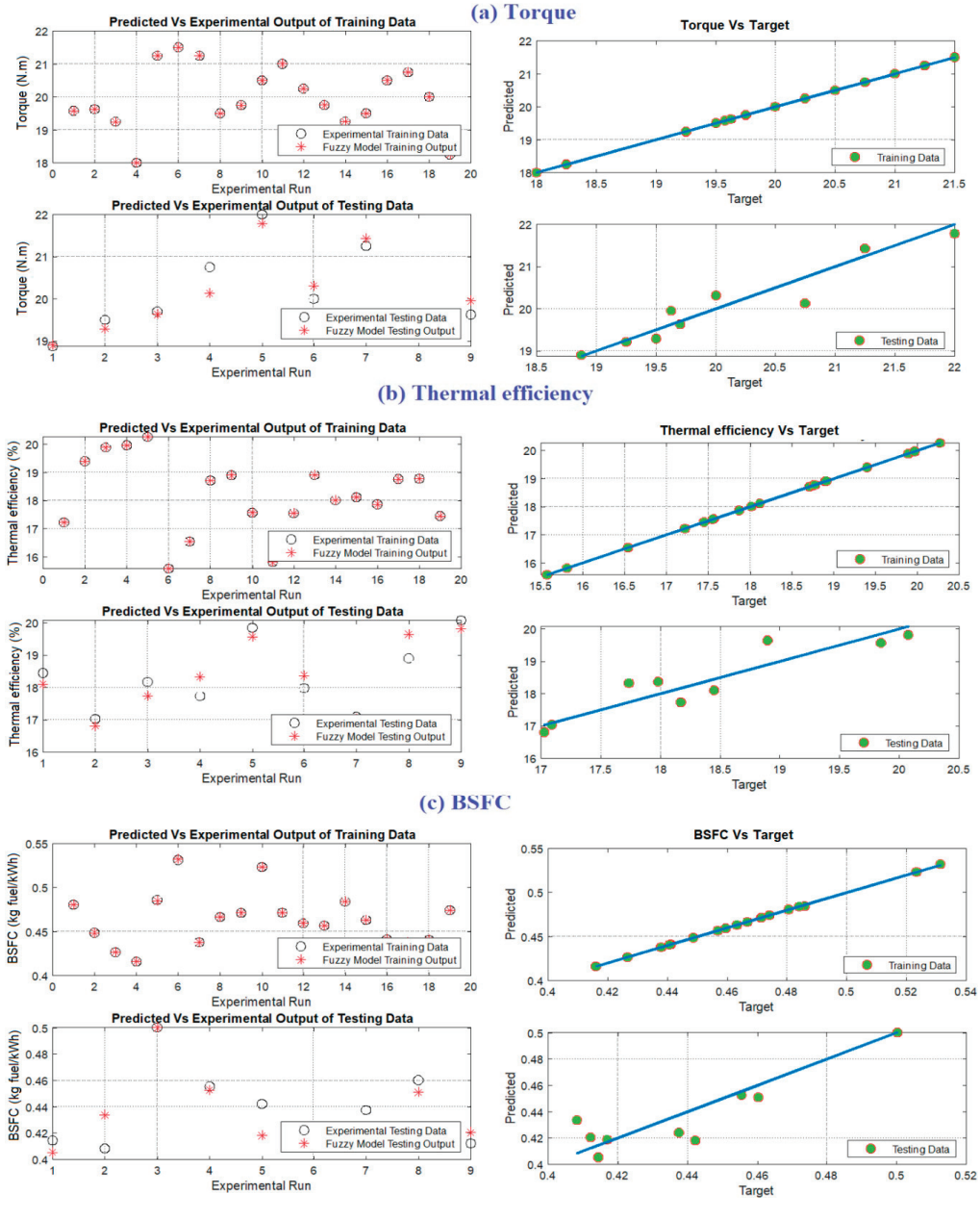

Figure 8. Fuzzy models' prediction precision.

The whole values of the output with the input space may be shown once the fuzzy model has been established. Figure 9 illustrates the 3D surfaces created, using fuzzy-based modeling, to simulate the CI engine's performance. The colored contours enable us to recognize the input–output function's nature and to characterize the minimum and maximum regions.

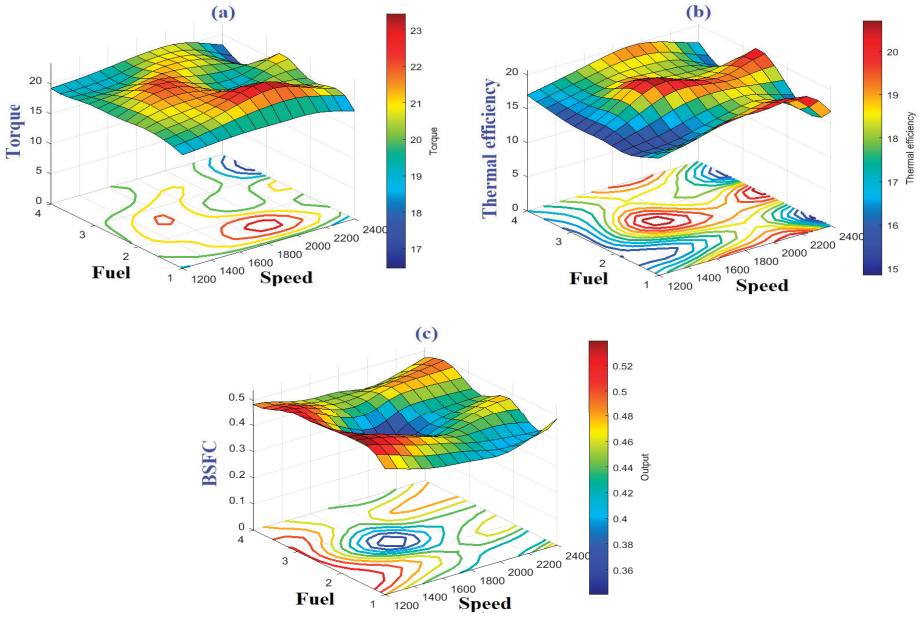

Figure 9. The 3D Surfaces of the fuzzy-based models, (**a**) brake torque, (**b**) brake thermal efficiency, and (**c**) BSFC. Note: Fuel (1 for diesel, 2 for palm oil, 3 for sunflower oil and 4 for corn oil).

The membership functions of the fuzzy model for the CI engine are displayed in Figure 10. The two inputs' membership functions (MFs) were determined to be Gaussian-shape, which is better for providing a smooth prediction surface. A Gaussian MF is defined by two parameters {m, σ}; m indicates the Gaussian curve's mean, and σ represents the curve's spread. This is a more natural method to show the distribution of data. The subtractive clustering technique, depending on the number of formed clusters, determines the number of MFs for each input.

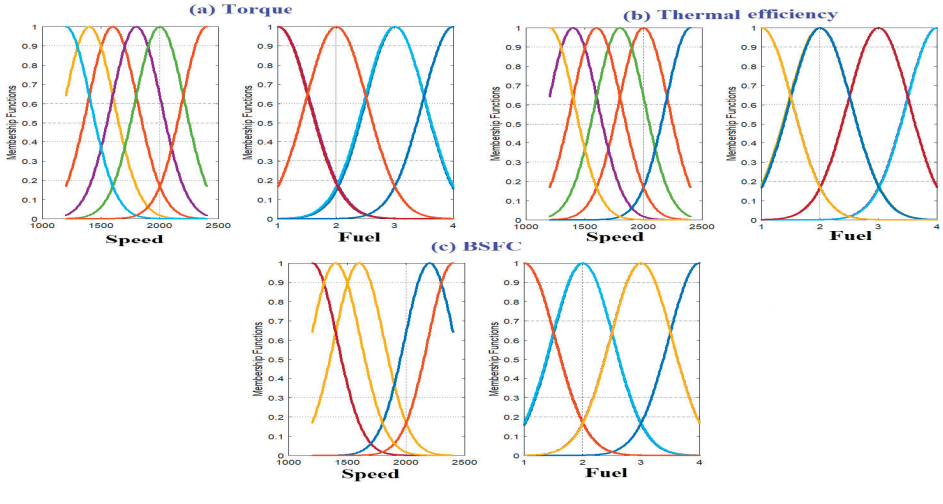

Figure 10. The membership functions of fuzzy models; (**a**) BT, (**b**) BTE, and (**c**) BSFC. (Each color represents fuzzy membership function).

3.3.2. Parameter Optimization

The PSO algorithm is used to calculate the optimal engine speed and best fuel type, based on the fuzzy-based model of the CI engine, which maximizes the output BT and BTE, while momentarily minimizing the BSFC. The number of searching agents is 20 and the number of iterations is 100. The cost objective function is demonstrated in Equation (8), and the optimization statement is as follows: identify the ideal values of the controlling variables (S and F) that optimize CI engine performance within their established constraints.

$$\text{Cost function} = -\text{BT (S, F)} - \text{BTE (S, F)} + \text{BSFC (S, F)} \quad (8)$$

where, BT (S, F), BTE (S, F), and BSFC (S, F) are the three outputs of the fuzzy models, respectively, for BT, BTE, and BSFC. S and F are the inputs (speed and fuel type). The negative sign in Equation (8) indicates that the optimization process is being treated as a maximization problem, rather than a minimization. Numerically merging the outputs in the cost function has the physical meaning of optimizing all of them simultaneously. The cost function terms have been converted to a dimensionless quantity that has been divided by the maximum value.

Based on the optimization process, the optimal engine speed is 1648 rpm, and the best fuel is sunflower oil. Under this condition, the BT, BTE, and BSFC values are 21.482, 19.71, and 0.41, respectively. The graph of the iterative values of engine speed, as in Figure 11, demonstrated that the 100 iterations are sufficient to reach the optimal point before the end of the optimization procedure.

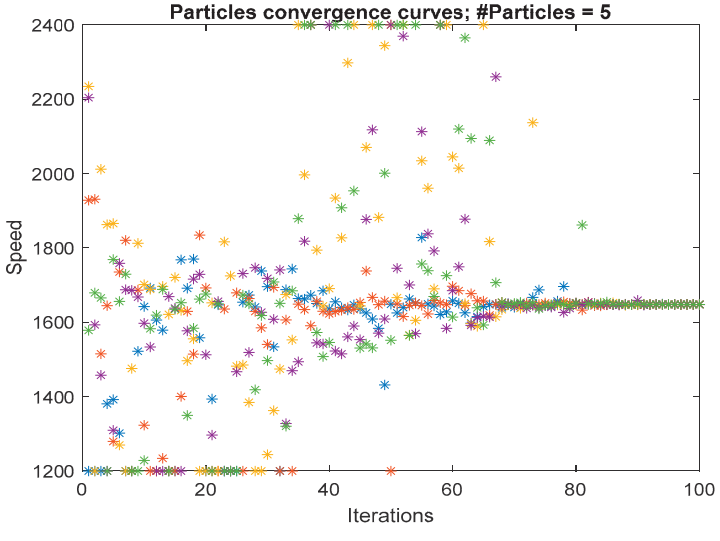

Figure 11. The convergence curve of the engine speed during the optimization process. (There are five different particles. Each color corresponds to one particle.)

3.3.3. Response Surface Methodology (RSM)

In the context of complicated interactions, RSM may be used to assess the relative importance of various elements. It is an effective method for evaluating many process variables [106]. RSM developed a polynomial model to describe and predict the data. It guarantees perfect interactions between the independent variables and no lack of fit related

to surface curvature [107]. The second-order quadratic polynomial model may be defined using the following relation:

$$Y = B_0 + \sum_{i=1}^{k} B_i x_i + \sum_{i=1}^{k} B_{ii} x_i^2 + \sum\sum_{i<j} B_{ij} x_i x_j \quad (9)$$

where, Y denotes the predicted output response; B_0, B_i, B_{ii}, and B_{ij} denote the regression coefficients; k is the number of factors; x_i denotes the factors.

Based on ANOVA, and considering the design matrix presented in Table 7, the first output response, BT, is modeled and displayed in Table 8. The model F-value of 20.93 in this table indicates that the model is significant. Due to noise, there is only a 0.01% chance that an F-value will display such a large amount. The model terms are significant if the p-values are less than 0.05. In this scenario F, S^2, F^2, and F^3 are significant model variables. The model terms are not significant if the value is higher than 0.1. In terms of actual factors, the following relationship may be utilized to generate BT predictions:

$$\begin{aligned} \mathrm{BT} = {} & 10.0285 - 0.002455\mathrm{S} + 11.06832\mathrm{F} - 0.0003\mathrm{SF} + 5.32552 \times 10^{-6}\mathrm{S}^2 \\ & -4.09844\mathrm{F}^2 - 2.83482 \times 10^{-7}\mathrm{S}^2\mathrm{F} + 0.000296\mathrm{SF}^2 - 1.62760 \times 10^{-9}\mathrm{S}^3 + 0.401190\mathrm{F}^3 \end{aligned} \quad (10)$$

Table 7. ANOVA design matrix.

Study Type	Response Surface	Subtype	Randomized
Design Type	Central Composite	Runs	28.00
Design Model	Quadratic	Blocks	No Blocks

Table 8. ANOVA table for first output response (BT).

Source	Sum of Squares	df	Mean Square	F-Value	p-Value	
Model	22.88	9	2.54	20.93	<0.0001	significant
S (speed)	0.1552	1	0.1552	1.28	0.2731	
F (fuel)	1.22	1	1.22	10.02	0.0054	
SF	0.1407	1	0.1407	1.16	0.2961	
S^2	9.36	1	9.36	77.06	<0.0001	
F^2	8.69	1	8.69	71.57	<0.0001	
S^2F	0.0540	1	0.0540	0.4447	0.5133	
SF^2	0.3919	1	0.3919	3.23	0.0892	
S^3	0.1465	1	0.1465	1.21	0.2866	
F^3	2.03	1	2.03	16.70	0.0007	
Residual	2.19	18	0.1214			
Cor Total	25.06	27				

Table 9 shows the ANOVA statistics for the second output response. The model F-value of 15.77 indicates that the model is statistically significant. Due to noise, there is only a 0.01% chance that an F-value will be this large. The model terms are significant if their p-values are less than 0.05. In this situation S, S^2, and F^2 are crucial model variables. The model terms are not significant if their values are higher than 0.1000. The following relationship can be utilized to construct BTE predictions, in terms of actual variables:

$$\mathrm{BTE} = -1.21079 + 0.024263\mathrm{S} - 2.14003\mathrm{F} - 0.000028\mathrm{SF} - 6.43799 \times 10^{-6}\mathrm{S}^2 + 0.418537\mathrm{F}^2 \quad (11)$$

Table 9. ANOVA table for second output response (BTE).

Source	Sum of Squares	df	Mean Square	F-Value	p-Value	
Model	32.15	5	6.43	15.77	<0.0001	significant
S	4.62	1	4.62	11.33	0.0028	

Table 9. *Cont.*

Source	Sum of Squares	df	Mean Square	F-Value	*p*-Value
F	0.3366	1	0.3366	0.8254	0.3735
SF	0.0044	1	0.0044	0.0109	0.9178
S^2	22.28	1	22.28	54.64	<0.0001
F^2	4.90	1	4.90	12.03	0.0022
Residual	8.97	22	0.4078		
Cor Total	41.12	27			

Table 10 displays the ANOVA statistics for the third output response. The F-value of 17.07 for the model indicates that it is significant. Due to noise, there is only a 0.01% chance that an F-value will appear this large. The model terms are significant if the *p*-values are less than 0.05. In this case S, S^2, and F^2 are important significant model variables. The model terms are not significant if the value is higher than 0.1000. The following relationship can be utilized to construct BSFC predictions in terms of actual variables:

$$\text{BSFC} = 0.959687 - 0.000626\text{S} + 0.054752\text{F} + 1.48809 \times 10^{-7}\text{SF} + 1.65947 \times 10^{-7}\text{S}^2 - 0.010605\text{F}^2 \quad (12)$$

Table 10. ANOVA table for third output response (BSFC).

Source	Sum of Squares	df	Mean Square	F-Value	*p*-Value	
Model	0.0216	5	0.0043	17.07	<0.0001	significant
S	0.0035	1	0.0035	13.70	0.0012	
F	0.0001	1	0.0001	0.5526	0.4651	
SF	1.240×10^{-7}	1	1.240×10^{-7}	0.0005	0.9825	
S^2	0.0148	1	0.0148	58.62	<0.0001	
F^2	0.0031	1	0.0031	12.47	0.0019	
Residual	0.0056	22				
Cor Total	0.0271	27				

Table 11 shows the statistical analysis of the ANOVA models. The anticipated R^2 value of 0.7278 for the BT model is rather close to the adjusted R^2 value of 0.8692; that is, the difference is less than 0.2. The signal-to-noise ratio is measured with sufficient precision. It is preferable to have a ratio of more than four. The signal-to-noise ratio of 16.795 suggests a good signal. The design space may be navigated using this concept. The anticipated R^2 value of 0.6130 for the second model, the BTE, is in reasonable agreement with the corrected R^2 value of 0.7322; that is, the difference is less than 0.2. The appropriate precision ratio is 13.368 and shows that the signal is sufficient. The design space may be navigated using this concept. The projected R^2 value of 0.6274 for the third model, BSFC, is in reasonable agreement with the adjusted R^2 value of 0.7485; that is, the difference is less than 0.2. The appropriate precision ratio is 13.807, indicating that the signal is sufficient. The design space may be navigated using this concept. The 3D response surface plots for three output responses, using RSM, are shown in Figure 12. In detail, Figure 11 shows the map variation between the engine speed and different types of fuels on the *y*-axis, where values of 1, 2, 3, and 4, represent pure diesel, palm, sunflower, and corn biodiesel fuel, respectively. The outputs are BT, BTE, and BSFC, displayed in Figure 12a–c, respectively. The physical meanings of Figure 12 were analyzed in Section 3.1, whereas comparison of the predicted and actual values of output responses is presented in Figure 13. In general, the average R^2 value for both training and testing is 0.783 and 0.656, respectively.

Table 11. Statistical analysis of the ANOVA model.

First ANOVA Model of Brake Torque			
Std. Dev.	0.3485	R^2	0.9128
Mean	20.01	Adjusted R^2	0.8692
C.V.%	1.74	Predicted R^2	0.7278
		Adeq Precision	16.7946
Second ANOVA Model of R_z			
Std. Dev.	0.6386	R^2	0.7818
Mean	18.24	Adjusted R^2	0.7322
C.V.%	3.50	Predicted R^2	0.6130
		Adeq Precision	13.368
Third ANOVA Model of BSFC			
Std. Dev.	0.0159	R^2	0.7951
Mean	0.4559	Adjusted R^2	0.7485
C.V.%	3.49	Predicted R^2	0.6274
		Adeq Precision	13.8074

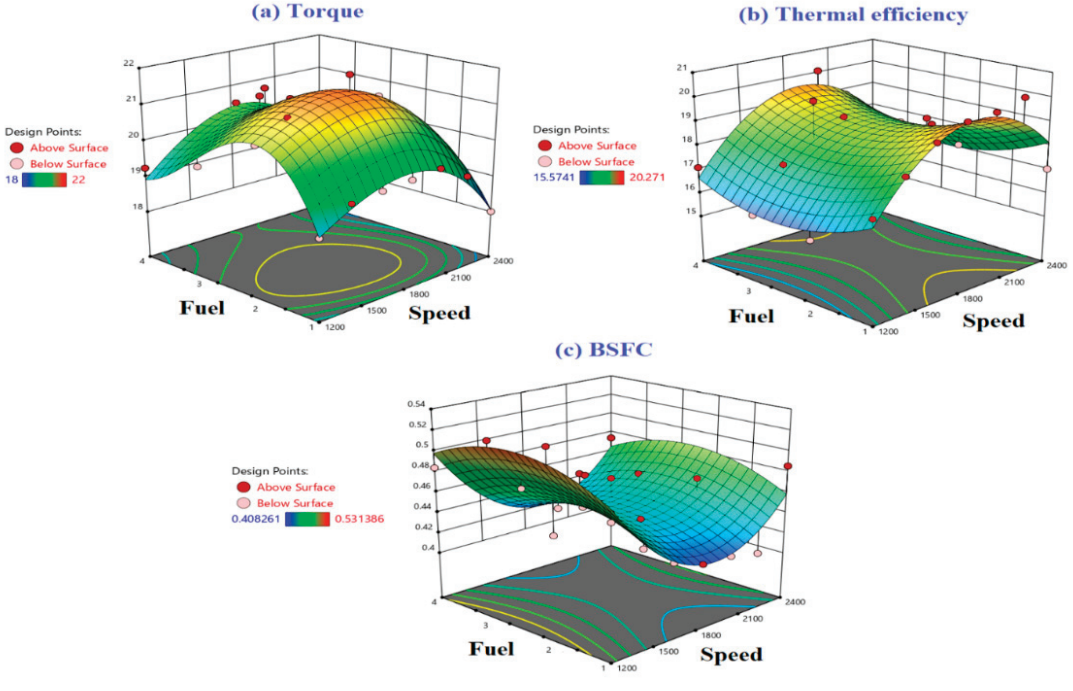

Figure 12. 3D response surface plots for three output responses.

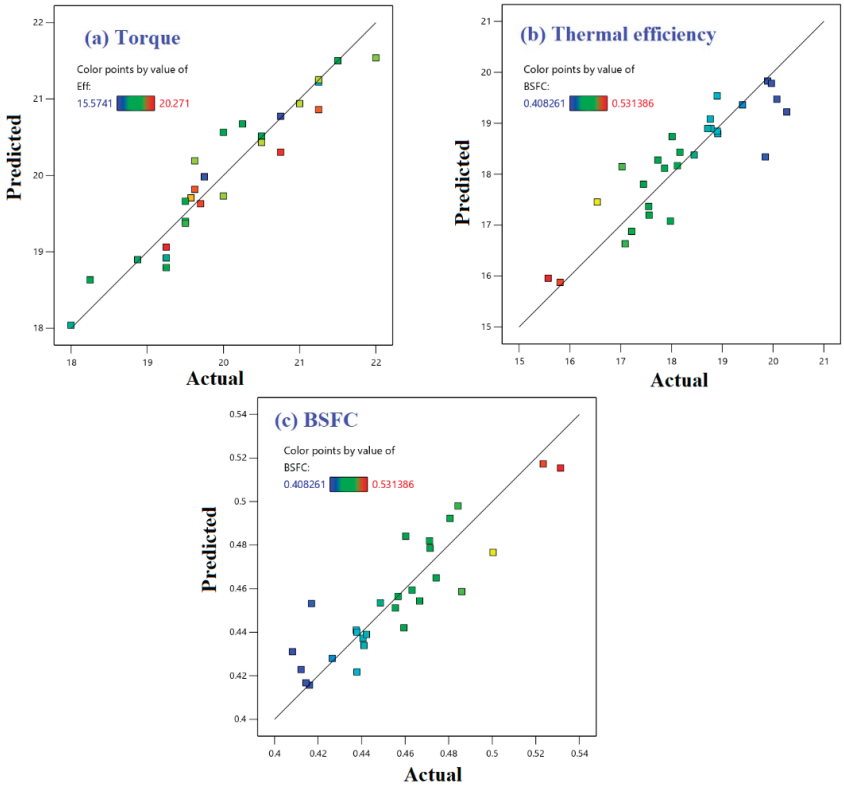

Figure 13. Comparison of the predicted and actual values of output responses.

3.3.4. Optimization-Based Response Surface Methodology (RSM)

The best input parameters and related output performance from the RSM-based optimization method are presented in Table 12. The best performance is achieved using corn oil, with an engine speed of 1862.7 rpm. Under this condition, the overall performance is increased by 0.268%, 1.9%, and 5.9%, as compared to pure diesel, palm oil, and sunflower oil, respectively.

Table 12. Optimization-based RSM.

Oil Type	Speed (rpm)	Torque (N.m)	Change (%)	Efficiency (%)	Change (%)	BSFC (kg_f/kWh)	Change (%)	Overall (%)
Diesel	1841.06	19.8057	0.0	19.8637	0.0	0.415	0.0	0.0
Palm Oil	1845.55	21.5087	+8.599	18.9295	−4.703	0.438	−5.542	−1.647
Sunflower	1844.47	20.9137	+5.594	18.8297	−5.205	0.44	−6.024	−5.635
Corn	1862.71	20.4353	+3.179	19.5726	−1.465	0.421	−1.446	0.268

3.4. Comparison Study

In summary, the average R^2 values for training and testing, using fuzzy logic, are 1 and 0.84801, respectively, whereas the average R^2 values for both training and testing are 0.783 and 0.656, respectively. Therefore, in comparison with the ANOVA, the average R^2 value, using fuzzy-based modeling, has been increased by 27.7% and 29.3%, for training and testing, respectively.

Twenty-eight experiments, using four different types of fuel (pure diesel, corn biodiesel, palm biodiesel, and sunflower biodiesel) were carried out. As a result, each fuel was tested seven times, relating to seven different speeds (1200 to 2400, step 200 rpm). The first experiment was used as a baseline to compare the three determinants, in terms of BT, BTE, and BSFC, to find the best improvement. The optimum improvement was selected according to the following equations:

$$\text{The optimum\% of improvement} = \text{\% of improvement of torque} + \text{\% of improvement of thermal efficiency} + \text{\% of improvement of BSFC} \tag{13}$$

$$\begin{aligned}&\text{\% of improvement @ specified speed}\\ &= \frac{(\text{Torque @ specified speed} - \text{Torque @ reference})}{\text{Torque @ reference}}\\ &+ \frac{(\text{Thermal efficiency @ specified speed} - \text{Thermal efficiency @ reference})}{\text{Thermal efficiency @ reference}}\\ &+ \frac{(\text{BSFC @ reference} - \text{Thermal efficiency @ specified speed})}{\text{Thermal efficiency @ reference}}\end{aligned} \tag{14}$$

Based on the particle swarm optimization process, the optimal engine speed is 1648 rpm, and the best fuel is sunflower oil. Under this condition, the overall performance has been increased by 2.065% and 8.256%, as compared to the experimental results and RSM. The performance comparison of experimental, RSM, and proposed strategy is presented in Table 13.

Table 13. Performance comparison of experimental, RSM and proposed strategy.

Method	Fuel Type	Speed (rpm)	Torque (N.m)	Change (%)	Efficiency (%)	Change (%)	BSFC (kg_f/kWh)	Change (%)	Overall (%)
Experimental	Sunflower Oil	1600	21.25	0.0	19.848	0.0	0.4169	0.0	0.00
RSM	Corn Oil	1862.71	20.4353	−3.834	19.5726	−1.388	0.421	−0.969	−6.191
Proposed	Sunflower Oil	1648	21.482	1.092	19.71	−0.696	0.41	1.669	2.065

4. Conclusions

The impact of utilizing various biodiesel blends, such as corn, sunflower, and palm biodiesels on the performance of a CI engine were examined experimentally in this research paper. According to the experimental observations and main findings, the most important outcomes can be concluded as follows:

- When compared to pure diesel, all biodiesel blends boost brake power. Because of its slightly higher calorific value and higher oxygen content, palm biodiesel offers the highest brake power increase of 8.7%, compared to other biodiesel blends.
- On average, there is a reduction in BTE of 6.7%, 4.4%, and 2.4% for palm, sunflower, and corn biodiesels, respectively, as compared to pure diesel. For all the biodiesel blends, BSFC increases, while heating value decreases. However, in this case, the increase in brake-specific fuel consumption is more significant. This explains why biodiesel blends have a poorer BTE, despite their low heating value. Furthermore, biodiesel mixes have a shorter ignition delay than pure diesel, implying that combustion starts sooner. More heat is lost to the atmosphere, as a result of the shorter ignition delay, necessitating more power for the piston to perform the compression stroke.
- Palm, sunflower, and corn biodiesels had an average increase in BSFC of 7.4%, 4.9%, and 2.5%, respectively, compared to pure diesel. Because biodiesel blends have a lower calorific value than pure diesel, they consume more fuel to provide the same braking power output.
- Palm biodiesel has the highest kinematic viscosity, resulting in poor fuel atomization and mixture formation, as well as a larger BSFC rise than the other test fuels.

- The physical and chemical characteristics of biodiesel blends, such as oxygen content, cetane number, calorific value, kinematic viscosity, and latent heat of vaporization have a direct impact on combustion efficiency.
- The average R^2 value, utilizing a fuzzy-based model, has been increased by 27.7% and 29.3%, for training and testing, respectively, as compared to ANOVA.
- Based on the optimization process using PSO, the optimal engine speed is 1648 rpm, and the best fuel is sunflower oil.
- Using the proposed strategy (integration between fuzzy logic and PSO), the overall performance has been increased by 2.065% and 8.256%, as compared to the experimental results and RSM.

Author Contributions: Conceptualization, A.A., H.R. and M.A.-Z.; methodology, A.A., H.R., H.A. and W.A.; software, H.R., A.A.A., H.A. and M.R.G., validation, A.A., H.A. and R.M.G.; formal analysis, A.A., M.A.-Z. and H.R.; investigation, A.A., H.R. and A.O.M.; resources, H.R.; data curation, A.A., H.R., M.A.-Z. and W.A.; writing—original draft preparation, A.A., H.R., H.A. and A.O.M.; writing—review and editing, A.A., H.R. and A.O.M.; visualization, A.A., H.R., H.A. and R.M.G.; supervision, A.A. and H.R.; project administration, A.A., A.A.A. and H.R.; funding acquisition, H.R., A.A.A. and R.M.G. All authors have read and agreed to the published version of the manuscript.

Funding: Princess Nourah bint Abdulrahman University Researchers Supporting Project number (PNURSP2022R138), Princess Nourah bint Abdulrahman University, Riyadh, Saudi Arabia.

Institutional Review Board Statement: Not applicable.

Informed Consent Statement: Not applicable.

Acknowledgments: We would like to thank Princess Nourah bint Abdulrahman University Researchers Supporting Project number (PNURSP2022R138), Princess Nourah bint Abdulrahman University, Riyadh, Saudi Arabia.

Conflicts of Interest: The authors declare no conflict of interest.

Nomenclatures

AI	artificial intelligence
ANFIS	adaptive network-based fuzzy inference system
ANN	artificial neural network
ANOVA	analysis of variance
ASTM	American Society for Testing and Materials
B_0, B_i, B_{ii}, and B_{ij}	regression coefficients
BP	brake power
BSFC	brake specific fuel consumption
BT	brake torque
BTDC	before top dead center
BTE	brake thermal efficiency
c_1, c_2	a cognitive and social factor
CFPP	cold filter plugging point
CN	cetane number
CO	carbon monoxide
DC	direct current
F	fuel type
FS	full scale
FSD	full scale deflection
FTIR	Fourier-transform infrared spectroscopy
g_{best}	the global best
K	number of factors
M	mean of the gaussian curve
MF	fuzzy membership function of the input
MSE	mean square error

N	rotation engine speed
NOx	nitrogen oxides
NREL	national renewable energy laboratory
P_{best}	best solution
PSO	particle swarm optimization
R	outcome function
r	random value
RMS	root mean square
RMSE	root mean square error
rpm	revolution per minute
RSM	response surface methodology
RTD	resistance temperature detectors
R^2	coefficient of determination
S	speed
SFC	specific fuel consumption
TBHQ	tert-butylhydroquinone
V	velocity
vol.	volume
W_R	uncertainty error
Wt.	weight
x	Variable, factors
Y	predicted output response
ω	realistic error
σ	spread of the curve

References

1. Chaichan, M.T. Performance and Emission Characteristics of CIE Using Hydrogen, Biodiesel, and Massive EGR. *Int. J. Hydrogen Energy* **2018**, *43*, 5415–5435. [CrossRef]
2. Aladayleh, W.; Alahmer, A. Recovery of Exhaust Waste Heat for ICE Using the Beta Type Stirling Engine. *J. Energy* **2015**, 1–8. [CrossRef]
3. Alahmer, A.I.; Adaileh, W.M.; Al Zubi, M.A. Monitoring of a Spark Ignition Engine Malfunctions Using Acoustic Signal Technique. *Int. J. Veh. Noise Vib.* **2014**, *10*, 201–213. [CrossRef]
4. Zacharczuk, W.; Andruszkiewicz, A.; Tatarek, A.; Alahmer, A.; Alsaqoor, S. Effect of Ca-Based Additives on the Capture of SO_2 during Combustion of Pulverized Lignite. *Energy* **2021**, *231*, 120988. [CrossRef]
5. Gomaa, M.R.; Al-Dmour, N.; AL-Rawashdeh, H.A.; Shalby, M. Theoretical Model of a Fluidized Bed Solar Reactor Design with the Aid of MCRT Method and Synthesis Gas Production. *Renew. Energy* **2020**, *148*, 91–102. [CrossRef]
6. Borowski, G.; Alsaqoor, S.; Alahmer, A. Using Agglomeration Techniques for Coal and Ash Waste Management in the Circular Economy. *Adv. Sci. Technol. Res. J.* **2021**, *15*, 264–276. [CrossRef]
7. Taghizadeh-Alisaraei, A.; Ghobadian, B.; Tavakoli-Hashjin, T.; Mohtasebi, S.S. Vibration Analysis of a Diesel Engine Using Biodiesel and Petrodiesel Fuel Blends. *Fuel* **2012**, *102*, 414–422. [CrossRef]
8. Dal, H.; Emiroğlu, A.O.; Bilge, H.; Şen, M. Experimental Investigation of the Effects of Chicken and Turkey Biodiesel Blends on Diesel Engine Noise Emissions. *Int. J. Environ. Sci. Technol.* **2019**, *16*, 5147–5154. [CrossRef]
9. Alahmer, A. Reduction a Particulate Matter of Diesel Emission by the Use of Several Oxygenated Diesel Blend Fuels. *Int. J. Therm. Environ. Eng.* **2014**, *7*, 45–50.
10. Gomaa, M.R.; Mustafa, R.J.; Al-Dmour, N. Solar Thermochemical Conversion of Carbonaceous Materials into Syngas by Co-Gasification. *J. Clean. Prod.* **2020**, *248*, 119185. [CrossRef]
11. Dey, S.; Deb, M.; Das, P.K. An Investigation of Diesohol-Biodiesel Mixture in Performance-Emission Characteristics of a Single Cylinder Diesel Engine: A Trade-off Benchmark. *Int. J. Automot. Mech. Eng.* **2019**, *16*, 7464–7479. [CrossRef]
12. Bae, C.; Kim, J. Alternative Fuels for Internal Combustion Engines. *Proc. Combust. Inst.* **2017**, *36*, 3389–3413. [CrossRef]
13. Hasan, A.O.; Osman, A.I.; Ala'a, H.; Al-Rawashdeh, H.; Abu-jrai, A.; Ahmad, R.; Gomaa, M.R.; Deka, T.J.; Rooney, D.W. An Experimental Study of Engine Characteristics and Tailpipe Emissions from Modern DI Diesel Engine Fuelled with Methanol/Diesel Blends. *Fuel Process. Technol.* **2021**, *220*, 106901. [CrossRef]
14. Reang, N.M.; Dey, S.; Deb, M.; Deb Barma, J. Effect of Diesel-biodiesel-alcohol Blends on Combustion, Performance, and Emission Characteristics of a Single Cylinder Compression Ignition Engine. *Environ. Prog. Sustain. Energy* **2021**, e13752. [CrossRef]
15. Song, J.T.; Zhang, C.H. An Experimental Study on the Performance and Exhaust Emissions of a Diesel Engine Fuelled with Soybean Oil Methyl Ester. *Proc. Inst. Mech. Eng. Part D J. Automob. Eng.* **2008**, *222*, 2487–2496. [CrossRef]
16. Ramadhas, A.S.; Muraleedharan, C.; Jayaraj, S. Performance and Emission Evaluation of a Diesel Engine Fueled with Methyl Esters of Rubber Seed Oil. *Renew. Energy* **2005**, *30*, 1789–1800. [CrossRef]

17. Pinzi, S.; Garcia, I.L.; Lopez-Gimenez, F.J.; Luque de Castro, M.D.; Dorado, G.; Dorado, M.P. The Ideal Vegetable Oil-Based Biodiesel Composition: A Review of Social, Economical and Technical Implications. *Energy Fuels* **2009**, *23*, 2325–2341. [CrossRef]
18. Labeckas, G.; Slavinskas, S. Comparative Evaluation of the Combustion Process and Emissions of a Diesel Engine Operating on the Cetane Improver 2-Ethylhexyl Nitrate Doped Rapeseed Oil and Aviation JP-8 Fuel. *Energy Convers. Manag. X* **2021**, *11*, 100106. [CrossRef]
19. Graboski, M.S.; McCormick, R.L.; Alleman, T.L.; Herring, A.M. The Effect of Biodiesel Composition on Engine Emissions from a DDC Series 60 Diesel Engine. *Natl. Renew. Energy Lab.* **2003**. Available online: https://www.nrel.gov/docs/fy03osti/31461.pdf (accessed on 25 November 2021).
20. Broatch, A.; Tormos, B.; Olmeda, P.; Novella, R. Impact of Biodiesel Fuel on Cold Starting of Automotive Direct Injection Diesel Engines. *Energy* **2014**, *73*, 653–660. [CrossRef]
21. Rakopoulos, D.C.; Rakopoulos, C.D.; Giakoumis, E.G.; Dimaratos, A.M.; Founti, M.A. Comparative Environmental Behavior of Bus Engine Operating on Blends of Diesel Fuel with Four Straight Vegetable Oils of Greek Origin: Sunflower, Cottonseed, Corn and Olive. *Fuel* **2011**, *90*, 3439–3446. [CrossRef]
22. Sureshkumar, K.; Velraj, R.; Ganesan, R. Performance and Exhaust Emission Characteristics of a CI Engine Fueled with Pongamia Pinnata Methyl Ester (PPME) and Its Blends with Diesel. *Renew. Energy* **2008**, *33*, 2294–2302. [CrossRef]
23. Rakopoulos, C.D.; Antonopoulos, K.A.; Rakopoulos, D.C.; Hountalas, D.T.; Giakoumis, E.G. Comparative Performance and Emissions Study of a Direct Injection Diesel Engine Using Blends of Diesel Fuel with Vegetable Oils or Bio-Diesels of Various Origins. *Energy Convers. Manag.* **2006**, *47*, 3272–3287. [CrossRef]
24. Atmanlı, A.; Ileri, E.; Yüksel, B. Experimental Investigation of Engine Performance and Exhaust Emissions of a Diesel Engine Fueled with Diesel–n-Butanol–Vegetable Oil Blends. *Energy Convers. Manag.* **2014**, *81*, 312–321. [CrossRef]
25. Chacko, N.; Jeyaseelan, T. Comparative Evaluation of Graphene Oxide and Graphene Nanoplatelets as Fuel Additives on the Combustion and Emission Characteristics of a Diesel Engine Fuelled with Diesel and Biodiesel Blend. *Fuel Process. Technol.* **2020**, *204*, 106406. [CrossRef]
26. Gad, M.S.; Jayaraj, S. A Comparative Study on the Effect of Nano-Additives on the Performance and Emissions of a Diesel Engine Run on Jatropha Biodiesel. *Fuel* **2020**, *267*, 117168. [CrossRef]
27. Rajak, U.; Chaurasiya, P.K.; Nashine, P.; Verma, M.; Kota, T.R.; Verma, T.N. Financial Assessment, Performance and Emission Analysis of Moringa Oleifera and Jatropha Curcas Methyl Ester Fuel Blends in a Single-Cylinder Diesel Engine. *Energy Convers. Manag.* **2020**, *224*, 113362. [CrossRef]
28. Tasca, A.L.; di Capaci, R.B.; Tognotti, L.; Puccini, M. Biomethane from Short Rotation Forestry and Microalgal Open Ponds: System Modeling and Life Cycle Assessment. *Bioresour. Technol.* **2019**, *273*, 468–477. [CrossRef]
29. Dey, S.; Reang, N.M.; Das, P.K.; Deb, M. A Comprehensive Study on Prospects of Economy, Environment, and Efficiency of Palm Oil Biodiesel as a Renewable Fuel. *J. Clean. Prod.* **2021**, *286*, 124981. [CrossRef]
30. Yee, K.F.; Tan, K.T.; Abdullah, A.Z.; Lee, K.T. Life Cycle Assessment of Palm Biodiesel: Revealing Facts and Benefits for Sustainability. *Appl. Energy* **2009**, *86*, S189–S196. [CrossRef]
31. Jiaqiang, E.; Liu, T.; Yang, W.M.; Li, J.; Gong, J.; Deng, Y. Effects of Fatty Acid Methyl Esters Proportion on Combustion and Emission Characteristics of a Biodiesel Fueled Diesel Engine. *Energy Convers. Manag.* **2016**, *117*, 410–419.
32. Boudy, F.; Seers, P. Impact of Physical Properties of Biodiesel on the Injection Process in a Common-Rail Direct Injection System. *Energy Convers. Manag.* **2009**, *50*, 2905–2912. [CrossRef]
33. Erdoğan, S.; Aydın, S.; Balki, M.K.; Sayin, C. Operational Evaluation of Thermal Barrier Coated Diesel Engine Fueled with Biodiesel/Diesel Blend by Using MCDM Method Base on Engine Performance, Emission and Combustion Characteristics. *Renew. Energy* **2020**, *151*, 698–706. [CrossRef]
34. Patel, C.; Tiwari, N.; Agarwal, A.K. Experimental Investigations of Soyabean and Rapeseed SVO and Biodiesels on Engine Noise, Vibrations, and Engine Characteristics. *Fuel* **2019**, *238*, 86–97. [CrossRef]
35. Krishania, N.; Rajak, U.; Chaurasiya, P.K.; Singh, T.S.; Birru, A.K.; Verma, T.N. Investigations of Spirulina, Waste Cooking and Animal Fats Blended Biodiesel Fuel on Auto-Ignition Diesel Engine Performance, Emission Characteristics. *Fuel* **2020**, *276*, 118123. [CrossRef]
36. Singh, T.S.; Verma, T.N. Analysis of the Effect of Temperature on the Morphology of Egg Shell Calcium Oxide Catalyst: Catalyst Production for Biodiesel Preparation. *Sci. Iran.* **2020**, *27*, 2915–2923.
37. Nalgundwar, A.; Paul, B.; Sharma, S.K. Comparison of Performance and Emissions Characteristics of DI CI Engine Fueled with Dual Biodiesel Blends of Palm and Jatropha. *Fuel* **2016**, *173*, 172–179. [CrossRef]
38. Sanjid, A.; Masjuki, H.H.; Kalam, M.A.; Abedin, M.J.; Rahman, S.M.A. Experimental Investigation of Mustard Biodiesel Blend Properties, Performance, Exhaust Emission and Noise in an Unmodified Diesel Engine. *APCBEE Procedia* **2014**, *10*, 149–153. [CrossRef]
39. Ndayishimiye, P.; Tazerout, M. Use of Palm Oil-Based Biofuel in the Internal Combustion Engines: Performance and Emissions Characteristics. *Energy* **2011**, *36*, 1790–1796. [CrossRef]
40. Patel, C.; Agarwal, A.K.; Tiwari, N.; Lee, S.; Lee, C.S.; Park, S. Combustion, Noise, Vibrations and Spray Characterization for Karanja Biodiesel Fuelled Engine. *Appl. Therm. Eng.* **2016**, *106*, 506–517. [CrossRef]

41. Bhowmik, S.; Panua, R.; Ghosh, S.K.; Paul, A.; Debroy, D. Prediction of Performance and Exhaust Emissions of Diesel Engine Fuelled with Adulterated Diesel: An Artificial Neural Network Assisted Fuzzy-Based Topology Optimization. *Energy Environ.* **2018**, *29*, 1413–1437. [CrossRef]
42. Alahmer, A.; Ajib, S. Solar Cooling Technologies: State of Art and Perspectives. *Energy Convers. Manag.* **2020**, *214*, 112896. [CrossRef]
43. Rajak, U.; Nashine, P.; Singh, T.S.; Verma, T.N. Numerical Investigation of Performance, Combustion and Emission Characteristics of Various Biofuels. *Energy Convers. Manag.* **2018**, *156*, 235–252. [CrossRef]
44. Dey, S.; Deb, M.; Das, P.K. Application of Fuzzy-Assisted Grey Taguchi Approach for Engine Parameters Optimization on Performance-Emission of a CI Engine. *Energy Sources Part A Recover. Util. Environ. Eff.* **2019**, 1–17. [CrossRef]
45. Umeuzuegbu, J.C.; Okiy, S.; Nwobi-Okoye, C.C.; Onukwuli, O.D. Computational Modeling and Multi-Objective Optimization of Engine Performance of Biodiesel Made with Castor Oil. *Heliyon* **2021**, *7*, e06516. [CrossRef] [PubMed]
46. Ismail, H.M.; Ng, H.K.; Queck, C.W.; Gan, S. Artificial Neural Networks Modelling of Engine-out Responses for a Light-Duty Diesel Engine Fuelled with Biodiesel Blends. *Appl. Energy* **2012**, *92*, 769–777. [CrossRef]
47. Li, J.; Wu, D.; Attar, H.M.; Xu, H. Geometric Neuro-Fuzzy Transfer Learning for in-Cylinder Pressure Modelling of a Diesel Engine Fuelled with Raw Microalgae Oil. *Appl. Energy* **2022**, *306*, 118014. [CrossRef]
48. Salam, S.; Verma, T.N. An Empirical Investigation on the Influence of Operating Conditions on Internal Combustion Engine Behavior and Their Graded Significance. *Energy Sources Part A Recover. Util. Environ. Eff.* **2021**, 1–19. [CrossRef]
49. Salam, S.; Verma, T.N. Analysis of Significance of Variables in IC Engine Operation: An Empirical Methodology. *Energy Convers. Manag.* **2020**, *207*, 112520. [CrossRef]
50. Salam, S.; Choudhary, T.; Pugazhendhi, A.; Verma, T.N.; Sharma, A. A Review on Recent Progress in Computational and Empirical Studies of Compression Ignition Internal Combustion Engine. *Fuel* **2020**, *279*, 118469. [CrossRef]
51. Dey, S.; Reang, N.M.; Das, P.K.; Deb, M. Comparative Study Using RSM and ANN Modelling for Performance-Emission Prediction of CI Engine Fuelled with Bio-Diesohol Blends: A Fuzzy Optimization Approach. *Fuel* **2021**, *292*, 120356. [CrossRef]
52. Krishnamoorthi, M.; Malayalamurthi, R.; Sakthivel, R. Optimization of Compression Ignition Engine Fueled with Diesel-Chaulmoogra Oil-Diethyl Ether Blend with Engine Parameters and Exhaust Gas Recirculation. *Renew. Energy* **2019**, *134*, 579–602. [CrossRef]
53. Dey, S.; Reang, N.M.; Deb, M.; Das, P.K. Study on Performance-Emission Trade-off and Multi-Objective Optimization of Diesel-Ethanol-Palm Biodiesel in a Single Cylinder CI Engine: A Taguchi-Fuzzy Approach. Energy Sources Part A Recover. *Util. Environ. Eff.* **2020**, 1–21. [CrossRef]
54. Reang, N.M.; Dey, S.; Debbarma, J.; Deb, M. Effect of Linseed Methyl Ester and Diethyl Ether on the Performance–Emission Analysis of a CI Engine Based on Taguchi-Fuzzy Optimisation. *Int. J. Ambient Energy* **2019**, 1–15. [CrossRef]
55. Shirneshan, A.; Bagherzadeh, S.A.; Najafi, G.; Mamat, R.; Mazlan, M. Optimization and Investigation the Effects of Using Biodiesel-Ethanol Blends on the Performance and Emission Characteristics of a Diesel Engine by Genetic Algorithm. *Fuel* **2021**, *289*, 119753. [CrossRef]
56. Patil, A.R.; Desai, A.D. Parametric Optimization of Engine Performance and Emission for Various N-Butanol Blends at Different Operating Parameter Condition. *Alex. Eng. J.* **2020**, *59*, 851–864. [CrossRef]
57. Rith, M.; Gitano-Briggs, H.W.; Gonzaga, J.A.; Biona, J.B.M. Optimization of Control Factors for a Diesel Engine Fueled with Jatropha Seed Producer Gas on Dual Fuel Mode. *Int. Energy J.* **2019**, *19*, 149–158.
58. Ghanbari, M.; Mozafari-Vanani, L.; Dehghani-Soufi, M.; Jahanbakhshi, A. Effect of Alumina Nanoparticles as Additive with Diesel-Biodiesel Blends on Performance and Emission Characteristic of a Six-Cylinder Diesel Engine Using Response Surface Methodology (RSM). *Energy Convers. Manag. X* **2021**, *11*, 100091. [CrossRef]
59. Devarajan, Y.; Mahalingam, A.; Munuswamy, D.B.; Arunkumar, T. Combustion, Performance, and Emission Study of a Research Diesel Engine Fueled with Palm Oil Biodiesel and Its Additive. *Energy Fuels* **2018**, *32*, 8447–8452. [CrossRef]
60. Zahan, K.A.; Kano, M. Biodiesel Production from Palm Oil, Its by-Products, and Mill Effluent: A Review. *Energies* **2018**, *11*, 2132. [CrossRef]
61. Avhad, M.R.; Marchetti, J.M. A Review on Recent Advancement in Catalytic Materials for Biodiesel Production. *Renew. Sustain. Energy Rev.* **2015**, *50*, 696–718. [CrossRef]
62. Charusiri, W.; Vitidsant, T. Response Surface Methodology Optimization of Biofuels Produced by Catalytic Pyrolysis of Residual Palm Oil from Empty Fruit Bunch over Magnesium Oxide. *J. Chem. Eng. Jpn.* **2017**, *50*, 727–736. [CrossRef]
63. Sommani, P.; Mankong, N.; Vitidsant, T.; Lothongkum, A.W. Cracking of Used Vegetable Oil Mixed with Polypropylene Waste in the Presence of Activated Carbon. *ASEAN Eng. J.* **2015**, *4*, 16–24.
64. Ito, T.; Sakurai, Y.; Kakuta, Y.; Sugano, M.; Hirano, K. Biodiesel Production from Waste Animal Fats Using Pyrolysis Method. *Fuel Process. Technol.* **2012**, *94*, 47–52. [CrossRef]
65. Alptekin, E.; Canakci, M.; Sanli, H. Biodiesel Production from Vegetable Oil and Waste Animal Fats in a Pilot Plant. *Waste Manag.* **2014**, *34*, 2146–2154. [CrossRef] [PubMed]
66. Rajaseenivasan, T.; Srithar, K. Performance Investigation on Solar Still with Circular and Square Fins in Basin with CO_2 Mitigation and Economic Analysis. *Desalination* **2016**, *380*, 66–74. [CrossRef]
67. Al-Dabbas, M.; Alahmer, A.; Mamkagh, A.; Gomaa, M.R. Productivity Enhancement of the Solar Still by Using Water Cooled Finned Condensing Pipe. *Desalin. Water Treat.* **2021**, *213*, 35–43. [CrossRef]

68. Giakoumis, E.G.; Sarakatsanis, C.K. A Comparative Assessment of Biodiesel Cetane Number Predictive Correlations Based on Fatty Acid Composition. *Energies* **2019**, *12*, 422. [CrossRef]
69. Shehata, M.S.; Attia, A.M.A.; Razek, S.M.A. Corn and Soybean Biodiesel Blends as Alternative Fuels for Diesel Engine at Different Injection Pressures. *Fuel* **2015**, *161*, 49–58. [CrossRef]
70. Kim, J.-K.; Yim, E.S.; Jeon, C.H.; Jung, C.-S.; Han, B.H. Cold Performance of Various Biodiesel Fuel Blends at Low Temperature. *Int. J. Automot. Technol.* **2012**, *13*, 293–300. [CrossRef]
71. El-Araby, R.; Amin, A.; El Morsi, A.K.; El-Ibiari, N.N.; El-Diwani, G.I. Study on the Characteristics of Palm Oil–Biodiesel–Diesel Fuel Blend. *Egypt. J. Pet.* **2018**, *27*, 187–194. [CrossRef]
72. Tutunea, D.; Dumitru, I. Analysis of Performance and Emissions of Diesel Engine Using Sunflower Biodiesel. *IOP Conf. Ser. Mater. Sci. Eng.* **2017**, *252*, 12085.
73. Naureen, R.; Tariq, M.; Yusoff, I.; Chowdhury, A.J.K.; Ashraf, M.A. Synthesis, Spectroscopic and Chromatographic Studies of Sunflower Oil Biodiesel Using Optimized Base Catalyzed Methanolysis. *Saudi J. Biol. Sci.* **2015**, *22*, 332–339. [CrossRef] [PubMed]
74. Rezk, H.; Nassef, A.M.; Inayat, A.; Sayed, E.T.; Shahbaz, M.; Olabi, A.G. Improving the Environmental Impact of Palm Kernel Shell through Maximizing Its Production of Hydrogen and Syngas Using Advanced Artificial Intelligence. *Sci. Total Environ.* **2019**, *658*, 1150–1160. [CrossRef] [PubMed]
75. Rezk, H.; Arfaoui, J.; Gomaa, M.R. Optimal Parameter Estimation of Solar PV Panel Based on Hybrid Particle Swarm and Grey Wolf Optimization Algorithms. *Int. J. Interact. Multimed. Artif. Intell.* **2021**, *6*, 145–155. [CrossRef]
76. Gao, D.; Li, X.; Chen, H. Application of Improved Particle Swarm Optimization in Vehicle Crashworthiness. *Math. Probl. Eng.* **2019**, *2019*, 8164609. [CrossRef]
77. Alahmer, A.; Yamin, J.; Sakhrieh, A.; Hamdan, M.A. Engine Performance Using Emulsified Diesel Fuel. *Energy Convers. Manag.* **2010**, *51*, 1708–1713. [CrossRef]
78. Alahmer, A. Influence of Using Emulsified Diesel Fuel on the Performance and Pollutants Emitted from Diesel Engine. *Energy Convers. Manag.* **2013**, *73*, 361–369. [CrossRef]
79. Adaileh, W.M.; AlQdah, K.S. Performance of Diesel Engine Fuelled by a Biodiesel Extracted from a Waste Cocking Oil. *Energy Procedia* **2012**, *18*, 1317–1334. [CrossRef]
80. Lapuerta, M.; Armas, O.; Rodriguez-Fernandez, J. Effect of Biodiesel Fuels on Diesel Engine Emissions. *Prog. Energy Combust. Sci.* **2008**, *34*, 198–223. [CrossRef]
81. Walle Mekonen, M.; Sahoo, N. Combined Effects of Fuel and Intake Air Preheating for Improving Diesel Engine Operating Parameters Running with Biodiesel Blends. *J. Renew. Sustain. Energy* **2018**, *10*, 43103. [CrossRef]
82. Muralidharan, K.; Vasudevan, D.; Sheeba, K.N. Performance, Emission and Combustion Characteristics of Biodiesel Fuelled Variable Compression Ratio Engine. *Energy* **2011**, *36*, 5385–5393. [CrossRef]
83. Buyukkaya, E. Effects of Biodiesel on a DI Diesel Engine Performance, Emission and Combustion Characteristics. *Fuel* **2010**, *89*, 3099–3105. [CrossRef]
84. Ganapathy, T.; Gakkhar, R.P.; Murugesan, K. Influence of Injection Timing on Performance, Combustion and Emission Characteristics of Jatropha Biodiesel Engine. *Appl. Energy* **2011**, *88*, 4376–4386. [CrossRef]
85. Abdullah, Z.; Suhaimi, H.; Abdullah, A.; Taufik, M.F.; Mrwan, A.G. Effect of Pentanol-Diesel Fuel Blends on Thermo-Physical Properties, Combustion Characteristics, Engine Performance and Emissions of a Diesel Engine. *Int. J. Automot. Mech. Eng.* **2018**, *15*, 5435–5450. [CrossRef]
86. Fayad, M.A.; Chaichan, M.T.; Dhahad, H.A. Engine Performance and PM Concentrations from the Combustion of Iraqi Sunflower Oil Biodiesel under Variable Diesel Engine Operating Conditions. *J. Phys. Conf. Ser.* **2021**, *1973*, 12051.
87. Abedin, M.J.; Masjuki, H.H.; Kalam, M.A.; Varman, M.; Arbab, M.I.; Fattah, I.M.; Masum, B.M. Experimental Investigation of a Multicylinder Unmodified Diesel Engine Performance, Emission, and Heat Loss Characteristics Using Different Biodiesel Blends: Rollout of B10 in Malaysia. *Sci. World J.* **2014**, *2014*, 349858. [CrossRef] [PubMed]
88. Masum, B.M.; Kalam, M.A.; Masjuki, H.H.; Palash, S.M.; Fattah, I.M.R. Performance and Emission Analysis of a Multi Cylinder Gasoline Engine Operating at Different Alcohol–Gasoline Blends. *RSC Adv.* **2014**, *4*, 27898–27904. [CrossRef]
89. Stone, R. *Introduction to Internal Combustion Engines*, 3rd ed.; Springer: Berlin/Heidelberg, Germany, 1999.
90. Khiraiya, K.; Ramana, D.V.; Panchal, H.; Sadasivuni, K.K.; Doranehgard, M.H.; Khalid, M. Diesel-Fired Boiler Performance and Emissions Measurements Using a Combination of Diesel and Palm Biodiesel. *Case Stud. Therm. Eng.* **2021**, *27*, 101324. [CrossRef]
91. Tat, M.E.; Van Gerpen, J.H. Effect of Temperature and Pressure on the Speed of Sound and Isentropic Bulk Modulus of Mixtures of Biodiesel and Diesel Fuel. *J. Am. Oil Chem. Soc.* **2003**, *80*, 1127–1130. [CrossRef]
92. Szybist, J.P.; Boehman, A.L.; Taylor, J.D.; McCormick, R.L. Evaluation of Formulation Strategies to Eliminate the Biodiesel NOx Effect. *Fuel Process. Technol.* **2005**, *86*, 1109–1126. [CrossRef]
93. Altıparmak, D.; Keskin, A.; Koca, A.; Gürü, M. Alternative Fuel Properties of Tall Oil Fatty Acid Methyl Ester–Diesel Fuel Blends. *Bioresour. Technol.* **2007**, *98*, 241–246. [CrossRef]
94. Ramakrishnan, S.; Karthick, J.; Saravanan, S.; LakshmiNarayanaRao, G. Engine Analysis of Single Cylinder DI Diesel Engine Fuelled With Sunflower Oil, Sunflower Oil Methyl Ester and Its Blends. In *ASME Internal Combustion Engine Division Fall Technical Conference*; World Congress and Exhibition: Sacramento, CA, USA, 2006; Volume 42606, pp. 219–224.

95. Rahman, S.M.A.; Masjuki, H.H.; Kalam, M.A.; Abedin, M.J.; Sanjid, A.; Sajjad, H. Production of Palm and Calophyllum Inophyllum Based Biodiesel and Investigation of Blend Performance and Exhaust Emission in an Unmodified Diesel Engine at High Idling Conditions. *Energy Convers. Manag.* **2013**, *76*, 362–367. [CrossRef]
96. Sharon, H.; Karuppasamy, K.; Kumar, D.R.S.; Sundaresan, A. A Test on DI Diesel Engine Fueled with Methyl Esters of Used Palm Oil. *Renew. Energy* **2012**, *47*, 160–166. [CrossRef]
97. Huang, J.; Wang, Y.; Qin, J.; Roskilly, A.P. Comparative Study of Performance and Emissions of a Diesel Engine Using Chinese Pistache and Jatropha Biodiesel. *Fuel Process. Technol.* **2010**, *91*, 1761–1767. [CrossRef]
98. Ozsezen, A.N.; Canakci, M.; Turkcan, A.; Sayin, C. Performance and Combustion Characteristics of a DI Diesel Engine Fueled with Waste Palm Oil and Canola Oil Methyl Esters. *Fuel* **2009**, *88*, 629–636. [CrossRef]
99. Dulger, Z.; Kaplan, C. *Utilization of Sunflower Methyl Ester as a Diesel Engine Fuel*; SAE Technical Paper; SAE International: Warrendale, PA, USA, 2001. [CrossRef]
100. Lin, B.-F.; Huang, J.-H.; Huang, D.-Y. Experimental Study of the Effects of Vegetable Oil Methyl Ester on DI Diesel Engine Performance Characteristics and Pollutant Emissions. *Fuel* **2009**, *88*, 1779–1785. [CrossRef]
101. Canakci, M.; Ozsezen, A.N.; Arcaklioglu, E.; Erdil, A. Prediction of Performance and Exhaust Emissions of a Diesel Engine Fueled with Biodiesel Produced from Waste Frying Palm Oil. *Expert Syst. Appl.* **2009**, *36*, 9268–9280. [CrossRef]
102. Suryanarayanan, S.; Janakiraman, V.M.; Rao, G.L.N.; Sampath, S. Comparative Study of the Performance and Emission Characteristics of Biodiesels from Different Vegetable Oils with Diesel. 2008. Available online: https://www.sae.org/publications/technical-papers/content/2008-01-1581/ (accessed on 20 July 2021).
103. Rama Krishna Reddy, E.; Subbalakshmi, Y.; Dhana Raju, V.; Appa Rao, K.; Harun Kumar, M.; Rami Reddy, S.; Tharun Sai, P. Assessment of Performance, Combustion and Emission Characteristics of the Diesel Engine Powered with Corn Biodiesel Blends. *Int. J. Ambient Energy* **2019**, 1–9. [CrossRef]
104. Holman, J.P. *Experimental Methods for Engineers*, 8th ed.; McGraw-Hill Education: New York, NY, USA, 2011.
105. Alahmer, A.; Aladayleh, W. Effect Two Grades of Octane Numbers on the Performance, Exhaust and Acoustic Emissions of Spark Ignition Engine. *Fuel* **2016**, *180*, 80–89. [CrossRef]
106. Bai, Y.; Saren, G.; Huo, W. Response Surface Methodology (RSM) in Evaluation of the Vitamin C Concentrations in Microwave Treated Milk. *J. Food Sci. Technol.* **2015**, *52*, 4647–4651. [CrossRef] [PubMed]
107. Nwosu, C.; Ayodele, O.; Ibrahim, H. Optimization of Hydrogen Production via Catalytic Autothermal Reforming of Crude Glycerol Using Response Surface Methodology and Artificial Neural Network. *Int. J. Energy Res.* **2021**, *45*, 18999–19013. [CrossRef]

mathematics

MDPI

Article

Numerical Method for Solving of the Anomalous Diffusion Equation Based on a Local Estimate of the Monte Carlo Method

Viacheslav V. Saenko [1,2,*], Vladislav N. Kovalnogov [1], Ruslan V. Fedorov [1,*], Dmitry A. Generalov [1] and Ekaterina V. Tsvetova [1]

[1] Laboratory for Interdisciplinary Problems of Energy Production, Ulyanovsk State Technical University, 32, Severny Venets St., 432027 Ulyanovsk, Russia; kvn@ulstu.ru (V.N.K.); dmgeneralov@mail.ru (D.A.G); katf0k@mail.ru (E.V.T)

[2] S.P. Kapitsa Scientific Research Institute of Technology, Ulyanovsk State University, 42, L. Tolstoy St., 432017 Ulyanovsk, Russia

* Correspondence: vvsaenko@inbox.ru (V.V.S.); r.fedorov@ulstu.ru (R.V.F.)

Abstract: This paper considers a method of stochastic solution to the anomalous diffusion equation with a fractional derivative with respect to both time and coordinates. To this end, the process of a random walk of a particle is considered, and a master equation describing the distribution of particles is obtained. It has been shown that in the asymptotics of large times, this process is described by the equation of anomalous diffusion, with a fractional derivative in both time and coordinates. The method has been proposed for local estimation of the solution to the anomalous diffusion equation based on the simulation of random walk trajectories of a particle. The advantage of the proposed method is the opportunity to estimate the solution directly at a given point. This excludes the systematic component of the error from the calculation results and allows constructing the solution as a smooth function of the coordinate.

Keywords: anomalous diffusion equation; continuous time random walk; Monte Carlo method; local estimate

MSC: 58J65; 60J60; 65C05

Citation: Saenko, V.V.; Kovalnogov, V.N.; Fedorov, R.V.; Generalov, D.A.; Tsvetova, E.V. Numerical Method for Solving of the Anomalous Diffusion Equation Based on a Local Estimate of the Monte Carlo Method. *Mathematics* **2022**, *10*, 511. https://doi.org/10.3390/math10030511

Academic Editors: Camelia Petrescu and Valeriu David

Received: 30 December 2021
Accepted: 3 February 2022
Published: 5 February 2022

Publisher's Note: MDPI stays neutral with regard to jurisdictional claims in published maps and institutional affiliations.

Copyright: © 2022 by the authors. Licensee MDPI, Basel, Switzerland. This article is an open access article distributed under the terms and conditions of the Creative Commons Attribution (CC BY) license (https://creativecommons.org/licenses/by/4.0/).

1. Introduction

Anomalous diffusion processes are characterized by a power-law dependence of the width of the diffusion packet on time $\Delta(t) \propto D_\alpha t^\gamma$, where D_α is the diffusion coefficient [1–4]. Depending on the value of the exponent γ, different diffusion regimes are distinguished: $\gamma < 1/2$ (a sub-diffusion), $\gamma = 1/2$ (a normal diffusion), $\gamma > 1/2$ (a super-diffusion). If $\gamma = 1$, then the quasi-ballistic regime is established, if $\gamma > 1$, then this regime bears the name super-ballistic. More detailed information about various regimes can be found in the works [5–8].

The Continuous Time Random Walk (CTRW) model underlies the model of anomalous diffusion [9]. This model was first introduced in the work [10] and was further developed in the works [4,11–13] (see also survey articles [9,14,15]). The CTRW model describes the random walk of a particle using a hopping-trap mechanism. The random walk of a particle represents a sequence of instantaneous random jumps of the value R_i, $i = 1, 2, 3, \ldots$ and rest states with random rest times T_i, $i = 1, 2, 3, \ldots$, which successively change one another. With a power-law distribution of the free path value $p(x) \propto x^{-\alpha-1}, x \to \infty, 0 < \alpha \leqslant 2$ and rest time $q(t) \propto t^{-\beta-1}, t \to \infty, 0 < \beta \leqslant 1$, the width of the diffusion packet will grow according to the power law $\Delta(t) \propto D_\alpha t^\gamma$. Within this model, normal diffusion is obtained if the probability density of the path distribution $p(x)$ has a finite second moment $\langle R^2 \rangle < \infty$ [6], and the probability density of the rest time distribution $q(t)$ has the finite mathematical expectation $\langle T \rangle < \infty$ [7].

The asymptotic distribution of particles in the CTRW process was first obtained by M. Kotulski in the article [16]. Later, independently from M. Kotulski, these distributions were obtained in the article [17] in which these distribution were called fractional stable distributions. It is well known that the anomalous diffusion equation is an asymptotic description of the CTRW process. The articles [18–20] are devoted to the solution of the anomalous diffusion equation. These papers show that the solution of the anomalous diffusion equation is expressed through the classes of the fractional stable and stable distributions.

Anomalous diffusion generalizes normal diffusion to the case of considering transport processes in inhomogeneous and turbulent media. The model of anomalous diffusion was first used to describe charge transfer in amorphous semiconductors [10–13]. Later, the model of anomalous diffusion became widespread in the description of transport processes in turbulent plasma [21–27], propagation of cosmic rays in the galaxy [28–32], studying the diffusion of microRNA in the cell [33], the fluctuation of prices on exchanges and currency exchange rates [34]. The theory of combustion is one of the few areas where anomalous diffusion has not become widespread yet. However, recently, this direction has been intensively developing. The authors of [35,36] point out that anomalous diffusion occurs during heat transfer in low-dimensional systems. In the paper [37] devoted to the study of thermal radiation during the combustion of natural gas and acetylene, it was found that the combustion process was of a subdiffusion nature.

The assumption about the formation of anomalous diffusion in the combustion process allows introducing fractional differential equations of diffusion into consideration. In the papers [38–40], the effective thermal conductivity coefficient was obtained for the Levy–Fokker–Planck and fractional Boltzmann equations. The authors of [41–43] propose to use the fractional differential equation of diffusion to describe the combustion process

$$ {}_0D_t^{\beta} u = \partial_{xx} u + s(u), \quad t > 0, \quad 0 < x < L, $$

where ${}_0D_t^{\beta}$ is the fractional Riemann-Liouville derivative (Appendix A, A2) of the order $0 < \beta < 1$ in terms of time and ∂_{xx} is the classical second-order partial derivative with respect to the coordinate. The paper considers the problem when the source $f(u)$ is singular, and the initial and boundary conditions are chosen in the form $u(x,0) = u_0(x)$, $u(0,t) = u(L,t) = 0$. The paper [41] examines the damping effect in the framework of the investigated model, and the paper [42] explores the phenomenon of explosion and the possibility of describing this phenomenon with the help of the passage to the limit $\beta \to 0$. The authors of [44] examine a two-dimensional combustion model with a fractional time derivative. To solve the fractional-differential diffusion equation, the authors develop an adaptive finite-difference discontinuous Galerkin method. In the paper [45], the authors consider a fractional-differential combustion model with the first derivative with respect to time and a fractional derivative with respect to the spatial variable.

$$ \partial_t u = \frac{\partial^{\alpha}}{\partial |x|^{\alpha}} u + s(u), \quad u(x,0) = u_0(x), \quad u(a,t) = u(b,t) = 0. $$

Here, ∂_t is the partial time derivative, and $\frac{\partial^{\alpha}}{\partial |x|^{\alpha}}$ is the fractional-differential Riesz operator (A4). Using this fractional-differential model of combustion, the paper investigates the effect on the damping phenomenon of a quantity of the order of the fractional derivative α, the spatial size of the area under study, and the initial conditions. To solve the fractional-differential combustion equation, finite-difference methods of solving the equations are used. In the article [46], a fractional-differential generalization of the kinetic equation was obtained that describes the dependence of the radius of the ball on time in the model of combustion of a fireball, which was theoretically predicted by the Soviet physicist Ya.B. Zeldovich [47].

As we can see, the use of the anomalous diffusion model and the fractional-differential generalization of the diffusion equation for modeling combustion processes is only in the initial state. One of the reasons for this is the complexity of solving such kind of equations.

Finite-difference methods were used to solve fractional-differential diffusion equations in the works considered above [41–43,45]. However, in these works, fractional differential equations are studied in which only one of the derivatives has a fractional order: the time derivative or the coordinate derivative. In this paper, we will propose a method for the numerical solution to the anomalous diffusion equation with a fractional derivative in both time and coordinate and with a source of a special type.

$$ {}_0D_t^{\beta}\rho(x,t) = D\frac{\partial^{\alpha}}{\partial|x|^{\alpha}}\rho(x,t) + \frac{t^{-\beta}}{\Gamma(1-\beta)}\delta(x), $$

with boundary conditions $\rho(x,t) \to 0$ if $x \to \pm\infty$ and $\rho(x,t) = 0$, if $t < 0$. Here, $0 < \beta \leqslant 1$, $0 < \alpha \leqslant 2$, D is the generalized diffusion coefficient.

2. Master Equation of the CTRW Process

To obtain the master equation of the CTRW process, we use the approach proposed in the paper [48] and further developed in the paper [49]. Consider the collision density $f(\mathbf{r},\mathbf{p},t)$, where $\mathbf{r}$ is the radius of the particle vector, $\mathbf{p}$ is the particle impulse, and t is time. The value $f(\mathbf{r},\mathbf{p},t)d\mathbf{r}\,d\mathbf{p}\,dt$ is the number of collisions in the volume element, and $d\mathbf{r}$ is the vicinity of the point $\mathbf{r}$ for the time interval dt, at which the particle impulse takes the value from $\mathbf{p}$ to $\mathbf{p}+d\mathbf{p}$. We will consider the nonrelativistic case $\mathbf{p} = m\mathbf{v}$. Without losing generality, we will assume that $m = 1$. It was shown in the paper [49] that if there are n discrete states, the value $f(\mathbf{r},\mathbf{v},t)$ can be presented in the form

$$ f(\mathbf{r},\mathbf{v},t) = \sum_{j=1}^{n} f_j(\mathbf{r},\mathbf{v},t), \tag{1} $$

where

$$ f_j(\mathbf{r},\mathbf{v},t) = s_j(\mathbf{r},\mathbf{v},t) + \sum_{i=1}^{n} c_{ij}\int_0^t k_i(\tau)d\tau \int W_{ij}(\mathbf{\Omega}',\mathbf{\Omega})d\mathbf{\Omega}'\times $$
$$ \int f_i(\mathbf{r}-v'\mathbf{\Omega}'\tau, v'\mathbf{\Omega}', t-\tau)h_{ij}(v',v)dv'. \tag{2} $$

Here, $k_i(\tau)$ is the probability density distribution of residence time in the state i and c_{ij} are the probabilities of passing from the state i into the state j, $W_{ij}(\mathbf{\Omega}',\mathbf{\Omega})$ is the density of probability of the fact that before the collision, the velocity had its direction $\mathbf{\Omega}'$; after the collision, the direction obtained the value $\mathbf{\Omega}$, $h_{ij}(v',v)$ is the probability density of changing the velocity from the value v' to v, $s_j(\mathbf{r},\mathbf{v},t)$ is the density of the sources of new particles in the state j, $\mathbf{v} = v\mathbf{\Omega}$, $v = |\mathbf{v}|$, $d\mathbf{v} = dv\,d\mathbf{\Omega}$, the summation is carried out over all possible previous states. The quantities c_{ij}, $W_{ij}(\mathbf{\Omega}',\mathbf{\Omega})$, and $h_{ij}(v',v)$ have normalization

$$ \sum_{j=1}^{n} c_{ij} = 1, \quad \int W_{ij}(\mathbf{\Omega}',\mathbf{\Omega})d\mathbf{\Omega} = 1, \quad \int h_{ij}(v',v)dv = 1. \tag{3} $$

The passage from the collision density $f(\mathbf{r},\mathbf{v},t)$ to the phase density $\psi(\mathbf{r},\mathbf{v},t)$ is carried out with the help of the integral

$$ \psi(\mathbf{r},\mathbf{v},t) = \int_0^t K(\tau)f(\mathbf{r}-v\mathbf{\Omega}\tau, v\mathbf{\Omega}, t-\tau)d\tau, \tag{4} $$

where $K(t) = \int_t^{\infty} k(\tau)d\tau$. Substituting (1) in (4), we obtain that the phase density has the form of the sum

$$ \psi(\mathbf{r},\mathbf{v},t) = \sum_{j=1}^{n} \psi_j(\mathbf{r},\mathbf{v},t), \tag{5} $$

where

$$\psi_j(\mathbf{r},\mathbf{v},t) = \int_0^t K_j(\tau) f_j(\mathbf{r} - v\boldsymbol{\Omega}\tau, v\boldsymbol{\Omega}, t-\tau)d\tau, \tag{6}$$

where $K_j(t) = \int_t^\infty k_j(\tau)d\tau$. The physical interpretation of the latter expression is simple. To detect a particle in the state j of the vicinity $d\mathbf{r}$ of the point $\mathbf{r}$ with the velocity in the interval from $\mathbf{v}$ to $\mathbf{v} + d\mathbf{v}$ at a moment of time from t to $t + dt$, the particle is supposed to pass into this state in the point $\mathbf{r} - v\boldsymbol{\Omega}\tau$ at the moment of time $t - \tau$ and stay in this state some time more than τ. The passage to the particle density $\rho(\mathbf{r}, t)$ is carried out with the use of the integral

$$\rho(\mathbf{r},t) = \int \psi(\mathbf{r},\mathbf{v},t)d\mathbf{v}. \tag{7}$$

The system of Equations (2), (5) and (6) together with conditions (3) describe practically any process of random walk with n discrete states under fairly general assumptions about the scattering indicatrix $W_{ij}(\boldsymbol{\Omega}', \boldsymbol{\Omega})$ and the velocity redistribution law $h_{ij}(v', v)$. In this study, using these equations, we will obtain master equations that describe the CTRW process.

The CTRW process is determined in the following way. At random times T_1, $T_1 + T_2$, $T_1 + T_2 + \cdots + T_j$, the particle makes instantaneous jumps with the value $R_1, R_2, \ldots, R_j$. Random jumps R_i and random times T_i are independent between one another as well as between each other. Thus, in the CTRW process, there are two states: $j = 1$ is the state of rest and $j = 2$ is the state of motion. By definition, in the CTRW process, after each jump, the particle enters a state of rest, and after each state of rest, the particle makes a jump. This means that the probabilities of passing c_{ij} from the state i into the state j have the following values

$$c_{11} = 0, \quad c_{12} = 1, \quad c_{21} = 1, \quad c_{22} = 0. \tag{8}$$

The state of rest is consistent with the velocity $v = 0$, and infinite velocity $v_2 = \infty$ corresponds to the state of motion (instant jump). To write the equation for $f_2(\mathbf{r}, \mathbf{v}, t)$, we first assume that in state 2, the particle moves with some constant velocity v_2, and then, we will carry out the passage $v_2 \to \infty$. Taking account of the foregoing, we have

$$h_{21}(v', v) \equiv h_1(v) = \delta(v), \quad h_{12}(v', v) \equiv h_2(v) = \delta(v - v_2), \tag{9}$$

$\delta(x)$ is the Dirac delta function. Furthermore, we assume that the direction of motion of the velocity after each collision does not depend on the previous direction of motion

$$W_{12}(\boldsymbol{\Omega}', \boldsymbol{\Omega}) = W_{21}(\boldsymbol{\Omega}', \boldsymbol{\Omega}) = W(\boldsymbol{\Omega}). \tag{10}$$

We represent the density of sources for each of the states in the form

$$s_j(\mathbf{r},\mathbf{v},t) = \sigma_j s_j(\mathbf{r},t) h_j^s(v) W_1(\boldsymbol{\Omega}), \quad j = 1, 2. \tag{11}$$

Here, σ_j is the probability of the birth of a particle in the state j ($\sigma_1 + \sigma_2 = 1$), $h_j^s(v)$ is the initial velocity modulus distribution, $W_j(\boldsymbol{\Omega})$ is the velocity direction distribution, and $s_j(\mathbf{r}, t)$ is the spatio-temporal density of a source distribution. Without loss of generality, let us assume that a particle begins its history from a state of rest. Thus, without loss of generality, we assume that the particle starts its history from the state of rest. Thus,

$$\sigma_1 = 1, \quad \sigma_2 = 0, \quad h_1^s(v) = \delta(v), \quad h_2^s(v) = \delta(v - v_2), \quad W_1(\boldsymbol{\Omega}) = W_2(\boldsymbol{\Omega}) = W(\boldsymbol{\Omega}). \tag{12}$$

Taking account of (8)–(12) for the collision density $f_j(\mathbf{r},\mathbf{p},t)$, we obtain the system of two equations

$$f_1(\mathbf{r},\mathbf{v},t) = W(\mathbf{\Omega})\delta(v)\Big(s_1(\mathbf{r},t) + \int_0^t k_2(\tau)d\tau \int d\mathbf{\Omega}' \int f_2(\mathbf{r}-v'\mathbf{\Omega}'\tau, v'\mathbf{\Omega}', t-\tau)dv'\Big), \quad (13)$$

$$f_2(\mathbf{r},\mathbf{v},t) = W(\mathbf{\Omega})\delta(v-v_2)\int_0^t k_1(\tau)d\tau \int d\mathbf{\Omega}' \int f_1(\mathbf{r}-v'\mathbf{\Omega}'\tau, v'\mathbf{\Omega}', t-\tau)dv'. \quad (14)$$

From this relation, we can see that in the case when the transition probability densities $h_{ij}(v',v)$ and $W_{ij}(\mathbf{\Omega}',\mathbf{\Omega})$ do not depend on the previous value v' and $\mathbf{\Omega}'$, then the collision density can be represented in the form of a product $f_j(\mathbf{r},v\mathbf{\Omega},t) = W(\mathbf{\Omega})h_j(v)F_j(\mathbf{r},\mathbf{t})$, $j = 1,2$, where $h_1(v)$ and $h_2(v)$ have the form (9). Thus, we obtain

$$f_1(\mathbf{r},v\mathbf{\Omega},t) = W(\mathbf{\Omega})\delta(v)F_1(\mathbf{r},\mathbf{t}), \quad f_2(\mathbf{r},v\mathbf{\Omega},t) = W(\mathbf{\Omega})\delta(v-v_2)F_2(\mathbf{r},\mathbf{t}). \quad (15)$$

Now, substituting these relations in (13) and (14) performing the integration over $dv\,d\mathbf{\Omega}$, for $F_j(\mathbf{r},t), j = 1,2$ we get a system of equations

$$F_1(\mathbf{r},t) = s_1(\mathbf{r},t) + \int_0^t k_2(\tau)d\tau \int W(\mathbf{\Omega}')d\mathbf{\Omega}' \int F_2(\mathbf{r}-v'\mathbf{\Omega}'\tau, t-\tau)\delta(v'-v_2)dv' =$$
$$s_1(\mathbf{r},t) + \int_0^t k_2(\tau)d\tau \int F_2(\mathbf{r}-v_2\mathbf{\Omega}'\tau, t-\tau)W(\mathbf{\Omega}')d\mathbf{\Omega}', \quad (16)$$

$$F_2(\mathbf{r},t) = \int_0^t k_1(\tau)d\tau \int W(\mathbf{\Omega}')d\mathbf{\Omega}' \int F_1(\mathbf{r}-v'\mathbf{\Omega}'\tau, t-\tau)\delta(v')dv' = \int_0^t k_1(\tau)F_1(\mathbf{r},t-\tau)d\tau. \quad (17)$$

In the equation for $F_2(\mathbf{r},t)$, the condition of normalization $\int W(\mathbf{\Omega}')d\mathbf{\Omega}' = 1$ was used. The physical meaning of quantities $F_j(\mathbf{r},t)$ is simple enough. This is the density of collisions in a volume element $d\mathbf{r}$ of the point vicinity $\mathbf{r}$, as a result of which the particle passes into the state j for a period of time $t, t+dt$ for any value of the particle velocity.

Let us now pass from the collision density to the phase density $\psi_j(\mathbf{r},\mathbf{v},t)$ and then to the density of particles $\rho_j(\mathbf{r},t)$. For this purpose, we substitute the expressions (15) in (6)

$$\psi_1(\mathbf{r},\mathbf{v},t) = \int_0^t K_1(\tau)W(\mathbf{\Omega})\delta(v)F_1(\mathbf{r}-v\mathbf{\Omega}\tau, t-\tau)d\tau,$$
$$\psi_2(\mathbf{r},\mathbf{v},t) = \int_0^t K_2(\tau)W(\mathbf{\Omega})\delta(v-v_2)F_2(\mathbf{r}-v\mathbf{\Omega}\tau, t-\tau)d\tau.$$

Now, integrating each of these expressions over $dvd\mathbf{\Omega}$ in view of (5) and (7) for the particle density, we obtain the system of equations

$$\rho(\mathbf{r},t) = \rho_1(\mathbf{r},t) + \rho_2(\mathbf{r},t),$$
$$\rho_1(\mathbf{r},t) = \int_0^t K_1(\tau)F_1(\mathbf{r},t-\tau)d\tau,$$
$$\rho_2(\mathbf{r},t) = \int_0^t K_2(\tau)d\tau \int W(\mathbf{\Omega})F_2(\mathbf{r}-v_2\mathbf{\Omega}\tau, t-\tau)d\mathbf{\Omega}, \quad (18)$$

where $F_1(\mathbf{r},t)$ and $F_2(\mathbf{r},t)$ are determined by Equations (16) and (17). As one can see, the total particle density is the sum of the particle density in each of the states. It should be noted that this system of equations is not yet a system of master equations to describe the CTRW process. This system describes the random walk of a particle with two states: state 1 is rest, and state 2 is motion with a constant final velocity v_2.

To obtain the system of equations for the CTRW process, it is necessary to go to the limit $v_2 \to \infty$. It should be pointed out that in Equations (16) and (18), τ is an independent variable, which has the meaning of the time in the state of motion. Therefore, if we pass now to the limit $v_2 \to \infty$, then it means that $\tau \to 0$ and the probability is $k_2(\tau)d\tau = 0$. To

avoid this, it is necessary to pass to a new variable $\xi = v\tau$, which has the meaning of the free path of a particle. As a result, we obtain the system of equations

$$\rho_1(\mathbf{r},t) = \int_0^t Q(\tau)F_1(\mathbf{r},t-\tau)d\tau,$$
$$\rho_2(\mathbf{r},t) = \frac{1}{v_2}\int_0^{v_2 t} P(\xi)d\xi \int W(\mathbf{\Omega})F_2(\mathbf{r}-\xi\mathbf{\Omega},t-\xi/v_2)d\mathbf{\Omega},$$
$$F_1(\mathbf{r},t) = s_1(\mathbf{r},t) + \int_0^{v_2 t} p(\xi)d\xi \int F_2(\mathbf{r}-\xi\mathbf{\Omega}',t-\xi/v_2)W(\mathbf{\Omega}')d\mathbf{\Omega}',$$
$$F_2(\mathbf{r},t) = \int_0^t q(\tau)F_1(\mathbf{r},t-\tau)d\tau.$$

Here, for convenience, the following notation was introduced $p(\xi) = \frac{1}{v_2}k_2\left(\frac{\xi}{v_2}\right)$, $P(\xi) \equiv K_2\left(\frac{\xi}{v_2}\right) = \int_\xi^\infty p(y)dy$, $q(\tau) \equiv k_1(\tau)$, $Q(\tau) \equiv K_1(\tau)$.

Let us now pass in this system of equations to the limit $v_2 \to \infty$. From the equation for $\rho_2(\mathbf{r},t)$, it is seen that due to the presence of the multiplier $1/v_2$ before the sign of the integral $\rho_2(\mathbf{r},t) \to 0$ at $v_2 \to \infty$. There is a simple explanation for this fact. Since now the particle is moving with infinite velocity, it instantly moves from one point in space to another. As a result, the probability of detecting a particle in a state of motion in the time interval $t + dt$ is equal to zero and as a sequence, $\rho_2(\mathbf{r},t) = 0$. Thus, for the CTRW process, we arrive at the system of equations

$$\rho(\mathbf{r},t) = \rho_1(\mathbf{r},t) = \int_0^t Q(\tau)F_1(\mathbf{r},t-\tau)d\tau, \tag{19}$$
$$F_1(\mathbf{r},t) = s_1(\mathbf{r},t) + \int_0^\infty p(\xi)d\xi \int F_2(\mathbf{r}-\xi\mathbf{\Omega}',t)W(\mathbf{\Omega}')d\mathbf{\Omega}', \tag{20}$$
$$F_2(\mathbf{r},t) = \int_0^t q(\tau)F_1(\mathbf{r},t-\tau)d\tau. \tag{21}$$

As one can see, for the CTRW process, the particle distribution density $\rho(\mathbf{r},t)$ only the density of the spatial distribution of particles at rest is determined.

The obtained system of equations can be simplified, and it is possible to pass to the equation of the particle density only $\rho(\mathbf{r},t)$. For this purpose, we need to put Equation (21) into Equation (20). Then, we need to put the obtained equation for the collision density $F_1(\mathbf{r},t)$ into Equation (19) and change the integration order in terms of time. As a result, we get the equation for density

$$\rho(\mathbf{r},t) = \int_0^t Q(\tau)s_1(\mathbf{r},t)d\tau + \int_0^t q(\tau)d\tau \int_0^\infty p(\xi)d\xi \int W(\mathbf{\Omega})\rho(\mathbf{r}-\xi\mathbf{\Omega},t-\tau)d\mathbf{\Omega}. \tag{22}$$

This equation is the master equation of the CTRW process in three-dimensional space. The result obtained coincides with similar results obtained in the works [4,14,48].

Let us simplify the problem and consider the one-dimensional case. Let the random walk process occur along the axis x. In this case, the function $W(\mathbf{\Omega})$ takes the form

$$W(\mathbf{\Omega}) = W(\theta,\varphi) = \frac{1}{\sin\theta}(\omega_1\delta(\varphi) + \omega_2\delta(\varphi-\pi))\delta(\theta-\pi/2), \tag{23}$$

where ω_1 and ω_2 are probabilities of motion in the positive and negative direction of the axis Ox correspondingly and $\omega_1 + \omega_2 = 1$. Substituting now (23) in (22) and taking account that $\mathbf{\Omega} = (\sin\theta\cos\varphi, \sin\theta\sin\varphi, \cos\theta)$, $\rho(\mathbf{r},t) = \rho(x,y,z,t)$, $s_1(\mathbf{r},t) = s_1(x,y,z,t)$, $d\mathbf{\Omega} = \sin\theta d\theta d\varphi$ and integrating the resulting equation over the angular variables, we obtain

$$\rho(x,y,z,t) = \int_0^t Q(\tau)s_1(x,y,z,t)d\tau + \int_0^t q(\tau)d\tau \int_0^\infty p(\xi)(\omega_1\rho(x-\xi,y,z,t-\tau) + \omega_2\rho(x+\xi,y,z,t-\tau))d\xi.$$

Since we are considering random walks along the axis Ox, then

$$\rho(x,y,z,t) = \rho(x,t)\delta(y)\delta(z), \quad s_1(x,y,z,t) = s_1(x,t)\delta(y)\delta(z).$$

Substituting now these expressions into the previous equation and integrating over $dydz$, we finally get

$$\rho(x,t) = \int_0^t Q(\tau)s_1(x,t)d\tau + \int_0^t q(\tau)d\tau \int_0^\infty p(\xi)(\omega_1\rho(x-\xi,t-\tau) + \omega_2\rho(x+\xi,t-\tau))d\xi. \tag{24}$$

This equation describes one-dimensional walks of a particle in the CTRW process. The solution to this equation will be sought by the standard method of the Fourier–Laplace transform. Performing the Fourier–Laplace transform

$$\hat{\rho}(k,\lambda) = \int_0^\infty dt \int_{-\infty}^\infty e^{ikx-\lambda t}\rho(x,t)dx$$

we get that the solution to Equation (24) has the form

$$\hat{\tilde{\rho}}(k,\lambda) = \frac{1-\tilde{q}(\lambda)}{\lambda}\frac{\hat{\tilde{s}}_1(k,\lambda)}{1-\tilde{q}(\lambda)(\omega_1\hat{p}(k)+\omega_2\hat{p}(-k))}. \tag{25}$$

Here, $\hat{q}(\lambda)$ is the Laplace transform of density $q(t)$, $\hat{p}(k)$ is the Fourier transform of density $p(\xi)$, $\hat{s}_1(k,\lambda)$ is the Fourier–Laplace transform of source function $s_1(x,t)$ and

$$\int_0^\infty e^{-\lambda t}Q(t)dt = \frac{1-\hat{q}(\lambda)}{\lambda}.$$

3. the Equations of Anomalous Diffusion

The obtained Equation (24) is an exact description of the walk process, and its solution in Fourier–Laplace images (25) is its exact solution. However, it is possible to perform the inverse Fourier–Laplace transform of the solution (25) and to write down an equation describing the process of a walk, only if to consider the asymptotic solution at $t \to \infty$ and $x \to \infty$. The form of this equation is determined by two characteristics of the distribution of free path and rest time: mathematical expectation and variance [6,7,14]. If the variance of free paths $\langle R^2\rangle$ and rest times $\langle T^2\rangle$ are finite, then the random walk process is described by a standard diffusion equation. If the variance of rest time is finite $\langle T^2\rangle < \infty$, the mathematical expectation of free paths is finite ($\langle R\rangle < \infty$ and $\langle R^2\rangle = \infty$) or infinite ($\langle R\rangle = \infty$), then the random walk process is described with the anomalous diffusion equation with the first derivative with respect to time and fractional derivative with respect to the coordinate. In the case $\langle T\rangle = \infty$ and $\langle R^2\rangle < \infty$, we obtain the equation of anomalous diffusion with a fractional time derivative and a second coordinate derivative. In the case $\langle T\rangle = \infty$ and $\langle R^2\rangle = \infty$, then the random walk process is described with a fractional derivative equation in both time and coordinate. Based on the foregoing, we will consider all these cases separately.

At first, we consider the simplest case $\langle T\rangle < \infty$ and $\langle R^2\rangle < \infty$. Let rest times and free paths have the exponential distribution

$$q(t) = \nu e^{-\nu t}, \tag{26}$$

$$p(x) = \mu e^{-\mu x}. \tag{27}$$

Performing the Laplace transform of the density $q(t)$ and the Fourier transform of the density $p(x)$, we obtain

$$\tilde{q}(\lambda) = \frac{\nu}{\nu + \lambda}, \quad \hat{p}(k) = \frac{\mu}{\mu + ik}.$$

The asymptotic solution at $t \to \infty$ and $x \to \infty$ is of interest to us. According to Tauberian theorems, the behavior of the function at $t \to \infty$ or $x \to \infty$ corresponds to the behavior of the transformant at $\lambda \to 0$ or $k \to 0$. Expanding images $\tilde{q}(\lambda)$ and $\hat{p}(k)$ in a series and leaving one summand in the expansion $\tilde{q}(\lambda)$ and two summands in the expansion $\hat{p}(k)$, we obtain

$$\tilde{q}(\lambda) \approx 1 - \langle T \rangle \lambda, \tag{28}$$

$$\hat{p}(k) \approx 1 + i\langle R \rangle k - \frac{\langle R^2 \rangle}{2} k^2. \tag{29}$$

Here, we use the fact that $1/\nu = \langle T \rangle$, $1/\mu = \langle R \rangle$ and $1/\mu^2 = \langle R^2 \rangle$. We will consider symmetrical random walks ($\omega_1 = \omega_2 = 1/2$) with the point instantaneous source $s_1(x,t) = \delta(x)\delta(t)$. We substitute the expansions (28) and (29) in the solution (25). As a result, we obtain

$$\hat{\tilde{\rho}}(k,\lambda) = \frac{1}{\lambda + D_A k^2}, \quad D_A = \frac{\langle R^2 \rangle}{2\langle T \rangle},$$

where D_A is the diffusion coefficient. If we write this expression in the form

$$\lambda \hat{\tilde{\rho}}(k,\lambda) - 1 = -D_A k^2 \hat{\tilde{\rho}}(k,\lambda) \tag{30}$$

and take into account that

$$\int_0^\infty e^{-\lambda t} \frac{\partial f(t)}{\partial t} dt = \lambda \tilde{f}(\lambda) - \tilde{f}_0, \tag{31}$$

$$\int_{-\infty}^\infty e^{ikx} \frac{\partial^2 f(x)}{\partial x^2} dx = -k^2 \hat{f}(k), \tag{32}$$

where $\tilde{f}_0$ is the Laplace transform of the initial condition, then it is clear that (30) is nothing but the Fourier–Laplace transform of the diffusion equation

$$\frac{\partial \rho(x,t)}{\partial t} = D_A \frac{\partial^2 \rho(x,t)}{\partial x^2} \tag{33}$$

with zero boundary conditions at infinity and the initial condition $\rho(x,0) = \delta(x)$. As it is well known, the solution to this equation is expressed in terms of the normal distribution and has the form

$$\rho(x,t) = (4\pi D_A t)^{-1/2} \exp\{-x^2/(4D_A t)\}. \tag{34}$$

An important property of this solution is the self-semilarity of the density profile [9]. Self-similarity is understood as a special form of solution symmetry, which means that a change in the scale of some variables can be compensated by a change in the scale of other variables. In the case under consideration, the solution (34) can be represented in the form $\rho(x,t) = (2D_A t)^{-1/2} g(x(2D_A t)^{-1/2})$, where $g(x) = (2\pi)^{-1/2} \exp\{-x^2/2\}$ is the density of the normal law (or Gauss distribution). As we can see, the solution $\rho(x,t)$ at an arbitrary moment of time can be obtained from the density of normal law $g(x)$ by scaling transformation of coordinate and density. Thus, in the case under consideration, the width of diffusion packet grows according to the law $\Delta(t) \propto (2D_A t)^{1/2}$.

We consider the case $\langle T \rangle = \infty$ and $\langle R^2 \rangle < \infty$. Let us assume that free paths have the distribution (27), and the rest times are distributed according to the law

$$q(t) = \begin{cases} 0, & t < t_0 \\ \beta t_0^\beta t^{-\beta-1}, & t \geqslant t_0, \end{cases}, \quad 0 < \beta < 1. \tag{35}$$

A characteristic property of this distribution is that this distribution has moments of order $k < \beta$, i.e., $\langle T^k \rangle < \infty$, if $k < \beta$, and $\langle T^k \rangle = \infty$, if $k \geqslant \beta$. Considering this circumstance, in the work [50], it was shown that the Laplace transform of density (35) had the form

$$\tilde{q}(\lambda) \approx 1 - (\lambda t_0)^{\beta} \Gamma(1-\beta), \quad \lambda \to 0, \tag{36}$$

where $\Gamma(x)$ is Euler's gamma function. Now, let us substitute this expansion as well as the expansion (29) in Equation (25). As in the previous case, we will consider symmetrical random walks ($\omega_1 = \omega_2 = 1/2$) with the point instantaneous source $s_1(x,t) = \delta(x)\delta(t)$. As a result, from (25), we obtain

$$\hat{\tilde{p}}(k,\lambda) = \frac{\lambda^{\beta-1}}{\lambda^{\beta} + D_B k^2}, \quad D_B = \frac{\frac{1}{2}\langle R^2 \rangle}{t_0^{\beta}\Gamma(1-\beta)}.$$

We represent this equation in the form

$$\lambda^{\beta}\hat{\tilde{p}}(k,\lambda) = -D_B k^2 \hat{\tilde{p}}(k,\lambda) + \lambda^{\beta-1}.$$

To perform the inverse Fourier–Laplace transform of this expression, we will use the formulas (A3) and (32). As a result, the random walk process in the case under consideration is described with the fractional differential equation

$${}_0D_t^{\beta}\rho(x,t) = D_B \frac{\partial^2 \rho(x,t)}{\partial x^2} + \frac{t^{-\beta}}{\Gamma(1-\beta)}\delta(x)$$

with a diffusion coefficient D_B. In the work [18], it was shown that the solution to this equation has the form

$$\rho(x,t) = \left(D_B t^{\beta}\right)^{-1/2} q\left(x\left(D_B t^{\beta}\right)^{-1/2}; 2, \beta\right),$$

where $q(x;\alpha,\beta)$ is the density of a fractional-stable law [17,51,52]

$$q(x,\alpha,\beta) = \int_0^{\infty} g\left(xy^{\beta/\alpha};\alpha,0\right) g(y;\beta,1) y^{\beta/\alpha} dy. \tag{37}$$

Here, $g(x;\alpha,0)$ and $g(y,\beta,1)$ are the densities of symmetric and one-sided strictly stable laws [53,54] and $0 < \alpha \leqslant 2$, $0 < \beta \leqslant 1$.

We consider the case $\langle T \rangle < \infty$ and $\langle R^2 \rangle = \infty$. Let the rest times have the exponential distribution (26) and free paths have the power distribution

$$p(x) = \begin{cases} 0, & x < x_0 \\ \alpha x_0^{\alpha} x^{-\alpha-1}, & x \geqslant x_0, \end{cases}, \quad 0 < \alpha < 2. \tag{38}$$

As mentioned earlier, distributions of this kind have moments not exceeding α, i.e., $\langle X^k \rangle < \infty$, if $k < \alpha$ and $\langle X^k \rangle = \infty$, if $k \geqslant \alpha$. Since the parameter α takes values from the interval $0 < \alpha \leqslant 2$, then at values $0 < \alpha \leqslant 1$, the mathematical expectation of free paths $\langle R \rangle$ is infinite, and at values $1 < \alpha \leqslant 2$, the mathematical expectation is finite. In this regard, it is necessary to consider these two cases separately.

At first, we consider the case $0 < \alpha < 1$. Let us perform the Fourier transform of the density (38)

$$\hat{p}(k) = \alpha x_0^{\alpha} \int_{x_0}^{\infty} x^{-\alpha-1} e^{ikx} dx. \tag{39}$$

Integrating this expression once by parts, we obtain

$$\hat{p}(k) = e^{ikx_0} + ikx_0^{\alpha} \int_{x_0}^{\infty} x^{-\alpha} e^{ikx} dx.$$

In this integral, we change the integration variable $ikx = -t$. Then, we will pass to the redistribution of $k \to 0$ and keep the summands that do not exceed x^α. As a result, we obtain

$$\hat{p}(k) \approx 1 - (-ikx_0)^\alpha \int_0^{-i\infty} t^{-\alpha} e^{-t} dt. \tag{40}$$

Next, we will use the well-known result (see §1.5, the formula (31) in [55])

$$\int_0^\infty t^{\gamma-1} e^{-ct\cos\psi - ict\sin\psi} dt = \Gamma(\gamma) c^{-\gamma} e^{-i\gamma\psi},$$

where $-\frac{\pi}{2} < \psi < \frac{\pi}{2}$, $\Re\gamma > 0$, or $\psi = \pm\frac{\pi}{2}$, $0 < \Re\gamma < 1$. If we consider that $z = te^{i\psi}$, then this formula can be represented in the form

$$\int_0^{\infty e^{i\psi}} z^{\gamma-1} e^{-cz} dz = \Gamma(\gamma) c^{-\gamma}, \tag{41}$$

where $-\frac{\pi}{2} < \psi < \frac{\pi}{2}$, $\Re\gamma > 0$, or $\psi = \pm\frac{\pi}{2}$, $0 < \Re\gamma < 1$. Comparing this formula with the integral on the right-hand side (40), we obtain

$$\hat{p}(k) \approx 1 - (-ikx_0)^\alpha \Gamma(1-\alpha), \quad 0 < \alpha < 1. \tag{42}$$

Now, we consider the case $1 < \alpha < 2$. Integrating twice in parts the Fourier transform of the density (39), we get

$$\hat{p}(k) = e^{ikx_0} + \frac{ikx_0}{\alpha - 1} e^{ikx_0} + \frac{k^2 x_0^\alpha}{1-\alpha} \int_{x_0}^\infty x^{-\alpha+1} e^{ikx} dx.$$

Now we will change the integration variable $ikx = -t$ in this expression, and then, we will pass to the limit $k \to 0$. When passing to the limit, we keep only summands with a degree not exceeding α. As a result, we have

$$\hat{p}(k) \approx 1 + \frac{ikx_0}{\alpha - 1} + \frac{(-ikx_0)^\alpha}{\alpha - 1} \int_0^{-i\infty} t^{1-\alpha} e^{-t} dt.$$

If we use the formula (41) now, then we finally get

$$\hat{p}(k) \approx 1 + \frac{ikx_0}{\alpha - 1} + \frac{(-ikx_0)^\alpha}{\alpha - 1} \Gamma(2-\alpha), \quad 1 < \alpha < 2. \tag{43}$$

Thus, we have obtained asymptotic expressions for the Fourier transform of the free path distribution (38) for two cases: $0 < \alpha < 1$ and $1 < \alpha < 2$.

Now, we get back to the expression (25) and consider the multiplier $\omega_1 \hat{p}(k) + \omega_2 \hat{p}(-k)$. As in the previous cases, we will consider the symmetrical random walks ($\omega_1 = \omega_2 = 1/2$). Using the expression (42) and taking account of the relation $(-i)^\alpha + i^\alpha = \cos(\pi\alpha/2)$ for the case $0 < \alpha < 1$, we obtain

$$\omega_1 \hat{p}(k) + \omega_2 \hat{p}(-k) = 1 - Ck^\alpha, \quad C = x_0^\alpha \Gamma(1-\alpha)\cos(\pi\alpha/2).$$

Using the doubling formula for the Gamma function $\Gamma(2z) = (2\pi)^{-1/2} 2^{2z-1/2} \Gamma(z)$ $\Gamma(z + 1/2)$ and the symmetry formula $\Gamma(\frac{1}{2} + z)\Gamma(\frac{1}{2} - z) = \frac{\pi}{\cos(\pi z)}$, the coefficient C can be represented in the form

$$C = 2^{-\alpha} \frac{\sqrt{\pi} x_0^\alpha \Gamma\left(1 - \frac{\alpha}{2}\right)}{\Gamma\left(\frac{1}{2} + \frac{\alpha}{2}\right)}.$$

In the case $1 < \alpha < 2$, it is necessary to use the expression (43). As a result, we obtain

$$\omega_1 \hat{p}(k) + \omega_2 \hat{p}(-k) = 1 - C'k^\alpha, \quad C' = x_0^\alpha \frac{\Gamma(2-\alpha)}{\alpha - 1} \sin(\tfrac{\pi}{2}(\alpha - 1)),$$

where we also assume symmetrical random walks ($\omega_1 = \omega_2 = 1/2$). Using the doubling formula for the Gamma function and the symmetry formula $\Gamma(z)\Gamma(1-z) = \frac{\pi}{\sin(\pi z)}$, it is possible to show that $C' = C$. Thus,

$$\tfrac{1}{2}(\hat{p}(k) + \hat{p}(-k)) = 1 - Ck^{\alpha}, \quad \alpha \in (0,1) \cup (1,2). \tag{44}$$

Now, we substitute this expression and the expression (28) in the solution (25). As a result, we obtain

$$\hat{\hat{\rho}}(k,\lambda) = \frac{1}{\lambda + D_C k^{\alpha}}, \quad D_C = \frac{C}{\langle T \rangle}. \tag{45}$$

We rewrite this expression in the form

$$\hat{\hat{\rho}}(k,\lambda)\lambda - 1 = -D_C k^{\alpha} \hat{\hat{\rho}}(k,\lambda).$$

If we use now the relations (31) and (A5), then it is possible to perform the inverse Fourier–Laplace transform of this equation easily. As a result, we obtain

$$\frac{\partial \rho(x,t)}{\partial t} = D_C \frac{\partial^{\alpha} \rho(x,t)}{\partial |x|^{\alpha}} + \delta(x)\delta(t).$$

The solution to this equation can be obtained by performing the inverse Fourier–Laplace transform of the solution (45). It was done in the work [18], which showed that the solution to this equation has the form

$$\rho(x,t) = (D_C t)^{-1/\alpha} q\Big(x(D_C t)^{-1/\alpha}; \alpha, 1\Big),$$

where the density $q(x;\alpha,\beta)$ is determined by the expression (37).

It remains to consider the case $\langle T \rangle = \infty$ and $\langle R^2 \rangle = \infty$. Suppose the rest times have the distribution (35), and free paths are distributed according to the law (38). Since the parameter α takes the values in the range $0 < \alpha < 2$, then, as it was mentioned earlier, there is a necessity to consider two cases: $0 < \alpha < 1$ and $1 < \alpha < 2$. This is determined by the fact that when passing to the limit $k \to 0$, it necessary to take account of different summands in the expansion of the function image $p(x)$. However, such a passage to the limit has already been performed when considering the previous case. It was shown that in the case of symmetric random walks, the multiplier $\omega_1 \hat{p}(k) + \omega_2 \hat{p}(-k)$,which is a component of the expression (25) has the form (44). The Laplace transform of the density (35) was also obtained by us earlier. It has the form (36). Now, we substitute the expansions (36) and (44) in the solution (25) and will keep summands in the obtained expression that do not exceed k^{α} and λ^{β}. As a result, we get

$$\hat{\hat{\rho}}(k,\lambda) = \frac{\lambda^{\beta-1}}{\lambda^{\beta} + D_D k^{\alpha}}, \quad D_D = 2^{-\alpha} \frac{x_0^{\alpha}\sqrt{\pi}\Gamma(1-\frac{\alpha}{2})}{t_0^{\beta}\Gamma(1-\beta)\Gamma(\frac{1}{2}(1+\alpha))}.$$

Here, D_D is the diffusion coefficient. If we use the relations (A3) and (A5), it is possible to show easily that the obtained expression is the solution to the equation

$${}_0D_t^{\beta}\rho(x,t) = D_D \frac{\partial^{\alpha}\rho(x,t)}{\partial |x|^{\alpha}} + \frac{t^{-\beta}}{\Gamma(1-\beta)}\delta(x).$$

The paper [18] shows that the solution of this equation has the form

$$\rho(x,t) = \Big(D_D t^{\beta}\Big)^{-1/\alpha} q\Big(x\Big(D_D t^{\beta}\Big)^{-1/\alpha}; \alpha, \beta\Big),$$

where $q(x,\alpha,\beta)$ is the density of a fractional-stable law (37).

As we can see, in all considered cases, the asymptotic distribution of particles at $t \to \infty$ and $x \to \infty$ is described with equations of the same type. The difference between these equations lies only in the order of the derivative with respect to time or coordinate and in the diffusion coefficient. If we assume that the case $\langle T \rangle < \infty$ corresponds to the parameter value $\beta = 1$, and the case $\langle R^2 \rangle < \infty$ corresponds to the parameter value $\alpha = 2$, then the random walk process is described with the anomalous diffusion equation

$$ {}_0D_t^{\beta} \rho(x,t) = D \frac{\partial^{\alpha} \rho(x,t)}{\partial |x|^{\alpha}} + \frac{t^{-\beta}}{\Gamma(1-\beta)} \delta(x), \tag{46} $$

where $0 < \beta \leqslant 1$, $0 < \alpha \leqslant 2$, and the generalized diffusion coefficient D for different parameter values takes different values

$$ D = \begin{cases} D_A, & \beta = 1, \quad \alpha = 2, \\ D_B, & 0 < \beta < 1, \quad \alpha = 2, \\ D_C, & \beta = 1, \quad 0 < \alpha < 2, \\ D_D, & 0 < \beta < 1, \quad 0 < \alpha < 2. \end{cases} \tag{47} $$

As the paper [18] shows, the solution of this equation has the form

$$ \rho(x,t) = \left(Dt^{\beta} \right)^{-1/\alpha} q\left(x \left(Dt^{\beta} \right)^{-1/\alpha}; \alpha, \beta \right), \tag{48} $$

where $q(x;\alpha,\beta)$ is the density of a fractional-stable law (37). According to the properties of fractional-stable laws [51] in case of parameter values $\beta = 1, \alpha = 2$, the density $q(x;2,1)$ becomes the density of the normal law, and in case $\beta = 1$, the density $q(x;\alpha,1)$ is the density of a stable law. Thus, Equation (46) describes the random walk process in all considered cases. The transition from one case to another is carried out only by replacing the value of the generalized diffusion coefficient D. Different types of the generalized diffusion coefficient are determined by different distributions of the rest times and the value of a free path. It is seen from (48) that this solution possesses the self-semilarity property. Therefore, the diffusion packet expands with time according to the law with exponent $\gamma = \beta/\alpha$, i.e., $\Delta(t) \propto D^{1/\alpha} t^{\beta/\alpha}$. As we can see in the case of normal diffusion, we obtain well-known result $\Delta(t) \propto \sqrt{D_A} t^{1/2}$.

4. the Solution to the Equation of Anomalous Diffusion

As we can see from Section 2, the CTRW process is described by the integral transport equation, which in the one-dimensional case takes the form (24). Therefore, the Monte Carlo method can be used to find a solution to this equation. The advantage of Monte Carlo methods is that they allow one to find a solution in multidimensional problems, as well as for various boundary and initial conditions. In this paper, we consider the solution to the anomalous diffusion Equation (46) under the condition $\rho(x,t) = 0$ if $t < 0$ and $\rho(x,t) \to 0$ if $x \to \pm\infty$.

From Section 2, the simplest method of stochastic solution to the anomalous diffusion equation immediately follows (46), based on trajectory modeling and histogram density estimation. Each trajectory begins at the moment of time $t = 0$ from the origin of coordinates $x = 0$ from the state of rest. In the state of rest, the particle stays for a random time T_1. Then, with equal probability, the particle jumps to the right or to the left at a distance R_1. After that, the particles will enter a state of rest. Then, the process continues in the same way. The construction of the trajectory continues as long as the condition is met

$$ \sum_{k=1}^{N(T^*)} T_k \leqslant T^*, \tag{49} $$

where T^* is a given moment in time at which a solution is to be found. As soon as this condition is no longer met, the trajectory is terminated. Then, a new trajectory begins.

Depending on the parameter values α and β, the rest times T_k and free path values R_k have different distributions. As noted earlier, the determining parameters that influence the form of the differential equation are the mathematical expectation of the rest time $\langle R^2 \rangle$. If the mathematical expectation of the rest time has a finite value, then this corresponds to the case $\beta = 1$. If the variance of a free path has a finite value, then this corresponds to the case $\alpha = 2$. In this paper, exponential distributions are chosen as such distributions. Therefore, in the case $\beta = 1$, the rest times have the distribution (26). In the case $\alpha = 2$, free paths have the distribution (27). The values $0 < \beta < 1$ correspond to the case of the infinite mathematical expectation of the rest time. In this case, the rest times are distributed with the density (35). The values $0 < \alpha < 2$ correspond to the case of the infinite variance of free paths. In this case, free paths are distributed with the density (38). Thus, with the value $\beta = 1$, random times T_k, $k = 1, 2, \dots$ are modeled according to the formula $T = -\nu^{-1} \log(\zeta)$, and in the case $0 < \beta < 1$ according to the formula $T = t_0 \zeta^{-1/\beta}$. If $\alpha = 2$ random free paths R_k, $k = 1, 2, \dots$ are modeled according to the formula $R = -\mu^{-1} \log(\zeta)$. If $0 < \alpha < 2$, then $R = x_0 \zeta^{-1/\alpha}$. Here, ζ represents equally distributed random values on the segment $(0, 1]$.

To construct the simplest histogram estimate of the solution (46), all the region of interest $\Delta = [a, b]$ is broken down into disjoint intervals $\Delta_i = (x_i, x_{i+1}]$, $i = 1, 2, \dots M - 1$, $x_1 = a, x_M = b$. To construct a histogram, the trajectory is modeled until the condition is met (49). As soon as this condition ceases to be met, the trajectory is terminated, and the contribution from this trajectory is calculated

$$h_j(\Delta_i) = \frac{I(\Delta_i)}{\Delta_i}.$$

where $I(\Delta_i)$ is the interval indicator Δ_i

$$I(\Delta_i) = \begin{cases} 1, & x^* \in \Delta_i, \\ 0, & x^* \notin \Delta_i, \end{cases}$$

where x^* is the coordinate of a particle at a moment of time T^*. As a result, the density estimate for the interval Δ_i is given with the expression

$$\tilde{\rho}(\Delta_i, t) = \frac{1}{N} \sum_{j=1}^{N} h_j(\Delta_i), \tag{50}$$

where the summation is performed over an ensemble of N independent trajectories.

Despite the simplicity of this estimate, it has several disadvantages. Firstly, the estimate of the solution $\tilde{\rho}(\Delta_i, t)$ is sought for the interval Δ_i. This is the source of the systematic (horizontal) component of the error δ_x. Secondly, this estimate also contains the statistical component of the error $\hat{\delta}$, which decreases as $N^{-1/2}$ at $N \to \infty$. It is impossible to eliminate these errors completely; one can only reduce their value. However, a decrease in one of these values leads to an increase in the other value or to an increase in the calculation time.

It is possible to get rid of the systematic component of the error completely δ_x if to consider one of the varieties of a local estimate. As in the case of the histogram estimate, the problem is to determine the probability density of detecting a particle at the point x^* at a moment of time T^*. The main element of solving the problem of transport theory by the Monte Carlo method, trajectory modeling, remains unchanged. The difference lies in the estimation method. In the case of a local estimate, the probability of a particle hitting a point (x^*, T^*) is calculated assuming that the next collision is the final one. This probability

is calculated after each collision (state change) of the particle. As a result, for the CTRW process, this probability is given by the value

$$\psi(\xi, \tau) = \tfrac{1}{2} p(\xi) Q(\tau), \tag{51}$$

where $Q(\tau) = \int_{\tau}^{\infty} q(t)dt$. It should be pointed out that for the CTRW process, this probability is calculated only for the transition «rest»→«jump». For transitions «jump»→«rest», this probability will be equal to zero. As a result, the contribution to the density estimate from each individual trajectory has the form

$$h_j(x^*, T^*) = \sum_{i=1}^{K(T^*)} \psi(|x^* - x_i|, T^* - t_i),$$

where $K(T^*)$ is the number of state change acts «rest»→«jump» that occurred for the interval of time $(0, T^*)$. The density estimate takes the form

$$\tilde{\rho}(x^*, T^*) = \frac{1}{N} \sum_{j=1}^{N} h_j(x^*, T^*), \tag{52}$$

where the summation is performed over an ensemble of N independent trajectories.

As we can see, the local estimate evaluates the density at a given point x^*. This means that this estimate does not contain a systematic component of the error δ_x, which is connected with the finite value of the interval Δ_i, as it was in the histogram estimate. Moreover, since each individual trajectory contributes more than once, as was the case with the histogram estimate and $K(T^*)$ times, then this leads to a decrease in the statistical error.

The results of solving Equation (46) are given in Figures 1–3. In these figures, the points correspond to the results of the local estimation (52), the circles correspond to the results of the histogram estimation (50), and the solid curves correspond to the solution (48) with the corresponding diffusion coefficient determined from the relation (47). The solution results are given for different points in time. From Figure 1, it is clear that for the parameter value $\beta = 0.3$, the results of the local and histogram estimation coincide with the solution (48) at time $T^* = 10$. This means that by this time, the walk process has already entered the asymptotic regime. Thus, for the given parameter values, the estimate (52) can be used to solve Equation (46) at times $T^* \geqslant 10$. In the case $\beta = 0.6$ with the time values $T^* = 10$ and 100, it is clear (see Figure 1 on the right) that the results of the local estimate and solution (48) differ. This means that at such times, the random walk process has not yet reached the asymptotic regime. However, at times $T^* = 10^3$ and 10^4, the random walk process already reaches the asymptotic regime. This means that at times $T^* \geqslant 10^3$, the estimate (52) can be used to solve numerically Equation (46) for the given parameter values. Similar conclusions can be drawn for other presented solution results. For an exponential distribution of rest times and $\alpha = 0.7$ and $\alpha = 1.4$ (Figure 2), it is clear that the random walk process reaches the asymptotic regime at time $T^* = 10$. Thus, for the indicated values of the parameters, the estimate (52) can be used to solve Equation (46) at times $T^* \geqslant 10$. In the case $\beta = 0.7$ and $\alpha = 0.9$ (see Figure 3 on the left), the random walk process becomes asymptotic at time $T^* = 1000$, and for the values $\beta = 0.7$, $\alpha = 1.4$ (see Figure 3 on the right) at time $T^* = 100$.

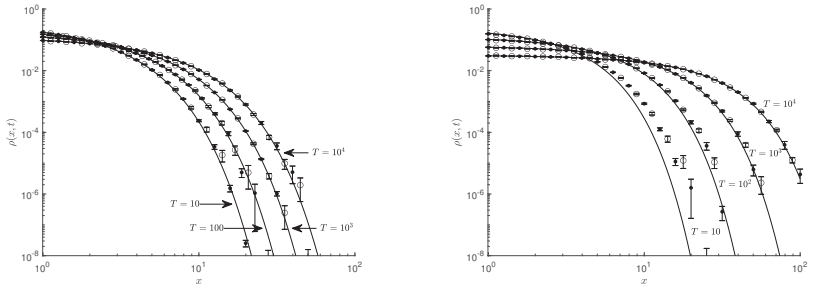

Figure 1. The solution to Equation (46) for the case of exponential distribution of free paths (27) and $\beta = 0.3$ (**on the left**) and $\beta = 0.6$ (**on the right**). The solutions are given for four values of time T, as indicated in the figures. The points are local estimate results (52), the circles are histogram estimation results (50), and the solid curve is the solution (48) with a generalized diffusion coefficient $D = D_B$.

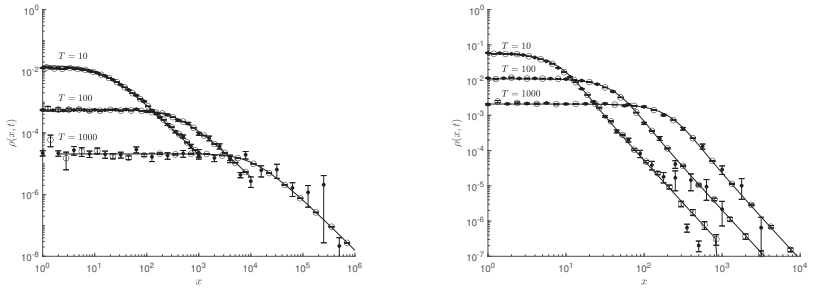

Figure 2. The solution to Equation (46) for the case of exponential distribution of rest times (26) and $\alpha = 0.7$ (**on the left**) and $\alpha = 1.4$ (**on the right**). The solutions are given for three values of time T, as indicated in the figures. The points are local estimate results (52), the circles are histogram estimation results (50), the solid curve is the solution (48) with a generalized diffusion coefficient $D = D_C$.

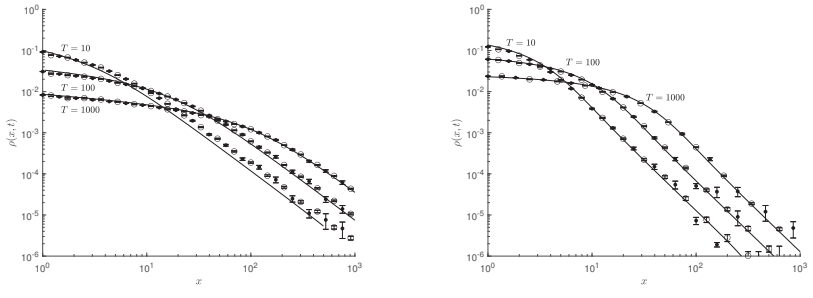

Figure 3. The solution to Equation (46) for the case $\beta = 0.7$, $\alpha = 0.9$ (**on the left**) and $\alpha = 1.4$ (**on the right**). The solutions are given for three values of time T, as indicated in the figures. The points are the results of a local estimate (52), the circles are histogram estimation results (50), and the solid curve is the solution (48) with a generalized diffusion coefficient $D = D_D$.

5. Conclusions

The use of the theory of anomalous diffusion and equations in fractional derivatives to describe combustion processes is only at the initial stage of research. At the moment, there are not many papers in which this approach is used to describe combustion processes. However, existing experimental studies (see, for example [37]) indicate the legitimacy of

this approach. One of the main difficulties in using equations in fractional derivatives is finding their solutions. Analytical methods for solving equations of this kind are only at the stage of development. Therefore, one of the main methods of solving equations in fractional derivatives is finite difference methods. In the papers [41–45], the numerical solution of the equation of anomalous diffusion is investigated, which is expressed in terms of derivatives of fractional order only in the case when one of the derivatives (or derivative with respect to time or derivative with respect to coordinate) is not of integer order. In this paper, we propose a numerical method for solving the anomalous diffusion equation in which both the time derivative and the coordinate derivative can be of non-integer order.

This paper considers the numerical method for solving the anomalous diffusion equation based on the use of a local estimate. This method is based on the idea of modeling random realizations of particle trajectories. However, unlike the histogram method for estimating the distribution density, each individual trajectory contributes to the estimate not once, but several times. In the proposed approach, after each act of a change in the state of a particle, the probability is calculated that to get to a given point with the coordinate x^* in a moment of time t^*, the following collision will turn out to be the final. For the considered model of walks, this probability has the form (51). This local estimate has several advantages over the histogram estimate. Since the density is estimated at a given point x^*, then this means that the result of the estimate does not contain a systematic component of the error δ_x. Specifying a set of points x_i^*, $i = 1, 2, \ldots, M$, it becomes possible to estimate the solution at several points at once. Moreover, one trajectory will contribute to all points at once x_i^*. As a result, the probability $\psi(\xi, \tau)$, determined by (51), is calculated after each act of changing the state of a particle; then, this leads to a considerable decrease in statistical error. Taking account of the fact that from one trajectory, the contribution can be calculated at once to all points x_i^*, $i = 1, 2, \ldots, M$ of a given set, this means that the desired solution can be constructed as a smooth function of the coordinate x.

In conclusion, one more important point should be noted. As shown in this study, the equation of anomalous diffusion (46) describes the asymptotic distribution (at $t \to \infty$) of particles in the CTRW process. A characteristic feature of this process is that the random rest times of a particle are characterized by a distribution with an infinite mathematical expectation $\langle T \rangle = \infty$, and the random free paths in the case of the exponent $\alpha \in (1, 2)$ are characterized by an infinite second moment $\langle R^2 \rangle = \infty$, and in the case of the exponent value $\alpha \in (0, 1]$, then by the infinite mathematical expectation $\langle R \rangle = \infty$. Taking into account that in the process of CTRW, a particle instantly moves from one point in space to another (instantaneous jumps), this leads to a non-physical result: in an arbitrarily small time interval, a particle can be at an arbitrarily large distance from the point of its previous position. It should be noted that the random walk process is also characterized by instantaneous jumps that leads to the diffusion Equation (33). However, as it was shown at the beginning of Section 3, to obtain normal diffusion, it is necessary to assume that the distributions of the rest time and the distribution of the jump value of a particle have a finite mathematical expectation and a finite variance. As a result, the instantaneous motion of a particle from one point in space to another is compensated by the small value of these jumps. In the case of a power-law distribution of the jump value (38), the probability of large jumps remains significant for any jump value. As the value decreases of α, this probability increases. This property is characteristic of power distributions. Therefore, when using the equation of anomalous diffusion (46) to describe combustion processes, especially in furnaces where the geometry is given, a certain amount of care must be taken. It should be understood that the solution to the anomalous diffusion equation decreases according to a power law at $x \to \infty$ and is different from zero in the entire space. The latter means that the probability of detecting a particle at an arbitrarily large distance from the source at an arbitrarily close moment of time to the initial time is different from zero. Taking account of the fact that this probability decreases according to a power law, then this probability will be significant, and it can no longer be neglected.

Author Contributions: Conceptualization, V.V.S.; methodology, V.V.S.; software, V.V.S.; validation, V.V.S., D.A.G. and E.V.T.; investigation, V.V.S.; writing—original draft preparation, V.V.S.; writing—review and editing, V.V.S., V.N.K. and R.V.F.; visualization, V.V.S., D.A.G. and E.V.T.; supervision, V.N.K.; project administration, R.V.F.; funding acquisition, V.N.K. and R.V.F. All authors have read and agreed to the published version of the manuscript.

Funding: This work was supported by the Megagrant of the Government of the Russian Federation in the framework of the federal project No. 075-15-2021-584.

Institutional Review Board Statement: Not applicable.

Informed Consent Statement: Not applicable.

Data Availability Statement: Not applicable.

Conflicts of Interest: The authors declare no conflict of interest.

Appendix A. Fractional Derivation Operators

Let us give the definitions and properties of some fractional differentiation operators which were used in the paper. The fractional Riemann–Liouville derivative of order $\nu > 1$ of the function $f(x)$ are the operators

$$
\begin{aligned}
{}_aD_x^\nu f(x) &= \frac{1}{\Gamma(n-\nu)}\frac{d^n}{dx^n}\int_a^x \frac{f(t)dt}{(x-t)^{\nu-n+1}},\\
{}^bD_x^\nu f(x) &= \frac{(-1)^n}{\Gamma(n-\nu)}\frac{d^n}{dx^n}\int_x^b \frac{f(t)dt}{(t-x)^{\nu-n+1}},
\end{aligned}
$$

where $n = [\nu]+1$, $\nu = [\nu]+\{\nu\}$ [56]. Here, $[\nu]$ is the integer part of number ν, and $\{\nu\}$ is the fractional part of number ν ($0 \leqslant \{\nu\} < 1$). The operator ${}_aD_x^\nu$ is called the left-sided Riemann–Liouville derivative, and the operator ${}^bD_x^\nu$ is the right-sided Riemann–Liouville derivative. The Fourier transform of these operators in the case $a = -\infty$ and $b = \infty$ has the form

$$
\int_{-\infty}^{\infty} e^{ikx}\,{}_{-\infty}D_x^\nu f(x)dx = (-ik)^\nu \hat{f}(k), \quad \int_{-\infty}^{\infty} e^{ikx}\,{}^{\infty}D_x^\nu f(x)dx = (ik)^\nu \hat{f}(k). \tag{A1}
$$

To generalize the fractional time derivative, we need the left-sided fractional Riemann–Liouville derivative of order $0 < \nu < 1$ for the function defined on the semiaxis $[0,\infty)$ [56]

$$
{}_0D_t^\nu f(t) = \frac{1}{\Gamma(n-1)}\frac{d}{dt}\int_0^t \frac{f(\tau)d\tau}{(t-\tau)^{\nu-n+1}} \tag{A2}
$$

The Laplace transform of this differentiation operator has the form

$$
\int_0^\infty e^{-\lambda t}\,{}_0D_t^\nu f(t)dt = \lambda^\nu \tilde{f}(\lambda). \tag{A3}
$$

The operator bears the name of the fractional Riesz derivative

$$
\frac{\partial^\nu}{\partial|x|^\nu} = \frac{-1}{2\cos(\pi\nu/2)}({}_{-\infty}D_x^\nu + {}^{\infty}D_x^\nu). \tag{A4}
$$

Using the definitions (A1) it is easy to show that

$$
\int_{-\infty}^{\infty} e^{ikx}\frac{\partial^\nu f(x)}{\partial|x|^\nu}dx = -|k|^\nu \hat{f}(k). \tag{A5}
$$

References

1. Metzler, R.; Glöckle, W.G.; Nonnenmacher, T.F. Fractional model equation for anomalous diffusion. *Phys. A Stat. Mech. Its Appl.* **1994**, *211*, 13–24. [CrossRef]
2. Fogedby, H.C. Lévy Flights in Random Environments. *Phys. Rev. Lett.* **1994**, *73*, 2517–2520. [CrossRef] [PubMed]
3. Shlesinger, M.F.; West, B.J.; Klafter, J. Lévy dynamics of enhanced diffusion: Application to turbulence. *Phys. Rev. Lett.* **1987**, *58*, 1100–1103. [CrossRef] [PubMed]
4. Klafter, J.; Blumen, A.; Shlesinger, M.F. Stochastic pathway to anomalous diffusion. *Phys. Rev. A* **1987**, *35*, 3081–3085. [CrossRef]
5. Chukbar, K.V. Stochastic transport and fractional derivatives. *J. Exp. Theor. Phys.* **1995**, *81*, 1025–1029.
6. Zolotarev, V.M.; Uchaikin, V.V.; Saenko, V.V. Superdiffusion and stable laws. *J. Exp. Theor. Phys.* **1999**, *88*, 780–787. [CrossRef]
7. Uchaikin, V.V. Subdiffusion and stable laws. *J. Exp. Theor. Phys.* **1999**, *88*, 1155–1163. [CrossRef]
8. Zaburdaev, V.Y.; Chukbar, K.V. Enhanced superdiffusion and finite velocity of Levy flights. *J. Exp. Theor. Phys.* **2002**, *94*, 252–259. [CrossRef]
9. Uchaikin, V.V. Self-similar anomalous diffusion and Levy-stable laws. *Physics-Uspekhi* **2003**, *46*, 821–849. [CrossRef]
10. Montroll, E.W.; Weiss, G.H. Random Walks on Lattices. II. *J. Math. Phys.* **1965**, *6*, 167. [CrossRef]
11. Scher, H.; Lax, M. Stochastic transport in a disordered solid. I. Theory. *Phys. Rev. B* **1973**, *7*, 4491–4502. [CrossRef]
12. Scher, H.; Lax, M. Stochastic transport in a disordered solid. II. Impurity conduction. *Phys. Rev. B* **1973**, *7*, 4502–4519. [CrossRef]
13. Scher, H.; Montroll, E. Anomalous transit-time dispersion in amorphous solids. *Phys. Rev. B* **1975**, *12*, 2455–2477. [CrossRef]
14. Metzler, R.; Klafter, J. The random walk's guide to anomalous diffusion: A fractional dynamics approach. *Phys. Rep.* **2000**, *339*, 1–77. [CrossRef]
15. Zaslavsky, G.M. Chaos, fractional kinetics, and anomalous transport. *Phys. Rep.* **2002**, *371*, 461–580. [CrossRef]
16. Kotulski, M. Asymptotic distributions of continuous-time random walks: A probabilistic approach. *J. Stat. Phys.* **1995**, *81*, 777–792. [CrossRef]
17. Kolokoltsov, V.N.; Korolev, V.Y.; Uchaikin, V.V. Fractional Stable Distributions. *J. Math. Sci.* **2001**, *105*, 2569–2576. [CrossRef]
18. Uchaikin, V.V. Montroll-Weiss problem, fractional equations, and stable distributions. *Int. J. Theor. Phys.* **2000**, *39*, 2087–2105. [CrossRef]
19. Mainardi, F.; Luchko, Y.; Pagnini, G. The fundamental solution of the space-time fractional diffusion equation. *Fract. Calc. Appl. Anal.* **2001**, *4*, 153–192.
20. Hanyga, A. Multi-dimensional solutions of space-time-fractional diffusion equations. *Proc. R. Soc. Lond. A* **2002**, *458*, 429–450. [CrossRef]
21. Carreras, B.A.; van Milligen, B.P.; Hidalgo, C.; Balbin, R.; Sanchez, E.; Garcia-Cortes, I.; Pedrosa, M.A.; Bleuel, J.; Endler, M. Self-Similarity Properties of the Probability Distribution Function of Turbulence-Induced Particle Fluxes at the Plasma Edge. *Phys. Rev. Lett.* **1999**, *83*, 3653–3656. [CrossRef]
22. Trasarti-Battistoni, R.; Draghi, D.; Riccardi, C.; Roman, H.E. Self-similarity, power-law scaling, and non-Gaussianity of turbulent fluctuation flux in a nonfusion magnetoplasma. *Phys. Plasmas* **2002**, *9*, 3369. [CrossRef]
23. Carreras, B.A.; van Milligen, B.P.; Pedrosa, M.A.; Balbin, R.; Hidalgo, C.; Newman, D.E.; Sanchez, E.; Frances, M.; Garcia-Cortes, I.; Bleuel, J.; et al. Self-similarity of the plasma edge fluctuations. *Phys. Plasmas* **1998**, *5*, 3632. [CrossRef]
24. Saenko, V.V. Self-similarity of fluctuation particle fluxes in the plasma edge of the stellarator L-2M. *Contrib. Plasma Phys.* **2010**, *50*, 246–251. [CrossRef]
25. Saenko, V.V. New Approach to Statistical Description of Fluctuating Particle Fluxes. *Plasma Phys. Rep.* **2009**, *35*, 1–13. [CrossRef]
26. Skvortsova, N.N.; Korolev, V.Y.; Maravina, T.A.; Batanov, G.M.; Petrov, A.E.; Pshenichnikov, A.A.; Sarksian, K.A.; Kharchev, N.K.; Sanchez, J.; Kubo, S. New possibilities for the mathematical modeling of turbulent transport processes in plasma. *Plasma Phys. Rep.* **2005**, *31*, 57–74. [CrossRef]
27. Hauff, T.; Jenko, F.; Eule, S. Intermediate non-Gaussian transport in plasma core turbulence. *Phys. Plasmas* **2007**, *14*, 102316. [CrossRef]
28. Lagutin, A.A. Anomalous diffusion of the cosmic rays in the fractal Galaxy. *Probl. At. Sci. Technol.* **2001**, *6*, 214–217.
29. Erlykin, A.D.; Lagutin, A.A.; Wolfendale, A.W. Properties of the interstellar medium and the propagation of cosmic rays in the Galaxy. *Astropart. Phys.* **2003**, *19*, 351–362.
30. Kermani, H.A.; Fatemi, J. Cosmic ray propagation in a fractal galactic medium Super-diffusion. *S. Afr. J. Sci. / Suid-Afr. Tydskr. Vir. Wet.* **2011**, *107*, 2–5. [CrossRef]
31. Ketabi, N.; Fatemi, J. A Simulation on the Propagation of Supernova Cosmic Particles in a Fractal Medium. *Trans. B Mech. Eng.* **2009**, *16*, 269–272.
32. Litvinenko, Y.E.; Effenberger, F. Analytical solutions of a fractional diffusion-advection equation for solar cosmic-ray transport. *Astrophys. J.* **2014**, *796*, 125. [CrossRef]
33. Burnecki, K.; Sikora, G.; Weron, A. Fractional process as a unified model for subdiffusive dynamics in experimental data. *Phys. Rev. E* **2012**, *86*, 041912. [CrossRef] [PubMed]
34. Romanovsky, M. Model space of economic events. *Phys. A Stat. Theor. Phys.* **1999**, *265*, 264–278. [CrossRef]
35. Dhar, A. Heat transport in low-dimensional systems. *Adv. Phys.* **2008**, *57*, 457–537.
36. Lepri, S.; Livi, R.; Politi, A. Thermal conduction in classical low-dimensional lattices. *Phys. Rep.* **2003**, *377*, 1–80. [CrossRef]

37. Souza, J.W.; Santos, A.A.; Guarieiro, L.L.; Moret, M.A. Fractal aspects in O_2 enriched combustion. *Phys. A Stat. Mech. Its Appl.* **2015**, *434*, 268–272. [CrossRef]
38. Li, S.N.; Cao, B.Y. International Journal of Heat and Mass Transfer Fractional Boltzmann transport equation for anomalous heat transport and divergent thermal conductivity. *Int. J. Heat Mass Transf.* **2019**, *137*, 84–89. [CrossRef]
39. Li, S.N.; Cao, B.Y. Anomalous heat diffusion from fractional Fokker–Planck equation. *Appl. Math. Lett.* **2020**, *99*, 105992. [CrossRef]
40. Li, S.N.; Cao, B.Y. Anomalies of lévy-based thermal transport from the lévy-fokker-planck equation. *AIMS Math.* **2021**, *6*, 6868–6881. [CrossRef]
41. Xu, Y.; Zheng, Z. Quenching phenomenon of a time-fractional diffusion equation with singular source term. *Math. Methods Appl. Sci.* **2017**, *40*, 5750–5759. [CrossRef]
42. Xu, Q.; Xu, Y. Extremely low order time-fractional differential equation and application in combustion process. *Commun. Nonlinear Sci. Numer. Simul.* **2018**, *64*, 135–148. [CrossRef]
43. Xu, Y. Quenching phenomenon in a fractional diffusion equation and its numerical simulation. *Int. J. Comput. Math.* **2018**, *95*, 98–113. [CrossRef]
44. Xu, Q.; Xu, Y. Quenching study of two-dimensional fractional reaction–diffusion equation from combustion process. *Comput. Math. Appl.* **2019**, *78*, 1490–1506. [CrossRef]
45. Wang, Z.; Xu, Y. Quenching of combustion explosion model with balanced space-fractional derivative. *Math. Methods Appl. Sci.* **2020**, *43*, 4472–4485. [CrossRef]
46. Pagnini, G. Nonlinear time-fractional differential equations in combustion science. *Fract. Calc. Appl. Anal.* **2011**, *14*, 80–93. [CrossRef]
47. Zeldovich, Y.B. *Theory of Combustion and Detonation of Gases*; Academy of Sciences (USSR): Moscow, Russia, 1944.
48. Uchaikin, V.V. Anomalous transport equations and their application to fractal walking. *Phys. A Stat. Mech. Its Appl.* **1998**, *255*, 65–92. [CrossRef]
49. Saenko, V.V. Anomalous Diffusion Equations with Multiplicative Acceleration. *J. Exp. Theor. Phys.* **2018**, *126*, 462–478. [CrossRef]
50. Saenko, V.V. The influence of the finite velocity on spatial distribution of particles in the frame of Levy walk model. *Phys. A Stat. Mech. Its Appl.* **2016**, *444*, 765–782.
51. Bening, V.E.; Korolev, V.Y.; Sukhorukova, T.A.; Gusarov, G.G.; Saenko, V.V.; Uchaikin, V.V.; Kolokoltsov, V.N. Fractionally stable distributions. In *Stochastic Models of Structural Plasma Turbulence*; Korolev, V.Y., Skvortsova, N.N., Eds.; Brill Academic Publishers: Utrecht, The Netherlands, 2006; pp. 175–244. [CrossRef]
52. Saenko, V.V. Integral Representation of the Fractional Stable Density. *J. Math. Sci.* **2020**, *248*, 51–66. [CrossRef]
53. Zolotarev, V.M. *One-Dimensional Stable Distributions*; Amer. Mat. Soc.: Providence, RI, USA, 1986.
54. Uchaikin, V.V.; Zolotarev, V.M. *Chance and Stability Stable Distributions and Their Applications*; VSP: Utrecht, The Netherlands, 1999; p. 569.
55. Bateman, H. *Higher Transcendental Functions.*; McGraw-Hill Book Company, Inc.: New York, NY, USA, 1953; Volume 1, p. 302.
56. Samko, S.G.; Kilbas, A.A.; Marichev, O.I. *Fractional Integrals and Derivatives—Theory and Application*; Gordon and Breach: New York, NY, USA, 1973.

mathematics

MDPI

Article

Roughness Scaling Extraction Accelerated by Dichotomy-Binary Strategy and Its Application to Milling Vibration Signal

Feng Feng [1], Meng Yuan [1], Yousheng Xia [1], Haoming Xu [1], Pingfa Feng [1,2,*] and Xinghui Li [1,3,*]

[1] Division of Advanced Manufacturing, Shenzhen International Graduate School, Tsinghua University, Shenzhen 518055, China; feng.feng@sz.tsinghua.edu.cn (F.F.); ym20@mails.tsinghua.edu.cn (M.Y.); xiays18@mails.tsinghua.edu.cn (Y.X.); xhm19@mails.tsinghua.edu.cn (H.X.)
[2] Department of Mechanical Engineering, Tsinghua University, Beijing 100084, China
[3] Tsinghua-Berkeley Shenzhen Institute, Tsinghua University, Shenzhen 518055, China
* Correspondence: feng.pingfa@sz.tsinghua.edu.cn (P.F.); li.xinghui@sz.tsinghua.edu.cn (X.L.)

Abstract: Fractal algorithms for signal analysis are developed from geometric fractals and can be used to describe various complex signals in nature. A roughness scaling extraction algorithm with first-order flattening (RSE-f1) was shown in our previous studies to have a high accuracy, strong noise resistance, and a unique capacity to recognize the complexity of non-fractals that are common in signals. In this study, its disadvantage of a long calculation duration was addressed by using a dichotomy-binary strategy. The accelerated RSE-f1 algorithm (A-RSE-f1) retains the three above-mentioned advantages of the original algorithm according to theoretical analysis and artificial signal testing, while its calculation speed is significantly accelerated by 13 fold, which also makes it faster than the typical Higuchi algorithm. Afterwards, the vibration signals of the milling process are analyzed using the A-RSE-f1 algorithm, demonstrating the ability to distinguish different machining statuses (idle, stable, and chatter) effectively. The results of this study demonstrate that the RSE algorithm has been improved to meet the requirements of practical engineering with both a fast speed and a high performance.

Keywords: roughness scaling extraction; fractal dimension; accelerated algorithm; Weierstrass–Mandelbrot function; milling vibration signal

MSC: 37M10

Citation: Feng, F.; Yuan, M.; Xia, Y.; Xu, H.; Feng, P.; Li, X. Roughness Scaling Extraction Accelerated by Dichotomy-Binary Strategy and Its Application to Milling Vibration Signal. *Mathematics* **2022**, *10*, 1105. https://doi.org/10.3390/math10071105

Academic Editors: Camelia Petrescu and Valeriu David

Received: 25 February 2022
Accepted: 28 March 2022
Published: 29 March 2022

Publisher's Note: MDPI stays neutral with regard to jurisdictional claims in published maps and institutional affiliations.

Copyright: © 2022 by the authors. Licensee MDPI, Basel, Switzerland. This article is an open access article distributed under the terms and conditions of the Creative Commons Attribution (CC BY) license (https://creativecommons.org/licenses/by/4.0/).

1. Introduction

Pioneered by the mathematician Mandelbrot [1,2], fractal geometry was established to investigate the morphological characteristics of filling space in the form of non-integer dimensions. Early studies have revealed that many features in nature have fractal characteristics, so fractal geometry is widely applied to a large variety of research areas, such as the influence of the fractal features of transects across vegetation on the arthropods living on its surface [3], the relationship between biological size and physiological function [4], and observations of the large-scale structure of the universe [5]. Follow-up studies found that fractals not only existed in features of nature, but also in various signals such as physiological electrical signals [6].

Fractal dimension (**FD**) is often used to measure the degree of geometric irregularity. Generally, the higher the complexity of the signal, the larger the corresponding **FD** value [7]. Therefore, many scholars have introduced **FD** into the research of signal processing in the medical field, such as electroencephalograms (EEG) [8] and electrocardiograms (ECG) [9–12], and have made remarkable achievements.

In recent years, signal fractals have been extended to the field of mechanical processing, such as the fractal characteristics of ultrasonic echoes and their application to nondestructive testing [13], the multifractal characteristics of ball mill dynamics [14], and the application

of vibration signal multifractals in fault diagnosis [15]. As a typical nonlinear signal, mechanical vibration has obvious fractal characteristics, and the complexity of the signal is closely related to the vibration state of the machine tool. Therefore, the fractal analysis of signals is also used to judge the machining status of machine tools. Ji et al. [16,17] proposed a multi-indicator chatter prediction method combining **FD**, power spectral entropy, and standard deviation. Zhuo et al. [18] identified chatter by calculating the **FD** of acceleration signals in thin-wall blade side milling. Chen et al. [19] proposed a multifractal method for chatter detection in milling processes. It can be seen that the application of **FD** in the field of manufacturing has been recognized.

There are various algorithms for calculating **FD**, including the box-counting (BC) algorithm [20], the Katz algorithm [21], and the Higuchi algorithm [22]. The Higuchi and box-counting algorithms have been widely used due to their practical applicabilities and fast speed [23–26]. In our previous study, a roughness scaling extraction (RSE) algorithm was proposed [27,28], and it has a higher accuracy and anti-noise performance compared with other traditional algorithms. The RSE algorithm can identify non-fractal features in signals [29], which is an ability that traditional fractal algorithms do not have. The RSE algorithm is based on the exponential relationship between scale (L) and root-mean-squared roughness (R_q), as shown in Equation (1). Firstly, Equation (2) is used to calculate the roughness values at each scale (L_i, R_{qi}), where $i = 1, 2, \ldots, n$ represents the serial number of the data point, and $\overline{y}$ represents the average of y_i, $\overline{y} = \frac{\sum_{i=1}^{n} y_i}{n}$, and then to obtain the dimension value $\boldsymbol{D}$ through Equation (3). $L = [L_1, L_2, \ldots, L_p]$ represents the signal length at different scales, as well as the number of signal points ($L_i = [L_{i-1} \times \delta]$, δ represents the scaling ratio).

$$R_q = AL^{2-D} \tag{1}$$

$$R_q = \sqrt{\frac{\sum_{i=1}^{n}(y_i - \overline{y})^2}{n}} \tag{2}$$

$$\log R_q = (2 - D)\log L + \log A \tag{3}$$

The key procedure of the RSE algorithm is the flattening modification of sub-sequences that are segmented out of the concerned signal. The RSE algorithm with first-order flattening (RSE-f1) is the most accurate for fractal signals. First-order flattening refers to first-order polynomial fitting of the sub-sequences, as shown in Equation (4), where the expressions of a, b, and x_i are shown in Equation (5). The sequence of the RSE-f1 algorithm consists of the elements m_i calculated by Equation (6).

$$\hat{y}_i = b + ax_i \tag{4}$$

$$a = \frac{\sum_{i=1}^{n} x_i y_i - n\overline{x}\,\overline{y}}{\sum_{i=1}^{n} x_i^2 - n\overline{x}^2};\ b = \overline{y} - a\overline{x}^2;\ x_i = i \tag{5}$$

$$m_i = y_i - \hat{y}_i \tag{6}$$

However, the disadvantage of the RSE algorithm is that calculations are time-intensive, which limits its application in practical engineering. Considering that the on-line recognition of the machining status of machine tools requires a fast response speed, the RSE algorithm needs to be accelerated to reflect the signal characteristics in a short delay of calculation. Therefore, an accelerated RSE-f1 (A-RSE-f1) algorithm based on a dichotomy and binary strategy is proposed in this paper. Based on theoretical analysis and artificial fractal signal testing, the A-RSE-f1 algorithm is much faster than the original RSE-f1 and the Higuchi algorithm, and it retains the high anti-noise performance of the RSE-f1 algorithm. Experimental results demonstrated that the A-RSE-f1 algorithm could distinguish the different machining statuses effectively of machining tools. In addition, the relationship between roughness and scale of the A-RSE-f1 algorithm is equivalent to that of the RSE-f1. Thus, the improvement does not change the fractal calculation principle of the algorithm.

2. Methods and Samples

2.1. Improvement of the RSE Algorithm

Specifically, the large scale sequence is divided into two small scale sequences, and the small scale sequence is divided successively until each subsequence contains only one element. In this way, it is guaranteed that sub-sequences at different scales do not overlap with each other and that the set of sub-sequences only covers the signal sequence, thus ensuring the calculation accuracy. It also adaptively changes the summation times of subsequence roughness according to the scale, which greatly improves the operation speed of the algorithm. As the formula and code of RSE-f0 are relatively simple, it is possible to find the core reason why the RSE algorithm requires a long time, so a dichotomy strategy was first used to preliminarily improve RSE-f0. In order to improve the accuracy of A-RSE-f0, it needs to carry out first-order flattening and realize random δ through a binary strategy, so as to obtain A-RSE-f1.

2.1.1. Accelerated RSE-f0 Algorithm

In order to accelerate the RSE algorithm, it must be clear what is taking the longest time in the program. Therefore, the pseudocode of the RSE algorithm without flattening (RSE-f0) can be written based on the above equations, as shown in Algorithm 1, where $stepN$ represents the number of subsequences of different lengths, and $subdata_i$, $R_q(m)_i$ represent the subsequence and roughness extracted for the i-th time at a certain scale, respectively. As the roughness of the small scale subsequence varies greatly in different positions of the signal sequence, it needs to be solved many times and then averaged, as shown in Lines 4 to 6 of the pseudocode. In order to ensure sufficient representativeness of the calculated roughness and a certain computational efficiency of the RSE-f0 algorithm, the roughness values of the 50 randomly selected sub-sequences are averaged as the final roughness value corresponding to the scale. However, it is this part of the operation that still greatly increases the time cost of the RSE-f0 algorithm. According to statistics, the 4∼6 lines of the pseudocode account for 99% of the calculation duration of the algorithm. It is understood that, when the sub-sequence scale is large, many of the 50 randomly selected sub-sequences can overlap, and when the sub-sequence scale is small, it is difficult to completely cover the signal by randomly selecting positions. Therefore, to accelerate the RSE-f0 algorithm, calculating the roughness adaptively while covering the entire signal is key.

Algorithm 1 RSE-f0 algorithm

Input: $data$: signal data; δ: scaling ratio; $minpixle$: the number of elements of the; smallest scale; $repeat_{num}$: the calculating times of the roughness of the same scale
Output: D: the dimension value of the signal

1: $stepN \leftarrow [\frac{\log(\frac{minpixle}{n})}{\log \delta}]$
2: $L \leftarrow N \times \delta^{[0\ to\ stepN-1\ do]}$, $R_q(1)$
3: **for** each $m \in [2, stepN]$ **do**
4: **for** each $i \in [1, repeat_{num}]$ **do**
5: $subdata_i$, $R_q(m)_i$
6: **end for**
7: $R_q(m) \leftarrow mean(R_q(m)_i)$
8: **end for**
9: $D \leftarrow 2 - \frac{\log R_q}{\log L}$

Aiming at this improvement, a preliminary accelerated algorithm based on RSE-f0 is proposed with a scaling ratio of 0.5. First, the dichotomy method is employed, thus the calculation flow is reversed, i.e., the roughness values are obtained from large sub-sequences to small ones in the original RSE-f0, while those in the A-RSE-f0 are from small sub-sequences to large ones. As sketched in Figure 1, each element in the sequence can be

regarded as a cell, and the combination of adjacent elements yields the next cell, which had twice the element number of the previous one. By analogy, the set of sub-sequences at various scales can be obtained, and the sub-sequences have no overlaps, which also ensures the full coverage of the signal. Obviously, based on the dichotomy method, the calculation times of the large-scale subsequence are shorter, while the calculation times of the small-scale subsequence are longer. For example, there are two sub-sequences after one scaling ($L_1 = 0.5 \times L$), while there are $\frac{1}{0.5^n}$ sub-sequences of the n-th scaling ($L_n = 0.5^n \times L$), which conforms to the previous goal of adaptively extracting the number of sub-sequences.

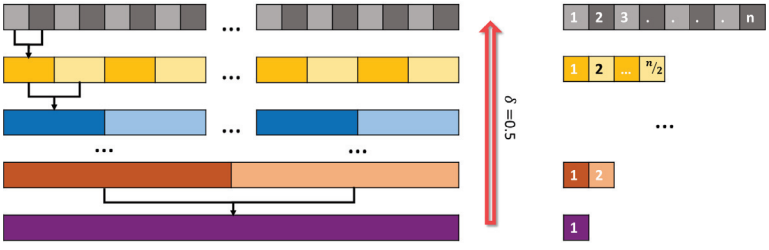

Figure 1. The schematic diagram of improving flow of A-RSE-f0 based on dichotomy method.

Further, the expression of the A-RSE-f0 algorithm is transformed, as shown in Equations (7) and (8). Equation (7) can be derived from Equation (1), where $A = \sum_{i=1}^{n} y_i^2$ and $B = \sum_{i=1}^{n} y_i$, thus obtaining Equation (8). The problem is then transformed into the construction of A and B matrices containing all scales by using the above dichotomy flow.

$$R_q^2 = \frac{\sum_{i=1}^{n} y_i^2}{n} - (\frac{\sum_{i=1}^{n} y_i}{n})^2 \tag{7}$$

$$R_q^2 = \frac{A}{n} - (\frac{B}{n})^2 \tag{8}$$

2.1.2. The Accelerated RSE-f1 Algorithm

The next aim of this study is to improve the RSE algorithm with first-order flattening (RSE-f1), whose accuracy is the highest [27]. The improved method based on the dichotomy idea can be extended to RSE-f1 as follows. Similar to that of A-RSE-f0, the expression of the A-RSE-f1 algorithm is also transformed. Equation (9) can be derived based on Equations (1) and (6). In Equation (9), $A = \sum_{i=1}^{n} y_i^2$, $C = \sum_{i=1}^{n} x_i y_i$ and $B = \sum_{i=1}^{n} y_i$ are set to obtain Equation (10). In this way, the problem is transformed into the construction of A, B, and C matrices containing various scales, and the solution of the intermediate parameters a and b. Thus, an A-RSE-f1 algorithm with $\delta = 0.5$ is obtained.

$$R_q^2 = \frac{\sum_{i=1}^{n} y_i^2 - a\sum_{i=1}^{n} x_i y_i - b\sum_{i=1}^{n} y_i}{n} \tag{9}$$

$$R_q^2 = \frac{A - aC - bB}{n} \tag{10}$$

However, in order to extend the scaling ratio of A-RSE-f1 to any value of δ to enhance its applicability, a binary strategy needs to be introduced. Specifically, extending to any δ is equivalent to the problem of extracting the subsequence between any two points in the signal sequence. Combined with Equations (9) and (10), the equivalent issue is how to quickly obtain the sum of the corresponding elements of the subsequence at any position.

For example, in order to obtain the sum from the first point to the P_{start}-th point in a sequence, the following operations can be conducted. Firstly, P_{start} is converted into binary numbers in the matrix constructed when $\delta = 0.5$ is used based on dichotomy. The i_{bin}-th bit in binary then corresponds to the i_{bin}-th row (a subsequence of length $2^{i_{bin}-1}$) and the $(P_{start} >> (i_{bin} - 1))$ column element of the matrix, where $>>$ represents the

right-shift operation in binary. The sum of all elements of the matrix corresponding to 1 in the binary number is the sum of the target sequence. As shown in Figure 2, if $P_{start} = 7$, it can be written as 111 after it is converted to binary. Its first digit (from right to left) is 1, corresponding to the first row and seventh column of the matrix. The second digit is also 1, corresponding to the second row and third column of the matrix. The third digit is also 1, corresponding to the third row and the first column of the matrix. The above three elements in the matrix are then summed, as shown in Equation (11). The problem is then transformed from a sum of seven elements to a sum of three elements, effectively reducing the time of summation and thus reducing the calculation duration. If the sum of elements between any two points is required, the sum from the first point to the P_{start}-th point $SUM_{P_{start}}$ and the sum from the first point to the P_{end}-th point $SUM_{P_{end}}$ can be obtained by the above algorithm, respectively, and the sum from the P_{start}-th point to the P_{end}-th point can then be obtained by $SUM_{P_{end}} - SUM_{P_{start}}$, as shown in Equation (12). Understandably, the overlapping elements cancel each other out while they are subtracted, resulting in a sum of the target elements, as shown in Figure 3.

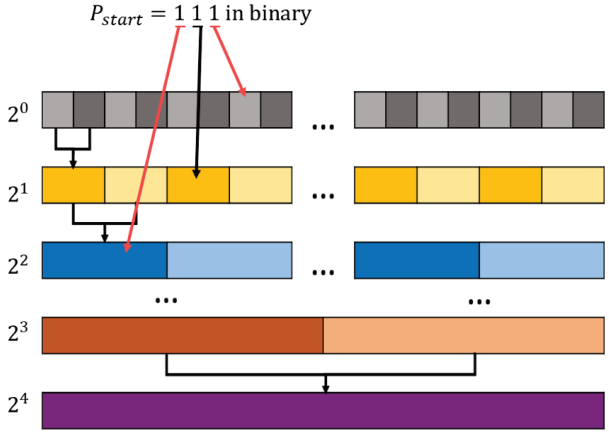

Figure 2. A diagram of the sum from the first point to the P_{start}-th (=7) point of the sequence in binary, which is employed for A-RSE-f1.

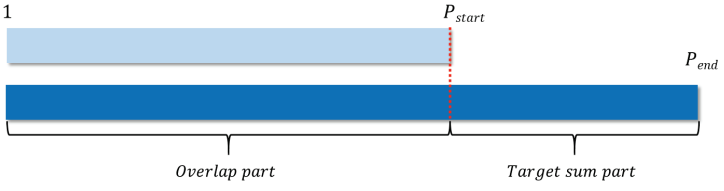

Figure 3. Diagram of summation of subsequence from P_{start} to P_{end}.

To summarize the above methods in a mathematical language, auxiliary matrices A, B, and C are denoted as ***TEMP***, as shown in Equation (11), where $\boldsymbol{TEMP}(i_{bin}, P >> (i_{bin} - 1))$ represents the element of the $(P >> (i_{bin} - 1))$ column of the i_{bin} row of the auxiliary matrix. In Equation (13), $\zeta(i)$ represents a two-valued function that returns 1 when the i_{bin} bit of the binary number is 1, and 0 when the i_{bin} bit is 0. After converting P_{start} into binary (P_{bin}), traverse all the elements in the auxiliary matrix corresponding to 1 contained in P_{bin}, and these values are then summed. Therefore, the number of summations in Equation (11) depends on the number of 1 s contained in the P_{bin}.

$$SUM_{p_{start}} = \sum \boldsymbol{TEMP}(i_{bin}, P_{start} >> (i-1))\zeta(i) \tag{11}$$

$$SUM = SUM_{P_{end}} - SUM_{P_{start}} \tag{12}$$

$$\zeta(i) = \begin{cases} 0 & \text{if the } i\text{-th bit of P in binary is 0} \\ 1 & \text{if the } i\text{-th bit of P in binary is 1} \end{cases} \tag{13}$$

In such a manner, the A-RSE-f1 algorithm achieved the aim of being adaptive and providing full coverage in the sub-sequence extraction based on the idea of a dichotomy so as to avoid repeated calculations caused by random selections with fixed times. The binary strategy was then used to reduce the summation times, thus further accelerating the summation process of corresponding elements. Compared with the RSE-f1 algorithm, the improvements of the A-RSE-f1 algorithm are based on equivalent operations via the dichotomy-binary strategy and thus do not change its principle, maintaining the accuracy of calculation.

2.2. Samples

2.2.1. Artificial Fractal and Non-Fractal Signals

As the true value of $\boldsymbol{D}$ cannot be obtained in prior for the actual fractal features, it is difficult to evaluate the advantages and disadvantages of different fractal algorithms by using signals from nature. Therefore, using a fractal function to generate ideal fractal signals or surfaces is an important approach to evaluate the performance of different fractal algorithms. The fractal function has the property of being continuous everywhere, but not differentiable [29]. The functions commonly used for generating fractal signals include the Weierstrass–Mandelbrot (W-M) function [30,31], the Monte Carlo function [32], the Takagi function [33], and the Brownian motion function [34]. Among them, the W-M function is widely used in the field of fractal analysis [35–39]. Moreover, the abnormal implementation of the W-M function enables it to generate non-fractal profiles or surfaces [29]. According to our previous research, actual signals or surfaces in nature also have non-fractal features, while traditional fractal algorithms (including Higuchi and box-counting) cannot recognize the complexity of non-fractal characteristics. Therefore, in this study, the W-M function is used to generate both fractal and non-fractal signals, so as to evaluate the performances of different algorithms.

The mathematical expression of the W-M function is shown in Equation (14), where $\boldsymbol{D}$ is the ideal ***Dimension*** value of the generated signals; γ is the density of frequencies in the signal; M is the number of superposed ridges; ϕ_n is a random phase shift; and n is a frequency index. Fifty groups of fractal signals for each $\boldsymbol{D}$, ranging from 0.1 to 2 with an interval of 0.1, were generated by the W-M function. Relevant pictures can be seen in the previous research [27]. It can be seen that, with the increase in the $\boldsymbol{D}$ value, the complexity of the curve is higher and the fluctuation of it is more severe.

$$W(x) = \sum_{n=0}^{M} \gamma^{(D-2)n} [cos\phi_n - cos(\gamma^n x + \phi_n)] \tag{14}$$

2.2.2. Milling Vibration Signals

In order to apply the A-RSE-f1 algorithm in practical engineering, it is not sufficient to test its performance only with the generated ideal fractal signals. It also needs to use real machining signals for verification purposes. Milling is one of the most important machining technologies in the field of manufacturing. However, the severe vibration of machine tools usually leads to the deterioration of workpiece surface quality, thus reducing work efficiency. Therefore, many methods to predict and suppress chatter have been proposed, including the establishment of a stability lobe diagram (SLD) [40], a cutting dynamics model [41], and online monitoring [42,43]. Recognizing the signal characteristics of machine tools is an important on-line monitoring method for preventing chatter [44–48]. For industries, an acceleration signal is generally recommended [49]. Therefore, the application effect of the A-RSE-f1 algorithm in practical engineering was verified by milling acceleration signals. The experimental equipment and data analysis are illustrated in Figure 4.

The machining signals used in this study were the acceleration signals of the machine tool spindle collected by the experimental equipment. The data acquisition process was carried out using an accelerometer fixed on the spindle of the machine tool. The data of the sensor were collected using the Simens LMS TestLab 17 software and finally transmitted to the computer. The vertical machining center was the EUMA DU810, and the accelerometer used was a PCB piezoelectric triaxial vibration sensor. The partial enlargement of the workbench and the workpiece surface obtained by two machining statuses (stable and chatter) are shown in Figure 4b. The data acquisition equipment was an LMSSCADASIII multi-channel data acquisition front end, as shown in Figure 4c.

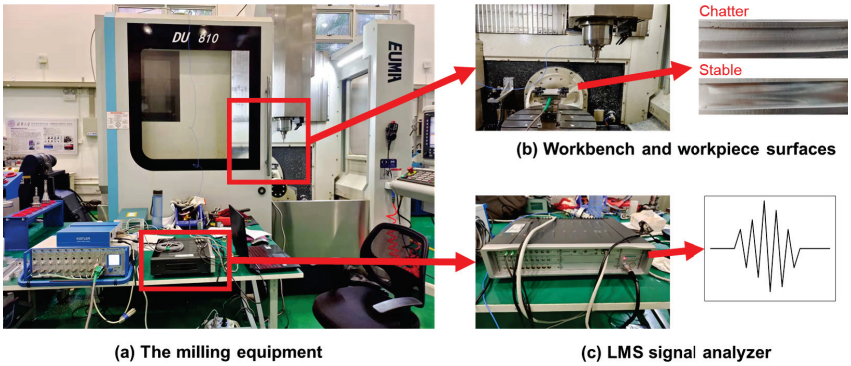

Figure 4. The final assembly of: (**a**) the milling equipment, (**b**) workbench and workpiece surfaces, and (**c**) LMS signal analyzer.

3. Results and Discussion

3.1. Ideal Fractal Signals Testing

In order to test the improvement effect of this study, the original RSE-f1, A-RSE-f1, Higuchi, and BC algorithms were used to calculate 20×50 artificial signals generated by the above W-M function. In this study, δ of the A-RSE-f1 has been extended to any value. Therefore, in order to evaluate the improved algorithm comparatively, the δ values of both A-RSE-f1 and RSE-f1 were set as $\delta = 0.85$.

Firstly, the calculated dimension (D_c) values by RSE-f1, A-RSE-f1, Higuchi, and BC algorithms were compared with the ideal dimension (D_i) values, as plotted in Figure 5. Obviously, when $\boldsymbol{D}$ value is less than 1, the calculation results of the Higuchi and BC algorithms are close to 1, while both the RSE-f1 and A-RSE-f1 algorithms could effectively approximate the D_i value. When the $\boldsymbol{D}$ value is above 1, the curves of RSE-f1, A-RSE-f1, and Higuchi are very close to D_i, but there is significant deviation in the BC curve.

To quantify the deviation of the above four algorithms, the logarithmic coordinate plot of the mean relative error (MRE) under different D_i were summarized, as shown in Figure 6. It can be seen that, when D_i is less than 1, the MRE values of RSE-f1 and A-RSE-f1 are much smaller than those of the Higuchi and BC algorithms, consistent with the results in Figure 5. These two traditional algorithms are completely invalid in the non-fractal region. When D_i is greater than 1, the MRE values of BC are generally greater than those of RSE-f1 and A-RSE-f1, while the Higuchi algorithm has a high accuracy when D_i is close to 2. It can also be observed in Figure 5 that the D_c values of the Higuchi algorithm are all larger than D_i, which is consistent with what is shown in Figure 6. By contrast, RSE-f1 and A-RSE-f1 both have high computational accuracy even in the non-fractal region, and their MREs are below 2% in the fractal region. Therefore, RSE-f1 and A-RSE-f1 are applicable to a wider range than are the other algorithms in terms of analyzing the signals of fractal and non-fractal regions.

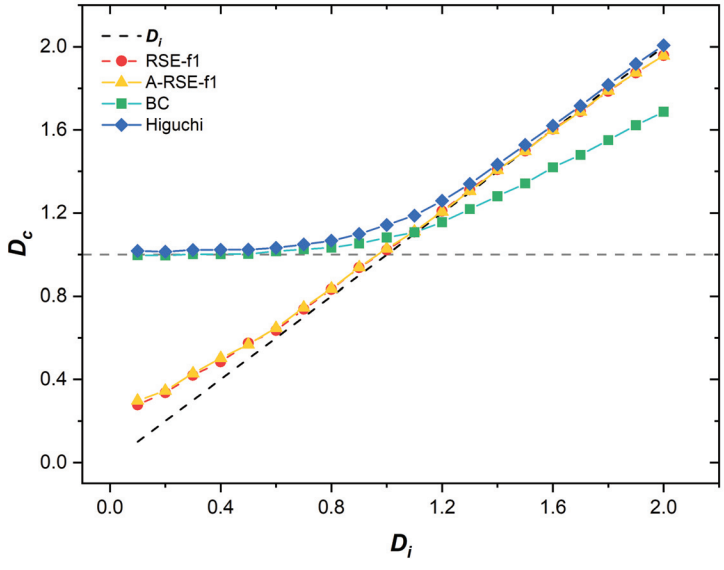

Figure 5. Comparision of the ideal dimension (D_i) and the calculated dimension (D_c) by RSE-f1, A-RSE-f1 Higuchi, and BC algorithms.

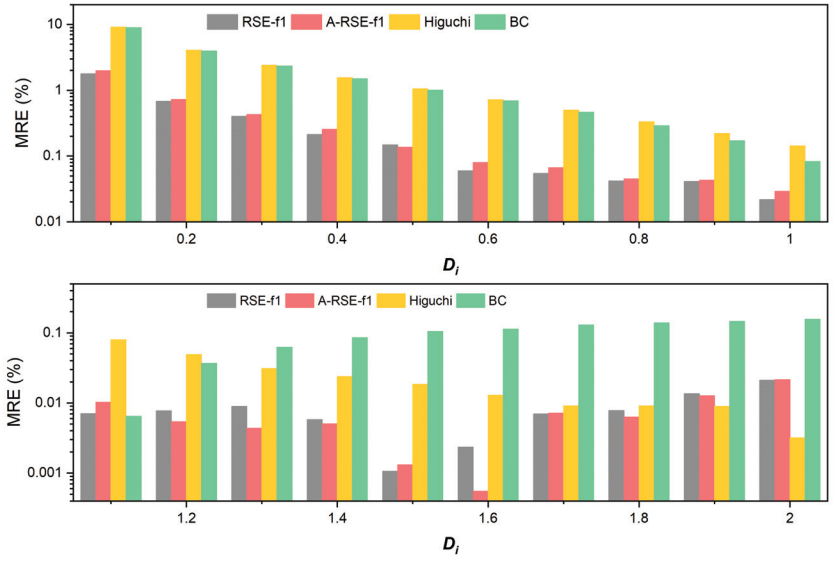

Figure 6. The logarithmic coordinate plot of the mean relative error (MRE) of RSE-f1, A-RSE-f1, Higuchi, and BC algorithms under different D_i values.

A major advantage of A-RSE-f1 compared with RSE-f1 is that its calculation speed is greatly accelerated. Figure 7 shows the single running duration (SRD) and standard deviation (STD) of the RSE-f1, A-RSE-f1, Higuchi, and BC algorithms. The calculation speed of A-RSE-f1 is significantly higher than that of the RSE-f1 algorithm by about 13 folds, and is also faster than that of the Higuchi algorithm, indicating that A-RSE-f1 based on a dichotomy and binary strategy has an advantage in terms of calculation speed. The

A-RSE-f1 algorithm only needs 7.8×10^{-3} s for a single running, which meets the practical engineering requirements. However, the RSE algorithm has the disadvantage of a large fluctuation in the results. As shown in Figure 7, the STD values of both RSE algorithms are higher than those of the Higuchi and BC algorithms, so multiple measurements are needed to eliminate such fluctuation.

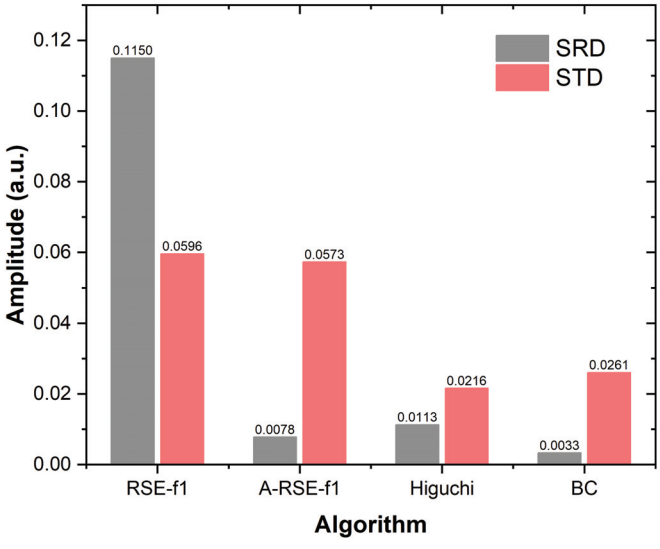

Figure 7. The single running Duration (SRD) and standard deviation (STD) of the RSE-f1, A-RSE-f1, Higuchi, and BC algorithms.

In essence, the collected signals in reality are always mixed with noise, which will reduce the efficiency of the calculations [50], so the algorithm must have an ability to resist noise. Therefore, the anti-noise performance of the RSE-f1, A-RSE-f1, Higuchi, and BC algorithms were also compared. The signal–noise ratios (SNRs) used in this study were $0, 5, \ldots, 50$ dB. As shown in Figure 8, the MRE values of the artificial signals after adding noise were calculated by the four algorithms. It can be seen that, when the D_i and SNR are both small, the anti-noise performance of all algorithms is low, because noise dominates the characteristics of the signals, and the D_c values are all close to 2, leading to large calculation errors. With the increase in SNR, the MRE values of all algorithms except BC gradually decrease, because the proportion of noise decreases. The BC algorithm shows an opposite trend in many cases. As indicated in Figure 5, the D_c values of the BC algorithm are low, and the deviation becomes larger with the increase in D_i. When D_i is large, noise plays a role in compensation, making BC more accurate, which is an interesting result. Globally, the MREs of the RSE-f1 and A-RSE-f1 algorithms are lower than those of the Higuchi and BC algorithms, demonstrating that the RSE-f1 algorithm has a strong anti-noise property, and its accelerated version, A-RSE-f1, retains this property.

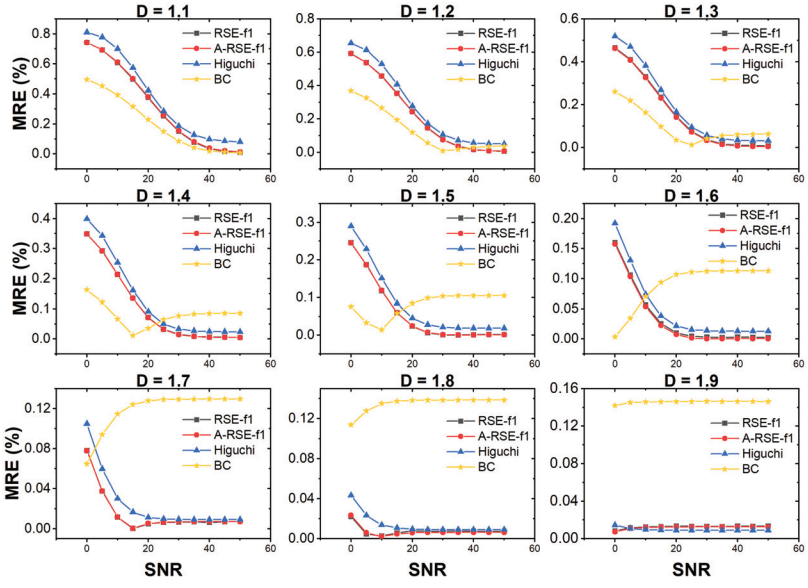

Figure 8. The comparision of anti-noise performances of RSE-f1, A-RSE-f1 Higuchi, and BC algorithms under different D_i and signal-noise-ratio (SNR) values.

3.2. Chatter Recognition in Milling

As shown in Figures 9 and 10, the typical acceleration signals of stable and chatter statuses are significantly different. The above signals were denoised by a five-order wavelet method, and the two sets of signals were calculated by the RSE-f1, A-RSE-f1, Higuchi, and BC algorithms. The length of the stable signal in Figure 9 is 30 s, of which 5–25 s is under a stable status of machining. The length of the chatter signal in Figure 10 is 13.5 s, of which 3.5–12 s is under a chatter status of machining. It can be seen that the calculation results of the RSE-f1, A-RSE-f1, and Higuchi algorithms vary accordingly, along with the operations and statuses of the milling process. The ***D*** values of stable milling are less than 1.4, and those of chatter milling are greater than 1.9. However, the ***D*** values calculated by the BC algorithm are about 1.5 in the stable milling and 1.7 in the chatter milling. The BC algorithm might not distinguish the acceleration signals of stable and chatter milling effectively and may not be suitable for the chatter recognition of acceleration signals. In addition, the ***D*** values of the idling status calculated by RSE-f1 and A-RSE-f1 are generally less than 1, indicating the non-fractal nature of the signals under such conditions. The Higuchi and BC algorithms cannot recognize non-fractal features, so their chatter recognition abilities are weaker. In particular, the ***D*** values of acceleration signals calculated by the Higuchi method in the idling status are basically the same as those in stable machining, as shown in Figure 9.

Vibration interference is an important factor restricting the development of computer numerical control (CNC) machine tool technology, including free vibration, forced vibration, and self-excited vibration. Chatter is a kind of complex, self-excited vibration, which is also the most serious form of vibration affecting the processing system. The real-time monitoring and recognition method can detect the status change of machine tools in time, so as to enable the suppression of the harm of chatter to workpiece and machine tools. However, the developments of chatter monitoring and suppression require recognition algorithms with both high accuracy and speed.

In order to further evaluate the application effect of A-RSE-f1 in signal recognition, 40 groups of milling acceleration signals (20 stable signals and 20 chatter signals) are

identified by the above four algorithms. The calculation durations for 40 groups of signals are listed in Table 1. The calculation durations are ordered as follows: RSE-f1 > Higuchi > A-RSE-f1 > BC. It can be seen that A-RSE-f1 is a significant improvement over RSE-f1 in terms of calculation speed and can thus meet the computing requirements of practical engineering applications.

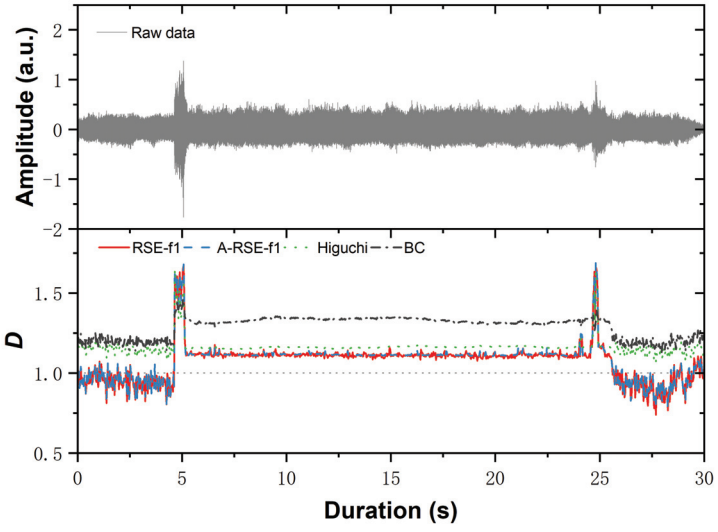

Figure 9. The acceleration signals of stable milling and ***D*** values of signal calculated by RSE-f1, A-RSE-f1, Higuchi, and BC algorithms.

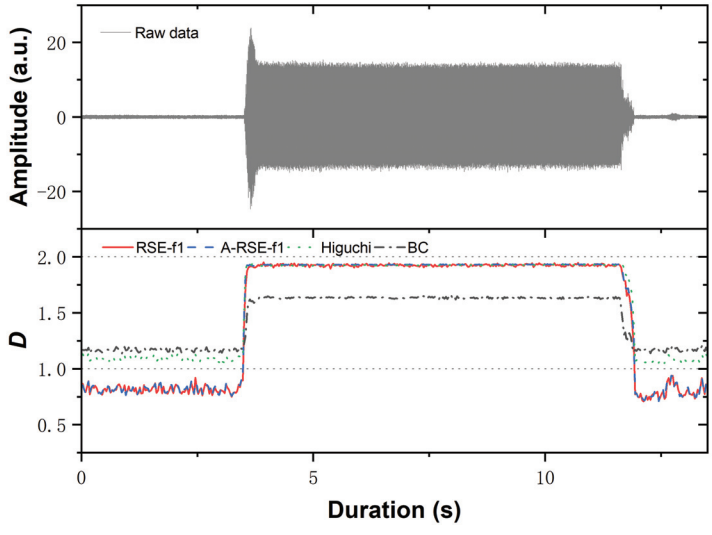

Figure 10. The acceleration signals of chatter status and ***D*** values of signal calculated by RSE-f1, A-RSE-f1, Higuchi, and BC algorithms.

Table 1. The calculation durations of RSE-f1, A-RSE-f1, Higuchi, and BC algorithms to process all 40 sets of vibration signals.

Algorithm	RSE-f1	A-RSE-f1	Higuchi	BC
Duration (s)	2439	157.7	249.1	65.41

Machining statuses can be idling, stable, or chatter. In order to ensure the consistent proportion of data in various machining statuses and the representativeness of signal samples, 100 ***D*** values were randomly selected from the results of 20 chatter signals in the idling stage and the machining stage and of 20 stable signals in the signal machining stage, respectively, so each machining status calculated by each algorithm has 2000 data points. The above data are plotted in Figure 11 and form the histogram of the ***D***-value distribution of 40 signals at different statuses calculated by the four algorithms. Obviously, the results of the RSE-f1, A-RSE-f1, and Higuchi algorithms have less overlap in the stable and chatter parts than the BC algorithm, indicating that these three algorithms can better identify the chatter characteristics of milling acceleration signals. As for idling and stable statuses, it can be seen that the RSE-f1 and A-RSE-f1 algorithms have the least overlap. As the acceleration signal of the machine tool spindle is relatively simple during idling, it embodies more non-fractal characteristics. The calculated ***D*** values of RSE-f1 and A-RSE-f1 are basically less than 1, which is consistent with the performance of actual machining, indicating that these two algorithms are applicable to a wider range. However, the Higuchi and BC algorithms cannot recognize non-fractal signals, so the calculation results of the idling part will partially overlap with stable processing.

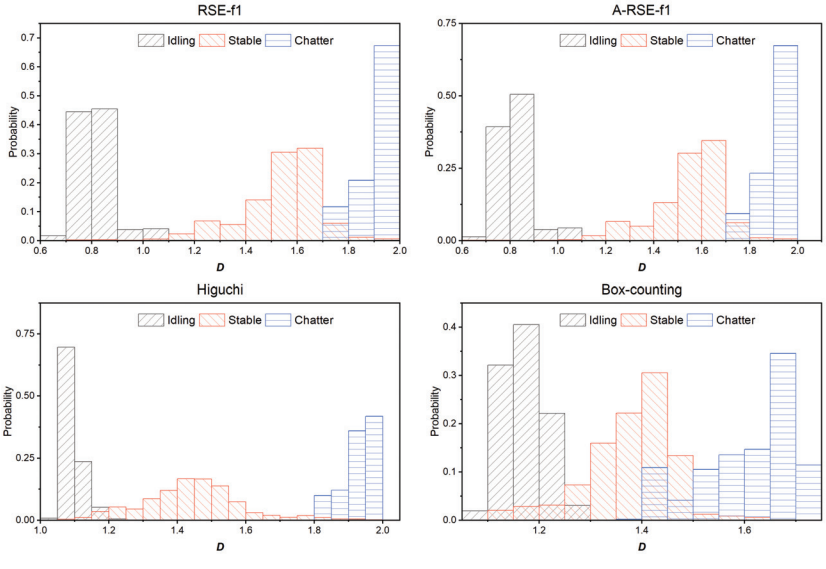

Figure 11. Histogram of ***D*** values distribution of 40 signals at different statuses calculated by RSE-f1, A-RSE-f1, Higuchi, and BC algorithms.

The A-RSE-f1 algorithm is significantly faster than the RSE-f1 algorithm and even faster than the Higuchi algorithm. Moreover, A-RSE-f1 can recognize non-fractal features, so the machining status of idling, stable, and chatter can be distinguished significantly according to the acceleration signal of the spindle of the machine tool. Although the calculation speed of the BC algorithm is faster, its accuracy and noise resistance are weak, and it is difficult to distinguish different machining statuses effectively. Therefore, the

A-RSE-f1 algorithm has the best comprehensive performance with a fast calculation speed, a high accuracy, strong noise resistance, and a wide application range, and can distinguish different processing statuses effectively.

3.3. Effects of Cutting Parameters

The establishment of a milling stability lobe diagram [51] is a method used to predict machining status, and the occurrence of chatter can be avoided by inducing stable cutting parameters under certain working conditions. Therefore, the selection of machining parameters is closely related to machining status and vibration signal. The influence of processing parameters on signal dimension will be explored below.

The experimental equipment is described in Section 2.2.2. The workpieces are 7075 120 mm × 120 mm × 10 mm aluminum alloy square plates, and the cutting tool is a tungsten steel 3-edge milling cutter with A diameter of 10 mm. A total of 36 groups of machining parameters, including changes in feed, cut depth, and speed, are summarized in Table 2. Fifty windows were randomly selected for each signal (each window contains 1024 data points), and 50 $\boldsymbol{D}$ values were calculated and averaged. According to the above analysis, the calculation results of RSE-f1 and A-RSE-f1 are almost the same, while the calculation duration of RSE-f1 is much longer, so only the A-RSE-f1, Higuchi, and BC algorithms were used for calculation. The calculation results are illustrated in Figure 12.

Table 2. 36 groups of machining parameters with various feed, cut depth and speed values.

No.	Speed (r/s)	Depth (10^{-3} m)	Feed (10^{-3} m/s)
1			8.3
2			9.2
3	50.0	1.0	10.0
...			...
13			18.3
14		0.5	
15		0.7	
16	150.0	0.9	6.7
...		...	
26		2.9	
27	50.0		
28	66.7		
29	83.3	1.0	5.0
...	...		
36	200.0		

As shown in Figure 12a, the $\boldsymbol{D}$ values calculated by the A-RSE-f1 and Higuchi algorithms all increased with the increase in the feed, among which the results of A-RSE-f1 show a more obvious upward trend. The feed per tooth can be expressed as $F/(3S)$, where F (m/s) represents the feed speed, and S (r/s) stands for spindle speed. The experimental tool has three teeth. Under the condition of the same speed and cutting depth, the larger the feed per tooth, the more likely it is to cause chatter, resulting in a higher $\boldsymbol{D}$ in the acceleration signal of the spindle. As shown in Figure 12b, the $\boldsymbol{D}$ values calculated by the A-RSE-f1 and Higuchi algorithms drop significantly when the cutting depth range is 0.5∼1.3 mm, indicating that the machine tool is prone to violent vibrations when the cutting depth is very small, consistent with the experimental phenomenon. When the cutting depth is greater than 1 mm, the $\boldsymbol{D}$ values of the acceleration signal are relatively stable, indicating that the cutting depth has little influence on the vibration of the machine tool within this range. However, a greater cutting depth can increase the cutting force of the tool, such that the tool can be more vulnerable to damage. As shown in Figure 12c, the $\boldsymbol{D}$ values calculated by the A-RSE-f1 and Higuchi algorithms generally show a downward trend along with the increase in spindle speed. This is similar to the situation in Figure 12a. As the spindle speed

increases, the feed per tooth decreases, so the possibility of chatter and the complexity of acceleration signal both decrease. However, a higher rotational speed can lead to a tool temperature that is too high, which becomes negative for machining. In addition, as shown in Figure 12, the calculation results of the BC algorithm are significantly different from those of the other algorithms, indicating that the BC algorithm is not sensitive to the changes of machining parameters, which further verifies that the BC algorithm is not suitable for the application to machining within the research scope of this study.

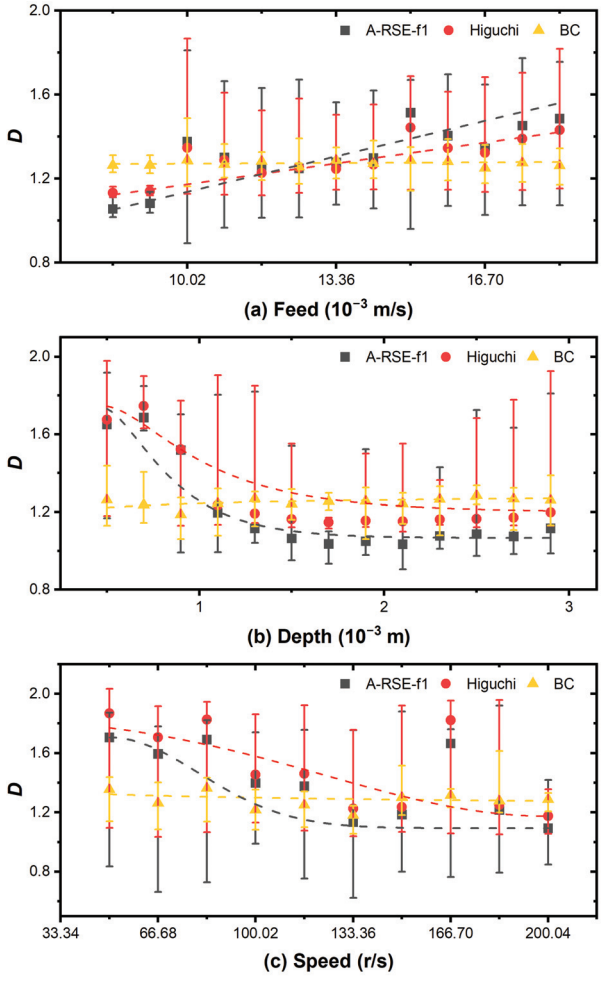

Figure 12. The calculation of *D* values of milling acceleration signal by A-RSE-f1, Higuchi, and BC algorithms, and the influences of: (**a**) feed, (**b**) cut depth, and (**c**) speed.

The variation range of the calculation results of the A-RSE-f1 algorithm is larger than the other two algorithms. This fact indicates that the A-RSE-f1 algorithm is more sensitive to the change in signal characteristics, and the algorithm can recognize more characteristics that the other algorithms cannot. In conclusion, under the working conditions of this experiment, a speed of 83.3∼150 r/s, a cutting depth of more than 1 mm, and a small feed are more appropriate machining parameters. Furthermore, the influences of each parameter on the machining status are coupled, while the establishment of the SLD preliminarily

predicts the speed and cutting depth range of stable machining but ignores the influence of the feed [52,53]. This issue will be further investigated in our future work.

4. Conclusions

In this study, an accelerated RSE-f1 (with first-order flattening) algorithm, A-RSE-f1, is proposed. Based on the strategy of a dichotomy, the random selection of a fixed number of sub-sequences in the RSE-f1 algorithm is changed to be adaptive and provide full coverage of the signal, avoiding redundant calculations. The auxiliary matrices are constructed based on a binary strategy to reduce the time of summation and further accelerate the algorithm. The improvement effect of the A-RSE-f1 algorithm is tested using fractal ($\boldsymbol{D}$ = 1∼2) and non-fractal ($\boldsymbol{D}$ = 0∼1) signals generated by the W-M function, and the engineering application of the A-RSE-f1 algorithm is demonstrated using 40 milling acceleration signals (20 chatter signals and 20 stable signals) of the machine tool spindle. In addition, the effects of different machining parameters on the acceleration signals and the $\boldsymbol{D}$ values are discussed. It should be noted that, due to differences in applicable parameters and signal characteristics in various experimental conditions, the experimental results analyzed by the A-RSE-f1 algorithm above are only verified within the experimental condition of this study, and the feasibility of its utilization under other experimental conditions will be investigated in our future work. The specific conclusions are as follows:

1. A-RSE-f1 is proposed based on a dichotomy and binary strategy. The A-RSE-f1 algorithm not only has been shown to be more accurate than the Higuchi and BC algorithms, but also is much faster than the original RSE-f1 algorithm by about 13 folds and 1.5-fold faster than the Higuchi algorithm. In the range of accuracy allowed, the lower scaling ratio δ can further improve the operation speed.
2. Through the verification of 40 groups of milling acceleration signals, it is shown that the RSE-f1 and A-RSE-f1 algorithms can recognize the machining signals of different statuses and can be applied to the chatter recognition of machine tools. The A-RSE-f1 algorithm can also identify the non-fractal characteristics of machining signals, which can play an important role in further studies of the physical significance of signal characteristics.
3. The single running duration of $\delta = 0.85$ of the A-RSE-f1 algorithm is only 7.8×10^{-3} s. In the range of accuracy allowed, the lower scaling ratio δ can further improve the operation speed. Therefore, A-RSE-f1 is promising in that it can meet the application requirements of practical engineering and can be used for chatter recognition through the acceleration signals in milling.

Author Contributions: Conceptualization, F.F. and Y.X.; Data curation, M.Y.; Funding acquisition, P.F.; Investigation, F.F.; Methodology, X.L.; Project administration, P.F.; Software, Y.X. and H.X.; Supervision, X.L.; Validation, H.X.; Writing—original draft, F.F. and M.Y.; and Writing—review and editing, X.L. All authors have read and agreed to the present version of the manuscript.

Funding: This study was supported by National Natural Science Foundation of China under Grant No. 51875311, Guangdong Basic and Applied Basic Research Foundation under Grant No. 2020A1515011199, and Shenzhen Natural Science Foundation under Grant No. WDZC20200817152115001.

Institutional Review Board Statement: Not applicable.

Informed Consent Statement: Not applicable.

Data Availability Statement: The data presented in this study are available from the corresponding author with reasonable request. Moreover, the codes of analysis and simulation on fractal profiles and surfaces have been established, and the collaboration investigation by using them is welcome by the authors.

Acknowledgments: The authors would like to thank Shaozhu Xiao, Xiangsong Zhang, Binbin Liu, Shaocong Wang, Junlong Huang, Jun Li, Yousheng Xia, and Zengxian Ma of Tsinghua University for their contributions to fractal studies in our lab.

Conflicts of Interest: The authors declare no conflict of interest.

References

1. Mandelbrot, B.B. Is nature fractal? *Science* **1998**, *279*, 783. [CrossRef]
2. Mandelbrot, B.B.; Mandelbrot, B.B. *The Fractal Geometry of Nature*; WH Freeman: New York, NY, USA, 1982; Volume 1.
3. Morse, D.R.; Lawton, J.; Dodson, M.; Williamson, M. Fractal dimension of vegetation and the distribution of arthropod body lengths. *Nature* **1985**, *314*, 731–733. [CrossRef]
4. Williams, N. Biology: Fractal geometry gets the measure of life's scales. *Science* **1997**, *276*, 34. [CrossRef] [PubMed]
5. Luo, X.; Schramm, D.N. Fractals and cosmological large-scale structure. *Science* **1992**, *256*, 513–515. [CrossRef] [PubMed]
6. Namazi, H.; Ala, T.S. Decoding of simple and compound limb motor imagery movements by fractal analysis of electroencephalogram (eeg) signal. *Fractals* **2019**, *27*, 1950041. [CrossRef]
7. Eke, A.; Herman, P.; Kocsis, L.; Kozak, L. Fractal characterization of complexity in temporal physiological signals. *Physiol. Meas.* **2002**, *23*, R1. [CrossRef]
8. Akar, S.A.; Kara, S.; Latifoğlu, F.; Bilgic, V. Investigation of the noise effect on fractal dimension of eeg in schizophrenia patients using wavelet and ssa-based approaches. *Biomed. Signal Process. Control* **2015**, *18*, 42–48. [CrossRef]
9. Raghav, S.; Mishra, A.K. Fractal feature based ecg arrhythmia classification. In Proceedings of the TENCON 2008—2008 IEEE Region 10 Conference, Hyderabad, India, 19–21 November 2008; pp. 1–5.
10. Pina-Vega, R.P.; Valtierra-Rodriguez, M.; Perez-Ramirez, C.A.; Amezquita-Sanchez, J.P. Early prediction of sudden cardiac death using fractal dimension and ecg signals. *Fractals* **2021**, *29*, 2150077–2151052. [CrossRef]
11. Marie, R.R.; Al Alfi, M.H. Identification of cardiac diseases from (ecg) signals based on fractal analysis. *Int. J. Comput. Technol.* **2014**, *13*, 4556–4565. [CrossRef]
12. Sharma, V. Deterministic chaos and fractal complexity in the dynamics of cardiovascular behavior: Perspectives on a new frontier. *Open Cardiovasc. Med. J.* **2009**, *3*, 110. [CrossRef]
13. Shoupeng, S.; Peiwen, Q. A fractal-dimension-based signal-processing technique and its use for nondestructive testing. *Russ. J. Nondestruct.* **2007**, *43*, 270–280. [CrossRef]
14. Budroni, M.A.; Pilosu, V.; Delogu, F.; Rustici, M. Multifractal properties of ball milling dynamics. *Chaos Interdiscip. J. Nonlinear Sci.* **2014**, *24*, 023117. [CrossRef]
15. Yu, Y.; Baoliang, L.; Jingshan, S.; Shixuan, Y. The application of vibration signal multi-fractal in fault diagnosis. In Proceedings of the 2010 Second International Conference on Future Networks, Sanya, China, 22–24 January 2010; pp. 164–167.
16. Ji, Y.; Wang, X.; Liu, Z.; Yan, Z.; Jiao, L.; Wang, D.; Wang, J. Eemd-based online milling chatter detection by fractal dimension and power spectral entropy. *Int. J. Adv. Manuf. Technol.* **2017**, *92*, 1185–1200. [CrossRef]
17. Ji, Y.; Wang, X.; Liu, Z.; Wang, H.; Jiao, L.; Wang, D.; Leng, S. Early milling chatter identification by improved empirical mode decomposition and multi-indicator synthetic evaluation. *J. Sound Vib.* **2018**, *433*, 138–159. [CrossRef]
18. Zhuo, Y.; Jin, H.; Han, Z. Chatter identification in flank milling of thin-walled blade based on fractal dimension. *Procedia Manuf.* **2020**, *49*, 150–154. [CrossRef]
19. Chen, Y.; Li, H.; Hou, L.; Bu, X.; Ye, S.; Chen, D. Chatter detection for milling using novel p-leader multifractal features. *J. Intell. Manuf.* **2020**, *33*, 1–15. [CrossRef]
20. Liebovitch, L.S.; Toth, T. A fast algorithm to determine fractal dimensions by box counting. *Phys. Lett. A* **1989**, *141*, 386–390. [CrossRef]
21. Katz, M.J. Fractals and the analysis of waveforms. *Comput. Biol. Med.* **1988**, *18*, 145–156. [CrossRef]
22. Higuchi, T. Approach to an irregular time series on the basis of the fractal theory. *Phys. D Nonlinear Phenom.* **1988**, *31*, 277–283. [CrossRef]
23. Kesić, S.; Spasić, S.Z. Application of higuchi's fractal dimension from basic to clinical neurophysiology: A review. *Comput. Methods Programs Biomed.* **2016**, *133*, 55–70. [CrossRef]
24. Khoa, T.Q.D.; Ha, V.Q.; Toi, V.V. Higuchi fractal properties of onset epilepsy electroencephalogram. *Comput. Math. Methods Med.* **2012**, *2012*. [CrossRef] [PubMed]
25. Miličić, S. Box-counting dimensions of generalised fractal nests. *Chaos Solit. Fractals* **2018**, *113*, 125–134. [CrossRef]
26. Valla, M.; Nedvěd, J.; Pavlík, D.; Adam, V.; Hubálek, J.; Trnková, L.; Kizek, R.; Provazník, I. Box Counting Method in Record, Processing and Evaluation of Genomic Signals. *J. Biochem. Technol. Hyderabad India* **2010**, *2*, 91–93.
27. Wang, S.; Zhang, J.; Feng, F.; Qian, X.; Jiang, L.; Huang, J.; Liu, B.; Li, J.; Xia, Y.; Feng, P. Fractal analysis on artificial profiles and electroencephalography signals by roughness scaling extraction algorithm. *IEEE Access* **2019**, *7*, 89265–89277. [CrossRef]
28. Zhou, G.; Wang, X.; Feng, F.; Feng, P.; Zhang, M. Calculation of fractal dimension based on artificial neural network and its application for machined surfaces. *Fractals* **2021**, *29*, 2150129–2151936. [CrossRef]
29. Li, Z.; Qian, X.; Feng, F.; Qu, T.; Xia, Y.; Zhou, W. A continuous variation of roughness scaling characteristics across fractal and non-fractal profiles. *Fractals* **2021**, *29*, 2150109–2150638. [CrossRef]
30. Majumdar, A.; Tien, C. Fractal characterization and simulation of rough surfaces. *Wear* **1990**, *136*, 313–327. [CrossRef]
31. Berry, M.V.; Lewis, Z.; Nye, J.F. On the weierstrass-mandelbrot fractal function. *Proc. R. Soc. Lond. A Math. Phys. Sci.* **1980**, *370*, 459–484.

32. Zou, M.; Yu, B.; Feng, Y.; Xu, P. A monte carlo method for simulating fractal surfaces. *Phys. A Stat. Mech. Its Appl.* **2007**, *386*, 176–186. [CrossRef]
33. Takagi, T. A simple example of the continuous function without derivative. *Collect. Pap. Teiji Takagi* **1973**, *1*, 5–6.
34. Falconer, K. *Fractal Geometry: Mathematical Foundations and Applications*; John Wiley & Sons: Hoboken, NJ, USA, 2004.
35. Chen, Z.; Liu, Y.; Zhou, P. A comparative study of fractal dimension calculation methods for rough surface profiles. *Chaos Solit. Fractals* **2018**, *112*, 24–30. [CrossRef]
36. Zuo, X.; Tang, X.; Zhou, Y. Influence of sampling length on estimated fractal dimension of surface profile. *Chaos Solit. Fractals* **2020**, *135*, 109755. [CrossRef]
37. Yao, K.; Chen, H.; Peng, W.; Wang, Z.; Yao, J.; Wu, Y. A new method on box dimension of weyl-marchaud fractional derivative of weierstrass function. *Chaos Solit. Fractals* **2021**, *142*, 110317. [CrossRef]
38. Kulesza, S.; Bramowicz, M. A comparative study of correlation methods for determination of fractal parameters in surface characterization. *Appl. Surf. Sci.* **2014**, *293*, 196–201. [CrossRef]
39. Liu, Y.; Wang, Y.; Chen, X.; Yu, H. A spherical conformal contact model considering frictional and microscopic factors based on fractal theory. *Chaos Solit. Fractals* **2018**, *111*, 96–107. [CrossRef]
40. Mohammadi, Y.; Ahmadi, K. Frequency domain analysis of regenerative chatter in machine tools with linear time periodic dynamics. *Mech. Syst. Signal Process.* **2019**, *120*, 378–391. [CrossRef]
41. Niu, J.; Jia, J.; Wang, R.; Xu, J.; Sun, Y.; Guo, D. State dependent regenerative stability and surface location error in peripheral milling of thin-walled parts. *Int. J. Mech. Sci.* **2021**, *196*, 106294. [CrossRef]
42. Rafal, R.; Pawel, L.; Krzysztof, K.; Bogdan, K.; Jerzy, W. Chatter identification methods on the basis of time series measured during titanium superalloy milling. *Int. J. Mech. Sci.* **2015**, *99*, 196–207. [CrossRef]
43. Aslan, D.; Altintas, Y. On-line chatter detection in milling using drive motor current commands extracted from cnc. *Int. J. Mach. Tools Manuf.* **2018**, *132*, 64–80. [CrossRef]
44. Ragab, A.; Yacout, S.; Ouali, M.-S.; Osman, H. Prognostics of multiple failure modes in rotating machinery using a pattern-based classifier and cumulative incidence functions. *J. Intell. Manuf.* **2019**, *30*, 255–274. [CrossRef]
45. Li, X.; Guan, X. Time-frequency-analysis-based minor cutting edge fracture detection during end milling. *Mech. Syst. Signal Process.* **2004**, *18*, 1485–1496. [CrossRef]
46. Cao, H.; Yue, Y.; Chen, X.; Zhang, X. Chatter detection in milling process based on synchrosqueezing transform of sound signals. *Int. J. Adv. Manuf. Technol.* **2017**, *89*, 2747–2755. [CrossRef]
47. Liu, C.; Zhu, L.; Ni, C. The chatter identification in end milling based on combining emd and wpd. *Int. J. Adv. Manuf.* **2017**, *91*, 3339–3348. [CrossRef]
48. Cuka, B.; Kim, D.-W. Fuzzy logic based tool condition monitoring for end-milling. *Robot. Comput.-Integr. Manuf.* **2017**, *47*, 22–36. [CrossRef]
49. Elangovan, M.; Sugumaran, V.; Ramachandran, K.; Ravikumar, S. Effect of svm kernel functions on classification of vibration signals of a single point cutting tool. *Expert Syst. Appl.* **2011**, *38*, 15202–15207. [CrossRef]
50. Elshorbagy, A.; Simonovic, S.; Panu, U. Noise reduction in chaotic hydrologic time series: Facts and doubts. *J. Hydrol.* **2002**, *256*, 147–165. [CrossRef]
51. Altintaş, Y.; Budak, E. Analytical prediction of stability lobes in milling. *CIRP Ann.* **1995**, *44*, 357–362. [CrossRef]
52. Jensen, S.; Shin, Y.C. *Stability Analysis in Face Milling Operations, Part 1: Theory of Stability Lobe Prediction*; ASME: New York, NY, USA, 1999.
53. Pour, M.; Torabizadeh, M.A. Improved prediction of stability lobes in milling process using time series analysis. *J. Intell. Manuf.* **2016**, *27*, 665–677. [CrossRef]

mathematics

MDPI

Article

Estimation of the Hurst Parameter in Spot Volatility

Yicun Li [1] and Yuanyang Teng [2,*]

[1] Business School, Zhejiang University City College, Hangzhou Yiyuan Technology Co., Ltd., Hangzhou 310015, China; 11820048@zju.edu.cn
[2] School of Management, Zhejiang University, Hangzhou Yiyuan Technology Co., Ltd., Hangzhou 310027, China
* Correspondence: 11620043@zju.edu.cn; Tel.: +86-183-5819-2972

Abstract: This paper contributes in three stages in a logic of the cognitive process: we firstly propose a new estimation of Hurst exponent by changing frequency method which is purely mathematical. Then we want to check if the new Hurst is efficient, so we prove the advantages of this new Hurst in asymptotic variance in the perspective compared with other two Hurst estimator. However, a purely mathematical game is not enough, a good estimation should be proven by reality, so we apply the new Hurst estimator into truncated and non-truncated spot volatility which fills the gap of previous literatures using 5-min price data (Source: Wind Financial Terminal) of 10 Chinese A-share industry indices from 1 January 2005 until 31 December 2020.

Keywords: spot volatility; change of frequency; roughness of volatility; hurst exponent; Chinese A-share market

MSC: 60F17; 91B70

Citation: Li, Y.; Teng, Y. Estimation of the Hurst Parameter in Spot Volatility. *Mathematics* **2022**, *10*, 1619. https://doi.org/10.3390/math10101619

Academic Editors: Camelia Petrescu and Valeriu David

Received: 7 April 2022
Accepted: 7 May 2022
Published: 10 May 2022

Publisher's Note: MDPI stays neutral with regard to jurisdictional claims in published maps and institutional affiliations.

Copyright: © 2022 by the authors. Licensee MDPI, Basel, Switzerland. This article is an open access article distributed under the terms and conditions of the Creative Commons Attribution (CC BY) license (https://creativecommons.org/licenses/by/4.0/).

1. Introduction

Since the seminal work of Black and Scholes [1], the price dynamics described by the following equation have been well-known to researchers in the fields.

$$\mathrm{dlog}S_t = \mu_t \mathrm{d}t + \sigma_t \mathrm{d}W_t,$$

where μ_t is a drift process, σ_t depicts the volatility process and W_t is standard Brownian motion. Since the constant volatility assumption of the model in Black and Scholes [1] contradicts empirical observation (see, for example, Fouque et al. [2]), more and more innovative models are proposed (see Hull and White [3]; Scott [4]; Stein and Stein [5]).

Despite these improvements in the above-mentioned stochastic volatility models, empirical studies have underlined the long-memory feature of the volatility of financial assets. To address this issue, a natural idea is to replace Brownian motion in the volatility process by fractional Brownian motion (fBm), which can describe the long memory property with the Hurst parameter $0.5 < H < 1$. Hence, Comte and Renault [6] proposed a fractional version of the Hull-White stochastic volatility model with the Hurst parameter $H > 0.5$ in fBm to model log-volatility and consider the option pricing problem in a long memory volatility environment. Other related research has been conducted by Comte et al. [7], Chronopoulou and Viens [8], Chronopoulou and Viens [9], Xiao and Yu [10].

Recent empirical studies have documented the roughness of historical volatility data and the implied roughness of option price data (see, e.g., Bennedsen et al. [11]; Bayer et al. [12]; Gatheral et al. [13]; Livieri et al. [14]; El Euch and Rosenbaum [15]). Early research conducted by Alòs et al. [16] investigated the short-time behavior of implied volatility by jump-diffusion models. Compared with Alòs et al. [16], Fukasawa and Takabatake [17] discussed self-similar stationary Gaussian noises such as fractional Gaussian noises, which indicate the volatility series. They extended the Whittle estimation method to

obtain asymptotically efficient estimators. Moreover, many studies have evaluated realized volatility forecasting performance of several models (see, e.g., Li et al. [18]; Wang et al. [19]; Wang et al. [20]) More precisely, Gatheral et al. [13] calibrated a model to the SP500 and NASDAQ indices, showing that the Hurst parameter of volatility should be close to 0.11. Other important indices, including the FTSE2, N2252, RUT2, DJI2, FCHI2, KS11, SSMI, IBEX2, NSEI, MXX, BVSP, GSPTSE, STOXX50E, FTSTI, FTSEMIB have also been studied. This indicates extremely rough directions for the volatility process, being much more irregular than those of standard stochastic volatility models driven by Brownian motion. Further empirical studies have confirmed the roughness of the log-volatility of thousands of stocks on the US equity market (Bennedsen et al. [11]). Livieri et al. [14] found that at-the-money short term volatility from SP500 options is also rough. Using high-frequency data for major volatility indices and the qth-order structure function (SF) method proposed by Gatheral et al. [13], Da Fonseca and Zhang [21] computed the volatility of major indices in the USA and showed the roughness of the volatility of volatility. Cao et al. [22] showed that even the elasticity of variance for the SP500 is rough. Takaishi [23] verified the roughness of Bitcoin volatility using MF-DFA based on Bitcoin tick data. Bennedsen et al. [11] verified the volatility roughness of many stocks. It has been shown recently that both the realized volatility and the option-implied volatility are rough. Recently, Fukasawa et al. [24] used a quasi-likelihood estimator to estimate the Hurst parameter of the S&P 500, FTSE 100, Nikkei 225, DAX, and Russell 3000 indices and found that the volatility is rough. Brandi and Di Matteo [25] computed the Hurst exponent on realized variance from the Oxford volatility library and found that the volatility is indeed rough with a Hurst exponent between 0.08 and 0.15. Alòs and León [26] provided a comprehensive discussion of rough volatility. With research progressing, spot volatility catches the eyes of researchers. Efficient estimation of spot volatility can be achieved by using Riemann-like integration. Applications of spot volatility are of great importance. For example, spot volatility can be used to detect the micro-structure of the of financial assets. It was also useful to explain jumps and co-jumps of volatility series as shown by Jacod and Todorov [27]. Moreover, spot volatility can be calibrated to implied volatility and play a key role in the option pricing. There are many publications about spot volatility in which it has been extensively studied (see, e.g., Fan and Wang [28]; Reno [29] and references therein).

This paper focuses on the roughness of spot volatility and proposes some interesting contributions:

- We propose a new Hurst exponent by changing the frequency method, prove consistency, and derive the asymptotic volatility of our estimator. Then we do simulations by the Monte Carlo method and compare our new Hurst estimator with existing Hurst exponents, showing its advantages.
- We introduce a non-parametric estimator for spot volatility based on the rough volatility environment proposed by Bayer et al. [12], and Gatheral et al. [13]. While Fan and Wang [28] proposed the same non-parametric estimator for spot volatility based on fractional stochastic volatility models with $H \in (1/2, 1)$, we extend this estimator for all $H \in (0, 1)$. The proof method established in this paper can be also applied to a general fractional stochastic volatility model with a bounded drift term.
- We employ the MF-DFA method proposed by Kantelhardt et al. [30] and qth-order SF method used by Gatheral et al. [13] to analyze the roughness of 10 industrial indices' spot volatility in the Chinese financial market. Then we compared two Hurst exponents of the least square method proposed by Berzin et al. [31] with our new Hurst exponents using empirical data. Gatheral et al. [13] proved the SF method in American markets, and their numeric results are similar to ours in Chinese markets. There is much evidence showing the roughness of volatility in different sectors and markets (see Guennoun et al. [32], Funahashi and Kijima [33], Neuenkirch and Shalaiko [34]. We confirmed that the Hurst exponent we propose is universal in other markets and sectors. Our results suggest that spot volatility is also rough, and has confirmed the

roughness of realized volatility (Bennedsen et al. [10]; Gatheral et al. [13]) and implied volatility (Livieri et al. [14]).

The rest of this paper is organized as follows. Section 2 introduces the non-parametric estimator for spot volatility from the rough stochastic volatility model proposed by Bayer et al. [12], and Gatheral et al. [13] and provides the asymptotic theory for the proposed non-parametric estimator. Section 3 presents the new estimator and investigates its asymptotic properties. Four popular methods for estimating the generalized Hurst exponent are also introduced in the later part of this Section. Section 4 presents some empirical studies. Section 5 discusses the contribution of this study with other research in the literature. Section 6 outlines the conclusion of our analysis. Components of proofs are collected in Appendix A.

2. The Spot Volatility Model

Modeling rough volatility is becoming increasingly popular and has important applications in finance. This is because rough volatility models must fit the volatility skew, which is defined as the derivative of the implied volatility surface under the Black-Scholes-Merton model with respective to log-strike price evaluated at-the-money. Moreover, rough volatility models must satisfy the mono-fractal scaling property of the historical volatility data, which means that for a given lag Δ, each q-th sample moment of the differences of log-volatility exhibits a power-scaling relationship with respect to this lag, i.e., $|\log \sigma_{t+\Delta_n} - \log \sigma_t|^q \propto \Delta^{qH}$ with $q > 0$ and $\Delta > 0$. Consequently, rough volatility models have important applications in finance, and the literature on estimating spot volatility is large. From the celebrated rough volatility model by Bayer et al. [12], Gatheral et al. [13] and Xiao and Yu [10], we assume that the asset price S_t follows the following dynamic:

$$\begin{cases} \frac{dS_t}{S_t} = \mu_t dt + \sigma_t dW_t \\ \sigma_t = \exp\{X_t\}, t \in [0, T] \\ dX_t = \alpha(m - X_t)dt + \nu dB_t^H \end{cases} \tag{1}$$

where S_t and σ_t are the price and volatility processes, respectively. Moreover, μ_t is a suitable drift term and satisfies $sup\{|\mu_t - \mu_s|, |t - s| \leq a\} = O_P(a^{1/2}\left|\log a\right|_{1/2})$, σt is the diffusion term, i.e., the spot volatility of the stock, $\alpha > 0$ is the speed of mean-reversion, m is the long term level of the variance, ν is the volatility of volatility, W_t is a Wiener process, i.e., a Brownian motion, and B_t^H is a fBm with Hurst parameter $H \in (0, 1)$. Following the idea of Bayer et al. [12] and Gatheral et al. [13], we assume that B_t^H is independent of W_t.

The model of (1) can describe both the mean reverting property and the roughness of the volatility. The self-similarity parameter, also called the Hurst parameter in the fBm, is a crucial criterion to test the roughness of the volatility. Consequently, estimating the Hurst parameter in the volatility has been the subject of active research and a challenging theoretical problem. In the literature, there exist many approaches for estimating the Hurst parameter, such as rescaled range, aggregated variance, aggregated absolute value, variance of residuals, log-periodogram regression, Whittle estimation, local Whittle estimation, novel time-varying generalized Hurst exponent methodology (see, for example, Kermarrec [35], Keshari Jena et al. [36], and Xiao et al. [37]) and so on. In this paper, we use MF-DFA proposed by Kantelhardt et al. [30] and the q-th order SF introduced by Gatheral et al. [13]. In what follows, we first introduce a non-parametric estimator for spot volatility in (1) then we introduce two methods for estimating the Hurst parameter.

The recent availability of high frequency data in finance has permitted more efficient ways of computing spot volatility. However, the estimation of the spot volatility from asset price observations is challenging because observed high frequency data are generally affected by noise-microstructure effects. Hence, following Fan and Wang [28], this subsection is devoted to the nonparametric estimation method for spot volatility in a rough volatility environment, which yields suboptimal convergence rates.

For any positive integer n, let $\Delta = T/n$ and $K(x)$ be a kernel with $\int_{-1}^{1} K(x)dx = 1$. Moreover, suppose that we observe S_{ti} at n discrete time points with $t_i = i\Delta = iT/n$,

i = 1, 2, . . . , n. Then, following the idea of Fan and Wang [28], we define the kernel type estimator for the spot volatility as:

$$\hat{\sigma}_t := \sqrt{\frac{1}{b}\sum_{t_i=t-b}^{t+b} K\left(\frac{t_i - t}{b}\right)\left(S_{t_i} - S_{t_{i-1}}\right)^2} \tag{2}$$

where b is a bandwidth.

The estimator (2) will be used for the continuous case as it is not jump robust and not noise robust. From Christensen et al. [38], we can see that the impact of jumps is negligible in the data studied here. Moreover, 5-min sampling data is commonly used and not affected by market micro-structure noise. Fan and Wang [28] impose the following assumptions for μ_t, σ_t and $K(x)$ provided by the following result.

When the price process is assumed to be present with jumps, the truncated estimator $\overline{\sigma}_t$ for the spot volatility can be calculated as:

$$\overline{\sigma}_t(k_n, \nu_n) = \sqrt{\frac{1}{k_n\Delta_n}\sum_{i=0}^{k_n-1}\left(Y_{(m+1+i)\Delta_n} - Y_{(m+i)\Delta_n}\right)^2 1_{\{|Y_{(m+1+i)\Delta_n} - Y_{(m+i)\Delta_n}| \le \nu_n\}}} \tag{3}$$

Hypothesis 1. *Suppose the following conditions are satisfied:*

A1 The diffusion term $\sigma_t$in (1) satisfies:

$sup\{|\sigma_s - \sigma_t|, |s-t| \le a\} = O_{\mathbb{P}}(a^{1/2}\left|log(a)\right|_{1/2})$ *and* $\sup_{0\le t\le T}\left|\sigma_t^2\right| = O_{\mathbb{P}}(1)$.

A2 For $i = 1, 2, \ldots, n, sup\{|\int_{t_{i-1}}^{t_i}(\sigma(s) - \sigma(t_{i-1}))dW_s|^2\} = O_{\mathbb{P}}\left(n^{-2+\eta}\right)$, *where η is an arbitrarily small number.*

A3 The drift term μ_t in (1) satisfies:

$$sup\{|\mu_t - \mu_s|, |t-s| \le a\} = O_{\mathbb{P}}(a^{1/2}\left|loga\right|_{1/2})$$

A4 Bandwidth b and kernel K satisfy $b \sim n^{-1/2}/log(n)$, $K(\cdot)$ *is twice differentiable with support* $[1,\ 1]$ *and* $\int_{-1}^{1} K(x)dx = 1$.

From Cheridito et al. [39], and for $\alpha > 0$, we can see that $X_t = \log(\sigma_t)$ defined by (1) is a stationary and ergodic if one chooses a suitable initial condition $X_0 = \mu + \sigma\int_{-\infty}^{0} e^{\kappa s}dB_s^H$. Moreover, we have the following important result.

Lemma 1. *For $\alpha > 0$, the random variable $X_t = log(\sigma_t)$ has normal distribution with mean $\left(1 - e^{-\alpha t}\right)m + X_0e^{-\alpha t}$ and*

$$VarX_t = H\upsilon^2\int_0^t z^{2H-1}\left(e^{-\alpha z} + e^{-\alpha(2t-z)}\right)dz \tag{4}$$

To verify the assumptions in Hypothesis 1, we state the following technical lemma.

Lemma 2. *For all $H \in (0,\ 1)$ and any $p \ge 1$, there exist positive constants C, such that*

$$\mathbb{E}|X_t|^p \le C \tag{5}$$

$$\mathbb{E}|X_t - X_s|^p \le C\left|t-s\right|^{pH} \tag{6}$$

for all $t,\ s \ge 0$.

We show below that Assumptions A1 and A2 of σ_t in Hypothesis 1 are satisfied for the volatility process in (1) as well as its super-positions.

Lemma 3. *Suppose that the volatility process is described by X_t in (1). Then conditions A1 and A2 in Hypothesis 1 are satisfied.*

Now, using the definition of μ_t and $K(x) = e^x 1_{(x\leq 0)}$, we can see that A3 and A4 in Hypothesis 1 are satisfied. Under assumption 1, Fan and Wang [28] provided the asymptotic theory for $\hat{\sigma}_t$, which is proposed by the following result.

Proposition 1. *Under the Hypothesis 1, we have:*

$$\sqrt{nb}\left(\hat{\sigma}_t^2 - \sigma_t^2\right) \xrightarrow{d} N\left(0, \sigma_t^4 \int_{-1}^{1} K^2(x)dx\right) \tag{7}$$

where $\xrightarrow{d}$ denotes convergence in distribution and $K(x)$ is defined in A4 of Hypothesis 1.

Moreover, let $M_n = \sup_{0\leq t\leq T} \sqrt{nb} \parallel \hat{\sigma}_t^2 - \sigma_t^2 \parallel$ and $\lambda(k) = \int_{-1}^{1} K^2(x)dx$ If σ_t is a stationary process, then we have

$$(2log\ n)^{1/2}\left(\frac{M_n}{\sqrt{\int_{-1}^{1} K^2(x)dx}} - d_n\right) \xrightarrow{d} exp\left(-2e^{-x}\right) \tag{8}$$

where

$$d_n = \begin{cases} (2log\ n)^{1/2} + \frac{log\ \lambda_1(K) - 0.5log\ \pi - 0.5log(log\ n)}{(2log\ n)^{1/2}}, \text{ if } \frac{K^2(-1)+K^2(1)}{2\lambda(K)} > 0 \\ (2log\ n)^{1/2} + \frac{log\left(\frac{1}{2\lambda(K)} \int [K'(x)]^2 dx\right) - log(2\pi)}{(2log\ n)^{1/2}}, \text{ otherwise.} \end{cases} \tag{9}$$

Remark 1. *The class of kernels $K(\cdot)$ which are allowed for the asymptotic theory in Proposition 2.1 include those in the existing literature. From Fan and Wang [28], we impose differentiability and some kind of Lipschitz regularity for $K(\cdot)$. Prominent kernel functions, such as the Gaussian kernel allow for the asymptotic theory in Proposition 1.*

Remark 2. *Using Proposition 1, we can construct an asymptotic confidence band for the unknown spot volatility process.*

Remark 3. *For the asymptotic theory of spot volatility in (2), we have to eliminate the jumps on inference for spot volatility. In the case of jump activity, we can use truncated power variations and multipower variations to eliminate the jumps asymptotically. In fact, whether we allow for discontinuous price processes or not, itis quite crucial from a statistical point of view, since the existence of jumps requires a significant modification of the involved statistics to ensure jump robustness. The extension of jumps is complicated and will be reported in later work.*

Remark 4. *Micro-structure noise in high-frequency data is a commonly accepted fact. The theory presented in Fan and Wang [28] is clearly not noise-robust. The extension of their theory to noise-robust estimators is a challenging but very interesting question.*

Remark 5. *Following the idea of Bayer et al. [11] and Gatheral et al. [13], we assume that there is no leverage effect in (1). Thus, the Brownian motion and the fBm in (1) are independent. Establishing the asymptotic theory of the estimator for the spot volatility in (1) will be pursued in a future study.*

3. Estimation Methods of the Hurst Exponent

In the literature, there exist many papers that describe different methods for estimating the Hurst parameter. For example, the parameter estimation method includes the exact maximum likelihood estimation and Whittle the maximum likelihood estimation. Semi-parametric estimation approaches involve the celebrated R/S statistic method, the modified R/S statistic method, Higuchi's method, detrended fluctuation analysis, the log-periodogram regression method and the local Whittle method. Non-parametric estimation includes the increment ratio method, the wavelet-based method and the quadratic variations approach. In this paper, we first introduce a new estimator, which is based on the change of frequency.

3.1. A New Hurst Exponent H_n

In this section we propose a new Hurst exponent estimator, which is:

$$\hat{H_n} = \frac{1}{2} - \frac{1}{2\ln 2} \ln\left(\frac{\sum_{k=1}^{2n-1} \left(\Delta_{2n,k}^{(2)} X\right)^2}{\sum_{k=1}^{n-1} \left(\Delta_{n,k}^{(2)} X\right)^2} \right)$$

where

$$\Delta_{n,k}^{(2)} X = X\left(t_{k+1}^n\right) - 2X(t_k^n) + X\left(t_{k-1}^n\right) \text{ and } t_k^n = kT/n$$

From the equation above, we have:

$$\hat{H_n} \to H \text{ a.s.}$$

$$2\ln 2\sqrt{n}\left(\hat{H_n} - H\right) \xrightarrow{d} \mathcal{N}\left(0; \sigma_H^2\right), \sigma_H^2 = \frac{3}{2}\Sigma_{11} - 2\Sigma_{12}.$$

$$\Sigma_{11} = 2(1 + \tfrac{2}{\left(4-2^{2H}\right)^2} \sum_{j=1}^{\infty} \hat{\rho}_H^2(j)), \Sigma_{22} = \tfrac{1}{2}\Sigma_{11},$$

$$\Sigma_{12} = \Sigma_{21} = \tfrac{1}{2^{2H}\left(4-2^{2H}\right)^2} \sum_{j\in\mathbb{Z}} \widetilde{\rho}_H^2(j),$$

$$\hat{\rho}_H(j) = \tfrac{1}{2}[-6|j|^{2H} - |j-2\Big|^{2H} - \left|j+2\right|^{2H} + 4|j-1\Big|^{2H} + 4\Big|j+1\Big|^{2H}],$$

$$\widetilde{\rho}_H(j) = \tfrac{1}{2}[|j+1|^{2H} + 2|j+2\Big|^{2H} - |j+3|^{2H} + |j-1\Big|^{2H} - 4\Big|j\Big|^{2H} - |j-3|^{2H} + 2|j-2|^{2H}].$$

Set $\mathrm{B^H} = \left\{\mathrm{B^H(t)} : \mathrm{t} \in [0, \mathrm{T}]\right\}, \mathrm{T} > 0$ as fBm.
We obtain:

$$V_{in,T}^{\hat{B}^H} = \sum_{k=1}^{in-1} \left(\Delta_{in,k}^{(2)} \hat{B}^H\right)^2, \Delta_{in,k}^{(2)} \hat{B}^H = \frac{\Delta_{in,k}^{(2)} B^H}{\sqrt{\mathrm{E}\left(\Delta_{in,k}^{(2)} B^H\right)^2}}\ i = 1, 2,$$

$$d_{k,j}^{\hat{B}^H, in} = \mathrm{E}\Delta_{in,k}^{(2)} \hat{B}^H \Delta_{in,j}^{(2)} \hat{B}^H, 1 \le j, k \le in-1, i = 1, 2,$$

$$c_{j,k}^{\hat{B}^H, 2n} = \mathrm{E}\Delta_{n,j}^{(2)} \hat{B}^H \Delta_{2n,k}^{(2)} \hat{B}^H, 1 \le j \le n-1, 1 \le k \le 2n-1,$$

$$\Delta_{in,k}^{(2)} \hat{B}^H = \hat{B}_{\frac{k+1}{in}T}^H - 2\hat{B}_{\frac{k}{in}T}^H + \hat{B}_{\frac{k-1}{in}T^H}^H, 1 \le k \le in-1, i = 1, 2.$$

Then we have following conclusion:

Theorem 1. *Suppose* $B^H = \left\{B^H(t) : t \in [0, T]\right\}, T > 0$ *is fBm, then:*

$$\mathbf{X}_n = \sqrt{n} \begin{pmatrix} n^{-1} V_{n,T}^{\hat{B}^H} - 1 \\ (2n)^{-1} V_{2n,T}^{\hat{B}^H} - 1 \end{pmatrix} \xrightarrow{d} \mathcal{N}(0; \Sigma_H), \Sigma_H = \begin{pmatrix} \Sigma_{11} & \Sigma_{12} \\ \Sigma_{12} & \Sigma_{22} \end{pmatrix}$$

where $\mathcal{N}(0;\Sigma_{\mathrm{H}})$ *is a Gaussian vector:*

$$\Sigma_{11} = 2(1+\tfrac{2}{(4-2^{2H})^2}\sum_{j=1}^{\infty}\hat{\rho}_H^2(j)), \Sigma_{22} = \tfrac{1}{2}\Sigma_{11},$$
$$\Sigma_{12} = \Sigma_{21} = \tfrac{1}{(4-2^{2H})^2}\sum_{j\in\mathbb{Z}}\widetilde{\rho}_H^2(j),$$

$$\begin{aligned}\hat{\rho}_H(j) = \;& \tfrac{1}{2}[-6|j|_{2H} - \left|j-2\right|_{2H} - |j+2|_{2H} + 4|j-1\Big|_{2H} + 4\Big|j+1\Big|_{2H}],\\ \widetilde{\rho}_H(j) = \;& \tfrac{1}{2^{2H+1}}[\left|j+1\right|^{2H} + 2\left|j+2\right|^{2H} - \left|j+3\right|^{2H} + \left|j-1\right|^{2H} - 4\Big|j\Big|^{2H}\\ & - |j-3|_{2H} + 2|j-2|_{2H}].\end{aligned}$$

Proof. The proof is similar to the proof of Theorem 4 in Kubilius [40]. However, since our result is slightly different from that in Kubilius [40], we provide brief derivations here.

To determine limiting distribution of $\mathbf{X}_n$, we compute a limiting moment generating function $\lim \mathrm{M}_{\mathrm{X_n}}(\lambda) = \mathrm{M}(\lambda)$.

Consider a centered Gaussian vector $\mathrm{G_n} = \left(\mathrm{G_n^{(1)}}, 1 \le \mathrm{i} \le 3\mathrm{n}-2\right)$

$$G_n^{(i)} = \Delta_{n,i}^{(2)}\hat{B}^H, 1 \le i \le n-1,$$
$$G_n^{(i)} = \sqrt{2^{-1}}\Delta_{2n,i+1-n}^{(2)}\hat{B}^H, n \le i \le 3n-2$$

And a diagonal matrix:

$$D_n = \mathrm{diag}\left(\underbrace{\lambda_1,\ldots,\lambda_1}_{n-1}, \underbrace{\lambda_2,\ldots,\lambda_2}_{2n-1}\right)$$

It is evident that $\mathrm{EG_n^{(i)}} = 0$ and $\mathrm{E}\left(\mathrm{G_n^{(i)}}\right)^2 = 1$ for all $1 \le \mathrm{i} \le \mathrm{n}-1$, $\mathrm{E}\left(\mathrm{G_n^{(i)}}\right)^2 = 2^{-1}$ for all $\mathrm{n} \le \mathrm{i} \le 3\mathrm{n}-2$. We denote the covariance matrix of the vector $\mathrm{G_n}$ by $\Sigma_{\mathrm{G_n}}$.

Set:

$$\widetilde{D}_n = \left(\Sigma_{\mathbf{G}_n}^{1/2}\right)^T D_n \Sigma_{\mathbf{G}_n}^{1/2}$$

We give bound on eigenvalues of $\widetilde{\mathrm{D}}_\mathrm{n}$. It is obvious that $\widetilde{\mathrm{D}}_\mathrm{n}$ is symmetric. Denote by $\|\mathrm{A_n}\| = \sup_{\|\mathrm{x}\|=1}\|\mathrm{A_n x}\|$ matrix A norm. For symmetric matrix $\widetilde{\mathrm{D}}_\mathrm{n}$ its norm is equal to its spectral norm, i.e., $\|\widetilde{\mathrm{D}}_\mathrm{n}\| = \rho(\widetilde{\mathrm{D}}_\mathrm{n}) := \max_\mathrm{k}|\lambda_\mathrm{k}(\widetilde{\mathrm{D}}_\mathrm{n})|$. Since norm $\|\cdot\|$ is submultiplicative norm then:

$$\begin{aligned}&\max_k\left|\lambda_k\left(\widetilde{D}_n\right)\right| = \|\widetilde{D}_n\| \le \|\Sigma_{\mathbf{G}_n}^{1/2}\|\cdot\|D_n\|\cdot\|\Sigma_{\mathbf{G}_n}^{1/2}\| = \|\Sigma_{\mathbf{G}_n}^{1/2}\|^2\cdot\|D_n\|\\ &= \rho((\Sigma_{\mathbf{G}_n}^{1/2})^2)\cdot\rho(D_n) = \rho(\Sigma_{\mathbf{G}_n})\cdot\rho(D_n) = \lambda_{max}(\Sigma_{\mathbf{G}_n})\cdot max\{|l_1|,|l_2|\}\end{aligned}$$

Now consider $\lambda_{\max}(\Sigma_{\mathrm{G_n}})$. In order to bound the maximal eigenvalue, we again make use of the fact that the latter does not exceed the maximal row sum of absolute values. Thus:

$$\lambda_{max}(\Sigma_{\mathbf{G}_n}) \le \max_j\sum_{i=1}^{3n-2}\left|(\Sigma_{\mathbf{G}_n})_{ij}\right|$$

Note that:

$$\begin{aligned}&(\Sigma_{\mathbf{G}_n})_{i,j+1-n} = \tfrac{1}{\sqrt{2}}\mathrm{E}\left[\Delta_{n,i}^{(2)}\hat{B}^H\Delta_{2n,j+1-n}^{(2)}\hat{B}^H\right]\\ &= \tfrac{1}{\sqrt{2}}E\left[\left(\Delta_{2n,2i+1}^{(2)}\hat{B}^H + \Delta_{2n,2i-1}^{(2)}\hat{B}^H + 2\Delta_{2n,2i}^{(2)}\hat{B}^H\right)\Delta_{2n,j+1-n}^{(2)}\hat{B}^H\right]\\ &= \tfrac{1}{\sqrt{2}}\left[d_{2i+1,j+1-n}^{\hat{B}^H,2n} + d_{2i-1,j+1-n}^{\hat{B}^H,2n} + 2d_{2i,j+1-n}^{\hat{B}^H,2n}\right]\end{aligned}$$

For $1 \leq i \leq n-1$ and $1 \leq j \leq 2n-1$, from Equations above, we can obtain:

$$\begin{aligned}\lambda_{max}\left(\sum_{\mathbf{G}_n}\right) &\leq \max_{1\leq j\leq n-1}\sum_{i=1}^{n-1}\left|d_{i,j}^{\hat{B}^H,n}\right| + \tfrac{1}{2}\max_{1\leq j\leq 2n-1}\sum_{i=1}^{2n-1}\left|d_{i,j}^{\hat{B}^H,2n}\right| \\ &+\tfrac{1}{\sqrt{2}}\max_{1\leq j\leq n-1}\sum_{i=1}^{2n-1}\left(\left|d_{i,2j+1}^{\hat{B}^H,2n}\right| + \left|d_{i,2j-1}^{\hat{B}^H,2n}\right| + 2\left|d_{i,2j}^{\hat{B}^H,2n}\right|\right) \\ &+\tfrac{1}{\sqrt{2}}\max_{1\leq j\leq 2n-1}\sum_{i=1}^{n-1}\left(\left|d_{2i+1,j}^{\hat{B}^H,2n}\right| + \left|d_{2i-1,j}^{\hat{B}^H,2n}\right| + 2\left|d_{2i,j}^{B^H,2n}\right|\right)\Bigg] \\ &\leq \max_{1\leq j\leq n-1}\sum\left|d_{i,j}^{\hat{B^H},n}\right| + \left(\tfrac{1}{2}+\tfrac{8}{\sqrt{2}}\right)\max_{1\leq j\leq 2n-1}\sum^{2n-1}\left|d_{i,j}^{\hat{B}^H,2n}\right| \leq 20\end{aligned}$$

Summing up, we come to conclusion that $\max_{k}\left|\lambda_k\left(\widetilde{D}_n\right)\right|$ is uniformly (in n, k) bounded by a finite constant depending only on λ_1, λ_2.

Note that:

$$\lambda^T\mathbf{Y}_n := \sqrt{n}(\lambda_1,\lambda_2)\begin{pmatrix} n^{-1}\left(V_{n,T}^{\hat{B}^H} - EV_{n,T}^{\hat{B}^H}\right) \\ (2n)^{-1}\left(V_{2n,T}^{\hat{B}^H} - EV_{2n,T}^{\hat{B}^H}\right)\end{pmatrix} = \frac{1}{\sqrt{n}}\left(\mathbf{G}_n^T D_n\mathbf{G}_n - \mathrm{E}\mathbf{G}_n^T D_n\mathbf{G}_n\right)$$

Recall that $G_n \overset{d}{=} \sqrt{\Sigma_{G_n}}Z_n$ with $Z_n \sim \mathcal{N}(0; I_{3n-2})$, where I_{3n-2} denotes an identity $3n-2$ matrix. So, one can determine the following equality:

$$\mathbf{G}_n^T D_n\mathbf{G}_n \overset{d}{=} \left(\Sigma_{\mathbf{G}_n}^{1/2}\mathbf{Z}_n\right)^T D_n\Sigma_{\mathbf{G}_n}^{1/2}\mathbf{Z}_n = \mathbf{Z}_n^T\left(\Sigma_{\mathbf{G}_n}^{1/2}\right)^T D_n\Sigma_{\mathbf{G}_n}^{1/2}\mathbf{Z}_n = \mathbf{Z}_n^T\widetilde{D}_n\mathbf{Z}_n$$

Let $\widetilde{D}_n = Q_n^T\Lambda\left(\widetilde{D}_n\right)Q_n$ be canonical representation of $\widetilde{D}_n$ via a diagonal matrix of eigenvalues and a corresponding orthogonal matrix of eigenvectors. Since the orthogonal transform does not change the distribution of Z_n, we have:

$$\mathbf{Z}_n^T\widetilde{D}_n\mathbf{Z}_n = \mathbf{Z}_n^T Q_n^T\Lambda\left(\widetilde{D}_n\right)Q_n\mathbf{Z}_n \overset{d}{=} \mathbf{Z}_n^T\Lambda\left(\widetilde{D}_n\right)\mathbf{Z}_n = \sum_{j=1}^{3n-2} Z_{n,j}^2\lambda_{n,j}$$

The estimation of eigenvalues of $\widetilde{D}_n$ shows that we can choose no $n^{-1/2}\max_k|\lambda_k(\widetilde{D}_n)| < 1/2$ for all $n \geq n_0$. To have $M_{Y_n}(\lambda)$ well defined, we assume that all n in the sequel satisfy this condition.

Now, the moment-generating function $M_{Y_n}(\lambda)$ we can be rewritten as:

$$M_{\mathbf{Y}_n}(\lambda) = \exp\left(-\frac{\mathbf{E}\mathbf{G}_n^T D_n\mathbf{G}_n}{\sqrt{n}}\right)\mathrm{E}\left[\exp\left(\sum_{j=1}^{3n-2} Z_{n,j}^2\frac{\lambda_{n,j}}{\sqrt{n}}\right)\right]$$

Thus:

$$\begin{aligned}M_{\mathbf{Y}_n}(\lambda) &= \exp\left(-\tfrac{\mathbf{E}\mathbf{G}_n^T D_n\mathbf{G}_n}{\sqrt{n}}\right)\prod_{j=1}^{3n-2} M_{\chi^2(1)}\left(\tfrac{\lambda_{n,j}}{\sqrt{n}}\right) \\ &= \exp\left(-\tfrac{\mathbf{E}\mathbf{G}_n^T D_n\mathbf{G}_n}{\sqrt{n}}\right)\left(\prod_{j=1}^{3n-2}\tfrac{1}{1-2\frac{\lambda_{n,j}}{\sqrt{n}}}\right)^{\frac{1}{2}} \\ &= \exp\left(-\tfrac{\mathbf{E}\mathbf{G}_n^T D_n\mathbf{G}_n}{\sqrt{n}} - \tfrac{1}{2}\sum_{j=1}^{3n-2}\log\left(1-2\tfrac{\lambda_{n,j}}{\sqrt{n}}\right)\right)\end{aligned}$$

By Maclaurin's expansion:

$$\log(1-x) = -x - \frac{x^2}{2} - \frac{x^3}{3} + o\left(x^3\right), x \to 0$$

Since $\max_{n,j}|\lambda_{n,j}|$ is uniformly bounded and $\sum_{j=1}^{3n-2}\lambda_{n,j} = \mathrm{tr}\left(\widetilde{D}_n\right) = E\left(Z_n^T\widetilde{D}_nZ_n\right) = E\left(G_n^TD_nG_n\right)$, we can rewrite the expression for $M_{Y_n}(\lambda)$ as follows

$$\begin{aligned} M_{\mathbf{Y}_n}(\lambda) &= \exp\left\{ -\frac{\mathbf{E}\mathbf{G}_n^T D_n \mathbf{G}_n}{\sqrt{n}} + \frac{1}{2}\sum_{j=1}^{3n-2}\left(2\frac{\lambda_{n,j}}{\sqrt{n}} + 4\frac{\lambda_{n,j}^2}{2n}\right) + O\left(\frac{1}{\sqrt{n}}\right)\right\} \\ &= \exp\left\{\frac{1}{n}\sum_{j=1}^{3n-2}\lambda_{n,j}^2\right\}\exp\left\{O\left(\frac{1}{\sqrt{n}}\right)\right\} \end{aligned}$$

Therefore, we can compute the limiting value of the first multiplier. By $\widetilde{D}_n$, definition:

$$\begin{aligned} \sum_{j=1}^{3n-2}\lambda_{n,j}^2 &= \mathrm{tr}(\widetilde{D}_n^2) = \mathrm{tr}(((\sqrt{\Sigma_{\mathbf{G}_n}})^T D_n \sqrt{\Sigma_{\mathbf{G}_n}})^2) = \mathrm{tr}((D_n\Sigma_{\mathbf{G}_n})^2) \\ &= \sum_{i=1}^{3n-2}\sum_{j=1}^{3n-2}(D_n\Sigma_{\mathbf{G}_n})_{ij}(D_n\Sigma_{\mathbf{G}_n})_{ji}. \end{aligned}$$

Note that equation above may be rearranged in the following way:

$$\begin{aligned} \sum_{i=1}^{3n-2}\sum_{j=1}^{3n-2}(D_n\Sigma_{\mathbf{G}_n})_{ij}(D_n\Sigma_{\mathbf{G}_n})_{ji} &= \frac{\lambda_1^2}{\left(4-2^{2H}\right)^2}\sum_{i=1}^{n-1}\sum_{j=1}^{n-1}\hat{\rho}_H^2(i-j) + \frac{\lambda_1\lambda_2}{\left(4-2^{2H}\right)^2}\sum_{i=1}^{n-1}\sum_{j=n}^{2n-1}\widetilde{\rho}_H(j,k) \\ &+ \frac{\lambda_2^2}{4\left(4-2^{2H}\right)^2}\sum_{i=1}^{2n-1}\sum_{j=1}^{n}\hat{\rho}_H^2(i-j) = \sum_{k=1}^{3} I_n^{(k)}. \end{aligned}$$

Therefore, to obtain a limiting expression for $M_{Y_n}(\lambda)$ it suffices to divide each sum by n and to calculate the corresponding limits. A standard calculation shows:

$$\begin{aligned} &\frac{1}{n\left(4-2^{2H}\right)^2}\sum_{i=1}^{n-1}\sum_{j=1}^{n-1}\hat{\rho}^2(i-j) \to 1 + \frac{2}{\left(4-2^{2H}\right)^2}\sum_{i=1}^{\infty}\hat{\rho}^2(k). \\ &\frac{1}{n}\frac{1}{\left(4-2^{2H}\right)^2}\sum_{j=1}^{n-1}\sum_{k=1}^{2n-1}\widetilde{\rho}_H^2(j,k) \to \frac{1}{\left(4-2^{2H}\right)^2}\sum_{m\in\mathbb{Z}}\widetilde{\rho}_H^2(m). \end{aligned}$$

Results obtained above imply that $M(\lambda) = \exp\left\{\frac{1}{2}\lambda^T\Sigma_H\lambda\right\}$. Thus:

$$\sqrt{n}\begin{pmatrix} n^{-1}(V_{n,T}^{\hat{B}^H} - EV_{n,T}^{\hat{B}^H}) \\ (2n)^{-1}(V_{2n,T}^{\hat{B}^H} - EV_{2n,T}^{\hat{B}^H}) \end{pmatrix} \xrightarrow{d} \mathcal{N}(0;\Sigma_H)$$

Application of Slutsky's theorem provides the required result. □

Theorem 2. *Let*

$$\hat{H}_n = \frac{1}{2} - \frac{1}{2\log 2}\log\left(\frac{\sum_{k=1}^{2n-1}\left(\Delta_{2n,k}^{(2)}X\right)^2}{\sum_{k=1}^{n-1}\left(\Delta_{n,k}^{(2)}X\right)^2}\right) \tag{10}$$

Then we can see that as $n \to \infty$, $\hat{H}_n \to H$

Moreover, we have:

$$2\log 2\sqrt{n}(\hat{H}_n^{(1)} - H) \xrightarrow{d} N(0, \sigma_H^2)$$

where

$$\sigma_H^2 = \frac{3}{2}\Sigma_{11} - 2\Sigma_{12} \tag{11}$$

Proof. The estimator $\hat{H}_n$ can be rewritten as:

$$\begin{aligned}\hat{H}_n &= \tfrac{1}{2} - \tfrac{1}{2\log 2}[(2H-1)\log\tfrac{1}{2} + \log\frac{(\frac{2n}{T})^{2H-1}V_{2n,T}^{(2)X}}{(\frac{n}{T})^{2H-1}V_{n,T}^{(2)X}}]\\ &= H - \tfrac{1}{2\log 2}\log\frac{(\frac{2n}{T})^{2H-1}V_{2n,T}^{(2)X}}{(\frac{n}{T})^{2H-1}V_{n,T}^{(2)X}},\end{aligned}$$

Using Theorem 1, the property of fractal Ornstein-Uhlenbeck and the Delta method, we can obtain:

$$2\log 2\sqrt{n}(\hat{H}_n^{(1)} - H) \xrightarrow{d} \mathcal{N}\left(0, \sigma_H^2\right), \sigma_H^2 = \frac{3}{2}\Sigma_{11} - 2\Sigma_{12}$$

$$\Sigma_{11} = 2(1 + \frac{2}{(4-2^{2H})^2}\sum_{j=1}^{\infty}\hat{\rho}_H^2(j)), \Sigma_{22} = \frac{1}{2}\Sigma_{11}$$

$$\Sigma_{12} = \Sigma_{21} = \frac{1}{2^{2H}(4-2^{2H})^2}\sum_{j\in\mathbb{Z}}\widetilde{\rho}_H^2(j)$$

$$\hat{\rho}_H(j) = \frac{1}{2}[-6|j|^{2H} - |j-2|^{2H} - |j+2|^{2H} + 4|j-1|^{2H} + 4|j+1|^{2H}],$$

$$\widetilde{\rho}_H(j) = \frac{1}{2}[|j+1|^{2H} + 2|j+2|^{2H} - |j+3|^{2H} + |j-1|^{2H} - 4|j|^{2H} - |j-3|^{2H} + 2|j-2|^{2H}]$$

□

3.2. Alternative Estimators for the Hurst Parameter

3.2.1. MF-DFA

In this subsection we introduce two different methods for estimating the Hurst exponent, as extracted from Kantelhardt et al. [30] and Gatheral et al. [13]. The first method is the MF-DFA proposed by Kantelhardt et al. [30] and allows multi-fractility. The MF-DFA has become a popular method to study the multi-fractal properties of various time series in finance since it may be applied to non-stationary time series. The second is the qth-order SF proposed by Gatheral et al. [13].

Let us consider the time series $x_i : i = 1, 2, \ldots, N$. Then, the MF-DFA involves the following five steps (most of the following algorithm is extracted from Kantelhardt et al. [30]):

(i) Compute the profile $Y(i)$ as follows:

$$Y(i) = \sum_{j=1}^{i}(x_j - \bar{x})$$

where $\bar{x}$ denotes the mean of x_i for the whole sample. Therefore, the profile $Y(i)$ is the cumulative sum of the return deviations from the sample mean.

(ii) Divide the profile $Y(i)$ into $Ns = \mathrm{int}\left(\frac{N}{s}\right)$ non-overlapping segments of equal length s, where s is referred to as the time scale. Since the length N of the series is often not

a multiple of the considered time scale s, a short part at the end of the profile may remain. In order not to disregard the short part at the end of the profile when N is not a multiple of s, the same procedure is repeated starting from the opposite end. Therefore, there will be 2Ns segments for a given time scale s. It is recommended that the value of the time scale, s, should satisfy $10 < s < \frac{N}{4}$.

(iii) Calculate the local trend for each of the 2Ns segments by a least-square fit of the series. Then determine the following variance $F^2(v,s)$:

$$F^2(v,s) \equiv \frac{1}{s}\sum_{i=1}^{s}\{Y[(v-1)s+i] - y_v(i)\}^2$$

For $v = Ns+1, Ns+2, \ldots, 2Ns$. Here, $y_v(i)$ is the fitting polynomial in segment v. The fitting polynomial captures the local trend. For example, let us consider segment v that is part of the first Ns segments. This segment includes the profiles $Y[(v-1)s+i]$, $i = 1, 2, 3 \ldots, s$. The local trend of the profile for the segment can be captured by fitting the following m-order polynomial:

$$Y[t] = \alpha + \beta_1 t + \beta_2 t^2 + \cdots + \beta_m t^m + \varepsilon, t = (v-1)s+1, \ldots, vs+1$$

Then, the fitting polynomial value $y_v(i)$ is given by:

$$y_v(i) = \hat{\alpha} + \widehat{\beta_1} t + \widehat{\beta_2} t^2 + \ldots + \widehat{\beta_m} t^m$$

where a "hat" above the parameters indicates the estimates obtained using the ordinary least squares method. In this study, we use the first-order polynomial.

(iv) Average over all segments to obtain the q-th order fluctuation function as follows $q \neq 0$:

$$F_q(s) \equiv \left\{\frac{1}{2Ns}\sum_{v=1}^{2Ns}\left[F^2(v,s)\right]^{q/2}\right\}^{1/q}$$

The q-th order fluctuations are similar to q-th order moments. However, in the MF-DFA, q can take negative values. The main purpose of using q-th order fluctuation has to do with the power-law, mentioned in the next step, which allows us to distinguish a multi-fractal model from a mono-fractal model. We are interested in how the generalized q dependent fluctuation functions $F_q(s)$ depend on the time scale s for different values of q. Hence, we must repeat steps 2 to 4 for several time scales, s. It is apparent that $F_q(s)$ will increase with increasing s. Of course, $F_q(s)$ depends on the DFA order m. By construction, $F_q(s)$ is only defined for $s \geq m+2$.

(v) Determine the scaling behavior of the fluctuation functions by analyzing log-log plots $F_q(s)$ versus s for each value of q. If the series x_i are long-range power-law correlated, $F_q(s)$ increases, for large values of s, as a power-law:

$$F_q(s) \sim s^{h(q)}$$

It is clear from the equation above that $F_0(s) = \lim_{q\to 0} F_q(s)$ and, therefore, $h(0) = \lim_{q\to 0} h(q)$, cannot be determined using the averaging procedure. Therefore, for $q = 0$, a logarithmic averaging procedure is employed as follows:

$$F_0(s) \equiv \exp\left\{\frac{1}{4Ns}\sum_{v=1}^{2Ns}\ln F^2(v,s)\right\} \sim s^{h(0)}$$

For each q (referred to as moment order), perform a linear regression of $\ln F_q(s)$ on $\ln(s)$ for all s. The slope of the regression will be the estimator of the generalized Hurst exponent $h(q)$.

3.2.2. The qth-Order SF Method

We also determined h(q) from the qth-order SF method used in Gatheral et al. [13]. In the spirit of Gatheral et al. [13], we assume that discrete observations of the spot volatility process, on a time grid with mesh Δ on [0, T] are $\sigma_0, \sigma_\Delta, \ldots, \sigma_{k\Delta}, \ldots, k \in \{0, \lfloor T/\Delta \rfloor\}$. Set $N = \lfloor T/\Delta \rfloor$, then for $q \geq 0$, we can define

$$m(q, \Delta) = \frac{1}{N} \sum_{k=1}^{N} \left| \log(\sigma_{k\Delta}) - \log\left(\sigma_{(k-1)\Delta}\right) \right|^q$$

Under the assumption that the log-spot-volatility process is stationary and that a law of large numbers holds, for some values of q we can see that qH has monofractual scaling properties which imply that

$$m(q, \Delta) \sim C\Delta^{qH}$$

As Δ tends to zero and with constant of proportionality C.

Let $\beta_1 = \log K_q$. We further use the market data via the regression

$$\log(m(q, \Delta)) = \beta_1 + \beta_2 \log \Delta + \epsilon \tag{12}$$

which provides an estimator:

$$H_{qSF} = \frac{\beta_2}{q} \tag{13}$$

For several orders of q, the regression of the slope in (12) against q reveals that the different orders of q lead to the same estimate of H as the one obtained when $q = 2$.

3.2.3. Two Least Square Estimation Methods

To test the roughness of the spot volatility, we must estimate the Hurst exponents. In fact, there exists a vast literature that describes different methods for estimating the Hurst parameter of the fractional Brownian motion (fBm) including parametric estimation methods, semi-parametric estimation and non-parametric estimation approaches. In this paper, we adopt two types of estimators for the Hurst parameter, which are proven to be strongly consistent and asymptotically normal.

Let $X_t = \log(\sigma t)$ as in model (1), and denotes $M_k(n) = \frac{1}{n-1} \sum_{i=0}^{n-2} \left(X_{(i+2)\Delta} - 2X_{(i+1)\Delta} + X_{i\Delta} \right)^k$, where $n \in \mathbb{N}^+ - 1, k \in \mathbb{R}^+$. The first estimator $\hat{H}_k$ of Hurst parameter H by the least squares estimation method introduced by Berzin et al. [31], is calculated as follows

$$\begin{aligned} \hat{H}_k &= -\tfrac{1}{k} \sum_{i=1}^{\ell} z_i \log(M_k(n_i)) \\ &= -\tfrac{1}{k} \sum_{i=1}^{\ell} z_i \log\left(\tfrac{1}{n_i - 1} \sum_{j=0}^{n_i - 2} \left(X_{(j+2)\Delta} - 2X_{(j+1)\Delta} + X_{j\Delta} \right)^k \right), \end{aligned} \tag{14}$$

where $n_i = r_i n, r_i \in \mathbb{N}^*, i = 1, \ldots, \ell$ and $z_i = \frac{y_i}{\sum_{i=1}^{\ell} y_i^2}$ and $y_i = \log(r_i) - \frac{1}{\ell} \sum_{i=1}^{\ell} \log(r_i)$.

Let $M_{\log}(n) = \frac{1}{n-1} \sum_{i=0}^{n-2} \log\left(\left| X_{(i+2)\Delta} - 2X_{(i+1)\Delta} + X_{i\Delta} \right| \right)$. The second estimator $\widetilde{H}_{\log}$ of H derived by the least square estimation method in Berzin et al. [31] is expressed as

$$\begin{aligned} \widetilde{H}_{\log} &= -\sum_{i=1}^{\ell} z_i M_{\log}(n_i) \\ &= -\sum_{i=1}^{\ell} z_i \tfrac{1}{n_i - 1} \sum_{j=0}^{n_i - 2} \log\left(\left| X_{(j+2)\Delta} - 2X_{(j+1)\Delta} + X_{j\Delta} \right| \right). \end{aligned} \tag{15}$$

The estimator $\hat{H}_k$ is an asymptotically unbiased strongly consistent estimator of H, and the estimator $\widetilde{H}_{\log}$ is an unbiased weakly consistent estimator of H. The asymptotic distribution of estimators $\hat{H}_k$ and $\widetilde{H}_{\log}$ can be found in Berzin et al. [31].

From remark 3.12 and remark 3.15 of Berzin et al. [31], asymptotic theory for $\hat{H}_k$ and $\widetilde{H}_{\log}$ there is a corollary. The estimator $\hat{H}_k$ is an asymptotically unbiased strongly consistent estimator of H and the estimator $\widetilde{H}_{\log}$ is an unbiased weakly consistent estimator of H. Furthermore, for $k = 2r_i = 2^{i-1}$ and $i = 1, \ldots, \ell$, we have:

$$\sqrt{n}\left(\hat{H}_k - H\right) \xrightarrow{d} \mathcal{N}\left(0, \sigma^2_{\hat{H}_k}\right)$$
$$\sqrt{n}\left(\hat{H}_{\log} - H\right) \xrightarrow{d} \mathcal{N}\left(0, \sigma^2_{\widetilde{H}_{\log}}\right)$$

where

$$\sigma^2_{\hat{H}_k} = \left(\frac{6}{\log(2)}\right)^2 \frac{1}{\ell^2(\ell^2-1)^2} \times \left(2 \sum_{i<j;i,j=1}^{\ell} 2^{-j}(2i-(\ell+1))(2j-(\ell+1)) \times \sum_{r=-\infty}^{+\infty} \rho^2_{1,2^{j-i}}(r) + \sum_{i=1}^{\ell} 2^{-i}(2i-(\ell+1))^2 \sum_{r=-\infty}^{+\infty} \rho^2_H(r)\right) \tag{16}$$

$$\begin{aligned}\sigma^2_{\widetilde{H}_{\log}} = \left(\frac{3}{\log(2)}\right)^2 \frac{1}{\ell^2(\ell^2-1)^2} \Bigg(2 \sum_{i<j;i,j=1}^{\ell} 2^{-j+1}(2i-(\ell+1))(2j-(\ell+1)) \\ \times \sum_{p=1}^{+\infty} (2p)! \left(\frac{1}{p(2p-1)!!}\right)^2 \sum_{r=-\infty}^{+\infty} \rho^{2p}_{1,2^{j-i}}(r) + \sum_{i=1}^{\ell} 2^{-i+1}(2i-(\ell+1))^2 \\ \times \sum_{p=1}^{+\infty} (2p)! \left(\frac{1}{p(2p-1)!!}\right)^2 \sum_{r=-\infty}^{+\infty} \rho^{2p}_H(r)\Bigg)\end{aligned} \tag{17}$$

$$\begin{aligned}\rho_{b,c}(x) = \frac{1}{2\left(4-2^{2H}\right)}(bc)^{-H}[-|x|^{2H} + 2|x-b|^{2H} - |x-2b|^{2H} \\ +2|x+c|^{2H} - 4|x+c-b|_{2H} + 2|x+c-2b|^{2H} - |x+2c|^{2H} \\ +2|x+2c-b|^{2H} - |x+2c-2b|^{2H}] \\ \rho_H(x) = \frac{-6|x|^{2H} + 4|x+1|^{2H} - |x+2|^{2H} - |x-2|^{2H} + 4|x-1|^{2H}}{2\left(4-2^{2H}\right)}\end{aligned}$$

3.3. Comparison of Asymptotic Variance of H_k, H_{log} and H_n

In this subsection, we compare Hurst exponents according to the three variance Formulas (11), (16) and (17). Although, in theory, H_k, H_{log} and H_n can eventually converge to the true value, in engineering practice, the value of ℓ, p, r cannot be very large, which means that there must be errors in the three Hurst exponent estimates under the condition of limited computing resources. Therefore, we try to compare the advantages and disadvantages of the three according to the asymptotic variance under different parameter values.

As can be seen from Table 1, with the increase in the number of ℓ, $\hat{\mathrm{H}}_{\mathrm{k}}$ and $\hat{\mathrm{H}}_{\log}$ have a downward trend, but overall, the asymptotic variance of $\hat{\mathrm{H}}_{\mathrm{k}}$ is less than $\hat{\mathrm{H}}_{\log}$. From this point of view, $\hat{\mathrm{H}}_{\mathrm{k}}$ is a better estimate.

Table 1. Comparison of asymptotic variance of H_k and H_{log}.

H.	ℓ	**0.1**	**0.2**	**0.3**	**0.4**	**0.5**	**0.6**	**0.7**	**0.8**	**0.9**
$\hat{H}_k$	2	61.43384	60.09544	58.74345	57.42546	56.19696	55.12336	54.28286	53.77096	53.7078
	5	9.179444	9.099669	8.987028	8.86357	8.745652	8.646854	8.57992	8.558286	8.597588
	10	2.973535	2.891396	2.820534	2.762025	2.716779	2.686191	2.672437	2.678699	2.709498
$\hat{H}_{log}$	2	165.8243	75.86426	74.52995	73.18453	71.87646	70.66238	69.6092	68.7972	68.32469
	5	11.05752	10.97854	10.86696	10.74497	10.62911	10.53315	10.47013	10.45383	10.50042
	10	3.51451	3.432525	3.361931	3.303832	3.259175	3.229411	3.216792	3.22461	3.257532

According to Figure 1 and Table 1, H_k is usually better than H_{log} when the parameter ℓ has a limited value. The variance of H_k is small, but H_{log} converges slightly faster with an increase of ℓ. In general, H_k is recommended in practice.

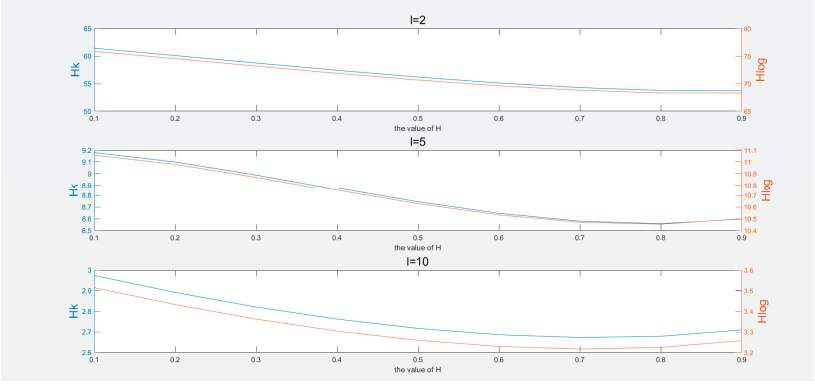

Figure 1. Comparison of asymptotic variance of H_k and H_{log}.

Next, given $\ell = 10$, compare the asymptotic variance of H_n with that of H_k and H_{log}. Table 2 shows the change of H values from 0.1 to 1. It can be seen that as the value of H increases, the error of H_n becomes smaller and smaller. When $H > 0.4$, the asymptotic variance of H_n is smaller than H_k and H_{log}.

Table 2. Comparison of asymptotic variance of H_n with H_k and H_{log}.

ℓ=10.									
H	0.1	0.2	0.3	0.4	0.5	0.6	0.7	0.8	0.9
$\hat{H}_k$	2.973535	2.891396	2.820534	2.762025	2.716779	2.686191	2.672437	2.678699	2.709498404
$\hat{H}_{log}$	3.51451	3.432525	3.361931	3.303832	3.259175	3.229411	3.216792	3.22461	3.257531806
$\hat{H}_n$	4.055571	3.812466	3.552612	3.280313	3	2.716159	2.433252	2.155608	1.887306706

A similar situation is shown in Figure 2. H_n decreases as the value of H increases; after 0.4, the asymptotic variance of H_n is less than that of H_k and H_{log}.

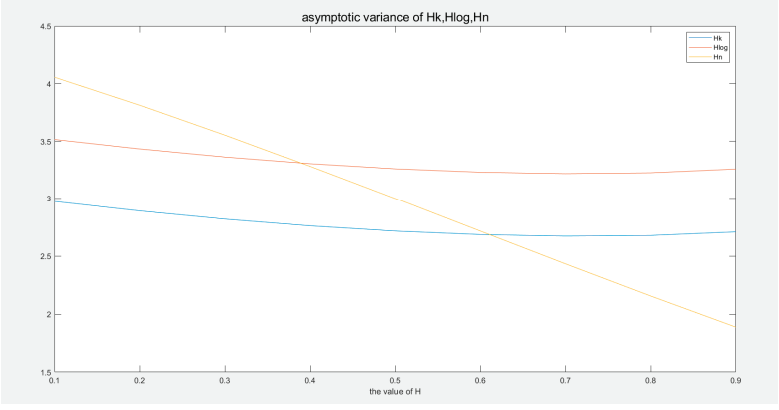

Figure 2. Comparison of asymptotic variance of H_n with that of H_k and H_{log}..

4. Research on the Roughness of Truncated and Non-Truncated Spot Volatility of Chinese A-Share Industry Indices Estimated by Five Hurst Exponents

4.1. Data Description

We collected Shanghai Composite Index and Shanghai Industrial Index series data from the WIND High-frequency database. The sampling frequency was set at 5 min, which allowed us to circumvent all the issues associated with micro-structure noise and thereby focus on questions pertinent to this paper. For assets in the Chinese stock market, we considered the Shanghai Composite Index (also named SSE Index), the most influential index in China's capital market, and the Shanghai Industrial Index series consisting of 10 primary industries.

The Shanghai Composite Index, published on 15 July 1991, is the first flagship index reflecting the overall market trend in Shanghai. It includes all the stocks listed on the Shanghai Stock Exchange, such as A shares and B shares, and is weighted by the total share capital, representing the 30-year development process of China's capital market. It is a symbol of China's capital market. The data set at our disposal ran from 1 January 2005 until 31 December 2020. We excluded weekends and holidays and kept only full trading days, which resulted in 3888 days. Thus, we obtained 48 observations for every trading day and obtained 186,624 observations for the SSE index. According to industry classification standards, the Shanghai Industrial Index series consists of 10 primary industries, such as the Energy Sector (SSE Energy), Raw Materials Sector (SSE Materials), Industrials Sector (SSE Industrials), Consumer Discretionary Sector (SSE ConsDisc), Consumer Staples Sector (SSE ConsStaples), Health Care Sector (SSE HealthCare), Financials Sector (SSE Financials), Information Technology Sector (SSE InfoTechnology), Telecommunication Services Sector (SSE TelecomSvc), and the Utilities Sector (SSE Utilities), which cover almost all samples of the Shanghai stock market and represent the development process of the relating industries. A detailed descriptions and interpretations for the ten indices are as follows:

1. Base date and base index. The base date of the Shanghai stock exchange industry index series is 9 January 2009, and the base index is 1000.

2. Index sample stocks selection. The sample stock space of series of the Shanghai industry index is composed of all sample stocks of Shanghai Index. Based on the international mainstream industry classification standards and the characteristics of China's listed companies, the listed companies are divided into 10 industries: energy, raw materials, industry, optional consumption, main consumption, medicine and health, finance and real estate, information technology, telecommunication business and public utilities.

3. Sample stock selection method. The stocks in the sample space are classified according to the industry classification standard, and all the stocks in their respective industries constitute the sample stocks of the corresponding industry index.

4. Index calculation and correction. The industry index series of Shanghai stock exchange adopts the Paasehe weighting method, and the weighted calculation formula is as follows.

Index in the reporting period = adjusted market value of sample stock in the reporting period/base period $\times$ 1000.

Specifically, adjust market value = stock price $\times$ adjusted capital stock. The adjusted capital stock is the capital stock after adjusting the capital stock of the sample stock by "grading and classifying".

5. Sample stock adjustment. When the Shanghai Stock Index adjusts the sample stocks, the industry index series of Shanghai stock index is adjusted accordingly. When the sample company has a special event, which leads to the change of its industry ownership, the sample stock of Shanghai stock exchange industry index series is adjusted accordingly.

The data set at our disposal run from 1 January 2010 until 31 December 2020, which results in 2673 days by keeping only full trading days. Thus, we obtain 48 observations for every trading day and obtain 128,304 observations for each industrial index.

4.2. Non-Truncated Spot Volatility

Ignoring the effects of jumps in the prices, we can apply the non-truncated estimator of Equation (2) to extract spot volatilities using the 5 min high-frequency data. The estimation procedure calculating with $\Delta_n = 5/240$ and $k_n = 96$ results in 1944 estimates of non-truncated spot volatility for the SSE Index and 1337 estimates of non-truncated spot volatilities for each industrial index. To give a brief insight into the properties of the 11 indices, Table 3 reports summary statistics for non-truncated spot volatility, where Std.Dev denotes standard derivation. Index abbreviations are given in the first column. The second to sixth columns contain some basic descriptive statistics for the indices, including the mean, minimal, median, maximal and standard deviation of the spot volatility estimates. Moreover, both skewness and kurtosis are presented in the last two columns of Table 3.

Table 3. Descriptive statistics for the non-truncated spot volatility and its logarithm.

stat_non_trunc	Mean	Min	Max	Median	Std.Dev	Skewness	Kurtosis
Panel A: Non-truncated Spot Volatility							
SSE index	0.00022	9.05×10^{-6}	0.00484	0.00010	0.00037	5.61360960	47.7565
SSE Energy	0.00025	1.48×10^{-5}	0.00613	0.00014	0.00045	6.96110970	69.8107
SSE Materials	0.00026	1.74×10^{-5}	0.00810	0.00014	0.00051	8.30235757	95.8771
SSE Industrials	0.00023	1.02×10^{-5}	0.00787	0.00010	0.00052	8.19252067	90.0560
SSE Cons Disc	0.00021	9.85×10^{-6}	0.00648	0.00011	0.00041	8.81983563	106.233
SSE Cons Staples	0.00020	1.14×10^{-5}	0.00659	0.00012	0.00037	9.56348181	128.357
SSE Health Care	0.00019	7.73×10^{-6}	0.00603	0.00011	0.00035	8.82946172	113.921
SSE Financials	0.00021	1.04×10^{-5}	0.00562	0.00011	0.00038	6.87344218	67.1841
SSE Info Technology	0.00031	2.28×10^{-5}	0.00727	0.00018	0.00048	7.08361470	76.6140
SSE Telecom Svc	0.00034	2.38×10^{-5}	0.00934	0.00018	0.00061	7.56650831	79.6772
SSE Utilities	0.00017	1.13×10^{-5}	0.00587	7.65×10^{-5}	0.00040	7.96280129	83.3764
Panel B: Logarithm of non-truncated spot volatilities							
SSE index	−9.0228	−11.6127	−5.3299	−9.1544	1.04418	0.48284956	2.92738
SSE Energy	−8.8034	−11.1212	−5.0932	−8.8651	0.93912	0.56099374	3.72217
SSE Materials	−8.7734	−10.959	−4.8149	−8.8504	0.92463	0.64137993	3.95554
SSE Industrials	−9.0030	−11.4906	−4.8435	−9.1269	0.95747	0.87836819	4.56345
SSE Cons Disc	−8.9992	−11.5282	−5.0387	−9.0412	0.92581	0.50655449	4.08381
SSE Cons Staples	−8.9353	−11.3815	−5.0212	−8.9969	0.82634	0.65934088	4.71016
SSE Health Care	−9.0657	−11.7707	−5.11096	−9.0936	0.94631	0.29717300	3.91282
SSE Financials	−8.9995	−11.4702	−5.1811	−9.0533	0.96055	0.43924226	3.75374
SSE Info Technology	−8.4958	−10.689	−4.9236	−8.5761	0.87165	0.45663801	3.65189
SSE Telecom Svc	−8.4808	−10.645	−4.6731	−8.5727	0.86341	0.78021763	4.49018
SSE Utilities	−9.3710	−11.3898	−5.1368	−9.4783	0.98057	0.94548892	4.67285

Panel A of Table 3 shows that mean values of the non-truncated spot volatility range from 0.0002 to 0.0003 for all indices. SSE TelecomSvc displays the highest standard deviation (i.e., 0.00061). Considering skewness and kurtosis, the SSE Index achieves the lowest values while the highest values are obtained for SSE ConsStaples. None of the series seems to be symmetric. Moreover, all the time series have positive skewness, which implies that the distributions have a long right tail.

As stated in Da Fonseca and Zhang [21], taking the logarithm has the well-known effect of reducing the discrepancies between variables and makes distributions closer to normal distributions. Panel B of Table 3 shows that skewness of the logarithm of non-truncated spot volatilities are much smaller, and the kurtosis are closer or a little bigger than 3.

The main reason for positive skewness and high kurtosis might be comprised of the effect of jumps which we don't filter in the data. Therefore, we next considered the case when there are jumps in the asset prices.

4.3. Truncated Spot Volatility

To consider the effect of jumps, we estimate the spot volatility using the truncated estimator of Equation (3) with $k_n = 96$, $\Delta_n = 5/240$ and $v_n = \sqrt{\Delta_n/250}$. Table 4 provides the basic descriptive statistics for the truncated spot volatility. As shown in Panel A of Table 4, the mean values and standard deviations of the truncated spot volatility indexes are all around 0.0001–0.0002. These positive values for the skewness of the spot volatility indexes indicate that all the spot volatility indexes are skewed right. The values for the kurtosis of the spot volatility indexes are always greater than 3, which indicates a heavy-tailed distribution. By taking the logarithm, Panel B of Table 4 shows that the skewness of the logarithm of truncated spot volatility of all the indices are near the expected value of zero, and the kurtosis of the logarithm of truncated spot volatility of all the indices are near the expected value of 3. Hence, the values of skewness and kurtosis of the logarithm of truncated spot volatility indexes are acceptable ranges for being normally distributed, which would make the Hurst parameter estimators maintain their good properties.

4.4. Hurst Exponent Estimation

By using the derived logarithm of non-truncated and truncated spot volatility series of the Composite Index and the 10 industrial indices data in the Chinese stock market, we calculated the Hurst parameter using the four Hurst parameter estimators, H_n,H_k,H_{log}, H_{qSF} in Section 2.

When we calculate the estimator H_{qSF} from (13) by the qth-order SF method, we should refine how the regression slope β_2 from regression (12) depends on the order q. By the mono-fractal scaling properties, we suppose $\beta_2 \sim Hq$, which leads us to a similar estimate of the Hurst exponent by (13).

By taking $q = 1$, 1.5, 2, 2.5, 3, 3.5 and conducting a linear regression of (12) for $\Delta = 1, 2, 3, \ldots, 100$, Figure 3 shows the linear relationship of β_2 and q based on logarithm forms of both non-truncated spot volatility and truncated spot volatility for the Shanghai Composite Index (SSE Index). Additional test results for the 10 industrial indices are shown in Figures 4 and 5. All the figures illustrate the approximate linear relationship between β_2 and q, which is consistent with the theoretical derivation in Gatheral et al. [13] and lead us to a similar estimate of the Hurst parameter by (13).

Table 4. Descriptive statistics for the truncated spot volatilities and their logarithms.

stat_trunc	Mean	Min	Max	Median	Std.Dev	Skewness	Kurtosis
Panel A: Truncated spot volatilities							
SSE index	0.00015	9.05×10^{-6}	0.00093	9.38×10^{-5}	0.00015	1.910627	6.71405
SSE Energy	0.00016	1.48×10^{-5}	0.00089	0.00011	0.00014	2.162615	8.26727
SSE Materials	0.00016	1.74×10^{-5}	0.00082	0.00012	0.00014	2.072311	7.87712
SSE Industrials	0.00014	1.02×10^{-5}	0.00090	0.0001	0.00013	2.476477	9.72460
SSE Cons Disc	0.00013	9.85×10^{-6}	0.00077	0.00010	0.00011	2.323363	9.81297
SSE Cons Staples	0.00014	1.14×10^{-5}	0.00081	0.00011	0.00010	2.505865	11.2342
SSE Health Care	0.00013	7.73×10^{-6}	0.00085	0.00010	0.00011	2.366167	10.4674
SSE Financials	0.00014	1.04×10^{-5}	0.00102	0.00010	0.00013	2.684608	12.6908
SSE Info Technology	0.00021	2.28×10^{-5}	0.00095	0.00016	0.00015	1.64547	5.96398
SSE Telecom Svc	0.00020	2.38×10^{-5}	0.00100	0.00016	0.00014	1.889841	7.25645
SSE Utilities	0.00010	1.01×10^{-5}	0.00086	7.26×10^{-5}	0.00012	3.081249	13.9049
Panel B: Logarithm of truncated spot volatilities							
SSE index	−9.1803	−11.612	−6.9750	−9.2744	0.88871	0.197569	2.41616
SSE Energy	−9.0321	−11.121	−7.0142	−9.0610	0.76953	0.124777	2.77233
SSE Materials	−8.9674	−10.959	−7.1063	−8.9712	0.74074	0.099774	2.73774
SSE Industrials	−9.1668	−11.490	−7.0048	−9.2100	0.76706	0.275856	3.15982
SSE Cons Disc	−9.1697	−11.528	−7.1616	−9.1632	0.76327	−0.04621	3.00242
SSE Cons Staples	−9.0922	−11.381	−7.1069	−9.1035	0.66098	0.002958	3.49107
SSE Health Care	−9.2145	−11.770	−7.069	−9.1831	0.78518	−0.28041	3.35773
SSE Financials	−9.1818	−11.470	−6.8844	−9.2013	0.79877	−0.00218	3.09299
SSE Info Technology	−8.6952	−10.689	−6.9569	−8.7076	0.6935	−0.10739	2.91148
SSE Telecom Svc	−8.6995	−10.645	−6.9032	−8.7227	0.65081	0.013933	3.01487
SSE Utilities	−9.4973	−11.507	−7.0505	−9.5307	0.8180	0.394645	3.19111

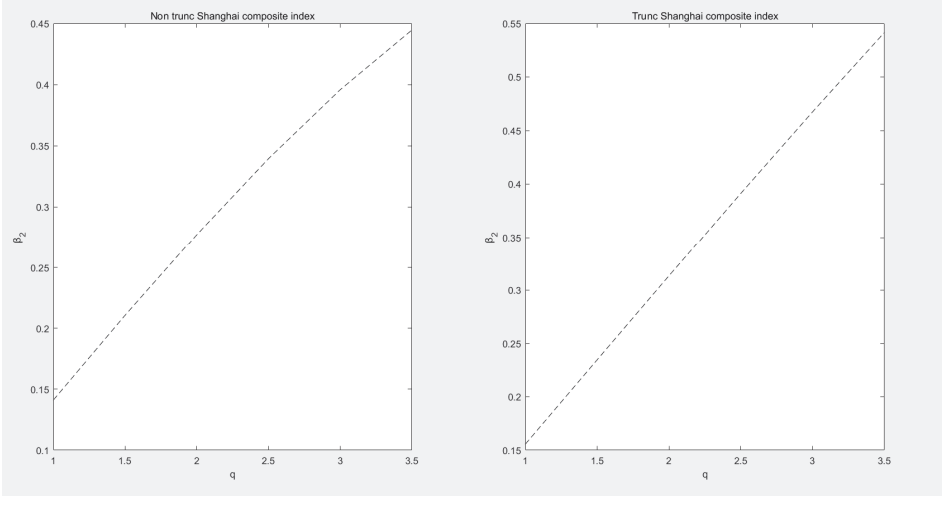

Figure 3. β_2 against q based on logarithm forms of both non-truncated spot volatility and truncated spot volatility for the Shanghai Composite Index (SSE Index).

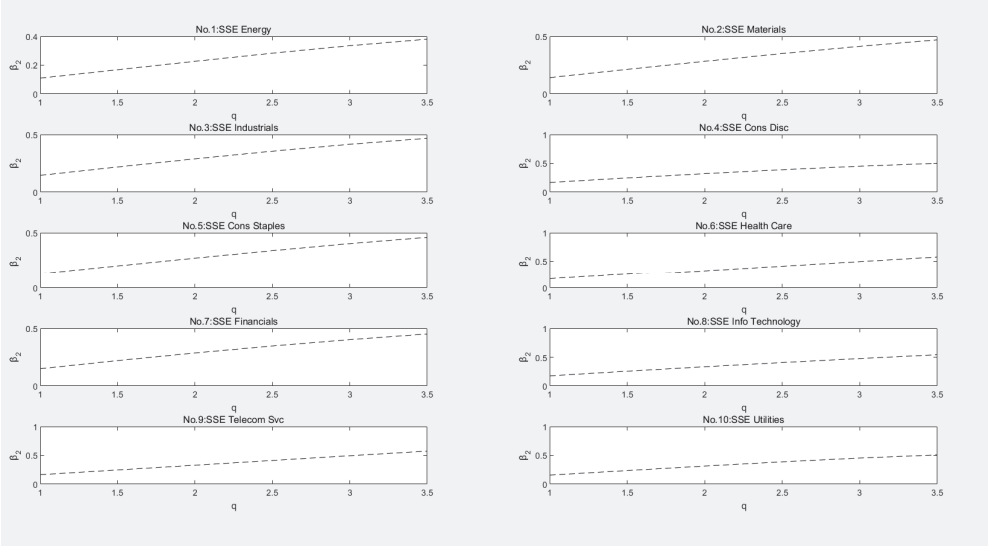

Figure 4. β_2 against q based on the logarithm of non-truncated spot volatility for the 10 industrial indices.

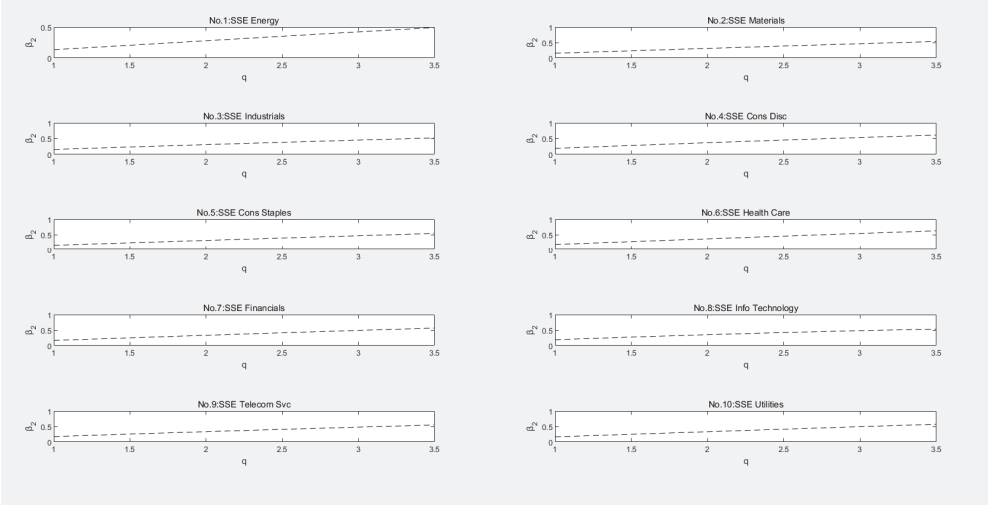

Figure 5. β_2 against q based on the logarithm of truncated spot volatility for the 10 industrial indices.

For all the indices, we can calculate the Hurst exponents by the five different Hurst exponent estimators using both non-truncated spot volatility and truncated spot volatility in logarithm forms. From the Hurst exponent estimation results listed in Table 5, we can see the Hurst exponents are all less than 0.5 for all the indices, no matter which Hurst exponent estimator we adopt, and whether or not price jumps are filtered. The results in Table 5 indicate the roughness in the log-volatility of the Composite Index and the 10 industrial indices in the Chinese stock market, consistent with findings in the literature, such as Gatheral et al. [13], Livieri et al. [14], Da Fonseca and Zhang [21] and Takaishi [23]; Bennedsen et al. [11]. Our study provides further evidence of the roughness in spot volatility.

Table 5. Hurst parameter estimates for the logarithm of spot volatilities.

Index	Log (Non-Truncated Spot Volatility)					Log (Truncated Spot Volatility)				
	H_k	H_{log}	H_{qSF}	H_n	MF-DFA	H_k	H_{log}	H_{qSF}	H_n	MF-DFA
SSE index	0.27	0.22	0.09	0.27	0.22	0.27	0.17	0.16	0.19	0.26
SSE Energy	0.33	0.28	0.06	0.33	0.23	0.33	0.22	0.05	0.24	0.26
SSE Materials	0.26	0.25	0.28	0.26	0.22	0.26	0.27	0.09	0.26	0.26
SSE Industrials	0.29	0.26	0.18	0.29	0.20	0.29	0.18	0.21	0.15	0.27
SSE Cons Disc	0.23	0.18	0.16	0.23	0.25	0.23	0.25	0.20	0.23	0.28
SSE Cons Staples	0.20	0.17	0.25	0.20	0.22	0.20	0.23	0.13	0.23	0.21
SSE Health Care	0.22	0.21	0.11	0.22	0.27	0.22	0.20	0.22	0.17	0.34
SSE Financials	0.23	0.24	0.27	0.23	0.15	0.23	0.21	0.11	0.20	0.23
SSE Info Technology	0.33	0.33	0.21	0.32	0.18	0.33	0.29	0.23	0.29	0.23
SSE Telecom Svc	0.37	0.38	0.10	0.37	0.21	0.37	0.31	0.21	0.30	0.25
SSE Utilities	0.27	0.22	0.09	0.27	0.22	0.27	0.33	0.15	0.28	0.26

5. Discussion

It is well-known that the constant volatility of Black and Scholes [1] is neither consistent with real volatility data nor consistent with implied volatility surfaces. Consequently, several popular stochastic volatility models driven by standard Brownian motions have been introduced in past decades to reproduce the stylized facts of time series observed for both the historical volatility and the implied volatility. Moreover, in order to take into account an apparent presence of long memory in the volatility process, Comte and Renault [6] first proposed a stochastic volatility model driven by fractional Brownian motion (fBm) with $H > 1/2$. Recently, prompted by new insights from realized volatility data, Gatheral et al. [13] and Bennedsen et al. [11] introduced rough volatility models driven by fBm with $H < 1/2$. Using absolute moments estimation and realized volatility as a proxy of true volatility, Gatheral et al. [13] estimate the Hurst exponent and found that it is close to 0.14 for both the log-volatility of the SP500 and the NASDAQ, together with other major indices. Moreover, the estimation of the Hurst exponent H is robust across time, scales and markets. More empirical studies of the log-volatility for thousands of stocks (see, e.g., Bennedsen et al. [11]) and implied volatility (see, e.g., Livieri et al. [14]) confirm the roughness of the volatility.

Since the spot volatility is of importance in several applications, including derivatives pricing, high-frequency trading, and risk management, it is t natural to assess whether spot volatility has a rough property, that is, to determine whether the spot volatility is rough.

Many publications consider the roughness of realized volatility and implied volatility. Gatheral et al. [13] showed the volatility roughness of SP500 index, Livieri et al. [14] showed that implied volatility is rough, too. Takaishi [23] studied Bitcoin and verified the roughness of volatilities in Bitcoin. Da Fonseca and Zhang [21] found the volatility of volatility is also rough. Bennedsen et al. [11] found the roughness of logarithmic volatility of thousands of stocks. There is much evidence showing the roughness of volatility in different sectors and markets (see Guennoun et al. [32], Funahashi and Kijima [33], Neuenkirch and Shalaiko [34]). However, spot volatility is still a problem, especially the comparison of truncated and non-truncated spot volatility. This paper fills the gaps in previous works.

Following the important work of Gatheral et al. [13], this study aims to provide further evidence of the roughness of logarithm spot volatility in the Chinese financial market. Using the non-parametric estimator proposed by Fan and Wang [28], this paper introduces a non-parametric spot volatility estimator for the fractional volatility model of (1) for all $H \in (0, 1)$. Using five different Hurst exponents, MF-DFA, qth-order SF, two Hurst estimations using the least square estimation method provided by Berzin et al. [31] and a new Hurst exponent by changing frequency method, this paper analyzed roughness of the log-realized volatility of 10 industrial indices in the Chinese financial market. We found that $h(q)$ calculated by five different Hurst exponents were all less 0.5. These results confirm the roughness of log-spot volatility.

Moreover, we propose a new Hurst estimation H_n by changing the data frequency method. This performs better when $H > 0.4$ in the perspective of asymptotic variance.

6. Conclusions

Volatility is very important in many aspects of the financial field. First, implied volatility is the key in option pricing relative to the realized volatility, and a model of realized volatility can be used to improve the option pricing effectiveness. Second, volatility is a way to measure risk. With the continuous development of the financial market, financial assets such as stocks, futures, bonds and foreign exchange are constantly enriched. No matter the kind of financial asset, price risk is always one of the core risks. The most direct manifestation of the sharp rise and fall of prices is the rise of volatility, so how to measure and predict volatility is a very important problem. Therefore, modeling and prediction of volatility is the answer to the basic problem of the financial risk, and its significance is self-evident. Third, volatility is an indicator of financial supervision on micro market behavior. Financial market supervision often faces a dilemma: on the one hand, we should encourage financial innovation, but innovation often brings new problems, such as new market risks or new institutional arbitragers. On the other hand, we should not be too conservative, otherwise it is easy to suppress market vitality and solidify market ecology; then we may lose the fairness of the market. With the popularity of financial big data, regulators have more micro-detailed data, which provides the possibility for fixed-point and local supervision. So how to mine and depict the behavior of market participants from massive data is an important problem. Macro and micro financial behaviors, related to the banker, money laundering, financial crises, credit default, and so on, have effects on market price. When the market price changes dramatically, this reflects volatility. Therefore, the volatility can become a tool and a starting point for supervision in the era of financial big data.

Since volatility modelling is so important, this section summarizes the contributions of studies of roughness of volatility, which is one its most important properties. First, we propose a Hurst estimation H_n by changing the data frequency method. Second, we prove the asymptotic variance of H_n and that of two Hurst estimations provided by Berzin et al. [31], and do simulations to find the advantages of H_n that H_n that work better than those of Berzin et al. [31] when $H > 0.4$. Third, since much literature verifies the roughness of volatility (including volatility of the SP500 index by Gatheral et al. [13], implied volatility of options by Livieri et al. [13], volatility of bitcoin by Takaishi [23], volatility of volatility by Da Fonseca and Zhang [21], and volatility of many stocks by Bennedsen et al. [11]), we fill a gap that verifies the roughness of truncated and non-truncated spot volatility by four different Hurst exponent estimations: H_n, H_k, H_{log}, H_{qSF}. We find that truncated spot volatility has a stronger roughness than that of non-truncated spot volatility.

This study also suggests several important directions for future research. The estimator methods of constructing the estimators and their asymptotic properties essentially depend on observations. The first suggestion is to include estimation error and microstructure noise into the analysis. The second suggestion is to construct a unified volatility model that correctly accounts for, if possible, all the stylized facts observed in the real data, such as volatility clustering, multi-fractality, roughness, mean-reversion and persistence. Another direction for future research is to discuss the pricing and hedging of volatility options in some rough volatility models. In such cases, efficient Monte Carlo methods and asymptotic approximations for computing option prices and hedge ratios should be employed, which might provide insight into the robustness of the results obtained herein.

Author Contributions: Methodology, Y.L.; software, Y.L.; formal analysis, Y.L.; writing—review and editing, Y.L.; validation, Y.T.; resources, Y.T. All authors have read and agreed to the published version of the manuscript.

Funding: This research received no external funding.

Institutional Review Board Statement: The study was conducted in accordance with the Declaration of Helsinki, and approved by the Institutional Review Board.

Informed Consent Statement: Not applicable.

Data Availability Statement: The data used to support the findings of this study are available from the corresponding author upon request.

Acknowledgments: All individuals included in this section have consented to the acknowledgement.

Conflicts of Interest: The authors declare that there are no conflicts of interest regarding the publication of this paper.

Appendix A

Proof of Lemma 1. We give brief derivations here.

From (1), for all $H \in (0, 1)$, we have

$$\begin{aligned} X_t &= \left(1-e^{-\alpha t}\right)m + X_0 e^{-\alpha t} + v\int_0^t e^{-\alpha(t-s)}dB_s^H \\ &= \left(1-e^{-\alpha t}\right)m + X_0 e^{-\alpha t} + vB_t^H - \alpha v e^{-\alpha t}\int_0^t e^{\alpha s}B_s^H ds \\ &= \left(1-e^{-\alpha t}\right)m + X_0 e^{-\alpha t} + \widetilde{X} \end{aligned} \tag{A1}$$

where $\widetilde{X}_t = \nu B_t^H - \alpha\nu e^{-\alpha t}\int_0^t e^{\alpha s}B_s^H ds$

Thus, X_t is normal distribution with mean $\left(1-e^{-\alpha t}\right)m + X_0 e^{-\alpha t}$. For the sake of convenience, we first consider the covariance of $\widetilde{X}_t$ and $\widetilde{X}_s$. Using the well known result, $R_H(s,t) = \frac{1}{2}(|t|^{2H} + |s|^{2H} - |t-s|^{2H})$, supporting t > s > 0, the covariance function of, $\widetilde{X}_t$ and $\widetilde{X}_s$ is given by:

$$\begin{aligned} \operatorname{cov}(\widetilde{X}_t, \widetilde{X}_s) = \mathbb{E}[&(-\alpha\nu e^{-\alpha t}\int_0^t e^{\alpha u}B_u^H du + \nu B_t^H)(-\alpha\nu e^{-\alpha s}\int_0^s e^{\alpha v}B_v^H dv + \nu B_s^H)] \\ &= -\tfrac{\alpha\nu^2}{2}e^{-\alpha t}\int_0^t e^{\alpha u}(u^{2H} + s^{2H} - |u-s|^{2H})du \\ &-\tfrac{\alpha\nu^2}{2}e^{-\alpha s}\int_0^s e^{\alpha v}(v^{2H} + t^{2H} - |v-t|^{2H})dv + \tfrac{\nu^2}{2}(t^{2H} + s^{2H} - |t-s|^{2H}) \\ &+\tfrac{\alpha^2\nu^2}{2}e^{-\alpha t-\alpha s}\int_0^t\int_0^s e^{\alpha u+\alpha v}(u^{2H} + v^{2H} - |u-v|^{2H})dudv = \tfrac{\nu^2}{2}\sum_{n=1}^{10} I_n \end{aligned} \tag{A2}$$

with

$$\begin{gathered} I_1 = -\alpha e^{-\alpha t}\int_0^t e^{\alpha u}s^{2H}du,\ I_2 = -\alpha e^{-\alpha t}\int_0^t e^{\alpha u}u^{2H}du,\ I_3 = \alpha e^{-\alpha t}\int_0^t e^{\alpha u}|u-s|^{2H}du \\ I_4 = -\alpha e^{-\alpha s}\int_0^s e^{\alpha v}t^{2H}dv,\ I_5 = -\alpha e^{-\alpha s}\int_0^s e^{\alpha v}v^{2H}dv,\ I_6 = \alpha e^{-\alpha s}\int_0^s e^{\alpha v}(t-v)^{2H}dv \\ I_7 = t^{2H} + s^{2H} - (t-s)^{2H},\ I_8 = \alpha^2 e^{-\alpha t-\alpha s}\int_0^t e^{\alpha v}dv\int_0^s e^{\alpha u}u^{2H}du \\ I_9 = \alpha^2 e^{-\alpha t-\alpha s}\int_0^s e^{\alpha u}du\int_0^t e^{\alpha v}v^{2H}dv \\ I_{10} = -\alpha^2 e^{-\alpha t-\alpha s}\int_0^t\int_0^s e^{\alpha u+\alpha v}|u-v|^{2H}dudv \end{gathered}$$

The first two integrals are equal to:

$$I_1 = s^{2H}\left(e^{-\alpha t}-1\right) \text{ and } I_2 = -e^{-\alpha t}\int_0^t u^{2H}de^{\alpha u} = -t^{2H} + 2He^{-\alpha t}\int_0^t e^{\alpha u}u^{2H-1}du$$

By changing variables and integration by parts, we can obtain:

$$\begin{aligned} I_3 = &\quad \alpha e^{-\alpha t}\int_0^s e^{\alpha u}(s-u)^{2H}du + \alpha e^{-\alpha t}\int_s^t e^{\alpha u}(u-s)^{2H}du \\ = &\quad \alpha e^{-\alpha t+\alpha s}\int_0^s e^{-\alpha z}z^{2H}dz + \alpha e^{-\alpha t+\alpha s}\int_0^{t-s} e^{\alpha z}z^{2H}dz \\ = &\quad -e^{-\alpha t+\alpha s}\Big(e^{-\alpha s}s^{2H} - 2H\int_0^s e^{-\alpha z}z^{2H-1}dz - e^{\alpha(t-s)}(t-s)^{2H} \\ &\quad +2H\int_0^{t-s} e^{\alpha z}z^{2H-1}dz\Big) \\ = &\quad -e^{-\alpha t}s^{2H} + (t-s)^{2H} + 2He^{-\alpha t+\alpha s}\int_0^s e^{-\alpha z}z^{2H-1}dz \\ &\quad -2He^{-\alpha t+\alpha s}\int_0^{t-s} e^{\alpha z}z^{2H-1}dz. \end{aligned}$$

Similarly, we can have:

$$I_4 = t^{2H}(e^{-\alpha s} - 1), I_5 = -s^{2H} + 2He^{-\alpha s}\int_0^s e^{\alpha v} v^{2H-1} dv$$
$$I_6 = \alpha e^{-\alpha s+\alpha t}\int_{t-s}^t e^{-\alpha z} z^{2H} dz = -e^{-\alpha s+\alpha t}\int_{t-s}^t z^{2H} de^{-\alpha z}$$
$$= -e^{-\alpha s} t^{2H} + (t-s)^{2H} + 2He^{-\alpha s+\alpha t}\int_{t-s}^t e^{-\alpha z} z^{2H-1} dz$$
$$I_8 = e^{-\alpha t-\alpha s}\left(e^{\alpha t} - 1\right)\int_0^s u^{2H} de^{\alpha u} = \left(1 - e^{-\alpha t}\right)s^{2H} - 2He^{-\alpha s}\left(1 - e^{-\alpha t}\right)\int_0^s e^{\alpha u} u^{2H-1} du$$
$$I_9 = (1 - e^{-\alpha s})t^{2H} - 2He^{-\alpha t}(1 - e^{-\alpha s})\int_0^t e^{\alpha v} v^{2H-1} dv$$

Then, we consider the term I_{10}, which can be represented as:

$$\begin{aligned} I_{10} = \quad & -\alpha^2 e^{-\alpha t-\alpha s}\int_0^s \int_0^v e^{\alpha u+\alpha v}(v-u)^{2H} du dv \\ & -\alpha^2 e^{-\alpha t-\alpha s}\int_0^s \int_v^s e^{\alpha u+\alpha v}(u-v)^{2H} du dv \\ & -\alpha^2 e^{-\alpha t-\alpha s}\int_s^t \int_0^s e^{\alpha u+\alpha v}(v-u)^{2H} du dv \\ = \quad & -2\alpha^2 e^{-\alpha t-\alpha s}\int_0^s \int_0^v e^{\alpha u+\alpha v}(v-u)^{2H} du dv \\ & -\alpha^2 e^{-\alpha t-\alpha s}\int_s^t \int_0^s e^{\alpha u+\alpha v}(v-u)^{2H} du dv \\ & = I_{10}^1 + I_{10}^2 \end{aligned}$$

Using the change of variables u − v = z, the change of order of integration, and integration by parts, we obtain:

$$I_{10}^1 = -2\alpha^2 e^{-\alpha t-\alpha s}\int_0^s e^{2\alpha v}\int_0^v e^{-\alpha z} z^{2H} dz dv$$
$$= -2\alpha^2 e^{-\alpha t-\alpha s}\int_0^s e^{-\alpha z} z^{2H}\int_z^s e^{2\alpha v} dv dz$$
$$= -2\alpha^2 e^{-\alpha t-\alpha s}\int_0^s e^{-\alpha z} z^{2H}\frac{e^{2\alpha s} - e^{2\alpha z}}{2\alpha} dz$$
$$= -\alpha e^{-\alpha t+\alpha s}\left(\int_0^s e^{-\alpha z} z^{2H} dz - \int_0^s e^{\alpha u} u^{2H} du\right)$$
$$= e^{-\alpha t} s^{2H} - 2He^{-\alpha t+\alpha s}\int_0^s e^{-\alpha z} z^{2H-1} dz + e^{-\alpha t} s^{2H} - 2He^{-\alpha t-\alpha s}\int_0^s e^{\alpha u} u^{2H-1} du$$

Now, we consider I_{10}^2, First we deal with the case of t > 2s. Using the change of variables u − v = z in the inner integral, changing the order of integration, and integrating with respect to v, we obtain:

$$I_{10}^2 = -\alpha^2 e^{-\alpha t-\alpha s}\int_s^t \int_{v-s}^v e^{-\alpha z+2\alpha v} z^{2H} dz dv$$
$$= -\alpha^2 e^{-\alpha t-\alpha s}\left(\int_0^s \int_s^{z+s} e^{-\alpha z+2\alpha v} z^{2H} dv dz + \int_s^{t-s} \int_z^{z+s} e^{-\alpha z+2\alpha v} z^{2H} dv dz\right.$$
$$\left. + \int_{t-s}^t \int_z^t e^{-\alpha z+2\alpha v} z^{2H} dv dz\right)$$
$$= -\alpha^2 e^{-\alpha t-\alpha s}\left(\int_0^s e^{-\alpha z} z^{2H}\frac{e^{2\alpha(z+s)} - e^{2\alpha s}}{2\alpha} dz\right.$$
$$\left. + \int_s^{t-s} e^{-\alpha z} z^{2H}\frac{e^{2\alpha(z+s)} - e^{2\alpha z}}{2\alpha} dz + \int_{t-s}^t e^{-\alpha z} z^{2H}\frac{e^{2\alpha t} - e^{2\alpha z}}{2\alpha} dz\right)$$
$$= \tfrac{-\alpha}{2} e^{-\alpha t+\alpha s}\int_0^{t-s} e^{\alpha z} z^{2H} dz - \tfrac{-\alpha}{2} e^{-\alpha t-\alpha s}\int_s^t e^{\alpha z} z^{2H} dz - \tfrac{-\alpha}{2} e^{-\alpha t+\alpha s}\int_0^s e^{-\alpha z} z^{2H} dz$$
$$+ \tfrac{-\alpha}{2} e^{-\alpha s+\alpha t}\int_{t-s}^t e^{-\alpha z} z^{2H} dz$$
$$= e^{-\alpha s} t^{2H} - e^{-\alpha t} s^{2H} - He^{-\alpha s+\alpha t}\int_{t-s}^t e^{-\alpha z} z^{2H-1} dz + He^{-\alpha t+\alpha s}\int_0^s e^{-\alpha z} z^{2H-1} dz$$
$$-He^{-\alpha t-\alpha s}\int_s^t e^{\alpha z} z^{2H-1} dz + He^{-\alpha t+\alpha s}\int_0^{t-s} e^{\alpha z} z^{2H-1} dz - (t-s)^{2H}$$

Similarly, one can verify that the above formula follows in the case of s < t < 2s. Finally, summing up all the terms, we obtain:

$$\begin{array}{c} \mathrm{Cov}(X_t, X_s) = \mathrm{Cov}\left(\widetilde{X}_t, \widetilde{X}_s\right) \\ = \frac{H\nu^2}{2}(-e^{-\alpha t+\alpha s}\int_0^{t-s} e^{\alpha z} z^{2H-1}dz + e^{\alpha t-\alpha s}\int_{t-s}^{t} e^{-\alpha z} z^{2H-1}dz \\ -e^{-\alpha t-\alpha s}\int_s^t e^{\alpha z} z^{2H-1}dz + e^{-\alpha t+\alpha s}\int_0^s e^{-\alpha z} z^{2H-1}dz \\ +2e^{-\alpha t-\alpha s}\int_0^t e^{\alpha z} z^{2H-1}dz) \end{array} \tag{A3}$$

Moreover, using (A3), for all $H \in (0,\ 1)$, we have:

$$\mathrm{Var}X_t = \mathrm{Var}\widetilde{X}_t = H\nu^2 \int_0^t z^{2H-1}(e^{-\alpha z} + e^{-\alpha(2t-z)})dz \tag{A4}$$

Which implies (4). □

Proof of Lemma 2. From (A1), we can easily obtain:

$$\mathbb{E}[\mathrm{X_t}] = \mathrm{m}(1 - \mathrm{e}^{-\alpha \mathrm{t}}) + \mathrm{X_0}\mathrm{e}^{-\alpha \mathrm{t}} \tag{A5}$$

Moreover, using (4) in Lemma 1, we have:

$$\mathrm{Var}[X_t] = H\nu^2 \int_0^t z^{2H-1}(e^{-\alpha z} + e^{-\alpha(2t-z)})dz \to \frac{H\Gamma(2H)}{\alpha^{2H}} \tag{A6}$$

where $\alpha\ > 0$ as $\mathrm{t} \to \infty$.

Since the random variable X_t has normal distribution, we can obtain (5) using (A5) and (A6). Now, we consider (6). For convenience, we assume $\mathrm{t}\ \geq\ \mathrm{s}\ \geq\ 0$ and $p = 2$. Thus, we show that

$$\mathbb{E}(X_t - X_s)^2 \leq \mathrm{C}|t-s|^{2H} \tag{A7}$$

Using the fact $X_t = X_0 + \alpha\int_0^t (m - X_s)ds + \nu B_t^H$, we obtain:

$$|X_t - X_s| \leq |\alpha m(t-s)| + \alpha\int_s^t |X_u|du + \nu\left|B_t^H - B_s^H\right| \tag{A8}$$

Therefore, using (5), we obtain:

$$\begin{array}{c} \mathbb{E}(X_t - X_s)^2 \leq 3|\alpha m(t-s)|^2 + 3|\alpha|^2\mathbb{E}(\int_s^t |X_u|du)^2 + 3\nu^2\mathbb{E}\left(B_t^H - B_s^H\right)^2 \\ \leq 3|\alpha m(t-s)|^2 + 3|\alpha|^2(t-s)\int_s^t \mathbb{E}|X_u|^2 du + 3\nu^2(t-s)^{2I} \\ \leq \mathrm{C}|t-s|^2 \end{array}$$

Thus, (A7) is proved. Since $X_t - X_s$ has a normal distribution, (6) follows from (A7) in the standard way. □

Proof of Lemma 3. First, using (5) and (A6), one can easily check the condition

$$\mathbb{E}\left[\sigma_t^2\right] = \mathbb{E}[e^{2X_t}] = e^{2\mathbb{E}[X_t]+2\mathrm{Var}[X_t]} \leq C$$

Which implies:

$$\underset{0\leq t\leq T}{sup}\left|\sigma_t^2\right| = O_p(1) \tag{A9}$$

From (A9), we can see that the second condition of A1 in Hypothesis 1 is satisfied. Since $\mathrm{e^y}$ is a continuous function of y and $\mathrm{X_t}$ is $\mathrm{H}\ -\epsilon$ Hölder continuous with any small ϵ, using Lemma 2 and (A9), we have:

$$E\left|\sigma_t - \sigma_s\right| = E|e^{X_t} - e^{X_s}| = E|e^{X_s}\left(e^{X_t - X_s} - 1\right)| \leq e^{X_s}(e^{C|t-s|^{pH}-1}) \leq C|t-s|^{pH} \tag{A10}$$

Which implies $sup\{|\sigma_s - \sigma_t|, |s-t| \leq a\} = O_{\mathbb{P}}(a^{1/2}|\log(a)|^{1/2})$. Hence the condition of A1 in Hypothesis 1 is satisfied. For the condition A2 in Hypothesis 1, using (A10), we obtain:

$$sup|\int_{t_{i-1}}^{t_i}(\sigma(s)-\sigma(t_{i-1}))dW_s|^2 \leq 2\log(n)sup|\int_{t_{i-1}}^{t_i}(\sigma(s)-\sigma(t_{i-1}))^2ds| \leq \frac{C\log(n)}{n^2}$$

Which implies A2 in Hypothesis 1. □

Proof of Proposition 1. From Lemma 3, we can see that assumptions A1 and A2 of σ_t in Hypothesis 1 are satisfied for the volatility process in (1). From the definition of M_n, we can see that M_n has the same asymptotic distribution as $\sup_{0\leq t\leq T}|\sigma_t^2|$. Hence, we can obtain the desired results. □

References

1. Black, F.; Scholes, M. The Pricing of Options and Corporate Liabilities. *J. Political Econ.* **1973**, *81*, 637–654. [CrossRef]
2. Fouque, J.-P.; Papanicolaou, G.; Sircar, K.R. *Derivatives in Financial Markets with Stochastic Volatility*; Cambridge University Press: Cambridge, UK, 2000.
3. Hull, J.; White, A. The pricing of options on assets with stochastic volatilities. *J. Financ.* **1987**, *42*, 281–300. [CrossRef]
4. Scott, L.O. Option Pricing when the Variance Changes Randomly: Theory, Estimation, and an Application. *J. Financ. Quant. Anal.* **1987**, *22*, 419. [CrossRef]
5. Stein, E.M.; Stein, J.C. Stock Price Distributions with Stochastic Volatility: An Analytic Approach. *Rev. Financ. Stud.* **1991**, *4*, 727–752. [CrossRef]
6. Comte, F.; Renault, E. Long memory in continuous-time stochastic volatility models. *Math. Financ.* **1998**, *8*, 291–323. [CrossRef]
7. Comte, F.; Coutin, L.; Renault, E. Affine fractional stochastic volatility models. *Ann. Financ.* **2012**, *8*, 337–378. [CrossRef]
8. Chronopoulou, A.; Viens, F.G. Estimation and pricing under long-memory stochastic volatility. *Ann. Financ.* **2012**, *8*, 379–403. [CrossRef]
9. Chronopoulou, A.; Viens, F.G. Stochastic volatility and option pricing with long-memory in discrete and continuous time. *Quant. Financ.* **2012**, *12*, 635–649. [CrossRef]
10. Xiao, W.; Yu, J. Asymptotic theory for estimating drift parameters in the fractional vasicek model. *Econ. Theory* **2019**, *35*, 198–231. [CrossRef]
11. Bennedsen, M.; Lunde, A.; Pakkanen, M.S. Decoupling the Short- and Long-Term Behavior of Stochastic Volatility. *J. Financ. Econ.* **2021**, 1–46. [CrossRef]
12. Bayer, C.; Friz, P.; Gatheral, J. Pricing under rough volatility. *Quant. Financ.* **2016**, *16*, 887–904. [CrossRef]
13. Gatheral, J.; Jaisson, T.; Rosenbaum, M. Volatility is rough. *Quant. Financ.* **2018**, *18*, 933–949. [CrossRef]
14. Livieri, G.; Mouti, S.; Pallavicini, A.; Rosenbaum, M. Rough volatility: Evidence from option prices. *IISE Trans.* **2018**, *50*, 767–776. [CrossRef]
15. El Euch, O.; Rosenbaum, M. The characteristic function of rough Heston models. *Math. Financ.* **2019**, *29*, 3–38. [CrossRef]
16. Alòs, E.; León, J.A.; Vives, J. On the short-time behavior of the implied volatility for jump-diffusion models with stochastic volatility. *Financ. Stoch.* **2007**, *11*, 571–589. [CrossRef]
17. Fukasawa, M.; Takabatake, T. Asymptotically efficient estimators for self-similar stationary Gaussian noises under high frequency observations. *Bernoulli* **2019**, *25*, 1870–1900. [CrossRef]
18. Li, X.; Wei, Y.; Chen, X.; Ma, F.; Liang, C.; Chen, W. Which uncertainty is powerful to forecast crude oil market volatility? New evidence. *Int. J. Financ. Econ.* **2020**, 1–19. [CrossRef]
19. Wang, D.; Xin, Y.; Chang, X.; Su, X. Realized volatility forecasting and volatility spillovers: Evidence from Chinese non-ferrous metals futures. *Int. J. Financ. Econ.* **2020**, *26*, 2713–2731. [CrossRef]
20. Wang, X.; Xiao, W.; Yu, J. Modeling and forecasting realized volatility with the fractional Ornstein–Uhlenbeck process. *J. Econ.* **2021**. [CrossRef]
21. Da Fonseca, J.; Zhang, W. Volatility of volatility is (also) rough. *J. Futur. Mark.* **2019**, *39*, 600–611. [CrossRef]
22. Cao, J.; Kim, J.-H.; Kim, S.-W.; Zhang, W. Rough stochastic elasticity of variance and option pricing. *Financ. Res. Lett.* **2019**, *37*, 101381. [CrossRef]
23. Takaishi, T. Rough volatility of Bitcoin. *Financ. Res. Lett.* **2019**, *32*, 101379. [CrossRef]
24. Fukasawa, M.; Takabatake, T.; Westphal, R. Is volatility rough? *arXiv* **2019**, arXiv:1905.04852.
25. Brandi, G.; Di Matteo, T. Multiscaling and rough volatility: An empirical investigation. *arXiv* **2022**, arXiv:2201.10466.
26. Alòs, E.; León, J. An Intuitive Introduction to Fractional and Rough Volatilities. *Mathematics* **2021**, *9*, 994. [CrossRef]
27. Jacod, J.; Todorov, V. Testing for common arrivals of jumps for discretely observed multidimensional processes. *Ann. Stat.* **2009**, *37*, 1792–1838. [CrossRef]

28. Fan, J.; Wang, Y. Spot volatility estimation for high-frequency data. *Stat. Interface* **2008**, *1*, 279–288. [CrossRef]
29. Renò, R. Nonparametric estimation of the diffusion coefficient of stochastic volatility models. *Econ. Theory* **2008**, *24*, 1174–1206. [CrossRef]
30. Kantelhardt, J.W.; Zschiegner, S.A.; Koscielny-Bunde, E.; Havlin, S.; Bunde, A.; Stanley, H. Multifractal detrended fluctuation analysis of nonstationary time series. *Phys. A Stat. Mech. Appl.* **2002**, *316*, 87–114. [CrossRef]
31. Berzin, C.; Latour, A.; León, J.R. *Inference on the Hurst Parameter and the Variance of Diffusions Driven by Fractional Brownian Motion*; Springer: Cham, Switzerland, 2014; Volume 216, p. 200.
32. Guennoun, H.; Jacquier, A.; Roome, P.; Shi, F. Asymptotic Behavior of the Fractional Heston Model. *SIAM J. Financ. Math.* **2018**, *9*, 1017–1045. [CrossRef]
33. Funahashi, H.; Kijima, M. Does the Hurst index matter for option prices under fractional volatility? *Ann. Financ.* **2017**, *13*, 55–74. [CrossRef]
34. Neuenkirch, A.; Shalaiko, T. The order barrier for strong approximation of rough volatility models. *arXiv* **2016**, arXiv:1606.03854.
35. Kermarrec, G. On Estimating the Hurst Parameter from Least-Squares Residuals. Case Study: Correlated Terrestrial Laser Scanner Range Noise. *Mathematics* **2020**, *8*, 674. [CrossRef]
36. Jena, S.K.; Tiwari, A.K.; Dogăn, B.; Hammoudeh, S. Are the top six cryptocurrencies efficient? evidence from time-varying long memory. *Int. J. Financ. Econ.* **2020**. [CrossRef]
37. Xiao, W.; Zhang, W.; Xu, W. Parameter estimation for fractional Ornstein–Uhlenbeck processes at discrete observation. *Appl. Math. Model.* **2011**, *35*, 4196–4207. [CrossRef]
38. Christensen, K.; Oomen, R.C.; Podolskij, M. Fact or friction: Jumps at ultra high frequency. *J. Financ. Econ.* **2014**, *114*, 576–599. [CrossRef]
39. Cheridito, P.; Kawaguchi, H.; Maejima, M. Fractional Ornstein-Uhlenbeck processes. *Electron. J. Probab.* **2003**, *8*, 1–14. [CrossRef]
40. Kubilius, K. CLT for quadratic variation of Gaussian processes and its application to the estimation of the Orey index. *Stat. Probab. Lett.* **2020**, *165*, 108845. [CrossRef]

mathematics

MDPI

Article

Effects of Magnetic Fields, Coupled Stefan Blowing and Thermodiffusion on Ferrofluid Transport Phenomena

Rohana Abdul Hamid [1,2], Roslinda Nazar [3,*], Kohilavani Naganthran [4,5,*] and Ioan Pop [6]

[1] Centre of Excellence for Social Innovation & Sustainability (CoESIS), Universiti Malaysia Perlis, Arau 02600, Malaysia; rohanahamid@unimap.edu.my
[2] Boundary Layer Research Group, Institute of Engineering Mathematics, Faculty of Applied and Human Sciences, Universiti Malaysia Perlis, Arau 02600, Malaysia
[3] Department of Mathematical Sciences, Faculty of Science and Technology, Universiti Kebangsaan Malaysia, Bangi 43600, Malaysia
[4] Institute of Mathematical Sciences, Faculty of Science, Universiti Malaya, Kuala Lumpur 50603, Malaysia
[5] Center for Data Analytics, Consultancy and Services, Faculty of Science, Universiti Malaya, Kuala Lumpur 50603, Malaysia
[6] Department of Mathematics, Babeş-Bolyai University, 400084 Cluj-Napoca, Romania; ipop@math.ubbcluj.ro
* Correspondence: rmn@ukm.edu.my (R.N.); kohi@um.edu.my (K.N.)

Abstract: The paramagnetic feature of ferrofluid allows it to be utilised in electronic devices and improvise fluid circulation in transformer windings. Hence, the present article aims to conduct the numerical study of ferrofluid boundary layer flow along with the Stefan blowing, velocity and thermal slip, and Soret effects within the stagnation region over a stretching/shrinking surface. The governing equations were solved numerically using the bvp4c function in the MATLAB computing package. Based on the results, a stronger magnetic field of ferrofluid was needed to identify the numerical solutions past the shrinking surface, while the Stefan blowing diminished the solution's availability. More than one solution is acquired for some specific values of the shrinking parameter, and the stability analysis validated that only one solution is reliable and stable.

Keywords: ferrofluidslip effect; Stefan blowing; thermodiffusion

MSC: 34B15; 76Dxx

Citation: Hamid, R.A.; Nazar, R.; Naganthran, K.; Pop, I. Effects of Magnetic Fields, Coupled Stefan Blowing and Thermodiffusion on Ferrofluid Transport Phenomena. *Mathematics* **2022**, *10*, 1646. https://doi.org/10.3390/math10101646

Academic Editors: Camelia Petrescu and Valeriu David

Received: 12 March 2022
Accepted: 9 May 2022
Published: 12 May 2022

Publisher's Note: MDPI stays neutral with regard to jurisdictional claims in published maps and institutional affiliations.

Copyright: © 2022 by the authors. Licensee MDPI, Basel, Switzerland. This article is an open access article distributed under the terms and conditions of the Creative Commons Attribution (CC BY) license (https://creativecommons.org/licenses/by/4.0/).

1. Introduction

The evaporation process is very beneficial in industries that require the removal of unwanted fluids, such as the food industry. To mention a few, evaporation is applied to concentrate milk, fruit juice, jams, jellies, and sugar solutions for crystallisation [1]. Furthermore, evaporation is crucial in the pulp and paper industry, where it is used in the drying section, which is the final and the most vital section to produce paper [2]. In a particular circumstance, the species transfer or mass transfer in evaporation can create a different fluid motion. The movement of the species from the interface to the free stream is called the blowing effect or the Stefan blowing effect because the concept originates from the Stefan problem of the mass transfer [3]. The formulations of the mass transfer are similar to the heat transfer equation, but in this problem, the present investigation involves the coupled blowing effect. Moreover, Fang and Jing [3], who introduced the influence of coupled Stefan blowing induced by species transport, suggested that the momentum and the concentration equations should be coupled because the species transfer and the flow field depend on each other. Then, Fang [4] revisited the work in [3] to examine the transport phenomena from the view of unsteady stagnation-point flow and solved analytically in terms of an incomplete Gamma function. After that, the coupled Stefan blowing impact has been considered in the boundary layer models under various settings and external forces,

for instance, in the bioconvection flow [5], magnetohydrodynamics [6], and anisotropic slip [7].

Since very few studies can be found regarding the Stefan blowing effect, we are interested in studying this problem with the addition of the Soret effect (or thermodiffusion), velocity slip, and thermal slip over a stretching or shrinking sheet in a ferrofluid. It is assumed in the present study that the movement of the species particles that is saturated at the surface results from the temperature gradient. This phenomenon is called thermophoresis or the Soret effect and has been studied by Ryskin and Pleiner [8], Ramreddy et al. [9], and Pal et al. [10] in nanofluids, while Arif et al. [11] studied it in a hybrid nanofluid. Furthermore, the study of the slip effect is necessary because the presence of the species blowing at the interface might contribute to the wall slip where the fluid velocity and temperature at the surface are not zero. It was also explained by Uddin et al. [12] that boundary slip occurs in a fluid that contains particulates, such as emulsions and suspensions. Hence, they studied the effects of the slip and the Stefan blowing in a nanofluid that contains gyrotactic microorganisms. On the other hand, many other researchers also considered the slip effect in their shrinking sheet problem, such as Singh and Chamkha [13], who reported the numerical analysis on the effects of the second-order slip on a permeable, vertical isothermal shrinking sheet. In addition, Mahapatra and Nandy [14], Aman et al. [15], and Merkin et al. [16] investigated the flow induced by the shrinking sheet with the slip effect near a stagnation point and obtained non-uniqueness solutions. This is in accordance with the result reported by [17], where the existence of the similarity solutions is guaranteed within the stagnation region past the shrinking surfaces.

On the other hand, we also aim to study the effect of the Stefan blowing in a ferrofluid that contains magnetite nanoparticles (Fe_3O_4). Apart from the nanofluids, which consider different types of nanoparticles as was examined by the theoretical works in [18–21], ferrofluid has become one of the essential fields of interest. Ferrofluid has properties that can be controlled and can absorb electromagnetic energy to increase heat when the external magnetic field is applied. Hence, ferrofluid is beneficial in many applications, such as biomedicine, solar system design, and technological applications, for example, dynamic sealing, damping, and doping of specialised materials [22]. Shokrollahi [23] identified that ferrofluid had been used in the mechanism for the early detection of cancer, as the contrast agent for the Magnetic Resonance Imaging (MRI), and in the development of an implantable artificial heart. In this problem, ferrofluid is numerically modelled using a single-phase approach. Henceforth, the base fluid and the magnetic nanoparticles are assumed in thermal equilibrium concerning their physical properties and moving with the same velocity. Ryskin et al. [24] described that most experiments on ferrofluids could be conducted as a single-phase model because the Lewis number of the ferrofluid is minimal. Several numerical studies of the ferrofluid used the single-phase model [25–28]. Recently, Hamid et al. [29] scrutinised the impact of viscous dissipation on dusty ferrofluid flow and heat transfer over a shrinking flat surface (single-phase model) and showed that the shear stress increases when the dust particles augment in the ferrofluid.

Acknowledging these valuable theoretical works reported within the scope of the magnetic field, ferrofluid flow, coupled Stefan blowing, and Soret impact, it was found that there is a research gap where the influences of the magnetic field, Soret coefficient, velocity slip, and thermal slip have not been examined on the ferrofluid flow past the moving surface. The numerical outputs are generated as the intensity of the external forces varies. More than one solution that elucidates the transport phenomena is identified, and stability analysis is implemented to justify the solution's stability. The present valuable work has significance in hydrometallurgical applications.

2. Mathematical Model

We examined a steady, two-dimensional, laminar, stagnation-point flow of a viscous and incompressible water-based ferrofluid with the velocity and thermal slips as shown in Figure 1, where x and y are the Cartesian coordinates considered past the moving

surface where the sheet moves in a manner of either stretching or shrinking, and normal to it, respectively. The sheet moves with a velocity defined as $u = \lambda U_w + U_{slip}$, where U_w and U_{slip} are the sheet velocity and slip velocity, respectively, and λ is the parameter that measures the stretching or shrinking rate. The free stream velocity is denoted by U_e. Meanwhile, the ferrofluid temperature, T at the surface is denoted as T_w. A transverse magnetic field was assumed to exist in the manner of normal to the surface where B_0 is the magnetic field strength. Additionally, it was assumed that no external electric field is available, and the electric field caused by the polarisation charges are omitted. We took that a binary fluid saturates the surface with dissolved species and magnetite ferroparticles (Fe_3O_4) in this problem. It was also assumed that the species' massive mass transfer occurred with velocity during the stretching/shrinking action $V_w(x)$ and generated a blowing effect [3]. It should be noted that the species does not interact with the magnetite nanoparticles.

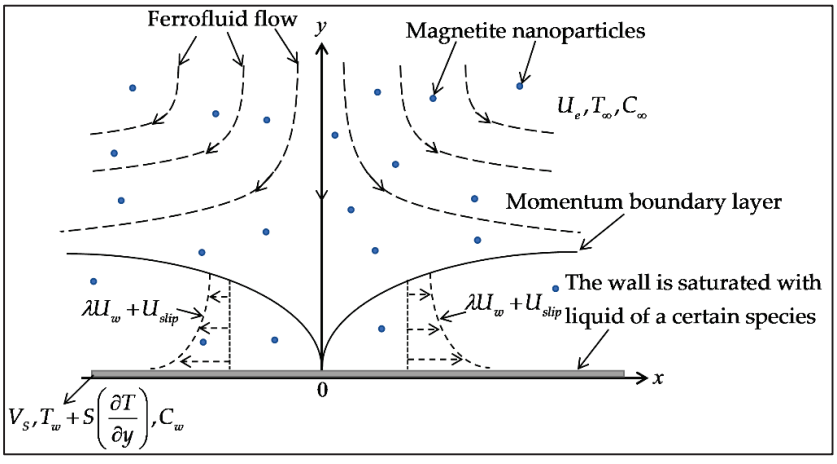

Figure 1. Present flow problem's physical model.

Based on these assumptions, the following mathematical model can be formulated [30]:

$$\frac{\partial u}{\partial x} + \frac{\partial v}{\partial y} = 0, \tag{1}$$

$$u\frac{\partial u}{\partial x} + v\frac{\partial u}{\partial y} = U_e\frac{dU_e}{dx} + \nu_{ff}\frac{\partial^2 u}{\partial y^2} - \frac{\sigma_{ff}B_0{}^2}{\rho_{ff}}(u - U_e), \tag{2}$$

$$u\frac{\partial T}{\partial x} + v\frac{\partial T}{\partial y} = \alpha_{ff}\frac{\partial^2 T}{\partial y^2}, \tag{3}$$

$$u\frac{\partial C}{\partial x} + v\frac{\partial C}{\partial y} = D_S\frac{\partial^2 C}{\partial y^2} + D_{CT}\frac{\partial^2 T}{\partial y^2}, \tag{4}$$

where u and v are the velocity components along with the directions x and y, respectively; ν_{ff} is the ferrofluid kinematic viscosity; σ_{ff} is the ferrofluid electrical conductivity; ρ_{ff} is the ferrofluid density; T is the temperature; α_{ff} is the ferrofluid thermal diffusivity; C is the species concentration; D_S is the species diffusivity; and D_{CT} is the Soret-type diffusivity. The boundary conditions at the sheet are ([15,31]):

$$\begin{aligned} &u = \lambda U_w + U_{slip} = \lambda cx + L\left(\frac{\partial u}{\partial y}\right), v = V_S = k(x)\frac{\partial C}{\partial y}, T = T_w + S\left(\frac{\partial T}{\partial y}\right), \\ &C = C_w \text{ at } y = 0, \\ &u \to U_e(x) = ax,\ T \to T_\infty,\ C \to C_\infty \text{ as } y \to \infty, \end{aligned} \tag{5}$$

where λ is the stretching parameter ($\lambda > 0$) or the shrinking parameter ($\lambda < 0$), a, c are the positive constants, L is the velocity slip parameter, S is the thermal slip parameter, and $k(x)$ signifies the blowing function. The effective properties of ferrofluid (subscript *ff*) may be conveyed in terms of the base fluid's properties (subscript f) and solid ferroparticles (subscript s) and the solid ferroparticles' volume fraction, ϕ, as follows [32]:

$$\begin{aligned} &\nu_{ff} = \frac{\mu_{ff}}{\rho_{ff}},\ \mu_{ff} = \frac{\mu_f}{(1-\phi)^{2.5}},\ \rho_{ff} = (1-\phi)\rho_f + \phi\rho_s, \\ &\alpha_{ff} = \frac{k_{ff}}{(\rho c_p)_{ff}},\ (\rho c_p)_{ff} = (1-\phi)(\rho c_p)_f + \phi(\rho c_p)_s, \\ &\frac{k_{ff}}{k_f} = \frac{k_s + 2k_f - 2\phi(k_f - k_s)}{k_s + 2k_f + \phi(k_f - k_s)},\ \frac{\sigma_{ff}}{\sigma_f} = 1 + \frac{3\left(\frac{\sigma_s}{\sigma_f} - 1\right)\phi}{\left(\frac{\sigma_s}{\sigma_f} + 2\right) - \left(\frac{\sigma_s}{\sigma_f} - 1\right)\phi}. \end{aligned} \tag{6}$$

We then introduced the following similarity variables as [30]:

$$\begin{aligned} &u = cxf'(\eta),\ v = -\sqrt{c\nu_f}f(\eta),\ \eta = \sqrt{c/\nu_f}y \\ &\theta(\eta) = \frac{T - T_\infty}{T_w - T_\infty},\ H(\eta) = \frac{C - C_\infty}{C_w - C_\infty}. \end{aligned} \tag{7}$$

Furthermore, it is a necessity for $f(0)$ to be independent of x, if and only if $k(x)$ and x vary inversely or $k(x) \propto \frac{1}{x}$ [31]. Eventually, the blowing function can be written in the following form: $k(x) = \frac{-\kappa\nu_f}{C_w - C_\infty}$, where the nondimensional blowing parameter κ is fixed to be within the range of $\kappa \geq 0$ to allow the model to be transformed into a similarity form. Substituting (7) into Equations (1)–(4) and boundary conditions (5) yielded the following simplified mathematical model,

$$\varepsilon_1 f''' + ff'' - f'^2 - \varepsilon_2 M(f' - A) + A^2 = 0, \tag{8}$$

$$\varepsilon_3 \theta'' + \Pr f\theta' = 0, \tag{9}$$

$$H'' + ScfH' + S_T Sc\theta'' = 0, \tag{10}$$

with the boundary condition:

$$\begin{aligned} &f(0) = \kappa H'(0),\ f'(0) = \lambda + \delta f''(0),\ \theta(0) = 1 + \delta_T\theta'(0),\ H(0) = 1, \\ &f'(\eta) \to A,\ \theta(\eta) \to 0,\ H(\eta) \to 0 \text{ as } \eta \to \infty, \end{aligned} \tag{11}$$

where

$$\begin{aligned} &\varepsilon_1 = \frac{\nu_{ff}}{\nu_f} = \frac{1}{(1-\phi)^{2.5}\left((1-\phi) + \phi\left(\rho_s/\rho_f\right)\right)},\ \varepsilon_2 = \frac{\sigma_{ff}/\sigma_f}{\left(1 - \phi + \phi\left(\rho_s/\rho_f\right)\right)}, \\ &\varepsilon_3 = \Pr\frac{\alpha_{ff}}{\nu_f} = \Pr\frac{k_{ff}/k_f}{\left(1 - \phi + \phi\frac{(\rho c_p)_s}{(\rho c_p)_f}\right)}. \end{aligned} \tag{12}$$

The other parameters are the velocity ratio A, the magnetic interaction parameter M, the Prandtl number Pr, the Schmidt number Sc, the Soret parameter S_T, the blowing parameter κ, the velocity slip parameter δ, and the thermal slip parameter δ_T, which are defined as:

$$A = \frac{a}{c},\ M = \frac{\sigma_f B_0^2}{a\rho_f},\ \mathrm{Pr} = \frac{\nu_f}{\alpha_f},\ Sc = \frac{\nu_f}{D_S},$$
$$S_T = \frac{D_{CT}(T_w - T_\infty)}{\nu_f(C_w - C_\infty)},\ \delta = L\sqrt{\frac{c}{\nu_f}},\ \delta_T = S\sqrt{\frac{c}{\nu_f}}. \tag{13}$$

The physical quantities that are important in the present work are the skin friction coefficient C_f and the local Nusselt number Nu_x, which are expressed as

$$C_f = \frac{\tau_w}{\rho_f U_w^2(x)},\ Nu_x = \frac{xq_w}{k_f(T_w - T_\infty)}, \tag{14}$$

The shear stress τ_w and the surface heat flux q_w are given by

$$\tau_w = \mu_{ff}\left(\frac{\partial u}{\partial y}\right)_{y=0},\ q_w = -k_{ff}\left(\frac{\partial T}{\partial y}\right)_{y=0}, \tag{15}$$

Hence, the dimensionless wall shear stress $C_f \mathrm{Re}_x^{1/2}$ and the dimensionless heat flux $Nu_x \mathrm{Re}_x^{-1/2}$ are defined as

$$C_f {\mathrm{Re}_x}^{1/2} = \frac{f''(0)}{(1-\phi)^{2.5}},\ Nu_x {\mathrm{Re}_x}^{-1/2} = -\frac{k_{ff}}{k_f}\theta'(0), \tag{16}$$

where $\mathrm{Re}_x = U_w(x)x/\nu_f$.

3. Stability Analysis

The stability analysis is started by introducing the non-dimensional time variable or τ as shown below

$$u = cxf'(\eta,\tau),\ v = -\sqrt{c\nu_f}f(\eta,\tau),\ \eta = \sqrt{c/\nu_f}y,\ \tau = ct,$$
$$\theta(\eta,\tau) = \frac{T - T_\infty}{T_w - T_\infty},\ H(\eta,\tau) = \frac{C - C_\infty}{C_w - C_\infty}. \tag{17}$$

Next, using (17), Equations (1)–(4) become the unsteady equations as follows:

$$\varepsilon_1\frac{\partial^3 f}{\partial\eta^3} + f\frac{\partial^2 f}{\partial\eta^2} - \left(\frac{\partial f}{\partial\eta}\right)^2 - \varepsilon_2 M\left(\frac{\partial f}{\partial\eta} - A\right) + A^2 - \frac{\partial^2 f}{\partial\eta\partial\tau} = 0, \tag{18}$$

$$\frac{\varepsilon_3}{\mathrm{Pr}}\frac{\partial^2\theta}{\partial\eta^2} + f\frac{\partial\theta}{\partial\eta} - \frac{\partial\theta}{\partial\tau} = 0, \tag{19}$$

$$\frac{\partial^2 H}{\partial\eta^2} + Scf\frac{\partial H}{\partial\eta} + ScS_T\frac{\partial^2\theta}{\partial\eta^2} - \frac{\partial H}{\partial\tau} = 0, \tag{20}$$

with the boundary conditions:

$$f(0,\tau) = \kappa\frac{\partial H(0,\tau)}{\partial\eta},\ \frac{\partial f(0,\tau)}{\partial\eta} = \lambda + \delta\frac{\partial f^2(0,\tau)}{\partial\eta^2},\ \theta(0,\tau) = 1 + \delta_T\frac{\partial\theta(0,\tau)}{\partial\eta},\ H(0,\tau) = 1,$$
$$\frac{\partial f(\eta,\tau)}{\partial\eta} \to A,\ \theta(\eta,\tau) \to 0,\ H(\eta,\tau) \to 0 \text{ as } \eta \to \infty. \tag{21}$$

Then, the linear stability of the solutions is determined by using the following:

$$f(\eta,\tau) = f_0(\eta) + e^{-\gamma\tau}J(\eta),\ \theta(\eta,\tau) = \theta_0(\eta) + e^{-\gamma\tau}Q(\eta),$$
$$H(\eta,\tau) = H_0(\eta) + e^{-\gamma\tau}B(\eta), \tag{22}$$

where $f_0(\eta)$, $\theta_0(\eta)$, and $H_0(\eta)$ indicate the steady solution of the Equations (8)–(10). Further, $J(\eta)$, $Q(\eta)$, and $B(\eta)$ are assumed to be small relative to $f_0(\eta)$, $\theta_0(\eta)$, and $H_0(\eta)$ so the disturbances are minimal [33]. Additionally, γ is the unknown eigenvalue and portrays the disturbance's growth (or decay) rate. Using (22) in (18)–(20) and setting $J(\eta) = J_0(\eta)$, $Q(\eta) = Q_0(\eta)$, and $B(\eta) = B_0(\eta)$ to test the steady flow solutions' stability, we obtain the following eigenvalues equations:

$$\varepsilon_1 J_0''' + f_0 J_0'' + f_0'' J_0 - 2 f_0' J_0' - \varepsilon_2 M J_0' + \gamma J_0' = 0, \tag{23}$$

$$\frac{\varepsilon_3}{\mathrm{Pr}} Q_0'' + f_0 Q_0' + J_0 \theta_0' + \gamma Q_0 = 0, \tag{24}$$

$$B_0'' + Sc\left(f_0 B_0' + J_0 H_0'\right) + S_T Sc Q_0'' + \gamma B_0 = 0, \tag{25}$$

and the boundary conditions become:

$$\begin{aligned} &J_0(0) = \kappa B_0'(0),\ J_0'(0) = \delta J_0''(0),\ Q_0(0) = \delta_T Q_0'(0),\ B_0(0) = 0, \\ &J_0'(\eta) \to 0,\ Q_0(\eta) \to 0,\ B_0(\eta) \to 0 \text{ as } \eta \to \infty. \end{aligned} \tag{26}$$

The range of possible eigenvalues γ in the Equations (23)–(25) can be obtained by resting either one of the outer boundary conditions of $J_0(\eta)$, $Q_0(\eta)$, or $B_0(\eta)$ [34]. This procedure is a must in executing the stability analysis because it is required only that the solution should not be exponentially large as τ approaches ∞. Thus, it is necessary to hold $J_0'(\infty) \to 0$ and replace it with a new boundary condition $J_0''(0) = 1$. Moreover, since any constant multiple of $J_0(\eta)$ is also considered a solution, $J_0''(0) = 1$ can be fixed without the loss of generality to solve Equations (23)–(25) as an initial value problem. This problem then can be solved via the bvp4c function to distinguish the stable and unstable solutions.

4. Results and Discussion

This section presents and discusses the numerical outputs generated via the bvp4c function. The thermophysical properties values of the magnetite ferroparticles given in Table 1 were utilised.

Table 1. Values of the physical properties ([25,35]).

Physical Properties	ρ(kg/m^3)	C_p(J/KgK)	k(W/mK)	$\sigma(\Omega m)^{-1}$
Base fluid	997.1	4179	0.613	0.05
Ferroparticle	5180	670	9.7	25,000

We also compared the previous work by Mahapatra and Gupta [36] and Khan et al. [30], as shown in Tables 2 and 3. It is apparent from these tables that the present study agrees relatively well with the previous works in the literature. Unless otherwise stated, the values for the parameters were chosen as the following: $\phi = 0.01$, $M = 1$, $A = 1$, Pr = 6.2, $Sc = 0.66$, $\kappa = 1$, $S_T = 1$, $\delta = 1$, and $\delta_T = 1$. The values of the Stefan blowing parameter κ were chosen to be positive because we considered the effects of the species blowing to the ambient.

Table 2. Comparison of $C_f \mathrm{Re}_x^{1/2}$ for pure water.

A	[36]	[30]	Present Values
0.1	–0.9694	–0.96938	–0.969386
0.2	–0.9181	–0.91810	–0.918107
0.5	–0.6673	–0.66726	–0.667264
2	2.0175	2.01750	2.017503
3	4.7293	4.72928	4.729282

Table 3. Comparison of $-C_f \mathrm{Re}_x^{1/2}$ for a water-based ferrofluid (Fe_3O_4) with the variation of M, ϕ and A.

Parameters			[30]	Present Values
M	ϕ	A		
0	0.01	0	1.03366	1.033668
		0.3	0.87801	0.878017
		0.5	0.66726	0.689728
	0.1	0	1.35914	1.359170
		0.3	1.15448	1.154506
		0.5	0.90690	0.906924
1	0.01	0	1.44703	1.447035
		0.3	1.12625	1.126254
		0.5	0.85391	0.853913
	0.1	0	1.77443	1.774455
		0.3	1.40123	1.401256
		0.5	1.06945	1.069473

The significant effect of the ferrofluid can only occur when there is an applied magnetic field. In this ferrofluid problem, we wanted to reveal the impact of the magnetic field when the Stefan blowing is present for the stretching/shrinking surface. Figure 2 shows the variations of the dimensionless wall shear stress, $C_f \mathrm{Re}_x^{1/2}$, with the stretching/shrinking parameter, λ, for different magnetic interaction parameter, M, and the Stefan blowing parameter, κ, when other parameters were set as $\phi = 0.01$, $A = 1$, and $\delta = 1$. One can see that there exist second solutions for specific values of λ in the figure. Evidently, samples of the velocity profiles with second solutions are presented in Figure 3. Hence, we performed the stability analysis, and the smallest eigenvalues for the first and second solutions of some selected parameters are depicted in Table 4. It is seen that the first solutions have the smallest eigenvalues consisting of positive values, but the second solutions have negative eigenvalues. Thus, the first solutions are stable, while the second solutions are not stable. Due to the second solutions' unstable state, the discussions are limited to the behaviours portrayed by the first solution.

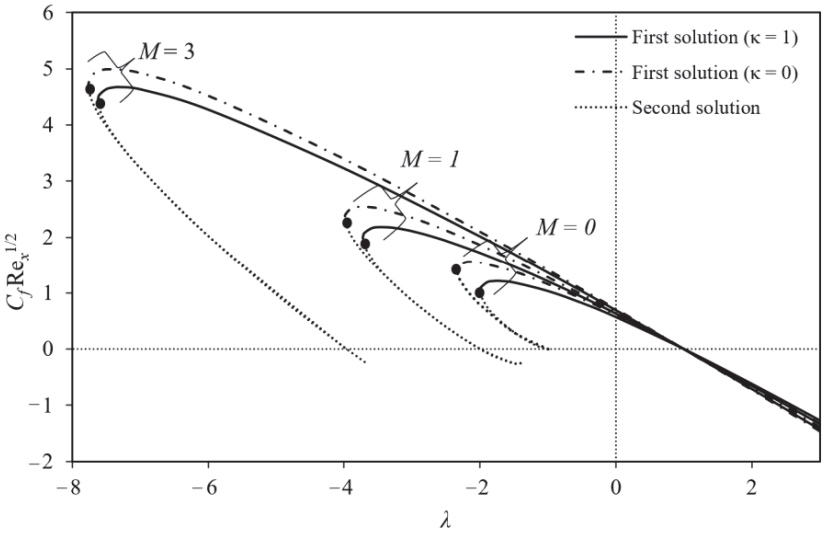

Figure 2. The variations of $C_f \mathrm{Re}_x^{1/2}$ with the stretching/shrinking parameter, λ, for different M and κ when $\phi = 0.01$, $A = 1$, and $\delta = 1$.

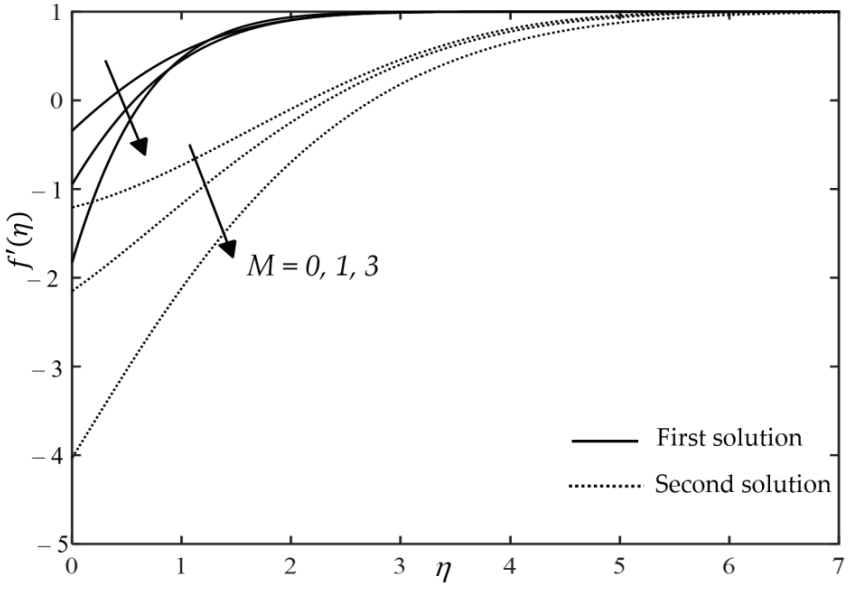

Figure 3. Velocity profiles for different M when $\phi = 0.01$, $A = 1$, $\kappa = 1$, and $\delta = 1$.

Table 4. Values of the smallest eigenvalues.

M	κ	λ	First Solution	Second Solution
0	0	−2	1.1610	−1.0347
		−2.3	0.3960	−0.3818
		−2.34	0.0607	−0.0603
	1	−1.8	0.8498	−1.0356
		−2	0.1383	−0.2353
		−2.006	0.0062	−0.0953
1	0	−3	2.1402	−1.8271
		−3.9	0.6383	−0.6135
		−3.98	0.2077	−0.2051
	1	−3	1.7442	−1.8234
		−3.7	0.4017	−0.5282
		−3.72	0.4011	−0.2867

Furthermore, it is also evident in Figure 2 that there is no wall shear stress when $\lambda = 1$, which indicates the ferrofluid moves at the same speed as the sheet. For $\lambda < 1$, all the values of $C_f \mathrm{Re}_x^{1/2}$ are positive, inferring that ferrofluid exerts the drag towards the surface. In the region $\lambda > 1$, the values of $C_f \mathrm{Re}_x^{1/2}$ are negative, indicating that the sheet's surface exerts the drag force on the ferrofluid. Moreover, Figure 2 also reveals that the increment in M increases the critical points' positions, wherein physically elucidating that boundary layer separation has been delayed. This observation is tally with the finding reported by Khan et al. [37]. This behaviour can be explained further where the magnetic field in the flow regime helps to sustain the kinetic energy of the fluid molecules, while preventing them from becoming drained. Conversely, Figure 2 shows that the increased influence of κ accelerates the boundary layer separation in the flow regime. The increased effect of κ depletes the fluid molecules' kinetic energy and, hence, contributes to the earlier boundary layer separation event.

To see more precise effects of the parameters in the region $\lambda > 1$, Figure 4 is plotted. In Figures 2 and 4, we can see that the magnetic interaction parameter, M, increases the magnitudes of $C_f \mathrm{Re}_x^{1/2}$ and broadens the range of solutions in the region $\lambda < 1$. On the other hand, the Stefan blowing parameter, κ, gives the opposite effect, i.e., decreases the magnitudes of $C_f \mathrm{Re}_x^{1/2}$ and reduces the range of solutions in the region $\lambda < 1$. It is also noticed that parameter M lessens the momentum boundary layer thickness, while the parameter κ gives the opposite effect, as shown in Figure 5. A possible explanation for these results may be that the applied magnetic field produced a Lorenz force that opposed the flows towards the surface and compressed the boundary layer. However, the increase in the Stefan blowing means that extra motion in the ferrofluid produced by the diffusion of the species increases the boundary layer thickness. The species are pushed away from the surface, and ultimately, the skin friction or the shear stress is reduced. On the other hand, Table 5 shows that increasing the volume fraction of the magnetite ferroparticles increases the wall shear stress even in the presence of the Stefan blowing over the shrinking sheet. The inclusion of more magnetite ferroparticles past the tightening state of the sheet causes the friction drag of the surface to be increased. Consequently, the momentum boundary layer becomes thinner and impacts the increased value of $C_f \mathrm{Re}_x^{1/2}$. It is worth highlighting that the effect of the Stefan blowing becomes insignificant with the presence of more magnetite ferroparticles volume fraction in the flow regime over the shrinking surface.

Table 5. Values of $C_f \mathrm{Re}_x^{1/2}$ for magnetite ferrofluid with variations of M, κ, and ϕ when $\lambda = -2$.

ϕ	M=0		M=1	
	κ=0	κ=1	κ=0	κ=1
0	1.496369	1.041150	1.810827	1.667498
0.01	1.544701	1.089054	1.861782	1.714116
0.05	1.744903	1.257814	2.079717	1.915632
0.1	2.016981	1.468133	2.390081	2.206845

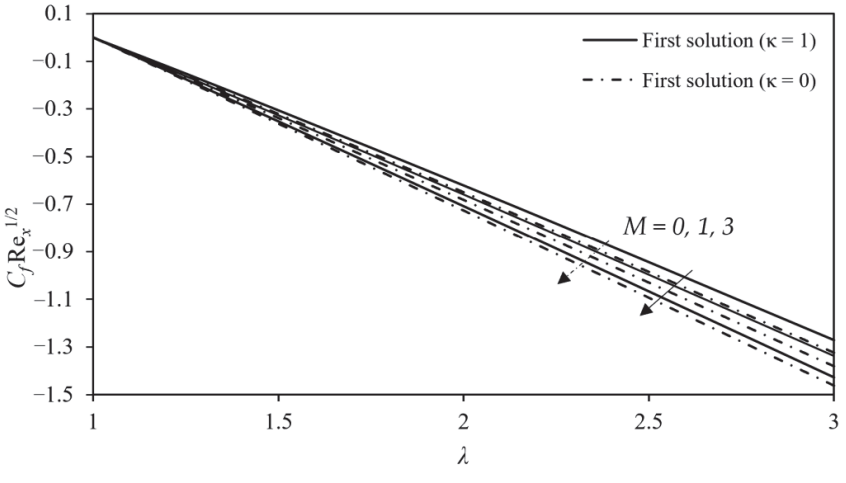

Figure 4. The behaviour of $C_f \mathrm{Re}_x^{1/2}$ towards the stretching parameter, λ, for different M and κ when $\phi = 0.01$, $A = 1$, and $\delta = 1$.

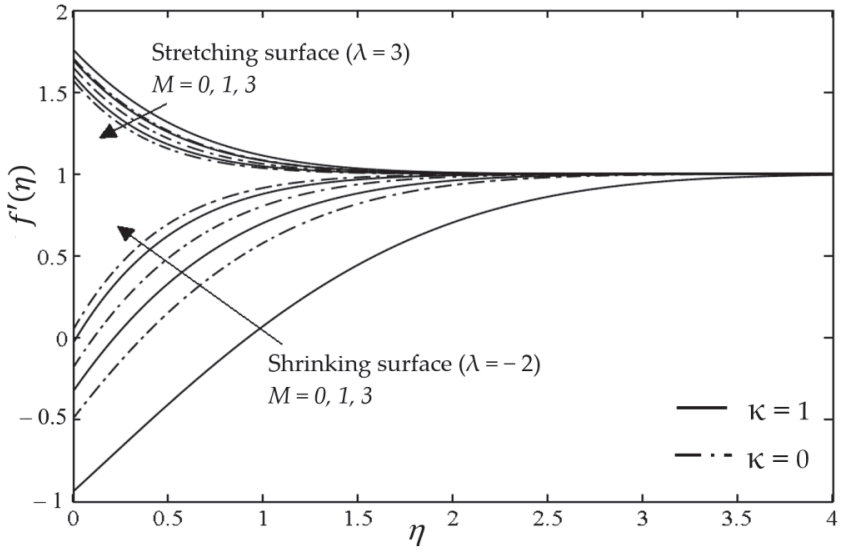

Figure 5. Impact of the magnetic parameter, M, on the velocity profiles for different κ and λ.

The dimensionless heat transfer coefficient, $Nu_x \mathrm{Re}_x^{-1/2}$, trends concerning the stretching/shrinking parameter, λ, for different values of the magnetic interaction parameter, M, and the Stefan blowing parameter, κ, are shown in Figure 6. Figure 6 illustrates the heat transfer rate behaviour with and without the Stefan blowing effect. For the case that considers the Stefan blowing effect, the values of $Nu_x \mathrm{Re}_x^{-1/2}$ increase with the increased effect of M. This can be explained from the aspect of species movement wherein the species also carry the heat while traveling, hence increasing the fluid temperature past the moving sheet. This essentially increased the surface heat flux and resulted in the enhanced values of $Nu_x \mathrm{Re}_x^{-1/2}$. Alternatively, for the situation where the Stefan blowing effect is absent, $Nu_x \mathrm{Re}_x^{-1/2}$ decreases when M intensifies. The diffusion of the species towards the ambient fluid may cause the deficiency of the ferrofluid on the surface and reduce the heat transfer rate past the moving sheet. Meanwhile, the effects of parameter M and parameter κ on the stretching/shrinking surface temperature profiles are displayed in Figure 7. These figures show that the heat transfer rate decreases, and the ferrofluid temperature distribution increases with the species Stefan blowing. The diffusion of the species towards the ambient fluid can cause the deficiency of the ferrofluid on the surface, reducing the rate of heat transfer. Another possible explanation is that the species also carry the heat while moving, consequently increasing the fluid temperature. In addition, Figures 6 and 7 also show that the magnetic interaction parameter, M, on the heat transfer coefficient and flow temperature is different in the regions $\lambda < 1$ and $\lambda > 1$. In the region $\lambda < 1$, the parameter M increases the heat transfer coefficient and reduces the temperature profiles. The opposite behaviour is observed in the region $\lambda > 1$. In this region, the ferrofluid flow slows down with the presence of a magnetic field. Consequently, this result produces a weaker convection and reduces the heat transfer. The present work infers that thermophoresis refers to the diffusion of the species particles saturated at the surface due to a temperature gradient. The effects of the thermophoresis or the Soret number parameter, $S_{T,}$ on the velocity and the temperature profiles are presented in Figures 8 and 9, respectively. It is apparent from these figures that the effect of parameter S_T is significant on the velocity profiles and the temperature profiles only when the Stefan blowing is present. As illustrated in Figures 8 and 9, when the

parameter $\lambda > 1$, the Soret number reduces the velocity and temperature distribution. In contrast with the stretching sheet state, the Soret number increases the shrinking sheet's velocity and temperature distribution.

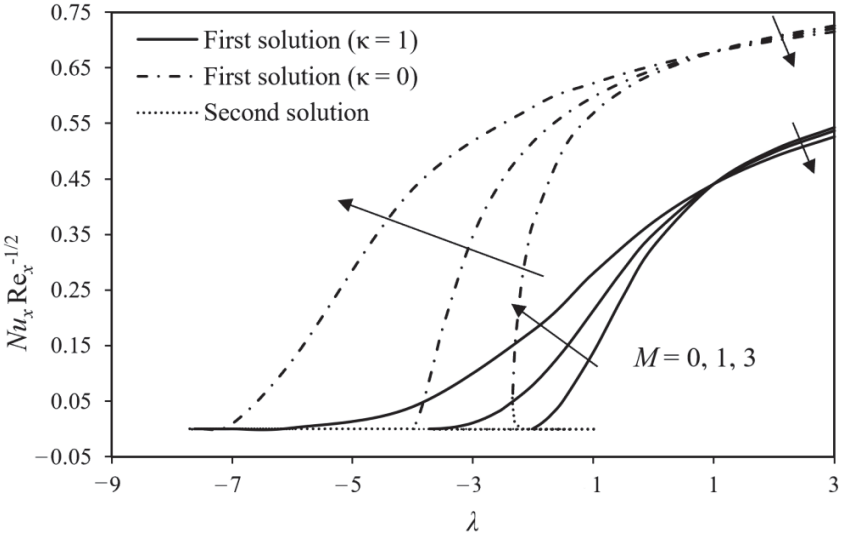

Figure 6. The variations of $Nu_x \mathrm{Re}_x^{-1/2}$ with the stretching/shrinking parameter, λ, for different M and κ when $\phi = 0.01$, $A = 1$, and $\delta_T = 1$.

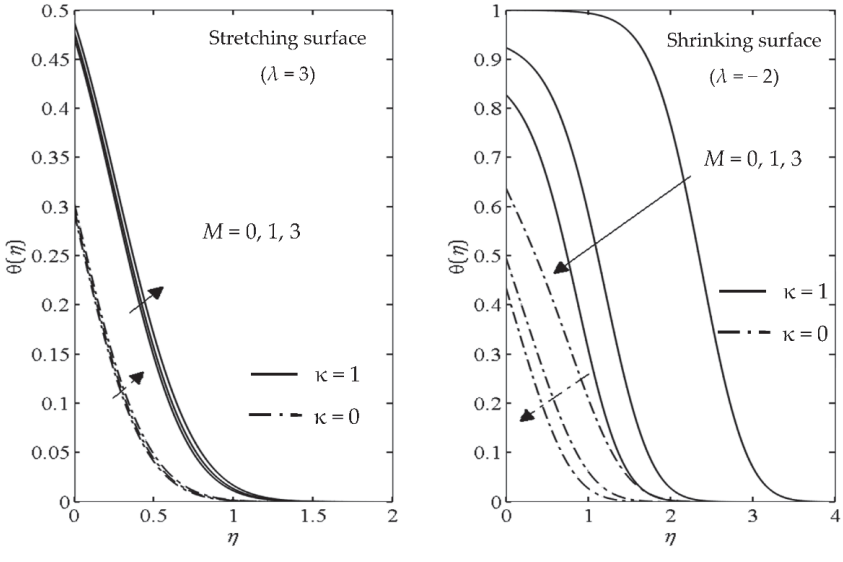

Figure 7. Effect of the magnetic interaction parameter, M, on the temperature profiles for different parameters κ and λ.

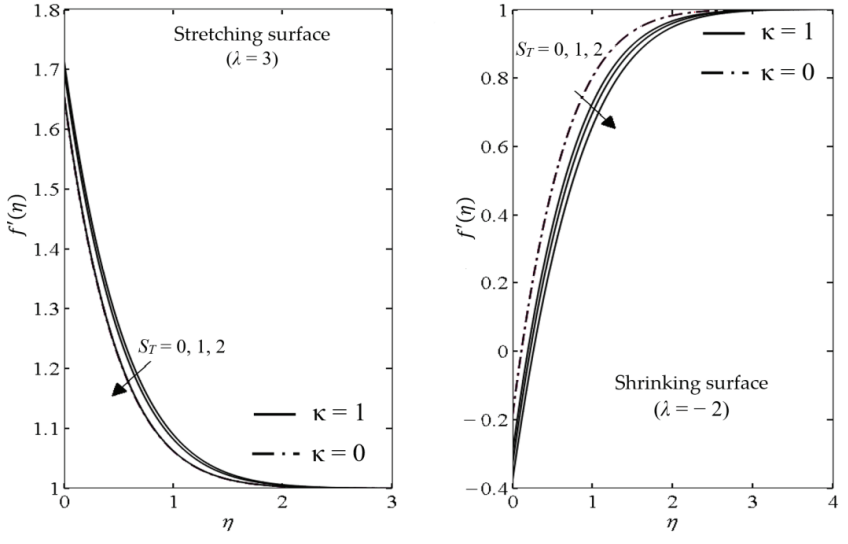

Figure 8. Influence of the Soret effect parameter, S_T, on the velocity profiles for different parameters κ and λ.

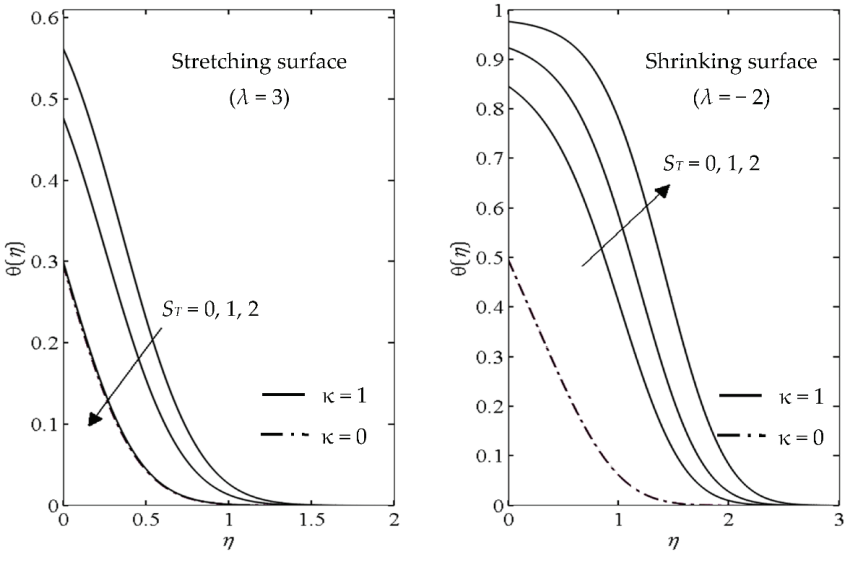

Figure 9. Influence of the Soret effect parameter, S_T, on the temperature profiles for different parameters κ and λ.

The flow with ultrafine particles is expected to experience a slip at the surfaces. Hence, the slip parameter was included, and the flow model is observed with the Stefan blowing effect. The impact of the velocity slip, δ, on the velocity profiles for different Stefan blowing intensities past the stretching/shrinking surfaces is depicted in Figure 10. For both surfaces, the velocity slip reduces the velocity distributions of the magnetite ferrofluid regardless of the Stefan blowing. Meanwhile, Figure 11 shows the effect of the thermal slip, δ_T, on the temperature profiles for the stretching and shrinking surfaces. Thermal slip has the effect of reducing the temperature distribution for both surfaces. The figure also shows that the temperature profiles are higher when the Stefan blowing is present. Lastly, we plotted the effects of the velocity ratio parameter, A, on the velocity and the temperature profiles as presented in Figures 12 and 13, respectively. The velocity ratio parameter is the ratio of the strength of the stagnation rates with the stretching/shrinking rates. In all the results above, we used $A = 1$, which means the strength of the stagnation flow and the stretching/shrinking flow are equal. As the parameter A increases, the strength of the stagnation flow probably exceeds the velocity of the stretching/shrinking flow and increases the acceleration of the external stream. Hence, we can see in Figure 12 that the velocity profiles will also increase for both surfaces. However, the thickness of the boundary layer reduces with parameter A, and a further reduction is noticed when the Stefan blowing is present for the stretching surface. Additionally, the thinning of the boundary layer thickness, as A increases, can be prevented when the Stefan blowing arises for the shrinking sheet. Furthermore, the parameter A reduces the temperature profiles, as shown in Figure 13. When the external stream of the stagnation velocity surpasses the stretching/shrinking velocity, the ferrofluid flow accelerates and produces a stronger thermal convection. This results in the increment of the heat transfer and reduces the temperature distribution.

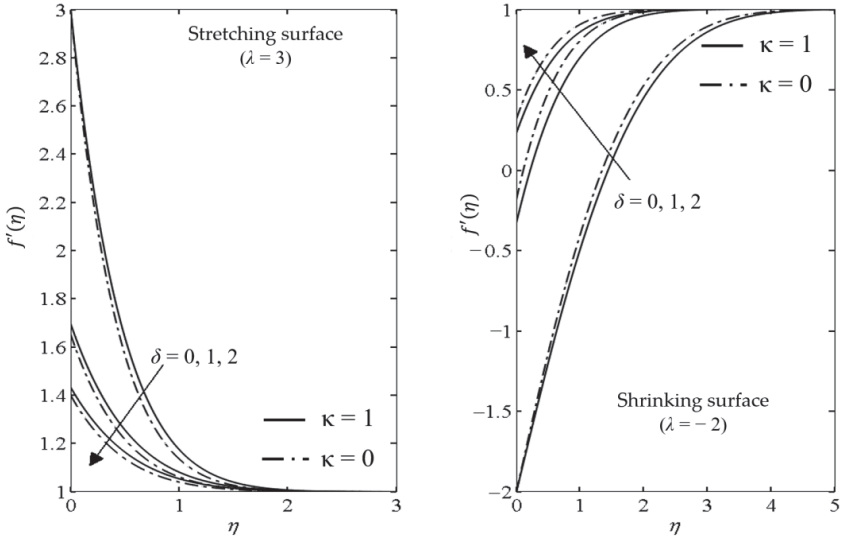

Figure 10. Effect of the velocity slip parameter, δ, on the velocity profiles for different parameters κ and λ.

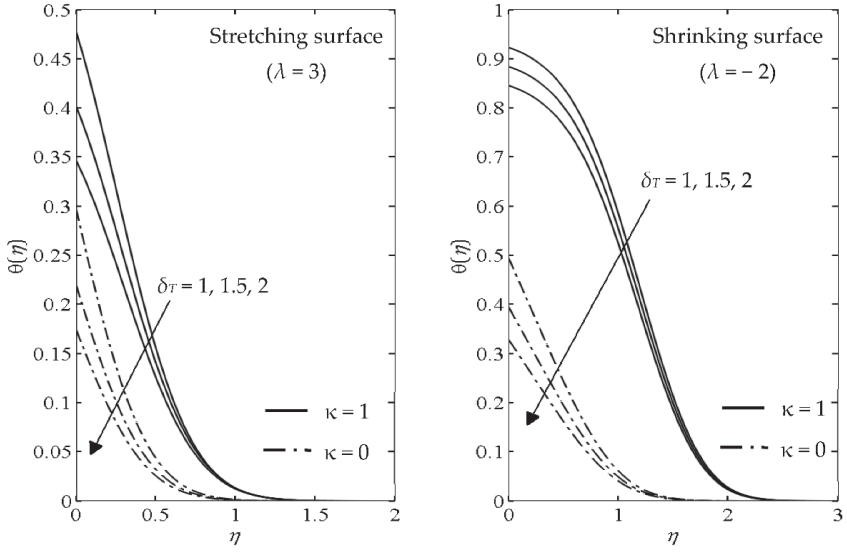

Figure 11. Effect of the thermal slip parameter, δ_T, on the temperature profiles for different parameters κ and λ.

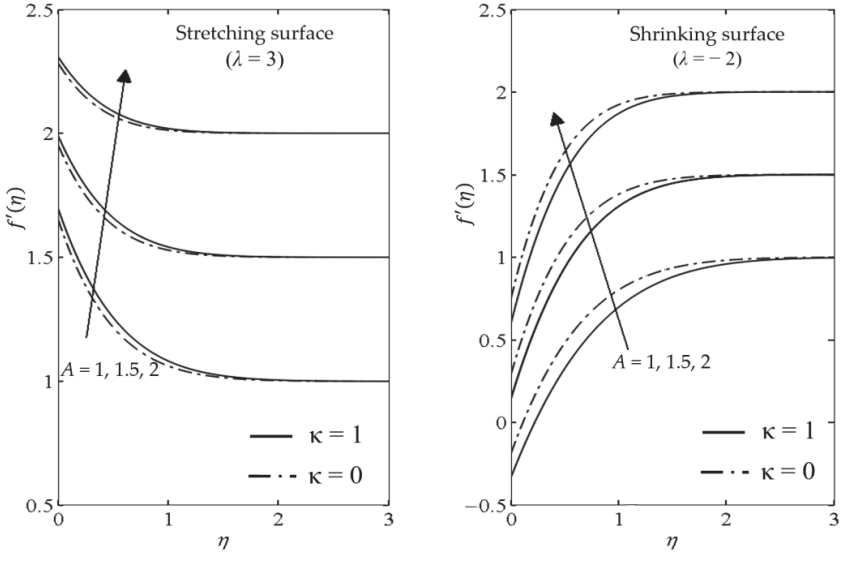

Figure 12. Effect of the velocity ratio parameter, A, on the velocity profiles for different parameters κ and λ.

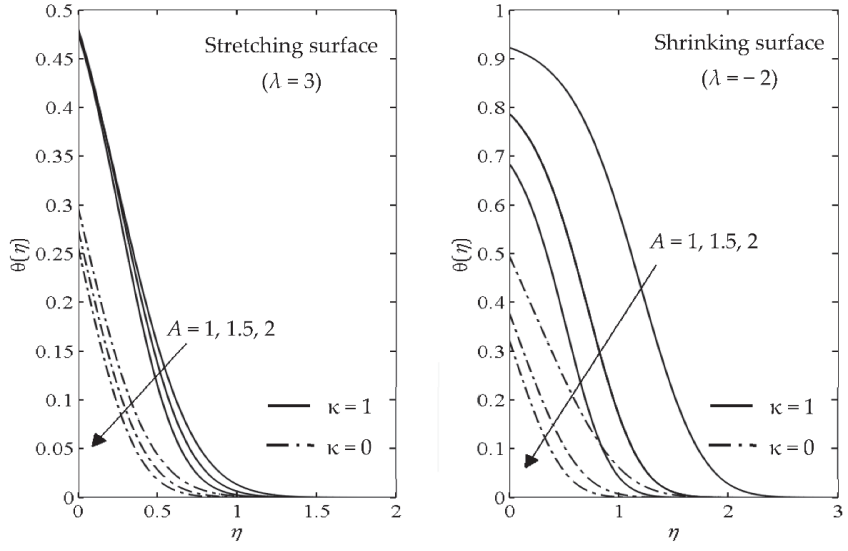

Figure 13. Effect of the velocity ratio parameter, A, on the temperature profiles for different parameters κ and λ.

5. Conclusions

The present theoretical work was devoted to examining upshots of the magnetic field, thermodiffusion, and slip on the magnetite ferrofluid flow when Stefan blowing is present. Overall, even though the increment in the magnetic field intensity in the flow regime increased the values of $C_f \mathrm{Re}_x^{1/2}$ past the moving surface, it deferred the boundary layer separation in the ferrofluid. In contrast, the Stefan blowing effect expedited the boundary layer separation when its intensity was increased. Next, the present work found that the heat transfer rate augmented if and only if the presence of the Stefan blowing was true, and vice versa. The Soret number lowered the velocity and temperature distribution past the stretching sheet, and vice versa, for the shrinking state case. Further, the increment effect of the velocity slip lowered the velocity distributions of the magnetite ferrofluid irrespective of the Stefan blowing influence. The increment effect of the thermal slip decreased the temperature distribution, while the Stefan blowing promotes the temperature distribution in the flow regime. The increment impact of the velocity ratio parameter, A, heightened the velocity profiles, but lowered the temperature profiles past the moving surface. Additionally, the effects of the thermodiffusion and the slip were more noticeable if Stefan blowing existed at the surface. Finally, the second solution was found in this problem, and through a stability analysis, the solutions were confirmed to be unstable.

Author Contributions: Conceptualization, R.A.H. and I.P.; methodology, R.A.H.; software, R.A.H.; validation, I.P., R.N. and K.N.; formal analysis, R.A.H., K.N., R.N. and I.P.; investigation, R.A.H. and R.N.; writing—original draft preparation, R.A.H. and K.N.; writing—review and editing, K.N., R.N. and I.P.; visualisation, I.P.; supervision, R.N.; project administration, K.N.; funding acquisition, R.N. All authors have read and agreed to the published version of the manuscript.

Funding: This research was funded by the Universiti Kebangsaan Malaysia research grant (GUP-2019-034) and the Malaysia Ministry of Education, grant number FRGS/1/2020/STG06/UNIMAP/02/4.

Institutional Review Board Statement: Not applicable.

Informed Consent Statement: Not applicable.

Data Availability Statement: Not applicable.

Conflicts of Interest: The authors declare no conflict of interest. The funders had no role in the design of the study; in the collection, analyses, or interpretation of data; in the writing of the manuscript, or in the decision to publish the results.

References

1. Toledo, R.T. *Fundamentals of Food Process Engineering*; Springer: New York, NY, USA, 2007; pp. 413–429.
2. Ghosh, A.K. *Fundamentals of Paper Drying-Theory and Application from Industrial Perspective*; IntechOpen: Vienna, Austria, 2011; pp. 535–582.
3. Fang, T.; Jing, W. Flow, heat, and species transfer over a stretching plate considering coupled Stefan blowing effects from species transfer. *Commun. Nonlinear Sci. Numer. Simul.* **2014**, *19*, 3086–3097. [CrossRef]
4. Fang, T. Flow and mass transfer for an unsteady stagnation-point flow over a moving wall considering blowing effects. *J. Fluids Eng.* **2014**, *136*, 71103. [CrossRef]
5. Uddin, M.J.; Kabir, M.N.; Alginahi, Y.; Bég, O.A. Numerical solution of bio-nano-convection transport from a horizontal plate with blowing and multiple slip effects. *Proc. Inst. Mech. Eng. Part C J. Mech. Eng. Sci.* **2019**, *233*, 6910–6927. [CrossRef]
6. Zohra, F.T.; Uddin, M.J.; Basir, M.F.; Ismail, A.I.M. Magnetohydrodynamic bio-nano-convective slip flow with Stefan blowing effects over a rotating disc. *Proc. Inst. Mech. Eng. Part N J. Nanomater. Nanoeng. Nanosyst.* **2020**, *234*, 83–97.
7. Zohra, F.T.; Uddin, M.J.; Ismail, A.I.M.; Bég, O.A.; Kadir, A. Anisotropic slip magneto-bioconvection flow from a rotating cone to a nanofluid with Stefan blowing effects. *Chin. J. Phys.* **2018**, *56*, 432–448. [CrossRef]
8. Ryskin, A.; Pleiner, H. Influence of a magnetic field on the Soret-effect-dominated thermal convection in ferrofluids. *Phys. Rev. E* **2004**, *69*, 46301. [CrossRef]
9. Ramreddy, C.; Murthu, P.V.S.N.; Chamkha, A.J.; Rashad, A.M. Soret effect on mixed convection flow in a nanofluid under convective boundary condition. *Int. J. Heat Mass Transf.* **2013**, *64*, 384–392. [CrossRef]
10. Pal, D.; Mandal, G.; Vajravalu, K. Soret and Dufour effects on MHD convective-radiative heat and mass transfer of nanofluids over a vertical non-linear stretching/shrinking sheet. *Appl. Math. Comput.* **2016**, *287-288*, 184–200. [CrossRef]
11. Arif, U.; Nawaz, M.; Selmi, A.L. Numerical study of simultaneous transport of heat and mass transfer in Maxwell hybrid nanofluid in the presence of Soret and Dufour effects. *Phys. Scr.* **2022**, *97*, 025207. [CrossRef]
12. Uddin, M.J.; Kabir, M.N.; Bég, O.A. Computational investigation of Stefan blowing and multiple-slip effects on buoyancy-driven bioconvection nanofluid flow with microorganisms. *Int. J. Heat Mass Transf.* **2016**, *95*, 116–130. [CrossRef]
13. Singh, G.; Chamkha, A.J. Dual solutions for second-order slip flow and heat transfer on a vertical permeable shrinking sheet. *Ain Shams Eng. J.* **2013**, *4*, 911–917. [CrossRef]
14. Mahapatra, T.R.; Nandy, S.K. Slip effects on unsteady stagnation-point flow and heat transfer over a shrinking sheet. *Meccanica* **2013**, *48*, 1599–1606. [CrossRef]
15. Aman, F.; Ishak, A.; Pop, I. Magnetohydrodynamic stagnation-point flow towards a stretching/shrinking sheet with slip effects. *Int. Commun. Heat Mass Transf.* **2013**, *47*, 68–72. [CrossRef]
16. Merkin, J.H.; Lok, Y.Y.; Pop, I. A note on the stagnation-point flow over a permeable shrinking sheet with slip effects. *Int. Commun. Heat Mass Transf.* **2016**, *71*, 101–107. [CrossRef]
17. Wang, C.Y. Stagnation flow towards a shrinking sheet. *Int. J. Non. Linear. Mech.* **2008**, *43*, 377–382. [CrossRef]
18. Song, Y.Q.; Obideyi, B.D.; Shah, N.A.; Animasaun, I.L.; Mahrous, Y.M.; Chung, J.D. Significance of haphazard motion and thermal migration of alumina and copper nanoparticles across the dynamics of water and ethylene glycol on a convectively heated surface. *Case Stud. Therm. Eng.* **2021**, *26*, 101050. [CrossRef]
19. Liu, H.; Animasaun, I.L.; Shah, N.A.; Koriko, O.K.; Mahanthesh, B. Further discussion on the significance of quartic autocatalysis on the dynamics of water conveying 47 nm alumina and 29 nm cupric nanoparticles. *Arab J. Sci. Eng.* **2020**, *45*, 5977–6004. [CrossRef]
20. Elnaqeeb, T.; Animasaun, I.L.; Shah, N.A. Ternary-hybrid nanofluids: Significance of suction and dual-stretching on three-dimensional flow of water conveying nanoparticles with various shapes and densities. *Z. Naturforsch. A* **2021**, *76*, 231–243. [CrossRef]
21. Animasaun, I.L.; Shah, N.A.; Wakif, A.; Mahanthesh, B.; Sivaraj, R.; Koriko, O.K. *Ratio of Momentum Diffusivity to Thermal Diffusivity: Introduction, Meta-Analysis, and Scrutinization*, 1st ed.; Chapman and Hall: London, UK; CRC: London, UK, 2022.
22. Scherer, C.; Neto, A.M.F. Ferrofluids: Properties and applications. *Brazillian J. Phys.* **2005**, *35*, 718–727. [CrossRef]
23. Shokrollahi, H. Structure, synthetic methods, magnetic properties and biomedical applications of ferrofluids. *Mater. Sci. Eng. C* **2013**, *33*, 2476–2487. [CrossRef]
24. Ryskin, A.; Müller, H.W.; Pleiner, H. Thermodiffusion effects in convection of ferrofluids. *Magnetohydrodynamics* **2003**, *39*, 51–55.
25. Hayat, T.; Qayyum, S.; Imtiaz, M.; Alzahrani, F.; Alsaedi, A. Partial slip effect in flow of magnetite-Fe_3O_4 nanoparticles between rotating stretchable disks. *J. Magn. Magn. Mater.* **2016**, *413*, 39–48. [CrossRef]
26. Imtiaz, M.; Hayat, T.; Alsaedi, A. Convective flow of ferrofluid due to a curved stretching surface with homogeneous-heterogeneous reactions. *Powder Technol.* **2017**, *310*, 154–162. [CrossRef]

27. Rashad, A.M. Impact of thermal radiation on MHD slip flow of a ferrofluid over a non-isothermal wedge. *J. Magn. Magn. Mater.* **2017**, *422*, 25–31. [CrossRef]
28. Abbas, Z.; Sheikh, M. Numerical study of homogeneous-heterogeneous reactions on stagnation point flow of ferrofluid with non-linear slip condition. *Chin. J. Chem. Eng.* **2017**, *25*, 11–17. [CrossRef]
29. Hamid, R.A.; Nazar, R.; Naganthran, K.; Pop, I. Dusty ferrofluid transport phenomena towards a non-isothermal moving surface with viscous dissipation. *Chin. J. Phys.* **2022**, *75*, 139–151. [CrossRef]
30. Khan, Z.H.; Khan, W.A.; Qasim, M.; Shah, I.A. MHD stagnation point ferrofluid flow and heat transfer toward a stretching sheet. *IEEE Trans. Nanotechnol.* **2014**, *13*, 35–40. [CrossRef]
31. Rosca, N.S.; Rosca, A.V.; Merkin, J.H.; Pop, I. Mixed convection flow, heat transfer, species concentration near the stagnation point on a vertical plate with Stefan coupled blowing. *Int. J. Numer. Methods Heat Fluid Flow* **2017**, *27*, 77–103. [CrossRef]
32. Rashad, A.M. Impact of anisotropic slip on transient three dimensional MHD flow of ferrofluid over an inclined radiate stretching surface. *J. Egypt. Math. Soc.* **2017**, *25*, 230–237. [CrossRef]
33. Zainal, N.A.; Nazar, R.; Naganthran, K.; Pop, I. Stability analysis of unsteady MHD rear stagnation point flow of hybrid nanofluid. *Mathematics* **2021**, *9*, 2428. [CrossRef]
34. Merkin, J.H. Mixed convection boundary layer flow on a vertical surface in a saturated porous medium. *J. Eng. Math.* **1980**, *14*, 301–313. [CrossRef]
35. Sheikholeslami, M.; Ganji, D.D. Nanofluid convective heat transfer using semi analytical and numerical approaches: A review. *J. Taiwan Inst. Chem. Eng.* **2016**, *65*, 43–77. [CrossRef]
36. Mahapatra, T.R.; Gupta, A.S. Heat transfer in stagnation-point flow towards a stretching sheet. *Heat Mass Transf.* **2002**, *38*, 517–521. [CrossRef]
37. Khan, U.; Waini, I.; Zaib, A.; Ishak, A.; Pop, I. MHD mixed convection hybrid nanofluids flow over a permeable moving inclined flat plate in the presence of thermophoretic and radiative heat flux effects. *Mathematics* **2022**, *10*, 1164. [CrossRef]

MDPI
St. Alban-Anlage 66
4052 Basel
Switzerland
Tel. +41 61 683 77 34
Fax +41 61 302 89 18
www.mdpi.com

Mathematics Editorial Office
E-mail: mathematics@mdpi.com
www.mdpi.com/journal/mathematics

MDPI
St. Alban-Anlage 66
4052 Basel
Switzerland

Tel: +41 61 683 77 34

www.mdpi.com

ISBN 978-3-0365-5940-7